

Universität der Bundeswehr München
Fakultät für Luft- und Raumfahrttechnik
Institut für Thermodynamik

**Real-Gas Effects and Single-Phase Instabilities
during Injection, Mixing and Combustion
under High-Pressure Conditions**

Christoph Dominik Traxinger, M.Sc.

Vollständiger Abdruck der von der
Fakultät für Luft- und Raumfahrttechnik
der Universität der Bundeswehr München
zur Erlangung des akademischen Grades eines

Doktor-Ingenieurs (Dr.-Ing.)

genehmigten Dissertation

Gutachter:

1. Prof. Dr. rer. nat. Michael Pfitzner
2. Prof. Dr.-Ing. habil. Bernhard Weigand

Die Dissertation wurde am 02.12.2020 bei der Universität der Bundeswehr München eingereicht und durch die Fakultät für Luft- und Raumfahrttechnik am 19.05.2021 angenommen. Die mündliche Prüfung fand am 11.06.2021 statt.

Preface

Die vorliegende Arbeit entstand während meiner Zeit als wissenschaftlicher Mitarbeiter am Institut für Thermodynamik der Universität der Bundeswehr München.

Mein erster Dank geht an meinen Doktorvater Prof. Dr. rer. nat. Michael Pfitzner, der es mir ermöglicht hat, mich in die Welt der Realgasthermodynamik, des Mehrkomponentenphasenzerfalls und der kompressiblen Strömungen zu stürzen und mein dabei gesammeltes Wissen in vielen unterschiedlichen Projekten einzubringen. Ihr stets offenes Ohr und viele interessante Diskussionen haben wesentlich dazu beigetragen, diese Arbeit erfolgreich abzuschließen. Des Weiteren bedanken ich mich ganz herzlich bei Prof. Dr.-Ing. habil. Bernhard Weigand für die Übernahme des Koreferats und bei Prof. Dr.-Ing. habil. Markus Klein für die Übernahme des Prüfungsvorsitzes. Ein weiterer Dank geht an Steffen Baab und Grazia Lamanna vom ITLR (Universität Stuttgart) für die enge und erfolgreiche Zusammenarbeit über die vergangenen Jahre und an Jan Matheis.

Der nächste Dank geht an das gesamte Thermodynamikinstitut. Ich habe die Arbeitsatmosphäre und die regen Diskussionen immer sehr genossen. Auch die gemeinsamen Unternehmungen (Skifahren, Wandern, Schlauchbootfahren, Kaffeefahrt nach Bremen usw.) haben die vergangenen fünf Jahre zu etwas unvergesslichem gemacht. Dies gilt insbesondere für Jannis Bonin, Arne Lampmann, Marco Vietze, Jens Trümner, Fabian Teschner, Axel Buck und Marvin Clifford Feike.

Aus fachlicher und freundschaftlicher Sicht möchte ich mich bei vier Personen ganz besonders bedanken, ohne die diese Arbeit so nicht möglich gewesen wäre. Anfangen will ich bei Hagen Müller. Vielen Dank für die tolle Einarbeitung und deine Offenheit. Deine Realgas-Schultern waren eine enorme Basis und der zentrale Ausgangspunkt für diese Arbeit. Auch unser gemeinsamer Besuch bei Martin Frank – du weißt jetzt was ein *Schoas* ist – im Vereinsheim bleibt unvergessen für mich. Mein Dank geht des Weiteren an Matthias Banholzer. Du hast für mich die Türe zu Hochgeschwindigkeitsströmungen aufgestoßen und damit für mich das Anwendungsfeld für thermodynamische Untersuchungen enorm erweitert. Unsere gemeinsamen Fußball- und Grillabende waren ein toller Ausgleich zum Unialltag. Als nächstes komme ich zu Julian Zips. Vielen, vielen Dank für alles. Es war eine überragende Zeit mit dir, die ich mir so nicht erträumen hätte können. Du warst mein Tor zur Verbrennung, bist mit mir in jede Schlacht gezogen und auch wieder heil und erfolgreich daraus hervorgegangen. Unsere Zeit im SFB, Konferenzreisen, Kochabende, Bierverköstigungen und vieles mehr werden in ewiger Erinnerung bleiben. Abschließend möchte ich mich noch bei Sebastian Ketterl bedanken. Trotz deiner Mitgliedschaft im Club der konstanten Dichte hattest du immer ein offenes Ohr für mich und hast auch nicht vor dem Korrekturlesen meiner Arbeit zurückgeschreckt. Unserem ersten Craftbier-Festival in Regensburg sind noch viele weitere Biere und Abende gefolgt. Vielen Dank für die gemeinsame tolle Zeit.

Mein herzlichster Dank geht an meine Familie. Danke Mama und Papa, dass ihr mir diesen Weg ermöglicht und mich stets unterstützt habt. Ohne eure Hilfe und euren Rückhalt wäre dieses Vorhaben nicht möglich gewesen. Dies gilt auch für meine drei Geschwister und die Familie Niedermeier. Ihr alle zusammen habt mir zu jeder Zeit beigestanden, ob ich nun Hilfe benötigte, ein offenes Ohr zum Auskotzen brauchte oder einfach nur mein Schneckenhaus, um an meiner Arbeit zu werkeln. Liebe Christina, dir danke ich hiermit noch einmal ausdrücklich fürs Korrekturlesen dieser Arbeit. Abschließend geht mein ganz besonderer Dank an meine Frau Sabrina. Mehr als 14 Jahre hast du mich bis zu diesem Punkt begleitet und ich hoffe es folgen noch viele weitere Jahre. Du bist mit mir durch Freud und Leid gegangen und warst stets mein größter Rückhalt. Damit ich diesen Weg gehen konnte, mustest du viele Entbehrungen hinnehmen und akzeptieren, dass ich lieber Paper am Strand las und abends auf der Terrasse programmierte. Vielen lieben Dank. Ohne dich wäre dieser Weg so nicht zu bewerkstelligen gewesen.

Abstract

Injection, mixing and combustion under high-pressure conditions are key processes in modern energy conversion machines. Driven by the demand for higher efficiency and reduction of pollutants, intensive investments are made in recent years in the further development of especially two types of fuel-fired engines: liquid-propellant rocket engines (LREs) and gas engines (GEs). This arises from the fact, that LREs will remain an essential component for payload launchers in the foreseeable future and that GEs fired with hydrogen or natural gas are a possible solution to gradually diversify towards cleaner energy conversion machines. Computational fluid dynamics (CFD) can contribute to a better understanding of the injection, mixing and combustion processes within these types of engines. Here, especially one thermodynamic topic is of paramount interest within recent years: phase separation processes under initially supercritical conditions. This work presents a CFD tool that enables the thorough investigation of these processes. Both a pressure- and a density-based solver framework are introduced. The first comprises different formulations of the pressure equation to cover a wide range of Mach numbers. A double-flux scheme specifically tailored for real-gas flows is the core of the density-based solver. The thermodynamic framework relies on a rigorous and fully conservative description of the thermodynamic state. Cubic equations of state and the departure function concept form the basis of the thermal and caloric closure. Consequently, real-gas effects are included inherently. Multicomponent phase separation processes are considered by means of a minimization of the Gibbs energy. For the investigation of the non-premixed combustion process, a tabulated combustion model based on the flamelet concept is employed. Overall, measurement data from five different experimental test campaigns are used to validate the numerical framework. Both Large-Eddy Simulations and Reynolds-Averaged Navier-Stokes simulations are performed. Most of the simulations are conducted with the pressure-based framework. In the first step, real-gas effects in underexpanded jets are investigated. Very good agreement with experimental speed of sound measurements is found. Further investigations demonstrate the importance of the consideration of real-gas effects to correctly capture the jet mixing process. Next, the phase separation process in an underexpanded argon jet is studied. In the fully developed jet, the single-phase instabilities are found downstream of the nozzle exit and upstream of the Mach disk. This is in excellent agreement with experimental Mie scattering measurements. Next, the possibility of phase separation under GE-like operating conditions is investigated. Two different fuels – hydrogen- and methane-based – are considered. For the latter, pronounced phase separation processes are found which are triggered by a strong expansion and a mixing with the ambient gas. No two-phase effects occur in the hydrogen-based fuel as the critical temperature of the less volatile component is dramatically lower as in the methane-based fuel. For the investigation of phase separation processes under LRE-like operating conditions a combined experimental and numerical study together with the University of Stuttgart is conducted. Three different test cases are defined. The characteristics of the phase formation process agree well between experiments and simulations. The single-phase instability is caused solely by a mixing process of the injected fuel with the ambient gas. Next, the prediction capabilities of the pressure- and the density-based solver are assessed in detail. For the pressure-based approach a very good agreement with three experimental test cases is found. The density-based method, in contrast, yields possibly nonphysical states indicated by a strong entrainment into the two-phase region. Finally, phase separation effects in a hydrogen and a methane flame under LRE-typical operating conditions are studied. Single-phase instabilities are found on both sides of the flamelet caused by the low temperatures and the presence of water. For the methane flame, a Large-Eddy Simulation for a reference experiment is conducted. The results show that the region of phase separation is mostly restricted to the oxygen core. The OH* emission images indicate that both flame length and shape are in good agreement with the experimental results.

Kurzfassung

Einspritzung, Mischung und Verbrennung unter Hochdruckbedingungen sind Schlüsselprozesse in modernen Energieumwandlungsmaschinen. Getrieben durch den Bedarf nach höherer Effizienz und Schadstoffreduzierung wird in den letzten Jahren die Weiterentwicklung von zwei Typen von Verbrennungsmaschinen stark vorangetrieben: Flüssigkeitsraketentreibwerke (LREs) und Gasmotoren (GEs). Dies resultiert aus der Tatsache, dass LREs in absehbarer Zukunft eine wesentliche Komponente für Nutzlastträgerraketen bleiben werden und dass mit Wasserstoff oder Erdgas befeuerte GEs eine mögliche Lösung für eine allmähliche Diversifizierung hin zu saubereren Energieumwandlungsmaschinen darstellen. Die numerische Strömungsmechanik (CFD) kann zu einem besseren Verständnis der Einspritz-, Mischungs- und Verbrennungsvorgänge innerhalb dieser Verbrennungsmaschinen beitragen. Dabei ist in den vergangenen Jahren vor allem ein Thema von besonderem Interesse: Phasenzerfallsprozesse unter ursprünglich überkritischen Bedingungen. Die vorliegende Arbeit liefert ein CFD-Werkzeug, das die genaue Untersuchung dieser Vorgänge ermöglicht. Es werden sowohl ein druck- als auch ein dichtebasierter Strömungslöser vorgestellt. Ersterer umfasst verschiedene Formulierungen der Druckgleichung, um einen weiten Bereich von Machzahlen abzudecken. Der dichte basierte Löser baut auf einem Double-Flux Schema auf, das speziell auf Realgasströmungen zugeschnitten ist. Die thermodynamische Schließung stützt sich auf eine vollständig konservative Beschreibung des thermodynamischen Zustands. Kubische Zustandsgleichungen und der Departure Function Ansatz werden für die thermische und kalorische Schließung verwendet. Realgaseffekte sind folglich inhärent enthalten. Phasenzerfallsvorgänge in Gemischen werden mittels einer Minimierung der Gibbs-Energie berücksichtigt. Für die Untersuchung nicht-vorgemischter Verbrennungsprozesse wird ein tabelliertes Verbrennungsmodell auf der Basis des Flamelet-Konzepts angewandt. Insgesamt werden Messdaten aus fünf verschiedenen experimentellen Testkampagnen zur Validierung des CFD-Werkzeugs herangezogen. Es werden sowohl Grobstruktursimulationen als auch Reynolds-gemittelte Navier-Stokes Simulationen durchgeführt. Für den Großteil der Simulationen wird ein druckbasierter Strömungslöser eingesetzt. Im ersten Schritt werden Realgaseffekte in unterexpandierten Jets untersucht. Die Simulationsergebnisse stimmen sehr gut mit den experimentellen Schallgeschwindigkeitsmessungen überein. Weiterführende Untersuchungen zeigen, wie wichtig die Berücksichtigung von Realgaseffekten für die korrekte Wiedergabe des Mischungsprozesses ist. Als nächstes wird der Phasenzerfallsprozess in einem unterexpandierten Argon-Jet analysiert. Im voll entwickelten Strahl tritt der Phasenzerfall stromabwärts des Düsenaustritts und stromaufwärts der Mach-Scheibe auf. Dies ist in hervorragender Übereinstimmung mit experimentellen Mie-Streuungsmessungen. Darauf aufbauend wird die Möglichkeit des Phasenzerfalls bei GE-ähnlichen Betriebsbedingungen untersucht. Zwei verschiedene Brennstoffe – auf Wasserstoff- und Methanbasis – werden berücksichtigt. Bei letzterem treten ausgeprägte Phasenzerfallseffekte auf, die durch eine starke Expansion und eine Vermischung mit dem Kammergas ausgelöst werden. Beim wasserstoffbasierten Brennstoff kommt es zu keinen Zweiphaseneffekten, da die kritische Temperatur der weniger flüchtigen Komponente sehr niedrig ist. Zur Untersuchung von Phasenzerfallsprozessen unter LRE-ähnlichen Betriebsbedingungen wird eine kombinierte experimentelle und numerische Studie zusammen mit der Universität Stuttgart durchgeführt. Es werden drei verschiedene Testfälle definiert. Die Charakteristika des Phasenzerfallsprozesses zeigen eine gute Übereinstimmung zwischen Experimenten und Simulationen. Der Phasenzerfall wird ausschließlich durch einen Vermischungsprozess des Brennstoffs mit dem Umgebungsgas verursacht. Als nächstes werden die Vorhersagefähigkeiten des druck- und des dichte basierten Lösers genauer bewertet und gegenübergestellt. Für den druckbasierten Ansatz wird eine sehr gute Übereinstimmung mit drei experimentellen Testfällen gefunden. Die dichte basierte Methode liefert hingegen möglicherweise nichtphysikalische Zustände, die durch ein starkes Ein dringen in das Zweiphasengebiet ersichtlich werden. Abschließend werden Phasenzerfallseffekte in einer Wasserstoff- und einer Methanflamme unter LRE-typischen Betriebsbedingungen untersucht. Zweiphasige Zustände treten auf beiden Seiten der Flamme auf und werden durch die niedrigen Temperaturen und die Anwesenheit von Wasser verursacht. Für die Methanflamme wird eine Grob struktursimulation zu einem Referenzexperiment durchgeführt. Die Ergebnisse veranschaulichen, dass der Bereich des Phasenzerfalls fast ausschließlich auf den Sauerstoffkern beschränkt ist. Die OH*-Emissionsbilder zeigen, dass sowohl die Flammenlänge als auch die Flammenform in guter Übereinstimmung mit den experimentellen Ergebnissen sind.

Contents

Contents	ix
List of figures	xiii
List of tables	xix
Nomenclature	xxi
I Fundamentals	1
1 Introduction	2
1.1 High-pressure injection, mixing and combustion	2
1.2 Injection and mixing under rocket-relevant conditions	4
1.3 High-pressure combustion under rocket-relevant conditions	9
1.4 Injection and mixing under gas engine relevant conditions	11
1.5 Objectives and outline	12
2 Governing equations	15
2.1 Conservation equations	15
2.2 Turbulence modeling	19
2.3 Large-Eddy Simulation	20
2.3.1 Filtered equations	21
2.3.2 Sub-grid scale models	22
2.4 Reynolds-Averaged Navier-Stokes simulation	24
2.4.1 Filtered equations	24
2.4.2 Turbulence model	25
II Numerics and modeling	27
3 Numerical methods	28
3.1 Finite volume method	28
3.1.1 Discretization of the solution domain	28
3.1.2 Spatial discretization	29
3.1.3 Temporal discretization	32
3.2 Numerical solution algorithms	34
3.3 Pressure-based solver framework	35
3.3.1 Formulation for subsonic flows	35
3.3.2 Extension for subsonic real-gas flows	36
3.3.3 Solution procedure	36
3.3.4 General extension for high-speed flows	38
3.3.5 Hybrid pressure-based approach for high-speed flows	39
3.4 Density-based solver framework	41
3.4.1 Spurious pressure oscillations	41
3.4.2 Double-flux method	43
4 Thermodynamics modeling	47
4.1 Fundamental properties and equations	47
4.2 Maxwell relations	52
4.3 Thermodynamic equilibrium	52

4.4	Departure function concept	54
4.5	Partial molar and specific properties	56
4.6	Ideal-gas model	57
4.6.1	Thermal and caloric equation of state	57
4.6.2	Transport properties	58
4.7	Real-gas model	59
4.7.1	Cubic equations of state	60
4.7.2	Multicomponent mixtures	63
4.7.3	Caloric and derived properties	65
4.7.4	Transport properties	69
4.8	Phase separation modeling in multicomponent fluids	69
4.8.1	Derivation of the tangent-plane distance criterion	70
4.8.2	Fugacity and fugacity coefficient	73
4.8.3	Evaluation of the tangent-plane distance criterion	74
4.8.4	Equilibrium flash	77
4.8.5	Caloric and transport properties in multiphase fluids	80
4.8.6	Compressibility and speed of sound in multiphase fluids	80
4.8.7	Realization in OpenFOAM	84
4.9	Characteristics of multicomponent phase equilibria	84
4.9.1	Construction of the phase envelope	85
4.9.2	Stability and criticality	88
4.9.3	Homogeneous nucleation in binary mixtures	91
5	Combustion modeling	95
5.1	Real-gas flamelet model	96
5.2	Reaction kinetics	99
III	Results	101
6	Mixing under supersonic flow conditions	102
6.1	Influence of real-gas effects	102
6.1.1	Experimental setup	102
6.1.2	Numerical setup	103
6.1.3	Results	106
6.1.4	Thermodynamic analysis	109
6.1.5	Summary	116
6.2	Phase separation in pure fluids	117
6.2.1	Experimental setup	117
6.2.2	Numerical setup	117
6.2.3	Results	119
6.2.4	Summary	122
6.3	Phase separation in multicomponent fuels	123
6.3.1	Introduction	123
6.3.2	Numerical setup	123
6.3.3	Probability of phase separation	124
6.3.4	Results	127
6.3.5	Summary	133
7	Mixing under subsonic flow conditions	135
7.1	Phase separation due to multicomponent mixing	135
7.1.1	Experimental setup	135
7.1.2	Numerical setup	136
7.1.3	Results	139
7.1.4	Summary	142

7.2	Comparison of fully- and quasi-conservative solvers	142
7.2.1	Introduction	142
7.2.2	Single-phase test case	143
7.2.3	Numerical setup	143
7.2.4	Results	144
7.2.5	Summary	150
8	Single-phase instability in high-pressure combustion	151
8.1	Thermodynamic closure	151
8.2	Test cases	152
8.3	Counterflow diffusion flames	152
8.3.1	General discussion	152
8.3.2	Phase separation	153
8.4	Large-Eddy Simulation	156
8.4.1	Test case and numerical setup	156
8.4.2	General flame features	157
8.4.3	Phase separation effects	158
8.4.4	Comparison with the experiment and the single-phase closure	158
8.5	Summary	159
IV	Summary and outlook	161
9	Summary	162
10	Outlook	167
Bibliography		169
A	Numerical flux schemes	189
A.1	Short overview	189
A.2	Derivation of the central-upwind scheme	190
A.3	Flux-vector splitting approach	194
B	Thermophysical properties	199
B.1	Critical properties, acentric factor and molar weight	199
B.2	High-pressure diffusion coefficients	199
C	Departure functions for the state equation due to Soave, Redlich and Kwong	201
D	Partial derivatives of the fugacity coefficient	203
D.1	Equation of state due to Peng and Robinson	203
D.2	Equation of state due to Soave, Redlich and Kwong	205
E	Solver instabilities due to real-gas thermodynamics	207
F	Additional material: Underexpanded jets	211
F.1	Validation of the hybrid pressure-based approach	211
F.2	Determination of the choked flow conditions	212
F.3	Assessment of the axial Mach disk position	213
G	Validation of the density-based solver	215
G.1	One-dimensional advection problem	215
G.2	Real-gas shock tube problem	216
G.3	Transcritical planar jet - pure fluid	217
G.4	Transcritical planar jet - binary mixture	218

List of figures

1.1	General reduced pressure-temperature diagram showing typical injection conditions for LREs and GEs: The solid black line denotes the vapor-pressure curve of a pure fluid determined by the critical point ($p_r = T_r = 1$). The dashed line corresponds to the Widom line. The iso-lines show constant compressibility factors Z	2
1.2	Exemplary shadowgraphs of an isobaric and a high-speed jet at supercritical injection conditions. Both images have been taken from the work of Baab et al. [14, 16]. Figure a) is reprinted from Fuel, volume 233, Baab, S., Steinhausen, C., Lamanna, G., Weigand, B. and Förster, F. J., <i>A quantitative speed of sound database for multi-component jet mixing at high pressure</i> , pp. 918–925, © (2018) with permission from Elsevier. Figure b) is reprinted by permission from Springer Nature Customer Service Centre GmbH: Springer Nature, <i>Experiments in Fluids</i> , Baab et al. [14], © (2016).	3
1.3	Approximated thermodynamic trajectories under GE-like and LRE-like injection conditions together with the relevant vapor-liquid equilibrium for a pure fluid (subfigure a) and a binary mixture (subfigure b). The subscripts HV and LV denote the high and the low volatile component of the mixture, respectively. An isopleth is a line of constant overall composition.	4
1.4	Injection of liquid N ₂ (90 K) into a pressurized test chamber: a) into subcritical N ₂ at 28 bar; b) into near-critical N ₂ at 35 bar; c) into supercritical N ₂ at 69 bar; d) into a binary N ₂ /He mixture at 69 bar. The figures have been taken from Mayer et al. [189]; reprinted by permission of the American Institute of Aeronautics and Astronautics, Inc.	6
1.5	Coaxial injection of liquid N ₂ (97 K, inner tube) and gaseous He (280 K, outer annulus) into a pressurized helium atmosphere at 10 bar and 60 bar, right images. On the left, a temperature-composition diagram together with the binary VLEs at the relevant pressures, the mixture critical locus and an exemplary mixing path are shown. The VLEs and the mixture critical locus have been calculated using the cubic equation of state of Peng and Robinson [226]. The shadowgraphs have been taken from Mayer et al. [189]; reprinted by permission of the American Institute of Aeronautics and Astronautics, Inc.	7
1.6	Spurious pressure oscillations during the injection of cryogenic nitrogen (71.5 K) into its own gas phase (332.2 K) at a pressure of 50 bar. The instantaneous snapshots of the temperature (a) and the pressure field (b) have been taken from Terashima and Koshi [311]. The density data have been obtained from CoolProp [27]. The figures a) and b) are reprinted from Journal of Computational Physics, volume 231, Terashima, H. and Koshi, M., <i>Approach for Simulating Gas-Liquid-Like Flows Under Supercritical Pressures Using a High-Order Central Differencing Scheme</i> , pp. 6907–6923, © (2012) with permission from Elsevier.	9
1.7	Shadowgraphies of methane/ethylene jets injected into a chamber filled with nitrogen: a) Variation of the NPR for a methane mole fraction of 90%; b) Variation of the injection temperature for a methane mole fraction of 10%. T_c and p_c are the respective critical mixture temperature and pressure. The images have been taken from the work of Lin et al. [170].	11
2.1	Energy spectrum of isotropic turbulence for $\text{Re} = 2.15 \times 10^5$ according to Pope [238]. The dashed line shows the 80% criteria $\mathcal{K}_\Delta^{80\%}$ for the LES resolution. In addition, computed and modeled wave number ranges in DNS, LES and RANS are shown (adopted from Poinsot et al. [236]).	19
3.1	Schematic of two control volumes sharing a common internal face f . The vector directions and the nomenclature represent the standard OpenFOAM terms.	29
3.2	Definition of the grid nodes (C, D and U) used to determine r in Eq. (3.15).	31

3.3	Flowchart of the pressure-based PIMPLE algorithm in OpenFOAM.	37
3.4	Definitions of the interpolation directions in OpenFOAM.	39
3.5	Influence of the filter width on a transcritical state change of supercritical oxygen at a pressure of 150 bar and a temperature range of $150 \text{ K} \leq T \leq 300 \text{ K}$	42
3.6	Influence of the filter width on an almost ideal state change of supercritical oxygen at a pressure of 150 bar and a temperature range of $500 \text{ K} \leq T \leq 1000 \text{ K}$	42
3.7	Variation of γ^* and $1/(\gamma^* - 1)$ for supercritical oxygen.	43
3.8	Flowchart of the double-flux method.	44
3.9	Schematic representation of the Euler fluxes on the LHS and RHS side of the cell face at $j + 1/2$ together with a theoretical variation of γ^*	45
4.1	Sketch of a closed system defining the first law of thermodynamics.	48
4.2	Schematic of an isolated system consisting of two subsystems.	53
4.3	Demonstration of the nonideal fluid behavior: a) $p\psi,p$ -diagram at $T = 293.15 \text{ K}$ for four different fluids; b) Variation of the compressibility factor Z of methane with pressure and temperature. The data for both figures have been taken from CoolProp [27].	59
4.4	Coexistence region of vapor and liquid for a general pure fluid: a) Influence of the selected critical parameter set (T_c, p_c vs. T_c, v_c) in cubic EoSs (adopted from Chou and Prausnitz [49]); b) Visualization of the van der Waals isotherm ($T < T_c$).	61
4.5	Demonstration of the corresponding states principle for three different fluids. The splines have been fitted through the available data points of the respective reduced temperature. The data have been taken from CoolProp [27].	62
4.6	Comparison of the PR-EoS [226] and the SRK-EoS [296] with reference data from CoolProp [27]: a) Density ρ for different alkanes from the homologue series at $p_r = p/p_c = 1.5$ and $T_r = T/T_c = 0.75$; b) Compressibility factor Z of methane, hydrogen and n-hexane at $T = 300 \text{ K}$	64
4.7	Representation of the multiphase state in the numerical simulation.	70
4.8	Schematic of a single- and a two-phase system at the same temperature T and pressure p . The illustration has been adopted from Firoozabadi [77].	70
4.9	Schematic representation of the variation of the molar Gibbs energy of mixing of a binary mixture as function of the trial phase composition w_1	71
4.10	Schematic representation of the TPD criterion of a generic binary mixture for a single-phase state (left) and a two-phase state (right).	72
4.11	Investigation of the 14 component Prudhoe Bay mixture [231] at four different pressure levels (10 bar, 30 bar, 50 bar and 70 bar): a) Vapor-liquid equilibrium; b) Speed of sound (solid: thermodynamic calculation, dashed: Wood's correlation [354]); c) Isentropic compressibility; d) Isenthalpic compressibility; e) Isothermal compressibility; f) Grüneisen parameter.	83
4.12	Flowchart visualizing the general procedure for solving and evaluating the multi-component VLE model in OpenFOAM.	84
4.13	Schematic of the vapor-liquid equilibrium of a generic multicomponent mixture together with the shape of the Gibbs energy at a fixed temperature.	85
4.14	Schematic of a binary VLE with a type I critical locus [335].	85
4.15	Comparison of the RE and HK [117] approaches for different binary mixtures. The experimental data have been taken from the literature [38, 52, 44, 304, 72].	90
4.16	Sketch of a binary mixture with a type III critical locus.	91
4.17	Illustration of the change of the normalized nucleation rate I with the subcooling.	92
4.18	Schematic of the formation free energy as function of the number of molecules for a binary mixture. The figures have been taken from Vehkämäki [340]; reprinted by permission from Springer Nature Customer Service Centre GmbH: Springer Nature, <i>Classical Nucleation Theory in Multicomponent Systems</i> by Vehkämäki, H. © (2010).	92
5.1	Schematic of non-premixed combustion: a) Turbulent diffusion flame emanating from a co-axial injection element; b) Concept of the counterflow diffusion flame approach.	95

5.2	Schematic procedure of the real-gas flamelet model.	99
6.1	Schematic of the test chamber used at the ITLR for the experimental investigations of high-pressure mixing processes. The figure has been taken from Baab et al. [14]; reprinted by permission from Springer Nature Customer Service Centre GmbH: Springer Nature, <i>Experiments in Fluids</i> , Baab et al. [14], © (2016).	102
6.2	Comparison of the PR-EoS [226] with reference data taken from CoolProp [27]. The evaluation is conducted for n-hexane at three different pressures, namely 300, 100 and 50 bar.	103
6.3	Schematic of the computational domain together with the major dimensions.	104
6.4	Mesh convergence study along the centerline for the case NPR60-T600. The near-nozzle region up to the Mach disk is shown in subfigure a. Far-field results are plotted in subfigure b including an evaluation of the speed of sound at the measurement position $x/D = 110$	105
6.5	Numerical simulation results of the underexpanded jets at a total reservoir temperature of 630 K.	106
6.6	Comparison of the speed of sound measurements [14, 80] with the simulation results. The dashed lines are linear regressions of the experimental data at identical axial positions.	107
6.7	Comparison of the average n-hexane field for the case NPR600-T577.	108
6.8	Comparison of the speed of sound taken from the RANS simulations with data a posteriori evaluated using CoolProp [27].	108
6.9	Concentration and velocity decay along the centerline for the three NPR150 cases. The curve fit was done manually to underline the self-similarity of the jets for sufficiently large distances from the source. Only every 5th point from the simulation results is shown and data points below $x/D \approx 45$ are excluded.	109
6.10	Comparison of the centerline concentration for the investigated n-hexane jets. Experimental data have been taken from the work of Baab et al. [14] and Förster et al. [80].	110
6.11	Change of the pressure and the compressibility factor along the center axis for the test case NPR150-T577.	110
6.12	Expansion path along the chamber centerline for the case NPR150-T577. Every 5th data point of the RANS simulation result is plotted and colored with the respective compressibility factor Z	111
6.13	Comparison of ideal and real gas RANS results for the case NPR150-T577. Only every 5th point from the simulations along the chamber centerline is shown.	112
6.14	Comparison of ideal and real gas RANS results for the case NPR150-T577 in terms of the speed of sound and the temperature along the centerline of the chamber.	112
6.15	Expansion of an underexpanded jet with the corresponding total enthalpy and static enthalpy characteristics. At the nozzle exit, the Mach number equals unity and hence the velocity is equal to the local speed of sound, i.e., the flow is choked.	113
6.16	Enthalpy-pressure diagram of n-hexane. The black lines show the two-phase region, the Widom line and eight isotherms. The colored lines highlight isenthalpic and isentropic state changes originating from the respective reservoir conditions (filled circle). The choked flow conditions and the post-shock states are marked by the white-filled dashed and bold circles, respectively.	114
6.17	Sketch of the adiabatic mixture concept for advection-controlled mixing.	115
6.18	Specific enthalpy and speed of sound along the adiabatic mixture path for the case NPR150-T577.	115
6.19	Comparison of the centerline concentration for the investigated n-hexane jets. Experimental speed of sound data were taken from Baab et al. [14] and Förster et al. [80] and have been post-processed using the adiabatic mixture concept.	116
6.20	Pressure-temperature diagram of argon together with an approximated isentropic expansion path for a perfect gas ($\text{Ar}: \gamma = 1.67$) from reservoir to chamber conditions.	118

6.21 Two-phase dome of argon calculated with the PR-EoS [226] for the pure fluid and for the binary mixture of argon and nitrogen $\mathbf{z} = [0.985, 0.015]$. The reference data have been taken from CoolProp [27] for pure argon.	118
6.22 Comparison of the near-nozzle flow structure by means of single-shot images. The experimental image (left) has been taken from Xiao et al. [360] who applied Schlieren measurements for the visualization. In the numerical simulation (right), the line-of-sight integrated magnitude of the streamwise density gradient $ \partial\bar{\rho}/\partial x $ is used to show the underexpanded flow structure. Reprinted by permission from Springer Nature Customer Service Centre GmbH: Springer Nature, <i>Flow, Turbulence and Combustion</i> , Xiao et al. [360], © (2019).	119
6.23 Visualization of the flow field downstream of the Mach disk by means of the averaged velocity. The experimental image has been taken from Xiao et al. [360]. Reprinted by permission from Springer Nature Customer Service Centre GmbH: Springer Nature, <i>Flow, Turbulence and Combustion</i> , Xiao et al. [360], © (2019).	119
6.24 Comparison of the mean axial velocity at four different axial positions in the cross-stream direction. The experimental data have been taken from Xiao et al. [360].	120
6.25 Comparison of the RMS velocity at four different axial positions in the cross-stream direction. The experimental data have been taken from Xiao et al. [360].	121
6.26 Visualization of the phase separation process upstream of the Mach disk. In the left figure, a single shot image of the Mie scattering is shown which has been taken from Fond et al. [79]. The right image shows an instantaneous snapshot from the present LES where the vapor mole fraction is used to highlight regions of phase separation (gray) and regions without phase separation (black). Reprinted by permission from Springer Nature Customer Service Centre GmbH: Springer Nature, <i>Experiments in Fluids</i> , Fond et al. [79], © (2018).	121
6.27 Pressure-temperature diagram of pure argon visualizing the expansion path of the underexpanded jet. The scatter data from the LES have been taken along the centerline.	122
6.28 Three dimensional view of the square duct chamber. The instantaneous iso-contour encloses the region of phase separation downstream of the nozzle exit. The back and the bottom planes show the averaged velocity and temperature fields, respectively.	122
6.29 Schematic of the numerical domain used to study possible phase separation processes under GE-like operating conditions.	124
6.30 VLEs of the binary nitrogen/hydrogen mixture. The dots in subfigure b are representing experimental data taken from the literature [303, 361, 288].	125
6.31 VLEs of the ternary methane/ethane/nitrogen mixture at two different temperatures (200 K and 160 K) and two different pressures (40 bar and 20 bar). The CNG composition is marked with a white dot. The colored dots represent experimental data taken from the literature [317].	126
6.32 VLEs of different binary mixtures of methane, ethane and nitrogen. The dots represent experimental data taken from the literature [304, 350, 140, 44, 38, 304, 52].	127
6.33 Snapshots of the temporal evolution of the underexpanded jet for the test case CNG-p600. In the left column, the fields of the temperature and the vapor fraction are superimposed. In the right column, a superposition of the pressure and the Mach number is shown.	128
6.34 Detailed view of different flow properties for the CNG-p600 test case at 40 μ s after injection. The snapshots have been taken at the tip of the jet and the view corresponds to the red box in Fig. 6.33. The yellow and orange boxes mark the sampling areas for Fig. 6.35.	129
6.35 Ternary phase diagrams for the CNG test-case CNG-p600. The colored points mark the sampling data highlighted in Fig. 6.34 by the appropriate colored boxes.	130
6.36 Comparison of the near-nozzle flow structures between the two CNG test cases CNG-p600 (upper half) and CNG-p300 (lower half).	131
6.37 Comparison of the near-nozzle flow structures for CNG (upper half) and CHG (lower half) at a total fuel pressure of 300 bar.	132

6.38 Evolution of the normalized jet penetration depth for both 300 bar cases. The colored lines show the analytical correlations of Abraham [5], Hill and Ouellette [119] and Gerold et al. [90].	133
7.1 Sketch of the experimental facility including the optical arrangement for the simultaneous shadowgraphy and elastic light scattering measurements.	135
7.2 Comparison of the thermodynamic framework for n-hexane at a pressure of 50 bar with reference data obtained from CoolProp [27]. The thermal state equation due to Peng and Robinson [226] is used. The viscosity is calculated based on the method of Chung et al. [51].	136
7.3 VLEs of the n-hexane/nitrogen mixture. The experimental reference data have been taken from the literature [72, 239].	137
7.4 Adiabatic mixtures of n-hexane and nitrogen for three different n-hexane temperatures at a pressure of 50 bar.	137
7.5 Results of the mesh convergence study in terms of the mean density $\langle \bar{\rho} \rangle$ and the corresponding root mean square $\sqrt{\langle \rho' \rho' \rangle}$ along the centerline of the chamber.	139
7.6 Fully developed jet structure of the T600 test case. Left: Experimental shadowgraphy image; Right: Line-of-sight integrated Laplacian of the density obtained from the LES result.	139
7.7 Comparison of experimental and numerical snapshots for the test case T600. \check{I} is the noise-corrected camera intensity I_{cam} normalized by the measured excitation intensity I_0	140
7.8 Comparison of LES scatter data with the adiabatic mixture concept, see Fig. 7.4. .	141
7.9 Comparison of experimental and numerical snapshots for the test case T560. \check{I} is the noise-corrected camera intensity I_{cam} normalized by the measured excitation intensity I_0	141
7.10 Comparison of experimental and numerical snapshots for the test case T480. \check{I} is the noise-corrected camera intensity I_{cam} normalized by the measured excitation intensity I_0	142
7.11 Comparison of mixture speed of sound data for the binary n-hexane/nitrogen mixture. The reference data have been taken from NIST Refprop [164].	144
7.12 Instantaneous flow field of the fully developed jet. For the conduction of the LES, the FC pressure-based solver has been used.	145
7.13 Variation of the mean density and its fluctuation along the center axis.	145
7.14 Comparison of the measured speed of sound data with the LES results along the axial centerline and in radial direction. The experimental data have been taken from Baab et al. [16].	146
7.15 Concentration and velocity decay along the centerline. The dashed line was fitted manually to the available LES data to study the self-similarity and to approximately mark the development region.	146
7.16 Schematic of the computational domain used for the simulation of the 2D planar jet configuration. The inlet height h is 1 mm.	147
7.17 Instantaneous flow field of the planar n-hexane jet injected into a quiescent nitrogen atmosphere simulated with the QC solver. The results are shown 0.5 ms after start of injection.	147
7.18 Temperature-composition diagram showing the results of the FC and QC solver for the single-phase speed of sound test case.	148
7.19 Vapor-liquid equilibrium of the binary n-hexane/nitrogen mixture at 50 bar together with the mixture critical point and the spinodal lines marking the region of intrinsic phase separation. The dash-dotted lines are lines of constant nucleation rate according to Fig. 4.17.	148
7.20 Temperature-composition diagrams of the T600 case. In subfigure a, the results of the FC and QC solver are shown. The result of a 1D diffusion problem employing the high-pressure diffusion coefficients due to Riazi and Whitson [258] is shown in subfigure b.	149
7.21 Schematic of the 1D diffusion problem together with the initial conditions.	149

7.22	Temperature-composition diagram of the T560 case with scatter data from FC and QC 2D planar jet simulations.	150
8.1	Comparison of the SRK-EoS [296] with reference data taken from NIST Refprop [164] for three different fluids (methane CH ₄ , oxygen O ₂ and hydrogen H ₂).	151
8.2	Validation of the binary water/oxygen mixture with experimental data [127] (solid: $k_{ij} = 0$; dash-dotted: $k_{ij} = 0.3$).	152
8.3	Results of the H ₂ and CH ₄ flames at a scalar dissipation rate $\chi_{st} = 1 \text{ s}^{-1}$	153
8.4	Thermodynamic analysis of the methane flamelet: a) Detailed view of the oxidizer-rich side; b) Detailed view of the fuel-rich side.	153
8.5	Comparison of the real-gas and the two-phase solution for the methane flamelet.	154
8.6	The flamelet results of the oxidizer-rich side superimposed onto the VLE of the binary mixture of water/oxygen at the appropriate pressure.	155
8.7	Thermodynamic analysis of the hydrogen flamelet: a) Detailed view of the oxidizer-rich side; b) Detailed view of the fuel-rich side.	155
8.8	Comparison of the real-gas and the two-phase solution for the hydrogen flamelet.	156
8.9	Computational domain of the LOx/CH ₄ test case.	156
8.10	Instantaneous view of the LOx/CH ₄ flame: The white line in (a) encloses the region of $f \leq 2 \times 10^{-4}$ and in (b) it represents the stoichiometric mixture fraction $f_{st} = 0.2$. In (c) the white line is drawn for $Z = 0.99$. In (d) the β -field is superimposed onto the mixture fraction field.	157
8.11	Scattered data from five independent time steps. States with phase separation are colored by the vapor mole fraction β . Black dots indicate a single-phase mixture or pure fluids.	158
8.12	Line-of-sight integrated OH* emission in comparison with the averaged experimental OH* radiation of Singla et al. [292]; reprinted from Proceedings of the Combustion Institute, volume 30, Singla, G., Scouflaire, P., Rolon, C. and Candel, S., <i>Transcritical Oxygen/Transcritical or Supercritical Methane Combustion</i> , pp. 2921–2928, © (2005) with permission from Elsevier.	159
A.1	Sketch of the piecewise reconstruction from cell to face values in central schemes.	191
A.2	Schematic of the KNP central-upwind scheme [149]. Left: Idea of the selection of the space-time control volumes. Right: Steps to evolve the numerical solution.	191
E.1	Reduced p,v -diagram of a pure fluid together with an approximated expansion path as it can occur during the direct injection in gas engines.	208
E.2	Sketch of a vapor-liquid equilibrium of a binary mixture with a type-I critical locus according to van Konynenburg and Scott [335].	209
F.1	Initial conditions of the 1D shock tube problem. Methane (CH ₄) is considered as fuel and a pressure ratio of 15 is investigated.	211
F.2	Results of the 1D shock tube problem after 0.5 ms.	212
F.3	Comparison of the axial position of the Mach disk in dependence of the NPR. The dashed line shows the correlation proposed by Crist et al. [55] and Ashkenas and Sherman [11]. The ideal-gas closure was used for case NPR150-T577.	213
G.1	Results of the 1D advection case after one flow through period.	215
G.2	Results of the real-gas shock tube problem at $t = 0.5 \text{ ms}$ in terms of density, pressure, velocity and temperature.	216
G.3	Schematic of the computational domain for the 2D cryogenic planar jet configuration. The inlet height h is 1 mm.	217
G.4	Density, temperature, speed of sound and pressure distributions of the 2D planar nitrogen jet configuration after 0.35 ms.	217
G.5	Results of the 2D planar jet break-up of n-dodecane into a nitrogen environment. The instantaneous fields of n-dodecane mass fraction, density, temperature and pressure are shown at $t = 0.35 \text{ ms}$	218

List of tables

1.1	Overview of experimental studies focusing on high-pressure multicomponent mixing under isobaric injection conditions. The chamber pressure and temperature as well as the injection temperature are denoted by p_{ch} , T_{ch} and T_{inj} , respectively.	5
1.2	Overview of typical combustion chamber pressures in LOx/H ₂ LREs with respect to the critical point of oxygen ($p_c = 50.43$ bar, $T_c = 154.58$ K).	9
2.1	Model constants of the k,ω - and k,ϵ -model used in the k,ω -SST-model [193].	26
4.1	Extensive and related intensive thermodynamic properties of the internal energy.	49
4.2	Conditions for the equilibrium of a closed system.	54
4.3	Parameters for the general cubic equation of state, see Eq. (4.95).	63
4.4	Definitions of the different compressibilities ψ and expansivities α	80
6.1	Available experimental data collected from Baab et al. [14] and Förster et al. [80].	103
6.2	Summary of the investigated underexpanded n-hexane test cases.	104
6.3	Solver setup for the investigation of real-gas effects in underexpanded jets.	105
6.4	Results for the grid independence study for case NPR60-T600.	105
6.5	Comparison of the post-shock temperature T_{ps} according to Eq. (6.3) and the RANS simulation results. The analytical post-shock temperature has been evaluated using CoolProp [27].	113
6.6	Numerical solver setup for the investigation of phase separation processes in pure fluids.	118
6.7	Volume fractions [%] of the hydrogen- and methane-based generic fuels CHG and CNG.	123
6.8	Overview of the boundary conditions for the three GE-like test cases.	124
6.9	Numerical solver setup for the investigation of phase separation processes in multi-component fuels under GE-like operating conditions.	125
6.10	Choked nozzle flow properties for the CNG and CHG test cases.	132
7.1	Operating conditions of the three different test cases for the investigation of multi-component phase separation under high-pressure conditions.	138
7.2	Numerical solver setup for the investigation of multicomponent phase separation.	138
7.3	Different meshes used for the grid convergence study with respect to the resolution of the injector ($\Delta r = D/n_{\text{cells}}$).	138
7.4	Experimental conditions for the single-phase test case taken from Baab et al. [16]. The nozzle exit temperature T_e and velocity u_e were estimated based on the assumption of an isentropic flow inside the injector.	143
7.5	Setup of the pressure-based solver for the comparison of FC and QC schemes.	144
7.6	Setup of the density-based solver for the comparison of FC and QC schemes.	144
8.1	Operating conditions of the considered LRE-like flames.	152
8.2	Numerical solver setup for the investigation of the high-pressure combustion case.	157
A.1	Constants used in the AUSM ⁺ -up scheme for all speeds [171].	197
B.1	Critical properties, acentric factor and molar weight of the applied fluids.	199
F.1	Numerical solver setup for the validation of the hybrid pressure-based approach.	211
G.1	Numerical solver setup for the validation of the density-based solver.	215

Nomenclature

In the following, only the specific (mass-related) variables are listed. Mole-related properties are denoted by \square in this work.

Latin symbols

A	[\cdot]	Dimensionless attractive parameter
A	[m^2]	Surface area or cross-section area
a	[$kg\ m^5\ s^{-2}\ mol^{-2}$]	Attractive term of the cubic state equation
a	[$m\ s^{-1}$]	Speed of propagation
\check{a}	[$m^3\ s^{-1}$]	Volumetric flux related to the speed of propagation
\mathbf{a}		Coefficient matrix in the finite volume method
a_N	[$kg\ m^{-3}\ s^{-1}$]	Matrix coefficient of the pressure equation for cell neighbors
a_P	[$kg\ m^{-3}\ s^{-1}$]	Matrix coefficient of the pressure equation for cell owners
a_s	[$m\ s^{-1}$]	Speed of sound
B	[\cdot]	Dimensionless repulsive parameter
b	[$m^3\ mol^{-1}$]	Repulsive term of the cubic state equation
\mathbf{b}		Vector of sources in the finite volume method
b_P	[$kg\ m^{-2}\ s^{-2}$]	Source/explicit contribution in the pressure equation for cell owners
C	[\cdot]	General constant in the cubic state equation
C_D	[\cdot]	Discharge coefficient
C_p	[$J\ K^{-1}$]	Heat capacity at constant pressure
C_v	[$J\ K^{-1}$]	Heat capacity at constant volume
c_i	[$mol\ m^{-3}$]	Molar concentration of species i
c_p	[$J\ kg^{-1}\ K^{-1}$]	Specific heat at constant pressure
c_v	[$J\ kg^{-1}\ K^{-1}$]	Specific heat at constant volume
D	[m]	Diameter
D	[$m^2\ s^{-1}$]	Diffusion coefficient
d	[m]	Distance between cell centers
d_{\perp}	[m]	Wall-nearest distance
d_i	[\cdot]	Share of the feed of species i in the TPD criterion
E	[J]	Internal energy
e	[$J\ kg^{-1}$]	Specific internal energy
e_0	[$J\ kg^{-1}$]	Reference specific internal energy
F	[J]	Helmholtz free energy
F_1	[\cdot]	Blending function in the k,ω -SST-model
F_2	[\cdot]	Blending function in the k,ω -SST-model
f	[$J\ kg^{-1}$]	Specific Helmholtz free energy
f	[Pa]	Fugacity
f	[\cdot]	Mixture fraction
f'^2	[\cdot]	Variance of the mixture fraction
f_a	[\cdot]	Scaling function in the AUSM scheme
f_i	[Pa]	Fugacity of species i
G	[J]	Gibbs energy
g	[$J\ kg^{-1}$]	Specific Gibbs energy
H	[J]	Enthalpy
H_P	[$kg\ m^{-2}\ s^{-2}$]	Operator used in the pressure equation of OpenFOAM
h	[$J\ kg^{-1}$]	Specific enthalpy

h_i	[J kg ⁻¹]	Partial enthalpy of species i
I	[\cdot]	Normalized nucleation rate
J	[m ⁻³ s ⁻¹]	Nucleation rate
j_i	[kg m ⁻² s ⁻¹]	Diffusive species flux of species i
K	[m ⁻³ s ⁻¹]	Kinetic pre-factor
K_i	[\cdot]	Equilibrium ratio of component i
k	[m ² s ⁻²]	Turbulent kinetic energy
k_f	[m ²]	Nonparallel part of the face normal vector
$k_{b,r}$	[l mol ⁻¹ s ⁻¹]	Reverse rate constant of the r -th reaction
$k_{f,r}$	[l mol ⁻¹ s ⁻¹]	Forward rate constant of the r -th reaction
k_{ij}	[\cdot]	Binary interaction coefficient
L	[m]	Characteristic length
l_i	[\cdot]	Amount of species i in the liquid phase
M	[kg mol ⁻¹]	Molar weight
Ma_p	[\cdot]	Low Mach number contribution in the AUSM ⁺ -up scheme for all speeds
m	[kg]	Mass
\dot{m}	[kg s ⁻¹]	Mass flow rate
m_t	[kg]	Total mass of the mixture
N_c	[\cdot]	Number of components
N_r	[\cdot]	Number of reactions
n	[mol]	Mole number
n_i	[\cdot]	Face normal vector in the i -th direction
n_t	[mol]	Total mole number of the mixture
P_i	[kg ^{1/4} m ³ s ^{-1/2} mol ⁻¹]	Parachor factor of species i
p	[Pa]	Pressure
p_u	[Pa]	Low Mach number contribution in the AUSM ⁺ -up scheme for all speeds
Q	[J]	Absorbed heat
\mathbf{Q}	[J mol ⁻²]	Hessian matrix of the Helmholtz free energy with respect to the mole number
q	[J s ⁻¹ m ⁻²]	Diffusive heat flux
R	[J kg ⁻¹ K ⁻¹]	Specific gas constant
r	[\cdot]	Function of successive gradients
r	[m]	Radius
S	[J K ⁻¹]	Entropy
S	[m ²]	Surface of the cell in the finite volume method
S_f	[m ²]	Face normal vector in the finite volume method
S_{ij}	[s ⁻¹]	Rate of strain tensor
s	[J kg ⁻¹ K ⁻¹]	Specific entropy
T	[K]	Temperature
TPD	[J mol ⁻¹]	Tangent-plane distance
t	[s]	Time
tm	[\cdot]	Modified TPD criterion
u	[m s ⁻¹]	Velocity
u	[\cdot]	Model parameter in the cubic state equation
\mathbf{U}		Vector of conservative variables
V	[m ³]	Volume
v	[m ³ kg ⁻¹]	Specific volume
v_i	[\cdot]	Amount of species i in the vapor phase
v_i	[m ³ kg ⁻¹]	Partial volume of species i
W	[J]	Work done on the system
W_i	[\cdot]	Formal mole number of species i in the modified TPD criterion
w	[\cdot]	Model parameter in the cubic state equation

w_i	[·]	Mole fraction of species i in the trial phase
x, y, z	[m]	Cartesian coordinates
x_i	[·]	Mole fraction of species i in the liquid phase
Y_i	[·]	Mass fraction of species i
y_i	[·]	Mole fraction of species i in the vapor phase
Z	[·]	Compressibility factor
z_i	[·]	Mole fraction of species i in the overall mixture/feed

Calligraphic symbols

α	[·]	Coefficients of the NASA polynomials
\mathcal{B}		Extensive property
β		Specific property of \mathcal{B}
\mathcal{C}	[·]	Curve in the state space
C_1	[Pa s]	Constant in the Sutherland model
C_2	[K]	Constant in the Sutherland model
δ	[m ⁻¹]	Diffusion driving force
\mathcal{E}	[m ³ s ⁻²]	Energy spectrum of turbulent flow
\mathcal{F}		Flux in the hyperbolic conservation law
\mathcal{G}		Vector of objective functions
\mathcal{H}		Numerical flux in the hyperbolic conservation law
\mathcal{J}		Jacobian matrix of the vector of objective functions
\mathcal{K}	[m ⁻¹]	Wave number of turbulent motion
\mathcal{L}	[m]	Length scale of turbulent motion
m	[J]	State property
$m_{(i)}$	[·]	i -th order polynomial in the AUSM scheme for the interface Mach number
$\mathcal{P}_{(i)}$	[·]	i -th order polynomial in the AUSM scheme for the interface pressure
\mathcal{P}_k	[kg m ⁻¹ s ⁻³]	Production of turbulent kinetic energy
\mathcal{P}_{sgs}	[·]	Joint probability density function
\mathcal{P}_ω	[kg m ⁻³ s ⁻²]	Production of turbulent dissipation
q_i	[mol]	Mole number of species i in the second phase
\mathcal{S}	[kg m ⁻³ s ⁻¹]	Source term
\mathcal{S}		Specification parameter
\mathcal{T}	[s]	Variable used for the time integration
t	[·]	Tangent to the Gibbs energy of mixing
u	[·]	General property used in central schemes
\mathcal{V}	[·]	Interpolation factor in the CD scheme
\mathfrak{w}	[·]	Staggered grid property in central flux schemes
\mathcal{X}		Vector of independent variables for the construction of the phase envelope
x		Thermodynamic variable in the Legendre transformation
y		Fundamental equation in the Legendre transformation

Greek symbols

α_f	[·]	Weighting factor in central flux schemes
α_i	[·]	Substituted variable in Newton's method of the TPD criterion
α_p	[K ⁻¹]	Thermal compressibility
β	[·]	Vapor (mole) fraction
β_m	[·]	Vapor mass fraction
β_v	[·]	Vapor volume fraction

Γ	[·]	Mass-based coefficient in the determination of the diffusion driving force
Γ_{BD}	[·]	Blending factor applied in the BD scheme
γ	[·]	Specific heat ratio
Δ	[m]	Filter width
ΔG	[J]	Free reversible energy of formation for a critical droplet
Δm^0	[J]	Difference in the hypothetical gas state
ΔT	[K]	Subcooling
Δt	[s]	Time step
Δx	[m]	Representative cell dimension or cell width in 1D
$\Delta^* \mu_i$	[J mol ⁻¹]	Difference of the chemical potential of liquid and vapor
δ_f	[m ²]	Parallel part of the face normal vector
δ_{ij}	[·]	Kronecker delta
ϵ	[m ² s ⁻³]	Turbulent kinetic energy dissipation rate
ζ	[m]	Variable used in the spatial integration
Θ	[·]	General constant for the blending in the k,ω -SST-model
ϑ		Table values in the flamelet model
κ	[·]	Function of the acentric factor in the cubic state equation
Λ	[·]	Multiplicative parameter in first-order functions
λ	[J s ⁻¹ m ⁻¹ K ⁻¹]	Thermal conductivity
λ_i	[·]	i -th eigenvalue of the speed of propagation
λ^{TPD}	[·]	Eigenvalue used in the solution of the TPD criterion
λ^{flash}	[·]	Eigenvalue used in the solution of the Tpn -flash
μ	[kg m ⁻¹ s ⁻¹]	Dynamic viscosity
μ	[J mol ⁻¹]	Chemical potential of the pure fluid
μ_i	[J mol ⁻¹]	Chemical potential of component i
μ_i^*	[·]	Normalized chemical potential of component i
ν	[·]	Stoichiometric coefficient
Ξ	[kg m ⁻³]	Mass density of the general scalar variable
ξ	[·]	General scalar variable
ρ	[kg m ⁻³]	Density
σ	[kg s ⁻²]	Surface tension
τ	[kg m ⁻¹ s ⁻²]	Viscous stress tensor
Φ_f	[m ³ s ⁻¹]	Volumetric flux through face f
ϕ_f	[kg s ⁻¹]	Mass flux through face f
ϕ	[·]	Grüneisen parameter
φ	[·]	Fugacity coefficient of the pure fluid
φ_i	[·]	Fugacity coefficient of species i
χ	[s ⁻¹]	Scalar dissipation rate
Ψ	[s ² m ⁻²]	Pseudo-compressibility used in the hyperbolic pressure equation
Ψ_h	[s ² m ⁻²]	Partial derivative of the density with respect to the pressure at isenthalpic conditions
ψ	[m s ² kg ⁻¹]	Compressibility
Ω	[m ³]	Cell volume
ω	[s ⁻¹]	Specific turbulent dissipation rate
ω	[·]	Acentric factor
ω_f	[m ³ s ⁻¹]	Volumetric flux in central flux schemes
$\dot{\omega}_k$	[kg m ⁻³ s ⁻¹]	Source term of species k

Dimensionless numbers

CFL_a	Acoustic Courant-Friedrichs-Lowy number
CFL_c	Convective Courant-Friedrichs-Lowy number

Da	Damköhler number
Le	Lewis number
Ma	Mach number
Pr	Prandtl number
Re	Reynolds number
Sc	Schmidt number

Constants

a_1	0.31	Constant in the k,ω -SST-model
a_{Riazi}	1.07	Constant in the diffusion model of Riazi and Whitson
C_{ad}	0.04	Constant in the localized artificial dissipation approach
C_f	0.7	Constant in the jet penetration correlation of Abraham
C_S	0.17	Smagorinsky constant
C_t	0.0161	Constant in the jet penetration correlation of Abraham
C_V	0.07	Constant in the Vreman sub-grid model
C_W	0.325	Constant in the WALE model
C_χ	2	Constant in the variance equation of f
C_μ	0.09	Constant in the k,ω - and k,ϵ -model
K_P	0.25	Constant in the AUSM ⁺ -up scheme for all speeds
K_u	0.75	Constant in the AUSM ⁺ -up scheme for all speeds
k_B	$1.380658 \times 10^{-23} \text{ J K}^{-1}$	Boltzmann constant
N_A	$6.02214076 \times 10^{23} \text{ mol}^{-1}$	Avogadro constant
\mathcal{R}	$8.314472 \text{ J mol}^{-1} \text{ K}^{-1}$	Universal gas constant
α	k,ω : 0.555; k,ϵ : 0.44	Constant in the k,ω - and k,ϵ -model
β	k,ω : 0.075; k,ϵ : 0.0828	Constant in the k,ω - and k,ϵ -model
β^{AUSM}	0.125	Constant in the AUSM ⁺ -up scheme for all speeds
β^*	0.09	Constant in the k,ω -SST-model
Γ	3.0 ± 0.1	Scaling parameter in jet penetration depth correlations
η	[0.11, 0.2766, 0.5, 1.0]	Constants in the Runge-Kutta time integration scheme
π	3.141593	Pi
σ^{AUSM}	1.0	Constant in the AUSM ⁺ -up scheme for all speeds
σ_k	k,ω : 0.85; k,ϵ : 1.0	Constant in the k,ω - and k,ϵ -model
σ_ω	k,ω : 0.5; k,ϵ : 0.856	Constant in the k,ω - and k,ϵ -model

Subscripts

0	Initial state of interest in the HK method
$1/2$	Interface value in the AUSM scheme
C	Grid node in the BD scheme
c	Critical property
ch	Chamber
D	Grid node in the BD scheme
ext	Extinction
F	Fuel
f	Face value
HV	High volatile component
h	Isenthalpic
inj	Injection
j	Cell index
L	Left-hand sided face state
LV	Low volatile component
l	Left-hand side extent of the Riemann fan
m	Mean value in the AUSM scheme

md	Mach disk
max	Maximum value
min	Minimum value
mix	Contribution of the ideal or nonideal mixing behavior
N	Neighbor cell
n_i	Iso-composition in terms of mole numbers
Ox	Oxidizer
P	Owner cell
p	Isobaric
ps	Post-shock
R	Right-hand sided face state
r	Reduced with respect to the critical point
r	Right-hand side extent of the Riemann fan
rev	Reversible
S	Isentropic
s	Isentropic
st	Stoichiometric
\mathcal{T}	Reference time
T	Isothermal
t	Turbulent or total
U	Grid node in the BD scheme
V	Isochoric
v	Isochoric
Y	Iso-composition in terms of mass fractions
z	Iso-composition in terms of mole fractions

Superscripts

-	Reconstruction direction
+	Reconstruction direction
∞	Extrapolated value in the dominant eigenvalue method
0	Hypothetical/ideal gas state
(0)	Fundamental function for the Legendre transformation
I/II	Theoretical thermodynamic subsystems
*	Real-gas property in the double-flux method
(c)	Convective part of the Eulerian flux
e	Eulerian
flash	Tpn -flash
k	Iteration step
(k)	k -th Legendre transform
l	Liquid phase
n	Time level
PE	Phase envelope
(p)	Pressure part of the Eulerian flux
pure	Thermodynamic property of the pure fluid
RE	Rapid estimate
r	Residual part of the state function
ref	Reference state in the departure function formalism
rg	Real-gas
s	Surface
sgs	Sub-grid scale
sp	Stationary point
tp	Two-phase
v	Viscous
v	Vapor phase

$\hat{\square}$	Variable for integration
$\tilde{\square}$	Favre-averaged variable
$\tilde{\tilde{\square}}$	Piecewise polynomial reconstruction in central schemes
$\bar{\square}$	Filtered variable
$\bar{\bar{\square}}$	Piecewise constant approximation in central schemes
\square'	Resolved fluctuation
\square''	Unresolved fluctuation

Abbreviations

AUSM	Advection Upstream Splitting Method
BD	Blended Differencing
CD	Central Differencing
CFD	Computational Fluid Dynamics
CHG	Compressed Hydrogen Gas
CNG	Compressed Natural Gas
CNT	Classical Nucleation Theory
CP	Critical Point
CSP	Corresponding States Principle
CV	Control Volume
DEM	Dominant Eigenvalue Method
DI	Direct Injection
DLR	German Aerospace Center (German: Deutsches Zentrum für Luft- und Raumfahrt)
DNS	Direct Numerical Simulation
ECN	Engine Combustion Network
ELS	Elastic Light Scattering
EoS	Equation of State
FC	Fully Conservative
GE	Gas Engine
GRI	Gas Research Institute
HK	Heidemann and Khalil
HV	High Volatile
ICE	Internal Combustion Engine
ITLR	Institute of Aerospace Thermodynamics
KNP	Kurganov, Noelle and Petrova
KT	Kurganov and Tadmor
LES	Large-Eddy Simulation
LHS	Left-Hand Side
LG	Liquid-Gas
LITA	Laser-Induced Thermal Acoustics
LLG	Liquid-Liquid-Gas
LOx	Liquid-like Oxygen
LRE	Liquid-propellant Rocket Engines
LV	Low Volatile
LxF	Lax and Friedrichs
MKL	Math Kernel Library
MUSCL	Monotonic Upstream-centered Scheme for Conservation Laws
NASA	National Aeronautics and Space Administration
NIST	National Institute of Standards and Technology
NM	Newton's Method
NPR	Nozzle Pressure Ratio
NT	Nessyahu and Tadmor

ODE	Ordinary Differential Equation
PDF	Probability Density Function
PIMPLE	Acronym combining PISO and SIMPLE
PISO	Pressure-Implicit with Splitting of Operators
PLIF	Planar Laser Induced Fluorescence
PMAL	Parallel Memory Abstraction Layers
PR	Peng and Robinson
QC	Quasi Conservative
QUICK	Quadratic Upstream Interpolation for Convective Kinematics
RANS	Reynolds-Averaged Navier-Stokes
RE	Rapid Estimate
RHS	Right-Hand Side
RK	Redlich and Kwong
RMS	Root Mean Square
RR	Rachford-Rice
SGS	Sub-Grid Scale
SIMPLE	Semi-Implicit Method for Pressure Linked Equations
SRK	Soave, Redlich and Kwong
SSM	Successive Substitution Method
SSME	Space Shuttle Main Engine
SST	Shear Stress Transport
TCI	Turbulence Chemistry Interaction
TPD	Tangent-Plane Distance
TVD	Total Variation Diminishing
UD	Upwind Differencing
VLE	Vapor-Liquid Equilibrium
vdW	van der Waals
WALE	Wall-Adapting Local Eddy-viscosity

Part I

FUNDAMENTALS

1 Introduction

1.1 High-pressure injection, mixing and combustion

Injection, mixing and combustion under high-pressure conditions are key processes in modern energy-conversion machines. In general, large operating pressures are preferred in many conversion processes to extract the maximum energy from the available fuel and convert it to, for instance, mechanical power or thrust. Although a lot of progress has been made in recent decades, the demands for efficiency improvements still leave much work and open questions [28, 362, 217, 156, 178, 29]. In the last few years, major research efforts have been undertaken to understand and study two types of fuel-fired engines in particular: liquid-propellant rocket engines (LREs) and gas engines (GEs). This arises from the fact, that LREs will remain an essential component for payload launchers in the foreseeable future and that GEs fired with hydrogen or natural gas are a possible solution to gradually diversify towards cleaner energy conversion machines. A common feature of LREs and GEs is that the injection and combustion process take place under high-pressure conditions. This has distinct reasons: In LREs, the specific impulse is proportional to the pressure and hence a larger combustion chamber pressure results in a higher propulsion efficiency [306]. In spark-ignited GEs, direct injection (DI) is considered to be a preferable approach compared to port-fuel injection [61, 111] as DI offers, for instance, a higher volumetric efficiency and a greater flexibility with respect to the control of the fuel-air mixture preparation. As gaseous fuels exhibit a much smaller density compared to liquid fuels, high injection pressures are necessary for injecting sufficiently large fuel masses into the cylinder.

For both engine types, the high combustion chamber pressures result in supercritical injection conditions, i.e., the injection pressures lie above the critical point of the pure fluids ($p_r = p/p_c > 1$ for both fuel as well as oxidizer). Figure 1.1 shows a general pressure-temperature (p - T) diagram of a pure fluid where typical injection conditions found in LREs and GEs are marked. The temperature and the pressure have been reduced by their respective critical values and the critical point (CP) is marked by the black dot which determines the vapor-pressure curve (solid black line). In this region, liquid and vapor coexist and both surface tension effects as well as vaporization and condensation processes take place. Consequently, the vapor-pressure curve separates the pure liquid from the pure gas state under subcritical pressure ($p < p_c$) conditions. Above the critical point

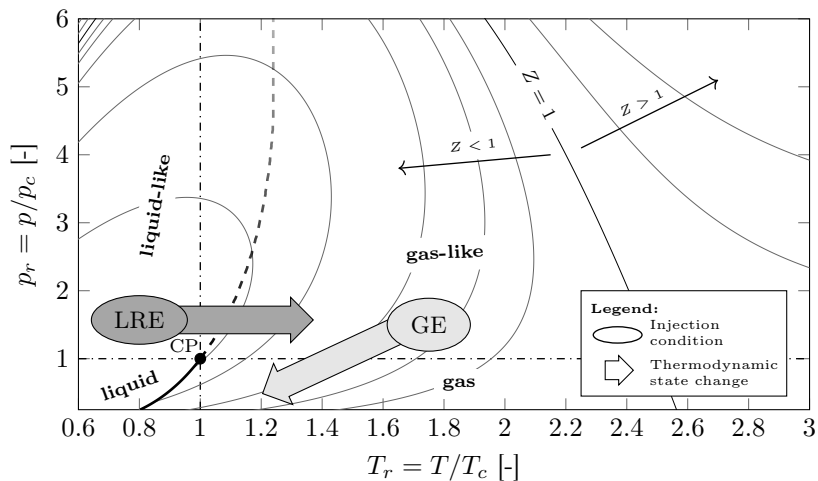


Figure 1.1: General reduced pressure-temperature diagram showing typical injection conditions for LREs and GEs: The solid black line denotes the vapor-pressure curve of a pure fluid determined by the critical point ($p_r = T_r = 1$). The dashed line corresponds to the Widom line. The iso-lines show constant compressibility factors Z .

($p > p_c$), the fluid behaves either liquid-like (high density) or gas-like (low density). As surface tension effects vanish under supercritical pressure conditions, the transition between both states is continuous. Both regions are separated by the Widom line [291] (dashed line) which is usually determined based on the maximum of the specific heat under isobaric conditions.

Different injection characteristics arise in both engine types due to the different injection densities (LRE: liquid-like/large; GE: gas-like/small) and nozzle pressure ratios (NPRs). The NPR is the pressure ratio between the fluid in the reservoir and the chamber into which the fluid is injected. In LREs, the injection process inside the combustion chamber can be considered roughly isobaric (small/vanishing NPR). After injection, the fluid transitions from a liquid-like to a gas-like state by interaction with its surrounding, see Fig. 1.1. This process is commonly termed transcritical injection [221] as the fluid crosses the critical point during mixing and heating. Due to the supercritical pressure conditions, the occurring density variation is temperature induced and steep density gradients are present in the region of the Widom line. No phase separation effects occur under pure fluid conditions and therefore the mixing process is dominated by turbulence and diffusion effects. Within experiments, this process is indicated by finger-like structures at the jet periphery and the jet gradually dissolves into the environment, see Fig. 1.2a. In contrast, GEs feature high NPRs between the fuel reservoir and the combustion chamber. This results in the formation of high-speed jets with underexpansion and distinct flow features like shocks and expansion waves, see Fig. 1.2b. Therefore, strong pressure and temperature changes occur during the injection process mainly induced by fluid dynamics effects, cf. Fig. 1.1.

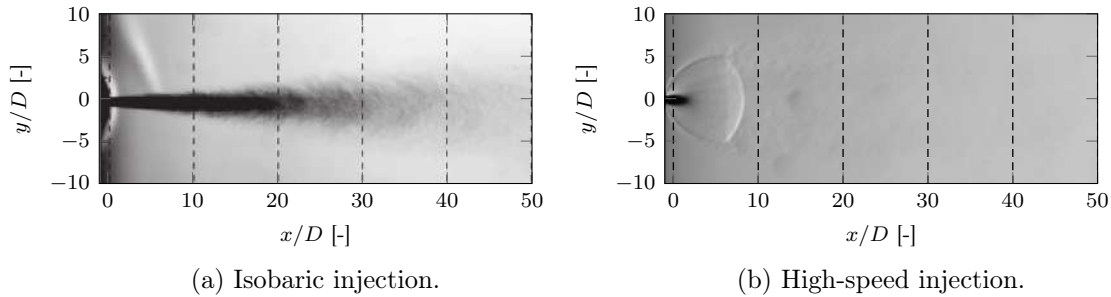


Figure 1.2: Exemplary shadowgraphs of an isobaric and a high-speed jet at supercritical injection conditions. Both images have been taken from the work of Baab et al. [14, 16]. Figure a) is reprinted from Fuel, volume 233, Baab, S., Steinhausen, C., Lamanna, G., Weigand, B. and Förster, F. J., *A quantitative speed of sound database for multi-component jet mixing at high pressure*, pp. 918–925, © (2018) with permission from Elsevier. Figure b) is reprinted by permission from Springer Nature Customer Service Centre GmbH: Springer Nature, *Experiments in Fluids*, Baab et al. [14], © (2016).

A common feature of both types of engines are the relatively low injection temperatures (LRE: $T_r < 1$; GE: $1 < T_r < 2$). The elevated pressure conditions and the moderate temperatures result in the presence of real-gas effects which are indicated by a nonunity compressibility factor Z , see Fig. 1.1. Under real-gas conditions ($Z \neq 1$), the ideal-gas assumption ($Z = 1$) is not valid anymore as intermolecular forces are present resulting in a nonlinear behavior of the fluid properties. Consequently, the thermodynamic properties depend on both temperature as well as pressure. Due to the initially supercritical pressure conditions, a single-phase state is assumed in most investigations. Recent experimental and numerical investigations [87, 86, 314, 71, 298, 357, 170, 169, 15], however, suggest that this assumption has to be questioned and further careful studies are necessary to better understand the possible recurrence of phase separation processes under initially supercritical pressure conditions. Under GE-like injection conditions, phase separation might be triggered due to the strong simultaneous changes in both pressure and temperature during the expansion process from reservoir to chamber conditions. In Fig. 1.3a, a pressure-specific volume (p - v) diagram is shown with focus on the approximated expansion process in GEs and the vapor-liquid equilibrium (VLE) of a pure fluid. Depending on the minimum pressure during the expansion, the dew-point line can be crossed and phase separation might occur. In

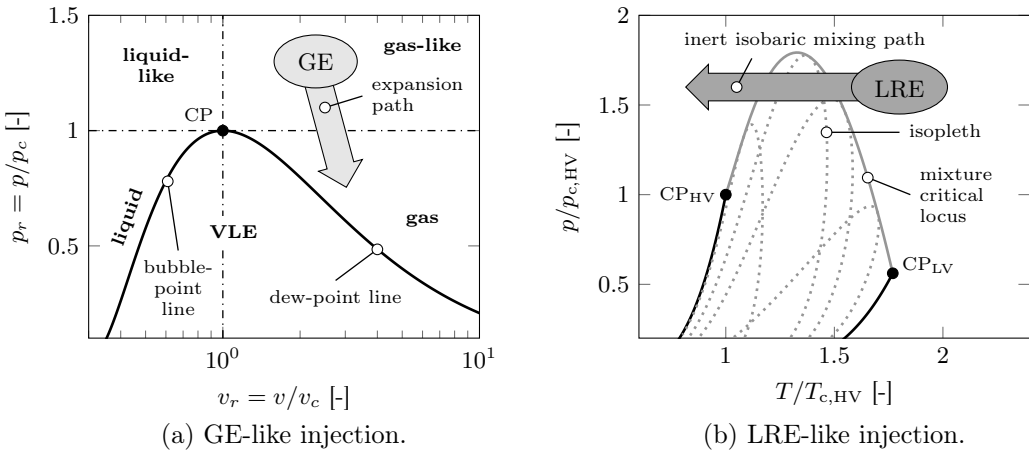


Figure 1.3: Approximated thermodynamic trajectories under GE-like and LRE-like injection conditions together with the relevant vapor-liquid equilibrium for a pure fluid (subfigure a) and a binary mixture (subfigure b). The subscripts HV and LV denote the high and the low volatile component of the mixture, respectively. An isopleth is a line of constant overall composition.

contrast, under LRE-like conditions, phase separation is primarily triggered by the mixing of the injected fluid with its surrounding. In multicomponent fluids, the critical points of the pure fluids degenerate to a critical locus which extent depends on both the fluids forming the mixture and the thermodynamic properties pressure, temperature and composition. As the critical locus can by far exceed the critical point of the pure components, phase separation can also occur under initially supercritical injection conditions, see Fig. 1.3b. Therefore, the term supercritical has to be used with caution when multicomponent mixtures are investigated as it might not be possible to define a single, representative critical point which marks the border between subcritical and supercritical conditions. In addition, the critical locus can have various forms and shapes, see, e.g., van Konynenburg and Scott [335], which further increases the complexity of the investigation and of the predictability of this thermodynamic process. This can get even more complex when looking at the combustion process under LRE-like conditions where species are produced and consumed by the reaction process. Here, fuel and oxidizer are typically injected separately through a coaxial injection element and the conditions are initially supercritical. Due to mixing and reaction processes, the single-phase assumption might be violated locally.

In the following, an overview regarding studies on high-pressure injection, mixing and combustion with a special focus on phase separation effects under initially supercritical conditions is given. Three different topics, which are relevant for the present work, are covered: (1) Injection and mixing under LRE-like conditions, (2) High-pressure combustion under LRE-like conditions and (3) Injection and mixing under GE-like conditions.

1.2 Injection and mixing under rocket-relevant conditions

Experimental investigations

Table 1.1 provides an overview of experimental studies focusing on multicomponent mixing under high-pressure conditions. The earliest investigation dates back to 1971 and was conducted by Newman and Brzustowski [209]. In this first systematic study on high-pressure fluid injection, liquid carbon dioxide (CO_2 : $p_c = 73.74$ bar, $T_c = 304.12$ K) was injected through a circular nozzle into a pressurized chamber filled with a binary mixture of nitrogen (N_2 : $p_c = 33.96$ bar, $T_c = 126.19$ K) and carbon dioxide. The chamber pressure and temperature were changed from sub- to supercritical conditions with respect to the critical point of CO_2 . Large changes in the jet disintegration process from a classical liquid spray break-up (two-phase) to a gas/gas mixing (single-phase) were reported. Especially, in the near-critical cases, the break-up process of the jet was very sensitive with respect to the chamber conditions which in turn underlines the complexity

Table 1.1: Overview of experimental studies focusing on high-pressure multicomponent mixing under isobaric injection conditions. The chamber pressure and temperature as well as the injection temperature are denoted by p_{ch} , T_{ch} and T_{inj} , respectively.

Reference	Year	Injectant	Chamber	p_{ch} [bar]	T_{ch} [K]	T_{inj} [K]	Mixture-induced phase separation
Newman and Brzustowski [209]	1971	CO_2	$\text{CO}_2 + \text{N}_2$	62 - 90	295 - 333	295	x
Woodward and Talley [356, 355]	1994 & 1996	N_2	$\text{N}_2 + \text{He}$	28 - 69	280 - 310	88 - 115	✓
Mayer et al. [189]	1998	$\text{N}_2 + \text{He}^a$	He	10 - 60	300	97	✓
Oschwald et al. [220]	1999	$\text{N}_2 + \text{H}_2^b$	N_2	40	118 - 140	300	x
Telaar et al. [310]	2000	$\text{N}_2 + \text{He}^c$	N_2	10 - 60	300	97	✓
Segal and Polikov [282]	2008	FK^d	N_2	1.4 - 40.5	293 - 452	300 - 564.5	x
Roy and Segal [266]	2010	FK	N_2	19.3 - 32.7	385.9 - 540.2	391.4 - 479.6	x
Roy et al. [265]	2013	FK	N_2	23.2 - 34.6	304.3 - 480.7	441.0 - 577.7	✓
Manin et al. [179]	2014	$\text{C}_{12}\text{H}_{26}$	N_2	20 - 80	700 - 1200	363	✓
Muthukumaran and Vaidyanathan [206, 207]	2015 & 2016	FK	$\text{N}_2 \& \text{He}$	13.2 - 24.7	317.6 - 458.6	405.7 - 471.9	✓
DeSouza and Segal [65]	2017	FK	N_2	14.5 - 27.0	339.6 - 533.6	291.1 - 480.7	✓
Baab et al. [16]	2018	$\text{C}_5\text{H}_{12}^e$ $\text{C}_6\text{H}_{14}^f \& \text{FK}$	N_2	39.5 - 50	296	500 - 630	x

^aA coaxial injector has been used where He has been injected through the annulus at 280 K.

^bA coaxial injector has been used where H_2 has been injected through the annulus at 270 K.

^cA coaxial injector has been used where He has been injected through the annulus at 280 K.

^dAbbreviation for fluoroketone, here: 2-trifluoromethyl-1,1,2,4,4,5,5-nonafluoro-3-pentanone.

^eChemical formula for n-pentane.

^fChemical formula for n-hexane.

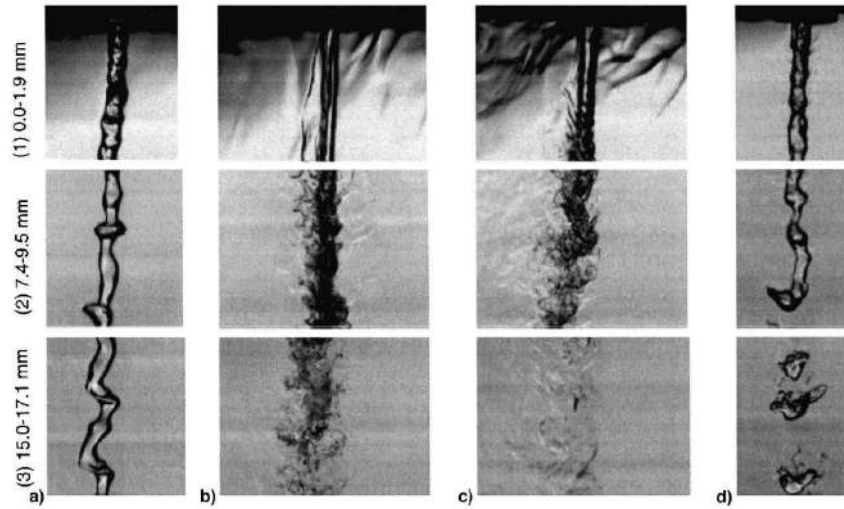


Figure 1.4: Injection of liquid N₂ (90 K) into a pressurized test chamber: a) into subcritical N₂ at 28 bar; b) into near-critical N₂ at 35 bar; c) into supercritical N₂ at 69 bar; d) into a binary N₂/He mixture at 69 bar. The figures have been taken from Mayer et al. [189]; reprinted by permission of the American Institute of Aeronautics and Astronautics, Inc.

of assessing the true thermodynamic state (single- or two-phase) in multicomponent mixtures. First clear evidence of high-pressure mixture-induced phase separation under engine-relevant conditions was reported by Woodward and Talley [356, 355] in 1996. By injecting pure nitrogen N₂ into its own gas phase and altering the pressure from sub- to supercritical conditions, Woodward and Talley [356, 355] demonstrated a transition from a fully subcritical jet with surface tension effects and droplets to a supercritical, single-phase jet with stringy fluid structures and an absence of droplet formation, see Figs. 1.4a-c. Introducing helium (He: $p_c = 2.3$ bar, $T_c = 5.2$ K) into the high-pressure chamber, i.e., filling the chamber with a binary mixture of N₂ and He, brought the jet back to a subcritical fluid behavior with a distinct interface and evidence of surface tension, see Fig. 1.4d. Two years later, similar findings were reported by Mayer et al. [189] for an identical binary mixture. In contrast to Woodward and Talley [355], Mayer et al. [189] used a coaxial injector where they injected liquid N₂ (97 K) through the inner tube and gaseous He (280 K) through the outer annulus into a test chamber filled with He (In 2000, Telaar et al. [310] did identical investigations with N₂ as chamber gas). The shadowgrams from the investigations of Mayer et al. [189] are shown in Fig. 1.5 right. By changing the pressure from 10 bar to 60 bar, an unambiguous visual difference in the jet mixing process occurs from a subcritical disintegration process with clear evidence of large droplets and ligaments to a rather diffuse mixing process where the inner dense core appears black. Thermodynamic analyses of this binary N₂/He-system show that the critical mixing temperature at 60 bar is at 125.7 K [188, 323] and therefore parts of the inner mixing layer might undergo a mixture-induced phase separation process which might be hidden by the dark jet core. This a posteriori analysis is shown in more detail in Fig. 1.5 left. Following the exemplary mixing path (here: ideal (linear) mixing is assumed for simplicity), the trajectory clearly crosses both VLE regions at 10 bar and 60 bar. This further underlines the expectation that the mixture at 60 bar might be found locally in a subcritical state. Unfortunately, the interpretation of the shadowgraph alone is not straightforward and bears uncertainties as, for instance, discussed by Lamanna et al. [158]. Therefore, more suitable measurement techniques apart from sole shadowgraphy are necessary to properly assess phase separation phenomena at elevated pressure conditions.

After these first groundbreaking studies the interest in mixture-induced phase separation got somewhat lost and a lot of groups focused on the basic understanding of supercritical pure fluid jets, see the review articles of Chehroudi [45] and Oschwald et al. [221]. More recent experimental studies have brought back scientific interest in the phenomenon of mixture-induced phase separation: For instance, in 2013, Roy et al. [265] injected initially supercritical fluoroketone (FK) into a supercritical nitrogen atmosphere and used planar laser induced fluorescence (PLIF) as mea-

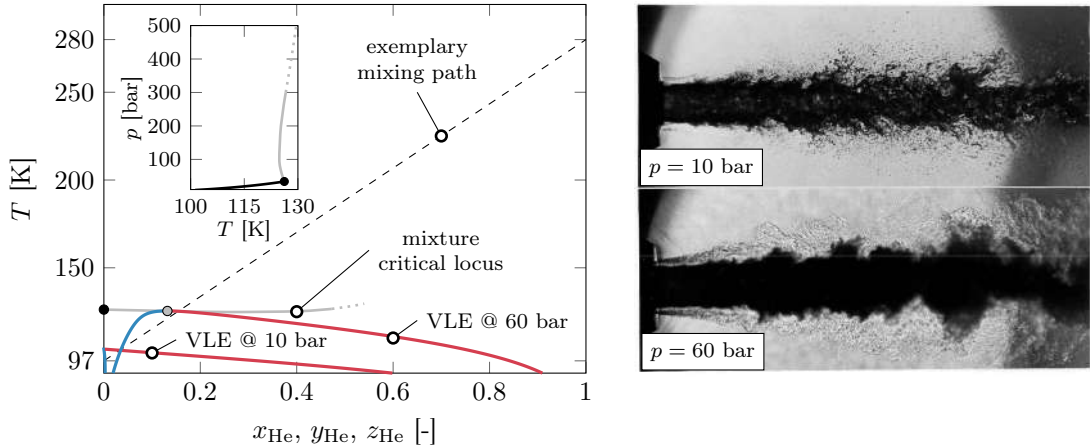


Figure 1.5: Coaxial injection of liquid N₂ (97 K, inner tube) and gaseous He (280 K, outer annulus) into a pressurized helium atmosphere at 10 bar and 60 bar, right images. On the left, a temperature-composition diagram together with the binary VLEs at the relevant pressures, the mixture critical locus and an exemplary mixing path are shown. The VLEs and the mixture critical locus have been calculated using the cubic equation of state of Peng and Robinson [226]. The shadowgraphs have been taken from Mayer et al. [189]; reprinted by permission of the American Institute of Aeronautics and Astronautics, Inc.

surement technique to visualize the jet structure up to a downstream position of 20 times the jet diameter. For sufficiently low ambient temperatures and far downstream from the injector (> 10 times the injector diameter), Roy et al. [265] found droplets and ligaments at the periphery of the jet which indicated mixture-induced phase separation. Manin et al. [179] performed high-speed long-distance microscopy experiments where n-dodecane (C₁₂H₂₆) was injected into a high-pressure, high-temperature chamber filled with nitrogen. Their investigations mainly focused on observations after the end of the injection. For sufficiently high chamber temperatures, Manin et al. [179] reported a transition from an atomization to a diffusion-driven mixing process with an absence of surface tension effects. In 2015 and 2016, Muthukumaran and Vaidyanathan [206, 207] followed the work of Roy et al. [265] and conducted PLIF measurements to study the thermodynamic behavior of binary jets emerging from an elliptical [206] and a circular [207] orifice. In the experiments, fluoroketone was injected into a pressurized chamber filled with either nitrogen or helium. Similar as in the experiments of Roy et al. [265], droplets occurred at the jet periphery at sufficiently low ambient temperatures. Furthermore, a dependency of the two-phase phenomenon on the pressure was found which was attributed to density changes of the injectant induced by the variation of the reservoir pressure. Using the identical setup as Roy et al. [265], DeSouza and Segal [65] focused on the effect of the density ratio between chamber gas and injectant on the jet break-up process and conducted a total of 48 measurements. Based on three selected cases, the change in the jet topology from a subcritical breakup to a supercritical turbulent mixing process was studied by means of both PLIF and shadowgraphy. DeSouza and Segal [65] found that both temperature and pressure influence the disintegration characteristics and that gas/gas mixing occurred when both chamber and injectant conditions are supercritical.

Numerical simulations

In the field of numerical simulations under high-pressure engine-relevant conditions, multicomponent phase separation processes were considered for the first time in studies focusing on the vaporization of isolated droplets. Among others, Manrique and Borman [180], Umemura [327], Litchford and Jeng [174], Delplanque and Sirignano [63], Yang and Shuen [363], Haldenwang et al. [107] and Sirignano and Delplanque [294] investigated the thermodynamic behavior of isolated transcritical droplets subjected to a gaseous environment. Upon exceeding the mixture critical temperature, a transition from a sharp to a diffuse interface occurs. A review of trans- and supercritical vaporization and mixing in liquid-fueled propulsion systems can be found in the work

of Yang [362]. With the beginning of the 21st century, Bellan and coworkers started excessive studies on the thermodynamic behavior and transport anomalies in mixing layers under supercritical conditions, see, e.g., Bellan [28], Okong'o and Bellan [217, 218, 219] or Selle et al. [285]. For an inert n-heptane/nitrogen mixing layer, Okong'o and Bellan [217] compared their simulation data to the a posteriori calculated critical locus of the binary mixture. They reported that the local temperature is always larger than the mixture critical temperature and therefore concluded that the fluid is supercritical throughout the complete simulation domain. In contrast, Masi et al. [184] investigated a mixing layer containing a mixture of five different species where n-heptane C₇H₁₆ represents the fuel, nitrogen N₂ and oxygen O₂ the oxidizer air and carbon-dioxide CO₂ and water H₂O the two main combustion products. Masi et al. [184] found negative values in the mass-diffusion matrix indicating a counter-gradient diffusion and hence a spinodal decomposition, i.e., a possible intrinsic triggering of a phase separation process. This effect was mainly traced back to the presence of water. In a recent investigation of Castiglioni and Bellan [43], the statement of possible spinodal decomposition was revised and stated that the negative matrix values only result in an uphill diffusion effect. In addition, three different Diesel surrogates and their mixtures with air were compared to their spinodal locus and single-phase stability was reported for the Diesel-engine cold-ignition regime.

In 2014, Qiu and Reitz [244] were the first to employ a multicomponent vapor-liquid equilibrium model [246, 248, 244, 247] in computational fluid dynamics (CFD) and to evaluate the thermodynamic stability of the mixture state during run-time. In their study, Qiu and Reitz [244] investigated the jets of Roy et al. [265] and demonstrated that numerical simulations are able to represent mixture-induced phase separation. However, the simulations of Qiu and Reitz [244] showed two-phase effects in the near-injector region. In contrast, Roy et al. [265] reported droplets far downstream which is a clear discrepancy between the experimental and numerical results. This in turn underlines the challenges and difficulties in the thermodynamic investigation of the jet break-up process. Applying the same numerical framework and motivated by the work of Dahms et al. [57], Qiu and Reitz [245] studied in a follow-up work the injection and mixing process under Diesel-like conditions. In their numerical investigation, Qiu and Reitz [245] injected n-dodecane into three different high-pressure, high-temperature nitrogen atmospheres similar to those of the Engine Combustion Network (ECN) Spray A test case [232, 58]. Using the adiabatic mixture concept proposed by Siebers [289], Qiu and Reitz [245] studied possible phase separation processes in an a priori analysis and compared single-phase (dense-gas) with two-phase (thermodynamic equilibrium) results pointing out large temperature differences between both approaches. In their CFD simulations, local condensation processes were reported for all three chamber conditions consistent with the a priori analysis demonstrating the possibility of subcritical mixing even under high temperature ambient gas conditions. Following the work of Qiu and Reitz [245], Mattheis and Hickel [185] performed Large-Eddy Simulations (LESs) of the ECN Spray A case [232] and found very good agreement between measurement and simulation data. Similar to previous works of other groups, see, e.g., Lacaze et al. [153], their scatter plots of temperature vs. nitrogen concentration closely followed the adiabatic mixture concept. In addition, Mattheis and Hickel [185] compared results obtained with their fully-conservative (FC) to those from a quasi-conservative (QC) scheme proposed by Terashima and Koshi [311]. The authors reported a significantly higher temperature field in the result of the QC scheme compared to the FC scheme. It is therefore not surprising that the QC result clearly deviated from the adiabatic mixture concept.

The development of QC schemes is motivated by the fact that FC schemes in combination with real-gas equations of state suffer from numerical difficulties which usually manifest themselves in spurious pressure oscillations. In Figs. 1.6a and b, the problem is demonstrated by means of instantaneous temperature and pressure fields taken from the work of Terashima and Koshi [311]. Here, liquid-like nitrogen (71.5 K) is injected into its own gas phase at a temperature of 332.2 K and a supercritical pressure of 50 bar. Nonphysical pressure oscillations in the order of ± 20 bar occur. These result in a failure of the numerical simulation and are closely related to the steep density gradient during the transcritical injection process, see Fig. 1.6 left. To overcome such problems, different strategies have been suggested in the literature: Schmitt et al. [281, 279] employed an energy correction procedure in addition to an artificial viscosity approach which reduces nonphysical noise induced by the steep density gradients. Following the works of Karni [135] and Abgrall [3],

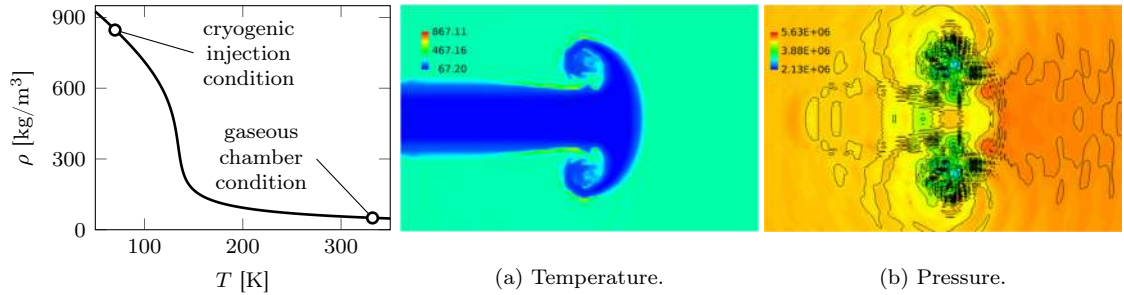


Figure 1.6: Spurious pressure oscillations during the injection of cryogenic nitrogen (71.5 K) into its own gas phase (332.2 K) at a pressure of 50 bar. The instantaneous snapshots of the temperature (a) and the pressure field (b) have been taken from Terashima and Koshi [311]. The density data have been obtained from CoolProp [27]. The figures a) and b) are reprinted from Journal of Computational Physics, volume 231, Terashima, H. and Koshi, M., *Approach for Simulating Gas-Liquid-Like Flows Under Supercritical Pressures Using a High-Order Central Differencing Scheme*, pp. 6907–6923, © (2012) with permission from Elsevier.

Terashima and Koshi [311] replaced the energy conservation equation with a transport equation for the pressure and were able to conserve the pressure equilibrium across contact interfaces. More recently, Ma et al. [177] followed the pioneering work of Abgrall and Karni [4] and Billet and Abgrall [32]. Ma et al. [177] extended the double-flux method [4, 32] to real-gas flows and combined it with an additional entropy-stabilized scheme to avoid nonphysical thermodynamic states during the time marching process. Despite representing a highly robust scheme, the extended double-flux approach is deemed QC and results in temperature fields which can significantly differ from those obtained with the FC schemes [177, 178]. Recently, Lacaze et al. [156] proposed a so-called enthalpy-based approach where they combined a classical flux-limited density-based method [155] with a pressure transport equation similar to the work of Terashima and Koshi [311]. The flux-limited scheme is inspired by the work of Swanson and Turkel [308] and is a blending of a third-order quadratic upstream interpolation for convective kinematics (QUICK) scheme with a robust first-order upwind scheme in combination with a convective flux limiter adapted for real-gas flows [155, 156]. By combining this basic approach with the pressure transport equation, a FC scheme without spurious pressure oscillations is created. The energy conservative character of the newly proposed approach was demonstrated by comparing temperature-composition scatter data from their numerical simulations with the adiabatic mixing concept. Recently, Ma et al. [178] investigated the mixing behavior of both FC and QC schemes. In accordance with other investigations [153, 185, 156], the FC results closely follow the adiabatic mixture assumption. For the QC double-flux scheme, Ma et al. [178] showed that the results of their investigated cases closely resemble an isochoric mixing approach where a linear behavior of the molar/specific volume is assumed in mixture space.

1.3 High-pressure combustion under rocket-relevant conditions

Nowadays, main stage liquid-propellant rocket engines are typically operated at elevated combustion chamber pressures up to more than 200 bar. Table 1.2 provides an overview of several LREs using liquid-like oxygen (LOx) and hydrogen (H₂) as propellant combination. Especially the space

Table 1.2: Overview of typical combustion chamber pressures in LOx/H₂ LREs with respect to the critical point of oxygen ($p_c = 50.43$ bar, $T_c = 154.58$ K).

Rocket engine	Vinci	Vulcain 1	Vulcain 2	LE-7A	SSME (RS-25)
$p/p_{c,O_2}$ [-]	1.21	1.98	2.33	2.38	4.10

shuttle main engine (SSME) stands out with a combustion chamber pressure of approximately 200 bar. The other engines have chamber pressures in the range of 100 bar. The very high pressures and temperatures during the combustion process make the conduction of experiments very challenging and costly. Therefore, many researchers focus on the numerical investigation of the combustion process in LREs. A comprehensive overview on the experimental work and the most important findings during the past two decades can be found in the PhD thesis of Cutrone [56] and in the overview paper of Haidn et al. [106]. In the following, the focus is put on numerical investigations of high-pressure combustion under LRE-relevant conditions with focus on real-gas modeling and investigation of possible phase separation processes.

First outstanding numerical investigations of reacting flows under LRE-like conditions were done by Oefelein [214] in 2005. In his work, Oefelein [214] characterized a supercritical LOx/H₂ flame emanating from a shear-coaxial injector using Direct Numerical Simulation (DNS) and LES. The results indicated the large influence of the LOx core onto the flame structure. Due to the steep thermodynamic gradients in the near injector region, a re-circulation zone occurs near the injector posttip which provides the main flame-holding mechanism and effectively separates the fuel from the oxidizer. Another approach apart from DNS and LES to study non-premixed reacting flows at representative operating conditions is the analysis of one-dimensional counterflow diffusion flames. Amongst others, Ribert et al. [259], Lacaze and Oefelein [154] and Banuti et al. [22, 24, 23] conducted detailed investigations of LOx/H₂ flames: Ribert et al. [259] focused on the dependency of the flame thickness and the heat release on pressure and strain rate in physical space and quantified the influence of Soret and Dufour effects. Lacaze and Oefelein [154] performed a detailed analysis of strain effects, pressure and temperature boundary conditions as well as real-fluid effects on the flame structure in both physical and mixture fraction space to develop a tabulated combustion model. Banuti et al. [22] investigated the transition of the thermodynamic state of LOx from a liquid-like state to a gas-like state to an ideal-gas state. They concluded that the real-gas effects are mainly limited to the pure oxygen and thus mixing occurs under ideal gas conditions.

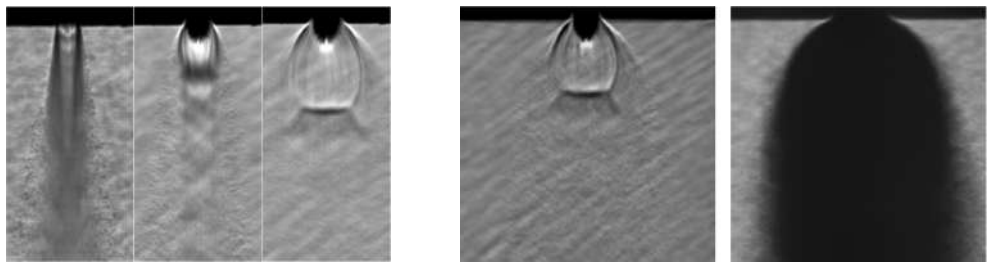
In recent years, the reusability of the LREs is getting more and more into the focus. In this context, the most promising propellant combination is LOx/methane (CH₄), see, e.g., Zurbach et al. [371] or Preclik et al. [242]. Consequently, many researchers focused on methane combustion and performed studies on one-dimensional LOx/CH₄ counterflow diffusion flames. Kim et al. [142] solved the real-gas flamelet equations in the mixture fraction space and established a library of the thermo-chemical state incorporating oxygen/methane chemistry and real-gas thermodynamics. Lapenna et al. [160] analyzed unsteady non-premixed LOx/CH₄ flamelets at supercritical pressures to study the effects of pressure and strain on autoignition, re-ignition and quenching. Slightly out of the scope of the LRE conditions, Juanós and Sirignano [133] used both steady air/methane as well as air/water-vapor/methane flamelets between 1 and 100 bar to investigate the pressure effects of these propellants and the required modeling.

Inspired by the inert investigations on mixture-induced phase separation effects some of these research groups performed a posteriori analysis of possible single-phase instabilities [154, 22, 160, 23]. All of them came to the finding that multi-phase effects do not occur and the mixture always stays in a single-phase state. A deficiency of these studies was that these groups applied a rapid estimation (RE) method for the determination of the mixture critical locus. Unfortunately, RE methods produce severe deviations from the real critical locus in complex mixtures like they occur during the combustion process. Therefore, evaluations of the thermodynamic state based on RE methods are prone to considerable uncertainties. Recently, Banuti et al. [24] used a high fidelity method a posteriori and pointed out that phase separation might be possible under rocket-relevant conditions but further investigations are necessary. Gaillard et al. [86] derived a diffuse-interface all-pressure flame model including water as a disperse phase. Using this framework, they investigated oxygen/hydrogen flames at rocket-relevant conditions and reported a possible occurrence of liquid water. Recent experimental investigations of Theron et al. [314] further underline this finding and give rise to the expectation that a pure single-phase treatment of the high-pressure combustion process under LRE-like conditions might not correctly reflect the actual thermodynamic state.

1.4 Injection and mixing under gas engine relevant conditions

Experimental investigations

Large injection pressures are key features in DI engines to provide an efficient fuel/oxidizer preparation [124] and sufficiently high fuel mass flow rates into the combustion chamber. As a result of the latter, the flow inside the injector nozzle is typically choked and an underexpanded jet is forming downstream of the nozzle exit to adjust the fuel jet to ambient conditions. The expansion characteristic of the underexpanded jet strongly depends on the pressure ratio between the fuel reservoir p_t and the ambient p_{ch} , i.e., the nozzle pressure ratio $NPR = p_t/p_{ch}$. According to Franquet et al. [81], four different scenarios are possible with increasing NPR: (1) weak underexpansion with a normal shock at the nozzle exit, (2) a moderately underexpanded jet with a diamond-like structure, (3) a highly underexpanded jet with a barrel structure and (4) an extremely underexpanded jet with a unique barrel with one single strong shock. This shock is usually termed Mach disk and its size and distance depends on the pressure ratio [55]. In Fig. 1.7a, shadowgraphs of three different jets at different NPRs are shown. The NPR increases from left to right resulting in a stronger manifestation of the first shock barrel downstream of the nozzle exit. Due to the moderate injection temperatures, these flow structures can be accompanied by both real-gas effects, cf. Fig. 1.1, and condensation processes resulting from the strong expansion downstream of the nozzle, cf. Fig. 1.3a. The latter is shown in Fig. 1.7b, where the reduction of the injection temperature brings the fuel jet from a single-phase (left) to a two-phase (right) state. Similar to the discussion of the subsonic mixing cases before, the jet structure occurs as a dark opaque core. Here, the assessment of the thermodynamic state based on the sole shadowgram bears a lot of uncertainties [158]. Experimentally, the occurrence of possible condensation processes was reported for the first time by Wu et al. [357, 358] who conducted a systematic study where supercritical ethylene was injected into nitrogen. The findings of Wu et al. [357] were later confirmed by Edwards et al. [71] by means of numerical simulations. Recently, Baab et al. [15] investigated underexpanded n-hexane jets by means of Elastic Light Scattering (ELS) and found phase separation effects. Based on a slight variation of the injection temperature of 3-4 K close to the critical temperature, Baab et al. [15] reported a change in the disintegration regime from near-critical flashing to gaseous jets with embedded fuel condensation. The latter effects were also reported by Fond et al. [79] who investigated extremely underexpanded argon jets using Mie scattering measurements. The authors detected bright regions upstream of the Mach disk and in the outer shear layer indicating a possible phase separation process.



p_t/p_c	1.17	1.29	1.38	1.16	1.15
p_t/p_{ch}	2.20	9.20	37.5	35.7	36.7
T_{inj}/T_c	1.46	1.46	1.46	1.23	1.03

(a) Pressure variation for $z_{CH_4} = 0.9$.(b) Temperature variation for $z_{CH_4} = 0.1$.

Figure 1.7: Shadowgraphies of methane/ethylene jets injected into a chamber filled with nitrogen: a) Variation of the NPR for a methane mole fraction of 90%; b) Variation of the injection temperature for a methane mole fraction of 10%. T_c and p_c are the respective critical mixture temperature and pressure. The images have been taken from the work of Lin et al. [170].

Numerical simulations

Over the past years, different groups have conducted numerical investigations to study the characteristics of underexpanded jets. Most of them neglected real-gas thermodynamics and therefore focused on the fluid dynamics aspects of the injection process: Yu et al. [365] investigated a pulsed underexpanded fuel jet in a combined experimental and numerical study. In their investigation, Yu et al. [365] applied PLIF in the experiment and compared the measurements with LESs. Overall, the LES was able to reproduce the basic physics of the underexpanded jet and showed good agreement with the experiment in terms of the shock structures. Using a similar configuration, Vuorinen et al. [343] investigated the effect of the NPR on the characteristics of underexpanded jets. Again, PLIF and LES were applied. Good agreement between numerical and experimental data in terms of the Mach disk dimensions and structures were found. In addition, the dependency of the Mach disk width on the NPR was studied and compared successfully with available data from the literature. Using probability density functions of the concentration, Vuorinen et al. [343] showed that the mixing of the fuel with the ambient gas improves with increasing NPR. Following the investigations of Vuorinen et al. [343], Hamzehloo and Aleiferis [108, 109, 111] conducted several investigations on underexpanded hydrogen and methane jets and studied the mixing process under engine-relevant conditions: In their first study, Hamzehloo and Aleiferis [108] reported that the main mixing was observed downstream of the Mach disk and particularly close to the jet boundaries. In their subsequent work [109], they extended their studies to elevated pressure conditions. For a constant NPR, they found that a higher ambient pressure resulted in a faster formation of the final Mach disk position. This effect was attributed to the faster establishment of the supersonic flow conditions inside the nozzle. In their most recent study, Hamzehloo and Aleiferis [111] applied both LES and Reynolds-Averaged Navier-Stokes (RANS) simulations and compared the results against various data from the literature. They concluded that the RANS approach is able to predict key characteristics of underexpanded jets and that penetration and spreading rates are similar to those found in the LES. Similar findings were reported by Gorlé and Ham [98] and Gorlé and Iaccarino [99].

One of the first numerical studies on underexpanded real-gas jets was published by Khalil and Miller [139] in 2004 who studied the expansion of an initially supercritical carbon dioxide jet. The authors applied the Redlich-Kwong [251] equation of state and reported not negligible deviations of the temperature between the ideal- and the real-gas closure. The most significant real-gas effects were found downstream of the Mach disk. In contrast, the position of the Mach disk as well as the minimum pressure were not greatly affected. For the investigation of underexpanded hydrogen jets, similar findings have been reported by Mohamed and Paraschivoiu [199], Cheng et al. [46], Khaksarfard et al. [138] and Bonelli et al. [39]. Recently, Hempert et al. [118] investigated underexpanded methane jets under real-gas conditions. Their comparison of the ideal- and the real-gas results showed unacceptable deviations between both closure models and hence the necessity to consider real-gas effects. Regarding numerical simulations focusing on phase separation processes in underexpanded jets only very little information is available in the literature. Lin et al. [169] compared their perfect gas simulation *a posteriori* to the VLE of the binary mixture and hereby discussed a possible occurrence of two-phase effects. As already mentioned, Edwards et al. [71] investigated the ethylene jets of Wu et al. [357] and confirmed the findings of the experiments.

1.5 Objectives and outline

Although there seems to be some evidence for the possible occurrence of phase separation processes during high-pressure injection, mixing and combustion there is no common agreement and understanding of these phenomena yet. The major reason is that under engine-relevant high-pressure conditions experiments and numerical simulations are still very challenging. To contribute to a better understanding the present work deals with the introduction and validation of a CFD tool which enables the numerical investigation of these processes under GE- and LRE-like conditions. Consequently, the tool has to be able to treat low- and high-speed flows, represent ideal- and real-gas effects and consider phase separation processes in multicomponent mixtures.

The work is structured as follows: In Sec. 2, the governing equations together with the turbulence modeling applied in the present work are introduced. Both LES and RANS turbulence closures are discussed in Secs. 2.3 and 2.4. The numerical methods applied in this work are presented in Sec. 3. In a first step, the underlying concept of the finite volume method and its realization in the CFD code are discussed in Sec. 3.1. After that, both a pressure- and a density-based solver approach are presented in Secs. 3.2 - 3.4. The thermodynamic closure is introduced in Sec. 4. This includes a fundamental introduction into real fluid thermodynamics in Secs. 4.1 - 4.5 followed by the discussion of the applied ideal- and real-gas models in Secs. 4.6 and 4.7. Based on that, the vapor-liquid equilibrium model is introduced in Sec. 4.8. Finally, in Sec. 4.9, important characteristics of multicomponent phase equilibria are discussed. In Sec. 5, the transcritical combustion model applied in the present work is introduced briefly. After that, the results are presented in the following three sections: First, real-gas effects and the possibility of phase separation in high-speed jets are assessed in Sec. 6. Second, mixture-induced phase separation under inert LRE-like conditions is investigated in Sec. 7. Third, the possibility of locally subcritical thermodynamic states in high-pressure combustion is discussed in Sec. 8. Finally, an overall summary and outlook to future work are given in Secs. 9 and 10, respectively.

2 Governing equations

Computational fluid dynamics relies on the description of the fluid motion by a set of nonlinear partial differential equations. Although gases and liquids have significantly different fluid properties, both obey the same law of motions and can be treated as a continuum under the conditions relevant for this thesis [75]. Applying the Eulerian approach, the flow at a fixed location may be described by the time history of the flow properties. The state at this fixed location can be changed by convection, diffusion and source/sink terms. In this chapter, the basics for the mathematical description of fluid motion are presented. The underlying conservation equations are introduced in Sec. 2.1. Next, the modeling ideas of turbulence are discussed in Sec. 2.2. In the following two Secs. 2.3 and 2.4, the turbulence modeling approaches in this work are described briefly.

2.1 Conservation equations

For a pure compressible fluid, the temporal change of the flow is governed by the conservation of mass, momentum and energy. In multicomponent flows, the set of conservation equations has to be supplemented by transport equations for the different species. In this work, nuclear fusion, radiation or volume forces like, for instance, gravitation are neglected. Einstein's summation convention is applied to present the conservation equations in a Cartesian coordinate system. A detailed derivation and discussion of these governing equations can be found in the textbooks of, e.g., Anderson [7], Blazek [37], Ferziger and Perić [75], Wesseling [348] or Kuo [146].

Conservation of mass

In all fluid systems considered in this work, mass is an extensive property which is conserved. Hence, mass can neither be created nor destroyed and the temporal change of mass inside a control volume equals the masses crossing the enclosing surfaces. In differential form, the mass conservation reads

$$\frac{\partial \rho}{\partial t} + \frac{\partial (\rho u_i)}{\partial x_i} = 0, \quad (2.1)$$

where ρ is the density, t is the time and u_i is the velocity in the direction x_i .

Conservation of momentum

The derivation of the momentum equation relies on Newton's second law which states that a variation of momentum of a material volume is caused by the net force acting on the volume. In the present work, the forces result from the pressure p and the deformation of the fluid element expressed by the viscous stress tensor τ . Applying these principles, the resulting differential equations describe the motion of a viscous fluid and are commonly referred to as Navier-Stokes equations:

$$\frac{\partial (\rho u_i)}{\partial t} + \frac{\partial (\rho u_i u_j)}{\partial x_j} = -\frac{\partial p}{\partial x_i} + \frac{\partial \tau_{ij}}{\partial x_j}. \quad (2.2)$$

For Newtonian fluids, the shear stress is proportional to the velocity gradient. Applying Stokes' hypothesis, the viscous stress tensor can be expressed as:

$$\tau_{ij} = 2\mu \left(S_{ij} - \frac{1}{3}\delta_{ij}S_{kk} \right). \quad (2.3)$$

Here, μ is the dynamic viscosity, S_{ij} is the rate of strain tensor

$$S_{ij} = \frac{1}{2} \left(\frac{\partial u_i}{\partial x_j} + \frac{\partial u_j}{\partial x_i} \right) \quad (2.4)$$

and δ_{ij} denotes the Kronecker delta which is one for $i = j$ and zero for $i \neq j$.

Conservation of energy

The first law of thermodynamics is the basis for the derivation of the energy conservation equation. The law states that energy can neither be created nor destroyed. Therefore, the total energy of an isolated system is constant and energy can be transformed from one form into another. As a result, the temporal variation of the energy in a control volume is caused by the work acting on the volume and the net heat fluxes. Different forms of the energy conservation equation exist [146, 236] since thermodynamic quantities can be converted into each other. In the present work, the conservation of energy is described in a form based on the static specific enthalpy h^1

$$\frac{\partial(\rho h)}{\partial t} + \frac{\partial(\rho u_i h)}{\partial x_i} = \frac{\partial p}{\partial t} + u_i \frac{\partial p}{\partial x_i} - \frac{\partial q_i}{\partial x_i} + \tau_{ij} \frac{\partial u_i}{\partial x_j}. \quad (2.5)$$

Here, q_i denotes the heat flux in the direction x_i which is in general caused by conduction, diffusion and Dufour effects [146]. The exact modeling of the heat flux in this work will be discussed after the introduction of the species transport equations. The fourth term on the right-hand side of Eq. (2.5), $\tau_{ij} \partial u_i / \partial x_j$, is the source term due to viscous heating and therefore describes the dissipation caused by viscous stresses.

Species transport equations

For the complete mathematical description of inert and reacting multicomponent flows, the mass, momentum and energy equations have to be supplemented with transport equations for the different species. In the present work, the number of species N_c ranges from a minimum of two for binary (inert) mixtures up to a maximum of 53 different species in methane/oxygen combustion for the largest reaction mechanism employed in the present work. The species transport equations are convection-diffusion equations describing the temporal variation of the mass fraction Y_k of component k in the flow field:

$$\frac{\partial(\rho Y_k)}{\partial t} + \frac{\partial(\rho u_i Y_k)}{\partial x_i} = -\frac{\partial j_{k,i}}{\partial x_i} + \dot{\omega}_k \quad k = 1, \dots, N_c. \quad (2.6)$$

The mass fraction Y_k represents the proportion of the species k in the total mixture and can therefore be calculated as:

$$Y_k = \frac{m_k}{m_t} = \frac{m_k}{\sum_{i=1}^{N_c} m_i} \quad k = 1, \dots, N_c. \quad (2.7)$$

Here, m_k and m_t denote the mass of component k and the total mass of the mixture, respectively. Per definition, the mass fractions of all components sum up to unity, i.e., $\sum_{i=1}^{N_c} Y_i = 1$, and therefore only $N_c - 1$ species transport equations have to be solved in the numerical simulation. In the species transport equation (2.6), $j_{k,i}$ denotes the flux due to diffusion and Soret effects into the direction x_i . Its mathematical modeling will be discussed in the next section together with the approach for the heat flux. The last term in Eq. (2.6), $\dot{\omega}_k$, represents the source term of species k due to reactions. Under inert flow conditions, $\dot{\omega}_k$ is zero as no chemical reactions take place. In reacting flows, the modeling of the chemical source term relies on suitable reaction mechanisms.

Modeling of the diffusive heat and species fluxes

For the modeling of the heat and species diffusion fluxes in Eqs. (2.5) and (2.6), approaches of different fidelity and complexity are available in the literature, see the textbooks of, for instance, Hirschfelder et al. [121] or Poling et al. [237]. To reduce the numerical effort to an acceptable level, a widely applied assumption in application-relevant numerical simulations is the neglect of Soret and Dufour effects. This is also done in the present work and could possibly lead to small errors under

¹The absolute enthalpy will be used exclusively in this work which is the sum of the sensible enthalpy and the enthalpy of formation. As a result, the energy conservation equation does not include a heat release term due to reactions, see, e.g., Poinsot and Veynante [236]. This fact is advantageous for the derivation and formulation of the applied combustion model. In nonreacting flows, the application of the absolute enthalpy has no big advantages except for the fact that the absolute enthalpy approach is slightly more efficient in terms of computing time.

high-pressure conditions depending on the investigated configuration. For a reacting LOx/H₂ case under supercritical pressure conditions, Oefelein [215] showed that both effects (Soret and Dufour) are negligible. In contrast, investigations from the group of Bellan [217, 93] demonstrate that in inert mixing processes the Soret effect might not be negligible. However, the investigations also showed that the diffusion flux due to the species gradient is dominating by far. Based on the DNS results of a binary nitrogen/carbon-dioxide jet, Gnanaskandan and Bellan [93] reported that the Soret term is approximately two orders of magnitude smaller than the mass fraction gradient term.

Neglecting Dufour and Soret effects, the diffusion fluxes of heat and species can be written in the following general form according to Gaillard et al. [87, 92]:

$$j_{k,i} = - \sum_{j=1}^{N_c} \rho Y_k D_{kj} \mathcal{d}_{j,i} \quad k = 1, \dots, N_c , \quad (2.8)$$

$$q_i = -\lambda \frac{\partial T}{\partial x_i} + \sum_{k=1}^{N_c} h_k j_{k,i} . \quad (2.9)$$

Here, D_{ij} is the multicomponent diffusion coefficient, which is generally a function of temperature, pressure and composition. Furthermore, $\mathcal{d}_{j,i}$ is the diffusion driving force of the j -th species in the direction x_i , λ is the thermal conductivity, T is the temperature and h_k is the partial enthalpy of species k . For moderate temperature gradients, the diffusion driving force is proportional to the gradient of the normalized chemical potential of component i , μ_i^* , under isothermal conditions

$$\mathcal{d}_{j,i} = z_j \left. \frac{\partial \mu_j^*}{\partial x_i} \right|_T , \quad (2.10)$$

where z_j is the mole fraction of the j -th species. In accordance to the mass fraction definition in Eq. (2.7), the mole fraction describes the amount of a constituent denoted by its mole number n_i in the total mixture n_t :

$$z_i = \frac{n_i}{n_t} = \frac{n_i}{\sum_{j=1}^{N_c} n_j} . \quad (2.11)$$

Per definition, all mole fractions in a mixture sum up to unity, i.e., $\sum_{i=1}^{N_c} z_i = 1$. Furthermore, mass and mole fractions can be converted into each other as

$$Y_i = \frac{M_i}{M} z_i \quad i = 1, \dots, N_c , \quad (2.12)$$

where M_i and M are the molar weights of species i and the mixture, respectively. The molar weight of the mixture can be calculated as a weighted sum, i.e.,

$$M = \sum_{i=1}^{N_c} z_i M_i . \quad (2.13)$$

The chemical potential is closely related to phase separation processes. According to Gaillard et al. [87], in the low Mach number limit, i.e., $dp = 0$, the diffusion driving force can be further simplified to

$$\mathcal{d}_{j,i} = z_j \left. \frac{\partial \mu_j^*}{\partial x_i} \right|_{T,p} = \sum_{k=1}^{N_c} \left(\frac{Y_j M}{\mathcal{R} T} \frac{\partial^2 g}{\partial Y_j \partial Y_k} \Big|_{T,p} \frac{\partial Y_k}{\partial x_i} \right) . \quad (2.14)$$

Here, g is the specific (mass-related) Gibbs energy and \mathcal{R} is the universal gas constant which has a value of $8.314472 \text{ J}(\text{mol K})^{-1}$. Applying nonideal Stefan-Maxwell relations and assuming a binary mixture, the diffusion flux vector of component 1 can be determined as [87]

$$j_{1,i} = -\rho \Gamma D_{12} \frac{\partial Y_1}{\partial x_i} , \quad (2.15)$$

where the mass-based coefficient Γ is expressed as

$$\Gamma = -\frac{\partial^2 g}{\partial Y_1 \partial Y_2} \Big|_{T,p} \frac{M_1 M_2}{M \mathcal{R} T} . \quad (2.16)$$

Therefore, under nonideal conditions, the diffusion flux vector \mathbf{j}_k is proportional to the second derivative of the Gibbs energy. This derivative is again closely related to phase separation processes as it is linked to the limit of spinodal decomposition: $\Gamma = 0$ [87]. Thermodynamic stability therefore holds if and only if $\Gamma > 0$. Moreover, the diffusion process vanishes at the chemical stability limit $\Gamma = 0$ and leads to nonmixing layers [87].

In the present work, nonideal mixing phenomena for the modeling of the diffusion fluxes are neglected. Nevertheless, the knowledge about the proportionality between the diffusion process and the partial derivatives of the Gibbs energy is essential for future investigations as more detailed simulations, e.g., DNS, demands for more accurate modeling approaches. Under ideal diffusion conditions, the species diffusion fluxes can be modeled based on Fick's law:

$$j_{k,i} = -\rho D \frac{\partial Y_k}{\partial x_i} \quad k = 1, \dots, N_c . \quad (2.17)$$

Here, the driving force for the diffusion process is the gradient of the mass fraction. A mean diffusion coefficient D for all species is assumed. The diffusion coefficient is deduced from the assumption of a unitary Lewis number Le which is defined as

$$Le = \frac{\lambda}{\rho c_p D} , \quad (2.18)$$

where c_p denotes the specific heat at constant pressure. This assumption is also applied in the flamelet approach which is the basis for the tabulated combustion model in this work. Recent investigations [370] on methane/oxygen combustion show that this assumption is acceptable for rocket-relevant conditions. However, when the molar weights of the species differ too much from each other, for instance in hydrogen/oxygen flames, this assumption may lead to inaccuracies, see, e.g., Pohl et al. [235]. Recently, Yao et al. [364] investigated the influence of different diffusion models on the prediction of single-phase instabilities in high-pressure flames. No significant effects were reported making the unity Lewis number approach an appropriate choice for the present investigations.

Applying the unitary Lewis number assumption to the formulation of the diffusive heat flux according to Eq. (2.9), an enthalpy-based formulation can be derived. The basis for this derivation is the total differential of the specific enthalpy. In a general multicomponent fluid, the enthalpy is a function of pressure, temperature and composition, i.e., $h = h(p, T, \mathbf{Y})$, where $\mathbf{Y} = [Y_1, \dots, Y_{N_c}]$ denotes the vector of mass fractions. Therefore, the spatial derivative of the specific enthalpy can be written as:

$$\begin{aligned} \frac{\partial h}{\partial x_i} &= \frac{\partial h}{\partial T} \Big|_{p, \mathbf{Y}} \frac{\partial T}{\partial x_i} + \frac{\partial h}{\partial p} \Big|_{T, \mathbf{Y}} \frac{\partial p}{\partial x_i} + \sum_{j=1}^{N_c} \frac{\partial h}{\partial Y_j} \Big|_{T, p, Y_{k \neq j}} \frac{\partial Y_j}{\partial x_i} \\ &= c_p \frac{\partial T}{\partial x_i} + \frac{\partial h}{\partial p} \Big|_{T, \mathbf{Y}} \frac{\partial p}{\partial x_i} + \sum_{j=1}^{N_c} h_j \frac{\partial Y_j}{\partial x_i} . \end{aligned} \quad (2.19)$$

Applying this total derivative together with Fick's law from Eq. (2.17) and the unitary Lewis number assumption to Eq. (2.9) yields:

$$q_i = -\frac{\lambda}{c_p} \left(\frac{\partial h}{\partial x_i} - \frac{\partial h}{\partial p} \Big|_{T, \mathbf{Y}} \frac{\partial p}{\partial x_i} \right) . \quad (2.20)$$

In the low Mach number regime, contributions due to pressure changes to the heat flux are usually negligible and therefore the diffusive heat flux under subsonic flow conditions is modeled as

$$q_i = -\frac{\lambda}{c_p} \frac{\partial h}{\partial x_i}. \quad (2.21)$$

This approach is well-known from ideal-gas simulations where the enthalpy is solely a function of temperature and composition. The enthalpy-based formulation of the heat flux is beneficial for the solver stability as the divergence of the heat flux vector can be handled implicitly.

2.2 Turbulence modeling

Under engineering-relevant conditions, most flows are turbulent. First scientific studies on turbulence date back to the work of Osborne Reynolds in the 19th century. By means of experimental investigations, Reynolds demonstrated the transition between the laminar and the turbulent flow regime. Based on his observations, Reynolds suggested that this transition is directly linked to the ratio between inertial and viscous forces. This ratio was later termed Reynolds number

$$\text{Re} = \frac{\rho u L}{\mu}, \quad (2.22)$$

where L denotes the characteristic length of the flow. In engineering applications, like it is the case in the present work, the Reynolds number is in the order of $\mathcal{O}(10^5)$ or even higher. Therefore, the flow is prevalently turbulent as the nonlinear convective term by far exceeds the linear viscous term. An advantage of turbulent flows compared to laminar flows is the more efficient transport and mixing of the different fluids [238] which is desired in most technical applications.

In general, the motion of the fluid in a turbulent flow is three-dimensional, transient, irregular, random and chaotic. Turbulence can be seen as a composite of a large collection of mutually interacting and continuously evolving three-dimensional eddies which size range typically covers several orders of magnitude. This process can be described mathematically in terms of an energy spectrum ε being a function of the wave number $\mathcal{K} = 2\pi/\mathcal{L}$, where \mathcal{L} is the length scale of the motion. In Fig. 2.1, the energy cascade for isotropic turbulence at a representative Reynolds number $\text{Re} = 2.15 \times 10^5$ is shown. This so-called Kolmogorov spectrum illustrates the transfer

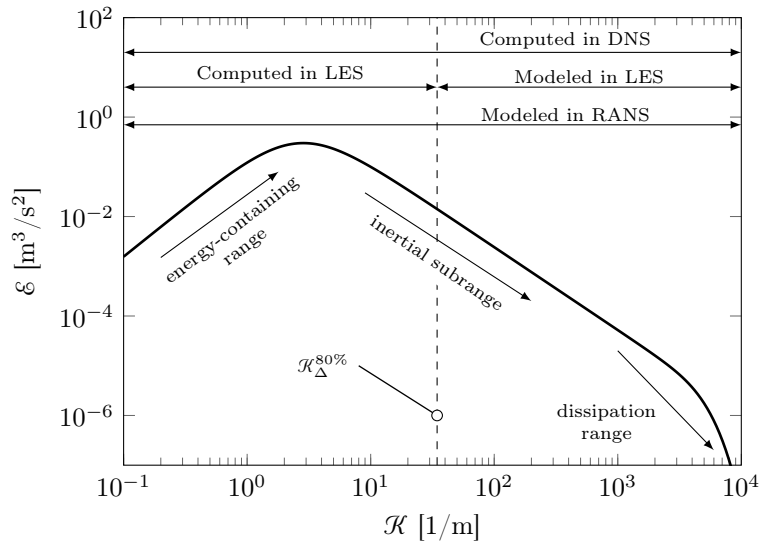


Figure 2.1: Energy spectrum of isotropic turbulence for $\text{Re} = 2.15 \times 10^5$ according to Pope [238]. The dashed line shows the 80% criteria $\mathcal{K}_\Delta^{80\%}$ for the LES resolution. In addition, computed and modeled wave number ranges in DNS, LES and RANS are shown (adopted from Poinsot et al. [236]).

of energy from large scales of motion to the small scales. The cascade can be divided into three sections: the energy-containing range, the inertial subrange and the dissipation range. On the largest scales (associated with the smallest wave numbers), the kinetic energy is extracted from the mean flow and therefore the biggest amount of energy is contained in the large eddies (energy-containing range). The size of these eddies is determined by the dimensions of the investigated geometry, for instance, the pipe diameter. In the inertial subrange, the energy spectrum is described by Kolmogorov's scaling law [238] $\mathcal{E}(\mathcal{K}) \propto \mathcal{K}^{-5/3}$. This is the wave number range, where energy is transferred from the larger scale eddies to the smaller eddies. The largest wave numbers of the cascade are associated with length scales smaller than the Kolmogorov length scale. This is the dissipation range in which most kinetic energy is dissipated due to viscous friction.

The most general way to simulate turbulent flows is to directly solve the conservation equations introduced in Sec. 2.1 without any averaging or approximation other than numerical discretization approaches [75]. Therefore, all motions present throughout the flow are represented. This approach is called Direct Numerical Simulation and covers the complete energy spectrum, see Fig. 2.1. Currently, the application of DNS is mostly limited to generic academic investigations like binary mixing layers, see, e.g., Bellan [29], as DNS is usually not affordable in most engineering applications. This results from the fact that the mesh size needed for a sufficient spatial resolution of all turbulent motions scales as $\text{Re}^{9/4}$ and the computing time as Re^3 [37]. In practical applications, the effects of turbulence have to be accounted for in an approximated manner by means of suitable modeling approaches. In the following, the two approaches applied in the current work – Large-Eddy Simulation (Sec. 2.3) and Reynolds-Averaged Navier-Stokes simulation (Sec. 2.4) – are introduced.

2.3 Large-Eddy Simulation

The concept of Large-Eddy Simulation is based on the idea that specific length scales of the energy cascade are discarded to reduce the range of scales that are resolved by the numerical simulation. This approach relies on Kolmogorov's hypothesis according to which large eddies are anisotropic and characterized by the boundary conditions, whereas small eddies are isotropic and universal [83, 88]. Therefore, the basic idea of the LES reduces to a scale separation. Large scales are resolved on the computational grid (grid scale) and the unresolved small scales are modeled (sub-grid scale) [83], see Fig. 2.1.

Mathematically, the scale separation is realized by means of a filtering approach using a high-pass filter which is also a low-pass filter in the wave number domain [88]. In physical space, the filtering operation is represented by a convolution product with the filter kernel \mathcal{G} [83, 236]

$$\bar{\xi}(x_i) = \int \xi(\zeta_i) \mathcal{G}(x_i - \zeta_i) d\zeta_i, \quad (2.23)$$

where $\bar{\xi}$ denotes the resolved part of the component ξ and ζ_i is the Cartesian integration variable. Different filter kernels can be used to perform the desired scale separation and a thorough discussion on this topic can be found in the textbooks of, e.g., Fröhlich [83] or Garnier et al. [88]. In the present work, the filter kernel corresponds to a box/top hat filter which can be denoted as [236]

$$\mathcal{G}(x_i) = \begin{cases} 1/\Delta^3, & \text{if } |x_i| \leq \Delta/2, i = 1, 2, 3 \\ 0, & \text{otherwise.} \end{cases} \quad (2.24)$$

According to Pope [238], Δ should be chosen such that 80% of the turbulent kinetic energy is resolved. In Fig. 2.1, the vertical dashed line $\mathcal{K}_\Delta^{80\%}$ marks the appropriate scale separation in the frequency domain for a Reynolds number $\text{Re} = 2.15 \times 10^5$.

In variable-density flows, it is advantageous to apply Favre-averaging to the different components. Favre-averaging is a density-weighted approach which does not produce undesired additional filtering terms in the governing equations and can be introduced according to Eq. (2.23) as [236]:

$$\tilde{\rho\xi} = \int \rho \xi(\zeta_i) \mathcal{G}(x_i - \zeta_i) d\zeta_i. \quad (2.25)$$

As a result of the filtering operation, an arbitrary quantity $\xi(x_i, t)$ of the flow field is decomposed into a low frequency part $\tilde{\xi}$ and a high frequency part ξ'' [88]:

$$\xi(x_i, t) = \tilde{\xi}(x_i, t) + \xi''(x_i, t) . \quad (2.26)$$

Here, $\tilde{\xi}$ is the Favre-average according to

$$\tilde{\xi} = \frac{\overline{\rho\xi}}{\bar{\rho}} \quad (2.27)$$

which represents the resolved part of the flow and covers all length scales being larger than the selected filter width Δ . The high frequency part ξ'' , which is not resolved on the grid, has to be modeled by a suitable sub-grid scale (SGS) model. In the following, the filtered equations and the applied SGS-models are introduced. More information on the concept of Large-Eddy Simulations can be found in the textbooks of, for instance, Fröhlich [83], Garnier et al. [88] or Sagaut [270].

2.3.1 Filtered equations

Based on the idea of scale separation, the filtered quantities are directly solved in the LES. Applying the Favre-averaging according to Eq. (2.27) to the low Mach number conservation equations (neglecting viscous heating and pressure contributions to the heat flux) yields the following set of filtered equations [236]:

$$\frac{\partial \bar{\rho}}{\partial t} + \frac{\partial(\bar{\rho}\tilde{u}_i)}{\partial x_i} = 0 , \quad (2.28)$$

$$\frac{\partial(\bar{\rho}\tilde{u}_i)}{\partial t} + \frac{\partial(\bar{\rho}\tilde{u}_i\tilde{u}_j)}{\partial x_j} = -\frac{\partial \bar{p}}{\partial x_i} + \frac{\partial[\bar{\tau}_{ij} - \bar{\rho}(\widetilde{u_i u_j} - \tilde{u}_i \tilde{u}_j)]}{\partial x_j} , \quad (2.29)$$

$$\frac{\partial(\bar{\rho}\tilde{h})}{\partial t} + \frac{\partial(\bar{\rho}\tilde{u}_i\tilde{h})}{\partial x_i} = \frac{\partial \bar{p}}{\partial t} + \overline{u_i \frac{\partial p}{\partial x_i}} + \frac{\partial}{\partial x_i} \left[\frac{\lambda}{c_p} \overline{\frac{\partial h}{\partial x_i}} - \bar{\rho} (\widetilde{u_i h} - \tilde{u}_i \tilde{h}) \right] , \quad (2.30)$$

$$\frac{\partial(\bar{\rho}\tilde{Y}_k)}{\partial t} + \frac{\partial(\bar{\rho}\tilde{u}_i\tilde{Y}_k)}{\partial x_i} = \frac{\partial}{\partial x_i} \left[\overline{\rho D \frac{\partial Y_k}{\partial x_i}} - \bar{\rho} (\widetilde{u_i Y_k} - \tilde{u}_i \tilde{Y}_k) \right] + \bar{\omega}_k \quad k = 1, \dots, N_c . \quad (2.31)$$

In accordance to Eqs. (2.3) and (2.4), the resolved part of the viscous stress tensor in Eq. (2.29) is modeled as:

$$\bar{\tau}_{ij} = \bar{\mu} \left(\frac{\partial \tilde{u}_i}{\partial x_j} + \frac{\partial \tilde{u}_j}{\partial x_i} - \frac{2}{3} \frac{\partial \tilde{u}_k}{\partial x_k} \delta_{ij} \right) . \quad (2.32)$$

Furthermore, the pressure velocity term in the filtered energy conservation equation (2.30) is approximated as [236]

$$\overline{u_i \frac{\partial p}{\partial x_i}} \approx \tilde{u}_i \frac{\partial \bar{p}}{\partial x_i} . \quad (2.33)$$

The filtered laminar diffusion fluxes in Eqs. (2.30) and (2.31) are modeled based on the gradient assumption [236]:

$$\frac{\lambda}{c_p} \overline{\frac{\partial h}{\partial x_i}} \approx \frac{\lambda}{c_p} \overline{\frac{\partial \tilde{h}}{\partial x_i}} \quad \text{and} \quad \overline{\rho D \frac{\partial Y_k}{\partial x_i}} \approx \bar{\rho} \overline{D} \frac{\partial \tilde{Y}_k}{\partial x_i} . \quad (2.34)$$

Due to the nonlinear convective terms in the momentum, energy and species equations, additional unresolved terms occur on the right-hand side. These terms represent the effect of the unresolved scales on the filtered flow properties. In the momentum equation (2.29), these terms can be interpreted as a turbulent stress tensor

$$\tau_{ij}^{\text{sgs}} = \bar{\rho} (\widetilde{u_i u_j} - \tilde{u}_i \tilde{u}_j) . \quad (2.35)$$

In the same way, the unresolved terms in the energy and species equations can be aggregated to a turbulent heat flux

$$q_i^{\text{sgs}} = \bar{\rho} (\widetilde{u_i h} - \tilde{u}_i \tilde{h}) \quad (2.36)$$

and a turbulent flux of the k -th species

$$j_{k,i}^{\text{sgs}} = \bar{\rho} \left(\widetilde{u_i Y_k} - \tilde{u}_i \tilde{Y}_k \right). \quad (2.37)$$

Here, the superscript sgs is used to distinguish the unresolved sub-grid scale part from its resolved counter-part. To model the unresolved terms, suitable modeling approaches are necessary.

In the species transport equation (2.31), the last term on the right hand-side denotes the filtered reaction rate $\bar{\omega}_k$ of component k . This term has to be modeled as the combustion process takes places on the smallest scales which are, as a result of the scale separation, cut-off in the LES. The demands on the determination of $\bar{\omega}_k$ are quite intense, as the combustion closure has to reflect the complex turbulence-chemistry interaction happening on the sub-grid scale level.

2.3.2 Sub-grid scale models

The unresolved SGS terms summarized in Eqs. (2.35) - (2.37) need to be modeled appropriately to represent the influence of the small scale motions onto the mean flow. The big advantage of Large-Eddy Simulations is that the small eddies are isotropic and universal. Therefore, the modeling of the unresolved terms is rather simple compared to Reynolds-Averaged Navier-Stokes simulations. In the RANS context, the entire range of turbulent scales has to be assimilated into a statistical approach. In the following, only the modeling approaches applied in the LESs in the present work are introduced. A more thorough discussion and introduction of SGS modeling in the context of Large-Eddy Simulations can be found in the textbooks of, for instance, Fröhlich [83], Pope [238] or Garnier et al. [88].

The applied SGS models are based on the eddy viscosity concept which was proposed by Boussinesq in the 19th century. The Boussinesq approximation relates the turbulent unresolved stress tensor τ_{ij}^{sgs} to the mean flow and introduces an eddy viscosity μ^{sgs} in analogy to the laminar Stokes' hypothesis:

$$\tau_{ij}^{\text{sgs}} = -2\mu^{\text{sgs}} \left(\tilde{S}_{ij} - \frac{1}{3} \tilde{S}_{kk} \delta_{ij} \right). \quad (2.38)$$

The eddy viscosity model assumes that turbulence is isotropic which agrees with the basic modeling idea of the LES. Due to the relation of the turbulent unresolved stresses to the rate of strain tensor based on the filtered velocity field, only the eddy viscosity has to be modeled. A similar approach can be applied to model the unresolved turbulent heat and species fluxes. The concept is termed gradient-diffusion hypothesis [238] and treats the turbulent fluxes analogously to their laminar counter-parts. After introducing the turbulent Prandtl number

$$\text{Pr}_t = \frac{\mu^{\text{sgs}} c_p}{\lambda^{\text{sgs}}} \quad (2.39)$$

and the turbulent Schmidt number

$$\text{Sc}_t = \frac{\mu^{\text{sgs}}}{\rho D^{\text{sgs}}} \quad (2.40)$$

in accordance to their laminar definitions, the unresolved turbulent heat and species fluxes can be expressed as:

$$q_i^{\text{sgs}} = -\frac{\lambda^{\text{sgs}}}{c_p} \frac{\partial \tilde{h}}{\partial x_i} = -\frac{\mu^{\text{sgs}}}{\text{Pr}_t} \frac{\partial \tilde{h}}{\partial x_i}, \quad (2.41)$$

$$j_{k,i}^{\text{sgs}} = -\bar{\rho} D^{\text{sgs}} \frac{\partial \tilde{Y}_k}{\partial x_i} = -\frac{\mu^{\text{sgs}}}{\text{Sc}_t} \frac{\partial \tilde{Y}_k}{\partial x_i}. \quad (2.42)$$

A species-independent turbulent diffusion coefficient D^{sgs} is applied as proportionality constant in the unresolved species fluxes. Therefore, only a single turbulent Schmidt number is necessary in the simulations. If not stated differently, a turbulent Schmidt and Prandtl number of unity will be used in the simulations, i.e., $\text{Sc}_t = \text{Pr}_t = 1$ which yields a unity turbulent Lewis number $\text{Le}_t = \text{Sc}_t/\text{Pr}_t = 1$. Comparing Eqs. (2.38) - (2.42) it gets obvious that all quantities except the eddy viscosity μ^{sgs} can be extracted from the resolved mean flow. In the present work, three different

eddy viscosity models are employed which can be expressed in the following general form [161]:

$$\mu^{\text{sgs}} = \bar{\rho} (C\Delta)^2 OP . \quad (2.43)$$

Here, C is a constant, Δ is the filter width and OP is an appropriate generic operator which relates the eddy viscosity to the filtered flow field. The filter width Δ is determined based on the cell volume Ω as $\Delta = \sqrt[3]{\Omega}$.

Smagorinsky model

The SGS model due to Smagorinsky [295] is the most common one and can be considered the pioneer sub-grid scale model for LES. The model is based on the equilibrium hypothesis which implies that the small scales of motion dissipate all the energy which they receive from the large scales [37]. According to Smagorinsky [295], the eddy viscosity can be computed as:

$$\mu^{\text{sgs}} = \bar{\rho} (C_S \Delta)^2 \sqrt{2 \tilde{S}_{ij} \tilde{S}_{ij}} . \quad (2.44)$$

Here, C_S is the Smagorinsky constant, which can take values between 0.1 and 0.2 depending on the investigated flow [88]. The theoretical value found by Lilly [168] is $C_S = 0.18$. This value is based on the assumption of a local equilibrium and a Kolmogorov spectrum together with a Kolmogorov constant of 1.4 [88]. In the present work, a Smagorinsky constant of 0.17 is used.

Vreman model

For combustion simulations, the sub-grid model due to Vreman [341] is applied following the work of Müller [202] and Zips et al. [368]. The Vreman model [341] is similarly compact as the approach of Samogrinsky [295] since it only needs the local filter width and the spatial derivatives of the velocity field. The algebraic equation to determine the eddy viscosity according to Vreman [341] reads

$$\mu^{\text{sgs}} = \bar{\rho} C_V \sqrt{\frac{B_\beta}{\alpha_{ij} \alpha_{ij}}} . \quad (2.45)$$

Here, C_V denotes the model constant which can be deduced from isotropic turbulence as $C_V \approx 2.5 C_S^2 = 0.07$. The other variables occurring in Eq. (2.45) can be determined from the filtered velocity field as follows:

$$B_\beta = \beta_{11}\beta_{22} - \beta_{12}^2 + \beta_{11}\beta_{33} - \beta_{13}^2 + \beta_{22}\beta_{33} - \beta_{23}^2 , \quad \beta_{ij} = \Delta^2 \alpha_{ki} \alpha_{kj} \quad \text{and} \quad \alpha_{ij} = \frac{\partial \tilde{u}_j}{\partial x_i} . \quad (2.46)$$

The advantage of the Vreman model [341] is that it is more favorable in laminar and transitional flows as the predicted dissipation is smaller in these regions compared to the model of Smagorinsky [295].

WALE model

The third SGS model used in this work is the Wall-Adapting Local Eddy-viscosity (WALE) model due to Nicoud and Ducros [211]. Following the work of Hamzehloo and Aleiferis [109, 110], this eddy viscosity approach is used in the simulation of high-speed jets for two reasons: First of all, the WALE model produces zero eddy viscosity in pure shear flows making it capable of reproducing turbulent transitional processes more accurately through the growth of unstable modes [211]. Second, for near-wall flows, it predicts the correct behavior of the turbulent viscosity. In the WALE model [211], μ^{sgs} is determined as:

$$\mu^{\text{sgs}} = \bar{\rho} (C_W \Delta)^2 \frac{\left(\tilde{S}_{ij}^d \tilde{S}_{ij}^d \right)^{2/3}}{\left(\tilde{S}_{ij} \tilde{S}_{ij} \right)^{5/2} + \left(\tilde{S}_{ij}^d \tilde{S}_{ij}^d \right)^{5/4}} . \quad (2.47)$$

Here, the eddy viscosity is proportional to the traceless symmetric part of the square of the velocity gradient tensor \tilde{S}_{ij}^d which can be calculated from the filtered velocity field as [161]

$$\tilde{S}_{ij}^d = \frac{1}{2} (\tilde{g}_{ij}^2 + \tilde{g}_{ji}^2) - \frac{1}{3} \tilde{g}_{kk}^2 \delta_{ij} \quad \text{with} \quad \tilde{g}_{ij} = \frac{\partial \tilde{u}_i}{\partial x_j}. \quad (2.48)$$

Furthermore, C_W is a model constant which Nicoud and Ducros [211] reported to be in the range of $0.55 \leq C_W \leq 0.60$ for homogeneous turbulence. More recent investigations [313] suggest a constant value of 0.325, which was also employed in the present work.

2.4 Reynolds-Averaged Navier-Stokes simulation

In RANS simulations, the complete turbulence spectrum has to be modeled and the solution of the filtered governing equations yields the mean flow field. This is in strong contrast to the LES approach where the mean of the fluctuating quantities does not vanish. In accordance to the LES, however, it is likewise advisable to apply Favre-averaging for the derivation of the filtered equations to avoid additional unclosed terms [146, 236]. As only the mean field is solved for in the RANS simulations, symmetries of the investigated geometries can be used. Therefore, the required computational power can be reduced drastically compared to LESs where the full geometry has to be taken into account. In the following, the applied RANS approach is introduced briefly including the filtered equations and the employed turbulence model. For a more thorough introduction and discussion of the RANS approach it is referred to the textbooks of, e.g., Kuo [146], Poinsot and Veynante [236] or Wilcox [351].

2.4.1 Filtered equations

Using the Favre-averaging, every component ξ of the flow field is split into a mean and a fluctuating part $\xi = \tilde{\xi} + \xi''$ whereby in the context of RANS simulations the mean of the fluctuation vanishes, i.e., $\xi'' = 0$. Applying this formalism to the inert conservation equations of mass, momentum, energy and species yields the following set of filtered equations [236]:

$$\frac{\partial \bar{\rho}}{\partial t} + \frac{\partial(\bar{\rho}\tilde{u}_i)}{\partial x_i} = 0, \quad (2.49)$$

$$\frac{\partial(\bar{\rho}\tilde{u}_i)}{\partial t} + \frac{\partial(\bar{\rho}\tilde{u}_i\tilde{u}_j)}{\partial x_j} = -\frac{\partial \bar{p}}{\partial x_i} + \frac{\partial(\bar{\tau}_{ij} - \bar{\rho}\widetilde{u''_i u''_j})}{\partial x_j}, \quad (2.50)$$

$$\frac{\partial(\bar{\rho}\tilde{h})}{\partial t} + \frac{\partial(\bar{\rho}\tilde{u}_i\tilde{h})}{\partial x_i} = \frac{\partial \bar{p}}{\partial t} + \overline{u_i \frac{\partial p}{\partial x_i}} + \frac{\partial}{\partial x_i} \left(\frac{\lambda}{c_p} \frac{\partial h}{\partial x_i} - \bar{\rho}\widetilde{u''_i h''} \right), \quad (2.51)$$

$$\frac{\partial(\bar{\rho}\tilde{Y}_k)}{\partial t} + \frac{\partial(\bar{\rho}\tilde{u}_i\tilde{Y}_k)}{\partial x_i} = \frac{\partial}{\partial x_i} \left(\rho D \frac{\partial Y_k}{\partial x_i} - \bar{\rho}\widetilde{u''_i Y''_k} \right) \quad k = 1, \dots, N_c. \quad (2.52)$$

Viscous heating and pressure contributions to the heat flux are neglected. In accordance with the LES, the stress tensor, the pressure velocity term and the laminar diffusion fluxes are modeled as follows [236]:

$$\bar{\tau}_{ij} = \bar{\mu} \left(\frac{\partial \tilde{u}_i}{\partial x_j} + \frac{\partial \tilde{u}_j}{\partial x_i} - \frac{2}{3} \frac{\partial \tilde{u}_k}{\partial x_k} \delta_{ij} \right), \quad \overline{u_i \frac{\partial p}{\partial x_i}} \approx \tilde{u}_i \frac{\partial \bar{p}}{\partial x_i}, \quad \overline{\frac{\lambda}{c_p} \frac{\partial h}{\partial x_i}} \approx \frac{\bar{\lambda}}{c_p} \frac{\partial \tilde{h}}{\partial x_i} \quad \text{and} \quad \overline{\rho D \frac{\partial Y_k}{\partial x_i}} \approx \bar{\rho} \bar{D} \frac{\partial \tilde{Y}_k}{\partial x_i}.$$

Three unclosed terms are remaining in the Favre-averaged conservation equations: the Reynolds stresses $\bar{\rho}\widetilde{u''_i u''_j}$ and the turbulent fluxes of the enthalpy $\bar{\rho}\widetilde{u''_i h''}$ and of the species $\bar{\rho}\widetilde{u''_i Y''_k}$. For the modeling of these terms, the Boussinesq approximation and the gradient-diffusion hypothesis [238] are applied:

$$\bar{\rho}\widetilde{u''_i u''_j} = -2\mu_t \left(\tilde{S}_{ij} - \frac{1}{3} \tilde{S}_{kk} \delta_{ij} \right), \quad (2.53)$$

$$\widetilde{\rho u_i'' h''} = -\frac{\mu_t}{\text{Pr}_t} \frac{\partial \tilde{h}}{\partial x_i}, \quad (2.54)$$

$$\widetilde{\rho u_i'' Y_k''} = -\frac{\mu_t}{\text{Sc}_t} \frac{\partial \tilde{Y}_k}{\partial x_i}. \quad (2.55)$$

Please note in Eq. (2.53) that the contribution due to the turbulent kinetic energy k is missing. In the applied open-source CFD tool OpenFOAM, this part is absorbed into the mean pressure to be able to treat LES and RANS formally identical which reduces the programming effort. For a more thorough discussion on this topic see, e.g., Pope [238] or Holzmann [122]. Furthermore it is noteworthy, that in Eqs. (2.54) and (2.55) the definitions of the turbulent Prandtl and Schmidt number are identical to the definitions in the LES, see Eqs. (2.39) and (2.40). Only the superscript sgs is replaced with a subscript t, which denotes the turbulent properties in the RANS context and therefore clearly distinguishes between sub-grid scale modeling in the LES and full turbulence modeling in the RANS simulation.

2.4.2 Turbulence model

In RANS simulations, the entire range of turbulent scales has to be assimilated by a model that is able to represent the effect of turbulence onto the mean flow. As the Boussinesq approximation is used in this thesis, three different types of turbulence models are generally available: algebraic, one- or two-equation models. An overview on the wide field of different models can be found in the works of, for instance, Leschziner [166] or Wilcox [351].

In the present work, the k,ω Shear Stress Transport (SST) model due to Menter [191, 192, 193] is employed which belongs to the class of two-equation eddy viscosity models. The k,ω -SST-model combines the k,ω -model of Wilcox [351] with the k,ϵ -model of Jones and Launder [132]. The former is advantageous in the boundary layer and the latter in the free shear flow making the k,ω -SST-model a universal turbulence model for a large number of different flow and boundary conditions. The variables k , ω and ϵ denote the turbulent kinetic energy, the specific rate of dissipation and the dissipation rate of the turbulent kinetic energy, respectively. These quantities can be related to each other as

$$\omega = \frac{\epsilon}{C_\mu k} = \frac{\epsilon}{\beta^* k} \quad (2.56)$$

and represent the length and time scales of the turbulence. Here, $C_\mu = 0.09$ is a constant which is used in the k,ω -model and k,ϵ -model. In the k,ω -SST-model, C_μ is replaced by β^* .

According to Menter [191, 192, 193], the two differential equations for k and ω solved in the k,ω -SST-model read:

$$\frac{\partial(\bar{\rho}k)}{\partial t} + \frac{\partial(\bar{\rho}\tilde{u}_i k)}{\partial x_i} = \mathcal{P}_k + \frac{\partial}{\partial x_i} \left[(\bar{\mu} + \sigma_k \mu_t) \frac{\partial k}{\partial x_i} \right] - \bar{\rho} \beta^* k \omega, \quad (2.57)$$

$$\frac{\partial(\bar{\rho}\omega)}{\partial t} + \frac{\partial(\bar{\rho}\tilde{u}_i \omega)}{\partial x_i} = \alpha \mathcal{P}_\omega + \frac{\partial}{\partial x_i} \left[(\bar{\mu} + \sigma_\omega \mu_t) \frac{\partial \omega}{\partial x_i} \right] - \beta \omega^2 + 2\bar{\rho}(1 - F_1) \sigma_\omega^2 \frac{1}{\omega} \frac{\partial k}{\partial x_i} \frac{\partial \omega}{\partial x_i}. \quad (2.58)$$

The partial differential equations of k and ω include production, transport (convection and diffusion) and dissipation terms. The temporal variation of k and ω together with the convective transport are on the left-hand side of Eqs. (2.57) and (2.58), whereby the other terms (production, diffusion and dissipation) are on the right-hand side.

In Eq. (2.57), \mathcal{P}_k denotes the production of turbulent kinetic energy. The mathematical formulation of this production term features a limiter to avoid the build-up of turbulence in stagnation regions [193]:

$$\mathcal{P}_k = \min(P_k, 10\beta^*\bar{\rho}k\omega) - \frac{2}{3}\bar{\rho}k\delta_{ij} \frac{\partial \tilde{u}_i}{\partial x_j} \quad \text{with} \quad P_k = \mu_t \frac{\partial \tilde{u}_i}{\partial x_j} \left(\frac{\partial \tilde{u}_i}{\partial x_j} + \frac{\partial \tilde{u}_j}{\partial x_i} \right). \quad (2.59)$$

The variable σ_k is a blended model constant, which will be discussed later together with the constants α , β and σ_ω . In Eq. (2.58), \mathcal{P}_ω is the production term in the ω -equation which is given

as:

$$\mathcal{P}_\omega = \bar{\rho} \frac{\partial \tilde{u}_i}{\partial x_j} \left(\frac{\partial \tilde{u}_i}{\partial x_j} + \frac{\partial \tilde{u}_j}{\partial x_i} \right) - \frac{2}{3} \bar{\rho} \omega \delta_{ij} \frac{\partial \tilde{u}_i}{\partial x_j}. \quad (2.60)$$

The variable F_1 in Eq. (2.58) denotes the blending function which performs the shift between the k,ω -model in the near-wall region ($F_1 = 1$) and the k,ϵ -model in the free-stream ($F_1 = 0$). According to Menter [192], F_1 is defined as

$$F_1 = \tanh(\xi^4) \quad \text{with} \quad \xi = \min \left[\max \left(\frac{\sqrt{k}}{\beta^* \omega d_\perp}, \frac{500 \bar{\mu}/\bar{\rho}}{d_\perp^2 \omega} \right), \frac{4\sigma_{\omega 2} k}{CD_\omega d_\perp^2} \right], \quad (2.61)$$

where d_\perp denotes the wall-nearest distance [201] and CD_ω is calculated as:

$$CD_\omega = \max \left(2\sigma_{\omega 2} \frac{1}{\omega} \frac{\partial k}{\partial x_i} \frac{\partial \omega}{\partial x_i}, 10^{-10} \right). \quad (2.62)$$

The blending function F_1 is further used to calculate the required model constants α , β , σ_k and σ_ω based on the constants of the k,ω -model (index: 1) and k,ϵ -model (index: 2). This is done based on a linear weighting

$$\Theta = F_1 \Theta_1 + (1 - F_1) \Theta_2, \quad (2.63)$$

where Θ can be replaced by the respective constant. In Tab. 2.1, the model constants (α_i , β_i , σ_{ki} and $\sigma_{\omega i}$) of the k,ω - and k,ϵ -model are listed. Finally, the eddy viscosity in the k,ω -SST-model is determined as:

$$\mu_t = \bar{\rho} \frac{a_1 k}{\max(a_1 \omega, \tilde{S} F_2)}. \quad (2.64)$$

Here, a_1 is a constant which takes the value 0.31 and \tilde{S} is the invariant measure of the strain rate, i.e., $\tilde{S} = \sqrt{2\tilde{S}_{ij}\tilde{S}_{ij}}$. In addition, F_2 is another blending function defined as:

$$F_2 = \tanh \left\{ \left[\max \left(\frac{2\sqrt{k}}{\beta^* \omega d_\perp}, \frac{500 \bar{\mu}/\bar{\rho}}{d_\perp^2 \omega} \right) \right]^2 \right\}. \quad (2.65)$$

Table 2.1: Model constants of the k,ω - and k,ϵ -model used in the k,ω -SST-model [193].

	α_i	β_i	σ_{ki}	$\sigma_{\omega i}$
1 (k,ω -model [351])	$5/9 = 0.555$	$3/40 = 0.075$	0.85	0.5
2 (k,ϵ -model [132])	0.44	0.0828	1.0	0.856

Part II

NUMERICS AND MODELING

3 Numerical methods

For the set of nonlinear conservation equations introduced in Sec. 2.1 only a few analytical solutions exist which are restricted to simple flow problems such as, for instance, Couette or potential flows [297]. For turbulent nonreacting or reacting flows in application-relevant (complex) geometries, an analytical solution of the conservation equations is very difficult or even impossible. Discretization allows the transformation of the set of partial differential equations into a corresponding system of algebraic equations [130]. The solution of this set of discretized equations yields values for the conservative and related/derived properties at a priori defined locations in time and space. This is known as numerical simulation and the solution depends on the initial and boundary conditions of the investigated flow problem. In this work, the implementation and treatment of initial and boundary conditions is not discussed as it does not significantly contribute to the overall understanding. Instead, it is referred to the textbook of Moukalled et al. [201] or the PhD theses of Jasak [130] and Rusche [269].

For nonmoving, constant volume meshes the discretization procedure of the flow problem consists of two essential steps [120]:

- 1) Temporal and spatial discretization of the solution domain.
- 2) Temporal and spatial discretization of the conservation equations.

In the present work, the finite volume method (FVM) is employed for the discretization. The advantages of the FVM compared to, e.g., the finite difference method are diverse. Two major advantages are: First, the conservation quantities are inherently conserved on a discrete level as the balance laws are discretized in an integral form. Second, complex geometries can be investigated as the spatial discretization can include any kind of general polyhedral shape. This kind of spatial discretization is often termed as unstructured grid/mesh and offers great freedom in mesh generation and manipulation.

This chapter is structured as follows: The realization of the FVM in the applied open-source tool OpenFOAM is presented in Sec. 3.1. This includes the discretization of the solution domain in Sec. 3.1.1 as well as the spatial and temporal discretization of the governing equations in Secs. 3.1.2 and 3.1.3, respectively. Next, the different methods for the pressure-velocity coupling are discussed in Sec. 3.2. In Sec. 3.3, a pressure-based solution framework is presented which is suitable for the numerical simulation of flows at all speeds. A density-based double-flux method specifically tailored for transcritical flows is introduced in Sec. 3.4. The pressure-based framework was implemented in OpenFOAM 4.1 [1]. The density-based method was realized in OpenFOAM v1806 [2]. More information on different numerical solver approaches can be found in the textbooks of, e.g., Hirsch [120], Blazek [37], Ferziger and Perić [75] or Moukalled et al. [201].

3.1 Finite volume method

3.1.1 Discretization of the solution domain

A general transient problem requires the discretization of the solution domain into a finite number of discrete grid points in time and space [120]. The solution at any time is only influenced by the history, i.e., the conditions at the previous time, as unsteady flows are parabolic in time [223]. This property makes the time a one-way coordinate [223] and an appropriate time step has to be prescribed which suits the required temporal resolution and stability criteria of the numerical method. The time step can be constant or variable depending on the local flow conditions. Combustion simulations were conducted using a constant time step. For inert simulations the convective/acoustic Courant-Friedrichs-Lowy (CFL) criterion was applied to determine a suitable time step.

The more difficult and time-consuming task is the spatial discretization of the flow problem. The spatial domain has to be subdivided into a finite number of control volumes (CVs). These cells have to be contiguous, i.e., not overlapping, and completely fill the domain [269]. The CVs have to

be arranged such that they resolve the parts of interest in the flow field. Their number has to be chosen such that the numerical solution of the governing equations is as independent as possible from the spatial discretization. OpenFOAM tools like, e.g., blockMesh and commercial meshers like, e.g., ANSYS ICEM CFD were used in the present work for the grid generation. A schematic of two arbitrary neighboring control volumes together with the nomenclature used in OpenFOAM is shown in Fig. 3.1. A CV is defined by a certain number of vertices which are connected via

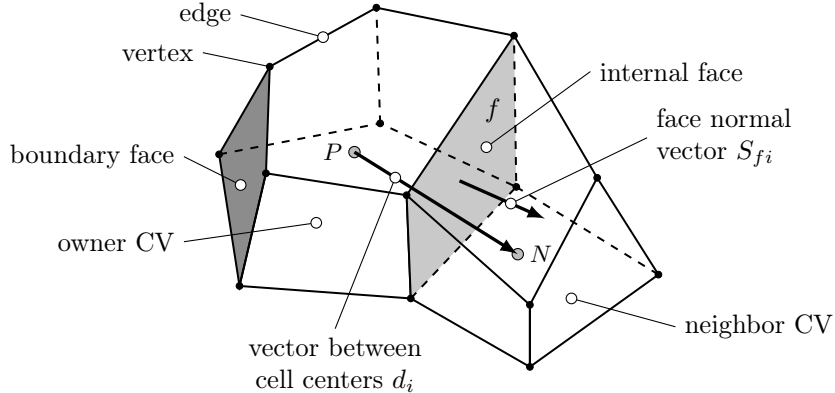


Figure 3.1: Schematic of two control volumes sharing a common internal face f . The vector directions and the nomenclature represent the standard OpenFOAM terms.

edges. These edges define faces which in turn bound the control volume and determine its size and volume. Faces can be of two types: Internal faces connect CVs in the internal mesh. Boundary faces constrain the solution domain and are the locations where boundary conditions are prescribed in OpenFOAM. The center of a CV is defined at its centroid [130] and is termed P for the owner CV and N for the neighbor CV, respectively. The terms owner and neighbor are defined based on the direction of the face normal vector S_{fi} of the internal face. The magnitude of S_{fi} is defined such that it is equal to the area of the face. The vector between two cell centroids is denoted as d_i . In OpenFOAM, dependent variables and other properties are stored at the cell centroids [269] resulting in a collocated mesh treatment. This arrangement allows for an arbitrary topology of the CV but demands reconstruction procedures for the interpolation of the cell-centered variables onto the faces of the CV which are an essential part of the spatial discretization of the balance laws. In staggered grid arrangements, in contrast, scalar variables are stored in the centroid of the CVs and velocities and momentum variables are located on the faces. This avoids odd-even decoupling/checkerboarding [120, 276]. However, for complex geometries the staggered approach is disadvantageous.

3.1.2 Spatial discretization

For the introduction of the spatial discretization of the balance laws, the conservation equation for a general scalar variable ξ is used:

$$\frac{\partial(\rho\xi)}{\partial t} + \frac{\partial(\rho\xi u_i)}{\partial x_i} = \frac{\partial}{\partial x_i} \left(\rho D_\xi \frac{\partial \xi}{\partial x_i} \right) + \mathcal{S}_\xi . \quad (3.1)$$

Here, the terms from left to right represent the temporal variation, convection, diffusion and sources of ξ , respectively. For an arbitrary control volume Ω_P with the cell center P the integral form of the transport equation of ξ reads:

$$\frac{\partial}{\partial t} \int_{\Omega_P} \rho\xi d\Omega + \int_{\Omega_P} \frac{\partial(\rho\xi u_i)}{\partial x_i} d\Omega = \int_{\Omega_P} \frac{\partial}{\partial x_i} \left(\rho D_\xi \frac{\partial \xi}{\partial x_i} \right) d\Omega + \int_{\Omega_P} \mathcal{S}_\xi d\Omega . \quad (3.2)$$

The volume integrals have to be approximated by means of numerical integration to arrive at a system of linear equations.

For solving the volume integrals of the transient and the source term, the midpoint rule is applied which yields the following approximation for both terms:

$$\int_{\Omega_P} \rho \xi d\Omega \approx \rho_P \xi_P \int_{\Omega_P} d\Omega = \rho_P \xi_P \Omega_P , \quad (3.3a)$$

$$\int_{\Omega_P} \mathcal{S}_\xi d\Omega \approx \mathcal{S}_{\xi,P} \int_{\Omega_P} d\Omega = \mathcal{S}_{\xi,P} \Omega_P . \quad (3.3b)$$

Here, ρ_P , ξ_P and $\mathcal{S}_{\xi,P}$ are the density, scalar variable and source term at the cell center P . This approach assumes that the values at the CV's centroid P are representative for the entire cell volume.

The convection and diffusion terms are integrated numerically using Gauss' theorem which converts the volume integrals into surface integrals. In the FVM, the CV is bounded by faces and the surface integral can therefore be transferred to the sum of integrals over all faces. For the spatial gradient of the general scalar variable ξ this concept reads:

$$\int_{\Omega_P} \frac{\partial \xi}{\partial x_i} d\Omega = \int_S \xi n_i dS = \sum_f \left(\int_f \xi n_i dS \right) \approx \sum_f \xi_f S_{fi} . \quad (3.4)$$

Here, S is the surface of the cell, n_i is the outward-pointing unity vector normal to the boundary S , ξ_f is the face-center value of ξ on face f and S_{fi} is the face area vector of face f in the direction x_i . In OpenFOAM, the face area vector is pointing outwards from the respective CV if f is owned by it [130], see Fig. 3.1. Therefore, the sum over the faces in Eq. (3.4) has to be split into the sums over the owned and neighboring faces:

$$\sum_f \xi_f S_{fi} = \sum_{owner} \xi_f S_{fi} - \sum_{neighbor} \xi_f S_{fi} . \quad (3.5)$$

Due to the global data structure in OpenFOAM, this convention is true for all summations over faces. For the sake of simplicity, the notation according to Eq. (3.5) is omitted in the following.

The convection term

Applying the Gauss theorem, the volume integral of the convection term in the general conservation equation (3.2) can be written as:

$$\int_{\Omega_P} \frac{\partial (\rho \xi u_i)}{\partial x_i} d\Omega = \int_S \rho \xi u_i n_i dS \approx \sum_f (\rho u_i)_f \xi_f S_{fi} = \sum_f \phi_f \xi_f . \quad (3.6)$$

Here, ϕ_f denotes the mass flux through the face f . The calculation of ϕ_f depends on the solver framework – pressure- or density-based – and is discussed in Secs. 3.3 and 3.4. The only fact which is important for now is the direction of the flux, i.e., if ϕ_f is greater than or smaller than zero or in other words if the flux is going inwards or outwards of the CV. This determines the upwind and downwind direction and therefore the numerical stencil for the face interpolation procedure. For the determination of the face value ξ_f three different schemes are available in OpenFOAM [130, 269]: central differencing (CD), upwind differencing (UD) and blended differencing (BD).

The most general interpolation approach is the CD scheme which is second-order accurate. The face value ξ_f is determined based on the centroid values of P and N as [130, 269, 100]

$$(\xi_f)_{CD} = \frac{\overline{fN}}{\overline{PN}} \xi_P + \left(1 - \frac{\overline{fN}}{\overline{PN}} \right) \xi_N = \mathcal{V} \xi_P + (1 - \mathcal{V}) \xi_N , \quad (3.7)$$

where \mathcal{V} is the interpolation factor [131]. Here, \overline{fN} is the distance between the internal face f and the neighbor centroid N and \overline{PN} is the distance between the owner and neighbor cell-centers P and N . The CD scheme is unbounded and can result in unphysical oscillations in convection dominated flows.

The simplest approach to overcome a violation of boundedness is the application of a UD scheme. In this case, the face value of ξ is determined according to the direction of the flux [130, 269, 100]:

$$(\xi_f)_{\text{UD}} = \begin{cases} \xi_P & \text{if } \phi_f > 0 \\ \xi_N & \text{if } \phi_f \leq 0 \end{cases}. \quad (3.8)$$

The UD scheme is first order accurate and introduces numerical diffusion into the simulation, i.e., the boundedness is guaranteed but the accuracy of the numerical result is reduced.

The blended differencing schemes combine the CD and UD approaches to yield a high-order bounded differencing scheme [131]. In OpenFOAM, BD schemes are realized as a linear combination of CD and UD applying a blending factor Γ_{BD} which depends on the local flow properties [130, 131, 100]:

$$(\xi_f)_{\text{BD}} = (1 - \Gamma_{\text{BD}})(\xi_f)_{\text{UD}} + \Gamma_{\text{BD}}(\xi_f)_{\text{CD}}. \quad (3.9)$$

Depending on the flow direction – upwind ($\phi_f > 0$) or downwind ($\phi_f \leq 0$) – the face values can be expressed as:

$$(\xi_f)_{\text{BD,upwind}} = [1 - \Gamma_{\text{BD}}(1 - \mathcal{V})]\xi_P + \Gamma_{\text{BD}}(1 - \mathcal{V})\xi_N, \quad (3.10)$$

$$(\xi_f)_{\text{BD,downwind}} = \Gamma_{\text{BD}}\mathcal{V}\xi_P + (1 - \Gamma_{\text{BD}}\mathcal{V})\xi_N. \quad (3.11)$$

The decisive part of the interpolation is now shifted towards the determination of the blending factor Γ_{BD} . This factor has to facilitate a smooth "switching" between the UD and CD schemes to avoid instabilities and convergence problems. In the present work, different limiter functions from the total variation diminishing (TVD) class are used like, e.g., van Leer [336], van Albada [332] or Minmod [264]. The selection of the appropriate TVD limiting scheme strongly depends on the considered flow problem. TVD approaches must fulfill the following basic conditions: maxima must be non-increasing, minima non-decreasing and no new local extrema may be created [37]. The limiter approaches can be written as function of successive gradients r :

$$\text{van Leer [336] limiter: } \Gamma_{\text{BD}} = \frac{r + |r|}{1 + |r|}, \quad (3.12)$$

$$\text{van Albada [332] limiter: } \Gamma_{\text{BD}} = \frac{r(r+1)}{r^2 + 1}, \quad (3.13)$$

$$\text{Minmod [264] limiter: } \Gamma_{\text{BD}} = \max(\min(r, 1), 0). \quad (3.14)$$

In general, r can be expressed as

$$r = \frac{\xi_C - \xi_U}{\xi_D - \xi_C}, \quad (3.15)$$

where the subscripts depend on the flow direction, see Fig. 3.2. In unstructured grids, the problem lies in the definition of the virtual grid point U [131, 60]. Therefore, the expression of r is usually re-cast in a function which only depends on the centroids C and D [60]:

$$r = \frac{2 \left(\frac{\partial \xi}{\partial x_i} \right)_C d_i^{CD}}{\xi_D - \xi_C} - 1. \quad (3.16)$$

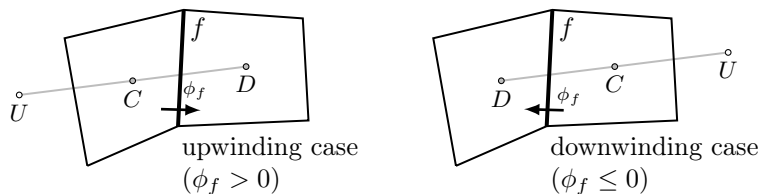


Figure 3.2: Definition of the grid nodes (C, D and U) used to determine r in Eq. (3.15).

Here, d_i^{CD} is the vector between the nodes C and D . Using the notation with owner and neighboring grid nodes P and N , r is expressed as follows in OpenFOAM:

$$r = \begin{cases} \frac{2\left(\frac{\partial \xi}{\partial x_i}\right)_P d_i}{\xi_N - \xi_P} - 1 & \text{if } \phi_f > 0 \\ \frac{2\left(\frac{\partial \xi}{\partial x_i}\right)_N d_i}{\xi_N - \xi_P} - 1 & \text{if } \phi_f \leq 0 \end{cases}. \quad (3.17)$$

The diffusion term

The volume integral of the diffusion term in Eq. (3.2) can be discretized similarly to the convection term as:

$$\int_{\Omega_P} \frac{\partial}{\partial x_i} \left(\rho D_\xi \frac{\partial \xi}{\partial x_i} \right) d\Omega = \int_S \rho D_\xi \frac{\partial \xi}{\partial x_i} n_i dS \approx \sum_f (\rho D_\xi)_f \left(\frac{\partial \xi}{\partial x_i} \right)_f S_{fi}. \quad (3.18)$$

The face value of $(\rho D_\xi)_f$ is determined using the CD scheme. The determination of the face normal gradient $(\partial \xi / \partial x_i)_f S_{fi}$ depends on the mesh topology.

For orthogonal meshes, i.e., the vectors d_i and S_{fi} are parallel, the face normal gradient is evaluated as [130]:

$$\left(\frac{\partial \xi}{\partial x_i} \right)_f S_{fi} = |S_{fi}| \frac{\xi_N - \xi_P}{|d_i|}. \quad (3.19)$$

Here, $|S_{fi}|$ and $|d_i|$ denote the magnitude of the face area vector and the vector between the centroids.

For nonorthogonal grids, as it is the case in most application-relevant meshes, the vectors d_i and S_{fi} are not parallel. Consequently, a correction term has to be introduced to achieve high accuracy. In this case, the determination of the face normal gradient is split up into two parts [130]:

$$\left(\frac{\partial \xi}{\partial x_i} \right)_f S_{fi} = \underbrace{|\delta_{fi}| \frac{\xi_N - \xi_P}{|d_i|}}_{\text{orthogonal}} + \underbrace{k_{fi} \left(\frac{\partial \xi}{\partial x_i} \right)_f}_{\text{nonorthogonal}}. \quad (3.20)$$

The decomposition of S_{fi} into the two vectors δ_{fi} and k_{fi} must satisfy

$$S_{fi} = \delta_{fi} + k_{fi}, \quad (3.21)$$

where δ_{fi} is parallel to d_i . The gradient term in the nonorthogonal contribution is determined by means of central differencing. In OpenFOAM, a so-called over-relaxed approach is employed to determine the parallel part of the vector [130]:

$$\delta_{fi} = \frac{d_i}{d_j S_{fj}} |S_{fk}|^2. \quad (3.22)$$

Consequently, k_{fi} can be calculated using Eq. (3.21).

3.1.3 Temporal discretization

In the previous section, the spatial discretization has been discussed which involves the transformation of volume and surface integrals to discrete algebraic equations based on the values at the centroids of the CVs. The application of these approaches yields the following semi-discrete form of the general conservation equation:

$$\frac{\partial (\rho_P \xi_P)}{\partial t} \Omega_P = - \sum_f \phi_f \xi_f + \sum_f (\rho D_\xi)_f \left(\frac{\partial \xi}{\partial x_i} \right)_f S_{fi} + \mathcal{S}_{\xi, P} \Omega_P = \mathfrak{L}(\xi_P^{\mathcal{T}}). \quad (3.23)$$

Here, $\mathcal{L}(\xi_P^{\mathcal{T}})$ is the spatial discretization operator at a reference time \mathcal{T} [201]. This operator can be expressed in an algebraic form for every CV of the grid [201]

$$\mathcal{L}(\xi_P^{\mathcal{T}}) = a_P \xi_P^{\mathcal{T}} + \sum_N a_N \xi_N^{\mathcal{T}} - b_P . \quad (3.24)$$

The sum \sum_N is taken over all neighboring CVs which influence the computational stencil around point P . After applying a discretization scheme to the transient term in Eq. (3.23), the general conservation equation can be written in the form of a system of algebraic equations [130]:

$$\mathbf{a}\boldsymbol{\xi} = \mathbf{b} . \quad (3.25)$$

Here, \mathbf{a} is a sparse matrix which contains the diagonal (a_P) and the off-diagonal (a_N) coefficients. The unknowns in the CVs are denoted by the vector $\boldsymbol{\xi}$ and the vector \mathbf{b} on the right-hand side contains the source terms of the respective centroids b_P .

In general, two kinds of time marching methods are available: explicit and implicit. When explicit time stepping is used, the spatial discretization operator $\mathcal{L}(\xi_P^{\mathcal{T}})$ contains only contributions from the previous time level. Hence, the time integration can be performed without solving a system of linear equations. In contrast, when implicit time integration schemes are applied, $\mathcal{L}(\xi_P^{\mathcal{T}})$ also depends on the values of the new – unknown – time level. This, in turn, implies the solution of the system of algebraic equations according to Eq. (3.25). The applied time marching schemes are presented in the following. In this work, the implicit Euler scheme is used in the combustion simulations and the second-order accurate backward method is applied in all inert pressure-based simulations. In the density-based solver, an explicit second-order four-stage low-storage Runge-Kutta scheme is employed. For the sake of simplicity the different time levels are denoted as

$$\Xi^{n+1} = \Xi(t + \Delta t), \quad \Xi^n = \Xi(t) \quad \text{and} \quad \Xi^{n-1} = \Xi(t - \Delta t) . \quad (3.26)$$

Here, Ξ is short for $\rho\xi$ and t and Δt denote the current time level and the time step, respectively.

Euler implicit

Expressing the face values in the FVM with cell values from the new time level yields the Euler implicit time integration scheme [130]:

$$\frac{\Xi_P^{n+1} - \Xi_P^n}{\Delta t} = \frac{1}{\Omega_P} \mathcal{L}(\xi_P^{n+1}) . \quad (3.27)$$

This time marching scheme is first-order accurate and more stable than the second-order implicit backward-differencing scheme introduced next.

Second-order implicit backward

Using the information of the current and the previous time level, the implicit backward differencing scheme can be deduced as [130]:

$$\frac{3\Xi_P^{n+1} - 4\Xi_P^n + \Xi_P^{n-1}}{2\Delta t} = \frac{1}{\Omega_P} \mathcal{L}(\xi_P^{n+1}) . \quad (3.28)$$

This time integration method is second-order accurate but the boundedness of the solution cannot be guaranteed.

Second-order four-stage low-storage Runge-Kutta

In density-based solvers, explicit Runge-Kutta (RK) time integration schemes are popular due to their ease of implementation. In contrast to the implicit time schemes which achieve accuracy by including multiple time steps, the Runge-Kutta schemes gain accuracy by introducing multiple stages [120]. In this work, a four stage, low storage variant is applied where only the last time step and the current Runge-Kutta stage have to be stored. The employed RK method can be written

in the following general form [37, 157]

$$\Xi_P^{(i)} = \Xi_P^n + \frac{\eta_i \Delta t}{\Omega_P} \mathcal{L}(\xi_P^{(i-1)}) \quad i = 1, 2, 3, 4, \quad (3.29)$$

where $\eta = [0.11, 0.2766, 0.5, 1.0]$. Here, $\xi_P^{(0)}$ corresponds to the solution of the last time step, i.e., ξ_P^n , and the final solution of the time marching procedure is $\Xi_P^{n+1} = \Xi_P^{(4)}$. The RK scheme can be implemented conveniently in terms of a four-stage loop where the new time level $t + \Delta t$ is updated gradually.

3.2 Numerical solution algorithms

The selection of the numerical algorithm is usually done with respect to the Mach number. The Mach number Ma is a dimensionless quantity that relates the local velocity $\|\mathbf{u}\|$ to the speed of sound a_s

$$\text{Ma} = \frac{\|\mathbf{u}\|}{a_s} \quad (3.30)$$

and is a measure for the presence of compressibility effects induced by the fluid flow¹. The different flow regimes can be roughly categorized as follows:

- Low-Mach regime: $\text{Ma} < 0.3$,
- Subsonic regime: $\text{Ma} < 0.8$,
- Transonic regime: $0.8 < \text{Ma} < 1.3$,
- Supersonic regime: $1.3 < \text{Ma} < 5.0$,
- Hypersonic regime: $\text{Ma} > 5.0$.

The big difference between the low and high Mach number regime is the role of the pressure [201]. In subsonic conditions (low Mach number), density and pressure as well as density and velocity are weakly coupled. Hence, the continuity equation acts as a constraint for the velocity field. In contrast, in high-speed flows changes in pressure induce significant variations in the density. As a result, the mass conservation equation can be applied to determine the density field. These facts result in two different types of numerical solver formulations which are widely used [120, 37]: pressure-based and density-based.

Historically, density-based solvers are applied for the numerical simulation of high Mach number flows. Density-based frameworks are a straightforward solution approach of the governing equations, i.e., their algebraic equivalences are solved. Therefore, the velocity and density fields are calculated from the momentum and mass conservation equations, respectively. The pressure field is obtained from a suitable thermal equation of state which can be written in the following pressure-explicit form

$$p = p(\rho, e, \mathbf{Y}), \quad (3.31)$$

where e denotes the specific internal energy. Density-based solvers have disadvantages when the Mach number approaches zero as density variations vanish in the incompressible limit and the problem becomes numerically ill-conditioned [37]. Different approaches have been developed to overcome these deficiencies which include, for instance, the introduction of an artificial compressibility, see, e.g., Chorin [48] or Choi and Merkle [47], or pre-conditioning, see, e.g., Turkel et al. [326] or Weiss and Smith [347].

Pressure-based solvers do not use the density as a primary variable but directly solve for the pressure. This type of solver can be therefore applied straightforwardly to incompressible cases. The pressure is solved in a Poisson-like equation which can be derived from the momentum and continuity equations. Therefore, the pressure is used to force mass conservation by manipulating the velocity field. The density field is either constant (incompressible case) or can be obtained

¹The term "compressibility effect" is used here from a fluid dynamics point of view. Under real-gas conditions, strong density variations can be introduced by the fluid behavior itself. This type of compressibility is superimposed onto the fluid dynamics part and should not be confused with each other.

from a suitable thermodynamic equation of state, i.e.,

$$\rho = \rho(p, h, \mathbf{Y}) . \quad (3.32)$$

By explicitly considering the pressure-density coupling in the pressure-based approach, this solver type can be applied to compressible flows, see, e.g., Moukalled and Darwish [200].

3.3 Pressure-based solver framework

For most of the numerical simulations presented within this work a pressure-based solution framework is applied. The main reason for this is the history of OpenFOAM, which was originally designed for this type of solver. The basis for the pressure-based solvers in OpenFOAM – formulation and nomenclature – can be found in the PhD thesis of Jasak [130]. In Sec. 3.3.1, the derivation of the pressure equation for subsonic flow conditions is shown. Next, the extension to real-gas flows is demonstrated in Sec. 3.3.2. After that, the solution procedure is discussed in Sec. 3.3.3 and finally the extension of the pressure equation towards the high Mach number regime is demonstrated in Secs. 3.3.4 and 3.3.5.

3.3.1 Formulation for subsonic flows

Applying the FVM to the momentum conservation equation (2.2) a semi-discrete form can be derived [130]

$$a_P u_{P,i} = b_{P,i} - \sum_N a_N u_{N,i} - \frac{\partial p}{\partial x_i} , \quad (3.33)$$

where the pressure gradient is not discretized yet. For a further simplification, Jasak [130] introduced the operator $H_{P,i}$ which contains the neighbor contributions a_N and the source terms $b_{P,i}$

$$H_{P,i}(u_i) = b_{P,i} - \sum_N a_N u_{N,i} . \quad (3.34)$$

Using this notation, the semi-discrete momentum equation and the velocity at the centroid P can be expressed as follows

$$a_P u_{P,i} = H_{P,i}(u_i) - \frac{\partial p}{\partial x_i} , \quad (3.35)$$

$$u_{P,i} = \frac{H_{P,i}(u_i)}{a_P} - \frac{1}{a_P} \frac{\partial p}{\partial x_i} . \quad (3.36)$$

These two equations form the basis for the realization of the pressure-based solver in OpenFOAM. Substituting Eq. (3.36) into the mass conservation equation (2.1) and applying the FVM again yields the final form of the pressure equation:

$$\frac{\delta \rho}{\delta t} + \frac{1}{\Omega_P} \sum_f \left[\left(\rho \frac{H_{P,i}}{a_P} \right)_f S_{fi} \right] - \frac{1}{\Omega_P} \sum_f \left[\left(\frac{\rho}{a_P} \right)_f \left(\frac{\partial p}{\partial x_i} \right)_f S_{fi} \right] = 0 . \quad (3.37)$$

Here, $\delta/\delta t$ is the operator for the discrete partial differentiation with respect to the time. This pressure equation (3.37) is elliptical in nature. In addition, it is important to note, that this pressure equation is different to the pressure equations applied in density-based solvers for stabilization purpose, see, e.g., Terashima and Koshi [311] or Lacaze et al. [156]. In real-gas flows, density-based frameworks suffer from spurious pressure oscillations. To overcome this issue, some groups replace the energy equation with a pressure transport equation, which should not be confused with Eq. (3.37). Another noteworthy fact is that in the LRE community, see, e.g., Ries et al. [261, 260] or Lapenna et al. [159, 160], Eq. (3.37) is sometimes referred to as low Mach approach, as it does not include any modifications for the pressure dependency of the density. Own investigations using the low Mach-type pressure equation showed, that this approach allows the simulation of moderate density stratifications in the subsonic regime like, for instance, the Mayer test cases [190]. For larger density ratios and, especially, under multicomponent conditions, the convergence behavior is not advantageous as the influence of the real-gas thermodynamics onto the pressure equation is

missing.

3.3.2 Extension for subsonic real-gas flows

Under real-gas conditions, thermodynamic properties depend on both temperature and pressure. For the stabilization of the solution procedure, Eq. (3.37) has to be modified to account for the density variations induced by temperature changes. Following typical pressure correction approaches in the literature, see, e.g., Ferziger and Perić [75] or Moukalled and Darwish [200], the density variation in the time derivative of Eq. (3.37) is approximated based on the total differential of the density $\rho = \rho(p, h, \mathbf{Y})$:

$$\begin{aligned} d\rho &= \frac{\partial \rho}{\partial p} \Big|_{h, \mathbf{Y}} dp + \frac{\partial \rho}{\partial h} \Big|_{p, \mathbf{Y}} dh + \sum_{i=1}^{N_c} \frac{\partial \rho}{\partial Y_i} \Big|_{h, p, Y_j \neq Y_i} dY_i \\ &= \Psi_h dp + \frac{\partial \rho}{\partial h} \Big|_{p, \mathbf{Y}} dh + \sum_{i=1}^{N_c} \frac{\partial \rho}{\partial Y_i} \Big|_{h, p, Y_j \neq Y_i} dY_i . \end{aligned} \quad (3.38)$$

Recasting this total differential into a Taylor series truncated after the first term and neglecting all variations except for the pressure, i.e., $dh = 0$ and $dY_i = 0$, gives

$$\rho = \rho^n + \Psi_h^n (p - p^n) . \quad (3.39)$$

Here, the superscript n refers to the last time or iteration step. Substituting Eq. (3.39) into Eq. (3.37) yields

$$\underbrace{\frac{\delta(\rho^n - \Psi_h^n p^n)}{\delta t}}_{\text{explicit}} + \underbrace{\frac{\delta \Psi_h^n p}{\delta t}}_{\text{implicit}} + \frac{1}{\Omega_P} \sum_f \left[\left(\rho \frac{H_{P,i}}{a_P} \right)_f S_{fi} \right] - \frac{1}{\Omega_P} \sum_f \left[\left(\frac{\rho}{a_P} \right)_f \left(\frac{\partial p}{\partial x_i} \right)_f S_{fi} \right] = 0 . \quad (3.40)$$

As a result of this substitution in the time derivative, the first term is evaluated explicitly while the second one is treated implicitly². With this modified pressure equation flows with larger density stratification can be simulated compared to the low Mach approach, cf. Eq. (3.37), and Eq. (3.40) is applied throughout this work for the simulation of subsonic flow problems.

3.3.3 Solution procedure

The pressure-based method is implemented in a segregated solution algorithm. A so-called PIMPLE approach is applied in OpenFOAM which is a combination of the Semi-Implicit Method for Pressure Linked Equations (SIMPLE) due to Patankar and Spalding [224] and the Pressure-Implicit with Splitting of Operators (PISO) method proposed by Issa et al. [126]. In Fig. 3.3, the basic structure of the numerical algorithm is illustrated.

In the following, the solution procedure of the PIMPLE algorithm is outlined shortly:

1. After the initialization of the simulation, the discretized momentum conservation equation is solved. The solution to the momentum equation yields the intermediate velocity field u_i^* which does not satisfy the mass conservation. In addition, two facts are important: First, the mass flux at the cell faces $\phi_f = (\rho u_i)_f S_{fi}$ in the convection term is taken from the last time/iteration step as it is only updated within the solution procedure of the pressure equation. Second, the matrix system for the momentum equations is set up without the pressure gradient as the different contributions of the discretized momentum equation are later used to construct the pressure equation according to Eq. (3.40).

²In OpenFOAM, the evaluation of the time derivative is realized by means of the function call `fvc :: ddt(rho) + psi * correction(fvm :: ddt(p))`. Here, fvc and fvm denote an explicit and an implicit evaluation of the time derivative, respectively, and psi corresponds to Ψ_h .

2. In the next step, the PISO loop is entered and the species transport and the energy conservation equations are solved. This solution structure differs from classical ideal-gas approaches where these transport equations are evaluated outside of the PISO loop. For the robustness of the solver under real-gas conditions, the consideration of the coupling between species, energy and pressure is essential, see, e.g., Jarczyk [128] or Jarczyk and Pfitzner [129]. After the mixture composition and the energy are updated, the thermodynamics closure is evaluated.
3. The next step involves the construction and evaluation of the pressure equation. First, the pseudo-velocity $H_{P,i}(u_i^*)(a_P)^{-1}$ is evaluated at the cell centroids [330] and is then interpolated onto the CV faces together with the density by means of a linear interpolation³. This step mimics the Rhee-Chow interpolation [256] in OpenFOAM and therefore avoids checkerboarding due to a missing contribution of the pressure value of the respective CV in the numerical stencil. For more details it is referred to the PhD thesis of Uroic [330] and the textbook of Moukalled et al. [201]. Next, the pressure equation is constructed and solved. Using the updated pressure field, the mass fluxes ϕ_f are updated which now contain the influence of the new pressure field and therefore satisfy mass conservation. Similarly, the velocity field is corrected according to Eq. (3.36). In addition, pressure contributions to the density are considered explicitly without invoking the thermodynamic closure by evaluating

$$d\rho = \Psi_h dp \quad (3.41)$$

before and after the evaluation of the pressure equation.

4. After convergence is achieved, the sub-grid/turbulence model is evaluated before advancing to the next time level.

Typically, the outer SIMPLE and the inner PISO loop are evaluated three and one times, respectively. On strongly nonorthogonal meshes, additional orthogonal corrections of the pressure equation are necessary. Usually, two additional corrections are sufficient to achieve a desirable convergence behavior.

³In OpenFOAM, the mass flux at the faces actually consists of two terms. The first one is the standard mass flux, i.e., the pseudo-velocity multiplied by the density and the surface area. The second contribution is termed fvc::ddtCorr(rho, U, phi) in OpenFOAM. This term cannot be found in the original PISO formulation and is an undocumented flux correction term. It accounts for the difference between the face velocity and the face flux due to nonequal face interpolation procedures and can be interpreted as a first order damping term. More details on this fact can be found in the work of Vuorinen et al. [342].

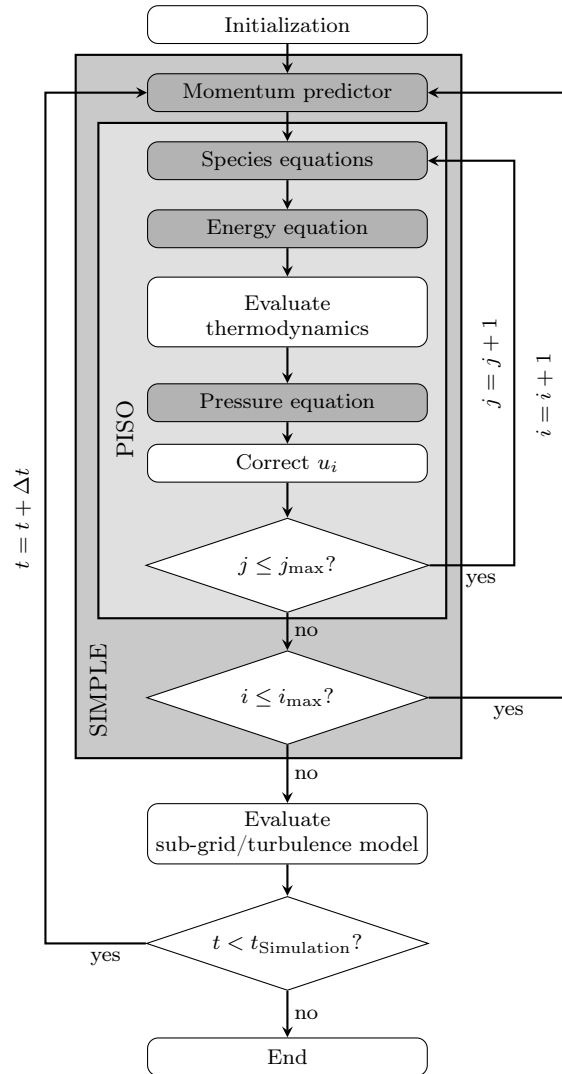


Figure 3.3: Flowchart of the pressure-based PIMPLE algorithm in OpenFOAM.

The time step is controlled by the convective Courant-Friedrichs-Lowy (CFL_c) number criterion

$$\text{CFL}_c = \frac{\|\mathbf{u}\| \Delta t}{\Delta x} \quad (3.42)$$

which relates the time step to a representative cell dimension Δx and the local velocity $\|\mathbf{u}\|$. In the present work, CFL_c numbers between 0.4 and 0.8 are applied.

3.3.4 General extension for high-speed flows

The governing equations of high-speed and compressible flows have a hyperbolic character which is the main reason why density-based solvers are so well suited for simulating this kind of flows [120]. To utilize the pressure-based approach for high-speed flows, the elliptical pressure equation (3.37) has to be adjusted to account for the variation of density with respect to pressure. In this way, the character of the pressure equation can be changed from purely elliptical to hyperbolic. This fact was noticed for the first time by Patankar [222] and was later also adopted by many other groups to extend their pressure-based solvers to high Mach numbers, see, e.g., Issa and Lockwood [125], Hah [104, 105], van Doormaal et al. [334], Rhie and Stowers [257] or Rincon and Elder [262].

The consideration of density variations with respect to pressure changes can be done straightforwardly as

$$\rho = \Psi p . \quad (3.43)$$

Independent of the fluid model, Ψ can be expressed as

$$\Psi = \frac{1}{ZRT} . \quad (3.44)$$

Here, R is the specific gas constant which can be calculated in a multicomponent mixture based on the mass-weighted sum of the different species. In addition, Z denotes the compressibility factor in Eq. (3.44) which is defined as:

$$Z = \frac{p}{\rho RT} . \quad (3.45)$$

For an ideal-gas ($Z = 1$ or $\rho = p(RT)^{-1}$), Ψ corresponds to the isothermal compressibility $\partial\rho/\partial p|_T = (RT)^{-1}$. In real fluids, the ideal gas behavior is a special case and Z is usually unequal to unity. The compressibility factor can be directly obtained from the thermodynamic equation of state. Note that Ψ in Eq. (3.43) and Ψ_h in Eq. (3.39) are not identical for real gases and care has to be taken in the numerical implementation. In OpenFOAM, two different basic thermodynamic libraries are available: rhoThermo and psiThermo. The first one is historically intended for incompressible cases and is therefore a good choice for the subsonic pressure-based framework. In contrast, the psiThermo library is intended for compressible flow problems and is, consequently, perfectly suited for the supersonic pressure-based framework. The basic difference in both thermodynamic classes lies in the call of the density field which is stored directly in a scalar field in the rhoThermo libraries. In the psiThermo libraries, the density is recalculated by means of Eq. (3.43), i.e., based on the current Ψ and p fields. As a result, the update of the density within the supersonic PISO loop, i.e., when the psiThermo libraries are used, is done using Eq. (3.43) instead of Eq. (3.41).

Applying Eq. (3.43) to the subsonic pressure equation (3.37) yields the basic form of the hyperbolic pressure equation

$$\frac{\delta(\Psi p)}{\delta t} + \frac{1}{\Omega_P} \sum_f \left[\left(\frac{H_{P,i}}{a_P} \right)_f S_{fi} (\Psi p)_f \right] - \frac{1}{\Omega_P} \sum_f \left[\left(\frac{\rho}{a_P} \right)_f \left(\frac{\partial p}{\partial x_i} \right)_f S_{fi} \right] = 0 . \quad (3.46)$$

This pressure equation can be used to simulate trans- and supersonic flows. However, in the current form, this approach can only be applied for investigating configurations with moderate density stratifications and without pronounced shock structures. For high-speed flows, like they occur during the fuel injection process under GE-like conditions, modifications have to be made as the current flux (pseudo-velocity) formulation and interpolation procedures in the standard Open-

FOAM libraries are prone to nonphysical pressure oscillations and simulation crashes. In general, a large number of different approaches exist. For the SIMPLE-family an excessive discussion and introduction can be found in the works of Moukalled and Darwish [59, 200, 201]. An implicitly coupled approach based on a Newton linearization was recently presented by Xiao et al. [359] yielding a highly robust numerical algorithm for all speeds. In the present work, Eq. (3.46) is augmented with a semi-discrete central-upwind flux scheme suited for high-speed flows which is derived and discussed in detail in appendix A. In the following, the most important details of the resulting hybrid pressure-based solver are outlined.

3.3.5 Hybrid pressure-based approach for high-speed flows

The hybrid pressure-based solver for high Mach number flows is based on the work of Greenshields et al. [101] and Kraposhin et al. [143]. Greenshields et al. [101] applied the semi-discrete central flux schemes of Kurganov and Tadmor [152] (KT) and Kurganov, Noelle and Petrova [149] (KNP) for the first time on arbitrary polyhedral meshes in OpenFOAM. The important step of this application is the replacement of the dimension-by-dimension reconstruction of cell values onto the cell interfaces with a face-by-face approach. Therefore, a genuinely multi-dimensional form of reconstruction, as for instance suggested by Kurganov and Petrova [150, 151], can be avoided which is usually not applicable on arbitrary polyhedral collocated meshes. Using the face-by-face approach, the central schemes are not applied along the Cartesian coordinates but rather along the face normal direction making it easily applicable for the FVM on arbitrary meshes. Therefore, the translation of the flux formulation into OpenFOAM and the reconstruction of cell values onto the faces are the central points of the implementation of the KT and KNP flux schemes in OpenFOAM. Recently, Kraposhin et al. [143] used the implementation and suggestions of Greenshields et al. [101] and included the semi-discrete central flux formulations together with the face-by-face reconstruction into the pressure-based solver. In this way, the flux formulation and interpolation is stabilized for the investigation of hyperbolic problems.

The key to incorporate the KT/KNP flux scheme into OpenFOAM is the understanding of OpenFOAM's interpolation procedure. The direction of the reconstruction is defined by the direction of the reconstruction procedure and not by the direction of the face normal vector as it is the case for the derivation of many central schemes, see, e.g., Kurganov [148] and appendix A.2. Therefore, left- and right-sided face values are associated with a positive and a negative reconstruction direction, respectively, see Fig. 3.4. In OpenFOAM, the interpolation of cell values onto the faces is done based on the blended differencing scheme introduced in Eqs. (3.10) and (3.11). To get left-hand side (LHS) and right-hand side (RHS) face values from the states stored at the cell centers, either a pseudo positive or negative flux has to be handed to the interpolation procedure, i.e., $pos = 1$ or $neg = -1$. In OpenFOAM, the call takes three different arguments, see Fig. 3.4. The first contains the values at the cell center (here: the density field ρ), the second defines the interpolation direction and the last argument is a key word (here: `reconstruct(rho)`) which enables

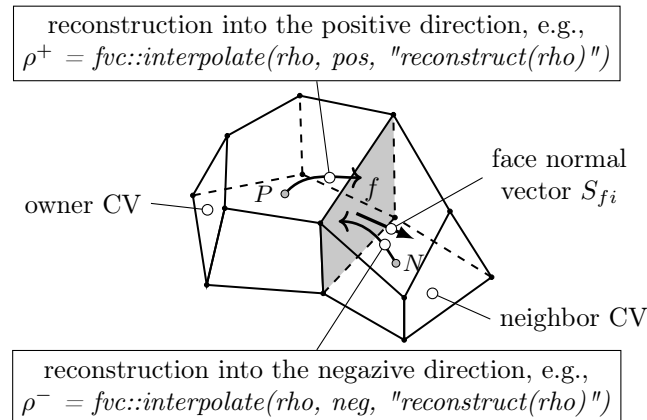


Figure 3.4: Definitions of the interpolation directions in OpenFOAM.

the run-time selection of any TVD scheme. The reconstruction procedure results in discontinuities at the cell interfaces. These discontinuities travel with left- and right-sided speeds of propagation which are the basis for the derivation of the family of central schemes. According to Greenshields et al. [101], the volumetric fluxes associated with the one-sided propagation speeds can be estimated as

$$\check{a}_f^+ = \max \left(\max \left(\Phi_f^+ + a_{s,f}^+ |S_{fi}|, \Phi_f^- + a_{s,f}^- |S_{fi}| \right), 0 \right) \quad (3.47)$$

and

$$\check{a}_f^- = \min \left(\min \left(\Phi_f^+ - a_{s,f}^+ |S_{fi}|, \Phi_f^- - a_{s,f}^- |S_{fi}| \right), 0 \right), \quad (3.48)$$

where $a_{s,f}^+$ and $a_{s,f}^-$ denote the left- and right-sided reconstructed speed of sounds, respectively, and $\Phi_f = (u_i)_f S_{fi}$ is the volumetric flux at the faces. As a result of the definition of the reconstruction directions in OpenFOAM, the one-sided propagation speeds have to be considered as maximum wave speeds into the respective directions of the face normal vector. This is in contrast to the definitions of the reconstruction directions as $a_{s,f}^+$ and $a_{s,f}^-$ are associated with the left- and right-handed side of the cell face, respectively.

In the present work, the KNP flux scheme [149] is employed exclusively. The reasons are discussed in the appendix A. Applying the above OpenFOAM definitions to the semi-discrete KNP flux scheme, cf. Eq. (A.24), yields the following volumetric flux of the general scalar variable ξ at the cell face $j + 1/2$ which is the face between the centroids at x_j and x_{j+1} :

$$(\Phi\xi)_{j+\frac{1}{2}} = \frac{\check{a}_{j+\frac{1}{2}}^+ (\Phi\xi)_{j+\frac{1}{2}}^+ - \check{a}_{j+\frac{1}{2}}^- (\Phi\xi)_{j+\frac{1}{2}}^-}{\check{a}_{j+\frac{1}{2}}^+ - \check{a}_{j+\frac{1}{2}}^-} - \frac{\check{a}_{j+\frac{1}{2}}^+ \check{a}_{j+\frac{1}{2}}^-}{\check{a}_{j+\frac{1}{2}}^+ - \check{a}_{j+\frac{1}{2}}^-} \left(\xi_{j+\frac{1}{2}}^+ - \xi_{j+\frac{1}{2}}^- \right). \quad (3.49)$$

For more details on the applied nomenclature refer to Sec. A.2 in the appendix. Following this expression and the idea of the face-by-face approach, the flux of a general scalar variable ξ in the FVM can be written as [101]

$$\sum_f \Phi_f \xi_f = \sum_f \frac{1}{\check{a}_f^+ - \check{a}_f^-} \left[\check{a}_f^+ \Phi_f^+ \xi_f^+ - \check{a}_f^- \Phi_f^- \xi_f^- - \check{a}_f^+ \check{a}_f^- \left(\xi_f^+ - \xi_f^- \right) \right]. \quad (3.50)$$

This formulation can be further simplified by introducing α^+ , α^- and the volumetric flux ω_f :

$$\alpha_f^+ = \frac{\check{a}_f^+}{\check{a}_f^+ - \check{a}_f^-}, \quad \alpha_f^- = 1 - \alpha_f^+ = -\frac{\check{a}_f^-}{\check{a}_f^+ - \check{a}_f^-} \quad \text{and} \quad \omega_f = \frac{\check{a}_f^+ \check{a}_f^-}{\check{a}_f^+ - \check{a}_f^-}. \quad (3.51)$$

Therefore, Eq. (3.50) can be re-written as:

$$\begin{aligned} \sum_f \Phi_f \xi_f &= \sum_f \left[\alpha_f^+ \Phi_f^+ \xi_f^+ + \alpha_f^- \Phi_f^- \xi_f^- - \omega_f \left(\xi_f^+ - \xi_f^- \right) \right] \\ &= \sum_f \left[\left(\alpha_f^+ \Phi_f^+ - \omega_f \right) \xi_f^+ + \left(\alpha_f^- \Phi_f^- + \omega_f \right) \xi_f^- \right]. \end{aligned} \quad (3.52)$$

Applying Eq. (3.52) to the general high-speed pressure equation (3.46) yields the hybrid pressure-based approach suggested by Kravoshin et al. [143]. In a first step, the volumetric fluxes on the left- and right-hand side of the face are expressed following Eq. (3.36):

$$\Phi_f^+ = (u_{P,i})_f^+ S_{fi} = \left(\frac{H_{P,i}}{a_P} \right)_f^+ S_{fi} - \left(\frac{1}{a_P} \frac{\partial p}{\partial x_i} \right)_f^+ S_{fi}, \quad (3.53)$$

$$\Phi_f^- = (u_{P,i})_f^- S_{fi} = \left(\frac{H_{P,i}}{a_P} \right)_f^- S_{fi} - \left(\frac{1}{a_P} \frac{\partial p}{\partial x_i} \right)_f^- S_{fi}. \quad (3.54)$$

In the next step, these volumetric fluxes are substituted into the KNP flux scheme, see Eq. (3.52), and ξ is replaced by the density ρ . In the final step, the flux formulation for the density is

substituted into the mass conservation equation and the densities in the transient, the pseudo-velocity and the volumetric flux terms are replaced by Eq. (3.43) yielding the final form of the hyperbolic pressure-equation:

$$\begin{aligned} \frac{\delta(\Psi p)}{\delta t} + \frac{1}{\Omega_P} \sum_f \left\{ \left[\alpha_f^+ \left(\frac{H_{P,i}}{a_P} \right)_f^+ S_{fi} - \omega_f \right] (\Psi p)_f^+ - \alpha_f^+ \left(\frac{\rho}{a_P} \right)_f^+ \left(\frac{\partial p}{\partial x_i} \right)_f^+ S_{fi} \right\} \\ + \frac{1}{\Omega_P} \sum_f \left\{ \left[\alpha_f^- \left(\frac{H_{P,i}}{a_P} \right)_f^- S_{fi} + \omega_f \right] (\Psi p)_f^- - \alpha_f^- \left(\frac{\rho}{a_P} \right)_f^- \left(\frac{\partial p}{\partial x_i} \right)_f^- S_{fi} \right\} = 0. \end{aligned} \quad (3.55)$$

This pressure equation allows the simulation of trans- and supersonic flows with ideal and real-gas effects. A thorough validation of this solver can be found in the work of Kraposhin et al. [143]. Further validations were conducted in the PhD thesis of Banholzer [20] and in Sec. F.1 of the appendix.

To conclude the section on the hybrid pressure-based approach, some final remarks are made regarding the implementation and handling:

1. In contrast to the subsonic pressure equation, the terms $H_{P,i}(a_P)^{-1}$ and $\rho(a_P)^{-1}$ are not reconstructed using a linear interpolation but rather TVD schemes to stabilize the solver.
2. All five terms in the pressure equation can be handled implicitly thanks to the replacement of ρ by the product Ψp . As a result, the left- and right-sided pressure-corrected face fluxes can be calculated straightforwardly in OpenFOAM by evoking the already implemented flux function. This yields a left- and right-sided face flux for the momentum, energy and species conservation equations. Note that the direct re-calculation of the face fluxes from the discretized pressure equation is in contrast to the subsonic approach, where the H by a-term is treated explicitly and therefore has to be added to the final face flux calculation.
3. Although the flux calculation is stabilized by a TVD-type reconstruction, the divergence terms in the conservation equations have to be discretized with the blended differencing schemes to avoid an unboundedness of the solution.

3.4 Density-based solver framework

3.4.1 Spurious pressure oscillations

A major problem in the numerical simulation of transcritical flows with density-based solvers is the occurrence of spurious pressure oscillations. This issue is closely related to underresolved gradients in the flow field as a result of the application of the LES. In DNS and RANS, these problems are not as pronounced because the gradients are either resolved or smeared out. Two different explanations can be given for the occurrence of nonphysical pressure oscillations under transcritical flow conditions. These are outlined shortly in the following whereby pure oxygen is considered as fluid.

Nonlinear fluid behavior

In density-based solvers, the solution of the mass and energy conservation equations yields the density and internal energy fields which define the thermodynamic state of the fluid. Both thermodynamic properties show strong nonlinearities under transcritical conditions. The filtering in the LES can therefore result in nonlinear responses in the derived properties like, for instance, the temperature or the pressure. To study this behavior in more detail, the work of Lacaze et al. [156] is followed and a transcritical state change of oxygen at a supercritical pressure of 150 bar is considered. A one-dimensional domain of 2 mm length is used which is resolved uniformly with 200 grid points. The temperature varies between 150 K and 300 K. The open-source fluid data base CoolProp [27] is applied to model the thermophysical behavior of oxygen. The impact of three different filter widths onto the filtered density and energy fields and the derived temperature and pressure values is shown in Fig. 3.5. The temperature field is almost unaffected by the filtering operation. In contrast, with increasing filter width the recalculated pressure shows a strong sensi-

tivity to the filtering operation and a large decrease of several bars occurs in the gradient region. This results from the nonlinear fluid behavior in the transcritical region and manifests itself as spurious pressure oscillations in the numerical simulation. Considering an identical case at larger temperatures, i.e., $500 \text{ K} \leq T \leq 1000 \text{ K}$, the nonideal fluid behavior is not significant anymore and therefore spurious pressure oscillations vanish. This fact is shown in Fig. 3.6 for a supercritical state change of oxygen at again 150 bar.

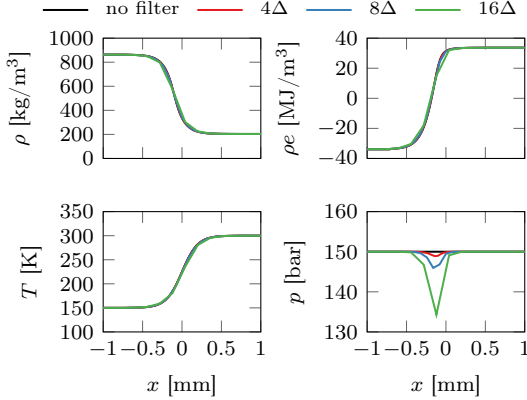


Figure 3.5: Influence of the filter width on a transcritical state change of supercritical oxygen at a pressure of 150 bar and a temperature range of $150 \text{ K} \leq T \leq 300 \text{ K}$.

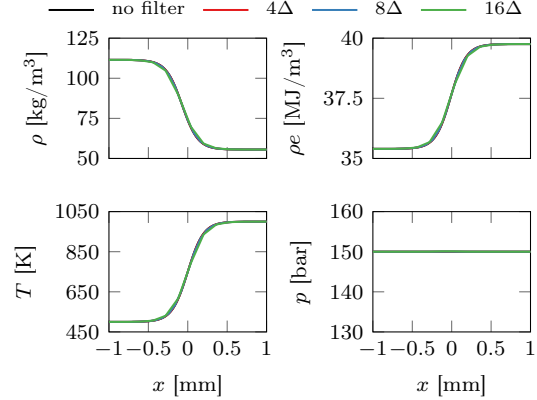


Figure 3.6: Influence of the filter width on an almost ideal state change of supercritical oxygen at a pressure of 150 bar and a temperature range of $500 \text{ K} \leq T \leq 1000 \text{ K}$.

Variation of the specific heat ratio and the reference energy

Since the work of Abgrall and Karni [4] it is known that fully-conservative Godunov-type schemes are not able to maintain the pressure equilibrium across material interfaces and therefore spurious pressure oscillations occur. The cause for these pressure oscillations can be traced back to a change of the reference internal energy e_0 and the specific heat ratio γ across the material front.

Let us follow the statements of Billet and Abgrall [32] and Ma et al. [177] and consider the one-dimensional Euler equations for mass, momentum and energy conservation:

$$\frac{\partial \rho}{\partial t} + \frac{\partial (\rho u)}{\partial x} = 0, \quad (3.56)$$

$$\frac{\partial (\rho u)}{\partial t} + \frac{\partial (\rho u^2)}{\partial x} = -\frac{\partial p}{\partial x}, \quad (3.57)$$

$$\frac{\partial (\rho e_t)}{\partial t} + \frac{\partial (\rho h_t)}{\partial x} = 0. \quad (3.58)$$

Here, the total enthalpy and energy are related by

$$h_t = e_t + \frac{p}{\rho} = e + \frac{u^2}{2} + \frac{p}{\rho}. \quad (3.59)$$

For the case of constant velocity u ($u \neq 0$) and pressure p at time level n , the discretized mass and momentum conservation equation can be further simplified as:

$$\delta \rho = -\frac{\Delta t}{\Delta x} u \Delta \rho, \quad (3.60)$$

$$\delta(\rho u) = -\frac{\Delta t}{\Delta x} u^2 \Delta \rho. \quad (3.61)$$

Here, the transient terms have been discretized using the first order Euler scheme [120]. In addition, the variables $\delta(\bullet)$ and $\Delta(\bullet)$ denote a temporal and a spatial variation, i.e., $\delta(\bullet) = (\bullet)^{n+1} - (\bullet)_j^n$

and $\Delta(\bullet) = (\bullet)_{j+1/2}^n - (\bullet)_{j-1/2}^n$. Substituting Eq. (3.60) into Eq. (3.61) yields

$$\delta(\rho u) = u \delta \rho . \quad (3.62)$$

Using the identity $\delta(\rho u) = \rho \delta u + u \delta \rho$, Eq. (3.62) can be further simplified to

$$u^{n+1} - u^n = 0 . \quad (3.63)$$

Therefore, during a single time step, the velocity equilibrium can be maintained across the material front. To study the behavior of the pressure, the energy conservation equation together with a suitable relation between specific internal energy and pressure is used. For a calorically perfect gas, this relation reads [177]

$$e = e_0 + \frac{p}{\rho(\gamma - 1)} = e_0 + \frac{pv}{\gamma - 1} . \quad (3.64)$$

Here, e_0 and γ are constants and denote the reference internal energy and the specific heat ratio, respectively. In addition, v is the specific volume being the inverse of the density ρ . For general fluids, the assumption of constant e_0 and γ usually does not hold and both can be nonlinear functions of pressure and temperature. However, Eq. (3.64) can still be applied when e_0 and γ are replaced by their respective nonlinear functions e_0^* and γ^* [177]:

$$e = e_0^* + \frac{pv}{\gamma^* - 1} . \quad (3.65)$$

Substituting this relationship into the energy conservation equation (3.58) and applying the same discretization approaches as for Eqs. (3.60) and (3.61) yields:

$$\delta(\rho e_0^*) + \frac{1}{\gamma^* - 1} \delta p + p \delta \left(\frac{1}{\gamma^* - 1} \right) = -\frac{\Delta t}{\Delta x} u \left[\Delta(\rho e_0^*) + \Delta \left(p \frac{\gamma^*}{\gamma^* - 1} \right) \right] . \quad (3.66)$$

Only in the case of constant e_0^* and γ^* the pressure equilibrium ($\delta p = 0$) can be maintained. In addition, Eq. (3.66) shows that oscillations in pressure can occur due to a variation of e_0^* and $(\gamma^* - 1)^{-1}$ in both space and time. As a result, in most practical simulations spurious pressure oscillations occur in regions where e_0^* and γ^* change. Especially under transcritical conditions, the variation of γ^* is very pronounced due to the presence of real-gas effects. In Fig. 3.7, the dependency of γ^* on the pressure and temperature is shown for supercritical oxygen. Near the critical temperature of oxygen ($T_{c,O_2} = 154.58$ K) the largest variations are found and this is therefore the region where strong spurious pressure oscillations can occur in fully-conservative schemes. To prevent such oscillations in the numerical simulation, the double-flux method is used in the present work.

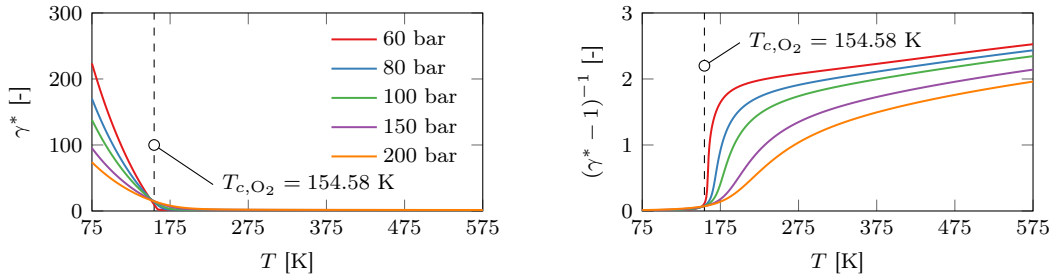


Figure 3.7: Variation of γ^* and $1/(\gamma^* - 1)$ for supercritical oxygen.

3.4.2 Double-flux method

The main idea of the double-flux approach is based on the findings of Eq. (3.66). To maintain the pressure equilibrium ($\delta p = 0$) across regions of varying ρe_0^* and γ^* both quantities have to be

frozen in the rectangular domain $[x_{j-1/2}, x_{j+1/2}] \times [t^n, t^{n+1}]$. This approach was first proposed in 2001 by Abgrall and Karni [4]. In 2003, Billet and Abgrall [32] generalized the double-flux method for temperature-dependent heat capacities. More recently, the double-flux method was extended to real-gas fluids by Ma et al. [177]. This extension is used in the present work to prevent spurious pressure oscillations under transcritical conditions.

As the double-flux method is implemented in a density-based solver framework, the governing equations are solved in an unmodified manner compared to the pressure-based approach introduced in Sec. 3.3. Applying the FVM for the discretization of the governing equations results in the following set of equations:

$$\Omega \frac{\partial \mathbf{U}}{\partial t} + \sum_f (\mathcal{H}_f^e - \mathcal{H}_f^v) \cdot \vec{S}_f = 0 \quad \text{with} \quad \mathbf{U} = [\rho, (\rho \mathbf{u})^T, \rho e_t, (\rho \mathbf{Y})^T]. \quad (3.67)$$

The vector \mathcal{H}_f^e represents the convective part of the numerical fluxes, i.e., the Euler system. The viscous numerical fluxes are denoted as \mathcal{H}_f^v . An important point in the implementation of the double-flux method is the choice of the scheme for the computation of the Euler fluxes. For the double-flux method, flux-vector splitting (FVS) schemes are generally applied which belong to the class of upwind schemes, see appendix A. In the present work, the suggestions of Billet and Abgrall [32] and Billet and Ryan [33] are followed and the AUSM⁺-up scheme [171] is employed.

Figure 3.8 shows the calculation procedure of the double-flux method. After the initialization, the time integration is started which is realized in the present work using the low-storage, four-stage RK scheme introduced in Sec. 3.1.3. Following the main idea of the double-flux method, the evaluation and the freezing of the isentropic exponent γ^* and the reference internal energy e_0^* in the spatial and temporal domain $[x_{j-1/2}, x_{j+1/2}] \times [t^n, t^{n+1}]$ is done prior to the start of the time marching. Based on the definition of the calorically perfect gas, γ^* and e_0^* are defined as [177]:

$$\gamma^* = \frac{\rho a_s^2}{p}, \quad (3.68)$$

$$e_0^* = e - \frac{p}{\rho(\gamma^* - 1)}. \quad (3.69)$$

These two quantities are therefore kept constant throughout a time step, see Fig. 3.8, which suppresses spurious pressure oscillations.

The second step of the double-flux method involves the evaluation of the Euler fluxes \mathcal{H}_f^e at the cell faces. This step can be split into two substeps:

1. Reconstruction of cell centered values onto the faces.
2. Evaluation of the Euler fluxes on the cell faces.

The interpolation of the values at the CV's centroid onto the faces is done as in the case of the hybrid pressure-based approach. The blended differencing scheme is employed as a basis for the interpolation procedure and TVD schemes are used to ensure boundedness, see Eqs. (3.10) and (3.11) and Sec. 3.3.5. In most flux-vector splitting

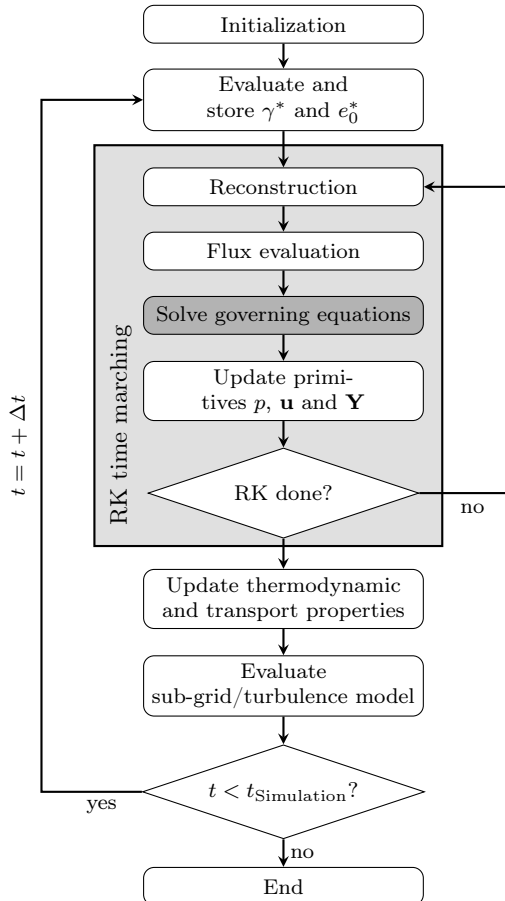


Figure 3.8: Flowchart of the double-flux method.

schemes the LHS and RHS face states are denoted by L and R , respectively. This notation is also adopted in the present case. Therefore, OpenFOAM's positive and negative directions correspond to the left- and right-hand sides of the face, respectively. The numerical flux at the cell face $j + 1/2$ can then be computed according to

$$\mathcal{H}_{j+1/2}^e := \mathcal{H}^e(\mathbf{U}_{j+1/2,L}, \mathbf{U}_{j+1/2,R}). \quad (3.70)$$

In appendix A.3, the numerical approach for the determination of the inviscid fluxes based on the AUSM⁺-up scheme [171] is presented. Since γ^* and e_0^* are frozen, the left-hand side and right-hand side values of these two quantities are different. Therefore, the convective energy fluxes on the LHS and RHS of a cell face are not identical, see Fig. 3.9. For instance, the total energy on the LHS of face $j + 1/2$ is calculated as:

$$(\rho e_t)_{j+1/2,L}^* = \frac{p_{j+1/2,L}}{\gamma_j^* - 1} + \rho_{j+1/2,L} e_{0,j}^* + \frac{1}{2} \rho_{j+1/2,L} \mathbf{u}_{j+1/2,L} \cdot \mathbf{u}_{j+1/2,L}. \quad (3.71)$$

Note the variables γ_j^* and $e_{0,j}^*$ in the first and second term on the right-hand side of the above equation. These two variables yield different energy fluxes at the shared face which in turn cause the quasi-conservative character of the double-flux method. Therefore, an energy conservation error is introduced which reduces with increasing mesh resolution [177]. However, in most practical simulations this error does not vanish and an erroneous energetic state has to be accepted to suppress spurious pressure oscillations.

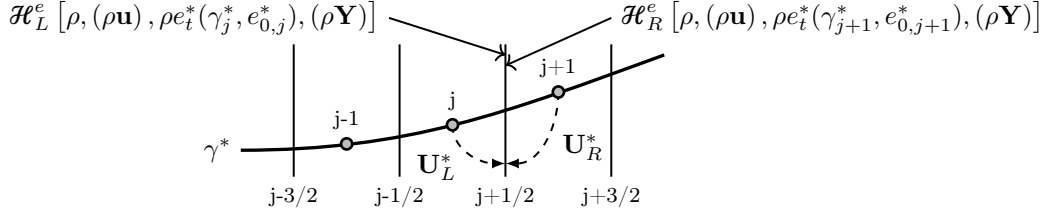


Figure 3.9: Schematic representation of the Euler fluxes on the LHS and RHS side of the cell face at $j + 1/2$ together with a theoretical variation of γ^* .

After the governing equations are solved, the primitive variables p , \mathbf{u} and \mathbf{Y} are updated. The velocity and mass fraction fields are obtained from the solution of the momentum equation and the transport equations of the different species. The pressure is evaluated by utilizing the calorically perfect gas assumption as [177]

$$p = (\gamma^* - 1) [(\rho e_t)^* - \rho e_0^* - 0.5 \rho \mathbf{u} \cdot \mathbf{u}], \quad (3.72)$$

where ρ , \mathbf{u} and $(\rho e_t)^*$ are solutions from the current iteration step.

At the end of a RK time step, the thermodynamic and transport properties are evaluated. For fully consistent thermodynamics, this includes an update of the internal energy from pressure, temperature and compositions, i.e., the pressure and the composition are taken from the double-flux method and the temperature is recalculated from the applied equation of state.

In contrast to the pressure-based solver, the acoustic CFL number is used to determine the time step

$$\text{CFL}_a = \frac{a_s \Delta t}{\Delta x} \quad (3.73)$$

which relates the time step to a representative cell dimension Δx and the local speed of propagation, here denoted as a_s . In the present work, CFL_a numbers between 0.2 and 0.4 are applied. A validation of the density-based solver can be found in appendix G.

4 Thermodynamics modeling

Classical thermodynamics allows the macroscopic analysis of energetic processes over a wide field of scientific and engineering problems. In the present work, the general purpose of the application of thermodynamics is to close the system of nonlinear conservation equations. In this way, relations between thermal and caloric properties are provided and different flow phenomena at engine-relevant conditions can be studied. This requires on the one hand a highly accurate thermodynamic framework which contains the most relevant physical effects. On the other hand, the evaluation of the thermodynamics closure should be as efficient as possible to provide a powerful numerical tool. This is especially important for LESs as computational meshes usually consist of several million CVs. The thermodynamic closure has to be evaluated at each time/iteration step to provide a robust coupling between conserved and derived properties. In the following, a thermodynamic framework is presented which comprises both requirements: accuracy and efficiency. The framework relies on a rigorous definition of the thermodynamic state based on classical equilibrium thermodynamics. This point is highly important to ensure the stability of the CFD simulation under real-gas conditions. Therefore, the complete thermodynamic framework is derived fundamentally in the present work to demonstrate its consistency and to enable the understanding of the relations between different thermodynamic properties.

This chapter is structured as follows: Starting in Sec. 4.1, the fundamental properties and equations of classical thermodynamics are introduced. In Sec. 4.2, the Maxwell relations are presented. The necessary conditions for the thermodynamic equilibrium are derived in Sec. 4.3. Next, the departure function formalism and the calculation of mass- and mole-related properties are introduced in Secs. 4.4 and 4.5, respectively. Based on these introductory sections of classical thermodynamics, the applied ideal- and real-gas models are presented in Secs. 4.6 and 4.7. The real-gas model is augmented in Sec. 4.8 with a vapor-liquid equilibrium model for multicomponent mixtures to enable the investigation of single-phase instabilities under high-pressure conditions. Finally, in Sec. 4.9, characteristics of multicomponent VLEs are discussed and the calculation procedures for different phase diagrams are introduced. The following discussions and presentations are based on the textbooks of Michelsen and Mollerup [196], Firoozabadi [77], Elliott and Lira [73], Poling et al. [237] and Lüdecke and Lüdecke [176]. In addition, the textbooks of Baehr and Kabelac [18], O'Connell and Haile [213], Tester and Modell [312], Sandler [272], Prausnitz et al. [241] and Stephan et al. [300, 301] provide supplementary useful information on thermodynamics for pure and multicomponent fluids.

4.1 Fundamental properties and equations

The foundations of classical thermodynamics are the first and second law of thermodynamics which state the following:

First law: The total energy of an isolated system is constant. Energy can neither be created nor destroyed but transferred from one form into another.

Second law: The total entropy of an isolated system is at a maximum under equilibrium conditions. Natural energy conversion and transfer processes are irreversible and therefore energy has different qualities.

Neither proofs nor exact mathematical definitions exist for these two laws. Both are postulates that rely on abundant human observations and can be understood as the summary of scientific studies over a long period of time that were never disproved. The second law thereby constrains the possibility of processes based on the first law, i.e., it restricts certain paths of energy conversion like, for instance, a one-by-one conversion of heat into work.

The second pillar of classical thermodynamics are state functions. These functions are used to describe the change of a system under equilibrium conditions. State functions have the property that they give one unique value for a set of state variables and that this value is independent of the

integration path, i.e., is not important how we arrive at the state. Thermodynamic state functions can be divided into zero and first order functions [196]. Intensive thermodynamic properties belong to the class of zero order functions. They are nonadditive and at the equilibrium their values are uniform throughout the system. Examples for intensive properties are, for instance, pressure, temperature, chemical potentials or concentrations. In contrast, extensive thermodynamic properties are first order functions which are additive and depend on the size of the system. Examples are internal energy, entropy, volume or mole numbers. The basic versions of the first and second law of thermodynamics are written in terms of extensive properties. Therefore, it is the ultimate goal in classical thermodynamics to express state changes in terms of intensive properties, e.g., pressure and temperature, which are measurable and hence accessible. In addition, these properties are more intuitive to handle and it is easier to prescribe them as boundary conditions in numerical simulations.

Internal energy

The starting point for the derivation of different state functions is the energy balance of a closed system, i.e., the first law of thermodynamics, [77]:

$$dE = dQ + dW . \quad (4.1)$$

Here, E , Q and W are the internal energy, the heat absorbed by the system and the work done across the boundaries of the system, see Fig. 4.1. For a reversible process, work and heat can be expressed as [176]

$$dQ = dQ_{\text{rev}} = T dS \quad (4.2)$$

based on the second law of thermodynamics and as

$$dW = dW_{\text{rev}} = -p dV . \quad (4.3)$$

Here, S and V denote the entropy and the volume, respectively. The negative sign in Eq. (4.3) results from the application of Newton's law and the fact that work added to the system has a positive sign per definition, i.e., for a compression ($dV < 0$) the work (dW) has to be larger than zero. Substituting Eqs. (4.2) and (4.3) into Eq. (4.1) yields the Gibbs fundamental equation [176] for a closed system:

$$dE = T dS - p dV . \quad (4.4)$$

Although this expression has been derived using reversible state changes, it is also valid for arbitrary (irreversible) processes, as E is a state variable, i.e., changes are independent of the path. Integrating Eq. (4.4) yields the internal energy as a function of the entropy and volume:

$$E = E(S, V) . \quad (4.5)$$

This formulation corresponds to a fundamental equation as it includes all necessary information of the thermodynamic system: a caloric equation of state $E = E(T, V)$, the entropy $S = S(T, V)$ and a thermal equation of state $p = p(T, V)$ [176]. To demonstrate this fact, the fundamental equation of E is expressed as total differential:

$$dE = \left. \frac{\partial E}{\partial S} \right|_V dS + \left. \frac{\partial E}{\partial V} \right|_S dV . \quad (4.6)$$

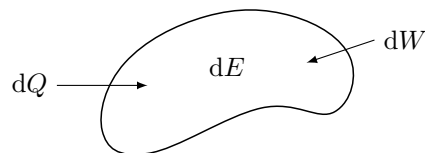


Figure 4.1: Sketch of a closed system defining the first law of thermodynamics.

Comparing this equation to Eq. (4.4), the intensive properties temperature and pressure are found as

$$T = \left. \frac{\partial E}{\partial S} \right|_V , \quad (4.7)$$

$$p = - \left. \frac{\partial E}{\partial V} \right|_S . \quad (4.8)$$

The fundamental equation of E can be extended to multicomponent mixture by representing the internal energy as a function of entropy, volume and composition

$$E = E(S, V, \mathbf{n}) . \quad (4.9)$$

Here, $\mathbf{n} = [n_1, \dots, n_{N_c}]$ is the vector of mole numbers which are extensive properties. The corresponding total differential of E therefore is

$$dE = \left. \frac{\partial E}{\partial S} \right|_{V, \mathbf{n}} dS + \left. \frac{\partial E}{\partial V} \right|_{S, \mathbf{n}} dV + \sum_{i=1}^{N_c} \left. \frac{\partial E}{\partial n_i} \right|_{S, V, n_j \neq i} dn_i = T dS - p dV + \sum_{i=1}^{N_c} \mu_i dn_i . \quad (4.10)$$

The third partial derivative of this total differential has been defined as

$$\mu_i = \left. \frac{\partial E}{\partial n_i} \right|_{S, V, n_j \neq i} \quad (4.11)$$

which is called the chemical potential of component i . The chemical potential has a function analogous to the temperature and the pressure [77]. All three intensive properties – T , p and μ_i – are related to extensive properties – S , V and n_i – and vice versa. Whenever a homogeneous system has gradients in intensive properties, transport of extensive properties occurs to bring the system into an equilibrium condition [196]. Therefore, a gradient in the intensive properties is a driving force for the transport processes of the extensive properties. The difference in temperature causes a heat flux, the difference in pressure results in bulk phase displacement and the difference in the chemical potential yields diffusion fluxes [77], see Tab. 4.1. Diffusion is therefore not caused by a composition gradient but by differences in the chemical potential as it was discussed in Sec. 2.1.

Table 4.1: Extensive and related intensive thermodynamic properties of the internal energy.

Extensive properties		Related intensive properties	
S	entropy	T	temperature
V	volume	$-p$	pressure
n_i	composition	μ_i	chemical potential

According to Eq. (4.9), in a homogeneous system, the internal energy is solely a function of the extensive variables S , V and \mathbf{n} . Therefore, the system is isotropic and the internal energy is a homogeneous function of degree one in the extensive variables [196, 77]. This permits the application of Euler's theorem to the fundamental definition of the internal energy as

$$E(\Lambda S, \Lambda V, \Lambda \mathbf{n}) = \Lambda E(S, V, \mathbf{n}) , \quad (4.12)$$

where Λ is a multiplication parameter [77]. The differentiation of this equation with respect to Λ yields

$$\left. \frac{\partial E}{\partial (\Lambda S)} \right|_{\Lambda V, \Lambda \mathbf{n}} \frac{d(\Lambda S)}{d\Lambda} + \left. \frac{\partial E}{\partial (\Lambda V)} \right|_{\Lambda S, \Lambda \mathbf{n}} \frac{d(\Lambda V)}{d\Lambda} + \sum_{i=1}^{N_c} \left. \frac{\partial E}{\partial (\Lambda n_i)} \right|_{\Lambda S, \Lambda V, \Lambda n_{j \neq i}} \frac{d(\Lambda n_i)}{d\Lambda} = E(S, V, \mathbf{n}) , \quad (4.13)$$

$$\left. \frac{\partial E}{\partial (\Lambda S)} \right|_{\Lambda V, \Lambda \mathbf{n}} S + \left. \frac{\partial E}{\partial (\Lambda V)} \right|_{\Lambda S, \Lambda \mathbf{n}} V + \sum_{i=1}^{N_c} \left. \frac{\partial E}{\partial (\Lambda n_i)} \right|_{\Lambda S, \Lambda V, \Lambda n_{j \neq i}} n_i = E(S, V, \mathbf{n}) . \quad (4.14)$$

Using $\Lambda = 1$ [77, 196] and replacing the remaining partial derivatives by T , $-p$ and μ_i based on Eqs. (4.7), (4.8) and (4.11) gives

$$E = TS - pV + \sum_{i=1}^{N_c} \mu_i n_i . \quad (4.15)$$

The differential form of this equation is

$$dE = T dS + S dT - p dV - V dp + \sum_{i=1}^{N_c} \mu_i dn_i + \sum_{i=1}^{N_c} n_i d\mu_i \quad (4.16)$$

and the comparison with Eq. (4.10) yields the Gibbs-Duhem equation [196]

$$S dT - V dp + \sum_{i=1}^{N_c} n_i d\mu_i = 0 \quad (4.17)$$

which demonstrates the importance of the connection between T , p and μ_i in multicomponent systems.

Other state functions

In common engineering problems, the fundamental equation $E = E(S, V, \mathbf{n})$ is undesirable as S and V might not be available. A different set of thermodynamic variables is usually preferred for convenience which are partial derivatives of the original variables [25]. This could be, for instance, the variable set (T, V, \mathbf{n}) where the entropy has been replaced by its related intensive property, i.e., the temperature T . This substitution is known as Legendre transformation which permits the transformation between different sets of independent variables without a loss of information [41]. The mathematical principle of the Legendre transformation is the basic theorem in line geometry [315, 25]. This principle states that a curve can be described completely by the tangents forming the envelope of the curve. A thorough discussion and introduction of the Legendre transformation can be found in the works of Beegle et al. [25], Michelsen and Mollerup [196] and Firoozabadi [77]. According to Beegle et al. [25], the k -th Legendre transform of the fundamental function $y^{(0)} = y^{(0)}(x_1, \dots, x_m)$ is

$$y^{(k)} = y^{(0)} - \sum_{i=1}^k \frac{\partial y^{(0)}}{\partial x_i} x_i . \quad (4.18)$$

The application of this method to the fundamental equation of the internal energy yields new fundamental equations with a different set of state properties which is shown in the following for three different cases. For this demonstration we consider a pure fluid system as starting point

$$E = E(S, V) = y^{(0)} \quad (4.19)$$

and will later extend the analysis to multicomponent systems. The first Legendre transform ($k = 1$) of the internal energy $E(S, V)$ is

$$y^{(1)} = y^{(0)} - \frac{\partial y^{(0)}}{\partial x_1} x_1 = E - \left. \frac{\partial E}{\partial S} \right|_V S = E - TS := F . \quad (4.20)$$

Here, the partial derivative of E with respect to S has been replaced with the temperature T according to Eq. (4.7). The resulting fundamental equation is known in classical thermodynamics as Helmholtz free energy F . Writing the differential of this fundamental equation

$$dF = dE - T dS - S dT \quad (4.21)$$

and substituting dE according to the Gibbs fundamental equation (4.4) yields

$$dF = -S dT - p dV . \quad (4.22)$$

Therefore, the Helmholtz free energy depends on the temperature T and the volume V , i.e.,

$$F = F(T, V) . \quad (4.23)$$

Hence, the entropy has been replaced with its corresponding intensive property and the Helmholtz free energy is a partial Legendre transform of the internal energy E from the (S, V) -space to the (T, V) -space.

In a similar way, other useful fundamental equations can be derived. Rearranging the variables of the internal energy as $E = E(V, S)$ and applying the first Legendre transformation yields

$$y^{(1)} = y^{(0)} - \frac{\partial y^{(0)}}{\partial x_1} x_1 = E - \left. \frac{\partial E}{\partial V} \right|_S V = E + pV := H \quad (4.24)$$

which is the definition of the enthalpy H . Writing the differential of H and replacing dE according to Eq. (4.4) it can be shown that the enthalpy is a function of pressure and entropy, i.e.,

$$H = H(p, S) . \quad (4.25)$$

Here, the volume has been replaced with its related intensive property – the pressure p .

Finally, a fourth fundamental equation can be derived using $E = E(S, V)$ and the second Legendre transformation:

$$y^{(2)} = y^{(0)} - \frac{\partial y^{(0)}}{\partial x_1} x_1 - \frac{\partial y^{(0)}}{\partial x_2} x_2 = E - \left. \frac{\partial E}{\partial S} \right|_V S - \left. \frac{\partial E}{\partial V} \right|_S V = E - TS + pV = H - TS := G . \quad (4.26)$$

This fundamental equation is called Gibbs energy G . The dependency analysis based on the differential of G shows that the Gibbs energy is a function of temperature and pressure

$$G = G(T, p) \quad (4.27)$$

which is convenient for many engineering applications as both properties – T and p – are accessible in measurements and their definition is intuitive.

In the next step, we can now apply these new fundamental equations of H , F and G straightforwardly to multicomponent fluids by replacing dE with Eq. (4.10). This yields the following total differentials for the enthalpy, Helmholtz free energy and Gibbs energy:

$$dH = T dS + V dp + \sum_{i=1}^{N_c} \mu_i dn_i , \quad (4.28)$$

$$dF = -S dT - p dV + \sum_{i=1}^{N_c} \mu_i dn_i , \quad (4.29)$$

$$dG = -S dT + V dp + \sum_{i=1}^{N_c} \mu_i dn_i . \quad (4.30)$$

Comparing these three formulations and Eq. (4.10), four equivalent definitions of the chemical potential exist

$$\mu_i = \left. \frac{\partial E}{\partial n_i} \right|_{S, V, n_j \neq i} = \left. \frac{\partial H}{\partial n_i} \right|_{S, p, n_j \neq i} = \left. \frac{\partial F}{\partial n_i} \right|_{T, V, n_j \neq i} = \left. \frac{\partial G}{\partial n_i} \right|_{T, p, n_j \neq i} \quad (4.31)$$

whereby the latter expression in terms of the Gibbs energy G is the best known one. However, the third definition based on the Helmholtz free energy F is better applicable in combination with most thermal equations of state as most are pressure-explicit, i.e., functions of T and V .

4.2 Maxwell relations

Using the first law of thermodynamics and the total differential of the internal energy, it could be shown that the first partial derivatives of the fundamental properties are related to the intensive (thermal) properties. Further important thermodynamic relations can be derived based on the second partial derivatives of the fundamental properties [176]. These relations are known as Maxwell relations and rely on the reciprocity relations of the partial derivatives [77]. Using Eqs. (4.7) and (4.8) yields the first Maxwell relation

$$\left. \frac{\partial T}{\partial V} \right|_S = - \left. \frac{\partial p}{\partial S} \right|_V . \quad (4.32)$$

Based on the enthalpy H , the Gibbs energy G and the Helmholtz free energy F three other Maxwell relations can be derived in an analogous manner:

$$\left. \frac{\partial T}{\partial p} \right|_S = \left. \frac{\partial V}{\partial S} \right|_p , \quad (4.33)$$

$$\left. \frac{\partial S}{\partial V} \right|_T = \left. \frac{\partial p}{\partial T} \right|_V , \quad (4.34)$$

$$\left. \frac{\partial S}{\partial p} \right|_T = - \left. \frac{\partial V}{\partial T} \right|_p . \quad (4.35)$$

Additional helpful Maxwell relations based on the total derivative of the internal energy and enthalpy are

$$\left. \frac{\partial S}{\partial T} \right|_V = \frac{\partial E / \partial T|_V}{T} = \frac{C_v}{T} \quad (4.36)$$

and

$$\left. \frac{\partial S}{\partial T} \right|_p = \frac{\partial H / \partial T|_p}{T} = \frac{C_p}{T} . \quad (4.37)$$

4.3 Thermodynamic equilibrium

Classical thermodynamics relies on the equilibrium assumption of the investigated system. According to the second law of thermodynamics, an isolated system reaches its equilibrium state by a spontaneous process which maximizes its entropy. At the same time this is a stationary point, i.e.,

$$dS = 0 . \quad (4.38)$$

To analyze the conditions for this equilibrium according to Eq. (4.38), the fundamental equation of the internal energy, Eq. (4.10), has to be rearranged into an equation for the entropy change [77]:

$$dS = \frac{dE}{T} + \frac{p}{T} dV - \sum_{i=1}^{N_c} \frac{\mu_i}{T} dn_i . \quad (4.39)$$

Let us now consider an isolated system consisting of two subsystems which are initially separated by a moving, diathermic and permeable wall, see Fig. 4.2. The properties of these two subsystems are denoted by $(\bullet)^I$ and $(\bullet)^{II}$, respectively. The application of the conservation principles results in the following basic relations:

$$dE^I + dE^{II} = 0 , \quad dV^I + dV^{II} = 0 \quad \text{and} \quad dn_i^I + dn_i^{II} = 0 \quad \text{with } i = 1, \dots, N_c .$$

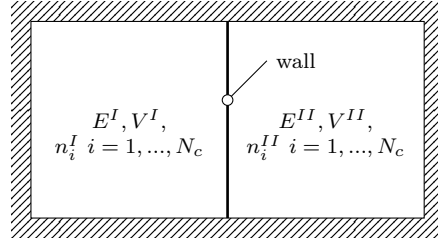


Figure 4.2: Schematic of an isolated system consisting of two subsystems.

Substituting these equalities into the maximum entropy principle yields

$$dS = dS^I + dS^{II} = \left(\frac{1}{T^I} - \frac{1}{T^{II}} \right) dE^I + \left(\frac{p^I}{T^I} - \frac{p^{II}}{T^{II}} \right) dV^I - \sum_{i=1}^{N_c} \left(\frac{\mu_i^I}{T^I} - \frac{\mu_i^{II}}{T^{II}} \right) dn_i^I = 0. \quad (4.40)$$

As E^I , V^I and n_i^I are independent variables, all three coefficients in the brackets must be zero to fulfill the constraint $dS = 0$. Therefore, the thermodynamic equilibrium of a system is defined at equal temperature, pressure and chemical potentials of the different components:

$$T^I = T^{II}, \quad (4.41a)$$

$$p^I = p^{II}, \quad (4.41b)$$

$$\mu_i^I = \mu_i^{II} \quad i = 1, \dots, N_c. \quad (4.41c)$$

Requirements for a spontaneous process

For the independent variables E , V and \mathbf{n} , the process towards the equilibrium occurs spontaneously when the entropy change δS is larger than the corresponding reversible change, i.e., when the entropy is maximized. To study the requirements of a spontaneous process for other variable combinations, we focus on a pure fluid system and replace the equality sign in the Gibbs fundamental equation (4.4) by an inequality and write

$$\delta S > \frac{\delta E}{T} + \frac{p}{T} \delta V \quad (4.42)$$

or more conveniently for the following derivations

$$\delta E < T \delta S - p \delta V. \quad (4.43)$$

Note, that the following considerations only hold for sufficiently small departures from the equilibrium [196].

For small changes, the fundamental equation of the enthalpy can be written as

$$\delta H = \delta E + \delta(pV) = \delta E + p \delta V + V \delta p. \quad (4.44)$$

Substituting δE according to Eq. (4.43) into this expression yields:

$$\delta H < T \delta S + V \delta p. \quad (4.45)$$

For an isentropic and isobaric system, the occurrence of a spontaneous process is therefore bounded to the condition

$$(\delta H)_{S,p} < 0. \quad (4.46)$$

Hence, the stationary point in an isentropic, isobaric system is at the global minimum of the enthalpy.

In a similar way, we can consider changes in the Helmholtz free energy

$$\delta F = \delta E - \delta(TS) = \delta E - T\delta S - S\delta T \quad (4.47)$$

and replace δE with Eq. (4.43) which yields

$$\delta F < -p\delta V - S\delta T. \quad (4.48)$$

Consequently, in an isothermal and isochoric system the equilibrium is reached by a spontaneous process that minimizes the Helmholtz free energy:

$$(\delta F)_{T,V} < 0. \quad (4.49)$$

Finally, the Gibbs energy G is applied to derive another spontaneous process. For small changes, the fundamental equation of G can be written as

$$\delta G = \delta E + \delta(pV) - \delta(TS) = \delta E + p\delta V + V\delta p - T\delta S - S\delta T. \quad (4.50)$$

Substituting Eq. (4.43) into this expression yields

$$\delta G < -S\delta T + V\delta p. \quad (4.51)$$

For a system with constant temperature and pressure, a spontaneous process must therefore proceed in such a way that

$$(\delta G)_{p,T} < 0. \quad (4.52)$$

As a result, the equilibrium of an isobaric, isothermal system is defined at the global minimum of the Gibbs energy. This condition is used to determine phase separation processes in multicomponent mixtures. However, we will see later that the definition based on the Helmholtz free energy can also be convenient for pressure-explicit equations of state. In Tab. 4.2, the equilibrium conditions depending on the state variables are summarized finally.

Table 4.2: Conditions for the equilibrium of a closed system.

Independent variables	State function to be minimized
E, V, \mathbf{n}	$-S$
S, p, \mathbf{n}	H
T, V, \mathbf{n}	F
p, T, \mathbf{n}	G

4.4 Departure function concept

The previous sections have shown that classical thermodynamics provides relations between different extensive and intensive properties. Experimentally, however, only properties like pressure or temperature are usually accessible. In terms of extensive properties, only changes can be measured and therefore an arbitrary zero has to be defined [196]. This results from the fact that changes in state properties do not depend on the path and therefore the selection of the reference zero is a matter of convenience [196]. A very convenient choice for the reference point is the gas state in the limit of zero pressure and density at a reference temperature T^{ref} . This concept is widely known as departure function formalism [196, 73, 237] and combines measurable data with fundamental equations. The idea of this method is as follows: A state property M at the thermodynamic state (T, V, \mathbf{n}) can be determined by means of a three-step procedure:

1. The gases are mixed at the reference temperature T^{ref} , zero pressure and zero density.
2. The mixture is heated from the reference temperature T^{ref} to the desired temperature T .
3. The heated gas mixture is compressed to the final volume V .

Mathematically, this procedure can be expressed as

$$m = \Delta m_{\text{mix}}^0 + \int_{T^{\text{ref}}}^T \left. \frac{\partial m^0}{\partial T} \right|_{V=\infty, \mathbf{n}} d\hat{T} + \int_{\infty}^V \left. \frac{\partial m}{\partial V} \right|_{T, \mathbf{n}} d\hat{V}. \quad (4.53)$$

The terms are arranged according to the description of the three-step procedure and $\hat{\square}$ denotes the integration variable. The next step is to rearrange the terms such that first the reference gas state is transferred to the desired T, V, \mathbf{n} -state, i.e., $m^0(T, V, \mathbf{n})$, and after that a correction $m^r(T, V, \mathbf{n})$ is carried out that accounts for the difference between the hypothetical gas state and the final state. This can be written as follows:

$$m = m^0(T, V, \mathbf{n}) + m^r(T, V, \mathbf{n}). \quad (4.54)$$

Here, both terms can be expressed as

$$m^0(T, V, \mathbf{n}) = \Delta m_{\text{mix}}^0 + \int_{T^{\text{ref}}}^T \left. \frac{\partial m^0}{\partial T} \right|_{V=\infty, \mathbf{n}} d\hat{T} + \int_{\infty}^V \left. \frac{\partial m^0}{\partial V} \right|_{T, \mathbf{n}} d\hat{V} \quad (4.55)$$

and

$$m^r(T, V, \mathbf{n}) = \int_{\infty}^V \left[\left. \frac{\partial m}{\partial V} \right|_{T, \mathbf{n}} - \left. \frac{\partial m^0}{\partial V} \right|_{T, \mathbf{n}} \right] d\hat{V}. \quad (4.56)$$

The latter expression $m^r(T, V, \mathbf{n})$ is called departure function as it accounts for the difference between the hypothetical gas state and the actual thermodynamic state.

To demonstrate the application of the departure function formalism, the Helmholtz free energy is considered as state function, i.e., $m = F$. Splitting F into the hypothetical and correction part yields

$$F = F^0 + F^r. \quad (4.57)$$

The hypothetical gas state can be determined according to Eq. (4.20) as

$$F^0 = E^0 - TS^0 = H^0 - (pV)^0 - TS^0, \quad (4.58)$$

where only hypothetical gas states are necessary to express F^0 . These are accessible based on measurements and theoretical approaches [237]. In the present work, the hypothetical gas state is evaluated by the ideal gas model. This model is introduced in Sec. 4.6. The departure contribution of the Helmholtz free energy reads

$$F^r = \int_{\infty}^V \left(\left. \frac{\partial F}{\partial V} \right|_{T, \mathbf{n}} - \left. \frac{\partial F^0}{\partial V} \right|_{T, \mathbf{n}} \right) d\hat{V}. \quad (4.59)$$

For the determination of both partial derivatives, we compare Eq. (4.29) with the total differential of $F(T, V, \mathbf{n})$

$$dF = \left. \frac{\partial F}{\partial T} \right|_{V, \mathbf{n}} dT + \left. \frac{\partial F}{\partial V} \right|_{T, \mathbf{n}} dV + \sum_{i=1}^{N_c} \left. \frac{\partial F}{\partial n_i} \right|_{T, V, n_j \neq i} dn_i \quad (4.60)$$

which yields

$$\left. \frac{\partial F}{\partial V} \right|_{T, \mathbf{n}} = -p. \quad (4.61)$$

Consequently, the residual part of F can be written as

$$F^r = \int_{\infty}^V (p^0 - p) d\hat{V}. \quad (4.62)$$

Both an ideal- and a real-gas pressure-explicit thermal equation of state of the form

$$p = p(T, V, \mathbf{n}) \quad (4.63)$$

are necessary to evaluate the departure function. It is noteworthy that no caloric real-gas model is necessary to determine the state function. Only ideal gas properties and a real-gas equation of state are needed to evaluate the Helmholtz free energy. We will see in the following that this is no exception but rather a rule which accounts for all other fundamental functions and related/derived properties.

The residual concept can also be applied to the variable set (T, p, \mathbf{n}) . In this case, the fundamental property m can be determined as

$$m = m^0(T, p, \mathbf{n}) + m^r(T, p, \mathbf{n}) . \quad (4.64)$$

The basic idea of the integration path of m^0 and m^r is identical to the (T, V, \mathbf{n}) -case, only the integration is performed from zero pressure instead of zero density:

$$m^0(T, p, \mathbf{n}) = \Delta m_{\text{mix}}^0 + \int_{T^{\text{ref}}}^T \frac{\partial m^0}{\partial T} \Big|_{p=0, \mathbf{n}} d\hat{T} + \int_0^p \frac{\partial m^0}{\partial p} \Big|_{T, \mathbf{n}} d\hat{p} \quad (4.65)$$

and

$$m^r(T, p, \mathbf{n}) = \int_0^p \left[\frac{\partial m}{\partial p} \Big|_{T, \mathbf{n}} - \frac{\partial m^0}{\partial p} \Big|_{T, \mathbf{n}} \right] d\hat{p} . \quad (4.66)$$

4.5 Partial molar and specific properties

In multicomponent fluids and mixtures, partial molar and specific properties play an important role as they describe the variation of an extensive property with respect to a variation in the mole number or mass. For the following derivations, an isobaric, isothermal single-phase system composed of various components is considered. Let \mathcal{B} be an extensive property that is in turn a homogeneous function of degree one. The partial molar property \underline{b}_i of \mathcal{B} at isobaric, isothermal conditions can be written as [196, 77]

$$\underline{b}_i := \frac{\partial \mathcal{B}}{\partial n_i} \Big|_{p, T, n_j \neq i} . \quad (4.67)$$

Using Euler's theorem with $\Lambda = 1$ we can therefore write

$$\mathcal{B} = \sum_{i=1}^{N_c} n_i \frac{\partial \mathcal{B}}{\partial n_i} \Big|_{p, T, n_j \neq i} \quad (4.68)$$

and recover the extensive property based on the partial molar properties and mole numbers of the different species. In a similar way, partial mass properties can be defined as

$$\underline{b}_i := \frac{\partial \mathcal{B}}{\partial m_i} \Big|_{p, T, m_j \neq i} \quad (4.69)$$

and the extensive property can be recalculated analogously according to

$$\mathcal{B} = \sum_{i=1}^{N_c} m_i \frac{\partial \mathcal{B}}{\partial m_i} \Big|_{p, T, m_j \neq i} . \quad (4.70)$$

Following this approach, intensive mole- and mass-related properties can be defined as

$$\underline{b} = \frac{\mathcal{B}}{n_t} = \sum_{i=1}^{N_c} z_i \underline{b}_i , \quad (4.71)$$

$$\beta = \frac{\mathcal{B}}{m_t} = \sum_{i=1}^{N_c} Y_i \beta_i . \quad (4.72)$$

4.6 Ideal-gas model

The major characteristic of gases is that they cover an available volume completely since the atoms and molecules of gases can move freely and have only weak attractive and repulsive forces [176]. Neglecting such forces and assuming that molecules/atoms of such gases are point masses, i.e., they do not possess an own volume, results in the ideal-gas model. Additional assumptions of this fluid model are: The molecules are in a constant random motion without a preferred direction in space. The collisions between the molecules and the boundaries are perfectly elastic. The pressure in the occupied volume is therefore only a result of the collisions between the molecules and the boundaries. Finally, the mean kinetic energy of the molecules is directly proportional to the temperature of the gas. In general, the ideal gas law is only valid at very low pressures and high temperatures. However, it has the charm that it can be derived straightforwardly from the kinetic gas theory. Therefore, it is a good choice to form the basis for the departure function formalism due to its sound theoretical character.

4.6.1 Thermal and caloric equation of state

In 1834, Clapeyron proposed the ideal gas law [162] by combining the empirical laws of Boyle, Charles, Avogadro and Gay-Lussac. The pressure-explicit form of this thermal equation of state (EoS) reads

$$p = \frac{n\mathcal{R}T}{V} \quad (4.73)$$

and links the pressure with the temperature, volume and mole number. Here, n can either be the mole number of a single component or of the mixture, i.e., $n = n_t$. Using the definition of the molar property according to Eq. (4.71), the ideal gas law can be written as

$$p\underline{v} = \mathcal{R}T . \quad (4.74)$$

The universal gas constant \mathcal{R} can be further related to the Avogadro constant N_A and the Boltzmann constant k_B as $\mathcal{R} = k_B N_A$.

Since the experimental work of Gay-Lussac [176] it is known that the internal energy and the enthalpy of an ideal gas are sole functions of the temperature. This fact can be also demonstrated theoretically using the already derived thermodynamic relations and the ideal gas law according to Eq. (4.73). Let us consider an iso-composition fluid and an isothermal state change. The derivative of the internal energy and the enthalpy with respect to the volume and the pressure can be written as

$$\left. \frac{\partial E}{\partial V} \right|_T = \left. \frac{\partial E}{\partial S} \right|_V \left. \frac{\partial S}{\partial V} \right|_T + \left. \frac{\partial E}{\partial V} \right|_S \quad \text{and} \quad \left. \frac{\partial H}{\partial p} \right|_T = \left. \frac{\partial H}{\partial S} \right|_p \left. \frac{\partial S}{\partial p} \right|_T + \left. \frac{\partial H}{\partial p} \right|_S . \quad (4.75)$$

Using the relations of extensive and intensive properties from the Secs. 4.1 and 4.2 both approaches can be re-formulated as

$$\left. \frac{\partial E}{\partial V} \right|_T = T \left. \frac{\partial p}{\partial T} \right|_V - p \quad \text{and} \quad \left. \frac{\partial H}{\partial p} \right|_T = -T \left. \frac{\partial V}{\partial T} \right|_p + V . \quad (4.76)$$

Both remaining partial derivatives can be expressed based on the ideal gas law according to Eq. (4.73) which yields

$$\left. \frac{\partial E}{\partial V} \right|_T = T \frac{n\mathcal{R}}{V} - p = p - p = 0 \quad \text{and} \quad \left. \frac{\partial H}{\partial p} \right|_T = -T \frac{n\mathcal{R}}{p} + V = -V + V = 0 . \quad (4.77)$$

This demonstrates that both the internal energy as well as the enthalpy of an ideal gas are not a function of the pressure and hence solely functions of the temperature. As a result, the heat

capacity, the molar enthalpy and the entropy of an ideal gas can be expressed as:

$$\underline{c}_p^0 = \underline{c}_p^0(T), \quad (4.78)$$

$$\underline{h}^0 = \underline{h}^0(T^{\text{ref}}) + \int_{T^{\text{ref}}}^T \underline{c}_p^0(\hat{T}) d\hat{T}, \quad (4.79)$$

$$\underline{s}^0 = \underline{s}^0(T^{\text{ref}}) + \int_{T^{\text{ref}}}^T \frac{\underline{c}_p^0(\hat{T})}{\hat{T}} d\hat{T} - \mathcal{R} \int_{p^{\text{ref}}}^p \frac{dp}{\hat{p}} = \underline{s}^0(T^{\text{ref}}) + \int_{T^{\text{ref}}}^T \frac{\underline{c}_p^0(\hat{T})}{\hat{T}} d\hat{T} - \mathcal{R} \ln\left(\frac{p}{p^{\text{ref}}}\right). \quad (4.80)$$

Here, $\underline{h}^0(T^{\text{ref}})$ is the molar enthalpy of formation at the reference temperature and $\underline{s}^0(T^{\text{ref}})$ is the reference molar entropy. The pressure term in the entropy equation results from the application of Eq. (4.28). In OpenFOAM, the reference temperature and pressure are 298.15 K and 1 bar, respectively. To model the temperature dependent part of the three quantities, the 7-coefficient NASA (abbreviation for: National Aeronautics and Space Administration) polynomials [97] are used in the present work. These polynomials read as follows [97]:

$$\frac{\underline{c}_p^0(T)}{\mathcal{R}} = a_1 + a_2 T + a_3 T^2 + a_4 T^3 + a_5 T^4, \quad (4.81)$$

$$\frac{\underline{h}^0(T)}{\mathcal{R}T} = a_1 + \frac{a_2 T}{2} + \frac{a_3 T^2}{3} + \frac{a_4 T^3}{4} + \frac{a_5 T^4}{5} + \frac{a_6}{T}, \quad (4.82)$$

$$\frac{\underline{s}^0(T)}{\mathcal{R}} = a_1 \ln(T) + a_2 T + \frac{a_3 T^2}{2} + \frac{a_4 T^3}{3} + \frac{a_5 T^4}{4} + a_7. \quad (4.83)$$

Here, a_i are constant coefficients which depend on the fluid. The set of coefficients in the NASA polynomials is split into two temperature intervals. The coefficients applied in the present work are taken from the work of Goos et al. [97]. Based on the concept of molar properties, the NASA polynomials can be extended to multicomponent mixtures by a molar weighting of the fluid specific coefficients.

4.6.2 Transport properties

For modeling the viscosity and the thermal conductivity, a large number of different approaches can be found in the literature. The most general models rely on the kinetic gas theory. Many other approaches have an empirical or semi-empirical character. A comprehensive overview on different modeling approaches can be found in the textbook of Poling et al. [237] or in the PhD thesis of Seidl [283].

In the present work, the viscosity and thermal conductivity of an ideal gas are used in RANS simulations of convection-dominated high-speed flows. Sutherland's law [305, 349] is employed to describe the temperature dependency of the viscosity as

$$\mu = C_1 \frac{T^{3/2}}{T + C_2}. \quad (4.84)$$

Here, C_1 and C_2 are species-dependent constants. In the present work, Sutherland's law is applied exclusively for the binary n-hexane/nitrogen mixture. Here, the required constants are $C_1 = 8.6 \times 10^{-7}$ Pa s and $C_2 = 400$ K for n-hexane and $C_1 = 1.44 \times 10^{-6}$ Pa s and $C_2 = 110$ K for nitrogen.

The thermal conductivity of an ideal gas is modeled using the modified Eucken equation due to Svehla [307]:

$$\lambda = \mu c_v^0 \left(1.32 + 1.77 \frac{R}{c_v^0} \right). \quad (4.85)$$

Here, c_v^0 is the isochoric heat capacity of an ideal gas. This property can be derived from the

definition of the enthalpy, see Eq. (4.24), and the ideal gas law, see Eq. (4.73), as

$$\frac{\partial h}{\partial T} = c_p^0 = \frac{\partial e}{\partial T} + R = c_v^0 + R. \quad (4.86)$$

This yields a relation between the isochoric and the isobaric heat capacity which reads

$$c_p^0 - c_v^0 = R. \quad (4.87)$$

The relation is strictly valid for ideal gases and for real gases the pressure dependency of the thermodynamic properties has to be taken into account.

4.7 Real-gas model

In general fluids, intermolecular forces and the volume of the molecules cannot be neglected as it is the case in the ideal gas model. In both liquids and gases, attractive and repulsive forces dictate the pVT -fluid behavior. Especially at high pressures and large densities, the application of the ideal gas law yields large inaccuracies which are not acceptable for high fidelity modeling of thermodynamic properties. Figure 4.3a shows a pV,p - diagram for four different application-relevant fluids together with the ideal gas law at a constant temperature of 293.15 K. As a result of the isothermal condition, the ideal gas law yields a fluid-independent straight line showing no pressure dependency. In

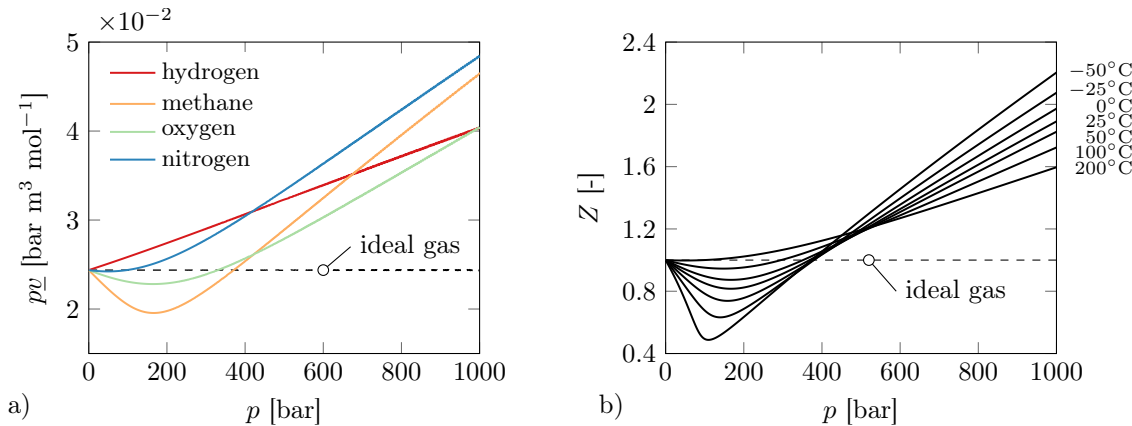


Figure 4.3: Demonstration of the nonideal fluid behavior: a) pV,p - diagram at $T = 293.15$ K for four different fluids; b) Variation of the compressibility factor Z of methane with pressure and temperature. The data for both figures have been taken from CoolProp [27].

contrast, for all four fluids under consideration large deviations from the ideal gas law are found. Only at zero pressure the lines converge towards the ideal-gas reference value. With larger pressure the difference between the nonideal (real) and ideal fluid behavior increases demonstrating the necessity of considering intermolecular forces in the fluid models. Figure 4.3b further emphasizes this by showing the variation of the compressibility factor Z of methane over a wide temperature and pressure range. For an ideal gas, the compressibility factor is a constant, i.e., $Z^0 = 1$. In the real fluid case, Z is generally unequal to unity and can be smaller or larger than one. Only in the zero pressure case and at a single point at elevated pressure the compressibility factor is equal to one. The connection of the high-pressure states with $Z = 1$ is known as Boyle curve [176] and marks the points where the real fluid behaves like an ideal gas, i.e., the intermolecular forces cancel each other.

For modeling the pVT -behavior of real fluids, a large number of different approaches can be found in the literature, see, for instance, the textbooks of Poling et al. [237] or Lüdecke and Lüdecke [176] or the papers of Valderrama [331], Wei and Sadus [345], Anderko [6] or Martin [183]. A review of different types of EoSs of different complexity and fidelity for both pure fluids and mixtures can

be found in the book of Sengers et al. [286]. According to Valderrama [331], the available real fluid EoSs can be put roughly into three different categories:

1. virial-type EoSs,
2. van der Waals EoSs,
3. molecular-based EoSs.

The virial-type EoSs are usually polynomial series of the pressure (Berlin form) or the inverse volume (Leiden form) [176, 237]. They are derived based on potential functions of the intermolecular interactions using statistical thermodynamics. Therefore, the first term of a virial EoS equals the ideal gas law and all additional terms account for corrections of the nonideal fluid behavior. One of the most widely applied and known representatives of the virial-type EoS group is the thermal EoS due to Benedict, Webb and Rubin [30] which has eight adjustable parameters. This enables a highly accurate representation of the pure fluid behavior but at the expense of relatively large computing times compared to simpler EoSs like the van der Waals-type EoSs. In addition, the adjustable parameters make the extension of virial-type EoSs to arbitrary mixtures and new fluids cumbersome and difficult. Regarding the difficulty in handling and the amount of required computational time, similar conclusions can be drawn for the molecular-based EoSs like, e.g., the PC-SAFT EoS [103]. These facts are especially problematic with respect to the conduction of LESs as the application of such costly EoSs is in contradiction to the idea of a powerful numerical tool. A very good compromise between efficiency and accuracy are van der Waals EoSs. This type of state equation has several advantages [331]: The evaluation of the EoS is relatively simple. Next, they can correctly predict the pVT -behavior of fluids over the entire range of liquid and gaseous states. Finally, these EoSs can be extended quite easily to arbitrary mixtures and if necessary they can be fitted conveniently to available experimental data. For these reasons, especially the branch of cubic (empirical) EoSs is very popular in LESs at engine-relevant conditions, see, e.g., the recent review papers of Bellan [29] or Oefelein [216]. Therefore, cubic empirical EoSs will be used in the present work to model the pVT -behavior of high-pressure fluids.

4.7.1 Cubic equations of state

Almost 150 years ago, van der Waals [333] (vdW) proposed for the first time ever a cubic EoS that was able to represent the pVT -behavior of liquids and gases, i.e., predict the coexistence of vapor and liquid at subcritical conditions, with a single EoS. The epoch-making character of this state equation is recognized in the fact that a whole group of EoSs is named after van der Waals. The common feature of this group is that they divide the intermolecular forces into a repulsive and an attractive term [345]. The pioneering EoS due to van der Waals [333], which accounts for both forces, reads

$$p = \frac{\mathcal{R}T}{\underline{v} - b} - \frac{a}{\underline{v}^2}. \quad (4.88)$$

Here, b is the co-volume of the molecules that reduces the available volume and can therefore be interpreted as a repulsive force, i.e., it increases the pressure compared to the ideal gas law. The parameter a accounts for the attractive forces and reduces the pressure compared to the ideal gas law. Setting a and b equal to zero, the ideal gas law according to Eq. (4.74) can be recovered.

General features

For the determination of the parameters a and b , the inflection point of the critical isotherm $T = T_c$ at the critical point is used. This characteristic point can be expressed mathematically as:

$$\left. \frac{\partial p}{\partial \underline{v}} \right|_{T=T_c} = \left. \frac{\partial^2 p}{\partial \underline{v}^2} \right|_{T=T_c} = 0. \quad (4.89)$$

As cubic EoSs are two parameter state equations, two of the three critical properties – pressure, temperature and volume – can be used to finally determine a and b based on the described equality in Eq. (4.89). Usually, p_c and T_c are employed. For the vdW-EoS [333] this yields the following

fluid specific equations for both parameters [176]:

$$a = 0.421875 \frac{\mathcal{R}^2 T_c^2}{p_c}, \quad (4.90)$$

$$b = \frac{1}{8} \frac{\mathcal{R} T_c}{p_c}. \quad (4.91)$$

As a result, the critical compressibility Z_c is fixed, i.e., Z_c is an EoS-dependent constant, and consequently the critical volume is also an EoS-dependent parameter. For the vdW state equation the critical compressibility is 0.375. This value is not in good agreement with most application-relevant fluids which can result in large deviations of the predicted liquid density, see Fig. 4.4a. In contrast, using T_c and v_c to determine a and b gives the correct critical volume at the expense of a wrong prediction of the critical pressure which is undesirable for the numerical investigation of high-pressure injection. A possible improvement for the prediction of the liquid density is the concept of volume translation which was proposed for the first time by Martin [182]. The idea is to alter the density at constant pressure and temperature by a constant or variable factor to get better agreement with experimental data. In the present work, this concept is not adopted as it is not yet well established for multicomponent mixtures [77]. An overview and a critical discussion of volume-translation methods under engine-relevant conditions can be found in the work of, for instance, Mattheis et al. [186]. Another possibility to overcome the described problem is the application of a three parameter EoS as it was proposed by Cismonti and Mollerup [53]. This state equation is a blended version of two cubic EoSs in order to combine their advantages and to arrive at a more universal state equation which is suitable for the representation of a large number of different fluids. Unfortunately, this type of EoS is also not very well established and not an alternative in the present work. As a result, standard cubic EoSs are employed and attention has to be paid to choose the EoS which is best suited for the investigated fluid and/or mixture.

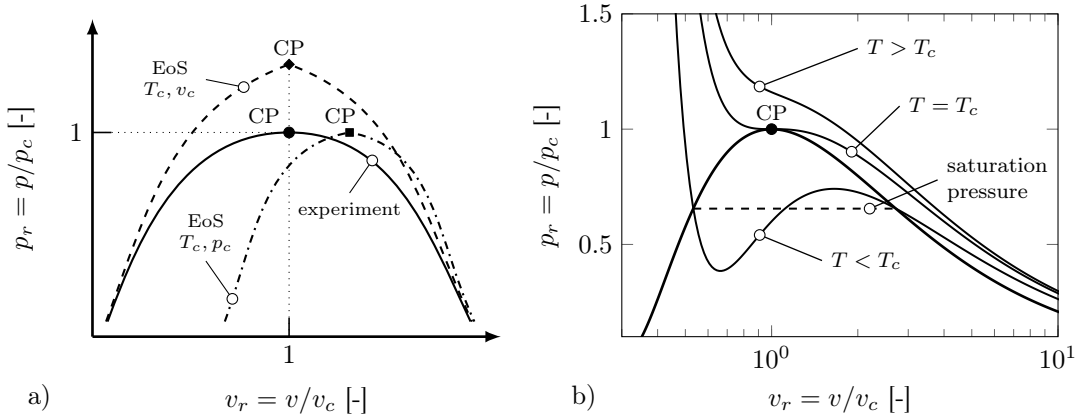


Figure 4.4: Coexistence region of vapor and liquid for a general pure fluid: a) Influence of the selected critical parameter set (T_c, p_c vs. T_c, v_c) in cubic EoSs (adopted from Chou and Prausnitz [49]); b) Visualization of the van der Waals isotherm ($T < T_c$).

A second important fact concerning cubic EoSs is their mathematical character with regard to the evaluation of the volume from a pressure-temperature pair. All cubic state equations are functions of third degree in the volume. To demonstrate this, the vdW-EoS [333] can be arranged into the following form

$$\underline{v}^3 - \left(\frac{\mathcal{R}T}{p} + b \right) \underline{v}^2 + \frac{a}{p} \underline{v} - \frac{ab}{p} = 0. \quad (4.92)$$

In general, the calculation of the volume for a given temperature and pressure can be done by employing, for instance, Cardano's method for cubic equations, see, e.g., Press et al. [243]. Care has to be taken under subcritical conditions $T < T_c$. Here, the cubic EoS forms a loop under isothermal conditions which is often called van der Waals isotherm/loop, see Fig. 4.4b. Therefore, the cubic EoS has three real solutions out of which the physically most meaningful solution has to

be selected. As an isothermal, isobaric system is considered for the evaluation of the volume, the root with the minimum Gibbs energy is usually the solution of choice.

A third characteristic of cubic EoSs is that they obey the corresponding states principle (CSP). The CSP states that for the same reduced pressure and temperature all fluids have the same reduced volume. Figure 4.5 visualizes the CSP for three different fluids – methane, oxygen and nitrogen – by means of a compressibility factor-reduced pressure plot. The data have been taken from CoolProp [27] and the spline was manually fitted to the respective normalized temperature T_r . It can be seen that by normalizing the pressure and temperature to the corresponding critical point the data collapse to a single curve for the respective reduced temperature. Therefore, generalized approaches based on the CSP – like the cubic EoSs – can be used to represent the pVT -behavior of different fluids. Mathematically, this can be demonstrated by re-writing the vdW-EoS [333] in the following reduced form:

$$\left(p_r + \frac{3}{v_r^2} \right) (3v_r - 1) = 8T_r . \quad (4.93)$$

Here, the variables have been normalized with the respective critical properties: $p_r = p/p_c$, $T_r = T/T_c$ and $v_r = v/v_c$.

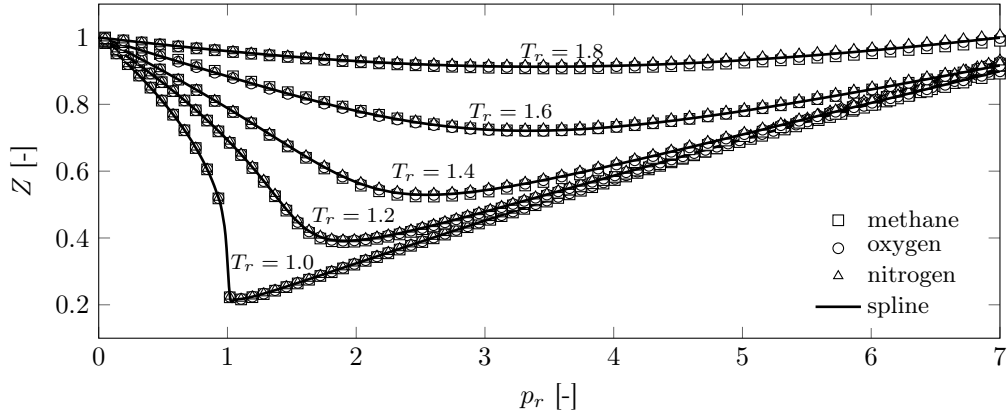


Figure 4.5: Demonstration of the corresponding states principle for three different fluids. The splines have been fitted through the available data points of the respective reduced temperature. The data have been taken from CoolProp [27].

Employed cubic EoSs

For the description of the pVT -behavior of most engine-relevant fluids, the vdW-EoS [333] is not accurate enough as a and b are only fluid-specific constants, see Eqs. (4.90) and (4.91). Historically, however, this EoS was a starting point for the development of a huge number of different modifications [331, 286]. The breakthrough for a lot of sophisticated improvements was made by Redlich and Kwong [251] (RK) in 1949 [240]. Redlich and Kwong [251] added the temperature dependency to the attractive term and could thereby drastically improve the prediction accuracy compared to the vdW-EoS [333]. A lot of different groups and researchers followed the idea of Redlich and Kwong [251] and deduced new improved cubic EoSs. A comprehensive overview on this topic is given in the work of Martin [183]. The most outstanding and most widely used EoSs resulting from this new development area are the state functions developed by Soave [296] (SRK-EoS) and Peng and Robinson [226] (PR-EoS). Based on the work of Redlich and Kwong [251], Soave [296] suggested to model the attractive term as a general function of the reduced temperature and the acentric factor ω , i.e., $a = a(T_r, \omega)$. The acentric factor was proposed by Pitzer [234] and is a measure for the difference between the molecular structure of the considered fluid and a perfectly spherical molecule ($\omega = 0$). The general approach for the determination of the attractive term

according to Soave [296] reads

$$a(T_r, \omega) = a_c \alpha(T_r, \omega) = C \frac{\mathcal{R}^2 T_c^2}{p_c} \left[1 + \kappa(\omega) \left(1 - \sqrt{\frac{T}{T_c}} \right) \right]^2. \quad (4.94)$$

Here, C is a constant which depends on the applied EoS and κ is a function of the acentric factor ω which is determined using experimental data. Peng and Robinson [226] followed an identical path to deduce their cubic EoS. As a result, the pressure-explicit form of both EoSs can be written as [253]:

$$p = \frac{\mathcal{R} T}{\underline{v} - b} - \frac{a(T_r, \omega)}{\underline{v}^2 + ub\underline{v} + wb^2} = \frac{\mathcal{R} T}{\underline{v} - b} - \frac{a_c \alpha(T_r, \omega)}{\underline{v}^2 + ub\underline{v} + wb^2}. \quad (4.95)$$

Here, u and w are EoS-dependent model constants. In Tab. 4.3, the definitions and the calculation of the different parameters for the SRK-EoS [296] and the PR-EoS [226] are summarized. As different approaches for the attractive term and different experimental vapor pressure data sets were used to derive these state equations, the model parameters and constants differ from each other. Consequently, the critical compressibilities are different, see Tab. 4.3. Therefore, both

Table 4.3: Parameters for the general cubic equation of state, see Eq. (4.95).

Parameter	SRK-EoS [296]	PR-EoS [226]
u	1	2
w	0	-1
a_c	$0.42748 \frac{\mathcal{R}^2 T_c^2}{p_c}$	$0.45724 \frac{\mathcal{R}^2 T_c^2}{p_c}$
$\alpha(T_r, \omega)$	$[1 + \kappa(\omega) \left(1 - \sqrt{\frac{T}{T_c}} \right)]^2$	
$\kappa(\omega)$	$0.480 + 1.574 \omega - 0.176 \omega^2$	$0.37464 + 1.54226 \omega - 0.26992 \omega^2$
b	$0.08664 \frac{\mathcal{R} T_c}{p_c}$	$0.07780 \frac{\mathcal{R} T_c}{p_c}$
Z_c	0.333	0.307

cubic EoSs are best suited for different fluids. In Fig. 4.6, this fact is elaborated in more detail. Figure 4.6a compares the predicted density for different alkanes from the homologue series at a fixed reduced temperature and pressure. The reference data have been taken from CoolProp [27]. For short-chain alkanes, the SRK-EoS [296] gives the best agreement. In contrast, with increasing chain length, the prediction accuracy of the PR-EoS [226] is getting better and surpasses the SRK-EoS [296]. Especially, for n-hexane, n-heptane and n-octane the PR-EoS [226] performs excellently. This is further emphasized in Fig. 4.6b where the prediction accuracy of both EoSs is evaluated for the isotherm $T = 300$ K and over a wide pressure range. For hydrogen only small differences between the SRK- and the PR-EoS are visible. The PR-EoS [226] gives a mean deviation from the reference data [27] of about -3.81% and the SRK-EoS of about -0.13%. In contrast, for n-hexane the mean deviation of the PR-EoS [226] is -1.38% and for the SRK-EoS [296] it is 10.46%. In the case of methane, the situation is reversed: The mean deviation of the PR-EoS [226] is 4.12% and for the SRK-EoS [296] it is -2.37%. Overall, the PR-EoS [226] is better suited for long-chain molecules whereas the SRK-EoS [296] is the better choice for small molecules.

4.7.2 Multicomponent mixtures

For the description of mixture properties, it is necessary to add the composition dependency to the thermal EoS, i.e.,

$$p = p(T, V, \mathbf{n}) = p(T, \underline{v}, \mathbf{z}). \quad (4.96)$$

This yields additional information about the mixture behavior but also increases the complexity of the thermodynamic model. In the present work, the one-fluid model is applied to represent the mixture properties. In this modeling approach the mixture is assumed to behave like a pure fluid with adjusted parameters [237]. Consequently, the modeling of the mixture reduces to finding

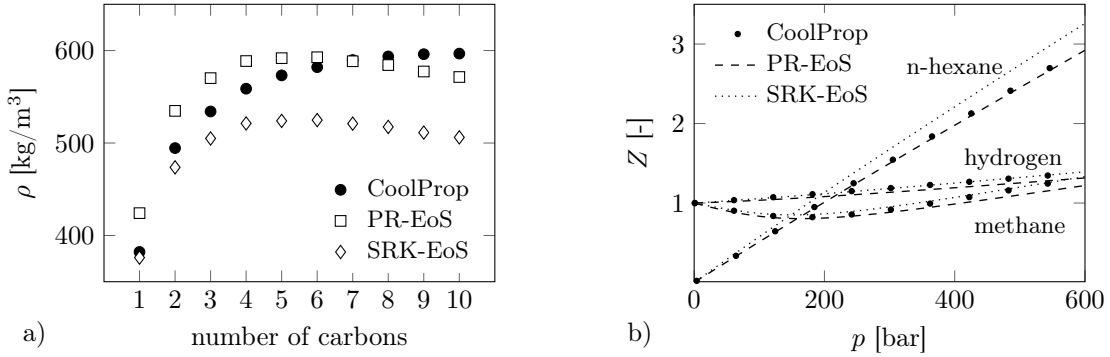


Figure 4.6: Comparison of the PR-EoS [226] and the SRK-EoS [296] with reference data from CoolProp [27]: a) Density ρ for different alkanes from the homologue series at $p_r = p/p_c = 1.5$ and $T_r = T/T_c = 0.75$; b) Compressibility factor Z of methane, hydrogen and n-hexane at $T = 300$ K.

appropriate expressions for the mixture-dependent attractive and repulsive parameters, i.e., $a = a(\mathbf{z})$ and $b = b(\mathbf{z})$. In the literature, many different mixture models can be found as up to now no analytically closed solution is known for the representation of multicomponent fluids. More information on different mixture models can be found in the textbooks of, for instance, Poling et al. [237] or Michelsen and Mollerup [196].

The representation of the repulsive force b in a multicomponent mixture is straightforward compared to the attractive force a . As b represents the finite extent of the different molecules, the overall co-volume of the mixture can be expressed as the arithmetic average of the individual components forming the multicomponent fluid

$$b = \sum_{i=1}^{N_c} z_i b_i . \quad (4.97)$$

Here, z_i is the mole fraction of component i which can be the mole fraction in the overall mixture or in every single phase (liquid or vapor). In the following, liquid and vapor mole fractions are denoted by $\mathbf{x} = [x_1, \dots, x_{N_c}]$ and $\mathbf{y} = [y_1, \dots, y_{N_c}]$, respectively. The co-volume b_i of the i -th component in the mixture can be calculated according to Tab. 4.3 and using the appropriate critical properties of the respective species.

The modeling of the attractive term a has to be done more carefully. In multicomponent mixtures many different contributions can occur simultaneously, for instance, various rotations, different aspect ratios, hydrogen bonding or size asymmetries [73]. All these different molecular interactions should be represented by the average attraction parameter a . To explain the idea of the mixing rule for a applied in this work, let us consider a binary mixture, i.e., a mixture consisting of two species (1) and (2), and follow the statements of Elliott and Lira [73]. In total, two different interactions between both molecules can be identified:

1. Interaction with itself (1+1 and 2+2),
2. Interaction with the other molecule (1+2 or 2+1).

The probability of finding the species (1) in the fluid is equal to its mole fraction z_1 [73]. Based on the conditional probability concept, the probability of a 1+1 interaction therefore is $z_1 z_1 = z_1^2$. Analogously, the probability of a 2+2 interaction is equal to z_2^2 . Consequently, the probabilities for cross interactions of the types 1+2 and 2+1 are $z_1 z_2$ and $z_2 z_1$. Denoting the parameters of the self-interaction forces with a_{11} and a_{22} , respectively, and the parameter for the cross-interaction as $a_{12} = a_{21}$ yields the following expression for the average interaction parameter of the multicomponent mixture [73]:

$$a = z_1^2 a_{11} + z_2^2 a_{22} + z_1 z_2 a_{12} + z_2 z_1 a_{21} = z_1^2 a_{11} + 2z_1 z_2 a_{12} + z_2^2 a_{22} = \sum_{i=1}^{N_c} \sum_{j=1}^{N_c} z_i z_j a_{ij} . \quad (4.98)$$

This type of mixing rule is called quadratic mixing rule [73]. Analogous to the co-volume, the diagonal elements of a_{ij} ($i = j$) can be determined based on the approaches listed in Tab. 4.3 and the critical properties of the respective pure species. For the determination of the off-diagonal elements of a_{ij} ($i \neq j$), a suitable modeling approach has to be used. In the present work, the pseudo-critical combination rules due to Reid et al. [253] are applied:

$$\begin{aligned}\omega_{ij} &= 0.5(\omega_i + \omega_j) , \quad \underline{v}_{c,ij} = \frac{1}{8} \left(\underline{v}_{c,i}^{1/3} + \underline{v}_{c,j}^{1/3} \right)^3 , \\ Z_{c,ij} &= 0.5(Z_{c,i} + Z_{c,j}) , \quad T_{c,ij} = \sqrt{T_{c,i}T_{c,j}}(1 - k_{ij}) , \\ p_{c,ij} &= Z_{c,ij} \mathcal{R} T_{c,ij} / \underline{v}_{c,ij} .\end{aligned}\tag{4.99}$$

In these equations, the indices i and j refer to the respective pure species and the index ij to the particular off-diagonal element ($i \neq j$) for which pseudo-critical parameters are evaluated based on the pure species. The resulting properties are called pseudo-critical as they do not represent the real critical point of the binary mixture. We will see later that the determination of the real critical point/locus of a mixture demands a more rigorous definition of criticality. Nonetheless, this fact does not render the combination rules inadequate as they include the binary interaction parameter k_{ij} . This parameter can be used to fit the equation of state to available experimental data and arrive at the desired description of the thermodynamic properties of interest. If not discussed explicitly, the binary interaction coefficient is set to zero in this work.

4.7.3 Caloric and derived properties

The departure function formalism in combination with the fundamental thermodynamic relations concludes the thermal and caloric single-phase real-gas closure. As the one-fluid mixture is employed in this work, the composition information is dropped in the following for the sake of simplicity and readability. The caloric properties are denoted as partial molar and specific properties like they occur in the governing equations. In the following, the derivations are demonstrated for the PR-EoS [226] and the respective expressions for the SRK-EoS [296] can be found in appendix C.

The basic difficulty in deriving the analytical expressions of the departure functions is the selection of the independent variables: (T, p) or (T, \underline{v}) . For both variable sets, the departure function formalism has been introduced in Sec. 4.4. Due to the difference in the hypothetical gas properties at (T, \underline{v}) and (T, p) , the residuals in Eqs. (4.56) and (4.66) are not necessarily identical [196, 213]:

$$\underline{m}^r(T, p) = \underline{m}^r(T, \underline{v}) + \underline{m}^0(T, \underline{v}) - \underline{m}^0(T, p) = \underline{m}^r(T, \underline{v}) + \Delta \underline{m}^0 .\tag{4.100}$$

The existence of a difference between the departure functions of both variable sets depends on the selection of \underline{m} . Evaluating the above relation for the first law conservation properties \underline{e} and \underline{h} yields

$$\underline{e}^r(T, p) = \underline{e}^r(T, \underline{v}) ,\tag{4.101}$$

$$\underline{h}^r(T, p) = \underline{h}^r(T, \underline{v}) .\tag{4.102}$$

Here, the choice of the independent variables is indiscriminate as \underline{e}^0 and \underline{h}^0 are not a function of the pressure p or the molar volume \underline{v} [213]. In contrast, the entropy of an ideal gas is a function of both temperature and pressure and therefore $\Delta \underline{s}^0$ is unequal to zero. This can be demonstrated by applying the Maxwell relations according to Eqs. (4.34), (4.35), (4.36) and (4.37) to the hypothetical part of the departure function of \underline{s} which yields:

$$\underline{s}^0(T, \underline{v}) = \Delta \underline{s}_{\text{mix}}^0 + \int_{T^{\text{ref}}}^T \frac{c_v}{T} dT + \mathcal{R} \int_{\infty}^{\underline{v}} \frac{d\underline{v}}{\underline{v}} ,\tag{4.103}$$

$$\underline{s}^0(T, p) = \Delta \underline{s}_{\text{mix}}^0 + \int_{T^{\text{ref}}}^T \frac{c_p}{T} dT - \mathcal{R} \int_0^p \frac{dp}{\hat{p}} .\tag{4.104}$$

This inequality in turn results in the following difference between both hypothetical gas approaches:

$$\underline{s}^0(T, \underline{v}) - \underline{s}^0(T, p) = \Delta \underline{s}^0 = \mathcal{R} \ln(Z) .\tag{4.105}$$

Consequently, the difference between both departure function formulations of the entropy is

$$\underline{s}^r(T, p) = \underline{s}^r(T, \underline{v}) + \mathcal{R} \ln(Z) . \quad (4.106)$$

As the molar Helmholtz free energy and the molar Gibbs energy are related to the entropy, $\Delta\underline{f}^0$ and $\Delta\underline{g}^0$ do also not vanish. The difference of the departure functions for the Helmholtz free energy and the Gibbs energy can be derived based on their fundamental definitions, cf. Eqs. (4.20) and (4.26), and read:

$$\underline{f}^r(T, p) = \underline{f}^r(T, \underline{v}) - \mathcal{R}T \ln(Z) , \quad (4.107)$$

$$\underline{g}^r(T, p) = \underline{g}^r(T, \underline{v}) - \mathcal{R}T \ln(Z) . \quad (4.108)$$

These findings form the basis for the evaluation of the departure function formalism which yields analytical expressions for the different required thermodynamic properties.

Let us start with the most fundamental property – the internal energy. The departure function of \underline{e} is

$$\underline{e}^r(T, p) = \underline{e}^r(T, \underline{v}) = \int_0^p \frac{\partial \underline{e}}{\partial p} \Big|_T d\hat{p} = \int_{\infty}^{\underline{v}} \left(T \frac{\partial p}{\partial T} \Big|_{\underline{v}} - p \right) d\underline{v} . \quad (4.109)$$

For an easier integration it is desirable to switch to the molar density $\underline{\rho}$ instead of the molar volume, i.e., $d\underline{v} = -d\underline{\rho}/\underline{\rho}^2$ which yields

$$\frac{\underline{e}^r}{\mathcal{R}T} = \int_0^{\underline{\rho}} \left(\frac{p}{\underline{\rho}\mathcal{R}T} - \frac{1}{\underline{\rho}} \frac{\partial p}{\partial T} \Big|_{\underline{\rho}} \right) \frac{d\underline{\rho}}{\underline{\rho}} = - \int_0^{\underline{\rho}} T \frac{\partial Z}{\partial T} \Big|_{\underline{\rho}} \frac{d\underline{\rho}}{\underline{\rho}} . \quad (4.110)$$

The required compressibility factor explicit version of the PR-EoS [226] is

$$Z = \frac{1}{1 - b\underline{\rho}} - \frac{a\underline{\rho}}{\mathcal{R}T (1 + 2\underline{\rho}b - \underline{\rho}^2b^2)} \quad (4.111)$$

and its partial derivative with respect to the temperature at constant density is

$$\frac{\partial Z}{\partial T} \Big|_{\underline{\rho}} = - \frac{\underline{\rho}}{1 + 2\underline{\rho}b - \underline{\rho}^2b^2} \frac{\frac{da}{dT} - \frac{a}{T}}{\mathcal{R}T} . \quad (4.112)$$

Here, the derivative of the attractive term with respect to the temperature reads

$$\frac{da}{dT} = \sum_{i=1}^{N_c} \sum_{j=1}^{N_c} z_i z_j \frac{da_{ij}}{dT} , \quad (4.113)$$

$$\frac{da_{ij}}{dT} = 0.45724 \frac{\mathcal{R}^2 T_{c,ij}^2}{p_{c,ij}} \frac{\kappa_{ij}}{\sqrt{T_{c,ij}}} \left(\frac{\kappa_{ij}}{\sqrt{T_{c,ij}}} - \frac{1 + \kappa_{ij}}{\sqrt{T}} \right) . \quad (4.114)$$

As a result, the analytical expression for the departure function of the internal energy is

$$\underline{e}^r = \frac{a - T \frac{da}{dT}}{\sqrt{8b}} \ln \left[\frac{\underline{v} + b(1 - \sqrt{2})}{\underline{v} + b(1 + \sqrt{2})} \right] . \quad (4.115)$$

The molar enthalpy \underline{h} can be derived based on its fundamental definition, cf. Eq. (4.24), as

$$\begin{aligned} \underline{h}^r &= \underline{e}^r + p\underline{v} - (p\underline{v})^0 = \underline{e}^r + p\underline{v} - \mathcal{R}T \\ &= p\underline{v} - \mathcal{R}T + \frac{a - T \frac{da}{dT}}{\sqrt{8b}} \ln \left[\frac{\underline{v} + b(1 - \sqrt{2})}{\underline{v} + b(1 + \sqrt{2})} \right] . \end{aligned} \quad (4.116)$$

For the derivation of the entropy, identical approaches can be used. Combining Eq. (4.106) with

the Maxwell relation of Eq. (4.34) and the ideal-gas law according to Eq. (4.74) yields the following expression

$$\begin{aligned}\frac{\underline{s}^r(T, p)}{\mathcal{R}} &= \frac{\underline{s}^r(T, \underline{v})}{\mathcal{R}} + \ln(Z) \\ &= \int_0^{\underline{\rho}} \left[-T \frac{\partial Z}{\partial T} \Big|_{\underline{\rho}} - (Z - 1) \right] \frac{d\underline{\rho}}{\underline{\rho}} + \ln(Z) .\end{aligned}\quad (4.117)$$

The integration of this equation for the PR-EoS [226] results in the following analytical formula

$$\underline{s}^r(T, p) = \mathcal{R} \ln \left[\frac{p(\underline{v} - b)}{\mathcal{R}T} \right] - \frac{da}{dT} \frac{1}{\sqrt{8b}} \ln \left[\frac{\underline{v} + b(1 - \sqrt{2})}{\underline{v} + b(1 + \sqrt{2})} \right] .\quad (4.118)$$

Based on the departure functions of the enthalpy and the entropy and the fundamental definition of the Gibbs energy according to Eq. (4.26), $\underline{g}^r(T, p)$ can be expressed as

$$\begin{aligned}\underline{g}^r(T, p) &= \underline{h}^r(T, p) - T\underline{s}^r(T, p) \\ &= p\underline{v} - \mathcal{R}T - \mathcal{R}T \ln \left[\frac{p(\underline{v} - b)}{\mathcal{R}T} \right] + \frac{a}{\sqrt{8b}} \ln \left[\frac{\underline{v} + b(1 - \sqrt{2})}{\underline{v} + b(1 + \sqrt{2})} \right] .\end{aligned}\quad (4.119)$$

This departure function is used to determine the physically most stable root of the cubic EoS. An evaluation of the hypothetical ideal-gas part is not necessary as this part is constant when different solutions are compared to each other. Analogous to the derivation of $\underline{g}^r(T, p)$, the residual part of the Helmholtz free energy $\underline{f}^r(T, p)$ can be calculated based on the departure functions of the internal energy and entropy and the fundamental definition of f , cf. Eq. (4.20), as

$$\begin{aligned}\underline{f}^r(T, p) &= \underline{e}^r(T, p) - T\underline{s}^r(T, p) \\ &= -\mathcal{R}T \ln \left[\frac{p(\underline{v} - b)}{\mathcal{R}T} \right] + \frac{a}{\sqrt{8b}} \ln \left[\frac{\underline{v} + b(1 - \sqrt{2})}{\underline{v} + b(1 + \sqrt{2})} \right] .\end{aligned}\quad (4.120)$$

This equation plays a key role in the derivation of the chemical potentials and its related properties.

Finally, five additional thermodynamic properties are necessary to conclude the single-phase real-gas closure: the partial derivative of the enthalpy with respect to the pressure at isothermal conditions $\partial h/\partial p|_T$, the isobaric and isochoric heat capacity (c_p and c_v), the speed of sound a_s and the partial derivative of the density with respect to the pressure at isenthalpic conditions $\partial \rho/\partial p|_h$. The starting point for the first derived property is the Gibbs fundamental equation in the enthalpy form

$$dh = Td\underline{s} + \underline{v}dp .\quad (4.121)$$

Together with the Maxwell relation of Eq. (4.35) and the thermodynamic chain rule

$$\frac{\partial \underline{v}}{\partial T} \Big|_p \frac{\partial p}{\partial \underline{v}} \Big|_T \frac{\partial T}{\partial p} \Big|_{\underline{v}} = -1\quad (4.122)$$

the partial derivative of the enthalpy with respect to the pressure can be written as

$$\frac{\partial h}{\partial p} \Big|_T = \underline{v} + T \frac{\partial p}{\partial T} \Big|_{\underline{v}} / \frac{\partial p}{\partial \underline{v}} \Big|_T .\quad (4.123)$$

Both partial derivatives on the right-hand side can be derived from any pressure-explicit EoS. For the PR-EoS [226], these two derivatives read:

$$\frac{\partial p}{\partial T} \Big|_{\underline{v}} = \frac{\mathcal{R}}{\underline{v} - b} - \frac{da/dT}{\underline{v}^2 + 2\underline{v}b - b^2} ,\quad (4.124)$$

$$\left. \frac{\partial p}{\partial \underline{v}} \right|_T = - \frac{\mathcal{R} T}{(\underline{v} - b)^2} + \frac{2a(\underline{v} + b)}{(\underline{v}^2 + 2\underline{v}b - b^2)^2}. \quad (4.125)$$

The heat capacities at constant pressure and volume can be derived based on the total differential of the enthalpy

$$dh = \left. \frac{\partial h}{\partial T} \right|_p dT + \left. \frac{\partial h}{\partial p} \right|_T dp = \underline{c}_p dT + \left. \frac{\partial h}{\partial p} \right|_T dp. \quad (4.126)$$

Substituting the definition of the enthalpy, cf. Eq. (4.24), and Eq. (4.123) into the above relation, the heat capacity at constant pressure and volume – \underline{c}_p and \underline{c}_v – can be related as

$$\underline{c}_p = \underline{c}_v - T \left(\left. \frac{\partial p}{\partial T} \right|_{\underline{v}} \right)^2 / \left. \frac{\partial p}{\partial \underline{v}} \right|_T. \quad (4.127)$$

Per definition, c_p can be derived by differentiating the enthalpy with respect to the temperature at constant pressure and hence reads

$$\underline{c}_p = \underline{c}_p^0(T, \mathbf{z}) - \mathcal{R} - T \frac{d^2 a / dT^2}{\sqrt{8b}} \ln \left[\frac{\underline{v} + b(1 - \sqrt{2})}{\underline{v} + b(1 + \sqrt{2})} \right] - T \left(\left. \frac{\partial p}{\partial T} \right|_{\underline{v}} \right)^2 / \left. \frac{\partial p}{\partial \underline{v}} \right|_T. \quad (4.128)$$

Here, the second derivative of the attractive term with respect to the temperature is

$$\frac{d^2 a}{dT^2} = \sum_{i=1}^{N_c} \sum_{j=1}^{N_c} z_i z_j \frac{d^2 a_{ij}}{dT^2}, \quad (4.129)$$

$$\frac{d^2 a_{ij}}{dT^2} = 0.45724 \frac{\mathcal{R}^2}{2T} \kappa_{ij} (1 + \kappa_{ij}) \frac{T_{c,ij}}{p_{c,ij}} \sqrt{\frac{T_{c,ij}}{T}}. \quad (4.130)$$

The speed of sound a_s can be deduced in a similar manner. In general, the thermodynamic sound velocity describes the speed at which a wave is propagating through a medium and is therefore defined as [77]

$$a_s = \sqrt{\left. \frac{\partial p}{\partial \rho} \right|_s}, \quad (4.131)$$

where s denotes the entropy and therefore an isentropic state change. Using the Maxwell relations according to Eqs. (4.36) and (4.37), the speed of sound can be expressed with already known thermodynamic quantities as

$$a_s = v \sqrt{- \left. \frac{c_p}{c_v} \frac{\partial p}{\partial v} \right|_T}. \quad (4.132)$$

Finally, the partial derivative of the density with respect to the pressure under isenthalpic conditions can be calculated as

$$\underline{\Psi}_h = \left. \frac{\partial \rho}{\partial p} \right|_{\underline{h}} = - \rho^2 \left. \frac{\partial \underline{v}}{\partial p} \right|_{\underline{h}}. \quad (4.133)$$

Using the chain rule

$$\left. \frac{\partial \underline{v}}{\partial p} \right|_{\underline{h}} \left. \frac{\partial h}{\partial \underline{v}} \right|_p \left. \frac{\partial p}{\partial h} \right|_{\underline{v}} = -1 \quad (4.134)$$

yields

$$\begin{aligned} \left. \frac{\partial \underline{v}}{\partial p} \right|_{\underline{h}} &= - \left. \frac{\partial h}{\partial p} \right|_{\underline{v}} / \left. \frac{\partial h}{\partial \underline{v}} \right|_p \\ &= - \left[\left. \frac{c_p^0}{\partial p} \frac{\partial T}{\partial p} \right|_{\underline{v}} + \left(\left. \frac{\partial h}{\partial p} \right|_{\underline{v}} \right)^r \right] / \left[\left. \frac{c_p^0}{\partial \underline{v}} \frac{\partial T}{\partial \underline{v}} \right|_p + \left(\left. \frac{\partial h}{\partial \underline{v}} \right|_p \right)^r \right]. \end{aligned} \quad (4.135)$$

Here, the required partial derivatives can be determined as follows:

$$\left(\frac{\partial h}{\partial p} \Big|_{\underline{v}} \right)^r = \underline{v} - \frac{\mathcal{R}}{\frac{\partial p}{\partial T} \Big|_{\underline{v}}} - \frac{T \frac{d^2 a}{dT^2} / \frac{\partial p}{\partial T} \Big|_{\underline{v}}}{\sqrt{8b}} \ln \left[\frac{\underline{v} + b(1 - \sqrt{2})}{\underline{v} + b(1 + \sqrt{2})} \right], \quad (4.136)$$

$$\left(\frac{\partial h}{\partial \underline{v}} \Big|_p \right)^r = p - \mathcal{R} \frac{\partial T}{\partial \underline{v}} \Big|_p - \frac{T \frac{d^2 a}{dT^2} \frac{\partial T}{\partial \underline{v}} \Big|_p}{\sqrt{8b}} \ln \left[\frac{\underline{v} + b(1 - \sqrt{2})}{\underline{v} + b(1 + \sqrt{2})} \right] + \frac{a - T \frac{da}{dT}}{\underline{v}^2 + 2\underline{v}b - b^2}. \quad (4.137)$$

All partial derivatives in these three final equations are known and therefore the thermodynamic closure of the real-gas single-phase framework is complete. It remains an appropriate iteration approach to deduce the temperature from either specific enthalpy and pressure (pressure-based solver) or from specific internal energy and density (density-based solver). In the present work, Dekker's method [243] is used which is a combination of the bisection and the secant method. Dekker's method is a first order method (linear convergence) and is constrained due to the application of the bisection approach. Therefore, it cannot diverge and always finds a solution. Divergence problems can occur when using Newton's method (quadratic convergence) in the transcritical case as the thermodynamic properties show very steep gradients in the region of the Widom line.

4.7.4 Transport properties

For the calculation of the high-pressure viscosity and thermal conductivity the method of Chung et al. [51, 50] is used. The required constants are taken from Poling et al. [237] as they yield better predictions under cryogenic conditions. The approach of Chung et al. [51, 50] relies on the Chapman-Enskog theory for diluted gases and is extended to high-pressure fluids based on empirical functions of the temperature and the pressure. Using combination rules, the method of Chung et al. [51, 50] can be applied to multicomponent mixtures. If both negative and positive acentric factors are present in the mixture, Chung's method [50] is known to produce oscillations [284]. One way to solve this problem is a mole-/mass-weighted average calculation based on the transport properties of each individual species, see, e.g., Ruiz et al. [267]. In the present work, negative acentric factors are set to zero when the viscosity and the thermal conductivity are evaluated to remove the anomalies.

4.8 Phase separation modeling in multicomponent fluids

The thermodynamic closure described in the previous Sec. 4.7 is commonly referred to as dense-gas approach as it assumes a single-phase behavior of the fluid. For a thermodynamically rigorous consideration of phase separation effects in a multicomponent system three requirements must be met at the solution of the phase equilibrium [19]:

1. The material balance must be satisfied.
2. The chemical potential of each species must be identical in all phases.
3. At constant temperature and pressure, the Gibbs energy must be at a minimum.

Especially the latter point is highly important which results from the application of the second law of thermodynamics and must not be intrinsically satisfied at the thermodynamic equilibrium. This fact is elaborated in more detail in the work of Baker et al. [19]. To check whether the single-phase state is at its global minimum of the Gibbs energy or not, the tangent-plane distance (TPD) criterion proposed by Michelsen [194] is used in the present work. If a crossing of the binodal is detected, a classical flashing approach is conducted which yields the species composition in the different phases. This modeling approach results in an Eulerian representation of the phase separation process. Therefore, a multiphase state is not represented by droplets and/or vapor bubbles but rather by a vapor fraction β which is the ratio between the mass of the vapor and the total mass in the system, see Fig. 4.7. Consequently, a vapor fraction between zero and one indicates a multiphase state in the numerical simulation. In the present work, a maximum of two phases is considered and a flat surface between both phases is assumed. Furthermore, the applied approach is only applicable for multicomponent mixtures.

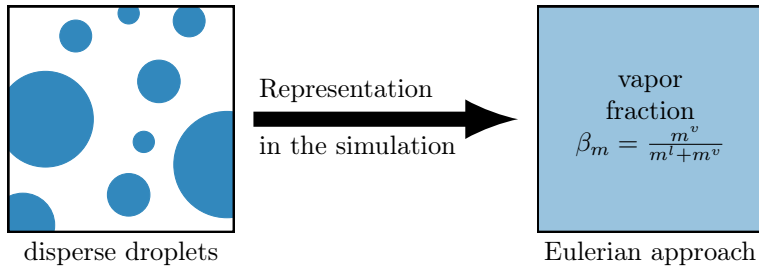


Figure 4.7: Representation of the multiphase state in the numerical simulation.

4.8.1 Derivation of the tangent-plane distance criterion

The starting point for the derivation of the tangent-plane distance criterion is a homogeneous single-phase system as it is sketched in Fig. 4.8 left. For this system (superscript: I), the Gibbs energy can be expressed as

$$G^I(p, T, \mathbf{n}) = \sum_{i=1}^{N_c} n_i \mu_i(p, T, \mathbf{n}) . \quad (4.138)$$

In the next step, a very small amount of a new phase at the identical temperature and pressure with a mole number of q is formed due to a spontaneous process. For this new system (superscript: II), see Fig. 4.8 right, the Gibbs energy can be written as

$$G^{II} = G(p, T, \mathbf{n} - q) + G(p, T, q) . \quad (4.139)$$

Here, the Gibbs energy of the new phase can be expressed as

$$G(p, T, q) = \sum_{i=1}^{N_c} q_i \mu_i(p, T, q) \quad (4.140)$$

and the Gibbs energy of the initial phase may be approximated using a Taylor series

$$G(p, T, \mathbf{n} - q) \approx G^I(p, T, \mathbf{n}) - \sum_{i=1}^{N_c} q_i \left. \frac{\partial G}{\partial n_i} \right|_{p, T, n_j \neq i} = G^I(p, T, \mathbf{n}) - \sum_{i=1}^{N_c} q_i \mu_i(p, T, \mathbf{n}) . \quad (4.141)$$

The difference of the Gibbs energy between the systems II and I can therefore be calculated as

$$\Delta G = G^{II} - G^I = \sum_{i=1}^{N_c} q_i [\mu_i(p, T, q) - \mu_i(p, T, \mathbf{n})] . \quad (4.142)$$

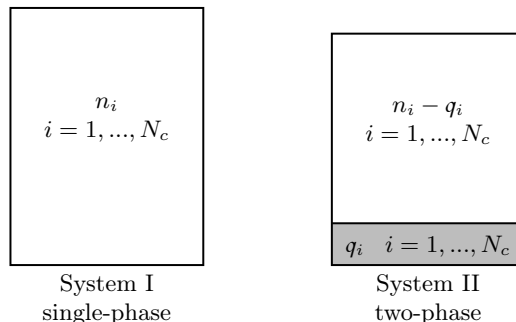


Figure 4.8: Schematic of a single- and a two-phase system at the same temperature T and pressure p . The illustration has been adopted from Firoozabadi [77].

Dividing this equation by the total mole number of the new phase q_t yields the molar formulation of the change in Gibbs energy

$$\underline{\Delta g} = \frac{\Delta G}{q_t} = \sum_{i=1}^{N_c} w_i [\mu_i(p, T, \mathbf{w}) - \mu_i(p, T, \mathbf{z})] , \quad (4.143)$$

where $\mathbf{w} = [w_1, \dots, w_{N_c}]$ is commonly referred to as trial phase composition as it is used to test the energetic state of the single-phase system. Based on the minimum Gibbs energy principle under isothermal, isobaric conditions, system I remains in its single-phase state if $\underline{\Delta g}$ is greater than zero for any feasible values of the trial phase \mathbf{w} . Consequently, for $\underline{\Delta g} < 0$, system I is not at its global minimum in Gibbs energy and the separation of a second phase yields a reduction in \underline{g} .

Equation (4.143) has a geometrical meaning. To demonstrate this, let us consider a binary mixture in which the molar Gibbs energy is

$$\underline{g}(w_1) = \sum_{i=1}^2 w_i \mu_i(w_1) . \quad (4.144)$$

For the sake of simplicity, the Gibbs energy of mixing $\underline{\Delta g}_{\text{mix}}$ is used for the following visual presentation which shows the same characteristics as the Gibbs energy \underline{g} and can be expressed as

$$\underline{\Delta g}_{\text{mix}} = \sum_{i=1}^{N_c} w_i [\mu_i(p, T, \mathbf{w}) - \mu_i^{\text{pure}}(p, T)] . \quad (4.145)$$

Here, μ_i^{pure} denotes the chemical potential of the pure component. Therefore, $\underline{\Delta g}_{\text{mix}}$ is a measure of the nonideal mixing behavior and the deviation from the ideal (linear) mixing state. In Fig. 4.9, a schematic representation of the normalized Gibbs energy of mixing as function of the trial phase composition w_1 is shown. At two different fixed overall compositions (z'_1 and z''_1) the tangents to the Gibbs energy curve ($t'(w_1)$ and $t''(w_1)$) are illustrated. Let us first focus on the feed composition z'_1 : The tangent intersects the Gibbs energy and the equation of this tangent can be expressed as

$$t'(w_1) = \underline{g}(z'_1) + \frac{\partial \underline{g}(z'_1)}{\partial w_1} [w_1 - z'_1] . \quad (4.146)$$

The derivative of Eq. (4.144) with respect to w_1 yields the required partial derivative of the molar Gibbs energy:

$$\frac{\partial \underline{g}}{\partial w_1} = \mu_1(w_1) - \mu_2(w_1) + w_1 \frac{\partial \mu_1}{\partial w_1} + w_2 \frac{\partial \mu_2}{\partial w_1} . \quad (4.147)$$

By applying the Gibbs-Duhem equation (4.17) at isothermal and isobaric conditions, the third and

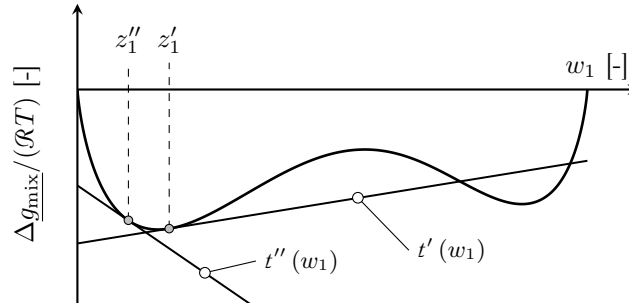


Figure 4.9: Schematic representation of the variation of the molar Gibbs energy of mixing of a binary mixture as function of the trial phase composition w_1 .

fourth term vanish and therefore the equation of the tangent can be written as

$$t'(w_1) = \sum_{i=1}^2 w_i \mu_i(z'_1) . \quad (4.148)$$

Calculating the difference between the Gibbs energy $\underline{g}(w_1)$ according to Eq. (4.144) and the tangent to the Gibbs energy at z'_1 according to Eq. (4.148) yields the TPD criterion for a binary mixture

$$TPD(w_1) = \sum_{i=1}^2 w_i [\mu_i(w_1) - \mu_i(z'_1)] . \quad (4.149)$$

Comparing Eqs. (4.143) and (4.149) it becomes obvious that both expressions are identical for a binary mixture. Therefore, we can write the TPD criterion for an arbitrary multicomponent mixture as

$$TPD(\mathbf{w}) = \sum_{i=1}^{N_c} w_i [\mu_i(\mathbf{w}) - \mu_i(\mathbf{z})] . \quad (4.150)$$

This equation was proposed for the first time by Michelsen [194] in 1982 and forms the basis for the consideration of multicomponent phase separation in this work. Using the TPD criterion it is possible to check whether the binodal of the VLE is crossed or not. Analogous to the discussion of Δg , the evaluation of TPD yields a statement regarding the global minimum of the Gibbs energy: If TPD is nonnegative for any feasible values of \mathbf{w} , the single-phase system persists and no further reduction of the Gibbs energy is possible, cf. the composition z''_1 in Fig. 4.9. In contrast, if TPD is negative for any \mathbf{w} , a spontaneous process occurs and the system splits up into one or more additional phases to yield a reduction in the overall Gibbs energy. In this case, the tangent intersects the Gibbs energy curve. To further illustrate the TPD principle, Fig. 4.10 shows TPD as a function of the trial phase composition w_1 for two different cases. On the left side in Fig. 4.10, a single-phase solution with $TPD \geq 0$ is shown. The mixture is at its minimum Gibbs energy, as the tangent to the Gibbs energy at the feed composition $\mathbf{z} = [0.15, 0.85]$ does not intersect the solid black curve. On the right side in Fig. 4.10, a single phase solution with a negative TPD is sketched. Here, the tangent at the overall composition $\mathbf{z} = [0.65, 0.35]$ intersects the Gibbs energy curve. Therefore, a phase separation leads to a reduction in the Gibbs energy. The resulting phase equilibrium is shown by the common tangent (gray line) and the gray dots which correspond to the dew- and bubble-point line, respectively. Regarding multicomponent mixtures, i.e., $N_c > 2$, the tangent-plane distance concept remains the same. The only difference is, that the Gibbs energy is forming a surface and the tangent at the overall composition is a hyper plane.

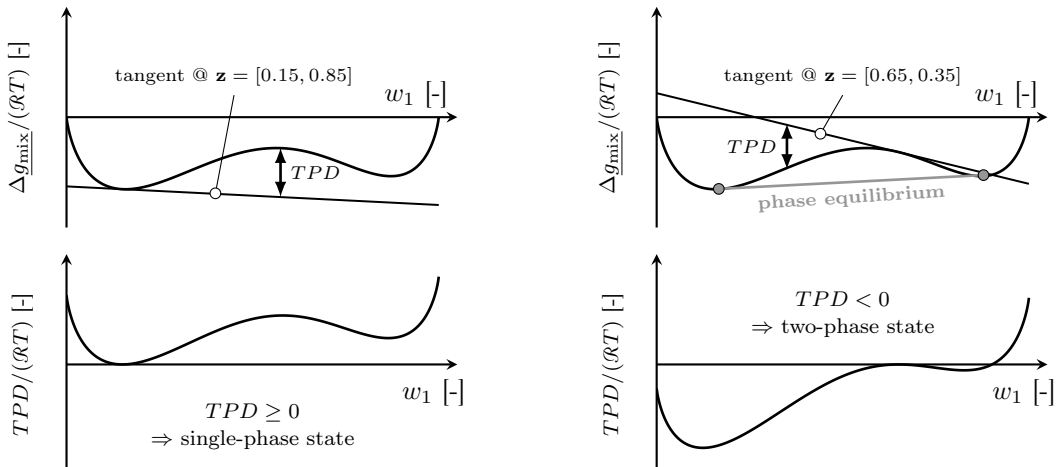


Figure 4.10: Schematic representation of the TPD criterion of a generic binary mixture for a single-phase state (left) and a two-phase state (right).

4.8.2 Fugacity and fugacity coefficient

For a better accessibility of the TPD method and the phase equilibrium evaluation for EoSs it is convenient to introduce the concept of the fugacity and the fugacity coefficient. First, the concept is derived for a pure fluid and then for multicomponent mixtures. The derivation closely follows the introduction in the textbooks of Michelsen and Mollerup [196] and Firoozabadi [77].

Pure fluid

Using the total differential of the Gibbs energy and its isothermal derivative with respect to the pressure, the difference of the chemical potential of a perfect gas at the pressure p and reference pressure p^{ref} can be expressed as

$$\mu^0(p, T) - \mu^0(p^{\text{ref}}, T) = \mathcal{R}T \ln(p/p^{\text{ref}}) . \quad (4.151)$$

To generalize this expression for real fluids, the fugacity f which equals the pressure for a perfect gas is defined:

$$\mathcal{R}T \ln\left(\frac{f(p, T)}{p^{\text{ref}}}\right) := \mu(p, T) - \mu^0(p^{\text{ref}}, T) . \quad (4.152)$$

Subtracting both equations from each other yields the definition of the fugacity coefficient φ

$$\mathcal{R}T \ln \varphi(p, T) := \mathcal{R}T \ln\left(\frac{f(p, T)}{p}\right) = \mu(p, T) - \mu^0(p, T) . \quad (4.153)$$

Therefore, the fugacity coefficient φ of a pure fluid can be determined based on the residual property of the molar Gibbs energy, see Eq. (4.119).

Multicomponent mixture

In perfect gas mixtures, the derivation of the fugacity and the fugacity coefficient relies on the definition of the Helmholtz free energy:

$$F^0(T, V, \mathbf{n}) := \sum_{i=1}^{N_c} n_i \left[\mu_i^0(p^{\text{ref}}, T) + \mathcal{R}T \ln\left(\frac{n_i \mathcal{R}T}{p^{\text{ref}} V}\right) - \mathcal{R}T \right] . \quad (4.154)$$

Using this formulation, the mixture Gibbs energy of a perfect gas ($Z = 1$) can be expressed as

$$\begin{aligned} G^0(p, T, \mathbf{n}) &= F^0(p, T, \mathbf{n}) + (pV)^0 = F^0(T, V, \mathbf{n}) + n\mathcal{R}T \\ &= \sum_{i=1}^{N_c} n_i \left[\mu_i^0(p^{\text{ref}}, T) + \mathcal{R}T \ln\left(\frac{n_i p}{n p^{\text{ref}}}\right) \right] \end{aligned} \quad (4.155)$$

which gives the following expression for the chemical potential of the i -th species

$$\mu_i^0(p, T, \mathbf{n}) = \mu_i^0(p^{\text{ref}}, T) + \mathcal{R}T \ln\left(\frac{z_i p}{p^{\text{ref}}}\right) . \quad (4.156)$$

In the next step, this equation is generalized to real fluids by defining the fugacity of the i -th component f_i as:

$$\mathcal{R}T \ln\left(\frac{f_i(p, T, \mathbf{n})}{p^{\text{ref}}}\right) := \mu_i(p, T, \mathbf{n}) - \mu_i^0(p^{\text{ref}}, T) . \quad (4.157)$$

For a perfect gas, f_i is equal to the partial pressure $z_i p$. Analogous to the pure component approach, the last two equations are subtracted from each other which yields the definition of the fugacity coefficient of component i :

$$\mathcal{R}T \ln \varphi_i(p, T, \mathbf{n}) := \mathcal{R}T \ln\left(\frac{f_i(p, T, \mathbf{n})}{z_i p}\right) = \mu_i(p, T, \mathbf{n}) - \mu_i^0(p, T, \mathbf{n}) = g_i^r(p, T, \mathbf{n}) . \quad (4.158)$$

As a result, φ_i can be calculated based on the departure function of the molar Gibbs energy of the i -th species in the mixture. To express $\ln \varphi_i(p, T, \mathbf{n})$ using a cubic pressure-explicit EoS it is convenient to switch to a formulation based on the temperature and the volume. In a first step, the partial derivative of the hypothetical perfect gas Helmholtz free energy, cf. Eq. (4.154), with respect to the molar number n_i is needed:

$$\mu_i^0(T, V, \mathbf{n}) = \frac{\partial F^0}{\partial n_i} \Big|_{T, V, n_j \neq i} = \mu_i^0(p^{\text{ref}}, T) + \mathcal{R}T \ln \left(\frac{n_i \mathcal{R}T}{p^{\text{ref}} V} \right). \quad (4.159)$$

Subtracting this expression from the definition of $\mu_i^0(p, T, \mathbf{n})$, i.e., Eq. (4.156), yields

$$\mu_i^0(p, T, \mathbf{n}) = \mu_i^0(T, V, \mathbf{n}) + \mathcal{R}T \ln(Z) \quad (4.160)$$

and $\ln \varphi_i(p, T, \mathbf{n})$ can be calculated as

$$\begin{aligned} \mathcal{R}T \ln \varphi_i(p, T, \mathbf{n}) &= \mu_i(p, T, \mathbf{n}) - \mu_i^0(p, T, \mathbf{n}) \\ &= \mu_i(T, V, \mathbf{n}) - \mu_i^0(T, V, \mathbf{n}) - \mathcal{R}T \ln(Z) \\ &= \frac{\partial F^r(T, V, \mathbf{n})}{\partial n_i} \Big|_{T, V, n_j \neq i} - \mathcal{R}T \ln(Z). \end{aligned} \quad (4.161)$$

The partial derivative of the residual part of the Helmholtz free energy is available by differentiating Eq. (4.120) with respect to the mole number n_i . For the PR-EoS [226] this yields the following expression for the fugacity coefficient of the i -th component in the mixture:

$$\ln \varphi_i(p, T, \mathbf{z}) = -\ln \left[\frac{p(v-b)}{\mathcal{R}T} \right] + \frac{b_i}{b} (Z-1) - \frac{a}{\sqrt{8b\mathcal{R}T}} \left(\frac{2 \sum_{j=1}^{N_c} z_j a_{ij}}{a} - \frac{b_i}{b} \right) \ln \left[\frac{v+b(1+\sqrt{2})}{v+b(1-\sqrt{2})} \right]. \quad (4.162)$$

Dimensionless tangent-plane distance criterion

The chemical potential of the i -th species can be obtained by using the definition of the fugacity of component i , cf. Eq. (4.157), and the definition of the fugacity coefficient $\varphi_i = f_i/(z_i p)$:

$$\mu_i = \mu_i^0(p^{\text{ref}}, T) + \mathcal{R}T \left[\ln(z_i) + \ln \left(\frac{p}{p^{\text{ref}}} \right) + \ln \varphi_i(\mathbf{z}) \right]. \quad (4.163)$$

Applying this equation to the expression of the TPD criterion, a normalized form can be derived

$$\begin{aligned} \frac{TPD(\mathbf{w})}{\mathcal{R}T} &= \frac{\sum_{i=1}^{N_c} w_i [\mu_i(\mathbf{w}) - \mu_i(\mathbf{z})]}{\mathcal{R}T} \\ &= \sum_{i=1}^{N_c} w_i [\ln(w_i) + \ln \varphi_i(\mathbf{w}) - \ln(z_i) - \ln \varphi_i(\mathbf{z})] \\ &= \sum_{i=1}^{N_c} w_i [\ln(w_i) + \ln \varphi_i(\mathbf{w}) - d_i]. \end{aligned} \quad (4.164)$$

This equation is convenient to handle as the required mole fractions and the fugacity coefficients are directly available. The last two terms on the RHS are aggregated in the variable d_i as this part is constant throughout the evaluation of the TPD criterion.

4.8.3 Evaluation of the tangent-plane distance criterion

The most obvious way to check the minimization of the Gibbs energy would be an exhaustive search in the complete mixture space. This, however, is very time-consuming and therefore Michelsen [194] suggests to locate the minima of the tangent-plane distance. If the TPD is negative at the minima, it is also negative at other trial phase compositions, cf. Fig. 4.10 right, and a phase separation

process leads to a lower Gibbs energy. Conversely, if the TPD is positive at the minima, the values of the TPD are also positive in the rest of the mixture fraction space, see Fig. 4.10 left. Therefore, the problem of the Gibbs energy minimization can be restricted to locating the minima of the TPD. A modified formulation (tm) of the TPD [196]

$$tm = 1 + \sum_{i=1}^{N_c} W_i [\ln(W_i) + \ln \varphi_i(\mathbf{W}) - d_i - 1] \quad (4.165)$$

allows an unconstrained minimization [196]. The vector $\mathbf{W} = [W_1, \dots, W_{N_c}]$ is formally treated as mole numbers. At the minimum of the TPD, the first order derivative vanishes and hence the stationary points (sp) are found at:

$$\frac{\partial tm}{\partial W_i} = \ln(W_i) + \ln \varphi_i(\mathbf{W}) - d_i = 0. \quad (4.166)$$

The modified tangent-plane distance criterion at the stationary point reads:

$$tm^{\text{sp}} = 1 - \sum_{i=1}^{N_c} W_i = 1 - W_T. \quad (4.167)$$

Hence, the condition for a reduction of the Gibbs energy due to a phase separation process can be reformulated as:

$$W_T = \sum_{i=1}^{N_c} W_i \geq 1. \quad (4.168)$$

A combination of first and second order methods allows for a stable and preferably fast solution of Eq. (4.166).

Under high-pressure conditions, the feed cannot be easily identified as liquid or vapor, which makes the initial selection of the trial phase not obvious. In the case of a liquid feed, Michelsen and Mollerup [196] recommend to search for a 'vapor-like' trial phase that minimizes tm . For a vapor phase, a 'liquid-like' trial phase should be used. In the high-pressure regime, a unique phase identification is not straightforward and both cases have to be investigated. However, a short-cut might be possible by utilizing the co-volume b calculated from the cubic EoS. If the specific volume is smaller than three times the co-volume, i.e., $\underline{v} < 3b$, it is advantageous to start on the vapor side. This approach can save time as the identification of one minimum of $tm < 0$ is sufficient to detect the necessity of an equilibrium phase separation process.

To initialize the trial phase composition the Wilson equation [353, 196] is used:

$$K_i = \frac{y_i}{x_i} = \frac{p_{c,i}}{p} \exp \left[5.373 (1 + \omega_i) \left(1 - \frac{T_{c,i}}{T} \right) \right] \quad i = 1, \dots, N_c. \quad (4.169)$$

Here, K_i is the so-called K-factor or equilibrium ratio which is the ratio of the vapor to the liquid mole fraction. Using Eq. (4.169) for an initial guess, a 'vapor-like' trial phase W_i can be found as

$$W_i = K_i z_i \quad i = 1, \dots, N_c. \quad (4.170)$$

In turn, the starting point for a 'liquid-like' trial phase reads

$$W_i = \frac{z_i}{K_i} \quad i = 1, \dots, N_c. \quad (4.171)$$

To find the minimum of tm based on the initial guess we start with some steps of first order successive substitution

$$\ln(W_i^{k+1}) = d_i - \ln \varphi_i(\mathbf{W}^k) \quad i = 1, \dots, N_c. \quad (4.172)$$

The superscript indicates the iteration step denoted by k and $k + 1$, respectively. The successive substitution method (SSM) usually converges to the minimum of tm , but the convergence rate is slow. The dominant eigenvalue method (DEM) is used to extrapolate and accelerate the calculation. Let \mathbf{W}^k be the solution in the k -th iteration step. Two more steps of SSM yield \mathbf{W}^{k+1} and \mathbf{W}^{k+2} . We then can compute the differences between the previous solutions as

$$\Delta \mathbf{W}^k = \mathbf{W}^{k+1} - \mathbf{W}^k \quad \text{and} \quad \Delta \mathbf{W}^{k+1} = \mathbf{W}^{k+2} - \mathbf{W}^{k+1}. \quad (4.173)$$

Using these two differences the eigenvalue can be calculated as:

$$\lambda^{\text{TPD}} = \frac{\sum_{i=1}^{N_c} (\Delta W_i^{k+1})^2}{\sum_{i=1}^{N_c} \Delta W_i^k \Delta W_i^{k+1}}. \quad (4.174)$$

The extrapolated trial phase composition \mathbf{W}^∞ can then be determined as:

$$\mathbf{W}^\infty = \mathbf{W}^{k+2} + \Delta \mathbf{W}^{k+1} \frac{\lambda^{\text{TPD}}}{1 - \lambda^{\text{TPD}}}. \quad (4.175)$$

One possibility to extrapolate is to monitor the eigenvalue λ^{TPD} . Another way, and that is what we prefer, is to execute the DEM after a certain number of SSM steps. The result of the extrapolation has to be compared to the previous SSM step in order to check the success of the DEM step. If the DEM converges to the minimum of tm , the new solution from Eq. (4.175) is accepted. Otherwise, we discard \mathbf{W}^∞ and go back to the SSM. If the SSM and DEM calculation do not lead to a fast convergence, it is advisable to switch to Newton's method (NM) to further accelerate the calculation. As suggested by Michelsen and Mollerup [196] a variable substitution is performed

$$\alpha_i = 2\sqrt{W_i} \quad i = 1, \dots, N_c. \quad (4.176)$$

The associated objective function reads

$$G_i^{\text{TPD}} = \frac{\partial tm}{\partial \alpha_i} = \sqrt{W_i} [\ln(W_i) + \ln \varphi_i - d_i] \quad i = 1, \dots, N_c \quad (4.177)$$

and the i, j -element of the corresponding Hessian matrix of tm can be obtained as

$$G_{ij}^{\text{TPD}} = \frac{\partial^2 tm}{\partial \alpha_i \partial \alpha_j} = \delta_{ij} + \sqrt{W_i W_j} \frac{\partial \ln \varphi_i}{\partial W_j} + \frac{1}{2} \frac{G_i^{\text{TPD}}}{\alpha_i} \delta_{ij}. \quad (4.178)$$

According to Michelsen and Mollerup [196], the last term in Eq. (4.178) can be neglected without affecting the convergence as it vanishes at the solution, i.e., the stationary point of tm . The Hessian is therefore computed according to

$$G_{ij}^{\text{TPD}} = \frac{\partial^2 tm}{\partial \alpha_i \partial \alpha_j} \approx \delta_{ij} + \sqrt{W_i W_j} \frac{\partial \ln(\varphi_i)}{\partial W_j}. \quad (4.179)$$

Here, $\frac{\partial \ln(\varphi_i)}{\partial W_j}$ is the partial derivative of the fugacity coefficient with respect to the mole number. The derivation and calculation of this derivative is shown in appendix D. A new α can be calculated based on Newton's method as

$$G^{\text{TPD}} \Delta \alpha + G^{\text{TPD}} = 0 \quad (4.180)$$

and $\boldsymbol{\alpha}^{k+1} = \boldsymbol{\alpha}^k + \Delta \boldsymbol{\alpha}$ which gives the new trial phase composition according to $\mathbf{W}^{k+1} = (\boldsymbol{\alpha}^{k+1}/2)^2$. If the new solution of the NM does not converge towards the stationary point of tm , the Newton step is discarded and we proceed with the SSM. Finally, when a minimum of the tangent-plane distance is found, the resulting TPD has to be calculated to evaluate a possible crossing of the binodal.

4.8.4 Equilibrium flash

When the TPD analysis gives a negative value at any of the stationary points a flash calculation has to be performed subsequently which yields the phase composition in the vapor (v) and liquid (l) phase. In this work, the multicomponent phase separation model is used together with the pressure-based solver. As a result, the enthalpy, the pressure and the composition define the thermodynamic state of the mixture. The equilibrium flash is designed as an isenthalpic $h = \text{const.}$, isobaric $p = \text{const.}$ and iso-composition $\mathbf{n} = [n_1, \dots, n_{N_c}] = \text{const.}$ flash, short *hpn*-flash.

In classical thermodynamics, the necessary condition for the existence of a phase equilibrium is the thermodynamic equilibrium, see Sec. 4.3, which includes in the multicomponent case the thermal equilibrium

$$T^v = T^l = T, \quad (4.181)$$

the mechanical equilibrium

$$p^v = p^l = p \quad (4.182)$$

and the chemical equilibrium. The latter can be expressed in terms of the equality of the chemical potentials between the liquid and the vapor phase

$$\mu_i^l(\mathbf{x}, p, T) = \mu_i^v(\mathbf{y}, p, T) \quad i = 1, \dots, N_c \quad (4.183)$$

or, equivalently, by the equality of the fugacities

$$f_i^l(\mathbf{x}, p, T) = f_i^v(\mathbf{y}, p, T) \quad i = 1, \dots, N_c. \quad (4.184)$$

In addition, the phase equilibrium in mixtures is characterized by the fulfillment of the mass conservation

$$y_i\beta + x_i(1 - \beta) = z_i \quad i = 1, \dots, N_c \quad (4.185)$$

and by the constraint that the mole fractions sum up to unity

$$\sum_{i=1}^{N_c} (y_i - x_i) = 0. \quad (4.186)$$

This definition of the phase equilibrium results in $2N_c+3$ unknowns, namely $\mathbf{x} = [x_1, \dots, x_{N_c}]$, $\mathbf{y} = [y_1, \dots, y_{N_c}]$, the vapor mole fraction β , T and p . Equations (4.184) - (4.186) give $2N_c+1$ relations to solve the flash. Hence, two unknowns have to be fixed to arrive at a solvable system of equations. Most commonly, the phase equilibrium calculations are conducted at fixed temperature and pressure, usually called *Tpn*-flash. This yields the most robust and reliable algorithms [196]. In the present work, the flashing problem is, however, defined by the specific enthalpy h , pressure p and the composition $\mathbf{z} = [z_1, \dots, z_{N_c}]$. This problem is solved by an 'overiteration'. The *hpn*-flash is implemented as a nested loop whereby in the inner loop a classical *Tpn*-flash is solved and in the outer loop the temperature is updated. As convergence criterion for the specific enthalpy we use:

$$\frac{|h^{\text{solver}} - [h^l(p, T, \mathbf{x})(1 - \beta_m) + h^v(p, T, \mathbf{y})\beta_m]|}{h^{\text{solver}}} < 1 \times 10^{-6}. \quad (4.187)$$

Here, β_m is the vapor mass fraction. For updating the temperature in the outer loop, the trust-region algorithm from the Intel® Math Kernel Library (MKL) is used.

To solve the *Tpn*-flash, the methods and recommendations described in the book of Michelsen and Mollerup [196] are followed strongly. Therefore, we switch to a formulation in terms of the equilibrium ratio $\mathbf{K} = [K_1, \dots, K_{N_c}]$ with elements

$$K_i = \frac{y_i}{x_i} = \frac{\varphi_i^l}{\varphi_i^v} \quad i = 1, \dots, N_c \quad (4.188)$$

which gives a clean and efficient formulation [77]. Combining Eqs. (4.185), (4.186) and (4.188)

yields the Rachford-Rice (RR) equation [250]

$$\mathcal{G}^{RR}(\beta) = \sum_{i=1}^{N_c} (y_i - x_i) = \sum_{i=1}^{N_c} z_i \frac{K_i - 1}{1 - \beta + \beta K_i} = 0 \quad (4.189)$$

with only one unknown, namely the vapor mole fraction β . Under the assumption of composition independent fugacity coefficients, i.e., an ideal mixture, the RR-equation can be solved by applying Newton's method as the function \mathcal{G}^{RR} is monotonically decreasing:

$$\mathcal{G}'^{RR}(\beta) = \frac{d\mathcal{G}^{RR}}{d\beta} = - \sum_{i=1}^{N_c} z_i \frac{(K_i - 1)^2}{(1 - \beta + \beta K_i)^2} < 0. \quad (4.190)$$

The liquid and the vapor mole fractions can be obtained at the solution ($\mathcal{G}^{RR} = 0$) as:

$$x_i = \frac{z_i}{1 - \beta + \beta K_i} \quad i = 1, \dots, N_c \quad (4.191)$$

and

$$y_i = \frac{K_i z_i}{1 - \beta + \beta K_i} \quad i = 1, \dots, N_c. \quad (4.192)$$

Based on these basic ideas, a successive substitution method can be designed giving a robust and reliable algorithm. As we are executing the flash only after a negative TPD analysis, the results from the TPD method can be used to initialize the flash calculation. If both sides of the TPD are tested, the equilibrium ratio is initialized as:

$$\mathbf{K} = \frac{\exp [\ln \varphi (\mathbf{W}^l)]}{\exp [\ln \varphi (\mathbf{W}^v)]}. \quad (4.193)$$

In the case of $\text{TPD} < 0$ at the liquid-like side

$$\mathbf{K} = \frac{\exp [\ln \varphi (\mathbf{W}^l)]}{\exp [\ln \varphi (\mathbf{z})]} \quad (4.194)$$

and for the gas-like side

$$\mathbf{K} = \frac{\exp [\ln \varphi (\mathbf{z})]}{\exp [\ln \varphi (\mathbf{W}^v)]} \quad (4.195)$$

are used as a first estimate for the K -factors. After the initialization, the Rachford-Rice equation (4.189) is solved to get the vapor fraction β and consequently the liquid and vapor composition. For a stable evaluation of the RR-equation, the existence of a solution in the interval $0 < \beta < 1$ is checked first:

$$\mathcal{G}^{RR}(0) = \sum_{i=1}^{N_c} [z_i (K_i - 1)] > 0 \quad (4.196)$$

and

$$\mathcal{G}^{RR}(1) = \sum_{i=1}^{N_c} \left(z_i \frac{K_i - 1}{K_i} \right) < 0. \quad (4.197)$$

If these two conditions hold, a root can be found in the interval $0 < \beta < 1$. Next, we try to set better initial estimates for β by improving its bounds. This also increases the reliability and stability of the algorithm [196], when highly volatile components ($K_i \gg 1$) for β close to 0 and very heavy components ($K_i \ll 1$) at β close to 1 are present. With Eqs. (4.191) and (4.192) the minimum β -value can be found for $K_i > 1$ as:

$$\beta_{min} = \frac{K_i z_i - 1}{K_i - 1}. \quad (4.198)$$

Contrarily, the maximum β -value can be obtained for $K_i < 1$ as:

$$\beta_{max} = \frac{1 - z_i}{1 - K_i} . \quad (4.199)$$

With these new bounds β_{min} and β_{max} a first initial guess for β can be made as

$$\beta = \frac{\beta_{min} + \beta_{max}}{2} \quad (4.200)$$

and the RR-equation can now be solved by applying Newton's method

$$\beta^{k+1} = \beta^k - \frac{\mathcal{G}^{RR}}{\mathcal{J}^{RR}} . \quad (4.201)$$

Usually, we set the convergence criterion to 1×10^{-6} for Eq. (4.189). After solving the RR-equation the liquid and vapor mole fractions can be obtained according to Eqs. (4.191) and (4.192). Using these compositions, the fugacity coefficients and the equilibrium factors \mathbf{K} are updated and the fulfillment of Eq. (4.184) is checked. Typically, the convergence criterion for the equality of the fugacities is set to 1×10^{-12} . If this tolerance is not met, the RR-Equation is re-evaluated to get a new guess for β and, hence, for \mathbf{x} and \mathbf{y} . This SSM is easy to implement and robust. Its convergence is good at the beginning but slow at the end. In the critical region, it might not converge. As for the TPD analysis, we switch to extrapolation and higher order methods to improve its convergence speed and success.

The dominant eigenvalue method is employed to extrapolate to an improved solution based on the previous iteration steps. We execute the DEM after some steps of SSM (usually every 5th step and renounce on the monitoring of the eigenvalue like we did it within the TPD analysis). The eigenvalue λ^{flash} used for the extrapolation of the equilibrium factors is computed based on the last three iteration steps (k , $k + 1$ and $k + 2$) as

$$\lambda^{\text{flash}} = \frac{\sum_{i=1}^{N_c} (\Delta K_i^{k+1})^2}{\sum_{i=1}^{N_c} \Delta K_i^k \Delta K_i^{k+1}} \quad (4.202)$$

with

$$\Delta \mathbf{K}^k = \mathbf{K}^{k+1} - \mathbf{K}^k \quad \text{and} \quad \Delta \mathbf{K}^{k+1} = \mathbf{K}^{k+2} - \mathbf{K}^{k+1} . \quad (4.203)$$

The extrapolated equilibrium factors \mathbf{K}^∞ can therefore be calculated as:

$$\mathbf{K}^\infty = \mathbf{K}^{k+2} + \Delta \mathbf{K}^{k+1} \frac{\lambda^{\text{flash}}}{1 - \lambda^{\text{flash}}} . \quad (4.204)$$

After the extrapolation we check the convergence criterion. If the step was in the right direction, i.e., the solution has been improved, we accept the result. Otherwise, we discard the DEM step and proceed with the SSM.

The second order Newton method is applied to further accelerate the calculation. According to Michelsen and Mollerup [196] the objective function for the NM reads

$$\mathcal{G}_i^{\text{flash}}(\mathbf{v}) = \ln(f_i^V) - \ln(f_i^L) = 0 \quad i = 1, \dots, N_c \quad (4.205)$$

with the vapor phase component amounts $\mathbf{v} = [v_1, \dots, v_{N_c}]$ as independent variables. The corresponding liquid amounts $\mathbf{l} = [l_1, \dots, l_{N_c}]$ can be retrieved from the material balance as

$$l_i = z_i - v_i \quad i = 1, \dots, N_c . \quad (4.206)$$

From the liquid and vapor amounts the liquid and vapor mole fractions can be computed as

$$l_i = (1 - \beta)x_i \quad \text{and} \quad v_i = \beta y_i \quad i = 1, \dots, N_c . \quad (4.207)$$

For solving N_c -coupled objective functions, we need the Jacobian matrix of $\mathcal{G}_i^{\text{flash}}$ with elements

$$\mathcal{J}_{ij}^{\text{flash}} = \frac{\partial \mathcal{G}_i^{\text{flash}}}{\partial v_j} = \frac{\partial \ln(f_i^v)}{\partial v_j} - \frac{\partial \ln(f_i^l)}{\partial v_j}. \quad (4.208)$$

The elements of this Jacobian can be calculated analytically as

$$\mathcal{J}_{ij}^{\text{flash}} = \frac{1}{\beta(1-\beta)} \left[\frac{z_i}{x_i y_i} \delta_{ij} - 1 + (1-\beta) \Phi_{ij}^v + \beta \Phi_{ij}^l \right] \quad (4.209)$$

with

$$\Phi_{ij} = n_t \frac{\partial \ln \varphi_i}{\partial n_j} \Bigg|_{p,T,n_k \neq j}. \quad (4.210)$$

The calculation of the partial derivatives of the fugacity coefficient with respect to the mole number from the applied cubic EoSs can be found in appendix D. Using Newton's method, the vapor flow can be corrected by

$$\mathcal{G}^{\text{flash}} \Delta \mathbf{v} + \mathcal{G}^{\text{flash}} = 0. \quad (4.211)$$

With the new vapor phase component amounts $\mathbf{v}^{k+1} = \mathbf{v}^k + \Delta \mathbf{v}$ the new liquid and vapor mole fractions can be re-calculated according to Eq. (4.207). If the Newton step did not converge towards the fulfillment of the objective function, the result of the NM is discarded and we start over with the SSM.

4.8.5 Caloric and transport properties in multiphase fluids

After the successful solution of the flashing problem, the thermodynamic and transport properties are updated consistently. Mass- and mole-based thermodynamic properties like the specific enthalpy h or density $\rho = 1/v$ can be calculated based on their liquid and vapor properties and by weighting these properties with the respective vapor fraction β . The mass specific enthalpy h , for instance, reads

$$h = (1 - \beta_m) h^l(p, T, \mathbf{x}) + \beta_m h^v(p, T, \mathbf{y}), \quad (4.212)$$

where β_m is the vapor mass fraction. For the transport properties, i.e., the thermal conductivity and the viscosity, a weighting of the liquid and vapor properties is also applied. In contrast to the calculation of the specific thermodynamic properties, this is thermodynamically not rigorous. This procedure is quite common, see, e.g., the work of Awad and Muzychka [12] for a more detailed discussion. In terms of compressibilities, however, fully consistent and rigorous properties have to be used and a weighting is inappropriate, as these thermodynamic quantities strongly affect the solver stability.

4.8.6 Compressibility and speed of sound in multiphase fluids

Three different definitions for the compressibility can be found in classical thermodynamics: the isothermal compressibility ψ_T , the isentropic compressibility ψ_s and the isenthalpic compressibility ψ_h . Their definitions are listed in Tab. 4.4. These three compressibilities can be related to each

Table 4.4: Definitions of the different compressibilities ψ and expansivities α .

Name	Symbol	Equation
Isothermal compressibility	ψ_T	$-\frac{1}{v} \frac{\partial v}{\partial p} \Big _T = \psi_s (1 + T \alpha_p \phi)$
Isentropic compressibility	ψ_s	$-\frac{1}{v} \frac{\partial v}{\partial p} \Big _s$
Isenthalpic compressibility	ψ_h	$-\frac{1}{v} \frac{\partial v}{\partial p} \Big _h = \psi_s (1 + \phi)$
Thermal expansivity	α_p	$\frac{1}{v} \frac{\partial v}{\partial T} \Big _p$

other by the Grüneisen parameter [9]

$$\phi = v \frac{\partial p}{\partial e} \Big|_v = \frac{v}{c_v} \frac{\partial p}{\partial T} \Big|_v = \frac{\rho}{T} \frac{\partial T}{\partial \rho} \Big|_s \quad (4.213)$$

which can also be expressed by other thermodynamic response functions [187] as

$$\phi = \frac{v \alpha_p}{c_v \psi_T} = \frac{\alpha_p a_s^2}{c_p}, \quad (4.214)$$

where α_p is the thermal expansivity. In fluids without hydrogen bondings the Grüneisen parameter is always greater than zero because this fluid type does not have density anomalies [187]. As a result, it can be deduced from the equations in Tab. 4.4 that

$$\psi_T > \psi_h > \psi_s. \quad (4.215)$$

It is important to distinguish between these three compressibilities and to choose the suitable one depending on the application and the numerical framework. In the present case, the isenthalpic compressibility is used in the subsonic pressure equation, compare Eq. (3.40), as the energy conservation equation is solved in an enthalpy form. The second compressibility being highly important within this study is the isentropic compressibility. The speed of sound a_s is a function of the inverse of the isentropic compressibility ψ_s and the density ρ :

$$a_s = \sqrt{\frac{\partial p}{\partial \rho}} \Big|_s = \sqrt{-v^2 \frac{\partial p}{\partial v}} \Big|_s = \frac{1}{\sqrt{\rho \psi_s}}. \quad (4.216)$$

In single phase systems, the calculation of the speed of sound and the isenthalpic compressibility is straightforward, see Sec. 4.7.3. In multiphase systems, however, the evaluation gets more complicated. This is also the case for measurements and therefore many researchers focus on the numerical investigation of the speed of sound in multicomponent, multiphase systems, see, e.g., Picard and Bishnoi [231], Firoozabadi and Pan [78], Nichita et al. [210] or Castier [42].

A simplified and very popular method for calculating the speed of sound in two-phase systems is the correlation of Wood [354]. This correlation is based on a volume-weighted approach of the bulk modulus respectively its inverse, the isentropic compressibility

$$\begin{aligned} \psi_s &= (1 - \beta_v) \psi_s^l(\mathbf{x}, p, T) + \beta_v \psi_s^v(\mathbf{y}, p, T) \\ &= \frac{(1 - \beta_v)}{\rho^l (a_s^l)^2} + \frac{\beta_v}{\rho^v (a_s^v)^2}, \end{aligned} \quad (4.217)$$

where β_v denotes the vapor volume fraction. Applying Eq. (4.217) to Eq. (4.216) yields Wood's correlation for the speed of sound in a two-phase mixture:

$$a_s = \left[\rho \left(\frac{(1 - \beta_v)}{\rho^l (a_s^l)^2} + \frac{\beta_v}{\rho^v (a_s^v)^2} \right) \right]^{(-1/2)}. \quad (4.218)$$

This correlation captures the basic trends of the variation of the speed of sound in the two-phase region but misses the abrupt/discontinues changes at the phase boundaries, see Nichita et al. [210] for a more thorough discussion. Different approaches can be found in the literature to numerically/analytically calculate the thermodynamic speed of sound in two-phase mixtures, see, e.g., Picard and Bishnoi [231], Firoozabadi and Pan [78], Nichita et al. [210] or Castier [42]. In this work, the approach devised by Nichita et al. [210] is followed as it is a general and efficient numerical scheme [42]. Here, it is possible to use the already implemented *Tpn*-flash as a basis to determine the thermodynamic speed of sound.

According to Tab. 4.4 the isothermal and the isentropic compressibility are related by the Grüneisen parameter. This relation can be re-casted as

$$\psi_s = \frac{\psi_T}{\gamma}, \quad (4.219)$$

where the ratio of the specific heats is denoted by $\gamma = c_p/c_v$. Applying basic mathematical and thermodynamic relations, Eq. (4.219) can be rewritten as [210]

$$\psi_s = \psi_T - \frac{\alpha_p^2 T v}{c_p}. \quad (4.220)$$

This basic derivation holds true for two-phase systems if the phase split is taken into account when evaluating the different properties and partial derivatives, for more details see Nichita et al. [210]. Equation (4.220) only contains partial derivatives with respect to the temperature T and the pressure p . Following Nichita et al. [210], these partial derivatives are evaluated numerically by applying Tpn -flashes at $(p, T \pm \epsilon)$ and $(p \pm \epsilon, T)$. These flashes converge very fast within 1-2 Newton iterations, since an excellent initial guess is available from the solved hpn -flash. Typically, we use a step size of 1×10^{-6} , i.e., $T \pm \epsilon = T(1 \pm 10^{-6})$ and $p \pm \epsilon = p(1 \pm 10^{-6})$.

For calculating the isenthalpic compressibility ψ_h we follow the same idea and rewrite the basic definition in such a way that it only contains partial derivatives with respect to temperature and pressure. This can be done by using the thermodynamic chain rules, the total derivative of the enthalpy with respect to temperature and pressure, the Gibbs fundamental equation in the enthalpy form and the Maxwell relations from Secs. 4.2 and 4.7.3. Applying these approaches to the definition of the isenthalpic compressibility yields

$$\psi_h = \frac{1}{v} \frac{-c_p \frac{\partial v}{\partial p} \Big|_T + v - T \frac{\partial v}{\partial T} \Big|_p}{\frac{c_p}{\frac{\partial v}{\partial T} \Big|_p}}. \quad (4.221)$$

This equation contains only partial derivatives with respect to the temperature and the pressure. As a result, the speed of sound a_s , the isenthalpic compressibility ψ_h and the partial derivative of the enthalpy with respect to the pressure at constant temperature $\partial h / \partial p \Big|_T$ of a multicomponent, two-phase system can be calculated numerically by solving the Tpn -flashes at $(p, T \pm \epsilon)$ and $(p \pm \epsilon, T)$.

Different research groups [231, 210, 42] used the Prudhoe Bay gas mixture to study the variation of the speed of sound inside the two-phase region by means of numerics and by applying the PR-EoS [226] to model the real-gas behavior. The Prudhoe Bay mixture contains 14 components with the following mole fractions listed in parentheses [231]: methane (83.3310%), ethane (9.6155%), propane (3.5998%), iso-butane (0.3417%), n-butane (0.4585%), iso-pentane (0.0403%), n-pentane (0.0342%), n-hexane (0.0046%), n-heptane (0.0003%), n-octane (0.0001%), toluene (0.0002%), nitrogen (1.4992%), oxygen (0.0008%) and carbon-dioxide (1.0738%). In Fig. 4.11a, the VLE of this 14 component mixture is shown together with the four pressure levels used in the further discussion. The VLE exhibits the typical pattern of an isopleth, i.e., the VLE of a mixture at constant overall composition. The sound speeds evaluated at the four different pressure levels are plotted in Fig. 4.11b. At the bubble-point line (low temperatures) a drastic, discontinuous jump is observed, which reduces with increasing pressure. For the lowest pressure (10 bar) the speed of sound is almost dropping by a factor of 30 as the fluid crosses the binodal and first vapor bubbles are forming. Afterwards, the temperature is increasing steadily. Consequently, the vapor fraction is rising and the same occurs for the speed of sound. A small discontinuity is also observed at the dew-point line (high temperatures). This jump gets larger with increasing pressure which is contrary to the behavior of a_s at the bubble-point line. Outside of the two-phase region the fluid behaves liquid-like to the left of the VLE resulting in an increase of a_s with reducing temperature. On the right-hand side of the VLE the speed of sound increases with a rising temperature as the

fluid behaves gas-like. The comparison of Wood's correlation [354] with the thermodynamic speed of sound in Fig. 4.11b underlines the statement that the correlation is able to capture the basic trend within the two-phase region but misses the significant drops of the speed of sound at the phase boundaries, compare Nichita et al. [210] for similar findings. This observation holds also for the isentropic compressibility as it behaves indirectly proportional to the speed of sound, see Fig. 4.11c.

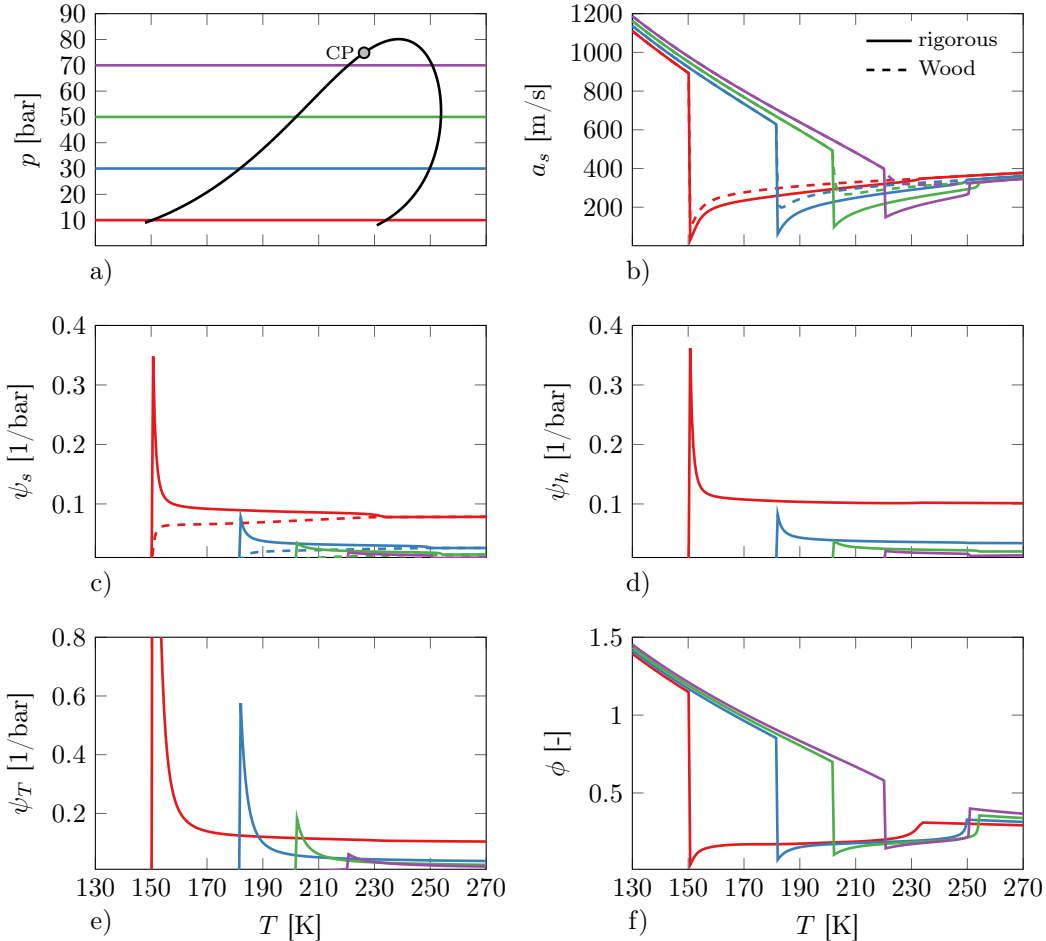


Figure 4.11: Investigation of the 14 component Prudhoe Bay mixture [231] at four different pressure levels (10 bar, 30 bar, 50 bar and 70 bar): a) Vapor-liquid equilibrium; b) Speed of sound (solid: thermodynamic calculation, dashed: Wood's correlation [354]); c) Isentropic compressibility; d) Isoenthalpic compressibility; e) Isothermal compressibility; f) Grüneisen parameter.

To further evaluate the numerical approach described above, the three compressibilities (ψ_s , ψ_h and ψ_T) are shown in Figs. 4.11c, d and e. The comparison of these plots indicates that the basic relation between the three compressibilities $\psi_T > \psi_h > \psi_s$, see Eq. (4.215), holds. Furthermore, Figs. 4.11c-e show that the isenthalpic and the isentropic compressibility are very similar within the VLE. In contrast, the isothermal compressibility ψ_T is much larger than ψ_h and ψ_s (note the scaling of the ordinate by a factor of two). The Grüneisen parameter in Fig. 4.11f exhibits a very similar pattern compared to the speed of sound outside as well as inside of the VLE. The accordance of the patterns of a_s and ϕ was also reported by Arp et al. [9], who investigated this kind of behavior for pure fluids.

4.8.7 Realization in OpenFOAM

In Fig. 4.12, the general calculation procedure for the consideration of multicomponent phase separation within the thermodynamic closure in OpenFOAM is shown. The first important step is the evaluation of the single-phase state based on the enthalpy, pressure and composition returned from the solver. After this, the TPD analysis is executed to check for a crossing of the binodal and hence for the necessity of a phase separation process. Two scenarios are possible: If TPD is larger than zero, the single-phase state stays homogeneous and we proceed with the evaluation of the thermodynamic and transport properties. In the case of a negative tangent-plane distance ($TPD < 0$), a phase separation is performed and an equilibrium flash is executed yielding the phase compositions of the vapor and the liquid phase. As this evaluation is cumbersome, a short-cut is introduced by utilizing the history of the previous iteration/time step. If the cell was already in a two-phase state, we assume the conservation of this state and directly proceed to the flashing procedure. We therefore execute a 'blind' flash and try to solve the two-phase problem for a certain number of iteration steps (usually 10 steps are performed). If we succeed, we can jump to the final evaluation of the thermodynamic and transport properties. In the unsuccessful case, we revert to the standard procedure, i.e., solving for the single-phase state and afterwards checking for the crossing of the binodal. The fast/short-cut flash approach can save a significant amount of time during the simulation, as the time steps are usually in the order of $\mathcal{O}(10^{-9})$ s to $\mathcal{O}(10^{-7})$ s and therefore the change of the flow properties is small. On top, there is an excellent initial guess for the flashing available.

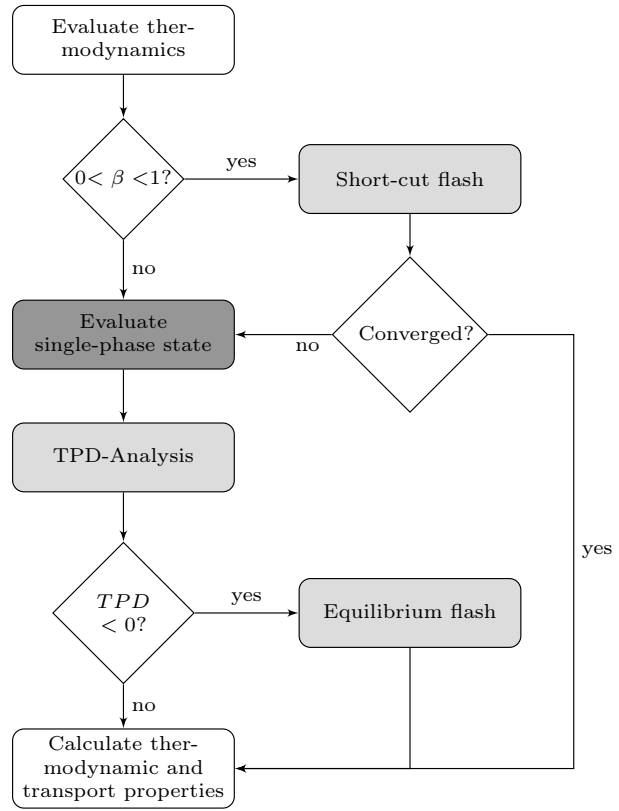


Figure 4.12: Flowchart visualizing the general procedure for solving and evaluating the multicomponent VLE model in OpenFOAM.

4.9 Characteristics of multicomponent phase equilibria

The thermodynamic closure introduced in the previous Sec. 4.8 enables the consideration of multicomponent phase separation within the numerical simulation. For the comparison with experimental VLE data and a posteriori analyses of the results, it is indispensable to study the VLE in different representation forms, i.e., thermodynamic diagrams. This gives knowledge at hand about the prediction capability of the applied thermodynamic framework and the specific characteristics of the investigated multicomponent VLE. In addition, the knowledge about different stability states of a thermodynamic system (stable, metastable or unstable) supports the assessment of the possibility of phase separation processes. Figure 4.13 shows a schematic of a multicomponent VLE at fixed pressure. The binodals, i.e., the equilibrium lines of vapor and liquid, occur at the state of equal fugacities in the different phases. The inside of the VLE can be further subdivided into a metastable and an unstable region. In the first region, the single-phase state can persist in the absence of large changes and nucleation and initial growth of droplets take place. In the latter, spinodal decomposition occurs and therefore phase separation is triggered intrinsically. The spinodal is determined at the critical point. Therefore, thermodynamic stability and criticality are

closely connected to each other. In the following, different approaches are presented to evaluate the different regions of the VLE. We will start with the construction of the phase envelope, i.e., the binodals, move on to the calculation of the limit of stability and end with a model for the calculation of binary nucleation.

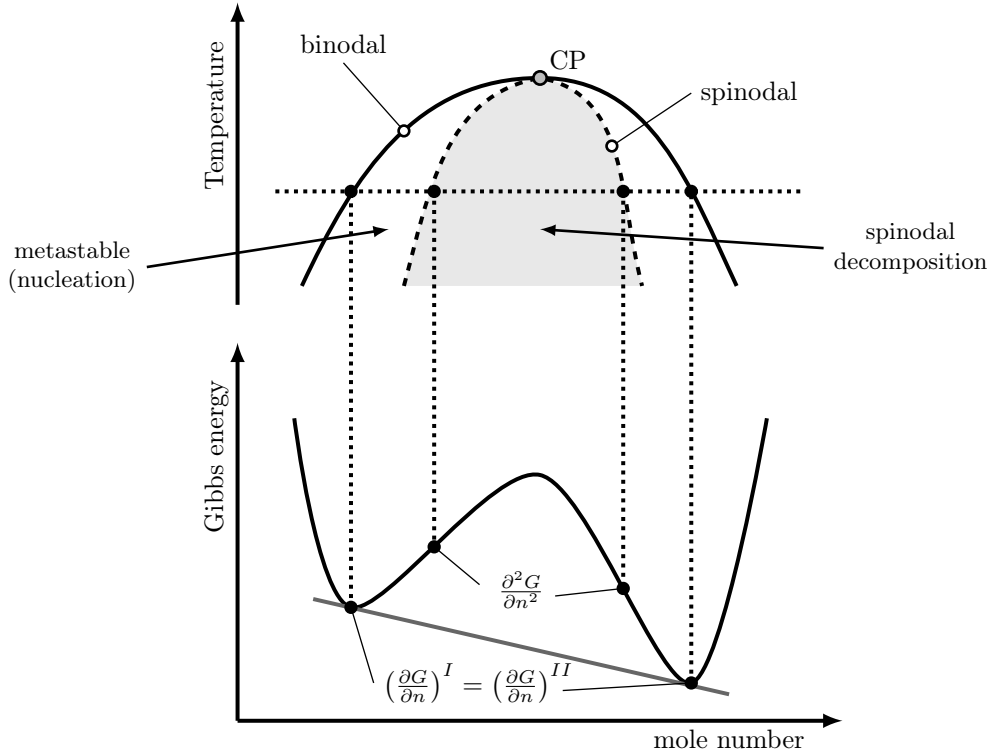


Figure 4.13: Schematic of the vapor-liquid equilibrium of a generic multicomponent mixture together with the shape of the Gibbs energy at a fixed temperature.

4.9.1 Construction of the phase envelope

Studies on multicomponent VLEs are usually carried out using three different diagram types: pressure-composition, temperature-composition and pressure-temperature diagrams. In Fig. 4.14, a schematic of the VLE of a binary mixture with a type I critical locus [335] is shown. The VLE of a multicomponent mixture has a certain extent in the pressure, temperature and composition space, see Fig. 4.14 left. For type I mixtures the VLE is determined by the vapor pressure curves of the pure components (solid black lines) and the critical locus (solid gray line) which connects the

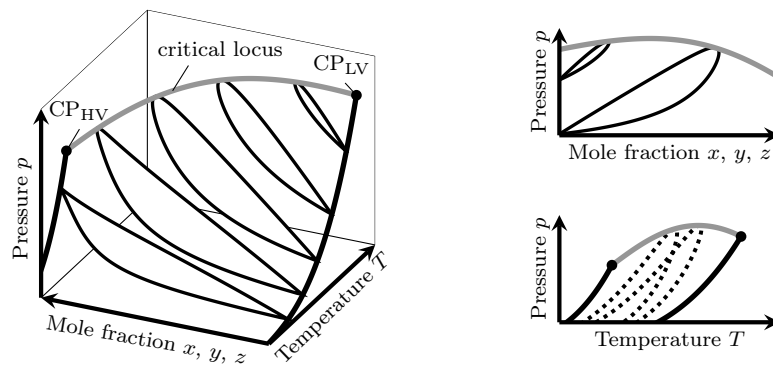


Figure 4.14: Schematic of a binary VLE with a type I critical locus [335].

critical point of the high volatile and the low volatile component. If the temperature or the pressure is subcritical for both pure components, the respective pressure-composition and temperature-composition diagrams show a lens-like shape which starts and ends at the vapor-pressure point of the HV and LV component. As soon as the critical point of one of the components is exceeded, the VLE is only unilaterally fixed at the vapor-pressure curve of the other component. Depending on the components of the mixture, both critical points might be exceeded. Therefore, VLEs occur which are not fixed at any vapor pressure curve and form an arbitrary shape in a certain region of the composition space. In addition to the composition diagrams, Fig. 4.14 shows a schematic of a pressure-temperature diagram including two isopleths (black dotted lines).

Pressure-composition and temperature-composition diagrams

For the calculation of pressure-composition and temperature-composition diagrams, the tools of the *Tpn*-flash presented in Sec. 4.8 can be used as a basis. In the present work, these approaches are combined with a trust region algorithm in MATLAB. The initial composition of the mixture at the start of the VLE construction has to be guessed and the *Tpn*-flash yields the composition of the liquid and the vapor phase. For the next steps, the trust region algorithm can be used as an excellent initial guess from the solved *Tpn*-flash is available. It is found to be most convenient to conduct two separate calculations: One down to the lowest pressure/temperature point of the VLE and one up to the highest pressure/temperature point. These points can be either critical points or states lying on the vapor-pressure curve of a pure fluid. The complete VLE can be assembled by combining both paths to a single phase envelope.

Iso-composition VLEs

The construction of phase envelopes at constant overall composition (isopleths) is a demanding task as different regions of the VLE are crossed: low and high pressures and temperatures, possible inflection points and the mixture critical point. According to Michelsen and Mollerup [196] it is therefore favorable to use a full Newton method as it yields the best convergence behavior. The only issue which has to be solved is the need for a good initial guess. The best idea is to start at a low pressure and then make the way around the phase envelope. At low pressures, the Wilson equation (4.169) yields a very good estimate for the start of the construction procedure. Subsequently, the solution of the last converged construction point is used to extrapolate a new initial guess. The resulting method reads as follows:

First we need to choose if we want to start at the bubble- or dew-point line by selecting the appropriate vapor fraction β . Similar to the discussion of the *Tpn*-flash we use the equilibrium ratio K_i to represent the composition and hence the vector of independent variables is

$$\mathcal{X} = [\ln K_i, T, p] \quad i = 1, \dots, N_c . \quad (4.222)$$

Therefore, $N_c + 2$ equations are necessary to solve the flashing problem. The most obvious choices are the equality of fugacities and the satisfaction of the mass conservation:

$$\mathcal{G}_i^{PE} = \ln K_i + \ln \varphi_i(p, T, \mathbf{y}) - \ln \varphi_i(p, T, \mathbf{x}) = 0 \quad i = 1, \dots, N_c , \quad (4.223)$$

$$\mathcal{G}_{N_c+1}^{PE} = \sum_{i=1}^{N_c} (y_i - x_i) = 0 . \quad (4.224)$$

Here, the superscript *PE* is an abbreviation for phase envelope. These objective functions \mathcal{G}^{PE} give $N_c + 1$ equations. The final equation is called specification equation [196] and is written as

$$\mathcal{G}_{N_c+2}^{PE} = \mathcal{X}_s - \mathcal{S} = 0 . \quad (4.225)$$

Here, s is the number in the variable set to be specified and \mathcal{S} is the objective value. In general, any variable from the vector of independent variables can be chosen. In the present work, the selection of the pressure for the specification equation is always sufficient, i.e., $\mathcal{X}_s = p$. For more complex VLEs, a sensitivity analysis for the specified variable might be necessary [196].

For the application of Newton's method, the Jacobian matrix of \mathcal{G}^{PE} is calculated analytically. Let us first focus on the $N_c \times N_c$ part of the Jacobian which generally reads:

$$\mathcal{J}_{ij}^{PE} = \frac{\partial \mathcal{G}_i^{PE}}{\partial \ln K_j} = \frac{\partial \ln K_i}{\partial \ln K_j} + \frac{\partial \ln \varphi_i^v}{\partial \ln K_j} - \frac{\partial \ln \varphi_i^l}{\partial \ln K_j}. \quad (4.226)$$

Looking at all three terms separately, the first term is equal to one if $i = j$ and is equal to zero if $i \neq j$. For the next term, the application of the chain rule yields

$$\frac{\partial \ln \varphi_i^v}{\partial \ln K_j} = \sum_{k=1}^{N_c} \frac{\partial \ln \varphi_i^v}{\partial y_k} \frac{\partial y_k}{\partial \ln K_j}, \quad (4.227)$$

where all partial derivatives are zero if $k \neq j$ and therefore the summation can be dropped and the second term reads

$$\frac{\partial \ln \varphi_i^v}{\partial \ln K_j} = \frac{\partial \ln \varphi_i^v}{\partial y_j} \frac{\partial y_j}{\partial \ln K_j}. \quad (4.228)$$

The partial derivative of $\partial y_j / \partial \ln K_j$ can be calculated as

$$\frac{\partial y_j}{\partial \ln K_j} = (1 - \beta) \frac{x_j y_j}{z_j}. \quad (4.229)$$

The analytical expression for the third term is analogous:

$$\frac{\partial \ln \varphi_i^l}{\partial \ln K_j} = \frac{\partial \ln \varphi_i^l}{\partial x_j} \frac{\partial x_j}{\partial \ln K_j}, \quad (4.230)$$

$$\frac{\partial x_j}{\partial \ln K_j} = -\beta \frac{x_j y_j}{z_j}. \quad (4.231)$$

The temperature derivatives can be calculated from the derivation of the fugacity coefficient with respect to the temperature:

$$\frac{\partial \mathcal{G}_i^{PE}}{\partial T} = 0 + \frac{\partial \ln \varphi_i^v}{\partial T} - \frac{\partial \ln \varphi_i^l}{\partial T}. \quad (4.232)$$

The analytical expressions for these partial derivatives can be found in Sec. D of the appendix. The same accounts for the required pressure derivatives:

$$\frac{\partial \mathcal{G}_i^{PE}}{\partial p} = 0 + \frac{\partial \ln \varphi_i^v}{\partial p} - \frac{\partial \ln \varphi_i^l}{\partial p}. \quad (4.233)$$

For the $N_c + 1$ objective function, the first N_c partial derivatives are

$$\frac{\partial \mathcal{G}_{N_c+1}^{PE}}{\partial \ln K_i} = \frac{\partial y_i}{\partial \ln K_i} - \frac{\partial x_i}{\partial \ln K_i}, \quad (4.234)$$

where both required partial derivatives can be calculated according to Eqs. (4.229) and (4.231). The partial derivatives with respect to the temperature and pressure are zero. For the final objective function $\mathcal{G}_{N_c+2}^{PE}$, the first $N_c + 1$ derivatives are zero and the last one is equal to one.

With the Jacobian matrix \mathcal{J}^{PE} the solution can be updated using Newton's method:

$$\mathcal{J}^{PE} \Delta \mathcal{X} + \mathcal{G}^{PE} = 0. \quad (4.235)$$

The convergence criterion for the solution is typically set to $\left| \sum_{i=1}^{N_c+2} \mathcal{G}_i^{PE} \right| \leq 1 \times 10^{-12}$. Having the new solution available, the new point on the phase envelope can be estimated as

$$\mathcal{X}(\mathcal{S} + \Delta \mathcal{S}) \approx \mathcal{X}(\mathcal{S}) + \frac{\partial \mathcal{X}}{\partial \mathcal{S}} \Delta \mathcal{S}. \quad (4.236)$$

Here, the partial derivative $\partial \mathcal{X} / \partial \mathcal{S}$ can be calculated from the differentiation of the objective function with respect to \mathcal{S}

$$\frac{\partial \mathcal{G}^{PE}}{\partial \mathcal{X}} \frac{\partial \mathcal{X}}{\partial \mathcal{S}} + \frac{\partial \mathcal{G}^{PE}}{\partial \mathcal{S}} = 0, \quad (4.237)$$

where $\partial \mathcal{G}^{PE} / \partial \mathcal{S} = [0, 0, \dots, -1]$.

4.9.2 Stability and criticality

Rigorous methods

In his classical work back at 1876, Gibbs [91] introduced the notions "thermodynamic stability" and "critical state" and hereby opened the gate to a rigorous definition of the critical point of pure fluids and the critical locus of a multicomponent mixture together with their related stability regions. Gibbs discovered that at the critical state two specific thermodynamic equations have to be obeyed. In the literature many different definitions of these two equations can be found and they all depend upon the thermodynamic variables considered as independent and upon the order of these variables. A very general way to derive these thermodynamic equations is the application of the Legendre transformation. According to Beegle et al. [26] and Reid and Beegle [252] the limit of stability and the criterion for criticality can be expressed as

$$y_{(N_c+1)(N_c+1)}^{(N_c)} = 0 \quad (4.238)$$

and

$$y_{(N_c+1)(N_c+1)(N_c+1)}^{(N_c)} = 0, \quad (4.239)$$

where the sub- and superscripts denote the order of the derivative and the variable. To demonstrate the effectiveness of this Legendre transformation, let us consider a pure fluid ($N_c = 1$) where the fundamental equation in terms of the internal energy reads $E = E(S, V) = y^{(0)}$. From Eq. (4.20) we already know that the first Legendre transform yields the Helmholtz free energy $y^{(1)} = E - TS = F$ which is a function of the volume and the temperature, i.e., $F = F(T, V)$. Applying Eqs. (4.238) and (4.239) to this fundamental equation yields the definition of the stability limit and the critical point of a pure fluid:

$$y_{(2)(2)}^{(1)} = \left. \frac{\partial^2 F}{\partial V^2} \right|_T = -\left. \frac{\partial p}{\partial V} \right|_T = 0 \quad (4.240)$$

and

$$y_{(2)(2)(2)}^{(1)} = \left. \frac{\partial^3 F}{\partial V^3} \right|_T = -\left. \frac{\partial^2 p}{\partial V^2} \right|_T = 0. \quad (4.241)$$

These expressions could have also been derived by intuition based on Fig. 4.4b. In Sec. 4.7.1, both equalities have been used without a proof to derive the attractive and repulsive parameters of the cubic EoSs, cf. Eq. (4.89).

Using the concept of the Legendre transformation, the conditions for the limit of stability and criticality can also be derived for multicomponent systems. Let us consider a binary thermodynamic system which is described by the thermodynamic properties pressure and temperature. For this kind of system the Gibbs energy is the fundamental equation which reads $y^{(2)} = G = G(T, p, n_1, n_2) = H - TS$, cf. Eq. (4.26). Therefore, the conditions for the limit of stability and criticality read:

$$y_{(3)(3)}^{(2)} = \left. \frac{\partial^2 G}{\partial n_1^2} \right|_{p,T,n_2} = \left. \frac{\partial \mu_1}{\partial n_1} \right|_{p,T,n_2} = 0 \quad (4.242)$$

and

$$y_{(3)(3)(3)}^{(2)} = \left. \frac{\partial^3 G}{\partial n_1^3} \right|_{p,T,n_2} = \left. \frac{\partial^2 \mu_1}{\partial n_1^2} \right|_{p,T,n_2} = 0. \quad (4.243)$$

This approach can be generalized for mixtures with $N_c > 2$ components. According to Peng and Robinson [227], the two thermodynamic equations for the limit of stability and the critical point

in the general case read:

$$\text{Limit of stability: } \mathcal{U} = \begin{vmatrix} \frac{\partial^2 G}{\partial n_1^2} \Big|_{T,p} & \frac{\partial^2 G}{\partial n_1 \partial n_2} \Big|_{T,p} & \cdots & \frac{\partial^2 G}{\partial n_1 \partial n_{N_c-1}} \Big|_{T,p} \\ \frac{\partial^2 G}{\partial n_2 \partial n_1} \Big|_{T,p} & \frac{\partial^2 G}{\partial n_2^2} \Big|_{T,p} & \cdots & \frac{\partial^2 G}{\partial n_2 \partial n_{N_c-1}} \Big|_{T,p} \\ \vdots & \vdots & & \vdots \\ \frac{\partial^2 G}{\partial n_{N_c-1} \partial n_1} \Big|_{T,p} & \frac{\partial^2 G}{\partial n_{N_c-1} \partial n_2} \Big|_{T,p} & \cdots & \frac{\partial^2 G}{\partial n_{N_c-1}^2} \Big|_{T,p} \end{vmatrix} = 0, \quad (4.244)$$

$$\text{Critical point: } \begin{vmatrix} \frac{\partial U}{\partial n_1} \Big|_{T,p} & \frac{\partial U}{\partial n_2} \Big|_{T,p} & \cdots & \frac{\partial U}{\partial n_{N_c-1}} \Big|_{T,p} \\ \frac{\partial^2 G}{\partial n_2 \partial n_1} \Big|_{T,p} & \frac{\partial^2 G}{\partial n_2^2} \Big|_{T,p} & \cdots & \frac{\partial^2 G}{\partial n_2 \partial n_{N_c-1}} \Big|_{T,p} \\ \vdots & \vdots & & \vdots \\ \frac{\partial^2 G}{\partial n_{N_c-1} \partial n_1} \Big|_{T,p} & \frac{\partial^2 G}{\partial n_{N_c-1} \partial n_2} \Big|_{T,p} & \cdots & \frac{\partial^2 G}{\partial n_{N_c-1}^2} \Big|_{T,p} \end{vmatrix} = 0. \quad (4.245)$$

Although the Legendre transformation is mathematically relatively convenient, the resulting governing equations are not always easily and intuitively to handle. Thankfully, other approaches have been found for the derivation of the thermodynamic equations which are easier to implement and specifically designed for pressure-explicit state equations. Another important fact regarding the limit of stability is the connection to numerical solver instabilities. This fact is further discussed in appendix E.

A widely used method for calculating the limit of stability and the critical locus is the one proposed by Heidemann and Khalil [117] (HK). Their mathematical formulation links the stability of a homogeneous phase and continuous small changes which do not trigger the appearance of a new phase [68]. To test the stability of the system, Heidemann and Khalil [117] use the temperature, the volume and the mole numbers as independent variables and therefore the stability conditions can be expressed in terms of the Helmholtz free energy F . For an isothermal variation in state and based on the fact that a change in volume does not qualify as a change in phase, the homogeneous phase is stable if the following criterion applies:

$$\left[F - F_0 - \sum_{i=1}^{N_c} \mu_{i,0} (n_i - n_{i,0}) \right] > 0. \quad (4.246)$$

Here, the subscript 0 refers to the initial state of interest. To evaluate the response of the system to allowable virtual processes Heidemann and Khalil [117] expressed the Helmholtz free energy by a Taylor series

$$\begin{aligned} \left[F - F_0 - \sum_{i=1}^{N_c} \mu_{i,0} \Delta n_i \right] &= \frac{1}{2!} \sum_j \sum_i \frac{\partial^2 F}{\partial n_j \partial n_i} \Big|_{T_0, V_0} \Delta n_i \Delta n_j \\ &+ \frac{1}{3!} \sum_k \sum_j \sum_i \frac{\partial^3 F}{\partial n_k \partial n_j \partial n_i} \Big|_{T_0, V_0} \Delta n_i \Delta n_j \Delta n_k + \mathcal{O}(\Delta n^4), \end{aligned} \quad (4.247)$$

where Δ indicates a variation. The stability of the homogeneous system is assured if the quadratic form in Eq. (4.247) is positive definite. For a test point to be on the limit of stability, the quadratic form has to be positive semi-definite. The limit of stability can therefore be found where the Hessian matrix \mathbf{Q} of the Helmholtz free energy with elements

$$Q_{ij} = \frac{\partial^2 F}{\partial n_i \partial n_j} \Big|_{T,V} \quad (4.248)$$

has a zero determinant, i.e., $\det(\mathbf{Q}) = 0$. This is equivalent to solving

$$\mathbf{Q} \cdot \Delta\mathbf{n} = 0 , \quad (4.249)$$

where $\Delta\mathbf{n}$ is a column vector, i.e., $\Delta\mathbf{n} = [\Delta n_1, \dots, \Delta n_{N_c}]$. Hence, \mathbf{Q} has a nullspace given by $N(\mathbf{Q}) = \mathbb{R}\mathbf{n}$. For calculating the critical point lying on the limit of stability the quadratic term in Eq. (4.247) must be zero and the first nonvanishing term in the Taylor series must be of even order [117]. This means, that the cubic form in Eq. (4.247)

$$\sum_k \sum_j \sum_i \frac{\partial^3 F}{\partial n_k \partial n_j \partial n_i} \Bigg|_{T_0, V_0} \Delta n_i \Delta n_j \Delta n_k = 0 \quad (4.250)$$

must vanish for $\Delta\mathbf{n}$ satisfying Eq. (4.249). Using this definition, the critical locus of a multicomponent mixture can be calculated. The second and the third partial derivatives of the Helmholtz free energy with respect to the mole numbers can be determined analytically from the cubic EoSs. Helpful details on the derivation of the equations and implementation of the method can be found in the literature [117, 195, 34].

Rapid estimation method

In the field of reacting flows under rocket-relevant conditions, Lacaze and Oefelein [154], Banuti et al. [22, 23] and Lapenna et al. [160] investigated hydrogen/oxygen and methane/oxygen flames and checked if thermodynamic states in these flames fall underneath the critical locus. In their investigations, a rapid estimate method [237] was used to calculate the mixture critical locus:

$$T_c^{RE} = \sum_{j=1}^{N_c} \frac{z_j v_{c,j}}{\sum_{i=1}^{N_c} z_i v_{c,i}} T_{c,i} , \quad (4.251)$$

$$p_c^{RE} = \frac{\sum_{j=1}^{N_c} \left(z_j \frac{p_{c,j} v_{c,i}}{T_{c,j}} \right) T_c^{RE}}{\sum_{j=1}^{N_c} z_j v_{c,j}} . \quad (4.252)$$

Here, $v_{c,i}$, $T_{c,i}$ and $p_{c,i}$ are the critical volume, temperature and pressure of the i -th species. This method is not based on a rigorous definition of the critical point/locus and therefore no good agreement with experimental data can be expected. In Fig. 4.15, the RE method is compared to the HK method for different binary mixtures. A binary mixture of nitrogen (N_2) and methane (CH_4) is shown in Fig. 4.15a which forms a critical locus of type I similar to the sketch in Fig. 4.14. A clear

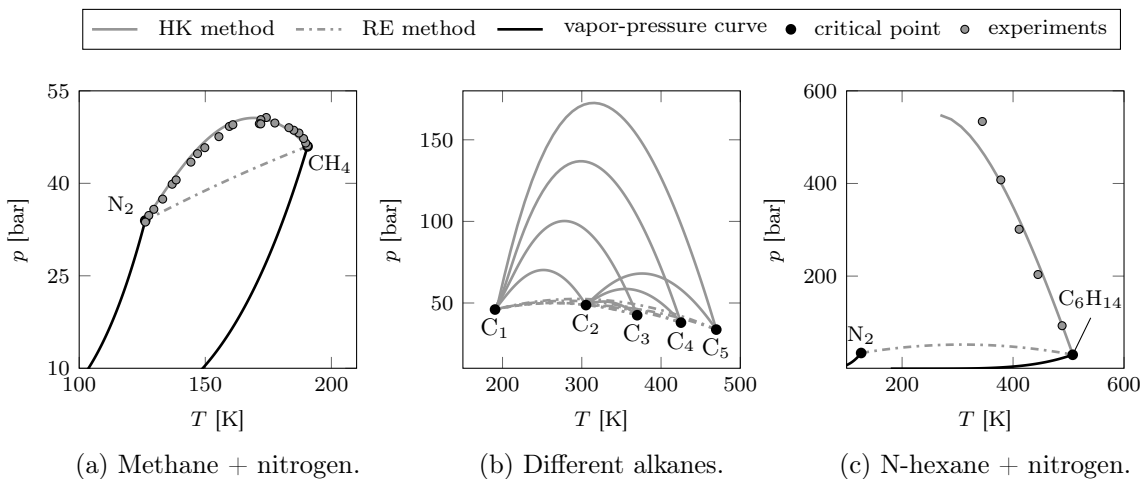


Figure 4.15: Comparison of the RE and HK [117] approaches for different binary mixtures. The experimental data have been taken from the literature [38, 52, 44, 304, 72].

difference can be seen between the two methods in terms of pressure values of the critical locus. As the HK method has a very good agreement with experimental data, it can be concluded that the RE method underpredicts the critical locus. This can be substantiated by comparing more different types of molecules. In Fig. 4.15b, the critical loci of the binary mixtures of various alkanes of the homologous series (methane C₁ to n-pentane C₅) are shown. A significant underestimation of the RE method becomes evident up to a factor of more than three for the binary mixture of methane and n-pentane. The RE method shows almost no superelevation with respect to the pressure values of the critical locus and hence the component with the highest critical pressure determines the maximum of the critical locus. This fact gets even worse if mixtures are investigated which do not form a type I critical locus. In Fig. 4.15c, a binary mixture of nitrogen (N₂) and n-hexane (C₆H₁₄) is plotted. This mixture has a critical locus of type III [335] which is characterized by very large pressure values for the liquid gas equilibrium (LG-Eq.) and a not complete miscibility of the two components [136]. Therefore, in type III mixtures a second liquid phase can appear and lead to a liquid-liquid-gas (LLG) equilibrium which is illustrated in Fig. 4.16. In addition, the extension of the state space with phase separation phenomena is drastically enlarged compared to the type I mixture, cf. Fig. 4.14. In Fig. 4.15c, the LG branch of the critical locus emerging from the low volatile component (C₆H₁₄) is plotted and compared to experimental data from the literature [72]. The HK method gives an excellent prediction up to a pressure of approximately 400 bar. The RE method completely fails in predicting the critical locus. It can therefore be concluded that it is highly important to use a thermodynamically consistent and rigorously derived approach rather than a rapid estimation method to investigate possible phase separation phenomena.

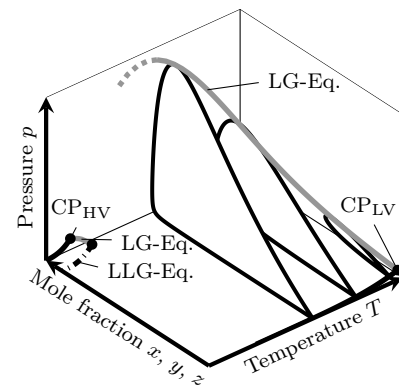


Figure 4.16: Sketch of a binary mixture with a type III critical locus.

4.9.3 Homogeneous nucleation in binary mixtures

The spinodal determines the region of intrinsic single-phase instability. However, in engineering applications phase separation – the relaxation of the metastable state towards the thermodynamic equilibrium – occurs before the stability limit is reached through the activated process of nucleation. To determine the onset of nucleation and therefore the return towards the thermodynamic equilibrium, a separate theory has to be applied. In the present work, the classical nucleation theory (CNT) extended to binary mixtures based on the work of Looijmans et al. [175] is employed.

In general, nucleation describes the situation when a system – single phase fluid/mixture – is put into a metastable (nonequilibrium) state [134]. Under these conditions, the expansion path does not follow the thermodynamic equilibrium resulting in a supersaturated/subcooled state. From a physical point of view, the metastable state corresponds to a local minimum of the free energy and hence is stable to small perturbations. Under metastable conditions, the chemical potential of the liquid phase is lower than in the vapor phase. This difference is the driving thermodynamic force for the occurrence of the phase separation process. The relaxation towards the thermodynamic equilibrium takes place when the system is able to overcome the energy barrier corresponding to a local maximum. This requires the stable formation of a small amount of the new phase called nucleus or embryo. The formation rate of droplets per unit time and space is called nucleation rate J and can be expressed based on the CNT in the following way [175]:

$$J = K e^{-\Delta G/(k_B T)} . \quad (4.253)$$

Here, K , ΔG and k_B denote the kinetic pre-factor, the free reversible energy of formation for a critical droplet and the Boltzmann constant. In the present work, we are not concerned with the absolute value of J but rather with its characteristic shape. Therefore, we restrict ourselves to the

investigation of the normalized nucleation rate

$$I = J/K = e^{-\Delta G/(k_B T)}, \quad (4.254)$$

as the exponential term determines the characteristic curve shape and the kinetic pre-factor K only scales it. For a more thorough discussion, the reader is referred to, e.g., Reiss [254]. An identical approach was followed by Jarczyk [128] to study nucleation phenomena in binary oxygen/hydrogen mixtures under LRE-like conditions. In Fig. 4.17, an example of the normalized nucleation rate as function of the subcooling is shown. With increasing subcooling

$$\Delta T = T(p^v) - T \quad (4.255)$$

the nucleation rate increases by several orders of magnitude within a small temperature range. In the present work, three different normalized nucleation rates are used: 10^{-200} , 10^{-100} and 10^{-50} . These nucleation rates are indicated in Fig. 4.17 by red dots. In this region, the subcooling is in the order of $\mathcal{O}(10)$ K.

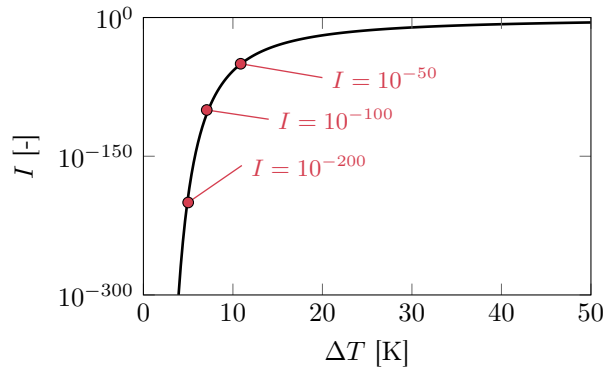


Figure 4.17: Illustration of the change of the normalized nucleation rate I with the subcooling.

The crucial point of the determination of the normalized nucleation rate I is the modeling of ΔG which is a function of the number of particles of both species forming the droplet, i.e., $\Delta G = \Delta G(n_1, n_2)$, see Fig. 4.18. Under metastable conditions, ΔG exhibits a saddle point corresponding to the lowest passage over the energy barrier. This saddle point is the location which has to be determined to calculate the composition of the embryo and as a result determines the nucleation rate based on the supersaturation. In the present work, the pioneering approaches of Wilemski [352] and Looijmans et al. [175] are followed to model the energy of formation ΔG . The applied macroscopic model consists of a droplet, its surface and the surrounding vapor. It is assumed that the droplet is incompressible and in a thermodynamic equilibrium with the surface.

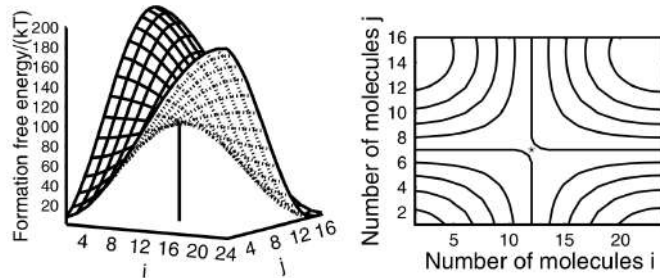


Figure 4.18: Schematic of the formation free energy as function of the number of molecules for a binary mixture. The figures have been taken from Vehkämäki [340]; reprinted by permission from Springer Nature Customer Service Centre GmbH: Springer Nature, *Classical Nucleation Theory in Multicomponent Systems* by Vehkämäki, H. © (2010).

The number of molecules in the droplet and the vapor are denoted by the superscripts l and v , respectively, and the number of surface molecules is an excess number defined as $n^s = n - n^l - n^v$. By considering a separate surface molecule number n^s , the effect of surface enrichment can be considered implicitly. According to Wilemski [352], the free formation energy reads:

$$\Delta G = (p - p^l) V^l + \sigma A + \sum_{i=1}^2 (\mu_i^l - \mu_i^v) n_i^l + \sum_{i=1}^2 (\mu_i^s - \mu_i^v) n_i^s . \quad (4.256)$$

Here, V^l and A are the volume and the surface area of the droplet. The surface tension of the droplet is denoted by σ . Under the assumption of thermodynamic equilibrium between surface and droplet and the assumption of a constant vapor pressure ($p = p^v$), Eq. (4.256) can be rewritten as

$$\Delta G = (p^v - p^l) V^l + \sigma A + \sum_{i=1}^2 \Delta \mu_i n_i^t , \quad (4.257)$$

where $\Delta \mu_i = \mu_i^l(p^l, T) - \mu_i^v(p^v, T)$ and $n_i^t = n_i^l + n_i^s$. Using the definition of the saddle point

$$\left. \frac{\partial \Delta G}{\partial n_i^t} \right|_{T,p} = 0 \quad i = 1, 2 , \quad (4.258)$$

the Gibbs-Duhem relation for the liquid

$$S^l dT - V^l dp^l + \sum_{i=1}^2 n_i^l d\mu_i^l = 0 , \quad (4.259)$$

the Gibbs adsorption equation for the droplet surface

$$S^s dT + A d\sigma + \sum_{i=1}^2 n_i^s d\mu_i^s = 0 , \quad (4.260)$$

the Laplace relation

$$p^l = p^v + 2\sigma/r \quad (4.261)$$

and expressions for the volume and the surface area of the spherical droplet

$$V^l = \sum_{i=1}^2 n_i^l \underline{v}_i^l = \frac{4}{3} \pi r^3 \quad (4.262)$$

$$A = 4\pi r^2 \quad (4.263)$$

yields the following equation

$$\Delta \mu_i = 0 . \quad (4.264)$$

In Eqs. (4.261) - (4.263), r and \underline{v}_i denote the droplet radius and the partial molar volume of species i , respectively. Finally, by applying the incompressible fluid assumption for the determination of the chemical potential

$$\mu_i^l(p^l, T) = \mu_i^l(p^v, T) + \underline{v}_i^l(p^l - p^v) \quad (4.265)$$

the Gibbs-Thomson or Kelvin equation

$$\mu_i^l(p^v, T) - \mu_i^v(p^v, T) + \frac{2\sigma \underline{v}_i^l}{r} = \Delta^* \mu_i + \frac{2\sigma \underline{v}_i^l}{r} = 0 \quad i = 1, 2 \quad (4.266)$$

can be derived, which is used to determine the composition of the liquid droplet. The energy of formation of the critical nucleus at the saddle point (subscript: sp) follows from Eqs. (4.257), (4.261) and (4.264) as

$$\Delta G_{sp} = \frac{1}{3} \sigma A . \quad (4.267)$$

The remaining parameter to be calculated is the surface tension σ . As the present work is concerned with injection, mixing and combustion under high-pressure conditions, i.e., supercritical pressure conditions with respect to the pure components, correlations for the pure fluids are not an option as surface tension effects vanish beyond the critical point. Therefore, the suggestion of Looijmans et al. [175] is followed and the Macleod-Sugden correlation [253] is employed to estimate the surface tension:

$$\sigma^{1/4} = \sum_{i=1}^{N_c} P_i (\underline{\rho_i}^l - \underline{\rho_i}^v) . \quad (4.268)$$

Here, the parameter P_i is the parachor factor of component i . In the present work, the CNT is used for the binary n-hexane/nitrogen mixture exclusively. The parachor factors for both fluids are taken from the literature [237, 255] and are set to $P_{C_6H_{14}} = 271 \text{ cm}^3 \text{ g}^{0.25}/(\text{s}^{0.5} \text{ mol})$ and $P_{N_2} = 60 \text{ cm}^3 \text{ g}^{0.25}/(\text{s}^{0.5} \text{ mol})$, respectively.

Having all necessary models at hand, the composition of the critical nucleus, the nucleation rates and the related subcooling/temperature can be determined. As n-hexane is a long-chain alkane, the PR-EoS [226] is used to describe the required gas and liquid properties. The calculation of the nucleation rate starts with the determination of the bulk composition of the nucleus. According to Looijmans et al. [175], a linear combination of the Kelvin equation is used:

$$\underline{v_2}^l \Delta^* \mu_1 - \underline{v_1}^l \Delta^* \mu_2 = 0 . \quad (4.269)$$

The partial molar volume of species i can be determined from the PR-EoS [226] as

$$\underline{v}_i = - \frac{\partial \underline{v}}{\partial p} \Big|_{T, \mathbf{z}} \left[\frac{\mathcal{R}T}{\underline{v} - b} + \frac{\mathcal{R}T b_i}{(\underline{v} - b)^2} - \frac{2 \sum_{j=1}^{N_c} z_j a_{ij}}{\underline{v}^2 + 2\underline{v}b - b^2} + \frac{2a(\underline{v} - b)b_i}{(\underline{v}^2 + 2\underline{v}b - b^2)^2} \right] . \quad (4.270)$$

The other necessary thermodynamic properties and partial derivatives can be found in Sec. 4.7.3. For a given pressure p , temperature T and vapor composition \mathbf{y} , Eq. (4.269) is solely a function of the nucleus composition and can be solved iteratively. Having the liquid bulk composition available, the droplet radius can be determined based on component 1 or 2 of the binary mixture using the Kelvin equation (4.266):

$$r = - \frac{2\sigma \underline{v}_i^l}{\Delta^* \mu_i} \quad i = 1 \text{ or } 2 . \quad (4.271)$$

Finally, the free energy of formation and the normalized nucleation rate can be calculated using Eqs. (4.267) and (4.254).

5 Combustion modeling

For the numerical simulation of reacting flows in the context of LES, models for the determination of the filtered source term $\bar{\omega}_k$ in the species transport equation (2.31) are required. As the combustion is taking place on the sub-grid scale level, the modeling approach has to reflect the complex turbulence-chemistry interaction (TCI). In general, a huge number of different methods can be found in the literature. The textbooks of, for instance, Poinsot and Veynante [236], Peters [230], Kuo [146] and Echekki and Mastorakos [69] give an overview on different combustion modeling approaches. Combustion models can be categorized into premixed and non-premixed approaches. In the premixed case, the key chemical reactants of combustion – fuel and oxidizer – are mixed before they pass through the reaction zone of the flame. In contrast, non-premixed combustion is characterized by the fact that oxidizer and fuel are injected separately into the combustion chamber. As a result, mixing and burning take place simultaneously. This is typically the case in liquid-propellant rocket engines where fuel and oxidizer are injected through co-axial injection elements into the combustion chamber. A schematic of a single co-axial injection element is shown in Fig. 5.1a. The oxidizer (here: oxygen) enters the combustor through the central circular pipe and is denoted by the mixture fraction $f = 0$. The fuel (here: methane or hydrogen) is injected through the circular annulus and equals the mixture fraction $f = 1$. Downstream of this co-axial injection element a turbulent non-premixed flame forms which position can be described by the stoichiometric mixture fraction f_{st} . In LOx/H₂ flames, the stoichiometric mixture fraction is

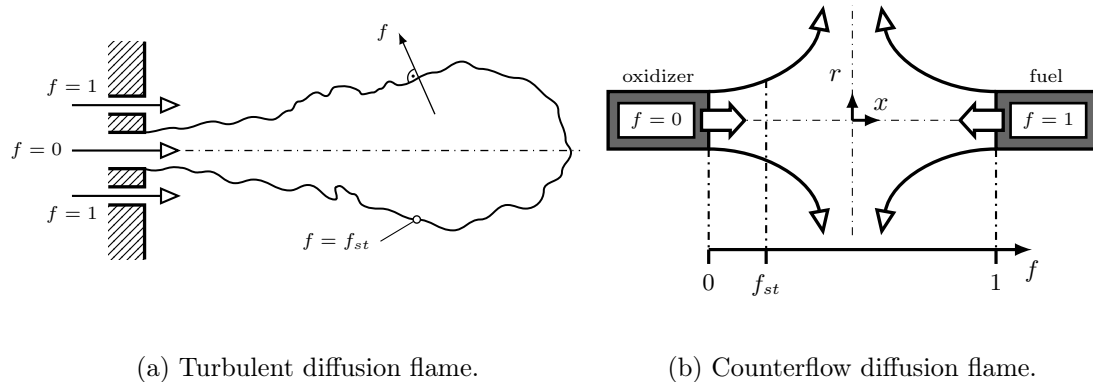


Figure 5.1: Schematic of non-premixed combustion: a) Turbulent diffusion flame emanating from a co-axial injection element; b) Concept of the counterflow diffusion flame approach.

0.1111 and in LOx/CH₄ flames f_{st} is equal to 0.2. The stoichiometric mixture is the region where the maximum temperature occurs in a flame. As the transport of fuel and oxidizer towards the flame is governed by diffusion, non-premixed flames are often called diffusion flames. In Fig. 5.1b, the corresponding generic configuration of a laminar counterflow diffusion flame is shown. Fuel and oxidizer are injected through opposite nozzles and inbetween a stationary flame occurs. This counterflow diffusion configuration is the basis for the combustion model applied in this work. In the present case, the model is specifically tailored for real-gas flows and enables an efficient and thermodynamically consistent treatment of the combustion process. In the following, only the most important details of this modeling approach are outlined. For a more thorough introduction and discussion refer to the paper of Zips et al. [368] or the related PhD theses of Zips [367] and Müller [202]. This chapter is structured as follows: In Sec. 5.1, the real-gas combustion model and its realization in the LES framework are described briefly. The required reaction and chemical kinetics are introduced in Sec. 5.2 which are necessary to finally close the applied combustion model.

5.1 Real-gas flamelet model

Originally, the flamelet model was proposed by Peters [228, 229, 230] in the 1980s. Recently, Lacaze and Oefelein [154] demonstrated the applicability of the flamelet approach for the numerical investigation of high-pressure combustion in LREs. The basic idea of the flamelet concept is that each element of a turbulent flame can be viewed as a small laminar flame called flamelet. In the stationary case, this implies that the flame structure is locally one-dimensional and depends on the mixture fraction coordinate f which is orthogonal to the surface of the stoichiometric mixture, i.e., the flame front, see Fig. 5.1a. The mixture fraction represents the proportion of fuel in the mixture and can be viewed as

$$f = \frac{\dot{m}_F}{\dot{m}_{Ox} + \dot{m}_F}, \quad (5.1)$$

where \dot{m}_F and \dot{m}_{Ox} denote the mass flow rate of the fuel and oxidizer, respectively. Many other definitions of the mixture fraction can be found in the literature, see, e.g., Peters [228, 230] or Poinsot and Veynante [236]. The mixture fraction is a passive scalar and enables the coupling between the turbulent flow and the combustion process. Consequently, parts of the governing equations can be replaced by appropriate transport equations for f . In the adiabatic combustion case, these are the species transport equations and the energy conservation equation. The stretching of the flame by means of turbulent motion can be described by the scalar dissipation rate χ . According to Peters [228, 230], χ acts as an inverse diffusion time and is defined as

$$\chi = 2D_f \left| \frac{\partial f}{\partial x_i} \right|, \quad (5.2)$$

where D_f is the diffusion coefficient of the mixture fraction.

Using the general idea of the stationary flamelet approach, a turbulent non-premixed flame can be represented by a brush of laminar counterflow diffusion flames which interact with the flow. This implies that the reactions take place in a thin layer and that the flame is thin compared to other flow parameters and wrinkling scales. Therefore, it is assumed that the chemical time scales are much smaller than the turbulent time scales which is equal to the assumption of Damköhler numbers $Da \gg 1$. In an axisymmetric configuration, see Fig. 5.1b, the governing equations reduce to a one-dimensional problem that can be solved in the mixture fraction space f by employing a coordinate transformation, see, e.g., Peters [230] or Poinsot and Veynante [236]. Under the assumption of a unitary Lewis number for all species ($Le_i = Le = 1$), the so-called flamelet equations read [230, 142]:

$$\rho \frac{\partial Y_k}{\partial t} = \rho \frac{\chi}{2} \frac{\partial^2 Y_k}{\partial f^2} + \dot{\omega}_k \quad k = 1, \dots, N_c, \quad (5.3)$$

$$\rho \frac{\partial h}{\partial t} = \rho \frac{\chi}{2} \frac{\partial^2 h}{\partial f^2}. \quad (5.4)$$

Here, isobaric conditions are assumed and therefore the set of the governing equations reduces to the species transport equations and the conservation equation of the energy in the enthalpy form. In the real-gas combustion community, many research groups write the energy conservation equation in the temperature form. This can result in inconsistencies which are thoroughly discussed in the work of Juanós and Sirignano [133]. In Eqs. (5.3) and (5.4), χ is an external parameter which correlates in the physical space with the inlet velocities of the fuel and the oxidizer. According to Peters [228], χ can be represented in the mixture fraction space by the following error function approach

$$\chi = \frac{\chi_{st}}{\pi} \exp \left(-2 [\operatorname{erfc}^{-1}(2f)]^2 \right), \quad (5.5)$$

where χ_{st} denotes the scalar dissipation rate at the stoichiometric point of the flame. As a result of this representation, a flamelet can be characterized by the mixture fraction f and the scalar dissipation rate at the stoichiometry χ_{st} . A scalar dissipation rate $\chi \approx 0$ corresponds to a very slow inflow of oxidizer and fuel into the configuration. In this case, almost no stretching of the flame occurs and the amount of time is sufficient for all reactions to take place. By increasing the inlet velocities or analogous χ , the residence time of the reactants inside the configuration decreases.

This increase in the scalar dissipation rate can be done until the extinction point $\chi = \chi_{ext}$ is reached. At this point, the convective time scales are too small compared to the chemical time scales and the flame is extinguished. In high-pressure flames with pure oxygen as oxidizer, this point is usually found for χ in the order of $\mathcal{O}(10^5)$.

To cover the full range of steady state flamelet realizations from $\chi \approx 0$ up to extinction, the flamelet equations (5.3) and (5.4) need to be solved for a distinct number of scalar dissipation rates in the bounds of $0 < \chi_{st} < \chi_{ext}$. Afterwards, the results can be stored in tables of the form $Y_k = Y_k(f, \chi_{st})$ and $h = h(f, \chi_{st})$ which is the basic idea of the classical flamelet approach [203]. In general, several open-source tools are available to solve the flamelet equations together with an ideal-gas closure, e.g., FlameMaster [233] or Cantera [96]. For the solution with real-gas EoSs, an in-house implementation in OpenFOAM considering real-gas and multicomponent phase separation effects is used. This approach enables the thorough thermodynamic investigation of the flame structure but, unfortunately, these calculations are too expensive for an efficient tabulation as the pressure has to be considered as an additional tabulation coordinate in the real-gas case. Therefore, an efficient real-gas flamelet tabulation method suggested by Zips et al. [368, 367] is employed in the present work. The real-gas flamelet model relies on the following two main assumptions:

1. Weak coupling between real-gas effects and chemical reactions.
2. Small fluctuations in pressure.

These assumptions enable a drastic simplification of the flamelet tabulation method in the real-gas case. In the first step, the counterflow diffusion flames are solved at the nominal combustion chamber pressure using the ideal-gas closure. In the next step, a correction of the thermodynamic state is conducted. Here, we make use of the fact that in the stationary case the enthalpy is a straight line in the mixture fraction space, i.e.,

$$h(f) = h(f=0) + [h(f=1) - h(f=0)] f. \quad (5.6)$$

As a result, the thermodynamic states are completely defined along the mixture fraction coordinate by means of the pressure p , the specific enthalpy h and the composition \mathbf{Y} . The latter are taken from the already solved ideal-gas flamelets. Using these states, the temperature, compressibilities etc. can be evaluated thermodynamically consistent.

Turbulence-chemistry interaction

The conduction of the LES yields filtered quantities which are used to access the a priori created flamelet tables. Therefore, the table values ϑ from the counterflow diffusion flame calculations have to be filtered using a Favre-filtered joint probability density function (PDF) $\tilde{\mathcal{P}}_{sgs}(f, \chi_{st}, p)$ for the mixture fraction, the scalar dissipation rate and the pressure:

$$\tilde{\vartheta} = \int_{p_{min}}^{p_{max}} \int_0^{\chi_{ext}} \int_0^1 \vartheta(\hat{f}, \hat{\chi}_{st}, \hat{p}) \tilde{\mathcal{P}}_{sgs}(\hat{f}, \hat{\chi}_{st}, \hat{p}) d\hat{f} d\hat{\chi}_{st} d\hat{p}. \quad (5.7)$$

Assuming statistical independence between f , χ_{st} and p the joint PDF can be written as

$$\tilde{\mathcal{P}}_{sgs}(f, \chi_{st}, p) = \tilde{\mathcal{P}}_{sgs}(f) \tilde{\mathcal{P}}_{sgs}(\chi_{st}) \tilde{\mathcal{P}}_{sgs}(p). \quad (5.8)$$

Therefore, only the modeling of the individual PDFs is necessary. In the present work, presumed PDF approaches are used for the Favre-filtering. For the mixture fraction, a β -distribution is employed which reads

$$\tilde{\mathcal{P}}_{sgs}(f) = f^{\alpha-1} (1-f)^{\beta-1} \frac{\Gamma(\alpha+\beta)}{\Gamma(\alpha)\Gamma(\beta)}. \quad (5.9)$$

Here, Γ is the gamma function and α and β define the shape of the PDF and are functions of the filtered mixture fraction \tilde{f} and its variance $\widetilde{f''^2}$:

$$\alpha = \tilde{f} \left[\frac{\tilde{f}(1-\tilde{f})}{\widetilde{f''^2}} - 1 \right], \quad (5.10)$$

$$\beta = \left(1 - \tilde{f}\right) \left[\frac{\tilde{f} \left(1 - \tilde{f}\right)}{\widetilde{f''^2}} - 1 \right]. \quad (5.11)$$

For the PDFs of the scalar dissipation rate and of the pressure, Dirac functions are applied:

$$\tilde{\mathcal{P}}_{sgs}(\chi_{st}) = \delta(\chi_{st} - \widetilde{\chi_{st}}), \quad (5.12)$$

$$\tilde{\mathcal{P}}_{sgs}(p) = \delta(p - \bar{p}). \quad (5.13)$$

The Dirac function is the simplest PDF and is a noticeable simplification compared to the β -shaped PDF for the mixture fraction. However, in contrast to the β -PDF it does not increase the size of the table which is in the present case quite important as the pressure is already an additional coordinate compared to the standard ideal-gas flamelet approach. In the present case, the thermo-chemical state which is stored in the tables is therefore defined as $\tilde{\vartheta} = \tilde{\vartheta}(\tilde{f}, \widetilde{f''^2}, \widetilde{\chi_{st}}, \bar{p})$. For a memory-optimized and preferably fast table access the Parallel Memory Abstraction Layers (PMAL) technique proposed by Weise and Hasse [346] is used. The database itself is stored in the HDF5-format.

Transport equations in the LES

To retrieve the local species composition and the required thermodynamic properties in the LES, a transport equation is solved for the filtered mixture fraction

$$\frac{\partial(\bar{\rho}\tilde{f})}{\partial t} + \frac{\partial(\bar{\rho}\tilde{u}_i\tilde{f})}{\partial x_i} = \frac{\partial}{\partial x_i} \left[\left(\frac{\bar{\mu}}{\text{Sc}} + \frac{\mu^{sgs}}{\text{Sc}_t} \right) \frac{\partial \tilde{f}}{\partial x_i} \right]. \quad (5.14)$$

A transport equation for its variance is used to model the unresolved fluctuations of the mixture fraction, cf. Kemenov et al. [137]:

$$\frac{\partial(\bar{\rho}\widetilde{f''^2})}{\partial t} + \frac{\partial(\bar{\rho}\tilde{u}_i\widetilde{f''^2})}{\partial x_i} = \frac{\partial}{\partial x_i} \left[\left(\frac{\bar{\mu}}{\text{Sc}} + \frac{\mu^{sgs}}{\text{Sc}_t} \right) \frac{\partial \widetilde{f''^2}}{\partial x_i} \right] - 2\bar{\rho}\tilde{\chi} + 2 \left(\frac{\bar{\mu}}{\text{Sc}} + \frac{\mu^{sgs}}{\text{Sc}_t} \right) \left(\frac{\partial \tilde{f}}{\partial x_i} \right)^2. \quad (5.15)$$

The scalar dissipation rate $\tilde{\chi}$ is evaluated according to Domingo et al. [66] and is decomposed into resolved and SGS contributions:

$$2\bar{\rho}\tilde{\chi} = 2\frac{\bar{\mu}}{\text{Sc}} \left(\frac{\partial \tilde{f}}{\partial x_i} \right)^2 + C_\chi \frac{\mu^{sgs}}{\text{Sc}_t} \frac{\widetilde{f''^2}}{\Delta^2}. \quad (5.16)$$

Here, Δ is the local filter size and the model constant is set to $C_\chi = 2$ according to Kemenov et al. [137]. In Eqs. (5.14) and (5.15), the gradient-diffusion hypothesis [238] is employed to describe the turbulent scalar fluxes. In particular, the molecular and turbulent Schmidt numbers (Sc and Sc_t) are introduced to relate the diffusion coefficients to the viscosity. Following the work of Cabrit and Nicoud [40] and Zips et al. [369, 370], both constants are set to $\text{Sc} = \text{Sc}_t = 0.7$ in the combustion simulation in this work.

Numerical procedure

In Fig. 5.2, the overall numerical procedure of the real-gas flamelet model is summarized. The model can be separated into three individual major steps:

1. Calculation of the flamelets at the nominal pressure employing the ideal-gas closure.
2. Application of the thermodynamic correction step to include real-gas effects.
3. Interference of the numerical solver with the generated and filtered tables.

Applying this model, different thermodynamic closures (single- and multi-phase) can be used to efficiently study the thermodynamic states in high-pressure combustion as these models only need to be exchanged in the correction step.

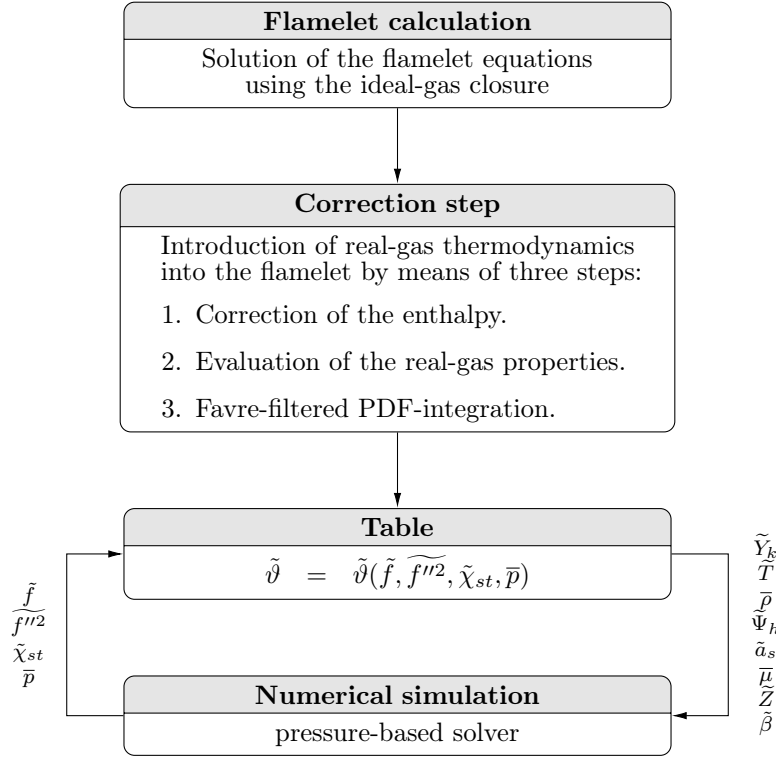


Figure 5.2: Schematic procedure of the real-gas flamelet model.

Stabilization of the numerical solver

High-pressure combustion under transcritical conditions can involve very large density stratifications. To avoid spurious pressure oscillations in the numerical simulation the pressure-based solver is stabilized employing a localized artificial dissipation concept μ^* . The approach applied in the present study is based on the work of Cook and Cabot [54] and reads [202]

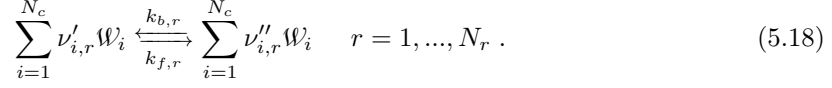
$$\mu^* = C_{ad} \bar{\rho} \tilde{a}_s \Delta^2 \left| \frac{\partial \tilde{Z}}{\partial x_i} \right|. \quad (5.17)$$

The artificial viscosity is added to the effective viscosity in Eqs. (5.14) and (5.15) in regions of high density gradients to avoid spurious oscillations. C_{ad} is a user-specified constant which is set to 0.04. The sensor, namely the local gradient of the compressibility factor, ensures that the effect of the artificial dissipation is limited to the narrow region of strong density gradients due to real-gas thermodynamics.

5.2 Reaction kinetics

Reaction mechanisms are used to determine the laminar source term $\dot{\omega}_k$ of the k -th species in Eq. (5.3). In the present work, the mechanism of O'Connaire et al. [212] is employed in LOx/H₂ combustion. The mechanism contains nine species ($N_c = 9$) and 19 reactions ($N_r = 19$) and has been used for the analysis of high-pressure hydrogen flames by Lacaze and Oefelein [154]. In the case of LOx/CH₄ combustion, the detailed mechanism developed at the Gas Research Institute (GRI) in the version 3.0 (short: GRI-3.0 [102]) is applied. This mechanism involves 53 species ($N_c = 53$) and 325 reactions ($N_r = 325$) and has been employed by Kim et al. [142] for operating conditions like they are investigated in the present work.

The process of chemical conversion during a combustion process can be described by elementary reactions which can be written in the form



Here, \mathcal{W}_i denotes the species i and the reactants and products of the chemical conversion process are on the LHS and RHS of the above equation, respectively. The stoichiometric coefficients of the forward and the reverse reactions of species i in the r -th reaction are $\nu'_{i,r}$ and $\nu''_{i,r}$. The associated rate constants are denoted by $k_{f,r}$ and $k_{b,r}$, respectively. Both constants are strongly temperature dependent and $k_{f,r}$ is modeled based on the empirical Arrhenius law [10]:

$$k_{f,r} = A_r T^{\beta_r} \exp\left(-\frac{E_{a,r}}{\mathcal{R}T}\right) . \quad (5.19)$$

Here, A_r , β_r and $E_{a,r}$ are the pre-exponential factor, the temperature exponent and the activation energy. All these values are given by the applied reaction mechanism. The reverse and the forward rate constants are related to each other by the equilibrium constants $K_{c,r}$ as

$$K_{c,r} = \frac{k_{f,r}}{k_{b,r}} = \left(\frac{p^{\text{ref}}}{\mathcal{R}T}\right)^{\sum_{i=1}^{N_c} (\nu''_{i,r} - \nu'_{i,r})} \exp\left(\frac{\Delta s_r^0}{\mathcal{R}} - \frac{\Delta h_r^0}{\mathcal{R}T}\right) . \quad (5.20)$$

Here, $p^{\text{ref}} = 101325$ Pa is the reference pressure and Δs_r^0 and Δh_r^0 denote the entropy and specific enthalpy changes during the conversion from reactants to products [147].

Having the rate constants of the reactions available, the reaction rates are expressed as

$$r_r = k_{f,r} \prod_{i=1}^{N_c} c_i^{\nu'_{i,r}} - k_{b,r} \prod_{i=1}^{N_c} c_i^{\nu''_{i,r}} , \quad (5.21)$$

where $c_i = Y_i \rho / M_i$ is the molar concentration of the i -th species. Next, the temporal change of c_i is determined as:

$$\frac{dc_i}{dt} = \sum_{r=1}^{N_r} (\nu''_{i,r} - \nu'_{i,r}) r_r \quad i = 1, \dots, N_c . \quad (5.22)$$

Finally, the source term $\dot{\omega}_i$ of component i can be calculated according to

$$\dot{\omega}_i = M_i \frac{dc_i}{dt} \quad i = 1, \dots, N_c . \quad (5.23)$$

The calculation of the concentration change according to Eq. (5.22) requires the solution of a system of ordinary differential equations (ODEs) comprising N_c equations and N_r summands. In the present work, conventional ODE-solvers like the semi-implicit Bulirsch-Stoer algorithm [17] are used.

Part III

RESULTS

6 Mixing under supersonic flow conditions

The first part of the results is concerned with mixing under GE-like injection conditions. The main focus is put on the resulting thermodynamic states and in particular on the possible occurrence of phase separation processes during the high-pressure injection. As supersonic flow conditions are prevailing in this chapter, the hybrid pressure-based approach is applied exclusively for the conduction of the numerical simulations. The following investigations are structured in three different parts which build upon each other. First, the influence of real-gas effects on the injection and mixing process is studied in Sec. 6.1. Second, the phase separation process in an extremely underexpanded pure argon jet is investigated in Sec. 6.2. Finally, the possibility of phase separation processes under GE-like conditions is the focal point in Sec. 6.3.

6.1 Influence of real-gas effects

Large parts of the following results and discussions are part of the journal article [319]:
Traxinger, C. and Pfitzner, M. Effect of nonideal fluid behavior on the jet mixing process under high-pressure and supersonic flow conditions. *Journal of Supercritical Fluids*, 172:105195, 2020.

6.1.1 Experimental setup

At the Institute of Aerospace Thermodynamics (ITLR) at the University of Stuttgart the mixing process of an initially supercritical jet under real-gas conditions is investigated experimentally. The jet experiments are performed in a cylindrical constant-volume test chamber where a single-hole injector of diameter $D = 0.236$ mm and length L of $L/D \approx 4.2$ is mounted into the front side end wall, see Fig. 6.1. The injector is equipped with two heater cartridges to control the injection temperature within ± 2 K. The chamber can be pressurized up to approximately 60 bar and the temperature inside the chamber corresponds to ambient conditions. Optical access is provided by three quartz windows. Recently, Baab et al. [14] and Förster et al. [80] used laser-induced thermal acoustics (LITA) to investigate the mixing process of highly underexpanded jets within this chamber. The speed of sound can be directly measured by extracting the frequency of the LITA signal and post-processing it using, for instance, the Fast Fourier transformation. From these two recent measurement campaigns [14, 80] a total of 14 injection experiments have been reported. The results of these experimental investigations [14, 80] are summarized in Tab. 6.1

and provide a valuable data base of speed of sound measurements regarding underexpanded jets under real-gas conditions. Note, that the measurements with a total injection temperature of 554 K from Baab et al. [14] and 553 K from Förster et al. [80] are aggregated and referred to as 553 K.

In the experiments [14, 80], two different fluids – fluoroketone/Novec 649 (FK) and n-hexane (C_6H_{14}) – have been injected through a single-hole injector into the test chamber filled with pure nitrogen (N_2) at rest. In the present work, the focus is put on the n-hexane cases. Here, nozzle

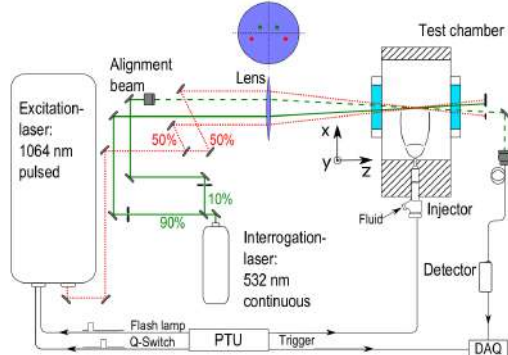


Figure 6.1: Schematic of the test chamber used at the ITLR for the experimental investigations of high-pressure mixing processes. The figure has been taken from Baab et al. [14]; reprinted by permission from Springer Nature Customer Service Centre GmbH: Springer Nature, *Experiments in Fluids*, Baab et al. [14], © (2016).

Table 6.1: Available experimental data collected from Baab et al. [14] and Förster et al. [80].

Fluid	NPR	p_t [MPa]	p_{ch} [MPa]	T_t [K]	T_{ch} [K]	x/D [-]
FK	12	6	0.5	500	295	80,110
FK	4	6	1.5	500	295	55,80,110
C_6H_{14}	600	30	0.05	553	295	110
C_6H_{14}	600	30	0.05	577	295	110,173
C_6H_{14}	600	30	0.05	600	295	110
C_6H_{14}	600	30	0.05	630	295	110
C_6H_{14}	150	30	0.2	553	295	55,80,110
C_6H_{14}	150	30	0.2	577	295	55,80,110,173
C_6H_{14}	150	30	0.2	600	295	55,110
C_6H_{14}	150	30	0.2	630	295	55,80,110
C_6H_{14}	60	30	0.5	577	295	173
C_6H_{14}	60	30	0.5	600	295	110
C_6H_{14}	60	30	0.5	630	295	110
C_6H_{14}	30	30	1	577	295	173

pressure ratios between 30 and 600 have been investigated. The total injection pressure p_t in the fuel reservoir equals 30 MPa and four different total injection temperatures T_t have been used: 553 K, 577 K, 600 K and 630 K. The speed of sound measurements were reported at four different nozzle exit distances depending on the operating conditions: $x/D = [55, 80, 110, 173]$. The chamber temperature T_{ch} corresponds to ambient conditions, i.e., 295 K. The chamber pressure p_{ch} was adjusted to meet the desired NPR.

6.1.2 Numerical setup

Thermodynamics

For describing the real-gas fluid behavior, the cubic EoS due to Peng and Robinson [226] is used. The required critical data and acentric factors of n-hexane and nitrogen can be found in Tab. B.1 in the appendix. In Fig. 6.2, the thermodynamic framework is validated for n-hexane at three different pressure levels. The reference data have been taken from CoolProp [27] and the discrete

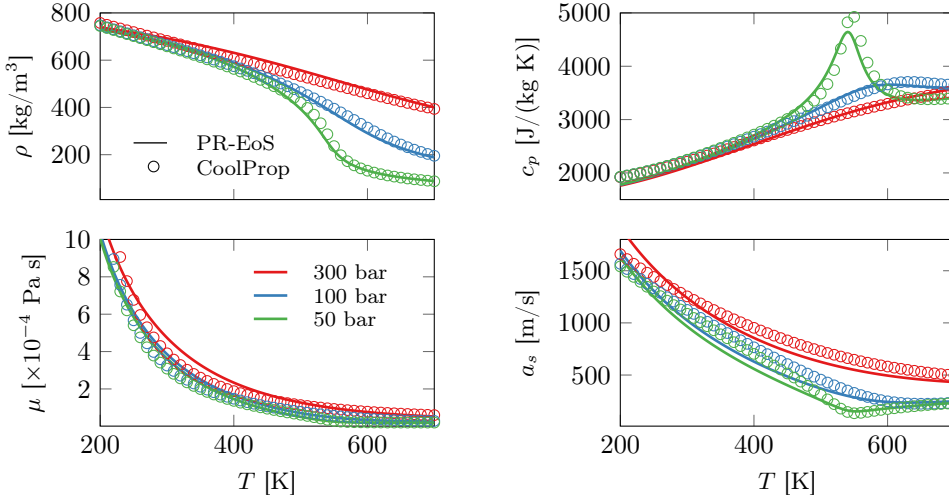


Figure 6.2: Comparison of the PR-EoS [226] with reference data taken from CoolProp [27]. The evaluation is conducted for n-hexane at three different pressures, namely 300, 100 and 50 bar.

pressures are selected such that they cover a large part of the supercritical pressure range ($p > p_c$) being present during the initial expansion process of the fuel jet into the chamber. Overall, a very good agreement with the high-fidelity data is achieved and it can be concluded that the PR-EoS [226] is a reasonably good choice for the present investigation. The discussion and comparison of mixture data is excluded for now and a critical and thorough assessment of the modeling error in the mixture space is conducted in Sec. 6.1.3.

Investigated test cases

Numerical simulations for eight of the twelve n-hexane test cases have been conducted and are listed in Tab. 6.2. The investigated test cases were selected in the following way: All low temperature cases ($T_t = 553$ K) have been excluded as a first a priori analysis showed that the expansion path of the underexpanded jet up to the Mach disk crosses the two-phase region of pure n-hexane. To keep the numerical effort at a reasonable level, all test cases with a single measurement point at $x/D = 173$ have also been excluded from this study. These are the two test cases at a total reservoir temperature of 577 K and NPRs of 30 and 60 (short: NPR30-T577 and NPR60-T577). This leaves us with a total number of eight test cases for which RANS simulations have been conducted and the focus is put on the measurement points $x/D = [55, 80, 110]$. Based on a priori evaluations of the molecular Prandtl number, the turbulent Prandtl and Schmidt numbers were set to 0.7 for both low NPR cases (60 and 150). For the NPR600 cases, Pr_t and Sc_t had to be decreased to a value of 0.4 to achieve a reasonable agreement with the experimental data. The possible reason for this decrease will be discussed later.

Table 6.2: Summary of the investigated underexpanded n-hexane test cases.

NPR	60	60	150	150	150	600	600	600
T_t [K]	600	630	577	600	630	577	600	630

Simulation domain

The computational domain consists of a high-pressure reservoir and a low-pressure chamber connected through a circular nozzle with a diameter of 0.236 mm according to the experimental setup [14, 80]. A sketch of the configuration is shown in Fig. 6.3. Initially, the low- and the high-pressure parts are separated by a virtual membrane which is removed at simulation start. At the inlet boundary of the high-pressure reservoir, total temperature and total pressure are prescribed with values taken from the experiments. Non-slip and adiabatic boundary conditions are employed at the solid walls. At the outlets of the low-pressure chamber, fixed static pressure boundary conditions are applied. Due to the investigation of different NPRs, the axial and radial extension (L_x and L_r) of the low-pressure chamber in the simulations are different. The lengths used in the present investigation are listed in the table in Fig. 6.3. The dimensions were chosen such, that the far field does not influence the near-nozzle jet structure. Especially in the NPR600 case, this resulted in an increase of the represented low-pressure chamber dimension by approximately a factor of two in the x - and y -direction compared to the low NPR cases. RANS simulations have been conducted which enable the utilization of the rotational symmetry of the flow field. A two degrees wedge configuration with symmetry boundary conditions on the opposite sides has been simulated. The solver settings are summarized in Tab. 6.3.

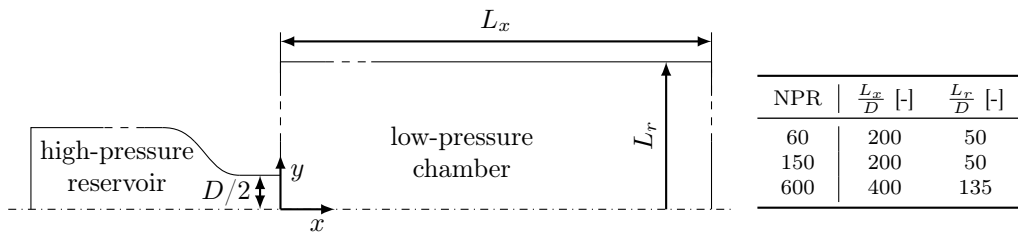


Figure 6.3: Schematic of the computational domain together with the major dimensions.

Table 6.3: Solver setup for the investigation of real-gas effects in underexpanded jets.

Solver	TVD-limiter	Turbulence closure	EoS
pressure-based (supersonic)	van Albada [332]	RANS with k,ω -SST-model [191, 192, 193]	PR-EoS [226]

Grid independence study

A grid independence study comprising four different meshes has been conducted for the NPR60-T600 case. Starting with an initial coarse resolution of 16 cells over the nozzle diameter – i.e., 8 cells in radial direction – for mesh1, the mesh was gradually refined three times with a 1.5 times higher cell number in each direction resulting in 24 (mesh2), 36 (mesh3) and 54 (mesh4) cells over the nozzle diameter. To evaluate the mesh convergence behavior in a first step, the mass flow rate at the nozzle exit \dot{m} is analyzed. In Tab. 6.4, the mesh resolution and the evaluated mass flow rates of the four different meshes are listed. While the mass flow rate still changes from mesh1 to mesh2

Table 6.4: Results for the grid independence study for case NPR60-T600.

	mesh1	mesh2	mesh3	mesh4
Orifice cells [-]	16	24	36	54
Cell count [-]	≈ 24000	≈ 53000	≈ 120000	≈ 272000
\dot{m} [g/s]	4.44	4.49	4.50	4.50

and from mesh2 to mesh3, a constant value of 4.50 g/s is achieved for the meshes 3 and 4 with 36 and 54 cells. To further judge the required mesh resolution, Fig. 6.4 shows the variation of the speed of sound along the chamber center axis for the four different meshes. The mesh dependence in the near-nozzle region – nozzle exit up to Mach disk position – is plotted in Fig 6.4a. From mesh1 to mesh2 a clear change in the expansion path for $x/D < 1$ and in the sharpness of the shock at the Mach disk is found. With increasing mesh resolution the variation of the speed of sound converges. For the refinement from mesh3 to mesh4 almost no significant changes become obvious. Similar findings in terms of the mesh convergence behavior can be found in the far-field, i.e., at the measurement location, see Fig. 6.4b. With increasing resolution the curves converge to each other and the changes from mesh3 to mesh4 are not significant. To further underline this

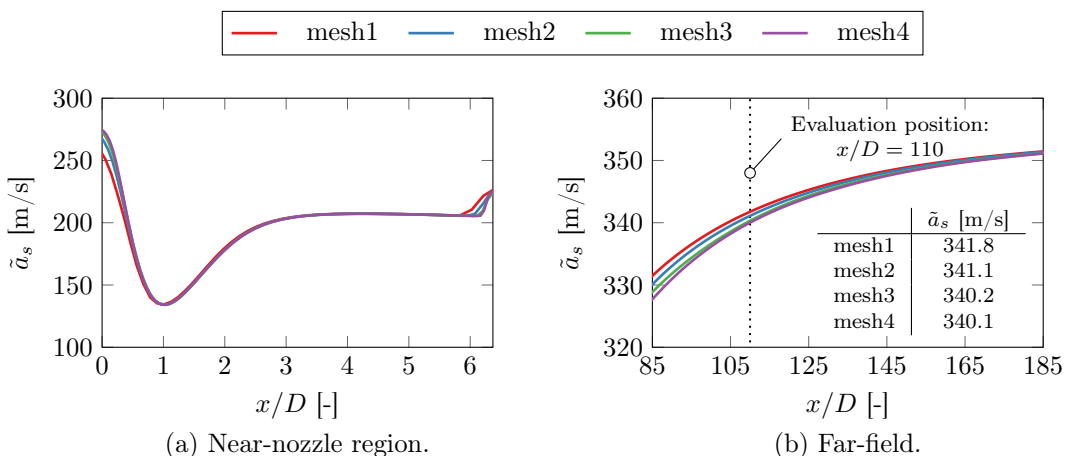


Figure 6.4: Mesh convergence study along the centerline for the case NPR60-T600. The near-nozzle region up to the Mach disk is shown in subfigure a. Far-field results are plotted in subfigure b including an evaluation of the speed of sound at the measurement position $x/D = 110$.

fact, the speed of sound has been evaluated at $x/D = 110$ which corresponds to the evaluation position in the experiment of the present case. A negligible change in the evaluated speed of sound is found from mesh3 to mesh4, see table in Fig. 6.4b. Therefore, grid independence is achieved for mesh3 and the flow is resolved sufficiently. All RANS simulation results presented in this section have been computed using mesh3.

6.1.3 Results

Comparison with experimental data

Before the experimental and numerical speed of sound data are compared to each other, the dependency of the overall flow field on the NPR is studied. In Fig. 6.5, the numerical simulation results for the NPRs 60, 150 and 600 are shown at a total reservoir temperature of 630 K. The NPR increases from top to bottom. Each upper half displays the temperature field, while the lower half shows the corresponding n-hexane mass fraction field. Note that all plots have the same temperature and mass fraction ranges. For all three cases, a highly underexpanded jet with a single shock barrel occurs. With increasing nozzle pressure ratio the size of this shock structure increases drastically. This accounts for both the axial and radial extent. A detailed investigation of the axial position of the Mach disk in dependency of the NPR can be found in Sec. F.3 of the appendix. In terms of the radial extent, the shock barrel grows by a factor of 1.75 from NPR 60 to 150 and more than doubles by a factor of 2.4 when going from NPR 150 to 600. As the Mach disk is the source for the subsequent mixing process of the injected fuel with the ambient gas, the extent of the overall flow field inside the chamber increases with increasing NPR. Looking at both the temperature and the mass fraction field in more detail, it can be seen, that the shock barrel prohibits the entrainment of nitrogen into this primary expansion structure. This fact was also reported and discussed recently by, e.g., Baab et al. [15] and Hamzehloo and Aleiferis [108]. With respect to the temperature, the barrel is the region of lowest temperature values in the overall flow field due to the strong expansion process after leaving the nozzle. The smallest temperature is found shortly upstream of the Mach disk. Downstream of the Mach disk the mass fraction and the temperature gradually decay towards the chamber conditions as a result of the steady mixing process with the ambient gas. For both the temperature and the mass fraction

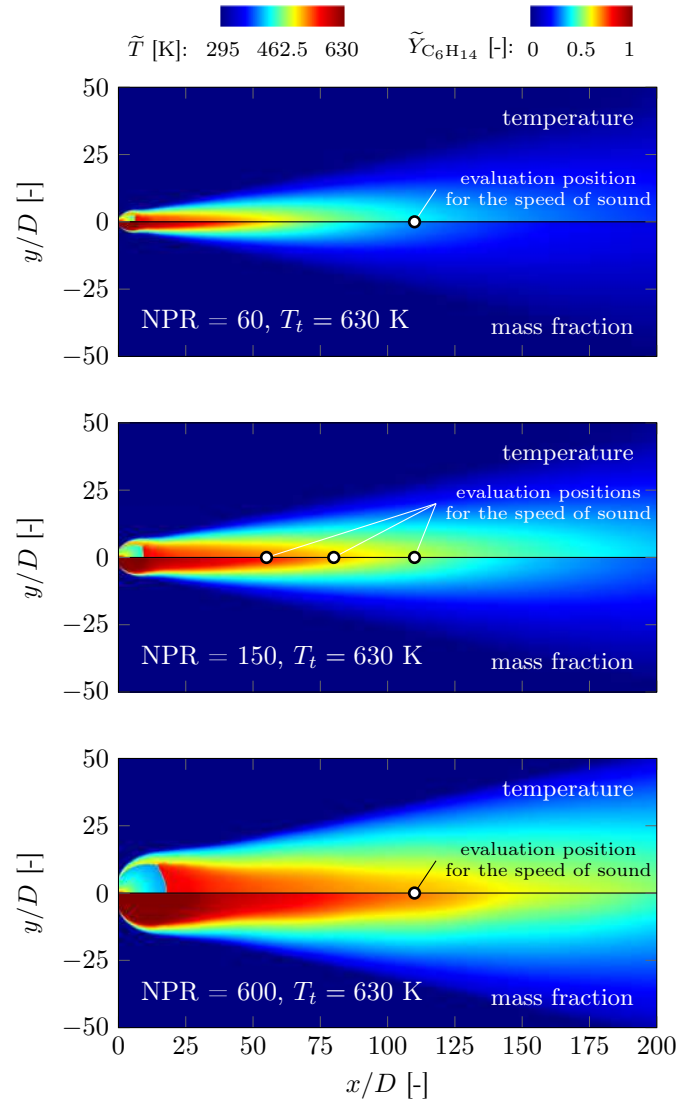


Figure 6.5: Numerical simulation results of the underexpanded jets at a total reservoir temperature of 630 K.

fact, the speed of sound has been evaluated at $x/D = 110$ which corresponds to the evaluation position in the experiment of the present case. A negligible change in the evaluated speed of sound is found from mesh3 to mesh4, see table in Fig. 6.4b. Therefore, grid independence is achieved for mesh3 and the flow is resolved sufficiently. All RANS simulation results presented in this section have been computed using mesh3.

field this decay occurs highly similar and is a first evidence of advection controlled mixing which will be examined in more detail later. In addition to the visualization of the flow field, Fig. 6.5 shows the measurement/evaluation points for the speed of sound data by means of white dots along the center axis. In the NPR 60 and 600 cases, only a single evaluation point at $x/D = 110$ is available. In the NPR60 case, this point lies outside the n-hexane potential core, while in the NPR600 case the evaluation point is found inside the core. For the NPR150 cases, three different positions at $x/D = [50, 88, 110]$ are used. The evaluation points are found partly inside and outside the potential core.

In Fig. 6.6, the comparison of the speed of sound data from the experimental measurements and the CFD simulations is shown. In accordance with the experiments [14, 80], the speed of sound was evaluated from the CFD results by using a sphere of diameter 200 μm and taking the average. Overall, a very good agreement is found and it can be concluded that the CFD framework is able to capture the mixing process over a wide temperature and NPR range. Almost all points lie

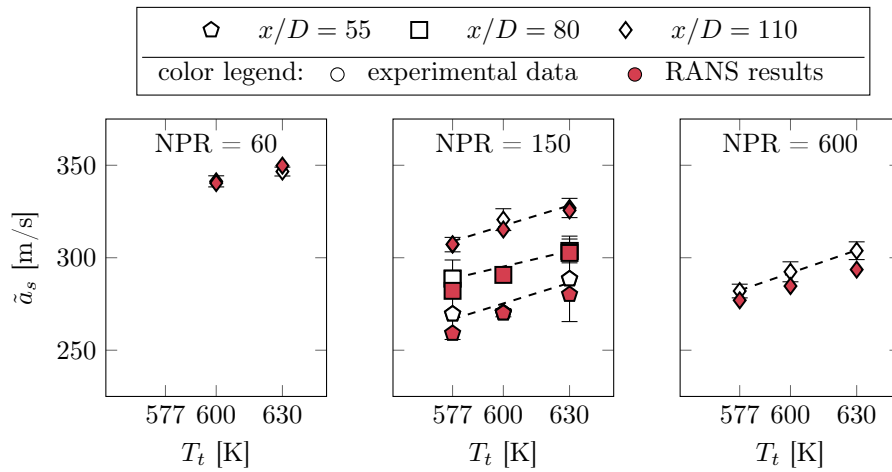


Figure 6.6: Comparison of the speed of sound measurements [14, 80] with the simulation results. The dashed lines are linear regressions of the experimental data at identical axial positions.

within the measurement uncertainty of the experiment. For the lowest NPR of 60, both simulations ($T_t = 600$ K and 630 K) excellently predict the measured speed of sound values at an axial position of $x/D = 110$. For the NPR150 cases a very good overall agreement is found. Data of both most downstream locations, i.e., $x/D = 80$ and 110, are predicted excellently for all three injection temperatures. At $x/D = 55$, small deviations are present for the injection temperatures $T_t = 577$ K and 630 K. However, note that at these two positions the measurement uncertainty in the experiment [14] is maximal and both RANS results lie within the uncertainty range. A possible reason for these large uncertainties and the deviations between CFD and experiment will be discussed later when the overall decay rate of the fuel jet is analyzed in more detail, see Sec. 6.1.3. For the NPR600 cases, a systematic underprediction of 2-3% is found for all three injection temperatures. However, the trend of a rising speed of sound value at $x/D = 110$ for increasing total reservoir temperatures is captured perfectly. Keep in mind that the turbulent Prandtl and Schmidt number had to be changed in the RANS simulations of the NPR600 cases to a value of 0.4 to correctly predict the sound velocity. Using the same Prandtl and Schmidt numbers ($\text{Pr}_t = \text{Sc}_t = 0.7$) as for the cases with NPR 60 and 150 resulted in an underprediction of the speed of sound of approximately 8-10%. To get more insight into this issue, a full 360-degrees Large-Eddy Simulation of the case NPR600-T577 has been conducted using the WALE sub-grid model [211]. The turbulent Prandtl and Schmidt numbers were set to one: $\text{Pr}_t = \text{Sc}_t = 1$. According to the suggestions of Hamzehloo and Aleiferis [111], the nozzle is resolved with 50 cells over the diameter. Very similar resolutions for reliable Large-Eddy Simulations of underexpanded jets were reported by, e.g., Vuorinen et al. [343] or Munday et al. [205]. The extent of the simulated low-pressure chamber equals the dimensions listed in Fig. 6.3 and yields a total mesh size of 12 million cells. The comparison of the experi-

mental and numerical speed of sound values at $x/D = 110$ shows very good agreement. The LES overpredicts the sound velocity by approximately 2.5% which is approximately the same amount as the RANS underpredicts it. In Fig. 6.7, the average n-hexane mass fraction fields from the LES and RANS simulation are compared to each other. Overall, the flow fields look similar in terms of the radial extent. However, for the axial variation deviations become obvious. In the RANS case, the decay of n-hexane is very continuous and the jet core gets gradually diluted with nitrogen. In contrast, a large entrainment of nitrogen in the LES case is first omitted up to $x/D \approx 40$. Farther downstream, the jet break-up is very intense and a lot of nitrogen mixes into the jet core leading to a very rapid dilution of n-hexane. As a result, the overall length of the potential core in the LES is shorter than in the RANS case and lower n-hexane mass fractions are present at and around the evaluation location ($x/D = 110$). The longer n-hexane potential core in the RANS simulations is therefore attributed to the turbulence modeling. Hence, a more thorough investigation on this issue would be necessary which is however out of scope of the present study. This will be kept for future investigations as the focus of the present study lies on the thermodynamic effects rather than on an in-depth investigation of the turbulence/sub-grid modeling in RANS and LES.

Assessment of the thermodynamic modeling error

In Fig. 6.2, the prediction capability of the PR-EoS [226] for pure n-hexane was compared to high-fidelity data taken from CoolProp [27]. The validation showed that both density and specific heat are predicted excellently by the PR-EoS [226] over a wide temperature and pressure range. Therefore, the representation of the general fluid state, i.e., the energetic state, can be considered highly accurate. However, for low temperatures notable deviations of the predicted sound velocity occur, see Fig. 6.2 bottom right. This in turn motivates the further assessment of possible thermodynamic modeling errors of a_s in the mixture space.

To quantify possible errors, we extracted pressure, temperature and composition from all RANS simulation results at the evaluation positions for the speed of sound. Based on these data, the sound velocities are re-evaluated using CoolProp [27]. For the treatment of alkane mixtures, the GERG-2008 EoS [144, 145] is used in CoolProp [27]. In Fig. 6.8, the sound velocity extracted from the RANS simulations $a_{s,RANS}$ – same as shown in Fig. 6.6 – and the a posteriori evaluated sound speed $a_{s,CoolProp}$ are compared to each other. Excellent agreement is found and the minimum and maximum error lie well below 1%. This is not unexpected as the mixing process occurs under almost ideal conditions. Therefore, modeling errors resulting from the thermodynamic framework should be minimal. Hence, the data can be used without hesitation for further studies that go beyond the mere comparison with experimental data.

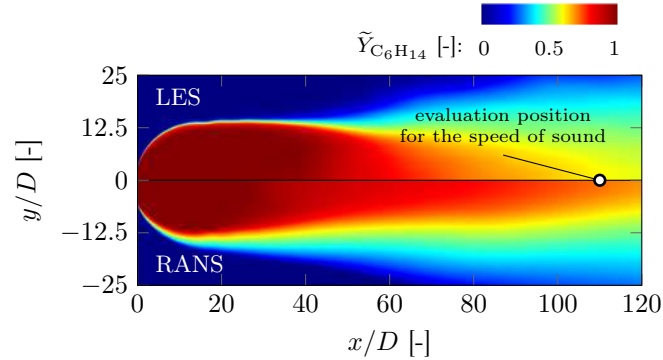


Figure 6.7: Comparison of the average n-hexane field for the case NPR600-T577.

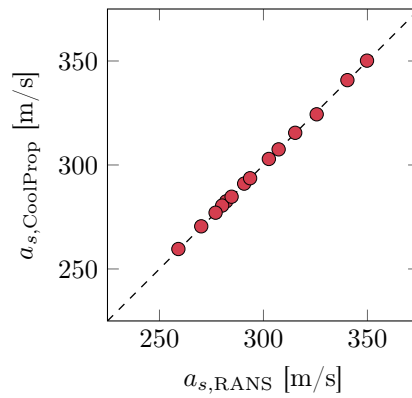


Figure 6.8: Comparison of the speed of sound taken from the RANS simulations with data a posteriori evaluated using CoolProp [27].

Concentration decay along the centerline

Turbulent jets released into a gaseous environment become self-similar at a sufficiently large distance from the source. In the present case, the source corresponds to the Mach disk as downstream of this shock structure the mixing process with the ambient gas takes place. As this process occurs under almost isobaric conditions, i.e., respective chamber pressure conditions, the jet growth and the axial decay rates of different properties correspond to ordinary compressible turbulent jets [366]. Experimental work of Birch et al. [35, 36] showed that for sufficiently large axial distances the centerline concentration and velocity are inversely proportional to the distance from the source. In Fig. 6.9, the decay of the n-hexane concentration and the velocity along the chamber axis are shown for the three different NPR150 cases. All three jets exhibit self-similarity for $x/D \gtrsim 90$. This is approximately the position of the second measurement point in the experiment and could be an explanation for the excellent agreement between experiment and simulations at $x/D = 80$ and $x/D = 110$, cf. Fig. 6.6. Upstream of $x/D \approx 90$, the values deviate from the dashed line as the jet structure is developing in this region and therefore self-similarity is not achieved yet. This in turn could be the reason for the large experimental uncertainty and the deviation between the experimental data and the CFD results.

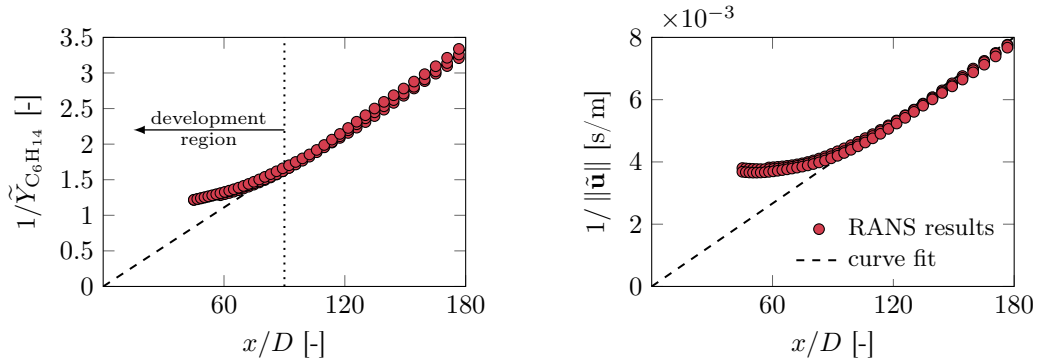


Figure 6.9: Concentration and velocity decay along the centerline for the three NPR150 cases. The curve fit was done manually to underline the self-similarity of the jets for sufficiently large distances from the source. Only every 5th point from the simulation results is shown and data points below $x/D \approx 45$ are excluded.

In addition to the speed of sound measurements, Baab et al. [14] and Förster et al. [80] reported mass fraction data which they recalculated from their measured sound speeds along the centerline. For the post-processing of the experimental data, Baab et al. [14] and Förster et al. [80] used thermodynamic data from NIST Refprop [165] together with the adiabatic mixture approach. This evaluation procedure and possible improvements are discussed in detail in the next section. In Fig. 6.10, the CFD and the experimental results are compared to each other. The data is grouped according to the axial measurement/evaluation positions ($x/D = [50, 80, 110]$). A systematic offset between the RANS results and the post-processed experimental data becomes obvious. The discrepancy increases with larger axial distance. In fact, the deviations can be traced back to real-gas effects which have to be considered in a consistent and thermodynamically rigorous way when mass fractions are deduced from, for instance, single-point speed of sound measurements.

6.1.4 Thermodynamic analysis

Nonideal fluid behavior

The mixing process downstream of the Mach disk leads to a gradual change of the energetic state and the composition. This in turn results in a variation of the speed of sound which is in general a function of pressure, temperature and composition. To better understand the mixing process and the influence of the nonideal fluid behavior, Fig. 6.11 shows the variation of the pressure and the compressibility factor along the centerline of the chamber. The data are taken from the case NPR150-T577. Up to the Mach disk position, a rapid expansion process occurs leading to a

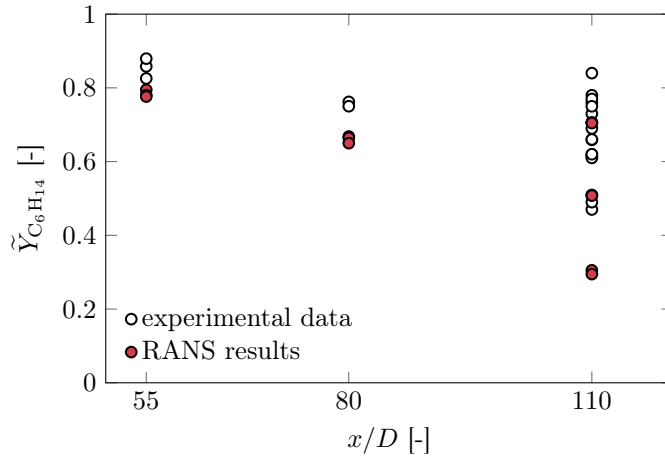


Figure 6.10: Comparison of the centerline concentration for the investigated n-hexane jets. Experimental data have been taken from the work of Baab et al. [14] and Förster et al. [80].

minimum pressure of ≈ 0.2 bar. Due to the strong shock, the flow is brought back to chamber conditions and therefore the pressure is almost constant downstream of the Mach disk. Therefore, the dilution of the jet takes place under almost isobaric conditions and hence the variation of the speed of sound is governed by the change in temperature and composition along the chamber axis. Due to the low pressure, mixing occurs under almost ideal gas conditions ($Z \approx 1$). However, upstream of the Mach disk the consideration of real-gas effects is mandatory as the compressibility factor is unequal to unity. Note that the minima of the compressibility factor and the pressure do not occur at an identical axial position. The minimum pressure value is found shortly upstream of the Mach disk location. In contrast, the minimum value of the compressibility factor ($Z \approx 0.4$) is located shortly downstream of the nozzle exit. To better understand this observation from a thermodynamic point of view, Fig. 6.12 shows the expansion path along the center axis in the pressure-temperature diagram of n-hexane. Every 5th point of the simulation data is plotted and colored with the respective compressibility factor. In addition, the vapor-pressure curve (solid black line) together with the Widom line (dash-dotted black line) of n-hexane are shown.

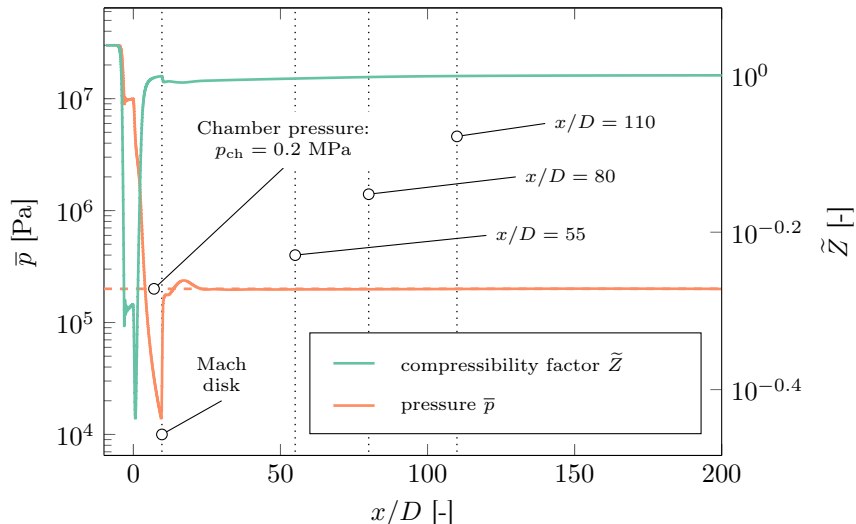


Figure 6.11: Change of the pressure and the compressibility factor along the center axis for the test case NPR150-T577.

For the determination of the Widom line the peak of the specific heat was used. Shortly upstream and downstream of the nozzle-exit the smallest compressibility factors are found. These scatter points with $Z < 1$ are all in the vicinity of the Widom line. As soon as the temperature and pressure in the expansion process are well below the critical point of n-hexane, the compressibility factor becomes close to unity and the non-ideal fluid behavior vanishes. However, this fact does not justify the application of the ideal-gas closure. The neglect of the real-gas effects on the simulation results will be examined in more detail in the following. Here, we will start with the determination of the post-shock state, as it is the source for the subsequent mixing process of the injected fuel and the ambient gas.

Post-shock state

In many investigations in the literature, the post-shock state is assumed to be at the chamber pressure and at a temperature being equivalent to the reservoir conditions, see, e.g., Harstad and Bellan [114], Baab et al. [15] or Förster et al. [80]. This is a valid assumption as long as the post-shock Mach number is below 0.4 (incompressible) and the fluid behaves like an ideal gas (enthalpy is only a function of the temperature, i.e., $h = h(T)$). In the present investigation, however, the latter assumption does not hold, as the injection conditions induce strong real-gas effects. Therefore, the thermodynamic state variables have both a temperature and a pressure dependency, i.e., $h = h(p, T)$.

To further elaborate this fact, Fig. 6.13 shows RANS results along the centerline for the case NPR150-T577. Both an ideal-gas and a real-gas equation of state have been employed to investigate the differences in the results induced solely by the thermodynamic closure. Overall, both expansion paths exhibit a kind of loop-like pattern in the pressure-temperature space with the maximum values at reservoir conditions and the minimum values at the Mach disk. The plot of the ideal-gas solution – marked with green dots – shows an almost straight line in the semi-log space ranging from the reservoir up to the Mach disk. This behavior can be attributed to two facts: First, because of the axial and radial shock structure, no mixing takes place and therefore only the pure fluid thermodynamic properties – here: n-hexane – govern the considered expansion path. Second, the expansion is rapid and almost adiabatic and therefore can be approximated as isentropic, i.e., the entropy s is constant. Assuming a perfect gas (constant heat capacity), the temperature and the pressure can be related in such an expansion process as

$$p/p_t = (T/T_t)^{\frac{\gamma}{\gamma-1}}. \quad (6.1)$$

Here, the reservoir condition is denoted by the index t and $\gamma = c_p/c_v$ is the isentropic exponent (here: $\gamma = 1.04$ for C₆H₁₄). The result of Eq. (6.1) is plotted in Fig. 6.13 as dotted line and underlines the assumption of an isentropic expansion process without mixing up to the Mach disk position. The strong normal shock brings the flow back to chamber pressure conditions (here: $p_{ch} = 2$ bar). Due to the application of the ideal-gas law, i.e., the enthalpy is solely a function of the temperature neglecting mixing processes, the post-shock temperature T_{ps} equals the reservoir condition (for an ideal gas: $T_{ps} = T_t = 577$ K), see Fig. 6.13.

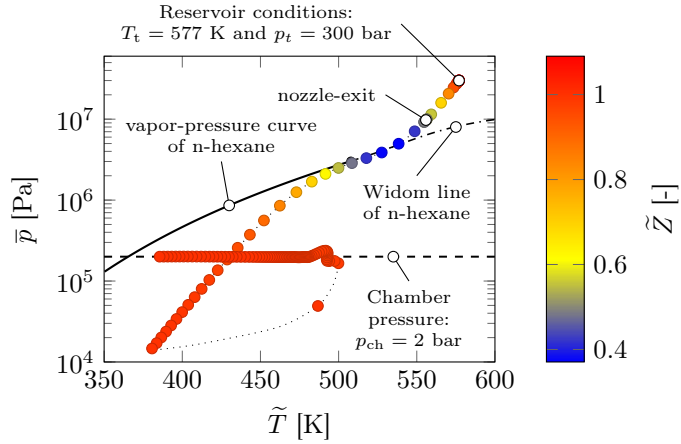


Figure 6.12: Expansion path along the chamber centerline for the case NPR150-T577. Every 5th data point of the RANS simulation result is plotted and colored with the respective compressibility factor Z .

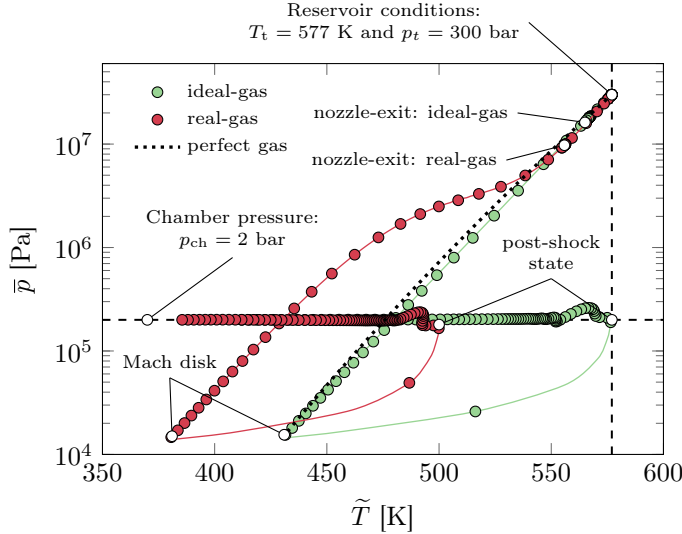


Figure 6.13: Comparison of ideal and real gas RANS results for the case NPR150-T577. Only every 5th point from the simulations along the chamber centerline is shown.

Looking at the real-gas results – shown as red dots in Fig. 6.13 – deviations with respect to the ideal gas solution are obvious. Due to the nonideal fluid behavior, the nozzle exit states are already different and the temperature and pressure in the real-gas case are lower compared to the ideal-gas solution. This fact gets more pronounced downstream of the nozzle: Here, the real-gas results show an s-shaped curve in the semi-log p, T -space resulting in overall smaller temperatures compared to the ideal-gas case throughout the whole expansion process from reservoir conditions up to the Mach disk. Comparing this curve shape to the ideal gas solution it can be concluded that the high-pressure and low-pressure branch of the expansion process are approximately governed by the ideal-gas behavior (compressibility factor $Z = pv(RT)^{-1} \approx 1$) as these branches are almost linear in the semi-log p, T -space. Identical conclusions have been drawn based on Fig. 6.12. With respect to the minimum expansion pressure, it is noteworthy that these pressure values are almost identical when comparing the ideal and the real gas results. The strong shock at the Mach disk brings the flow back to the chamber pressure. Due to the nonideal fluid behavior, the post-shock temperature is approximately 75 K lower compared to the ideal-gas solution. Hence, the assumption of an isothermal relation between the reservoir condition and the post-shock state does not hold in the real-gas case.

The consideration of real-gas effects within the simulation does not only alter the initial expansion process and the post-shock state but also changes the whole thermodynamic states along the nozzle and chamber axis. This can be seen in more detail in Fig. 6.14 where the speed of sound and the temperature are plotted along the chamber centerline. The comparison shows that the temperature level is reduced due to the consideration of real-gas effects which in turn results in lower values of the speed of sound. Overall, it can be concluded that the consideration of real-gas effects is mandatory for the prediction of the correct mixture

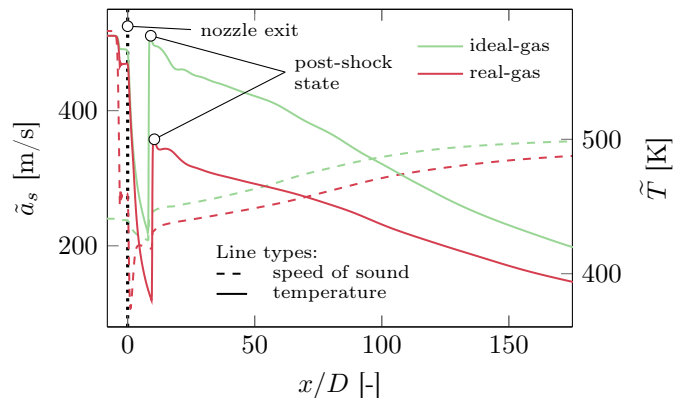


Figure 6.14: Comparison of ideal and real gas RANS results for the case NPR150-T577 in terms of the speed of sound and the temperature along the centerline of the chamber.

state and that the application of the ideal-gas law leads to severe deviations which are not acceptable for high-fidelity investigations and predictions of the disintegration process of fuel jets into a gaseous environment.

To correctly predict the post-shock state in underexpanded real-gas jets a priori, i.e., without using expensive and complex simulations, it is essential to start from the first law of thermodynamics. Considering an open system and under the assumption of a stationary process the first law of thermodynamics reads:

$$0 = \sum \dot{Q} + \sum \dot{W} + \sum (\dot{m}h_t) . \quad (6.2)$$

Here, \dot{Q} is the heat flux, \dot{W} is the power and $\dot{m}h_t$ is the transport of total specific enthalpy due to mass fluxes across the system boundaries. Assuming an adiabatic expansion (the expansion process is very fast and hence no significant heat flux is present) and combining it with the fact that no technical device is connected to the investigated flow system, we arrive at a flow with constant total specific enthalpy ($h_t = \text{const.}$). This resulting process is illustrated in Fig. 6.15. As our primary interest lies in the post-shock state, i.e., state 1 in Fig. 6.15, we apply the first law to the expansion structure upstream of the Mach disk (highlighted in gray). Therefore, the state change from point 0 to 1 in Fig. 6.15 is considered. Due to the fact that the velocity change is negligible between

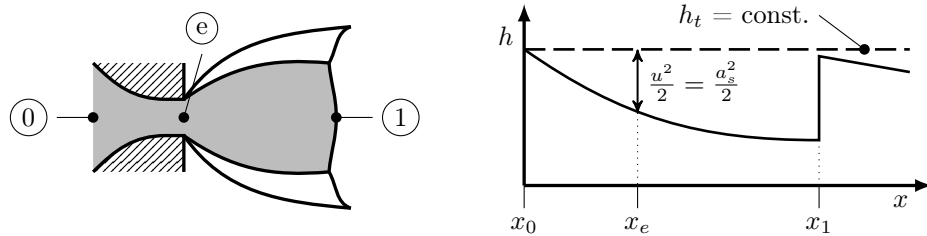


Figure 6.15: Expansion of an underexpanded jet with the corresponding total enthalpy and static enthalpy characteristics. At the nozzle exit, the Mach number equals unity and hence the velocity is equal to the local speed of sound, i.e., the flow is choked.

the reservoir and post-shock state, see Fig. 6.15, we arrive at a flow with constant enthalpy when looking at the inlet and outlet of our imaginary thermodynamic system between state 0 and 1 in Fig. 6.15, i.e., $h_t = h_0 = h_1$. As a result, the post-shock static temperature T_{ps} can be estimated from the total enthalpy at reservoir conditions and the chamber pressure as:

$$T_{ps} = T(h_t, p_{ch}) . \quad (6.3)$$

Here, it is of course important to apply a thermodynamic closure considering real-gas effects, i.e., $h = h(p, T)$. A comparison between the analytical results from Eq. (6.3) and the CFD results is shown in Tab. 6.5. The discrepancy between both results is well below 1%. In addition, the comparison between the reservoir temperature T_t and the post-shock temperature T_{ps} shows the influence of the real-gas effects on the post-shock temperature.

Table 6.5: Comparison of the post-shock temperature T_{ps} according to Eq. (6.3) and the RANS simulation results. The analytical post-shock temperature has been evaluated using CoolProp [27].

NPR T_t [K]	60			150			600		
	600	630	577	600	630	577	600	630	
T_{ps} Eq. (6.3) [K]	533.57	569.94	502.68	531.49	568.27	501.46	530.48	567.45	
T_{ps} RANS [K]	531.17	567.63	499.94	528.93	566.32	499.02	528.52	563.61	
Difference [K]	2.40	2.31	2.74	2.56	1.95	2.44	1.96	3.84	
Difference [%]	0.45	0.40	0.54	0.48	0.34	0.49	0.37	0.68	
$T_t - T_{ps}$ [K]	66.43	60.06	74.32	68.51	61.73	75.54	69.52	62.55	

To conclude the thermodynamic discussion of the post-shock state, Fig. 6.16 shows the enthalpy-pressure diagram of n-hexane. High-fidelity data from CoolProp [27] have been used for the presentation of this diagram. The two-phase region is defined by the two binodals – dew- and bubble-point line – and is determined by the critical point from where the Widom line (dash-dotted line) extends into the supercritical pressure regime. Eight isotherms are shown including three subcritical, the critical and four supercritical temperatures. The arrow on the top right of Fig. 6.16 shows the expansion direction for the pure n-hexane up to the Mach disk. The four total injection conditions are marked by the colored dots. Each colored horizontal line indicates an isenthalp, i.e., $h = h_t (p_t, T_t)$. By comparing the post-shock states at constant enthalpy with the isotherms at the corresponding reservoir conditions a clear difference is visible. While the isenthalps form a straight line in the h, p -diagram, the isotherms exhibit an s-like curve shape. For all reservoir and back-pressure conditions, an average deviation of approximately 70 K is found when comparing the isothermal with the isenthalpic approach. This is a result of the real-gas effects and in turn of the pressure dependency of the thermodynamic properties in this regime. Similar conclusions have been drawn from the detailed investigation of case NPR150-T577 based on Figs. 6.13 and 6.14.

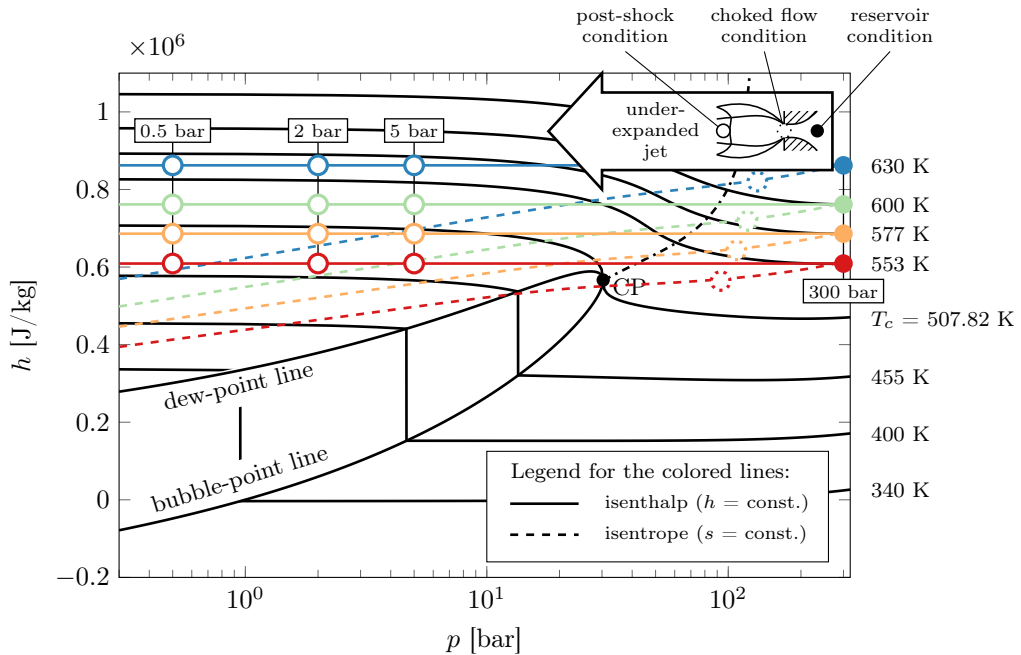


Figure 6.16: Enthalpy-pressure diagram of n-hexane. The black lines show the two-phase region, the Widom line and eight isotherms. The colored lines highlight isenthalpic and isentropic state changes originating from the respective reservoir conditions (filled circle). The choked flow conditions and the post-shock states are marked by the white-filled dashed and bold circles, respectively.

In addition to the discussion of the post-shock state, the exclusion of the low temperature cases ($T_t = 553$ K) from the present numerical investigation can be understood from Fig. 6.16. The dashed line emerging from the respective reservoir condition corresponds to the isentropic expansion path and the colored dot on this line marks the choked flow condition. The red dashed line clearly crosses the two-phase region and therefore a more sophisticated thermodynamic closure would be necessary to conduct the simulations. This topic will be addressed in Sec. 6.2 in more detail for a different test case.

Thermodynamically rigorous mixing approach

Building on the findings in the last section, a thermodynamically consistent 1D mixing approach is outlined in the following. This method enables the thermodynamically rigorous evaluation of thermodynamic properties from, e.g., measured speed of sound data in convection dominated

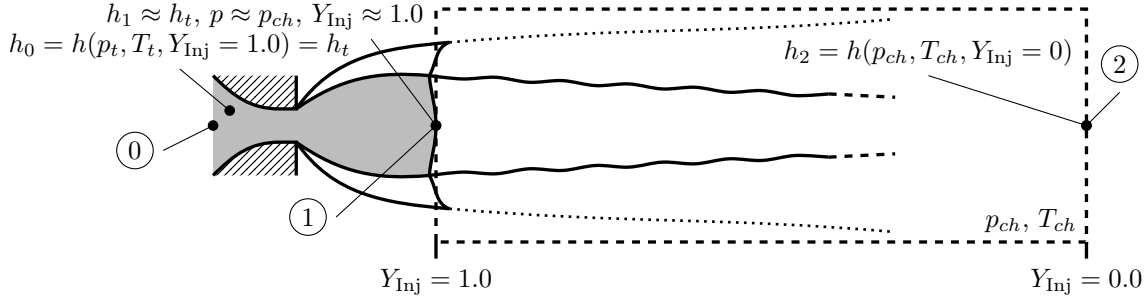


Figure 6.17: Sketch of the adiabatic mixture concept for advection-controlled mixing.

mixing. The basic concept is sketched in Fig. 6.17. The mixing approach spans from shortly downstream of the Mach disk up to a virtual point in the far field where the flow is fully mixed out and solely pure ambient gas is present. Therefore, the complete mixture space is covered. In the present high-speed cases, the mixing is advection-controlled. As a result, the transport of species and energy is controlled by means of convection and turbulent diffusion and hence both conservation properties are transported at the same rate. This fact allows the application of the adiabatic mixture concept which relies on the unitary Lewis number assumption which again implies the equality of species and energy transport. The big difference to previous investigations is not the introduction of this adiabatic mixture approach but the thermodynamically rigorous description of the post-shock state, which the mixture model relies on.

In general, the adiabatic mixture model for a binary mixture reads as follows

$$\dot{m}_{\text{mix}} = \dot{m}_1 + \dot{m}_2 , \quad (6.4a)$$

$$\dot{m}_{\text{mix}} h_{\text{mix}} = \dot{m}_1 h_1 + \dot{m}_2 h_2 , \quad (6.4b)$$

which can be deduced from the conservation of mass and energy under stationary conditions. In Eq. (6.4), the indexing of the pure fluid is chosen in accordance with Fig. 6.17 and the mixture is denoted by the index mix. Using Eq. (6.4), the mass fraction of the mixture along the mixing path can be expressed as

$$Y_{\text{mix}} = \frac{\dot{m}_1}{\dot{m}_1 + \dot{m}_2} \quad (6.5)$$

and therefore the mixture specific enthalpy reads

$$h_{\text{mix}} = Y_{\text{mix}} h_1 + (1 - Y_{\text{mix}}) h_2 . \quad (6.6)$$

Using this approach, the mass fraction at any axial position along the centerline can be deduced from the measured speed of sound data applying an iterative process. This can be done in the following way: The mixture space is completely defined by the mixing pressure, i.e., the chamber pressure, and the specific enthalpy in the mixture space, see Fig. 6.18. According to Eq. (6.6) and Fig. 6.18, the enthalpy forms a straight line which is defined by the chamber ($Y_{\text{N}_2} = 1$) and the reservoir/post-shock conditions ($Y_{\text{N}_2} = 0$). Therefore, the correct post-shock temperature including real-gas effects is inherently included. Under the assumption of a single-phase mixing process downstream of the Mach disk – as it is the case here – the thermodynamic state at every mixture location is fully

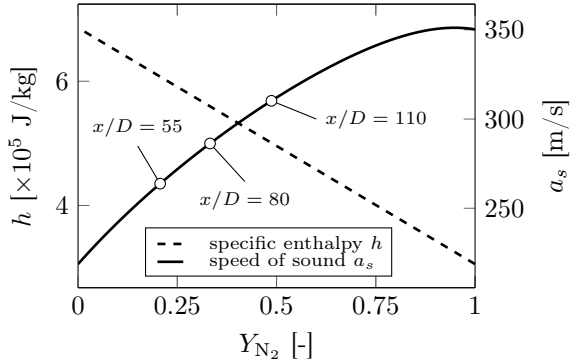


Figure 6.18: Specific enthalpy and speed of sound along the adiabatic mixture path for the case NPR150-T577.

defined by the enthalpy, pressure and mass fractions. Hence, every other thermodynamic property can be derived straightforwardly. It is just necessary to perform a line search along the mixture fraction and look for the appropriate speed of sound value. From Fig. 6.18 it becomes obvious that for most parts of the present study, there are unique values available. Only for nitrogen mass fractions larger than 90% the distribution is nonmonotonic and the mixture approach might fail. This, however, is of no concern in the present study as the n-hexane mass fractions are always greater than 20%.

In the final step, the described adiabatic mixing model is applied to evaluate the mass fractions a posteriori from the measured speed of sound data. The results of the post-shock corrected experimental data of Baab et al. [14] and Förster et al. [80] are shown in Fig. 6.19 in comparison to the RANS results. By rigorously considering real-gas effects for the determination of the post-shock state the newly post-processed mass fractions from the experimental data correspond very well to the RANS results. Comparing Figs. 6.10 and 6.19, a clear shift of the newly post-processed mass fractions towards lower values and therefore towards the CFD results occurs. In future studies, this agreement can be improved by several aspects: First, the current adiabatic mixing model neglects the kinetic energy of the flow. Second, the investigation of other fluids, e.g., fluoroketone, and lower NPRs can extend the data base for the analysis and show possible additional sensitivities apart from the sole thermodynamic aspects. When taking additional fluids into account, it is advisable to switch from mass to mole fractions following the work of Ewan and Moodie [74].

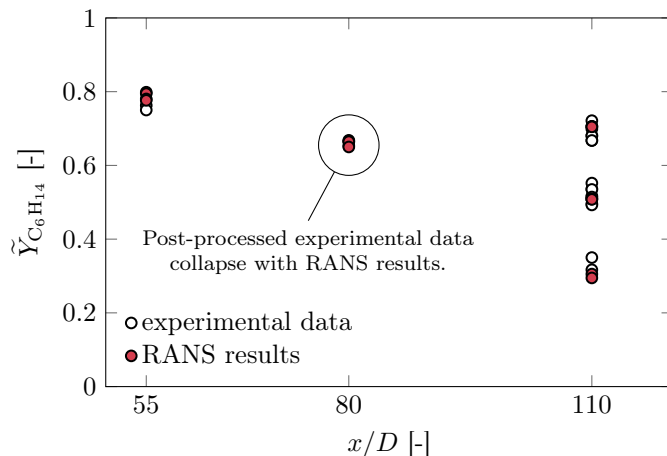


Figure 6.19: Comparison of the centerline concentration for the investigated n-hexane jets. Experimental speed of sound data were taken from Baab et al. [14] and Förster et al. [80] and have been post-processed using the adiabatic mixture concept.

6.1.5 Summary

In this section, numerical simulations have been conducted to study the mixing of highly underexpanded jets under engine-relevant conditions. Recent experimental data from Baab et al. [14] and Förster et al. [80] in terms of speed of sound measurements along the chamber center axis have been used to validate the CFD tool and study the jet mixing process. In total, eight different cases have been investigated where n-hexane has been injected through a single-hole injector into a chamber filled with nitrogen at rest. The cases selected for the present study cover a wide range of injection conditions: The reservoir temperatures comprise values from 577 K to 630 K and the NPRs vary between 60 and 600. Overall, very good agreement between the CFD results and the experimental data has been found. Especially in the regions of the fully developed jet, the prediction capability of the numerical framework is excellent.

Based on the successful validation of the CFD framework, a thorough analysis of the influence of the thermodynamic closure on the jet mixing process has been conducted. Neglecting the

pressure-dependency of the thermodynamic properties, i.e., real-gas effects, results in incorrect thermodynamic states throughout the complete jet mixing process from reservoir to chamber conditions. Most obvious, an average overprediction of the post-shock temperature of 70 K occurs for the present cases. This is caused by the erroneous energetic state when the ideal-gas law is applied as thermodynamic closure. This error further manifests in an overprediction of the temperature and consequently of the speed of sound along the chamber center axis. To evaluate and post-process thermodynamic properties in the mixing region downstream of the Mach disk from, e.g., measured speed of sound data, a thermodynamically rigorous determination of the post-shock state is necessary. Based on the present simulation results, an adiabatic mixture model has been deduced which enables a correct consideration of the energetic state. This in turn leads to a reliable prediction of additional thermodynamic data along the mixing path without applying costly and possibly complex numerical simulations. Using this new modeling approach, fuel mass fractions have been re-calculated from the measured speed of sound data from Baab et al. [14] and Förster et al. [80]. The post-shock corrected results nicely collapse to the simulation results and show the validity of the suggested mixture model.

6.2 Phase separation in pure fluids

Large parts of the following results and discussions are published in the journal article [321]: Traxinger, C., Zips, J., Banholzer, M., and Pfitzner, M. A pressure-based solution framework for sub- and supersonic flows considering real-gas effects and phase separation under engine-relevant conditions. *Computers & Fluids*, 202:104452, 2020.

6.2.1 Experimental setup

Recently, Fond et al. [79] and Xiao et al. [360] investigated underexpanded argon jets by means of experiments and numerical simulations. The main focus of both works [79, 360] was on the fluid-wall interaction in the confined channel and the velocity field in terms of first and second order moments. In their investigations [79, 360], argon Ar was injected into its own gas phase through a single-hole nozzle of diameter $D = 1.54$ mm. The low-pressure chamber is a square duct of 50 mm \times 50 mm. The nozzle-pressure ratio between the fluid reservoir upstream of the nozzle and the chamber is given as 120. The back-pressure in the chamber was set to 1 bar which yields a total reservoir pressure of 120 bar. Moderate temperatures were chosen for both the fluid reservoir ($T = 274$ K) and the chamber ($T = 285$ K) resulting in the presence of real-gas effects [360]. In addition, Fond et al. [79] reported the possibility of phase separation processes, as their single-shot images of the Mie scattering intensity showed bright regions upstream of the Mach disk. However, this was not numerically investigated by Xiao et al. [360] and therefore is one of the focal points of the following investigations.

6.2.2 Numerical setup

General settings

For the numerical investigation of the described argon jet, an LES has been conducted and the turbulence closure was achieved using the WALE [211] sub-grid model. For the temporal and spatial integration, second order accurate schemes were employed. According to the work of Xiao et al. [360], the Minmod limiter [264] is used to prevent an unboundedness of the solution. Following recent investigations of Hamzehloo and Aleiferis [111] the injector is resolved with 50 cells over the diameter resulting in a minimum cell size of ≈ 30 μm . The length of the square duct chamber was chosen as 100 mm to accurately capture the near-nozzle region up to approximately 60 mm. The length of the nozzle was set to ten times the injector diameter D , i.e., 15.4 mm, followed by an upstream reservoir supplying the high-pressure fluid to the nozzle. In total, the mesh comprises approximately 3.2 million cells. For the initialization of the simulation, the domain was separated into a high-pressure part (reservoir conditions: $p = 120$ bar and $T = 274$ K) and into a low-pressure part (chamber conditions: $p = 1$ bar and $T = 285$ K) left and right of the nozzle exit ($x = 0$ mm).

The thermodynamic closure has been achieved based on the Peng-Robinson [226] equation of state. As argon is a noble gas, this choice is not crucial for the present investigation. The required critical properties together with the acentric factor can be found in Tab. B.1 in the appendix. The solver settings are summarized in Tab. 6.6.

Table 6.6: Numerical solver setup for the investigation of phase separation processes in pure fluids.

Solver	TVD-limiter	Turbulence closure	EoS
pressure-based (supersonic)	Minmod [264]	LES with WALE [211]	PR-EoS [226]

Thermodynamics

In Fig. 6.20, the vapor pressure curve of argon (solid black line) from the triple point up to the critical point is shown. The triple point of a fluid marks the temperature and the pressure where three phases (solid, liquid and vapor) coexist in thermodynamic equilibrium. It therefore determines the lower end of the VLE. Based on Eq. (6.1), the approximated isentropic expansion path of a perfect gas (Ar: $\gamma = 1.67$) from reservoir conditions towards the chamber pressure is shown in the p,T -diagram. At a temperature of approximately 125 K the ideal expansion path crosses the VLE and consequently the two-phase region is entered across the dew-point line. As a result, a condensation process can be expected which has to be taken into account to investigate the actual thermodynamic expansion trajectory and to avoid solver instabilities caused by an erroneous (single-phase) treatment of the fluid in the numerical simulation. To enable the application of the VLE-model introduced in Sec. 4.8 for the present case, argon has been diluted with one mass percentage of nitrogen N₂ corresponding to a binary mixture with overall mole fractions of $\mathbf{z} = [0.985, 0.015]$. In Fig. 6.21, this assumption is evaluated in terms of the two-phase dome and the critical point. The reference data from CoolProp [27] and the PR-EoS [226] show the VLE of the pure fluid (argon). Comparing these two data sets, the binodal and the critical point are described very well by the PR-EoS [226], despite some small deviations at the bubble-point line. This could be expected, as argon is a noble gas. The comparison of the defined binary mixture to these two data sets yields very similar conclusions. The shape of the binary two-phase dome almost collapses with the prediction of the pure PR-EoS [226] in terms of both the binodal and the critical point. Therefore, it is concluded, that the application of the diluted binary mixture instead of the pure fluid is a reasonable approximation for the present investigation.

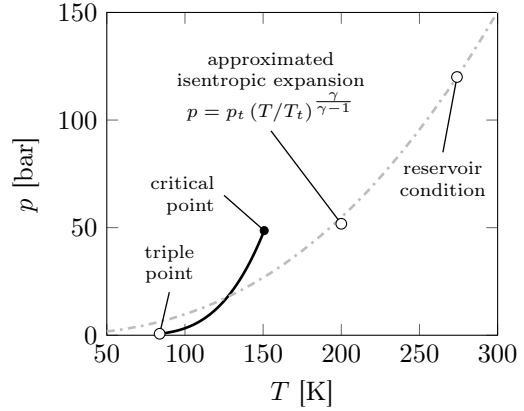


Figure 6.20: Pressure-temperature diagram of argon together with an approximated isentropic expansion path for a perfect gas (Ar: $\gamma = 1.67$) from reservoir to chamber conditions.

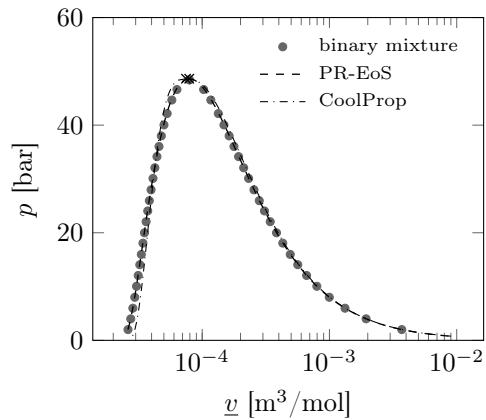


Figure 6.21: Two-phase dome of argon calculated with the PR-EoS [226] for the pure fluid and for the binary mixture of argon and nitrogen $\mathbf{z} = [0.985, 0.015]$. The reference data have been taken from CoolProp [27] for pure argon.

6.2.3 Results

Flow structure

In Fig. 6.22, the flow structure of the underexpanded jet forming downstream of the nozzle exit up to $x \leq 16$ mm is shown by means of instantaneous snapshots. The Schlieren image obtained from the experiments [360] is shown on the left-hand side and the right image depicts the simulation result. As a vertical knife edge is used in the experiments, the magnitude of the streamwise gradient of the density, i.e., $|\partial\bar{\rho}/\partial x|$, is evaluated for the visualization of the jet structure [287]. In addition, a line-of-sight integration has been conducted and the obtained intensity I has been stretched via the relation $\exp(-2.5I/I_{max})$ following Xiao et al. [360]. Both the experiment and the numerical simulation show an extremely underexpanded jet. The shock structure forming downstream of the nozzle exit is determined by the Mach disk separating the flow into the supersonic (upstream) and the subsonic (downstream) regime. The numerical simulation is able to capture the radial extent of the structure and the axial position of the Mach disk. According to Fond et al. [79], the Mach disk is located between 11.5 mm and 12.5 mm and hence no stationary behavior was reported which is in good agreement with the present LES.

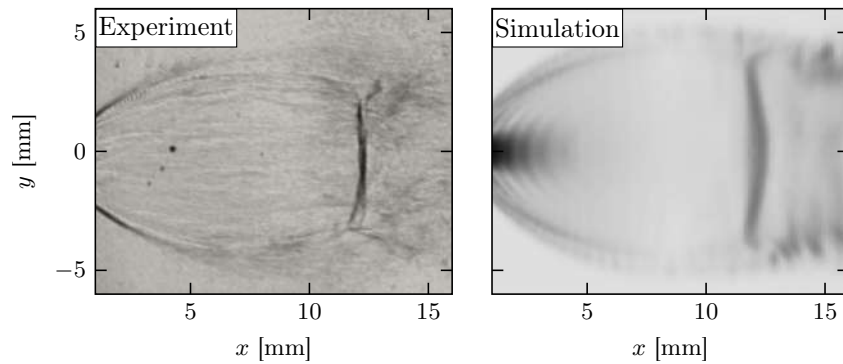


Figure 6.22: Comparison of the near-nozzle flow structure by means of single-shot images. The experimental image (left) has been taken from Xiao et al. [360] who applied Schlieren measurements for the visualization. In the numerical simulation (right), the line-of-sight integrated magnitude of the streamwise density gradient $|\partial\bar{\rho}/\partial x|$ is used to show the underexpanded flow structure. Reprinted by permission from Springer Nature Customer Service Centre GmbH: Springer Nature, *Flow, Turbulence and Combustion*, Xiao et al. [360], © (2019).

In Fig. 6.23, the velocity field downstream of the Mach disk is shown for $15 \text{ mm} \leq x \leq 60 \text{ mm}$ by means of the averaged velocity field. The left image shows the experimental result reported by Xiao et al. [360] which was obtained by means of Particle Image Velocimetry measurements

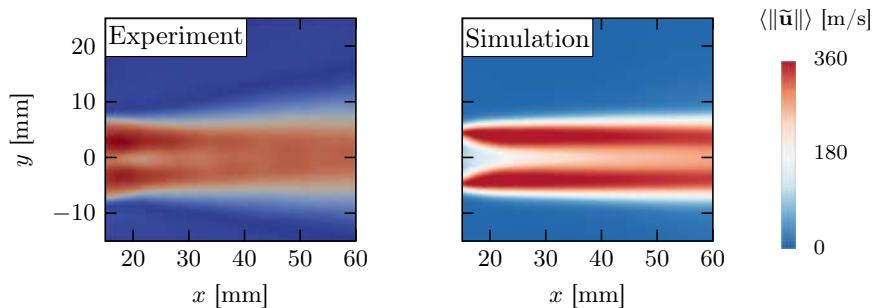


Figure 6.23: Visualization of the flow field downstream of the Mach disk by means of the averaged velocity. The experimental image has been taken from Xiao et al. [360]. Reprinted by permission from Springer Nature Customer Service Centre GmbH: Springer Nature, *Flow, Turbulence and Combustion*, Xiao et al. [360], © (2019).

and averaging 50 instantaneous shots. The numerical simulation result is depicted in the right image of Fig. 6.23. The value range and color-map are applied according to Xiao et al. [360]. In general, a good agreement between the experiment and the simulation is found. The width of the jet and high velocity regions are predicted well by the LES. However, the jet break-up in the LES is not as intense as in the experiments. This fact and the overall prediction quality of the numerical simulation can be further investigated based on averaged axial velocity profiles at different axial positions. In Fig. 6.24, experimental and numerical results at four different axial positions are shown downstream of the Mach disk. Overall, the comparison of the experiment

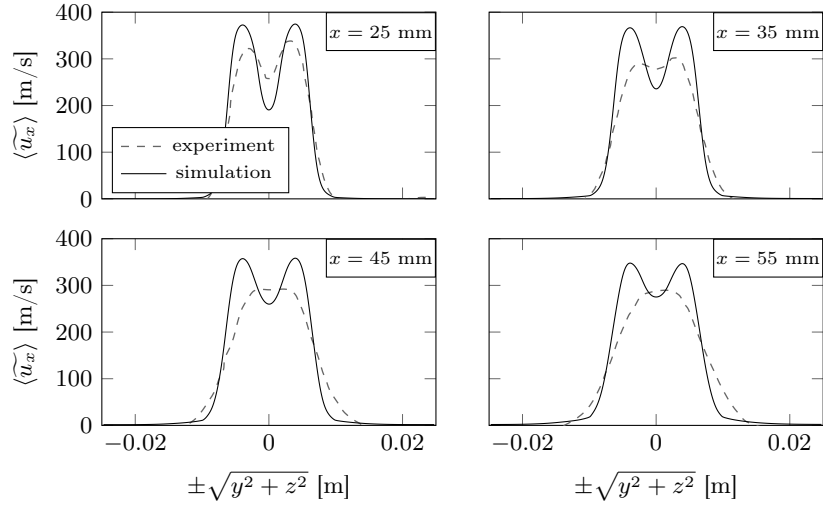


Figure 6.24: Comparison of the mean axial velocity at four different axial positions in the cross-stream direction. The experimental data have been taken from Xiao et al. [360].

and the simulation further underlines the good prediction capability of the LES. Particularly the width of the jet is captured very well throughout all four axial positions. In terms of the velocity distribution away from the center line, especially the first axial position ($x = 25$ mm) shows a very good agreement. For the three positions following downstream a reasonably good agreement is found. While the LES still features a pronounced slip line, this flow element is not visible in the experiments. In addition to the averaged axial velocities, Xiao et al. [360] also evaluated root mean square (RMS) values at the four axial positions. The comparison of the experimental RMS values and the second order moments extracted from the LES are shown in Fig. 6.25. Overall, a satisfactory agreement between the experiment and the simulation is found. Again, the agreement at the first axial position ($x = 25$ mm) is very good. Farther downstream, the general pattern is predicted quite well and the same accounts for the value range. In summary, for the comparison of the flow field it can be concluded that the agreement between experiment and simulation is good. The LES is able to capture the relevant flow characteristics from a fluid dynamics point of view especially in the near-nozzle region and therefore enables the investigation of possible phase separation processes.

Phase separation processes

In Fig. 6.26, experimental and numerical single-shot images are compared to each other. In both images, "bright" regions are found indicating a phase separation process upstream of the Mach disk. As two different properties are compared to each other, the application of a quantitative colormap is forgone and only a qualitative comparison is carried out. In terms of the experiment, the image on the left side of Fig. 6.26 shows the Mie scattering intensity taken from the work of Fond et al. [79]. As the edge of the laser sheet is starting at $x = 7.5$ mm, Mie scattering measurements have only been carried out by Fond et al. [79] downstream of this axial position. Furthermore, it has to be mentioned that the measurements have been conducted at a reservoir pressure of 125 bar. According to Crist et al. [55], this pressure difference results in an axial displacement of the Mach disk by ≈ 0.2 mm downstream. This is not of any concern in the

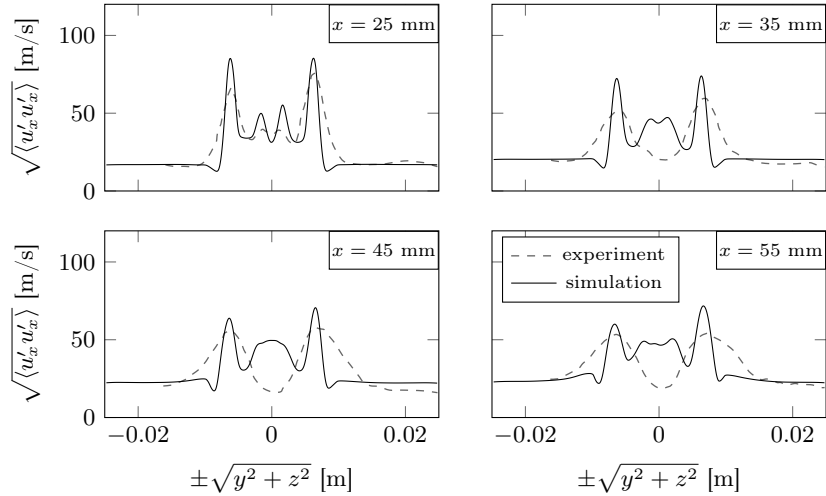


Figure 6.25: Comparison of the RMS velocity at four different axial positions in the cross-stream direction. The experimental data have been taken from Xiao et al. [360].

present study, as the Mach disk position anyway varies between an axial position of 11.5 mm and 12.5 mm in the experiment [79]. For the visualization of the phase separation process in the LES, the vapor fraction directly resulting from the *hpns*-flash was selected. The gray regions in Fig. 6.26 right indicate a vapor fraction less than one and hence areas of phase separation. In turn, black areas denote regions of single phase stability, i.e., areas of no phase separation. For a better comparability, a three-stage color-map was chosen for the visualization of the LES results. Comparing the single-shot images of the experiment and the LES, a very good agreement in terms of the phase separation process is found which is far better in terms of the radial and axial extent than the comparison shown in Fig. 6.22. As assumed by Fond et al. [79], single-phase instabilities are present upstream of the Mach disk and in the region of the reflected shocks, i.e., in the bright regions deduced from the Mie scattering measurements. Downstream of the Mach disk, no phase separation is present anymore, as the normal shock results in a large pressure and temperature recovery bringing the jet back into a single-phase state. In Fig. 6.27, scatter data from the present LES are shown in a pressure-temperature diagram of argon to further highlight the phase separation process. The data have been taken along the center axis and show the expansion path up to the Mach disk and downstream of it. Slightly upstream of the Mach disk the minimum pressure and temperature occur which are in this case approximately 3000 Pa and 62 K. When comparing this to the triple point of argon (6889.25 Pa and 83.81 K) it becomes obvious that the

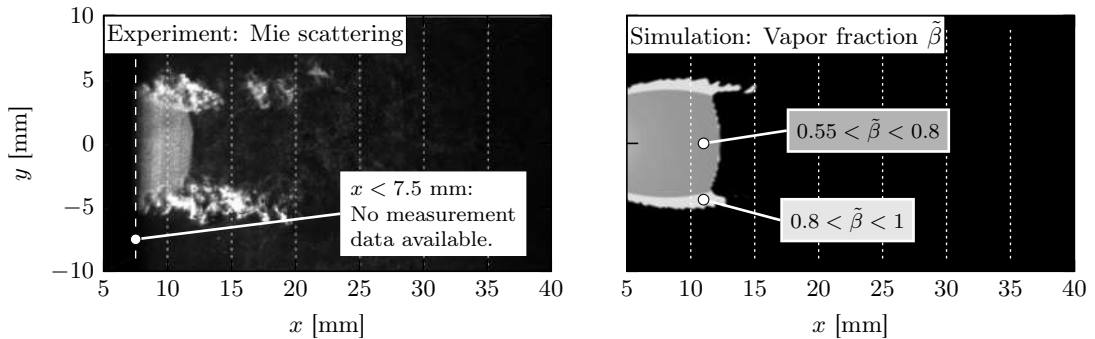


Figure 6.26: Visualization of the phase separation process upstream of the Mach disk. In the left figure, a single shot image of the Mie scattering is shown which has been taken from Fond et al. [79]. The right image shows an instantaneous snapshot from the present LES where the vapor mole fraction is used to highlight regions of phase separation (gray) and regions without phase separation (black). Reprinted by permission from Springer Nature Customer Service Centre GmbH: Springer Nature, *Experiments in Fluids*, Fond et al. [79], © (2018).

expansion path crosses the triple line and hence the occurrence of a solid phase might be possible. As the applied cubic EoS is only capable of representing vapor and liquid states and their equilibria, no statement can be made regarding the occurrence of ice and solid phases, respectively. Downstream of the Mach disk a large temperature increase is visible and the temperature rises from ≈ 62 K to over 200 K instantaneously due to the compression of the fluid. Finally, Fig. 6.28 shows a three dimensional view of the phase separation region downstream of the nozzle exit. As already discussed based on Fig. 6.26, the two-phase region is confined by the Mach disk and the area of reflected shock waves at the boundaries and slightly reaches into the beginning of the slip line. In the back and the bottom planes of Fig. 6.28, the mid-plane values of the averaged velocity and temperature fields are shown. The comparison of the iso-contour and these two flow fields underlines that phase separation occurs in the region of high velocity and low temperatures.

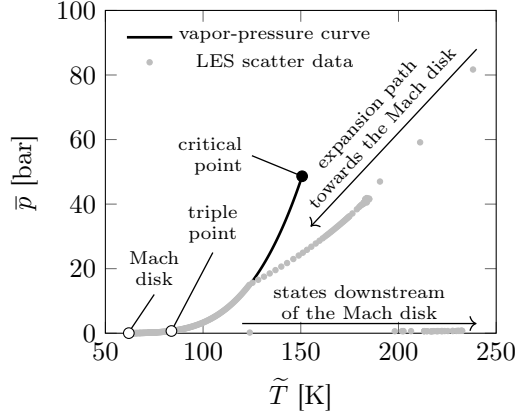


Figure 6.27: Pressure-temperature diagram of pure argon visualizing the expansion path of the underexpanded jet. The scatter data from the LES have been taken along the centerline.

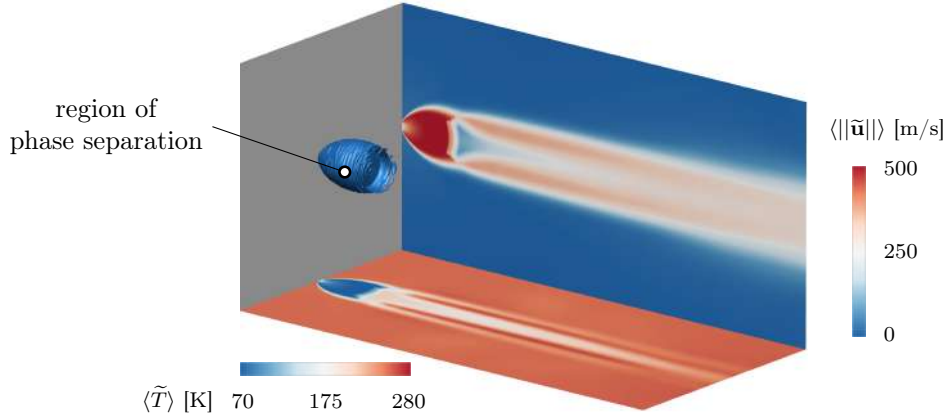


Figure 6.28: Three dimensional view of the square duct chamber. The instantaneous iso-contour encloses the region of phase separation downstream of the nozzle exit. The back and the bottom planes show the averaged velocity and temperature fields, respectively.

6.2.4 Summary

In this section, the phase separation process in an extremely underexpanded jet has been studied. Following the experiments of Fond et al. [79] and Xiao et al. [360], argon was injected into its own gas phase. The nozzle pressure ratio has been set to 120 and moderate injection and chamber temperatures have been chosen resulting in the presence of real-gas effects. To enable the application of the VLE model in the LES, argon has been diluted with one mass percentage of nitrogen. The comparison of this binary mixture with the VLE of pure argon shows very good agreement and justifies the approach for the present investigation.

In the first step, the fluid dynamics aspects of the supersonic jet have been studied: The comparison of the near-nozzle flow and shock structure by means of instantaneous snapshots showed a good agreement in terms of the radial and axial extent of the Mach disk. Additional comparisons of the flow field downstream of the Mach disk using axial mean and RMS velocity profiles further underlined the finding of the good prediction capability of the numerical framework. Especially the near-nozzle flow field is captured very accurately which is of major importance for the investigation of the phase separation phenomenon in the present study.

To study the single-phase instability downstream of the nozzle exit, single-shot images of the experimental Mie scattering intensity and the calculated vapor fraction field have been compared to each other. Excellent agreement is found and the LES is able to reproduce the phase separation process. Two-phase states occur upstream of the Mach disk and in the region of the reflected shock, i.e., in the characteristic shock barrel of the extremely underexpanded jet. This corresponds to the region of highest velocity and lowest temperature which is of course complementary. The scattering of the LES results into a pressure-temperature diagram of argon showed that the expansion is even such strong that it crosses the triple point and therefore the occurrence of a solid phase might be possible. Unfortunately, this phenomenon cannot be represented by the present thermodynamic framework and has to be postponed to future investigations.

6.3 Phase separation in multicomponent fuels

Large parts of the following results and discussions are published in the conference article [318]: Traxinger, C., Banholzer, M., and Pfitzner, M. Real-gas effects and phase separation in underexpanded jets at engine-relevant conditions. In *2018 AIAA Aerospace Sciences Meeting*, 2018.

6.3.1 Introduction

For the injection of gaseous fuels at GE-relevant conditions, detailed experiments and numerical simulations are lacking in the literature particularly with focus on possible phase separation processes. Based on the successful validation of the numerical framework in the last two Secs. 6.1 and 6.2, the CFD tool is now used in a predictive manner to investigate the possibility of phase separation processes under GE-like injection and operating conditions. In particular, the thermodynamic behavior of two application-relevant fuels is the focal point of the following study.

6.3.2 Numerical setup

Test cases

Two different GE-typical fuels are considered in the following study: a hydrogen-based and a methane-based fuel. In recent years, methane-based fuels have gained increasing popularity as many natural resources are still available. In addition, methane is the hydrocarbon with the least number of carbon atoms and hence the production of carbon dioxide is reduced compared to other fuels [90]. Following this argumentation, hydrogen is another interesting fuel for combustion engines as its combustion product is water vapor. Usually, the purity of hydrogen is not given for industrial applications like GEs. Therefore, nitrogen with a volume fraction of 0.1% is mixed with 99.9% hydrogen and defined as compressed hydrogen gas (CHG) in the present study. Methane-based fuels in internal combustion engines (ICEs) are usually termed compressed natural gas (CNG). A literature survey [198, 141, 64] showed that most of the CNG available in the industry consists of three main components: methane (CH_4), ethane (C_2H_6) and nitrogen (N_2). Concluding the CNG compositions available in these publications [198, 141, 64] a generic fuel mixture is defined and its composition is listed in Tab. 6.7 together with the composition of the CHG. The thermophysical properties of the pure components of the gas mixtures can be found in Tab. B.1 in the appendix.

Table 6.7: Volume fractions [%] of the hydrogen- and methane-based generic fuels CHG and CNG.

Fuel	Methane (CH_4)	Hydrogen (H_2)	Ethane (C_2H_6)	Nitrogen (N_2)
CHG	0.0	99.9	0.0	0.1
CNG	95.8	0.0	2.6	1.6

In ICEs, typical chamber pressures range from 5 to 80 bar, depending on the ICE-type and the start of injection. For the present investigation, an intermediate chamber pressure of 50 bar is

selected. Similar considerations lead to a maximum total fuel pressure of 600 bar [31, 324, 325, 123, 290]. In addition, a total fuel pressure of 300 bar is chosen to study the influence of the reservoir pressure onto the fuel injection process. This results in effective pressure ratios of 12 and 6, respectively. For the sake of simplicity, the injection and the chamber temperature are set to 300 K. Consequently, a total of three different numerical simulations are carried out and the boundary conditions for these test cases are summarized in Tab. 6.8. The cases CNG-p600 and CNG-p300 are used to study the effect of the pressure change. Both low-pressure cases (CNG-p300 and CHG-p300) are applied to investigate the effect of the fuel change.

Table 6.8: Overview of the boundary conditions for the three GE-like test cases.

Case	Reservoir	Chamber	p_t [bar]	p_{ch} [bar]	NPR [-]	T_t [K]	T_{ch} [K]
CNG-p600	CNG	Nitrogen (N_2)	600	50	12	300	300
CNG-p300			300	50	6		
CHG-p300	CHG	Nitrogen (N_2)	300	50	6	300	300

Solver settings

Following the investigations in Sec. 6.1, RANS simulations have been conducted using the k,ω -SST model [191, 192, 193]. Therefore, the rotational symmetry of the injection configuration has been used and only a two degrees wedge configuration with symmetry boundary conditions on the opposite sides has been simulated. The schematic of the numerical domain is shown in Fig. 6.29. According to the work of Banholzer et al. [21], the nozzle diameter D is set to 1.5 mm. The dimensions of the chamber in the axial and radial directions are $L_x/D = 80$ and $L_r/D = 70$, respectively. The computational setup of Hamzehloo and Aleiferis [108, 109] and a grid independence study performed by Banholzer et al. [21] lead to a required resolution of $\Delta x = \Delta r = D/40 = 0.0375$ mm which is very similar to the mesh topology used in Sec. 6.1. Therefore, a separate grid independence study is forgone for this investigation and the injector is resolved with 20 cells in radial direction. The thermodynamic closure has been achieved based on the SRK-EoS [296] as this state equation is very well suited for the reliable prediction of both short-chain hydrocarbons and hydrogen. Further important solver settings are listed in Tab. 6.9.

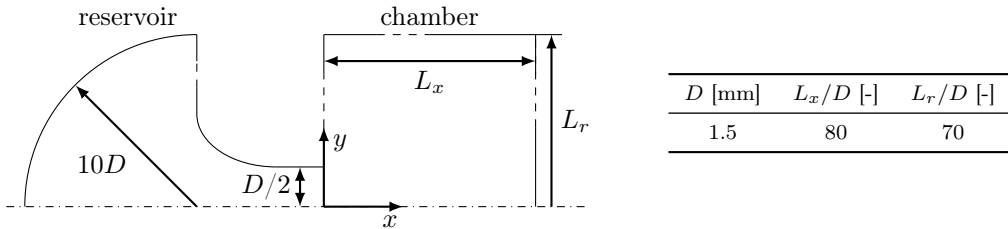


Figure 6.29: Schematic of the numerical domain used to study possible phase separation processes under GE-like operating conditions.

6.3.3 Probability of phase separation

At their reservoir conditions both fuels are in a single-phase state. As highly underexpanded jets can be expected due to the large prescribed pressure ratios, two different ways are feasible how the vapor-liquid equilibrium could be entered: First, by a strong expansion lowering the pressure and the temperature at constant overall feed composition. Second, by a nitrogen dilution of the fuel and a simultaneous expansion process.

In the CHG case, two fluids are forming the multicomponent mixture: hydrogen and nitrogen. Here, hydrogen is the high volatile and nitrogen is the low volatile component. Hence, nitrogen is defining the upper bound of the multicomponent critical locus in terms of the temperature at

Table 6.9: Numerical solver setup for the investigation of phase separation processes in multicomponent fuels under GE-like operating conditions.

Solver	TVD-limiter	Turbulence closure	EoS
pressure-based (supersonic)	van Albada [332]	RANS with k,ω -SST model [191, 192, 193]	SRK-EoS [296]

its critical temperature of 126.19 K, see Fig. 6.30a. Above this temperature no phase separation is expected and therefore a strong expansion and simultaneous reduction of the temperature is necessary to enter the multicomponent VLE. In Fig. 6.30b, some selected vapor-liquid equilibria at relevant temperatures (100.0 K, 107.7 K and 113.0 K) are shown. The comparison between the experimental data [303, 361, 288] and the SRK-EoS [296] shows a reasonably good agreement, especially in the low pressure region up to the chamber pressure of 50 bar. Above this pressure the prediction capability of the SRK-EoS [296] is getting worse with increasing pressure and decreasing temperature and the cubic EoS is overestimating the extension of the VLE in terms of pressure. As CHG is almost pure hydrogen, a phase separation at the overall feed composition of CHG can be excluded. To enter the VLE by means of a nitrogen dilution at the chamber pressure of 50 bar, the mixture must contain more than 30 mole-% of nitrogen at a temperature of 100 K. At the other two temperatures, a minimum of approximately 40 mole-% and 50 mole-% N₂, respectively, has to mix into the CHG to enter the VLE. Hence, the probability of phase separation for the CHG case can be considered low.

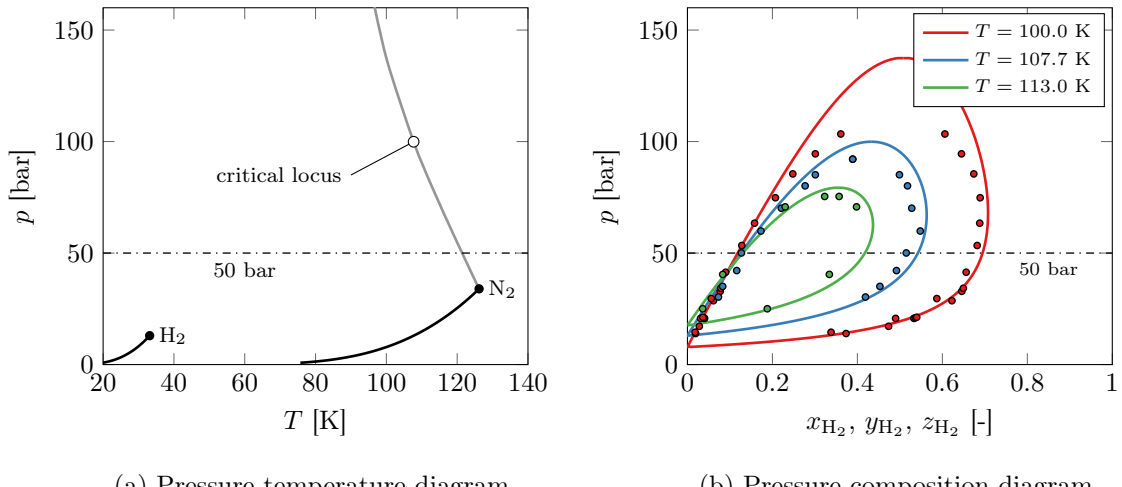


Figure 6.30: VLEs of the binary nitrogen/hydrogen mixture. The dots in subfigure b are representing experimental data taken from the literature [303, 361, 288].

For the CNG cases, the VLE and the probability of phase separation is significantly different. First, CNG is a ternary mixture and therefore the mixture space is increased by one dimension compared to the CHG. Second, nitrogen is now the high volatile component because methane and ethane have significantly higher critical temperatures, see Tab. B.1 in the appendix. Therefore, in the case of the CNG the critical locus has an upper bound at 305.32 K which is the critical temperature of ethane. This temperature in turn is almost three times larger than the critical temperature of nitrogen. The higher maximum critical temperature makes phase separation during the CNG injection significantly more probable than in the CHG case because the injection temperature and the critical temperature of ethane are almost identical. Figure 6.31 shows VLEs of the ternary methane/ethane/nitrogen mixture at two different pressures (40 bar and 20 bar) and two different temperatures (200 K and 160 K). The dew-point lines are shown in red and the bubble-point lines in blue while the experiments are represented by dots. The feed composition of CNG is marked by the white dot in each plot. To give a more detailed glance into these

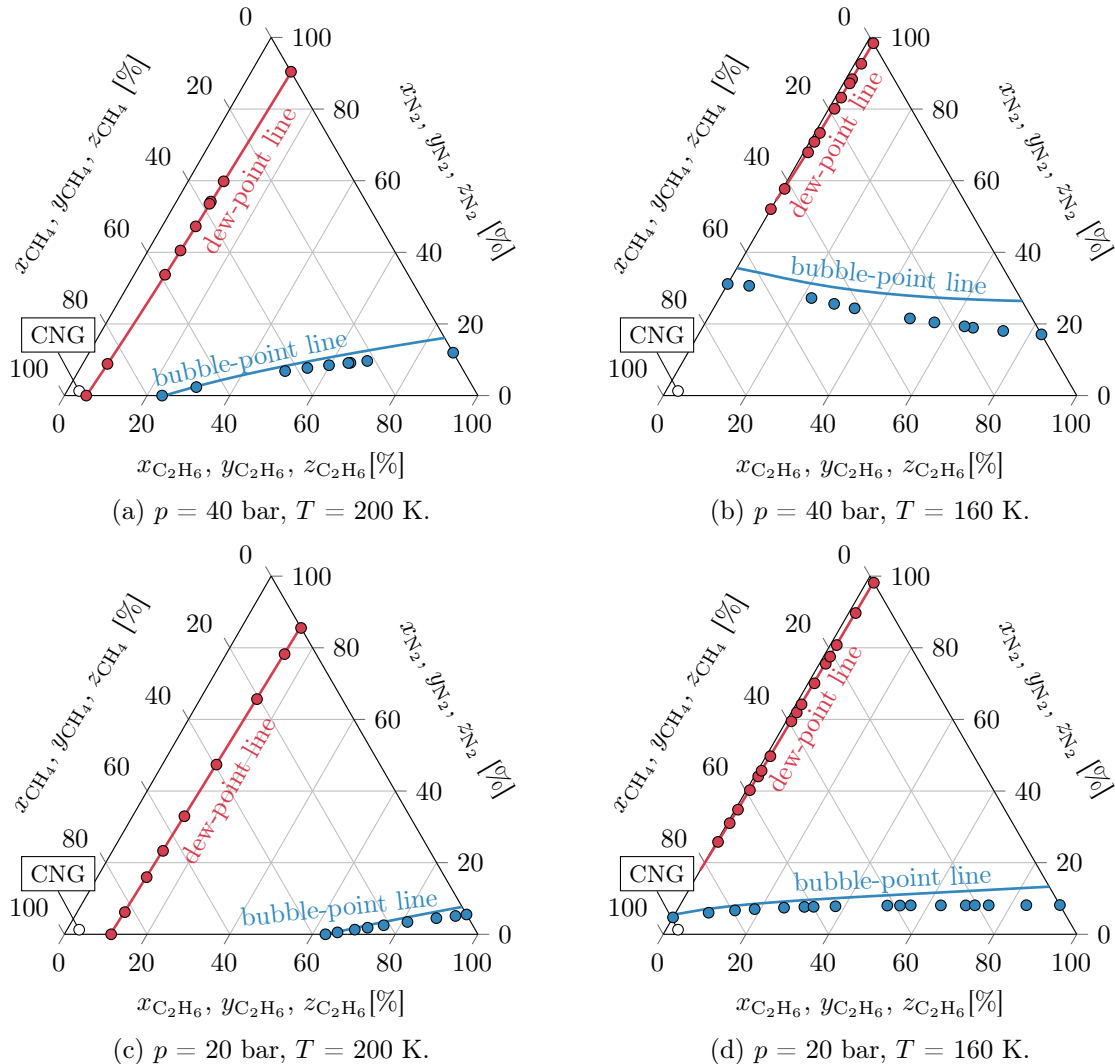


Figure 6.31: VLEs of the ternary methane/ethane/nitrogen mixture at two different temperatures (200 K and 160 K) and two different pressures (40 bar and 20 bar). The CNG composition is marked with a white dot. The colored dots represent experimental data taken from the literature [317].

ternary VLE-diagrams, the related binary mixtures are shown in pressure-composition diagrams in Fig. 6.32a for methane and nitrogen, Fig. 6.32c for ethane and nitrogen and Fig. 6.32d for ethane and methane. In the respective diagrams the two pressure levels (20 bar and 40 bar) are marked with dashed lines and the chamber pressure of 50 bar is indicated with a dash-dotted line. Especially in Fig. 6.32c, the deviations between the experimental data and the cubic EoS become very obvious. With decreasing temperature the prediction error is rising steadily. Similar findings can be made for the methane/nitrogen mixture, but compared to the ethane/nitrogen mixture the overall prediction accuracy is acceptable over the investigated pressure and temperature range. This latter finding can be further underlined based on Fig. 6.32b. Here the critical locus of the binary methane/nitrogen mixture is shown and the prediction of the SRK-EoS [296] with respect to the experimental data is excellent. Identical conclusions can be drawn for the ethane/methane mixture over the relevant pressure and temperature range, see Fig. 6.32d. These findings for the different binary mixtures transfer directly to the VLEs of the ternary CNG mixture. Apart from the 40 bar and 160 K diagram, see Fig. 6.31b, the comparison to the experimental data is very good, see Figs. 6.31a, c and d. Especially the dew-point line is predicted excellently by the SRK-EoS [296] and the already mentioned problems in terms of the prediction accuracy are obvious at the bubble-point line. In the present investigation, this issue is not of any concern as most of

the two-phase states will occupy the left bottom corner of the ternary VLE-diagram, where the prediction of the SRK-EoS [296] is very good. As the phase separation process is induced by condensation processes, the VLE will be entered across the dew-point line. Consequently, an excellent prediction concerning the onset of phase separation can be expected.

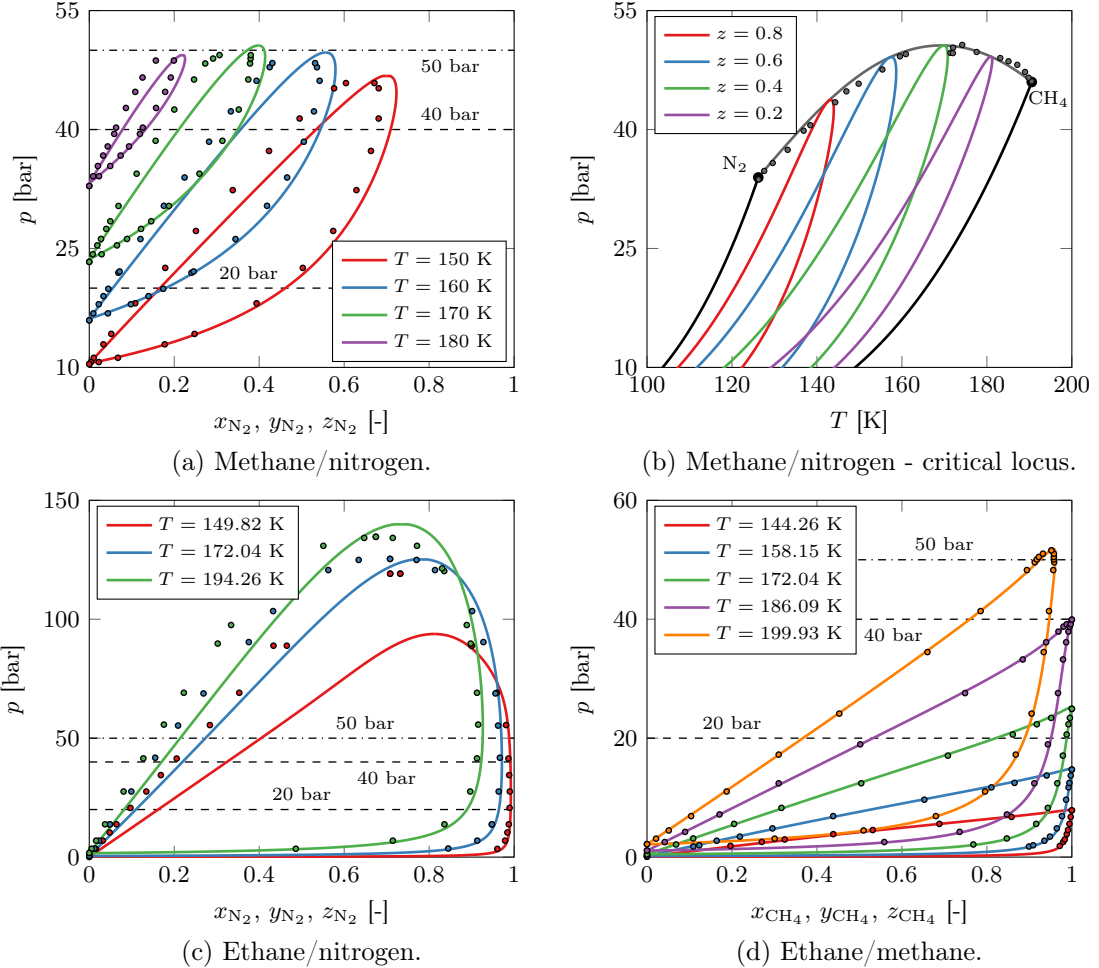


Figure 6.32: VLEs of different binary mixtures of methane, ethane and nitrogen. The dots represent experimental data taken from the literature [304, 350, 140, 44, 38, 304, 52].

6.3.4 Results

Detailed discussion of the CNG-p600 case

Figure 6.33 shows snapshots of the temporal evolution of the CNG-p600 case. Only the first $\approx 20\%$ of the chamber are shown which is sufficient to discuss the main fluid dynamics and thermodynamics effects happening during the transient part of the injection process. The left column shows the temperature distribution superimposed by the vapor fraction. In the right column, the pressure field is superimposed by the Mach number in which regions with $\text{Ma} < 1$ are excluded.

Looking at the overall flow field in the different snapshots a typical underexpanded jet can be seen. The static temperature as well as the static pressure are covering a wide range. The large values are caused by the compression process downstream of the tip of the jet and the low values are related to the strong expansion within the jet downstream of the nozzle exit. For a better visualization, the pressure is bounded to the upper limit of 50 bar. After the start of injection ($5 \mu\text{s}$), the fluid enters the mixing chamber and a Prandtl-Meyer expansion fan forms at the nozzle edge. The flow accelerates across the expansion fan and therefore the Mach number increases while the static pressure and temperature drop inside the jet. As the fuel penetrates further into

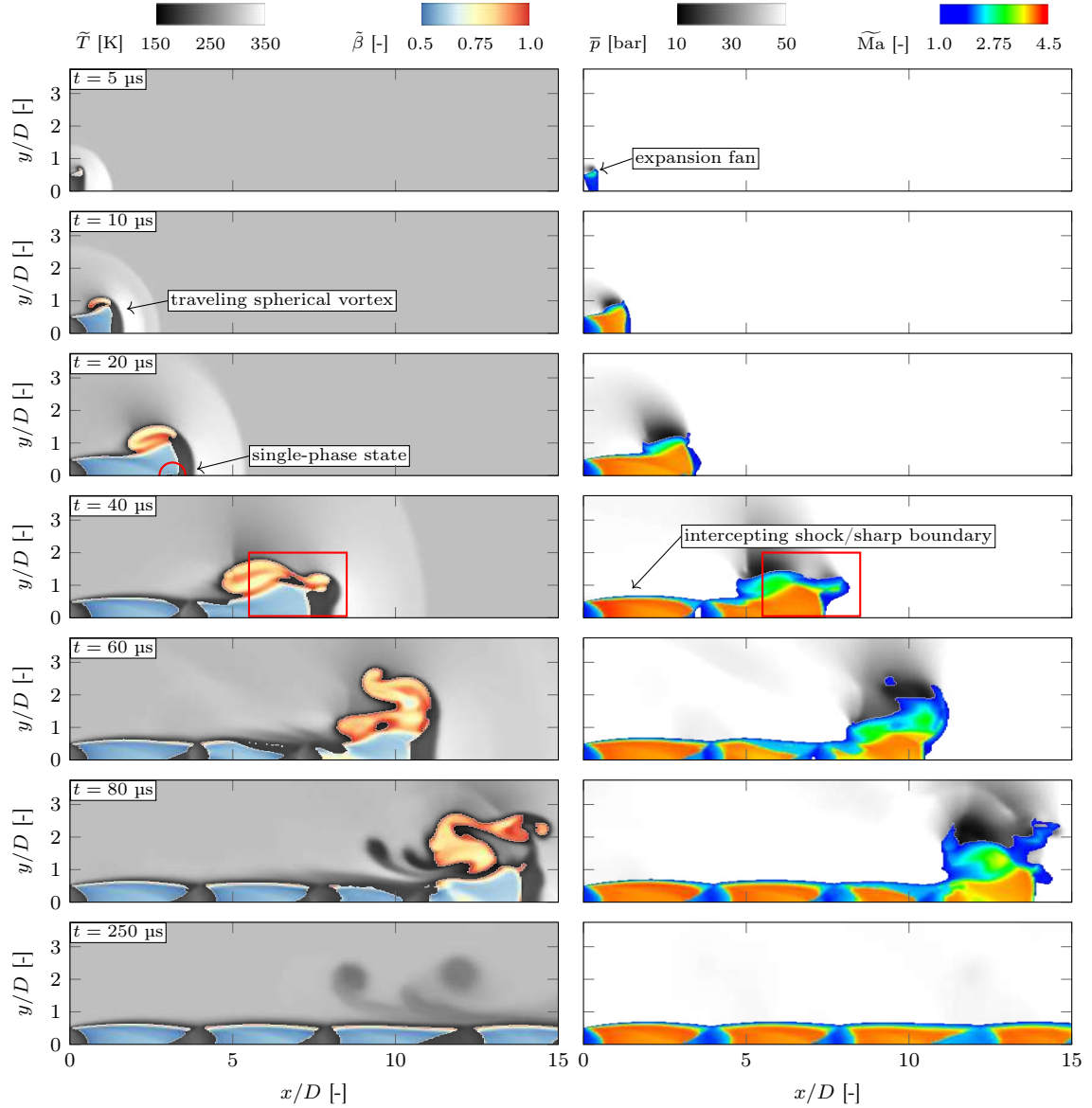


Figure 6.33: Snapshots of the temporal evolution of the underexpanded jet for the test case CNG-600. In the left column, the fields of the temperature and the vapor fraction are superimposed. In the right column, a superposition of the pressure and the Mach number is shown.

the chamber, a traveling spherical vortex occurs in front of the jet. This vortical structure is growing continuously and breaks up at approximately 60 μ s. The fluid inside this vortex gets pushed into the mixing chamber by the subsequent steady-state jet region which is apparent in the Mach number plots at $t = 60 \mu$ s and $t = 80 \mu$ s. Apart from this dominant vortex structure, shock phenomena inside the fuel jet can be observed during the injection process. These structures can be seen for the first time at 40 μ s. The expansion fans being present at the outer part of the jet interact with the free jet boundary leading to weak compression waves and an intercepting shock. This intercepting shock is – in the present case – reflected at the centerline resulting in a reflected shock. This shock is rather weak/oblique and therefore the flow remains at transonic/supersonic conditions. Downstream, the flow again accelerates quickly due to the large pressure ratios being present in the underexpanded jet until another shock structure forms. As time moves on and the fuel jet penetrates further through the chamber, several of these shock barrels arise along the jet. The last row in Fig. 6.33 shows the quasi-stationary jet after 250 μ s. Here, a total of four shock barrels are visible.

From the left column in Fig. 6.33 it is obvious that larger parts of the jet have entered the VLE which can be identified by the vapor fraction β ranging from 0.5 to 1. At 5 μs a first small region of single-phase instability forms near the nozzle trailing edge. This region results from the decrease of the static pressure and temperature inside the Prandtl-Meyer expansion fan. Related to this is a discontinuous drop in the speed of sound and in turn a nonlinear increase in the Mach number from approximately unity to Mach numbers ranging from two up to three. The subsequent expansion leads to a further decrease of pressure and temperature and at 10 μs a large part of the jet has entered the VLE. This trend continues until the formation of a first shock barrel takes place. The start of the formation of this shock structure can be seen in terms of a small single-phase region close to the centerline at $t = 20 \mu\text{s}$. At $t = 40 \mu\text{s}$ the first shock barrel is already fully developed and can be found at $x/D \lesssim 4$. Due to the shock and the accompanying increase in temperature and pressure, the jet gets back to a single-phase state downstream of the shock barrel. As the flow is accelerated after this shock, the continuous expansion again leads to a phase separation process. In the present case, this phenomenon appears several times during the propagation of the jet into the chamber and results in four distinct shock barrels containing one large region of two-phase flow each, see snapshots in Fig. 6.33 at $t = 250 \mu\text{s}$. Outside of this region with strong expansion, large areas of phase separation are also visible in the traveling spherical vortex. Compared to the jet center, the vapor fraction is larger and covers a wider range. This can be explained by taking a deeper look into the phase separation process itself and how it is triggered in these two different regions of the jet. This is done with results from the snapshot at $t = 40 \mu\text{s}$. Here, the focus is put on a small region at the jet tip marked by the red box in Fig. 6.33.

The detailed view of the red box in Fig. 6.33 is depicted in Fig. 6.34 in terms of six different properties. Beginning on the top left, the first snapshot reveals the large pressure gradient being present at the tip of the underexpanded jet. The minimum pressure of the first expansion wave is

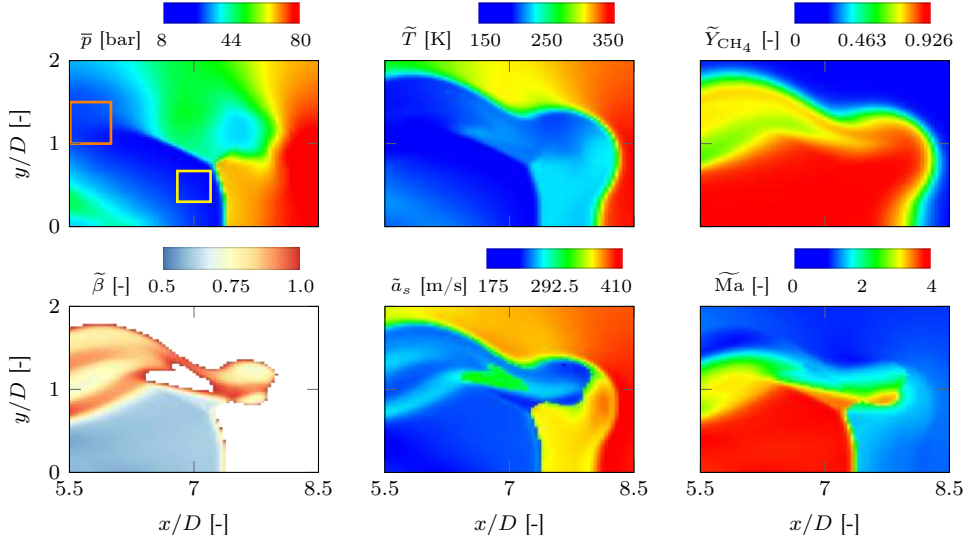


Figure 6.34: Detailed view of different flow properties for the CNG-p600 test case at 40 μs after injection. The snapshots have been taken at the tip of the jet and the view corresponds to the red box in Fig. 6.33. The yellow and orange boxes mark the sampling areas for Fig. 6.35.

approximately 8 bar while the compression process in front of the jet increases the fluid's pressure up to 80 bar being 1.6 times larger than the prescribed chamber pressure. Due to this strong expansion and compression, the static temperature (second frame) ranges approximately from 150 K to 350 K and shows a pattern which is similar to the static pressure. In the third frame, the mass fraction of methane is depicted. Due to the shock structures inside the core of the fuel jet virtually no nitrogen has mixed into this region which is therefore almost at the feed composition. In the region of the traveling spherical vortex, the opposite is true as the convection inside of this vortex is forcing the dilution of CNG with the surrounding chamber gas. Consequently, two regions with different phase separation mechanisms can be distinguished during the CNG injection process:

A phase separation solely caused by expansion and a phase separation triggered by expansion and nitrogen dilution. To emphasize these findings instantaneous results are extracted at the relevant positions marked by the yellow and orange boxes in Fig. 6.34 top left. The data are scattered in two ternary mixture diagrams in Fig. 6.35. The constant temperatures and pressures in these diagrams

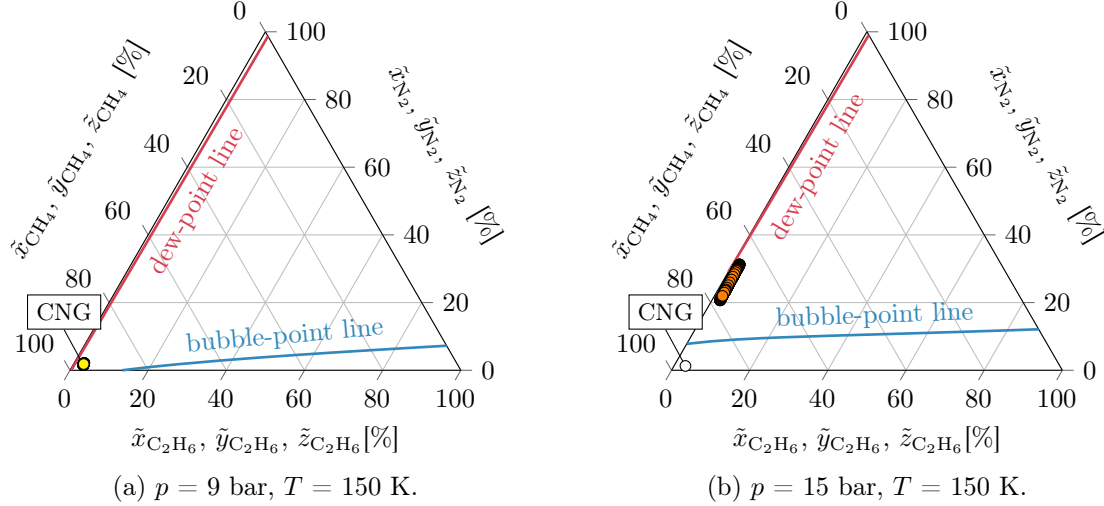


Figure 6.35: Ternary phase diagrams for the CNG test-case CNG-p600. The colored points mark the sampling data highlighted in Fig. 6.34 by the appropriate colored boxes.

were chosen such that the largest possible number of data points can be plotted. In Fig. 6.35a, the scattering data of the expansion induced phase separation (yellow) are shown. All data points are grouping around the feed composition as a result of the prevention of the mixing process by the pronounced shock structures. Due to the low temperature and pressure, the VLE covers almost the complete mixture space and all scatter points have entered the region of single-phase instability. Looking at Fig. 6.35b, the sole expansion would not have been sufficient to cross the binodal at this temperature and pressure. A dilution of the CNG with the surrounding nitrogen is necessary to enter the VLE. Due to the convective mixing inside the vortex, the individual mixtures contain more than 20 mole-% nitrogen and therefore single-phase instability is triggered by a combined expansion and mixing process. Going back to Fig. 6.34 the snapshot for the vapor fraction β in the bottom left corner can now be reconstructed. In the jet center, the variation of temperature, pressure and composition is low and therefore an almost constant β -value can be observed. Inside the vortex a wider range of β -values occurs due to the steady mixing with the surrounding nitrogen and also the wider pressure and temperature range. As already discussed earlier, the speed of sound and the Mach number exhibit a discontinuous jump as the mixture enters the VLE. The speed of sound drops significantly and the Mach number increases to values up to four.

Effects of the pressure change

In Fig. 6.36, the near-nozzle flow structures of both CNG cases (600 bar and 300 bar) are compared to each other in terms of snapshots at different times after injection. The single-shot images are a superposition of the temperature field with the corresponding vapor fraction field. Overall, the flow structures are very similar for both cases concerning fluid dynamics and thermodynamics aspects. For the case CNG-p300 a weaker expansion due to the lower pressure ratio of $\text{NPR} = 6$ can be seen compared to the case CNG-p600. Nevertheless, the expansion process is still sufficient to enter the VLE. The weaker expansion directly manifests itself in a larger vapor fraction in the jet core compared to the CNG-p600 case. In addition, the expansion is still strong enough to cause phase separation effects in the region of the traveling spherical vortex. In contrast to the 600 bar jet, the break-up of this vortical structure is weakened in its intensity and spatial extension. Due to the lower total fuel pressure and therefore a lower density and speed of sound at the nozzle exit, the penetration of the CNG-p300 jet is slower. Furthermore, the length of the stationary shock barrels is smaller by a factor of almost two.

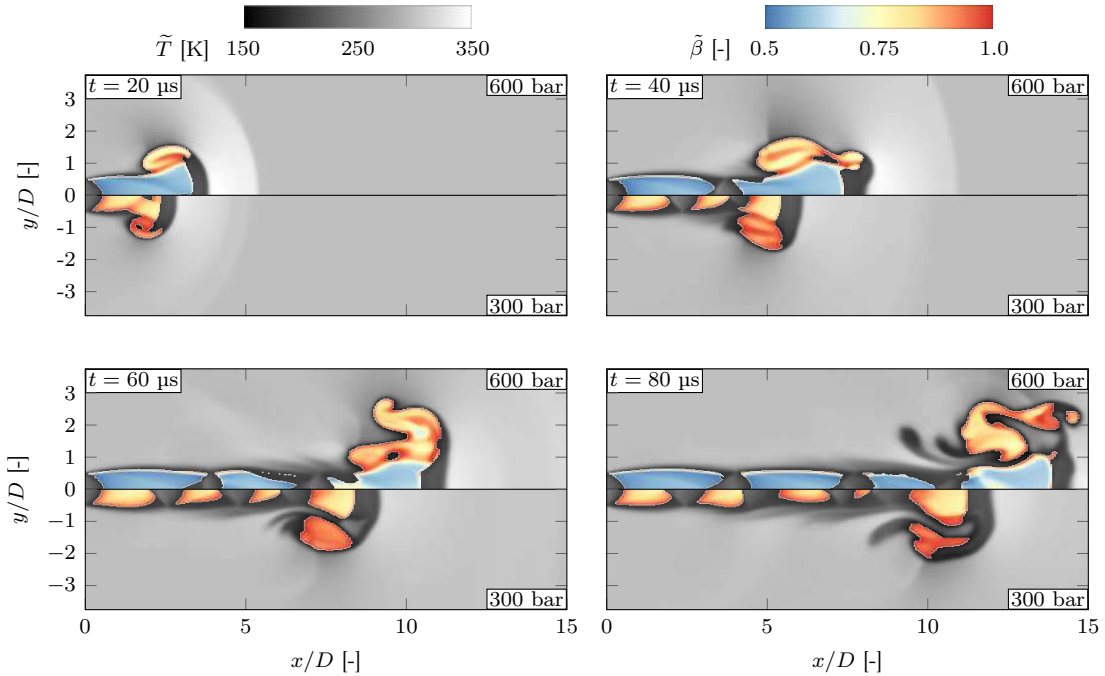


Figure 6.36: Comparison of the near-nozzle flow structures between the two CNG test cases CNG-600 (upper half) and CNG-p300 (lower half).

Effects of the fuel change

Figure 6.37 shows the effects of the fuel change from CNG to CHG for a total pressure of 300 bar in terms of the temperature field superimposed by the vapor fraction field. For the ease of presentation the temperature range is clipped to a minimum of 150 K. In the CHG case, however, temperatures down to 100 K in the region of the shock barrels occur. The shock and vortex structures are slightly more pronounced in the hydrogen case and cover a larger spatial extent compared to the CNG case. In contrast, the length of the shock barrels is a little bit shorter in the CHG case compared to the CNG case. Although the expansion of the CHG is much stronger (manifesting in a lower static temperature), the mixture remains in a single-phase state throughout the complete jet. As discussed based on Fig. 6.30, an expansion to 100 K in the undiluted CHG jet is by far not sufficient to enter the VLE of the binary mixture. In the region of the traveling spherical vortex, however, the dilution of the fuel with the surrounding nitrogen would be sufficient but here in turn the expansion is too weak to enter the VLE.

Another interesting aspect related to the change in fuel is the temporal evolution of the jet penetration depth. The knowledge of this process is of paramount interest for the transient mixing process of the jet and is, for instance, necessary to avoid the impingement of the jet onto the combustion chamber wall in piston engines. In the literature, different correlations for the evaluation of the axial jet penetration depth x_{tip} can be found. Gerold et al. [90] give a detailed introduction and an overview on the analytical derivation of the jet penetration depth and point out three different correlations including an own modification:

$$\text{Abraham [5]:} \quad x_{tip} = \sqrt{\frac{3C_f}{4\pi C_t}} \left(\frac{\dot{M}_e}{\rho_{ch}} \right)^{\frac{1}{4}} \sqrt{t}, \quad (6.7)$$

$$\text{Hill and Ouellette [119]:} \quad x_{tip} = \Gamma \left(\frac{\dot{M}_e}{\rho_{ch}} \right)^{\frac{1}{4}} \sqrt{t}, \quad (6.8)$$

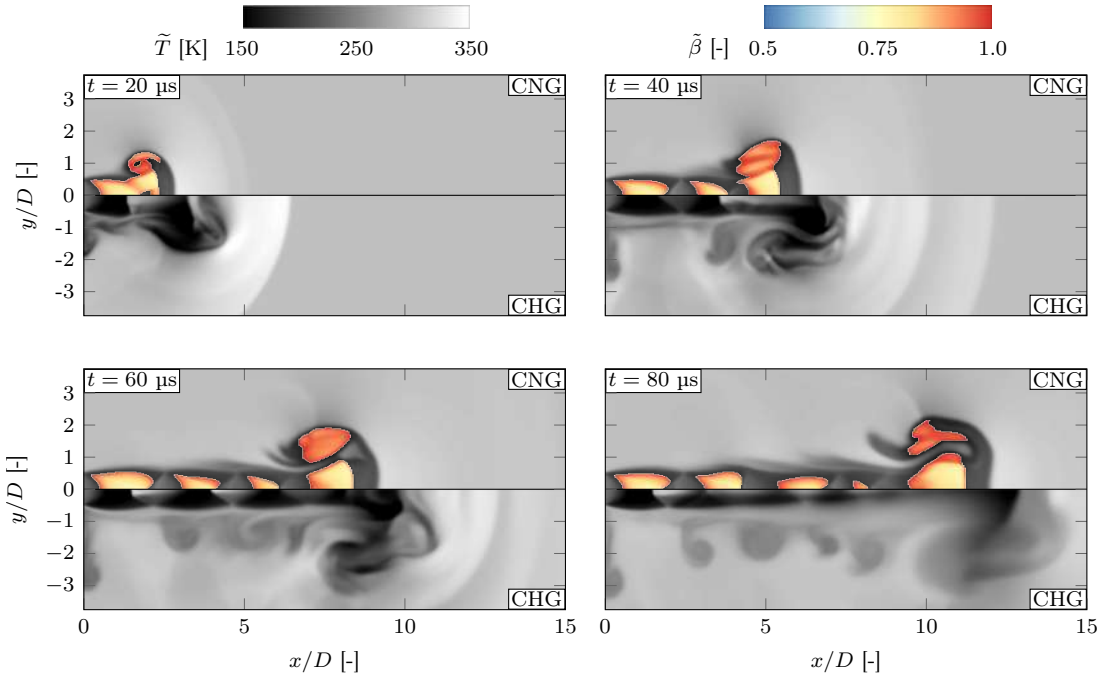


Figure 6.37: Comparison of the near-nozzle flow structures for CNG (upper half) and CHG (lower half) at a total fuel pressure of 300 bar.

$$\text{Gerold et al. [90]:} \quad x_{tip} = \Gamma \frac{(\dot{M}_e C_D)^{\frac{1}{4}} \rho_e^{\frac{1}{12}}}{\rho_{ch}^{\frac{1}{3}}} \sqrt{t}. \quad (6.9)$$

In these equations, C_f and C_t are scaling constants which according to Abraham [5] take the values of 0.7 and 0.0161, respectively. The discharge coefficient is denoted as C_D and is set to 1.0 in the present work corresponding to ideal flow conditions. Following the work of Gerold et al. [90], the model constant Γ in Eqs. (6.8) and (6.9) is 3.0 ± 0.1 . In the present work, the mean value $\Gamma = 3.0$ is used exclusively. The main influencing parameter of the penetration depth of the jet is the momentum flux \dot{M}_e being present at the nozzle exit. The momentum flux in a choked flow is defined as

$$\dot{M}_e = \rho_e a_{s,e}^2 A, \quad (6.10)$$

where A is the cross section of the nozzle and the choked flow conditions are denoted by the subscript e . The choked flow properties of the two fuels can be determined according to appendix F.2 and are summarized for the different operating conditions in Tab. 6.10.

Table 6.10: Choked nozzle flow properties for the CNG and CHG test cases.

Fuel	p_t [bar]	p_e [bar]	ρ_e [kg/m ³]	$a_{s,e}$ [m/s]	\dot{M}_e [kg m/s ²]
CNG	600	191.37	220.55	556.42	120.67
	300	124.66	148.87	439.36	50.78
CHG	300	148.09	13.65	1330.11	42.68

The normalized jet penetration depth x_{tip}/D tracked with a fuel mass fraction of 1% at the centerline is shown in Fig. 6.38 for the two low-pressure test cases CNG-p300 and CHG-p300. Up to ≈ 0.2 ms the CHG-p300-jet penetrates faster than the CNG-p300-jet with the same total pressure. In the beginning of the injection, the penetration curve of the CHG-jet shows a linear incline up to ≈ 0.1 ms. The reason for this behavior is the detachment of the jet from the centerline. A blocking cone is formed in front of the jet consisting of a higher pressure and therefore higher

density region which redirects the main flow away from the centerline towards the sides. This effect was also noticed for high pressure gas injections by other researchers, see, e.g., Hamzehloo and Aleiferis [109]. After the cone vanishes, the jet reattaches to the centerline. The penetration rate slows down considerably and is now proportional to the square root in time. The comparison of the injection profile of the numerical simulation with the analytical correlations shows an overall good agreement. The best agreement is found with the correlation of Hill and Ouellette [119].

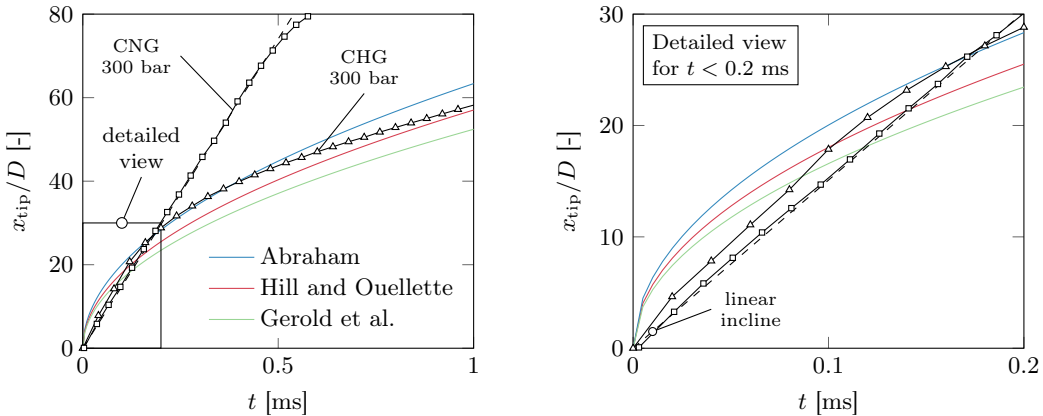


Figure 6.38: Evolution of the normalized jet penetration depth for both 300 bar cases. The colored lines show the analytical correlations of Abraham [5], Hill and Ouellette [119] and Gerold et al. [90].

The results for the injection profile of the CNG-p300 case are completely different. Not only in the beginning, but almost throughout the whole computational domain the linear incline remains. Shortly before 0.5 ms it can be seen that the linear incline changes to the typical curvature. One of the major reasons for this extraordinary behavior is the traveling spherical vortex. Figures 6.36 and 6.37 show large two-phase regions in this first vortical structure which remain present even for longer simulation times. Later, increasing temperatures and pressures lead to the disappearance of those, momentum gets lost and the jet slows down. The time of vanishing of the two-phase region and the time where the slope changes its characteristic is identical. As a result, the penetration behavior of an underexpanded jet with embedded two-phase regions differs significantly from the behavior and characteristics of a single-phase jet. Therefore, the analytical correlations available in the literature are not applicable under such conditions.

6.3.5 Summary

Three different engine-relevant test cases have been defined in the present section to study the thermodynamic behavior of typical GE-fuels during the high-pressure injection process. Two different fuels have been considered namely a compressed hydrogen gas (hydrogen + nitrogen) and a compressed natural gas (methane + ethane + nitrogen). Both fuels have been injected through a single-hole injector into a chamber pressurized with nitrogen at 50 bar. Two different nozzle pressure ratios have been chosen: 6 and 12. The initial temperatures in the fuel reservoir and the high-pressure chamber have been set to 300 K.

In a first step, the probability of phase separation processes has been assessed using thermodynamic phase diagrams. By comparing experimental VLE data from the literature to the predictions of the SRK-EoS [296], it was demonstrated that this state equation is well suited for the numerical investigation of phase separation processes under GE-like conditions. The a priori analysis indicated the large influence of the fuel composition on the possibility of single-phase instabilities during the injection process. In general, the higher the critical temperature of the low volatile component, the more likely it is that a phase separation process might occur. In the present case, this leads to the conclusion that hydrogen fuels will exclusively exhibit a single-phase behavior as nitrogen is the LV component in the mixture. In contrast, in CNGs larger molecules like methane and ethane are present which drastically increase the maximum critical temperature. Hence, phase separation processes are much more probable in GEs fired with CNGs.

The a priori findings could be confirmed based on RANS simulations. The detailed study of the 600 bar CNG case showed that phase separation is triggered as soon as the jet enters the chamber, namely in the region of the Prandtl-Meyer expansion fan. In the following, single-phase instabilities are found inside the shock barrels and within the traveling spherical vortex close to the jet tip. For the former, the VLE is entered due to the strong expansion solely. In the latter case, the phase separation phenomenon is triggered by a combined expansion and mixing process. Changing the injection pressure from 600 bar to 300 bar the reasons for the entrainment into the VLE remain identical. However, by decreasing the injection pressure the intensity of the phase separation effects is reduced. Switching from CNG to CHG, the single-phase instabilities completely vanished and a pure single-phase behavior was found. An analysis of the jet penetration depth as function of the time showed that correlations from the literature are applicable for the single-phase CHG cases. For the CNG case, large differences between the correlations and the CFD simulation occurred as the break-up of the spherical vortex and the reattachment of the jet to the centerline are drastically delayed by the presence of the two-phase phenomena. Therefore, classical correlations as suggested by, e.g., Abraham [5], Hill and Ouellette [119] or Gerold et al. [90] are not applicable under such injection conditions.

7 Mixing under subsonic flow conditions

In the second part of the results, the mixing under LRE-typical conditions is studied. As a result, the pressure conditions are initially supercritical with respect to the pure components and possible single-phase instabilities can therefore be triggered exclusively due to a mixing of the different components. The investigation is split into two different parts: In Sec. 7.1, the results of a combined experimental and numerical study are presented. Based on three different test cases, the transition from a dense-gas to a spray-like jet with embedded two phase regions is studied. Building on these findings, the thermodynamic mixing trajectories predicted by different numerical solver approaches (fully-conservative and quasi-conservative) are assessed in Sec. 7.2. This includes the investigation and discussion of both single-phase and two-phase cases.

7.1 Phase separation due to multicomponent mixing

Large parts of the following results and discussions are published in the journal article [320]: Traxinger, C., Pfitzner, M., Baab, S., Lamanna, G., and Weigand, B. Experimental and numerical investigation of phase separation due to multi-component mixing at high-pressure conditions. *Physical Review Fluids*, 4(7):074303, 2019.

7.1.1 Experimental setup

The injection experiments presented in this section have been conducted at the ITLR (University of Stuttgart) by Steffen Baab by using the same experimental test facility and fluids as described in Sec. 6.1. Consequently, n-hexane has been injected into a chamber filled with nitrogen. The chamber pressure was set to 50 bar which is supercritical with respect to both pure fluids ($p_{c,C_6H_{14}} = 3.0 \text{ MPa}$ and $p_{c,N_2} = 3.4 \text{ MPa}$). As the chamber cannot be heated, the temperature of the chamber gas corresponds to ambient conditions ($T = 293 \text{ K}$). A sketch of the experimental and optical setup used in the present study is shown in Fig. 7.1. In the following, only the most relevant details regarding the measurement equipment are discussed. An exhaustive introduction and discussion of the experimental facility regarding its design and qualification can be found in the work of Stotz et al. [302] and Baab et al. [13, 14]. Optical measurements have been carried out instead of speed

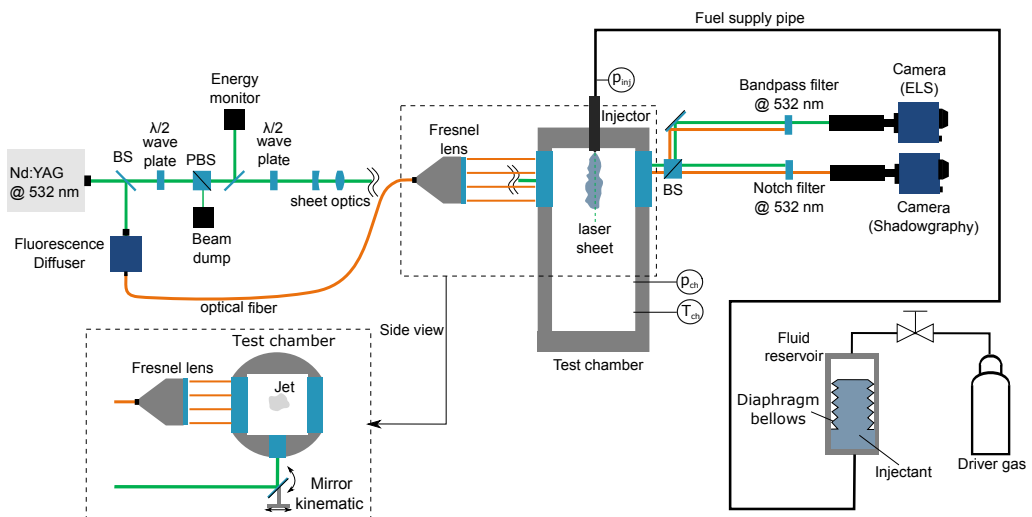


Figure 7.1: Sketch of the experimental facility including the optical arrangement for the simultaneous shadowgraphy and elastic light scattering measurements.

of sound measurements as the evaluation of the sound velocity under multiphase conditions is not feasible. Three quartz windows (two at the side walls, one at the bottom) enable optical access into the chamber. Parallel-light direct shadowgraphy in combination with planar 90 degree-elastic light scattering (ELS) have been used for the experimental jet analysis. In several recent studies, this choice has been shown suitable to assess both the geometric jet topology as well as the occurrence of two-phase regions embedded within the dense core region, see, e.g., Lamanna et al. [158] or Baab et al. [13]. The suitability of the ELS technique to capture phase separation at mesoscopic scale was discussed in detail in Baab et al. [16]. Therefore, only a short summary is given here. Basically, scattered intensities from a fluid jet illuminated by a light source are very sensitive to the size of the scattering particle/drop. Thus, signal magnitudes vary by several orders of magnitude among single-phase flow (molecular Rayleigh scattering) and two-phase flows with embedded – potentially very small – droplets, scattering in the Rayleigh or Mie regime [197]. As a matter of fact, molecular scattering intensities from single-phase flow are below the detection sensitivity of non-intensified cameras [197]. Observation of signals significantly above the detection limit therefore becomes an indicator for two-phase regions embedded in the flow. The above considerations also highlight the limitations of the ELS technique. The onset of nucleation, characterized by critical cluster sizes of the order of $20 - 30 \text{ \AA}$, will not be detected with the ELS method, which detection limit lies on the mesoscopic scale and hence in the size range of the order of $30 - 50 \text{ nm}$. From a practical point of view, this implies that the detection of phase separation with the ELS technique has a spatial and temporal offset compared to the onset of homogeneous/heterogeneous nucleation. Since non-equilibrium processes relax very rapidly to a quasi-equilibrium state, it must be expected that the inception of phase separation detected by the ELS technique will not differ substantially from the prediction of a vapor-liquid equilibrium model as it is applied in the numerical simulations.

7.1.2 Numerical setup

Thermodynamics

In the numerical simulations, the thermodynamics closure has been achieved based on the EoS due to Peng and Robinson [226]. The critical properties and acentric factors of n-hexane and nitrogen are listed in Tab. B.1 in the appendix. In Fig. 7.2, the prediction capability of the thermodynamic framework is evaluated for pure n-hexane at the chamber pressure of 50 bar and over a relevant temperature range. An excellent agreement is found with the reference data taken

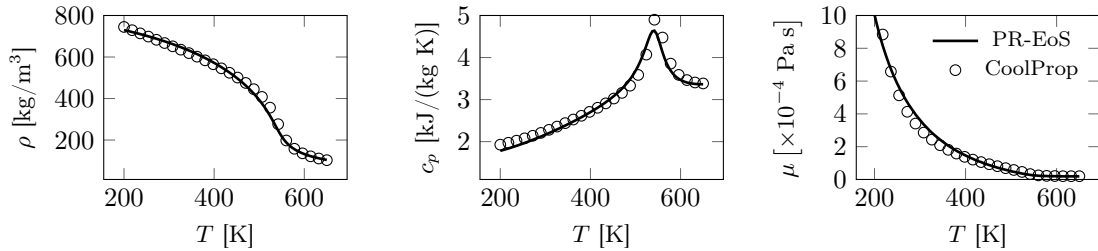


Figure 7.2: Comparison of the thermodynamic framework for n-hexane at a pressure of 50 bar with reference data obtained from CoolProp [27]. The thermal state equation due to Peng and Robinson [226] is used. The viscosity is calculated based on the method of Chung et al. [51].

from CoolProp [27] in terms of the density, the specific heat at constant pressure and the dynamic viscosity. The transition from the liquid-like to the gas-like state is captured very accurately. Therefore, an excellent prediction of the injection conditions can be expected. However, the crucial fact of this study is the prediction capability of the VLE of the binary n-hexane/nitrogen mixture. In Fig. 7.3, VLEs at relevant temperatures are shown in a pressure-composition diagram. The comparison with experimental data from the literature [72, 239] shows good agreement for the investigated pressure around 5 MPa. Especially the dew-point line shows very good agreement, which is of essential importance in this study.

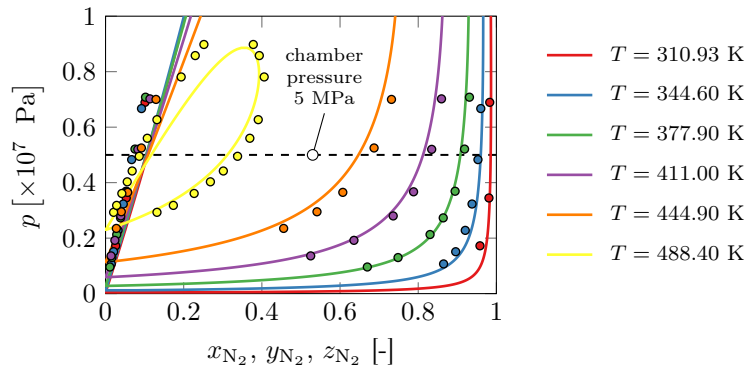


Figure 7.3: VLEs of the n-hexane/nitrogen mixture. The experimental reference data have been taken from the literature [72, 239].

Test cases

The focal point of this study is the investigation of the phase separation process under initially supercritical injection conditions. To define appropriate n-hexane injection temperatures, a priori studies of the expected thermodynamic mixing trajectories were conducted. In Fig. 7.4a, the VLE of the binary n-hexane/nitrogen mixture at the chamber pressure of 50 bar is shown. Based on a priori calculations of the adiabatic mixture considering phase separation three different injection temperatures have been selected for the present study. The corresponding theoretical mixing trajectories are shown in Fig. 7.4a as solid black lines. Small deviations from the estimated temperature profiles can, of course, occur due to heat transfer or viscous dissipation effects. As long as the temperature curve intersects the binodal, the onset of phase separation should not be affected. The validity of this assumption is verified in the result section. The temperatures selected as case

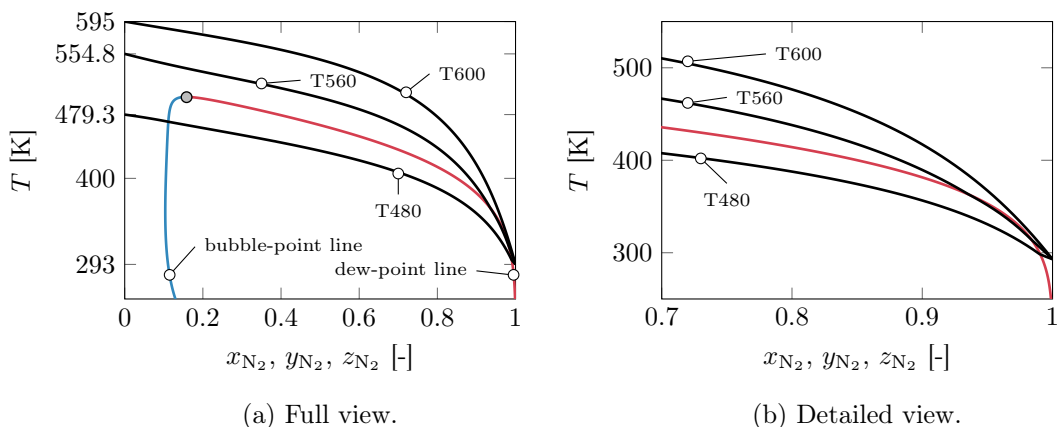


Figure 7.4: Adiabatic mixtures of n-hexane and nitrogen for three different n-hexane temperatures at a pressure of 50 bar.

names (T600, T560 and T480) correspond to the total temperature in the injector reservoir T_t . The static temperature T_e as well as the mean velocity at the nozzle exit u_e have been calculated based on the assumption of an isentropic nozzle flow. The conditions for the three selected test cases are summarized in Tab. 7.1. Reverting back to Fig. 7.4, case T480 shows strong two-phase effects and the adiabatic mixture fully penetrates the VLE. Both binodals – the bubble- and the dew-point line – are crossed. For the case T560, only minor two-phase effects can be expected. At very large nitrogen concentrations the adiabatic mixture intersects the VLE, see Fig. 7.4b. The adiabatic mixture of the T600 case does not cross the VLE and therefore a single-phase dense-gas jet should result.

Table 7.1: Operating conditions of the three different test cases for the investigation of multicomponent phase separation under high-pressure conditions.

Case	p_{ch} [bar]	T_{ch} [K]	T_t [K]	T_e [K]	u_e [m/s]	$Re_{C_6H_{14}}$ [-]
T480	50	293.0	480.0	479.3	51.0	8.23×10^4
T560	50	293.0	560.0	554.8	72.1	1.39×10^5
T600	50	293.0	600.0	595.0	90.3	1.45×10^5

Solver setup

For the detailed numerical investigation of the three different test cases, LESs have been conducted. As the injection cases are almost isobaric, the inlet boundary conditions were directly prescribed at the nozzle exit and the upstream fluid reservoir is not resolved as it was the case in the numerical investigation of the supersonic jets. Realistic inflow boundary conditions are necessary to accurately capture the jet breakup and mixing with the environmental gas. Based on the nozzle exit velocities u_e listed in Tab. 7.1, separate incompressible channel flow LESs were conducted and the velocity fields have been extracted and interpolated in time and space onto the inlet. Dirichlet boundary conditions were applied to prescribe the static temperature at the inlet according to Tab. 7.1 and the static pressure at the outlet, i.e., $p = 5$ MPa. The turbulence closure is achieved using the Smagorinsky [295] sub-grid model. The solver settings are summarized in Tab. 7.2.

Table 7.2: Numerical solver setup for the investigation of multicomponent phase separation.

Solver	TVD-limiter	Turbulence closure	EoS
pressure-based (subsonic)	limitedLinear	LES with Smagorinsky [295]	PR-EoS [226]

Grid convergence study

For a proper selection of the mesh resolution a grid convergence study for the case T600 has been conducted. Five different refinement levels were evaluated. The mesh topology in terms of the injector resolution is summarized in Tab. 7.3. A minimum number of 15 and a maximum

Table 7.3: Different meshes used for the grid convergence study with respect to the resolution of the injector ($\Delta r = D/n_{\text{cells}}$).

	very coarse	coarse	medium	fine	very fine
n_{cells}	15	21	30	45	60
Δr [\mu m]	15.73	11.24	7.87	5.24	3.93

number of 60 cells were used to resolve the injector in the radial direction corresponding to an approximate discretization of 16 μm and 4 μm , respectively. In Fig. 7.5, the results of the gradual mesh refinement in terms of the mean density and its corresponding root mean square along the chamber axis for $x/D \leq 30$ are shown. From the coarsest mesh to the medium mesh a gradual shortening of the density potential core can be observed, see Fig. 7.5a. Between the three finest mesh versions, the increase in resolution mainly has an influence on the RMS values, see Fig. 7.5b. Based on this study, it was decided to use the medium mesh with a resolution of 30 cells as the consideration of the multicomponent phase separation is already very costly. In addition, the resolution is sufficient for the present test case to properly resolve the large Reynolds number flow field and to investigate the mixture-induced phase separation process.

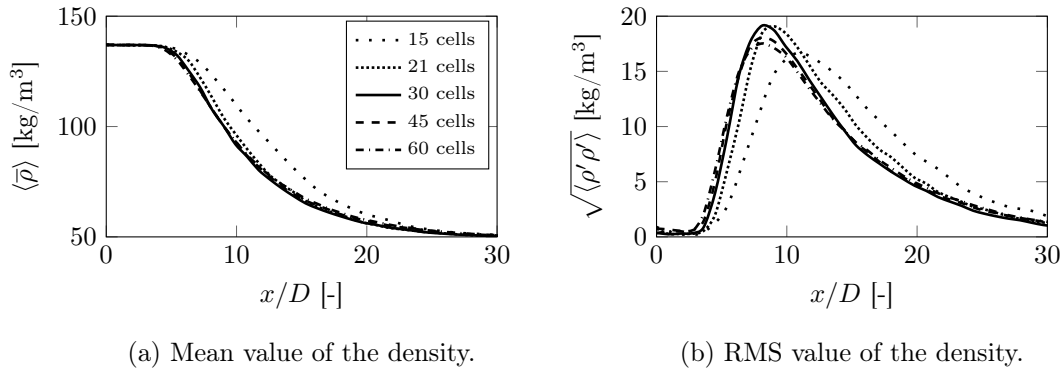


Figure 7.5: Results of the mesh convergence study in terms of the mean density $\langle \bar{\rho} \rangle$ and the corresponding root mean square $\sqrt{\langle \rho' \rho' \rangle}$ along the centerline of the chamber.

7.1.3 Results

Evaluation of the jet topology

In advance to the detailed thermodynamic analysis, the prediction capability of the numerical solver with respect to the fluid dynamics aspects is evaluated. Both experimental and numerical shadowgraphs of the high-temperature case T600 are used to compare the jet topology with each other. The shadowgraphy image in the LES has been obtained by performing a line-of-sight integration of the Laplacian of the density, i.e., $|\nabla \cdot \nabla \bar{\rho}|$, in accordance to the experiments [287]. In Fig. 7.6, the experimental and numerical results of the fully developed jet are shown up to an axial distance of $x/D = 45$. A highly turbulent jet is visible which gradually dissolves into the environment. In the experiment, almost no dark areas are present for $x/D \gtrsim 30$ which can be observed similarly in the LES. The dark core length extracted from the experimental data by means

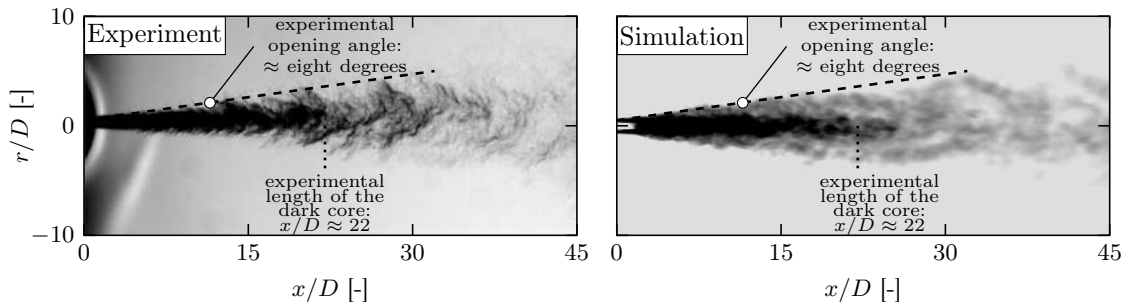


Figure 7.6: Fully developed jet structure of the T600 test case. Left: Experimental shadowgraphy image; Right: Line-of-sight integrated Laplacian of the density obtained from the LES result.

of a binarized image compares very well to the result of the numerical simulation. From a fluid dynamics point of view, both jets feature a similar opening angle of approximately eight degrees highlighted by the dashed line. This line was fitted to the shadowgraphy of the experiment and has been superimposed onto the LES results. Looking deeper into the jet topology, finger-like structures can be seen on the outer surface for $x/D \lesssim 15$. These are typical phenomena in supercritical jets and indicate a possible single-phase character of the jet mixing process. However, the assessment of the actual thermodynamic state based on sole shadowgraphy images is not sufficient [158] and therefore additional measurement techniques are necessary.

Investigation of phase separation phenomena

The discussion and investigation of mixture-induced phase separation processes is carried out based on experimental single-shot measurements and instantaneous LES results. Snapshots have been

taken at a time sufficiently large such that the jets are fully developed and can be considered as quasi-stationary. In the following figures, experimental results are always shown in the left column and LES results in the right column, respectively. In the experiment, the shadowgram and the simultaneously taken ELS image superimposed onto the corresponding shadowgram visualize both the flow structure as well as the thermodynamic state. The intensity from the ELS measurements is shown on a logarithmic scale comprising almost three orders of magnitude. Focus shall hence be put on the overall scattering characteristics rather than the quantitative evaluation of the measured signals. Values outside the color scale range have been cut off to emphasize the distinction between regions of negligible intensity \tilde{I} and two-phase regions within the jet, indicated by high scattering intensities. In the LES, flow structures are visualized by the instantaneous temperature field. To study the phase separation behavior, the vapor fraction is superimposed onto the temperature field to indicate regions of two-phase flow. By doing so, a direct (qualitative) comparison of the phase formation phenomena in the experiment and LES is provided.

The results of the case T600 are shown in Fig. 7.7. According to the discussion of Fig. 7.6, the experimental results show a jet being dissolved in the environment and finger-like structures emerging from the surface of the dark core. No significant (stable) ELS signal has been measured and as a result a single-phase state can be deduced. This finding agrees well with the LES results. The simulation does not predict any thermodynamically unstable mixture states which is underlined by the scatter plot shown in Fig. 7.8. Due to the assumption of an equal turbulent Prandtl and Schmidt number in the turbulence closure, the turbulent Lewis number is equal to one and hence all conditions in the LES strictly follow the adiabatic mixture line. As the experiment shows only very minor phase formation effects, it can be deduced that for the present test cases the mixture states in the experiment can also be found close to the adiabatic mixture line. Nevertheless, it has to be pointed out that this has not to be the case in every jet mixing process and the assumption of an adiabatic mixture can possibly lead to severe deviations from the actual mixture states. Another important aspect for these jets is that they are almost isobaric and are therefore not subjected to large fluctuations in pressure. Furthermore, the dew-point line does not show a strong dependency on the pressure close to the investigated pressure of 5 MPa, see Fig. 7.3, underlining the LES result (no phase separation process) and the experimental observation of the absence of a pronounced two-phase region within the jet. The minor signals determined in the experiment might result from spatial fluctuations of thermodynamic properties, heterogeneous nucleation or the local deviation from the adiabatic mixture concept. Downstream of $x/D \gtrsim 10$, these regions form in the outer shear layer but they are highly unstable and collapse instantaneously.

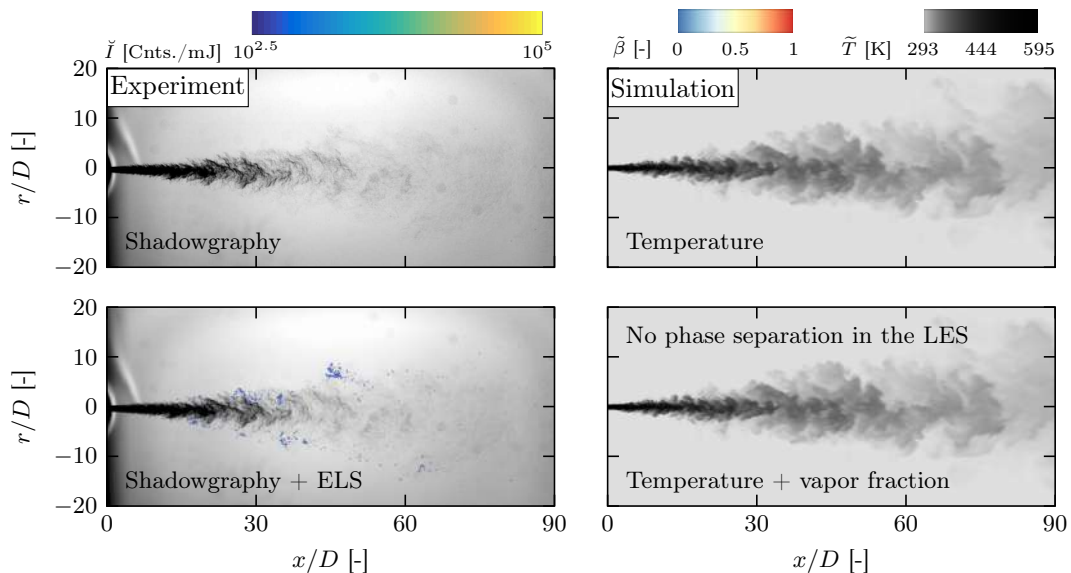


Figure 7.7: Comparison of experimental and numerical snapshots for the test case T600. \tilde{I} is the noise-corrected camera intensity I_{cam} normalized by the measured excitation intensity I_0 .

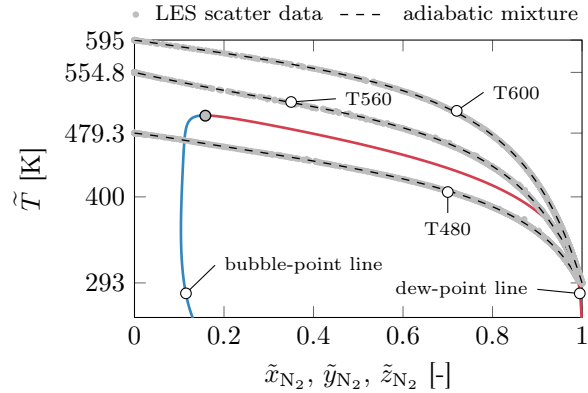


Figure 7.8: Comparison of LES scatter data with the adiabatic mixture concept, see Fig. 7.4.

A totally different picture results for the case T560, see Fig. 7.9. While the shadowgram resembles that for T600 in the near-nozzle region, a strong difference becomes apparent for $x/D \gtrsim 20$. Here, a dark region forms over the entire extension of the jet, which indicates the formation of a dense droplet cloud. This fact is clearly corroborated by a steep increase in the scattering intensity, which is initiated by droplet generation in the mixing layer for $x/D \gtrsim 10$. Further downstream, this flow mixes into the jet core, leading to a pronounced two-phase characteristic throughout the entire jet domain. In fact, this is proven by the LES result of case T560, where a large spatial area of the jet shows two-phase behavior. In agreement with the experimental observation, the LES regions showing two-phase flow are located in the outer shear layer, which merge towards the jet centerline downstream of $x/D \gtrsim 60$. Due to the only minor penetration of the VLE, the vapor fraction in the regions with phase separation is very close to unity. The minor penetration of the VLE can be understood in more detail in the scatter diagram shown in Fig. 7.8.

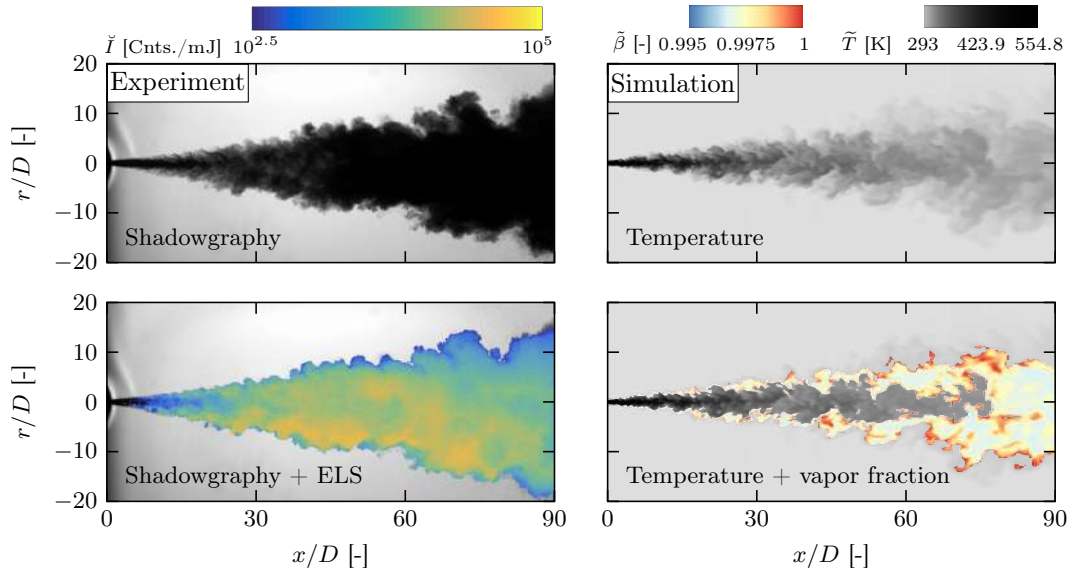


Figure 7.9: Comparison of experimental and numerical snapshots for the test case T560. \bar{I} is the noise-corrected camera intensity I_{cam} normalized by the measured excitation intensity I_0 .

For case T480, a drastic change in terms of flow phenomena occurs. A spray-like behavior similar to atomized jets can be seen in the experimental snapshots in Fig. 7.10. The corresponding shadowgram shows a constant dark core with distinct droplets visible in the outer jet region for $x/D \gtrsim 15$. This pronounced two-phase characteristic directly reflects in the strong scattering throughout virtually the entire jet domain. As in case T560, the presence of this strong phase

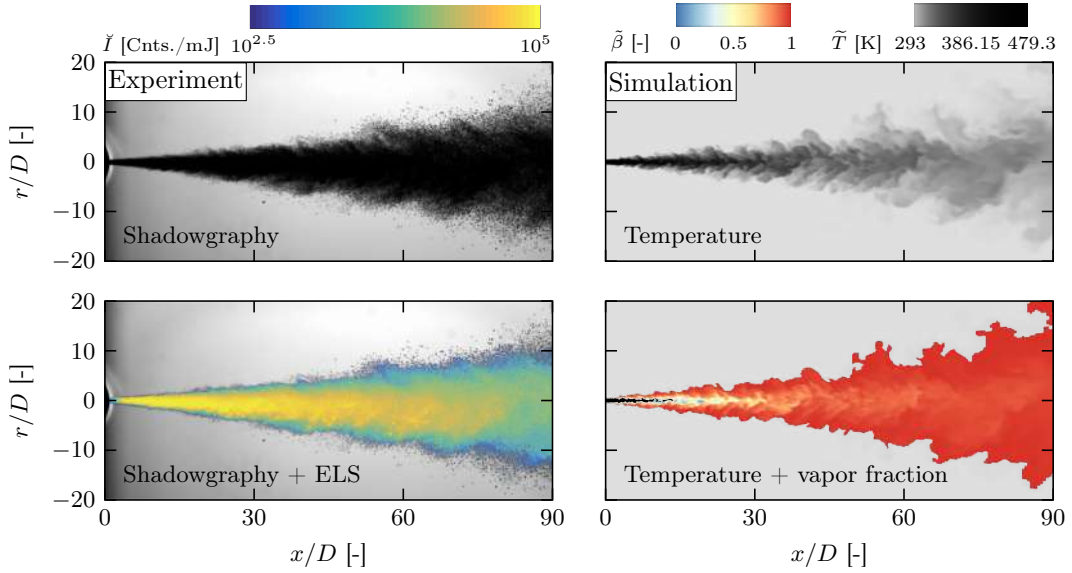


Figure 7.10: Comparison of experimental and numerical snapshots for the test case T480. \check{I} is the noise-corrected camera intensity I_{cam} normalized by the measured excitation intensity I_0 .

separation is confirmed by the LES where nearly the complete jet has entered the VLE, see Fig. 7.8. In contrast to the cases T560 and T600, the lowering of the injection temperature to 480 K leads to the fact that both binodals are crossed and the corresponding shadowgram shows a jet exhibiting spray-like behavior. Due to the Eulerian approach used in the LES, no individual droplets are resolved. Therefore, the spray-like character is represented in terms of the vapor fraction covering the whole range from zero to one whereby the lowest values are found in the core of the jet. A single-phase state is predicted only in the "dark" core close to the injector inlet and in a thin area at the outermost region of the jet.

7.1.4 Summary

Well synchronized experiments and numerical simulations of jet mixing at high-pressure conditions have been carried out to investigate mixture-induced phase separation processes in initially supercritical fluids. A multicomponent system consisting of n-hexane and nitrogen was chosen and a systematic study has been conducted at supercritical pressure with respect to the pure components. N-hexane has been injected into a chamber filled with pure nitrogen at (cold) ambient temperature. The test case conditions were defined by applying the adiabatic mixture concept considering phase separation. The injection temperatures were selected such that they lead to regimes in which the occurrence of phase separation is possible and triggered gradually by lowering the injection temperature. Three different test cases have been presented and discussed. Simultaneous shadowgraphy and elastic light scattering experiments have been conducted at the ITLR (University of Stuttgart) to capture both the flow structure as well as the phase separation. In addition, numerical simulations have been carried out by means of Large-Eddy Simulations with a VLE model. Experimental and numerical results show phase separation and the transition from a dense-gas to a spray-like jet. Characteristics of the formation process agree well between experiments and numerical simulations. The formation of a two-phase flow is initiated in the mixing layer some distance downstream of the nozzle and eventually mixes into the jet core at large distances.

7.2 Comparison of fully- and quasi-conservative solvers

7.2.1 Introduction

Recently, Ma et al. [178] investigated the mixing behavior of both FC and QC schemes. In accordance with other investigations, e.g., Lacaze et al. [153, 156] or Mattheis and Hickel [185], the FC

results closely follow the adiabatic mixture assumption. An identical behavior has been found in the last Sec. 7.1 for the results of the three n-hexane test cases, cf. Fig. 7.8. For the QC double-flux scheme, Ma et al. [178] showed that the results of their investigated cases closely resemble an isochoric mixing approach where a linear behavior of the specific volume in mixture fraction space is assumed. Therefore, the isochoric mixture model is governed by:

$$\dot{m}_{\text{mix}} = \dot{m}_1 + \dot{m}_2 , \quad (7.1)$$

$$\dot{m}_{\text{mix}} v_{\text{mix}} = \dot{m}_1 v_1 + \dot{m}_2 v_2 . \quad (7.2)$$

In addition, an isobaric process is assumed to arrive at a fully defined thermodynamic state. Applying the adiabatic and isochoric mixture model, Ma et al. [178] studied the experiments of Roy et al. [265] and Manin et al. [179]. Based on the comparison of the numerical and the experimental findings, Ma et al. [178] concluded that the adiabatic mixture model is unable to correctly predict the phase separation behavior under these high-pressure conditions. In contrast, very good agreement between the isochoric approach and the experimental findings was reported in this work [178]. Building on the good agreement between experimental and numerical investigations in the last Sec. 7.1, the findings of Ma et al. [178] are checked for these n-hexane test cases. An additional single-phase test case from the work of Baab et al. [16] is used to extend the basis of this investigation and add quantitative measurement data to it.

7.2.2 Single-phase test case

Recently, Baab et al. [16] carried out LITA measurements in subsonic jets under high-pressure conditions. The applied experimental setup is identical to the one used by Baab et al. [14] for the experimental investigation of the supersonic n-hexane jets, cf. Sec. 6.1. In total, five different cases have been reported by Baab et al. [16]. Here, the n-hexane case which corresponds to "Case 1" in Baab et al. [16] is used. The experimental conditions are listed in Tab. 7.4 and are very similar to the T600 case in Sec. 7.1. This test case was selected for two reasons: First of all, the same validated thermodynamic framework as in the previous Sec. 7.1 can be applied. Second, the measurement data are available for a wide range of axial positions from $x/D = 17$ up to $x/D = 80$. In addition, at $x/D = 35$ radial profiles of the measured speed of sound are also available for a range of $y/D \approx \pm 6$.

Table 7.4: Experimental conditions for the single-phase test case taken from Baab et al. [16]. The nozzle exit temperature T_e and velocity u_e were estimated based on the assumption of an isentropic flow inside the injector.

Injectant	Chamber	T_t [K]	p_t [MPa]	T_{ch} [K]	p_{ch} [MPa]	T_e [K]	u_e [m/s]
C ₆ H ₁₄	N ₂	630	5.49 ± 0.03	296	4.99 ± 0.04	627	91

7.2.3 Numerical setup

Thermodynamics

Following Secs. 6.1 and 7.1, the cubic EoS of Peng and Robinson [226] is applied to achieve the thermodynamic closure for the present test cases. The prediction quality of this state equation with respect to pure n-hexane and binary VLEs has been already studied in detail in Sec. 7.1, see Figs. 7.2 and 7.3. For the single-phase test case, the predictability of the mixture speed of sound is of major interest. In Fig. 7.11, high-fidelity data from NIST Refprop [164] are compared to the PR-EoS [226]. Here, the adiabatic mixture concept is employed to define the thermodynamic mixing states according to the experimental boundary conditions in Tab. 7.4. In NIST Refprop [164], the GERG-2008 EoS due to Kunz and Wagner [145] is used to describe the binary n-hexane/nitrogen mixture. A very good agreement between both thermodynamic models is achieved especially close to pure n-hexane. With increasing dilution of n-hexane with nitrogen, the PR-EoS [226] tends to slightly underpredict the speed of sound.

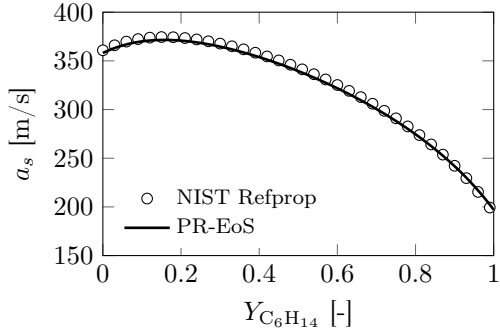


Figure 7.11: Comparison of mixture speed of sound data for the binary n-hexane/nitrogen mixture. The reference data have been taken from NIST Refprop [164].

Solvers

The settings applied in the FC pressure-based solver are identical to the ones in Sec. 7.1 and are summarized in Tab. 7.5.

Table 7.5: Setup of the pressure-based solver for the comparison of FC and QC schemes.

Solver	TVD-limiter	Turbulence closure	EoS
pressure-based (subsonic)	limitedLinear	LES with Smagorinsky [295]	PR-EoS [226]

The density-based double-flux solver is not employed for 3D simulations. Therefore, 2D planar jets are investigated in accordance to the works of Ma et al. [177, 178] and Lacaze et al. [156] to study the mixing behavior. Consequently, no sub-grid model is applied and laminar simulations have been conducted. The solver settings for the density-based solver are summarized in Tab. 7.6.

Table 7.6: Setup of the density-based solver for the comparison of FC and QC schemes.

Solver	TVD-limiter	Turbulence closure	EoS
density-based	limitedCubic	laminar	PR-EoS [226]

7.2.4 Results

Single-phase case - FC solver

In the first step, a 3D-LES of the single-phase speed of sound case has been conducted using the FC pressure-based approach. Following the mesh convergence study in Sec. 7.1, the injector is resolved with 30 cells over the diameter corresponding to a minimum cell size of 7.87 μm . For proper inflow boundary conditions, a separate incompressible channel flow LES was conducted in advance. From this simulation, the velocity field has been extracted over a sufficient amount of time and has been interpolated in time and space onto the inlet. A constant temperature of 627 K has been set at the n-hexane inlet. At the outlet, a pressure of 5 MPa has been prescribed.

In Fig. 7.12, instantaneous CFD results of the fully developed n-hexane jet are shown. Focusing on the temperature and mass fraction plots first, a highly turbulent mixing process of n-hexane with the gaseous nitrogen environment becomes visible. As soon as the fuel jet enters the chamber, it starts to break up and dissolves gradually into the environment. At the beginning only small vortical structures are visible at the jet boundary. Further downstream, the structures grow rapidly in size and spatial extent. Therefore, more and more ambient gas is entrained into the jet leading to a gradual reduction of the n-hexane mass fraction and the temperature. As species and energy are transported at the same rate in the present fully-conservative

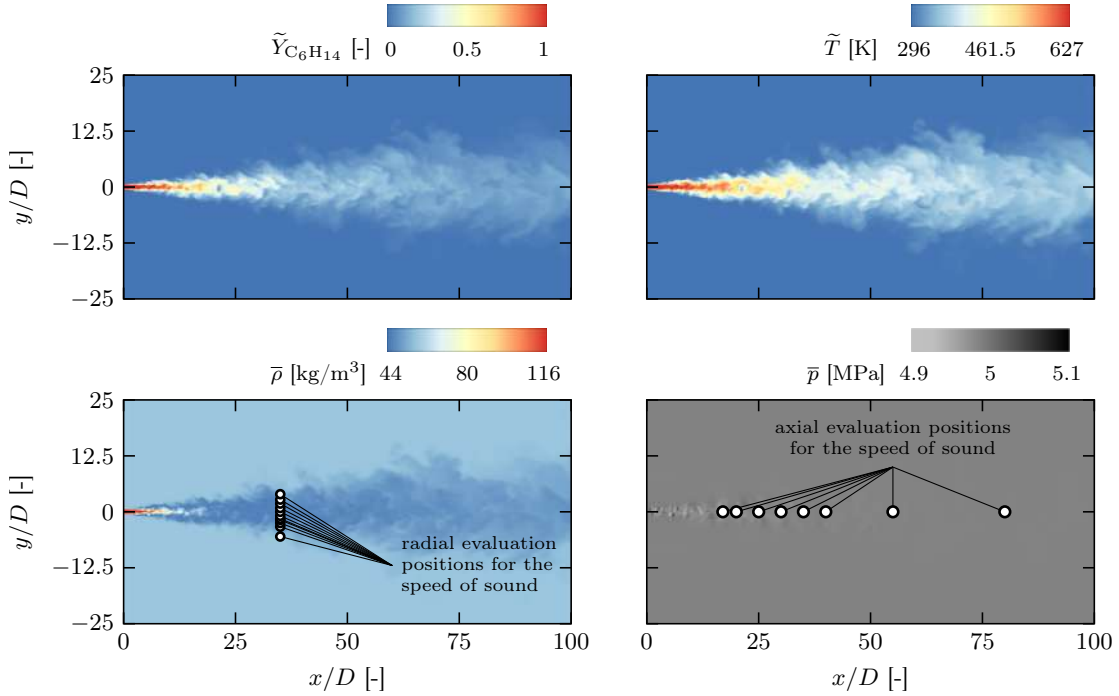


Figure 7.12: Instantaneous flow field of the fully developed jet. For the conduction of the LES, the FC pressure-based solver has been used.

framework, both fields appear similar. The decay of the temperature field towards the ambient conditions is somewhat smaller compared to the mass fraction field. Keep this in mind when we later examine the behavior of the QC solver. The variation of the density is shown in Fig. 7.12 bottom left. At the inlet, the largest density values are found and up to $x/D \approx 10$ a dark core – almost pure fluid – is present. Downstream of this dark core, most of the mixing process takes place and a lot of nitrogen is entrained into the jet. Therefore, a strong decay of the density is found. This can be understood in more detail in Fig. 7.13 where the variation of the mean density and its root mean square are plotted along the center axis of the chamber. Up to $x/D \approx 20$ a strong reduction of the density occurs which comes along with large fluctuations. At $x/D \approx 30$, the mean density begins to rise steadily. However, the values of the density lie well below the respective pure nitrogen reference value at chamber conditions highlighting the presence of real-gas effects. This decrease can also be seen in the instantaneous density field in Fig. 7.12 bottom left. In hydrogen/nitrogen mixtures under rocket-engine relevant conditions, it was reported by Müller et al. [204] that the real-gas mixing effects can also lead to a subcooling with respect to the injection temperatures. Finally, in Fig. 7.12 bottom right, the instantaneous pressure field is shown. The injection is almost isobaric and only at the periphery of the jet, pressure fluctuations resulting from the jet break-up process occur. Therefore, the change in the thermodynamic state is governed by changes in composition and energy

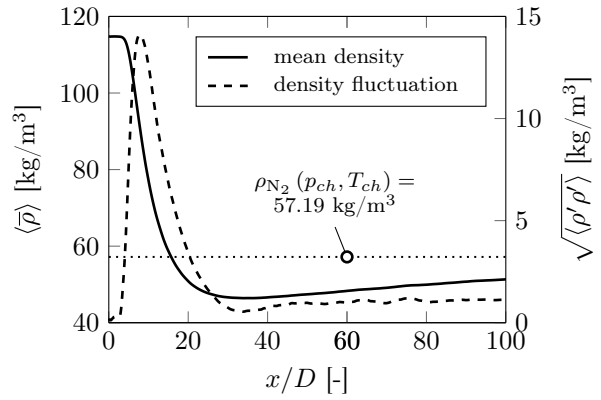


Figure 7.13: Variation of the mean density and its fluctuation along the center axis.

exclusively. In addition to the presentation of the flow field by means of snapshots, the contour plots of the density and the pressure in Fig. 7.12 show the axial and radial evaluation positions for the speed of sound data by means of white dots which are used in the following for a comparison between experimental measurements and numerical simulation results.

In Fig. 7.14, the time-averaged speed of sound results extracted from the LES are compared to the experimental data of Baab et al. [16]. Overall, a very good agreement is found demonstrating that the FC pressure-based solver is able to predict the mixing process of n-hexane into nitrogen. Focusing on the axial variation of the speed of sound, see Fig. 7.14a, small deviations are found for $x/D \leq 20$ whereby the first point lies within the measurement uncertainty and the second evaluation point underpredicts the measured speed of sound by roughly 3%. Downstream of

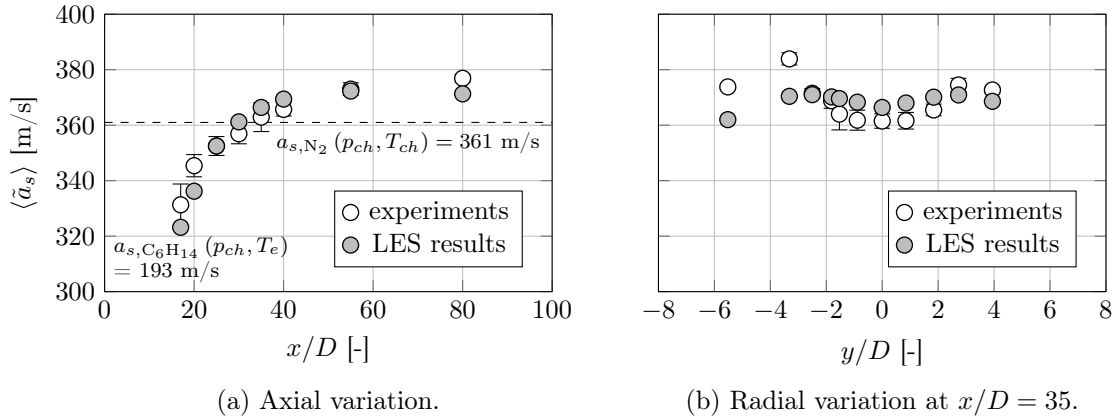


Figure 7.14: Comparison of the measured speed of sound data with the LES results along the axial centerline and in radial direction. The experimental data have been taken from Baab et al. [16].

$x/D = 20$, the agreement between CFD and experimental data is almost perfect. Only the comparison at $x/D = 80$ shows a small underprediction. However, this issue might be attributed to the PR-EoS [226]. The comparison of the applied thermodynamic framework with reference data from NIST Refprop [164] in Fig. 7.11 reveals that the PR-EoS [226] tends to slightly underestimate the speed of sound for large nitrogen mass fractions. In addition, nonideal mixing processes caused by diffusion might also play a role at this large distance. Unfortunately, the investigation of such processes using a fully resolved 3D simulation is out of scope for the present work as it would require much more computational power. In contrast to this issue, the explanation for the slight underestimation at $x/D \leq 20$ can be found with the help of the available data. The decay of the n-hexane mass fraction and the velocity along the center axis are plotted in Fig. 7.15. Downstream of $x/D \approx 25$ both profiles achieve self-similarity and follow the dashed-line which was manually fitted

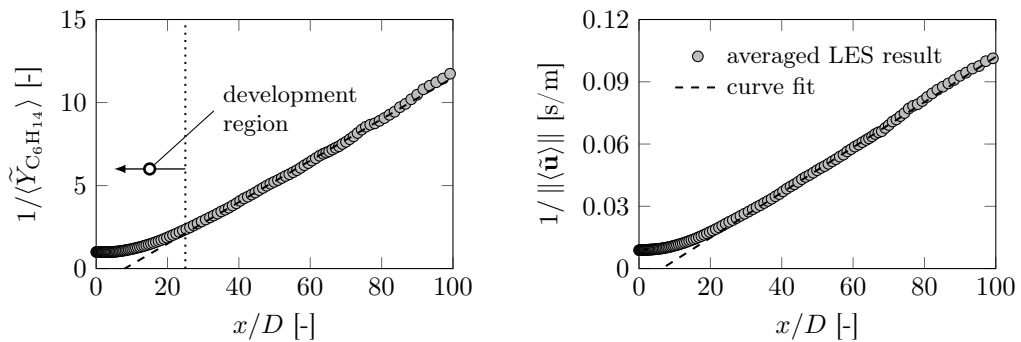


Figure 7.15: Concentration and velocity decay along the centerline. The dashed line was fitted manually to the available LES data to study the self-similarity and to approximately mark the development region.

to the LES data. Here, the centerline concentration and velocity are inversely proportional to the distance from the injector exit. This behavior in turn demonstrates that the first two measurement points ($x/D = 17$ and 20) lie within the development region where the average speed of sound values are more sensitive to the predicted turbulent flow field and the initial break-up process. It is assumed that this is the reason for the slight deviation between experiments and CFD.

Finally, in Fig. 7.14b the radial distribution of the speed of sound is compared. Overall, the trend is captured accurately by the LES. However, close to the centerline the CFD overpredicts the speed of sound. In contrast, for $y/D > 2$, the measurement data are slightly underpredicted. This fact can be attributed to the thermodynamic closure similar to the discussion at the axial position $x/D = 80$. Unfortunately, no statement is found in Baab et al. [16] concerning the measurement points at $y/D < -2$. Based on the current simulation results it is suspected that these points are not representative for the average jet break-up process. This assumption is further underlined by the slightly asymmetric behavior of the experimental data.

Single-phase case - FC vs. QC solver

In the following, a comparison between the FC pressure-based solver and the QC double-flux solver is carried out based on the single-phase test case. A 2D planar jet simulation has been conducted with the QC density-based solver. The configuration corresponds to Fig. 7.16 and the thermal boundary conditions are applied in accordance with Tab. 7.4. The inlet velocity was set to 100 m/s based on the work of Terashima and Koshi [311]. Following the work of Ma et al. [178], a uniform grid spacing is employed and the inlet is resolved with 50 cells. An identical configuration has been used for the validation of the density-based solver in Sec. G in the appendix. The instantaneous n-hexane mass fraction and temperature fields 0.5 ms after injection are shown in Fig. 7.17. A typical flow field of a 2D planar jet with large vortical structures can be seen. Due to the mixing of the injectant with the ambient gas, the mass fraction and temperature gradually decay towards the ambient conditions. However, in comparison to the FC temperature and mass fraction fields in Fig. 7.12, both flow fields from the QC solver occur highly different with respect to their decay rate. Especially, the temperature field tends very quickly towards the ambient temperature of 296 K giving rise to the expectation that the mixing behavior of the QC solver is quite different from the FC solver.

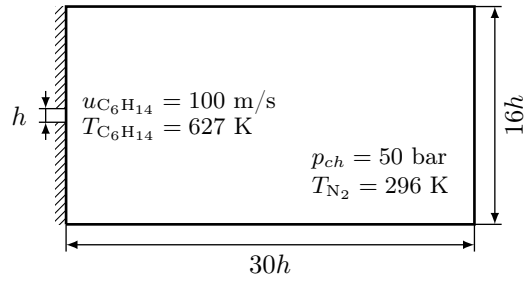


Figure 7.16: Schematic of the computational domain used for the simulation of the 2D planar jet configuration. The inlet height h is 1 mm.

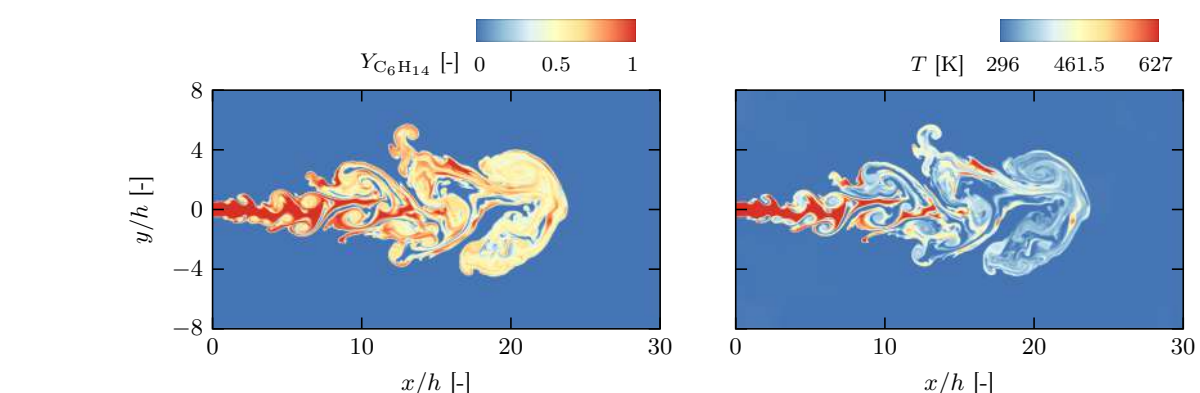


Figure 7.17: Instantaneous flow field of the planar n-hexane jet injected into a quiescent nitrogen atmosphere simulated with the QC solver. The results are shown 0.5 ms after start of injection.

To study this issue in more detail, the work of Ma et al. [178] and Lacaze et al. [156] is followed and the results of both solvers are scattered in a temperature-composition diagram in Fig. 7.18. A large deviation between both approaches becomes visible. The stronger temperature reduction in the QC case is apparent. An almost straight line between the injection conditions of pure nitrogen and n-hexane in the temperature-composition space results and the scatter data of the QC solver mimics the trend of an isochoric mixture. In contrast, the data of the FC solver taken from the present LES follow the adiabatic mixture concept closely. Both results are superimposed onto the VLE of the binary mixture at the corresponding chamber pressure of 50 bar. The results of the QC solver clearly penetrate the VLE region. This in turn yields a strong two-phase characteristic of the jet which would make the measurement of speed of sound impossible. In contrast, the scatter data of the FC solver do not cross the binodal and therefore a pure single-phase mixing behavior can be deduced which is in excellent agreement with the experiments [16]. This in turn underlines the applicability of the adiabatic mixture concept to study the overall mixing process under high-pressure conditions for the present n-hexane test cases. This fact, is elaborated in more detail in the next section using the multi-phase test cases from Sec. 7.1.

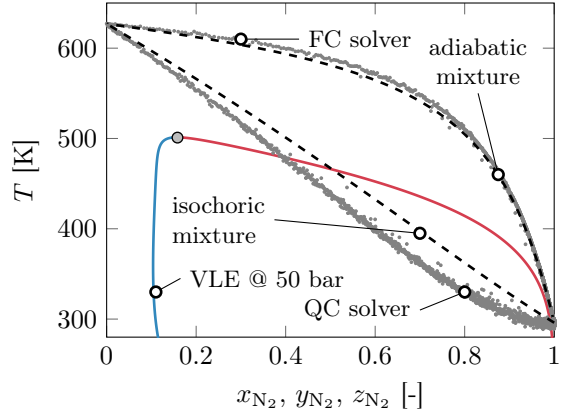


Figure 7.18: Temperature-composition diagram showing the results of the FC and QC solver for the single-phase speed of sound test case.

Multi-phase cases - FC vs. QC solver

In the following, the focus is put on both high temperature cases, i.e., T600 and T560, and the T480 case is excluded as the shadowgram in Fig. 7.10 clearly indicates a two-phase behavior. As a starting point for a thorough investigation, Fig. 7.19 shows the VLE of the binary n-hexane/nitrogen mixture at 50 bar. Unlike before, not only the equilibrium binodals are plotted but also the spinodal region and lines of constant nucleation rate are shown. The two spinodal curves (dashed lines) mark the region of intrinsic single-phase instability. However, this region will never be entered in engineering practice as the activated process of nucleation will trigger the formation of a stable phase a lot earlier. This is shown by the three red dash-dotted lines which correspond to the increasing nucleation rates $I = [10^{-200}, 10^{-100}, 10^{-50}]$ based on the discussion in Fig. 4.17. In practice, the mixing process crosses the dew-point line but due to a too high activation energy the

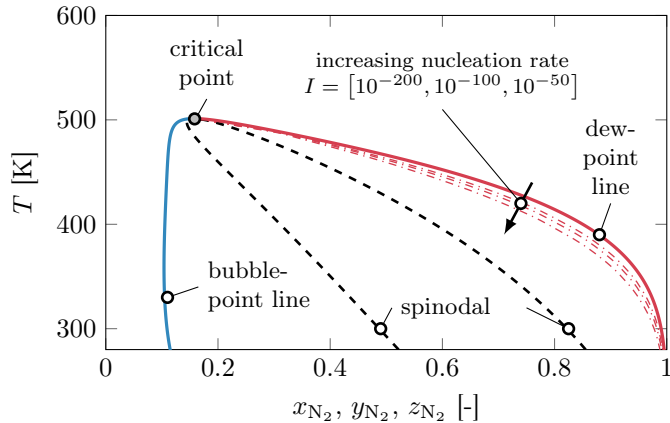


Figure 7.19: Vapor-liquid equilibrium of the binary n-hexane/nitrogen mixture at 50 bar together with the mixture critical point and the spinodal lines marking the region of intrinsic phase separation. The dash-dotted lines are lines of constant nucleation rate according to Fig. 4.17.

barrier to form a stable nucleus cannot be crossed. The mixing process continues in a single-phase state and the fluid becomes subcooled with respect to the equilibrium temperature. Therefore, the fluid exists in a metastable/nonequilibrium state. This process proceeds until the nucleation rate is high enough to overcome the energy barrier and to form a stable nucleus where the formation of a liquid phase can take place. After that, the nonequilibrium state quickly reverts back to equilibrium conditions governed by the typical macroscopic thermodynamics. This process takes place close to the dew-point line as it is indicated by the three dash-dotted red lines in Fig. 7.19.

2D planar jet simulations for both multi-phase test cases have been conducted with both solvers. In the following, no snapshots of the flow field are shown as they are similar to Fig. 7.17 and do not provide additional information apart from the already discussed facts. Therefore, the focus is put solely on the scattering of data into temperature-composition diagrams. In Fig. 7.20a, the results for the T600 case are shown. It is not surprising that the pattern of the scatter

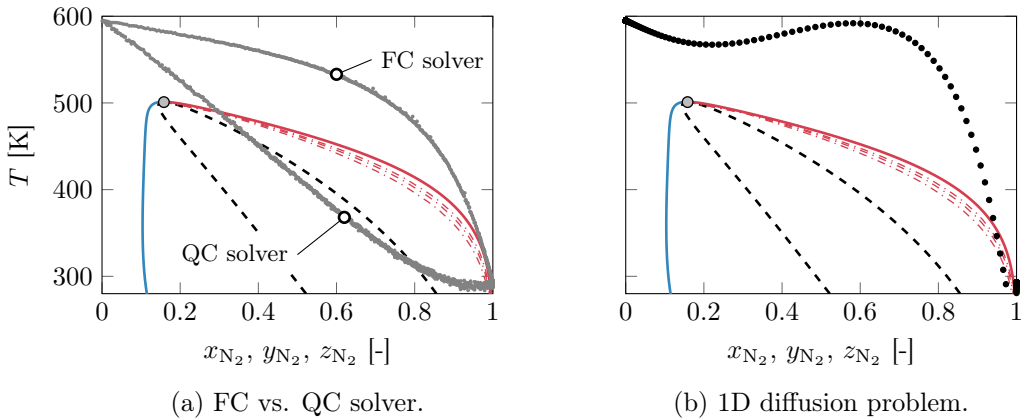


Figure 7.20: Temperature-composition diagrams of the T600 case. In subfigure a, the results of the FC and QC solver are shown. The result of a 1D diffusion problem employing the high-pressure diffusion coefficients due to Riazi and Whitson [258] is shown in subfigure b.

data looks very similar to the one discussed in Fig. 7.18. Compared to the single-phase speed of sound test case, the n-hexane reservoir temperature was lowered by 30 K and the ambient temperature is 293 K instead of 296 K. Therefore, the findings are identical but now it becomes obvious that the trajectory of the QC solver not only crosses the binodal but also gets inside the spinodal area which is in strong contradiction to the findings in the experiment where only a single-phase mixing process has been found. Depending on the combined shadowgraph/ELS image in Fig. 7.7 one might now argue that there are small signals at the jet periphery. From the experiments it is known that these regions are highly unstable and collapse instantaneously. Therefore, one reason could be small particles which would cause heterogeneous nucleation. Another possible reason could be nonideal transport phenomena. To further elaborate on this latter fact, a 1D diffusion problem was defined and the high-pressure diffusion coefficients due to Riazi and Whitson [258] are used, i.e., the unitary Lewis number assumption has been dropped. In Sec. B.2 of the appendix the diffusion model of Riazi and Whitson [258] is described in detail. A sketch of the 1D diffusion problem including the initial conditions is shown in Fig. 7.21. The domain has a length of 100 μm and is discretized with 1000 grid points. The result of the diffusion problem after 4.4 μs is shown in Fig. 7.20b. At this time, the temperature profile was found quasi-stationary. The comparison of the scatter data with the VLE demonstrates that diffusion can cause the unstable regions at the jet boundary as the path runs through the region of sufficiently large nucleation rates where the formation of a stable nucleus would be possible.

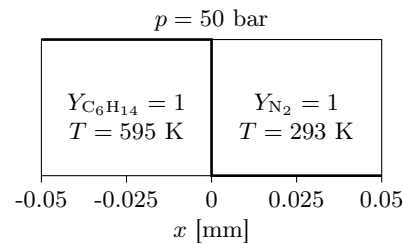


Figure 7.21: Schematic of the 1D diffusion problem together with the initial conditions.

Finally, Fig. 7.22 compares the results for the T560 case. Here, scatter data from both solvers indicate a penetration of the VLE whereby – from the fuel’s point of view – the trajectory generated by the QC solver enters the VLE approximately across the mixture critical point and leaves it across the dew-point line. The one generated by the FC solver, in contrast, enters and leaves the two-phase region across the dew-point line resulting in a kind of retrograde condensation behavior, i.e., the liquid mass fraction is increased and lowered but never reaches full saturation. Comparing these observations of the FC and QC solver, things are not as clear as in the T600 case. Looking at the experimental results, cf. Fig. 7.9, a dark shadowgram can be seen and the ELS signal covers wide regions of the jet. However, no droplets or similar structures are visible and therefore, a deep entry into the VLE as predicted by the QC solver is unlikely. Therefore, it is believed that the resulting thermodynamic mixing trajectory of the FC solver – i.e., an adiabatic mixture assumption – is much closer to the real mixing path than the trajectory described by the results of the QC solver. Especially when considering possible local nonideal diffusion processes which might help to activate the phase separation process in the conservative/adiabatic case.

7.2.5 Summary

In this section, the focus has been put on the investigation of the thermodynamic mixing trajectories predicted by different solver types under high-pressure real-gas conditions. Two different numerical solver approaches have been applied and compared to each other: A fully-conservative pressure-based approach and a quasi-conservative double-flux method. The latter type is quite popular in density-based real-gas solver frameworks as such schemes suppress spurious pressure oscillations caused by material interfaces. This property makes the solver robust in the application, which is desirable for the successful conduction of numerical simulations. However, the predicted thermodynamic mixing trajectory of the QC solver differs from a fully-conservative approach.

Overall, three different test cases have been used in this study where initially supercritical n-hexane was injected into a high-pressure chamber filled with nitrogen at rest. For the single-phase test case, speed of sound measurements are available in the literature [16]. The comparison with the LES results of the pressure-based framework showed a very good agreement. In contrast, the scatter plots of the QC solver strongly deviated from the FC results. The generated thermodynamic mixing trajectory of the QC solver penetrates the two-phase region of the binary mixture making speed of sound evaluations impossible. Using two experimental test cases (T600 and T560) on high-pressure mixture-induced phase separation from Sec. 7.1, the possibly nonphysical prediction of the QC scheme could be further confirmed. Overall, it has been found that a fully-conservative solver and the adiabatic mixture model are most suitable for an estimation of the thermodynamic mixing trajectory of the jet mixing process in the present cases.

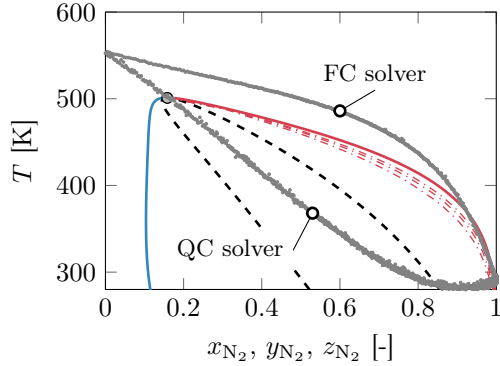


Figure 7.22: Temperature-composition diagram of the T560 case with scatter data from FC and QC 2D planar jet simulations.

8 Single-phase instability in high-pressure combustion

This final result section is concerned with the investigation of single-phase instabilities in diffusion flames under LRE-like conditions. In the literature, little is known about the possibility of such processes and thus no experimental investigations focusing on this particular thermodynamic phenomenon are available for comparison. Consequently, the focal point is to clarify whether phase separation can occur and, if so, what the major effects are. In the following, reacting cases for both LOx/H₂ and LOx/CH₄ flames at representative conditions taken from two well-known experiments are studied. First, fundamental investigations are performed using one-dimensional counterflow diffusion flames. Second, the results of the LOx/CH₄ flame are tabulated and applied in a Large-Eddy Simulation and compared to experiments in terms of OH* emission.

Large parts of the following results and discussions are published in the journal article [322]: Traxinger, C., Zips, J., and Pfitzner, M. Single-phase instability in non-premixed flames under liquid rocket engine relevant conditions. *Journal of Propulsion and Power*, 35(4):675–689, 2019.

8.1 Thermodynamic closure

For the thermodynamic representation of high-pressure hydrogen and methane flames, the SRK-EoS [296] is employed. In Fig. 8.1, the prediction capability is evaluated for the density of the pure fuels (H₂ and CH₄) and the pure oxidizer (O₂) at pressure and temperature conditions which are relevant for the present study. For all three fluids, a very good agreement between the prediction

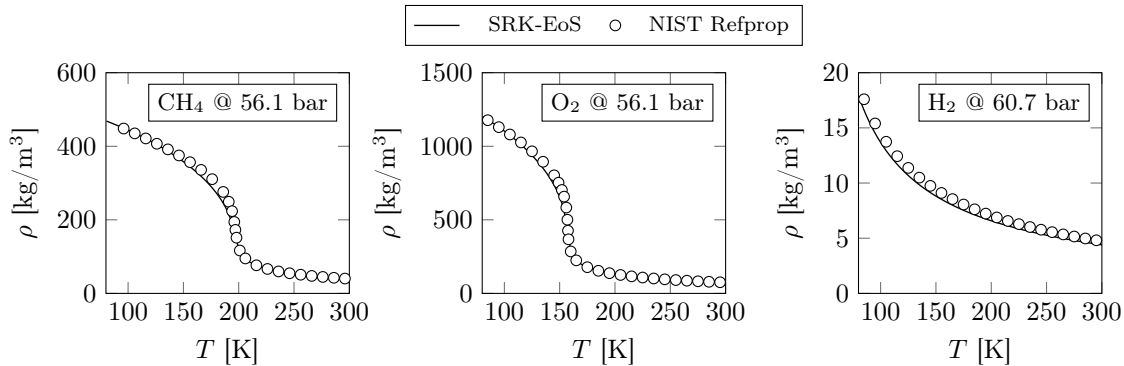


Figure 8.1: Comparison of the SRK-EoS [296] with reference data taken from NIST Refprop [164] for three different fluids (methane CH₄, oxygen O₂ and hydrogen H₂).

and the reference data from NIST Refprop [164] is found. Apart from the prediction of the thermodynamic single-phase properties, the accurate representation of the VLEs is of major importance in this study. In the pressure-composition diagrams in Figs. 6.30b, 6.32a and b, VLEs for the binary mixture of the two different fuels (hydrogen and methane) with nitrogen are shown. For both mixtures, the binary interaction parameter k_{ij} has been set to zero and the SRK-EoS [296] gives good results in the relevant pressure range ($p \lesssim 60$ bar). The third binary mixture, which is important for the present investigation, is oxygen/water (H₂O). This mixture occurs in the core of the flame where the cryogenic oxygen mixes with the combustion products. Water is a main combustion product and has a high critical temperature and pressure ($T_c = 647.1$ K and $p_c = 217.7$ bar) as well as strong hydrogen bondings. Due to the strongly associating character of water, cubic EoSs are usu-

ally not the optimal choice for a good prediction of its thermodynamic behavior [8]. However, the cubic EoSs are state of the art in the LRE community because of their relatively good accuracy for many fluids and mixtures and due to their efficiency. In Fig. 8.2, predicted and experimental data are compared for four different isopleths and the critical locus of the binary water/oxygen mixture. The solid lines correspond to $k_{ij} = 0$ and the dash-dotted lines to $k_{ij} = 0.3$. The binary water/oxygen mixture exhibits a critical locus of type III [335]. The comparison of the different binary interaction coefficients shows that a perfect fit of the experimental data with a single k_{ij} -value is not feasible. Using $k_{ij} = 0$ the critical locus can be predicted very well. By applying $k_{ij} = 0.3$ the predictions of the isopleths become more accurate but the calculated critical locus shows larger deviations from the experimental data. Furthermore, it has to be noticed that all the experimental data available in the literature [127] are for very large pressures ($p > 220$ bar). The operating conditions in the present test cases are however approximately 60 bar. Therefore, a sensitivity analysis for the binary interaction coefficient of water/oxygen within the flamelet calculation has been performed to assess its influence on the results. Four different binary interaction coefficients $k_{ij} = [0.0, 0.1, 0.2, 0.3]$ have been used for this analysis and no significant changes in the results were found. Therefore, $k_{ij} = 0.3$ is employed as binary interaction coefficient between water and oxygen as it fits the curve for $z_{\text{H}_2\text{O}} = 0.08$ in Fig. 8.2 very well and phase separation can only be expected at moderate temperature and hence low water mole fractions.

8.2 Test cases

The reference conditions investigated within this study are taken from two well-known combustion experiments. One is the experiment of Singla et al. [292] at the Mascotte test bench where methane is used as fuel. The other one is a model combustor named BKH [113] operated at the German Aerospace Center (DLR) Lampoldshausen which is fired with hydrogen. Both combustors are operated under rocket-relevant conditions. This implies that the pressure is supercritical with respect to the propellants' critical point and that the oxidizer is injected at a liquid-like state. The operating conditions of both test cases are listed in Tab. 8.1.

Table 8.1: Operating conditions of the considered LRE-like flames.

LOx/H ₂ flame						
p [MPa]	T_{O_2} [K]	T_{H_2} [K]	u_{O_2} [m/s]	u_{H_2} [m/s]	ρ_{O_2} [kg/m ³]	ρ_{H_2} [kg/m ³]
6.07	127	279	12.3	410	926.27	5.10
LOx/CH ₄ flame						
p [MPa]	T_{O_2} [K]	T_{CH_4} [K]	u_{O_2} [m/s]	u_{CH_4} [m/s]	ρ_{O_2} [kg/m ³]	ρ_{CH_4} [kg/m ³]
5.61	85	288	2.48	63.20	1180.08	41.79

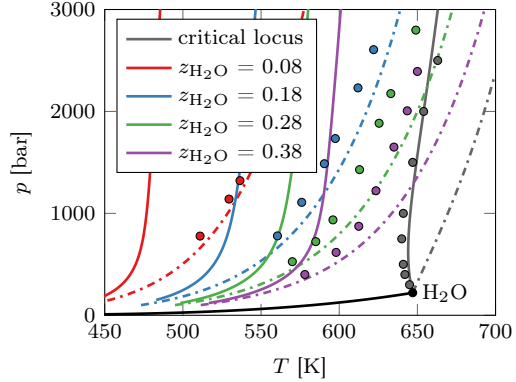


Figure 8.2: Validation of the binary water/oxygen mixture with experimental data [127] (solid: $k_{ij} = 0$; dash-dotted: $k_{ij} = 0.3$).

A sensitivity analysis for the binary interaction coefficient of water/oxygen within the flamelet calculation has been performed to assess its influence on the results. Four different binary interaction coefficients $k_{ij} = [0.0, 0.1, 0.2, 0.3]$ have been used for this analysis and no significant changes in the results were found. Therefore, $k_{ij} = 0.3$ is employed as binary interaction coefficient between water and oxygen as it fits the curve for $z_{\text{H}_2\text{O}} = 0.08$ in Fig. 8.2 very well and phase separation can only be expected at moderate temperature and hence low water mole fractions.

8.3 Counterflow diffusion flames

8.3.1 General discussion

For both nominal operating conditions listed in Tab. 8.1 laminar flamelet calculations have been performed with a scalar dissipation rate $\chi_{st} = 1 \text{ s}^{-1}$. In Fig. 8.3a, the temperature profiles of the two flames are plotted over the mixture fraction f . Two typical counterflow diffusion flame structures can be seen with a steep temperature gradient towards the oxidizer-rich side. The

maximum temperature is similar for both flames with different stoichiometric mixture fractions $f_{st,LOx/H_2} = 0.1111$ and $f_{st,LOx/CH_4} = 0.2$, respectively. Figure 8.3b shows the profiles of the density ρ and the compressibility factor Z of both counterflow diffusion flames. Especially for $f < 0.01$ (at the oxidizer-rich side) significant changes for both properties occur and the compressibility factor is unequal to unity. This can also be seen in the density profile which shows a strong decline over a small band in the mixture fraction space. At the fuel-rich side, real-gas effects ($Z \neq 1$) are also present. Looking at the pure fuels, methane has a compressibility factor of approximately 0.9 and hydrogen of 1.04 in the present test cases. Due to the steady temperature increase for $1 > f > f_{st}$ the real-gas feature gets lost gradually and therefore Z is close to one over a wide part of the mixture fraction space. Most of the mixing and combustion takes therefore place under almost ideal-gas conditions.

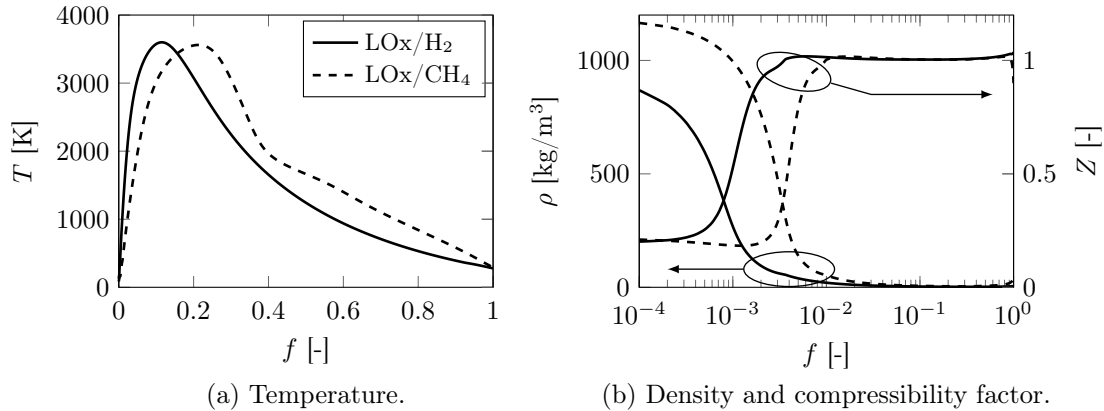


Figure 8.3: Results of the H_2 and CH_4 flames at a scalar dissipation rate $\chi_{st} = 1 \text{ s}^{-1}$.

8.3.2 Phase separation

Figure 8.4 shows the detailed analysis of the methane flame regarding phase separation. At both sides of the flamelet (oxidizer and fuel) the TPD analysis yields a negative value and therefore a phase separation was performed during the calculation of the flamelet. The separation of a second phase can be attributed to moderate temperatures and the presence of water in these two regions. On both sides the presence of H_2O is caused by diffusion as the reaction rate of water is almost

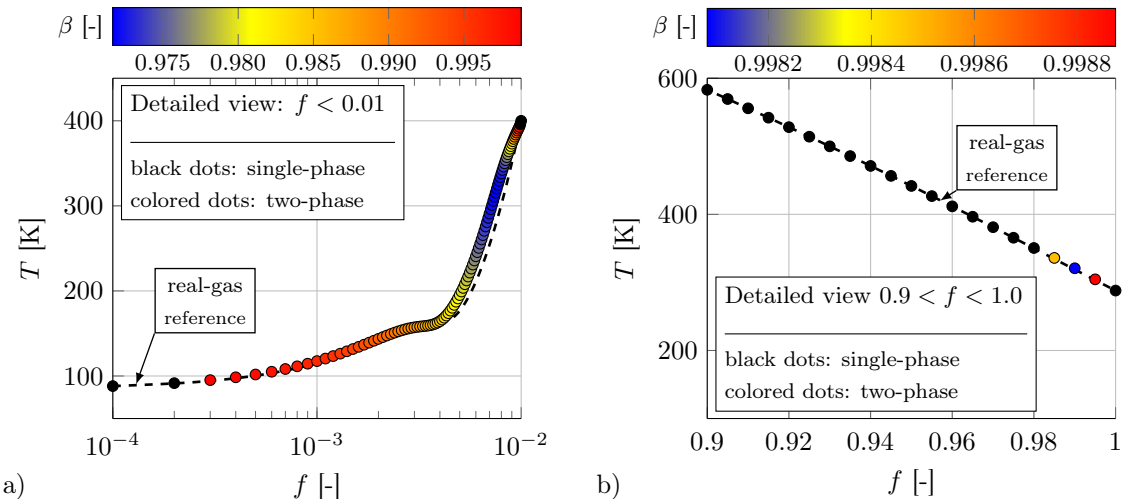


Figure 8.4: Thermodynamic analysis of the methane flamelet: a) Detailed view of the oxidizer-rich side; b) Detailed view of the fuel-rich side.

zero in these regions. Figure 8.4a shows a detailed view for $T < 450$ K and $f < 0.01$ by means of a scatter plot. Black dots indicate a homogeneous mixture and colored dots a two-phase state whereby the color corresponds to the vapor fraction β . As H_2O is the low volatile component in the mixture of the combustion products and only a small amount of it is present in the mixture, β is close to unity and ranges between 97% and 100%. Only three distinct points at the oxidizer side are in the single-phase state, namely $f = 0$ (pure oxygen, not shown in Fig. 8.4a), $f = 1 \times 10^{-4}$ and $f = 2 \times 10^{-4}$. All other points up to $f \approx 1 \times 10^{-2}$ have entered the VLE. Following the colored dots from left to right a continuous variation of β can be seen although the composition of the mixture varies due to diffusion and reaction. At $f = 3 \times 10^{-4}$ the dew-point line is crossed. Afterwards, the vapor fraction is reducing continuously until the minimum of approximately 0.97 is reached at $f \approx 8 \times 10^{-3}$. After the minimum is passed, β rises and the dew-point line is crossed again at $f \approx 1 \times 10^{-2}$. A similar behavior regarding the vapor fraction and the corresponding two-phase phenomena was found in Sec. 7.1 for the case T560 of the binary n-hexane/nitrogen mixture. On the fuel-rich side a very similar pattern occurs but here the vapor fraction drops only to a minimum of about 0.998 at $f \approx 0.99$, see Fig. 8.4b.

In both detailed views of Fig. 8.4 the real-gas reference case, i.e., without considering phase separation, is plotted as dashed line. The maximum difference in temperature occurs at the oxidizer-rich side and is approximately 50 K corresponding to a relative deviation of approximately 15%. For comparison, the maximum difference at the fuel-rich side is almost zero and hence negligible. Due to the consideration of the phase separation and hence the condensation of the fluid, the temperature of the two-phase case is larger. The entrainment into the VLE region has also an effect onto other thermodynamic properties. In Fig. 8.5, the real-gas and the two-phase solution are compared to each other for $f < 0.01$, where the largest deviations between both thermodynamic closures occur. The overall comparison reveals that the curve shapes are very similar but in the

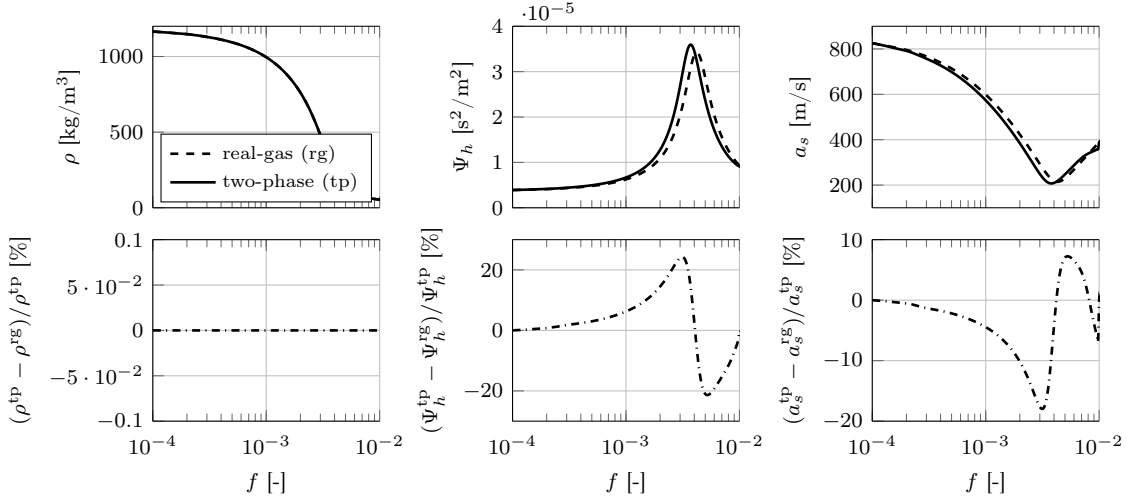


Figure 8.5: Comparison of the real-gas and the two-phase solution for the methane flamelet.

two-phase case they are shifted to lower mixture fractions. The shift leads to deviations up to approximately 20%. The main reason is the slightly higher temperature in the two-phase flamelet which is caused by the condensation of a small portion of gas indicated by β -values smaller than one. For derived properties like the compressibility and the speed of sound some additional features occur. As soon as the binodal is crossed, these properties can be subject to large changes as the fluid is not homogeneous anymore. In the present case, the speed of sound shows a slight drop when the VLE is entered. At the same position the compressibility has a discontinuity. Compared to the example of the Prudhoe Bay mixture (cf. Fig. 4.11) the drop in the sound velocity is minor and almost negligible for the methane flame. Therefore, the consideration of the phase equilibrium leads to higher temperatures in the region with phase separation and therefore to the shift in the characteristic values which can be attributed to the pseudo-boiling process in the real-gas case. Therefore, the solver stability is not significantly enhanced by considering the phase separation

process as it applies for inert injection cases. The reason for that is shown in Fig. 8.6a. Here, the results from the flamelet calculation are superimposed onto the VLE of the binary water/oxygen mixture. Note the logarithmic scale on the abscissa. The solid black line is the dew-point line and the dashed line the limit of stability. The metastable region is shown as a gray area. All of the scatter points lie within the metastable region. We therefore conclude that the homogeneity of the single-phase might continue although the VLE is entered as the phase separation process in this area is not triggered intrinsically. This agrees well with the only slight variation in thermodynamic properties, the stability of the solver and the general assumption of a supercritical combustion process. Similar results have been reported by Gaillard et al. [86] for a hydrogen/oxygen flame.

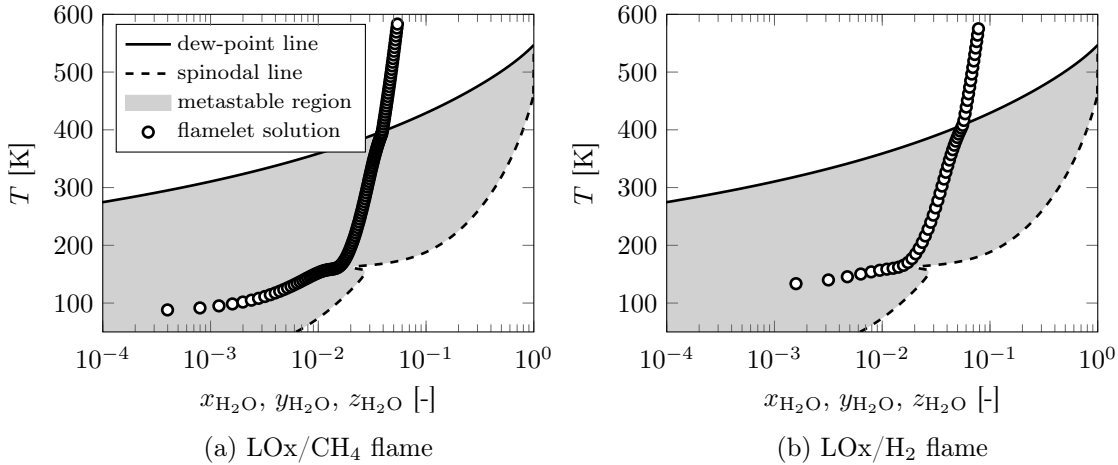


Figure 8.6: The flamelet results of the oxidizer-rich side superimposed onto the VLE of the binary mixture of water/oxygen at the appropriate pressure.

In Figs. 8.6b, 8.7 and 8.8, the phase separation effects occurring in the hydrogen counterflow diffusion flame of the LOx/H₂ test case are presented. The solution of the hydrogen flamelet leads to similar findings as the thoroughly discussed methane flamelet. Phase separation processes occur on both sides of the mixture fraction space and have similar effects on the solution and the derived thermodynamic properties.

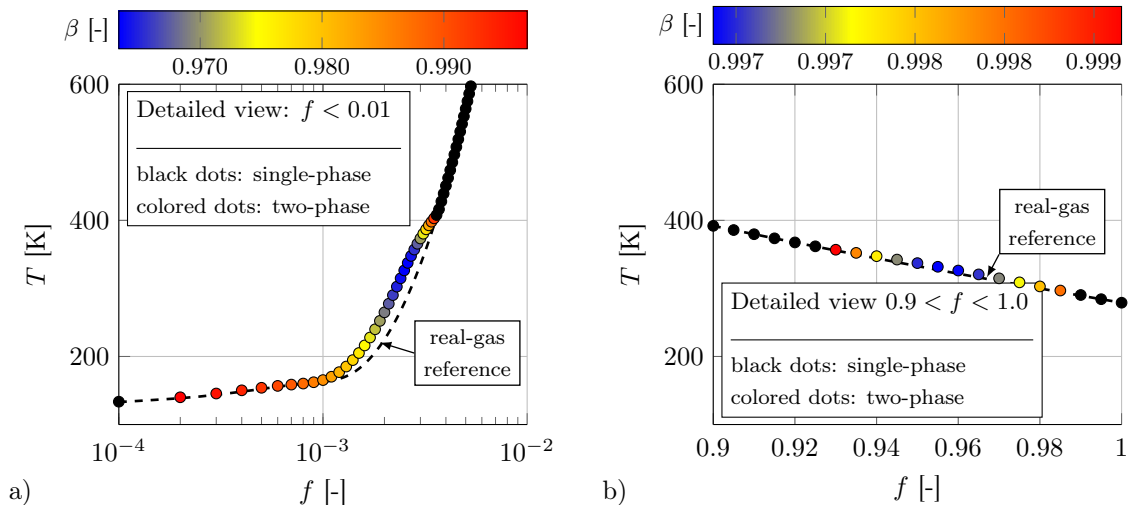


Figure 8.7: Thermodynamic analysis of the hydrogen flamelet: a) Detailed view of the oxidizer-rich side; b) Detailed view of the fuel-rich side.

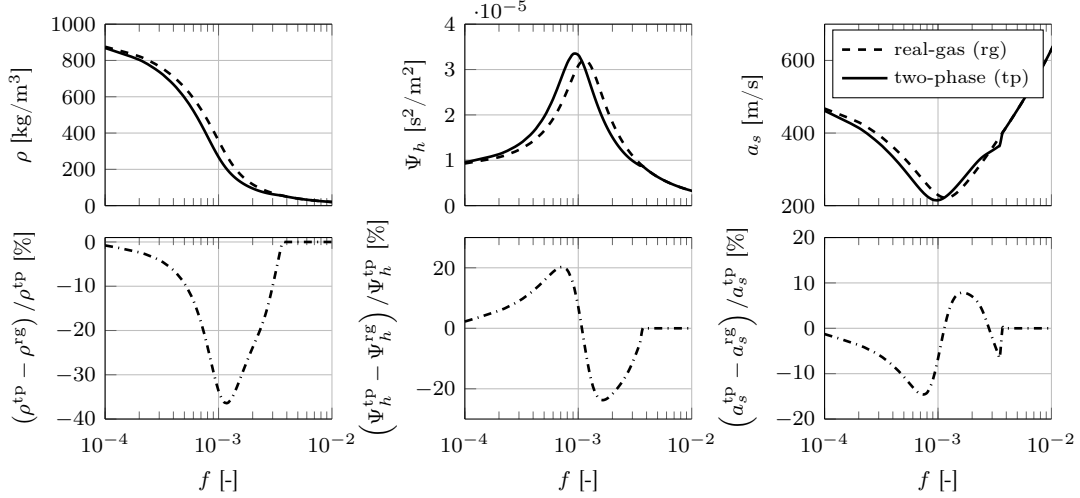


Figure 8.8: Comparison of the real-gas and the two-phase solution for the hydrogen flamelet.

8.4 Large-Eddy Simulation

8.4.1 Test case and numerical setup

For the evaluation of the role of real-gas and two-phase phenomena under rocket-like conditions, the combustion experiment of Singla et al. [292] conducted at the Mascotte test bench is chosen as a reference. This test case has previously been used by many other groups as validation case for numerical combustion simulations, see, e.g., Schmitt et al. [280, 279]. At an operating pressure of 56.1 bar, oxygen is injected in a liquid-like state at 85 K and the injection temperature of methane is 288 K, see Tab. 8.1. The combustion chamber is a 50 mm × 50 mm square duct with a length of 400 mm and a convergent-divergent nozzle at the outflow. Being a single-element test case, the propellants are supplied by one coaxial injection element with a 3.4 mm LOx pipe diameter, a CH₄ annulus height of 2.2 mm and a posttip width of 0.6 mm. As windows allow for optical access, Singla et al. [292] measured spontaneous emission of OH* and reported line-of-sight integrated results. The computational domain, see Fig. 8.9, is truncated after 150 mm. This length is sufficient to accommodate the flame and to avoid interactions with the outlet boundary. All walls are considered as adiabatic no-slip boundary conditions. Realistic turbulent inflow boundary conditions for LOx and CH₄ jets are generated using a separate incompressible LES at corresponding operating conditions with cyclic boundaries in axial direction. The turbulent velocity field of this precursor LES is extracted and interpolated in space and time onto the grid of the actual simulation. The grid consists of $\approx 16 \times 10^6$ cells with a minimum resolution at the injector of 0.2 mm in axial and 0.025 mm in radial direction. For more details on the grid and its resolution see the work of Zips et al. [368]. Figure 8.9 schematically shows the domain and the qualitative mesh resolution with reduced grid density. In Tab. 8.2, the numerical settings for the LES are summarized. The transcritical combustion model presented in Sec. 5 is employed. The table dimensions are $1011 \times 11 \times 7 \times 15$ in \tilde{f} , $\tilde{f}''^{1/2}$, $\tilde{\chi}_{st}$ and \tilde{p} .

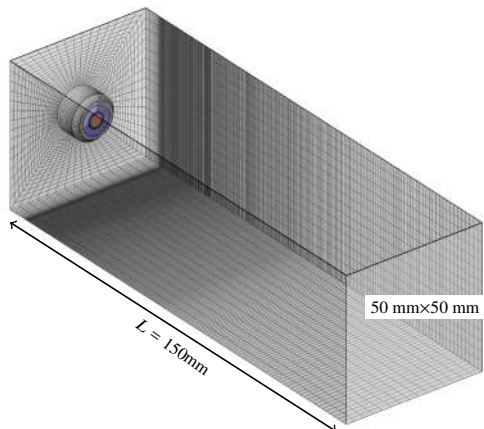


Figure 8.9: Computational domain of the LOx/CH₄ test case.

Table 8.2: Numerical solver setup for the investigation of the high-pressure combustion case.

Solver	TVD-limiter	Turbulence closure	EoS
pressure-based (subsonic)	van Leer [336]	LES with Vreman [341]	SRK-EoS [296]

8.4.2 General flame features

Figure 8.10 shows various instantaneous fields of the LOx/CH₄ flame using a central cut through the flame to provide a qualitative impression of the flame shape. The instantaneous temperature field, see Fig. 8.10a, shows that a thin diffusion flame emanates from the injector which is anchored at the posttip. The white line in Fig. 8.10a indicates the mixture fraction $f = 2 \times 10^{-4}$ and

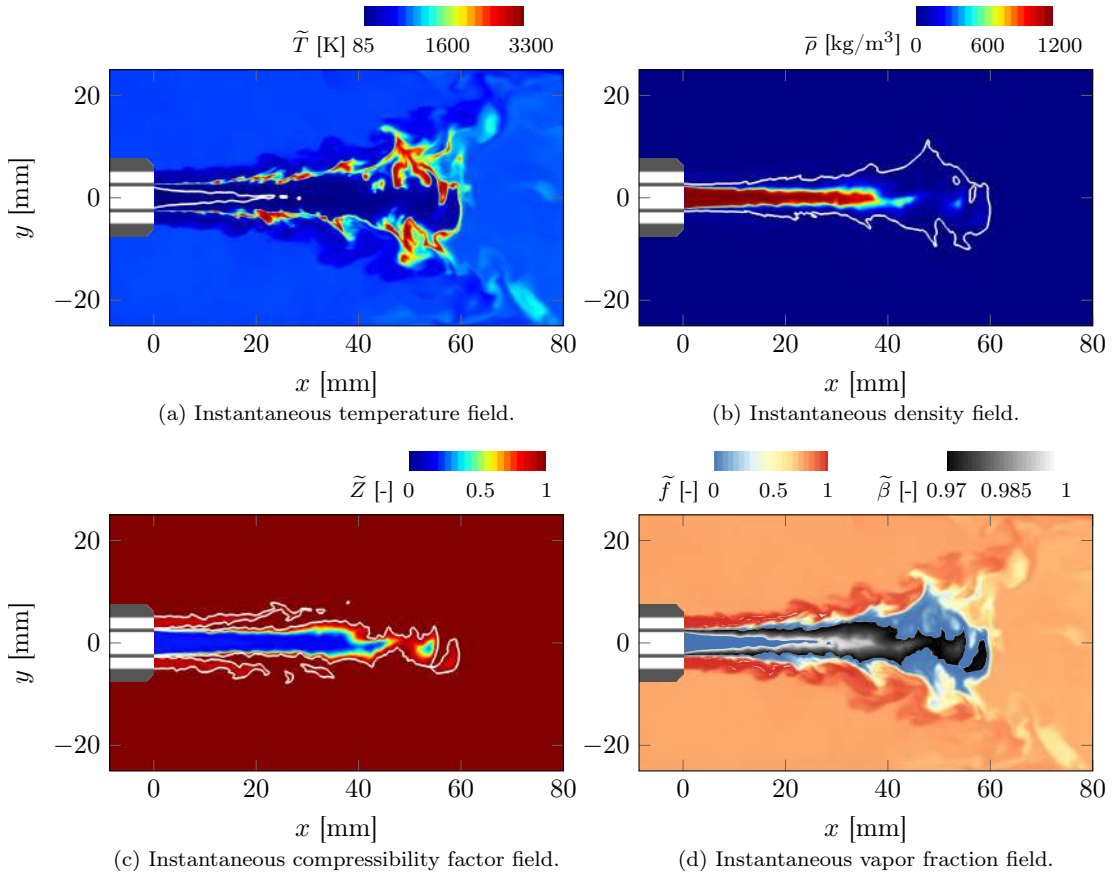


Figure 8.10: Instantaneous view of the LOx/CH₄ flame: The white line in (a) encloses the region of $f \leq 2 \times 10^{-4}$ and in (b) it represents the stoichiometric mixture fraction $f_{st} = 0.2$. In (c) the white line is drawn for $Z = 0.99$. In (d) the β -field is superimposed onto the mixture fraction field.

therefore encloses the region of (almost) pure oxygen. In Fig. 8.10b, the instantaneous density field is shown. Disintegration of the stable cold oxygen core starts at approximately 40 mm, where pockets of high-density fluid detach from the core and are transported downstream. There, they react with the surrounding fuel leading to the region of strongest chemical reactions. The white line in Fig. 8.10b denotes the stoichiometric mixture fraction $f_{st} = 0.2$ highlighting the position of the flame. In order to emphasize the real-gas character of the investigated flame, Fig. 8.10c shows the compressibility factor Z . The scale is truncated at unity and the region of real-gas behavior is highlighted by the white iso-line drawn for $Z = 0.99$. As already discussed based on Fig. 8.4, both the oxidizer as well as the fuel feature real-gas effects whereby the strongest deviation from the ideal gas state are present on the oxygen side.

8.4.3 Phase separation effects

Figure 8.10d shows the instantaneous vapor fraction field β superimposed onto the mixture fraction field f which is used to indicate the general flame structure and shape. In accordance to Fig. 8.4, β ranges between 97% and 100%. The largest region with phase separation is present within the LOx-core where combustion products and especially water mixes with the pure oxygen. Only for pure oxygen no phase separation was found as the injection and combustion is almost isobaric and therefore supercritical with respect to the critical point of oxygen. Minor areas of phase separation are also present around the pure fuel. In Fig. 8.10d, these regions are almost not visible, but Fig. 8.4b proves their presence as the counter-flow diffusion flame concept was used to build the thermo-chemical library accessed in the LES.

By comparing Figs. 8.10a, c and d it becomes obvious that the largest region of phase separation is enclosed by the iso-lines for $f = 2 \times 10^{-4}$ and for $Z = 0.99$. The resulting region is characterized by real-gas effects, moderate temperatures and the presence of water. In Fig. 8.11, these facts are further emphasized by means of scatter data extracted at five independent time steps in the mid-plane. Figure 8.11a shows the temperature T plotted over the H_2O mass fraction colored by the vapor fraction β . The scatter data form a kind of loop and the intersection separates the area of phase separation (left of the intersection) from the area with a homogeneous mixture. A very similar shape results for the scattering of the compressibility factor Z , see Fig. 8.11b. In this plot, the determination of the phase separation region for $Z \approx 1$ can be retraced in detail which is especially true for the oxidizer-rich side.

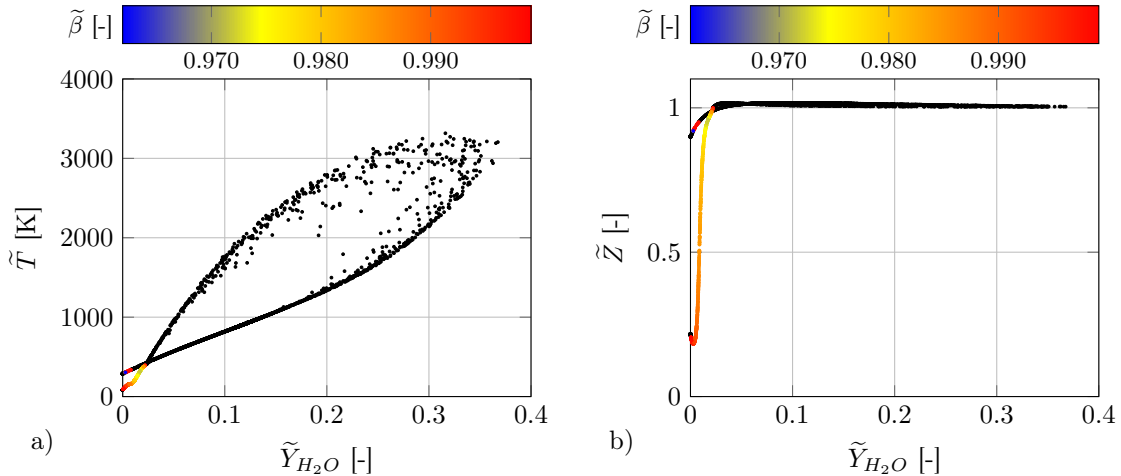


Figure 8.11: Scattered data from five independent time steps. States with phase separation are colored by the vapor mole fraction β . Black dots indicate a single-phase mixture or pure fluids.

8.4.4 Comparison with the experiment and the single-phase closure

For the present test case, experimental data is available from Singla et al. [292] in terms of OH^* emission images. In order to evaluate the numerical results the model of Fiala and Sattelmayer [76] is used to extract the OH^* emission from the simulation. Figure 8.12 compares the line-of-sight integrated OH^* radiation with the computational results. The characteristic flame shape is visible in both the simulations and the experiments. In the latter, a constant spreading angle is observed in the front part of the flame. Further downstream, expansion due to chemical conversion takes place and subsequently, an abrupt end of the reaction zone can be seen. The LES results properly reflect this behavior and a more detailed discussion on the characteristics of the flame shape can be found in the work of, for instance, Schmitt et al. [280, 279]. However, Singla et al. [292] did not publish the exact dimensions of the experimental field of view such that a more detailed validation is not possible. Nevertheless, the proportions of the flame in the LES in terms of shape and length indicate good agreement with the experiment.

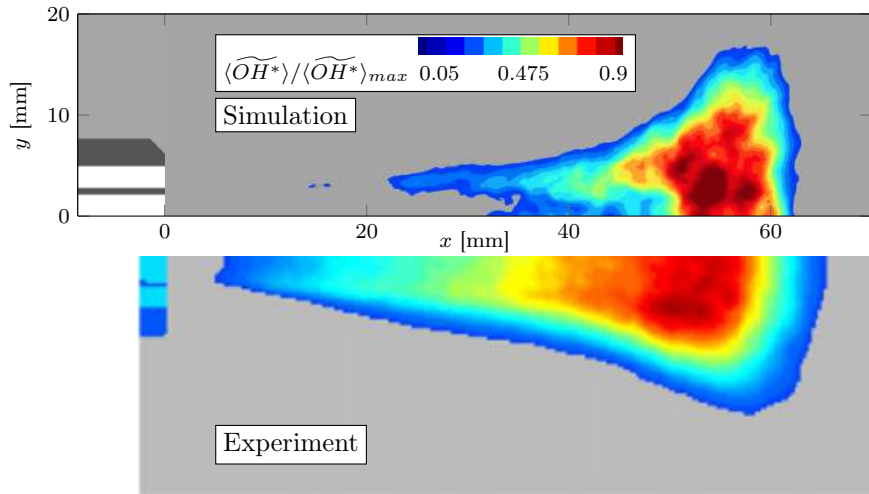


Figure 8.12: Line-of-sight integrated OH^* emission in comparison with the averaged experimental OH^* radiation of Singla et al. [292]; reprinted from Proceedings of the Combustion Institute, volume 30, Singla, G., Scouflaire, P., Rolon, C. and Candel, S., *Transcritical Oxygen/Transcritical or Supercritical Methane Combustion*, pp. 2921–2928, © (2005) with permission from Elsevier.

In comparison to the recent work of Zips et al. [368], where the same solver setup and the dense-gas approach is applied as thermodynamic closure, the flame shape and the overall results are almost identical. This is quite reasonable, as the a posteriori analysis of the flamelet results showed, that all thermodynamic states can be found in the stable or metastable region. Hence, the single-phase approach is applicable, as the physically forbidden (unstable) region of the VLE is not entered. Furthermore, the density was only marginally affected by the phase separation process and therefore the fluxes in the finite volume method remain almost identical.

8.5 Summary

In this final result section, the possibility of mixture-induced phase separation during high-pressure combustion in LOx/CH_4 and LOx/H_2 counterflow diffusion flames has been investigated. Pressure and propellant inlet temperatures have been set according to two well-known experiments featuring upper stage relevant conditions. General real-gas effects of the one-dimensional flames have been discussed for both propellant combinations. The phase separation analysis showed single-phase instabilities on both the oxidizer and the fuel side of the flamelets at moderate temperatures below $T \lesssim 400$ K. Stronger effects are observed at the oxidizer-rich side indicated by a minimum vapor fraction of approximately 0.97 compared to 0.998 at the fuel side in the case of LOx/CH_4 . For the LOx/H_2 case, similar results have been found.

By comparing the reference solution without phase separation to the result incorporating condensation effects, the following findings have been obtained: Deviations up to 40% between different thermodynamic properties have been found. However, the general profiles of the properties in mixture fraction space are not significantly affected by the phase separation process and therefore the deviations are mostly caused by a shift to lower mixture fraction values. The shift occurs due to the higher temperatures in the two-phase solution. These higher temperatures result from the gas condensation and the maximum difference in terms of the temperature is approximately 50 K. A comparison of the flamelet results with the vapor-liquid equilibrium of the binary water/oxygen mixture showed that the possible phase separation process is occurring within the metastable region. Therefore, phase separation is not triggered intrinsically. This in turn suggests that the widely applied dense-gas approach can be used as the physically forbidden (unstable) region of the VLE is not entered. In this area, the consideration of phase separation is essential as the homogeneity of the single phase is not given anymore.

The results of the one-dimensional LOx/CH₄ flames have been tabulated and used for the Large-Eddy Simulation of a single-element test case. The spatial extent of the phase separation phenomena is mostly restricted to a region around the LOx-core. This region is enclosed by the iso-line of almost pure oxygen and the transition to an ideal gas state. Line-of-sight integrated OH* emission images indicate that both flame length and shape are in good agreement with the experimental results. As expected from the one-dimensional analysis, the consideration of phase separation has no significant effect on the results and yields almost identical results compared to the dense-gas approach without phase separation.

Part IV

SUMMARY AND OUTLOOK

9 Summary

The focal point of this work is put on the numerical investigation of real-gas effects and phase separation phenomena during the injection, mixing and combustion process under high-pressure conditions. In particular, operating conditions like they occur in liquid-propellant rocket engines and gas engines are focused. In such energy conversion machines elevated pressure conditions are preferred to extract the maximum technical useful energy from the applied fuel and convert it to thrust or mechanical power. Usually, the operating pressure easily exceeds the critical point of the pure fluids, i.e., fuel and oxidizer. Therefore, injection, mixing and combustion take place under conditions which are initially supercritical with respect to the pure fluids. At such pressure conditions, the application of the ideal gas model is invalid. Real-gas effects are present and the fluid properties depend on both temperature and pressure. As a result of the initially supercritical pressure conditions, the dense-gas model is widely applied to model the thermodynamic behavior of both the pure fluids and the mixtures. This modeling approach takes into account real-gas effects but assumes a single-phase state. Recent experimental and numerical investigations, however, suggest that this assumption has to be questioned and further careful studies are necessary to better understand the possible occurrence of phase separation processes under initially supercritical pressure conditions.

Challenges

Three major challenges had to be tackled in this work to investigate the thermodynamic behavior of the fluids and the mixtures under LRE- and GE-like operating conditions:

1. Depending on the pressure ratio between fuel reservoir and mixing/combustion chamber, different fluid dynamic injection characteristics arise which have to be handled by the numerical solver. In LREs, subsonic – low Mach number – flow conditions are present yielding challenges with respect to the pressure-velocity coupling. Under GE-like injection conditions, high nozzle pressure ratios are present resulting in underexpanded – high Mach number – jets which are accompanied by strong expansion and shock structures. A pressure-based solver framework is presented in this work which enables the simulation of both flow problems. In the subsonic approach, real-gas thermodynamics is taken into account within the solver formulation to stabilize the CFD tool. For the simulation of high-speed jets, a hybrid pressure-based approach is applied. Here, the hyperbolic pressure equation is augmented with a central-upwind scheme to increase the robustness of the flow solver. In addition to these pressure-based solvers, a density-based double flux method is employed. Under real-gas and multicomponent conditions, such approaches are quite popular as they suppress spurious pressure oscillations. A flux-vector splitting scheme is applied which allows the simulation of low and high Mach number flows.
2. The operating conditions in LREs and GEs cover a wide range of thermodynamic states. In LREs, the oxidizer is injected at cryogenic temperatures and initially supercritical pressure conditions, i.e., in a liquid-like state. Afterwards a transcritical process takes place in which the fluid transitions from this high density state towards a gas-like (low density) state by interacting with its surrounding (mixing and heating). In GEs, underexpanded fluid jets are a common feature yielding strong variations in pressure and temperature. Phase separation processes can occur under both LRE- and GE-like operating conditions. To represent and cover all these possible scenarios in a single thermodynamic closure, a framework is presented in this work which relies on a rigorous and fully conservative description of the thermodynamic state. This is highly important for the stability of the numerical solver and enables at the same time a sound investigation of the thermodynamic states within high-pressure injection, mixing and combustion processes. The thermal and caloric closure are based on the cubic equations of state and the departure function formalism. This thermodynamic framework enables an accurate but also efficient description of the fluid state. The occurrence of a

possible multicomponent phase separation process is evaluated rigorously by means of a minimization of the Gibbs energy. This includes two separate evaluation procedures: a detection of the crossing of the binodal and a flashing approach yielding the composition of the liquid and the vapor phase.

3. Many LREs are operated with liquid-like oxygen and hydrogen. Recently, a lot of research effort is put into the better understanding of LOx/methane combustion. This propellant combination is a promising candidate for the reusability of LREs associated with significantly lower costs for space cargo transportation. However, LOx/CH₄ combustion involves a large number of species and reactions. This, in turn, results in a huge numerical effort making tabulated combustion models a promising candidate for the efficient numerical simulation and investigation of high-pressure combustion. Under LRE-typical conditions, i.e., non-premixed combustion, tabulation approaches based on the flamelet concept are widely used. In this work, a flamelet tabulation method specifically tailored for real-gas and high-pressure conditions is employed and coupled with the developed thermodynamic framework. The resulting combustion model facilitates the investigation of the possibility of single-phase instabilities during the combustion process under LRE-like operating conditions.

Using the developed CFD tools, real-gas effects and phase separation processes under GE- and LRE-like operating conditions are investigated in this work by means of numerical simulations. Overall, five different experimental test campaigns from the literature are employed to validate the numerical framework and lay a solid basis for more thorough and further investigations. For most of the simulations, the pressure-based solver framework is applied. Both Large-Eddy Simulations and Reynolds-Averaged Navier-Stokes simulations are performed.

Mixing under supersonic flow conditions

The first part of the results focuses on injection and mixing processes in extremely underexpanded jets. The applied reference experiments are taken from the literature and have been conducted at the Institute of Aerospace Thermodynamics at the University of Stuttgart. Here, a high fidelity test bench featuring a cylindrical constant-volume test chamber is available. A single-hole injector is mounted into the front side end wall. Temperature, pressure and purity of the fluids (injectant and chamber) can be controlled accurately and three quartz windows provide optical access into the test chamber. Eight different test cases are used in this work where speed of sound measurements along the centerline of the chamber are available in the literature. In all applied test cases, n-hexane is injected into a quiescent nitrogen atmosphere. RANS simulations of these cases are conducted in this work. A very good agreement is found between the experimental data and the simulation results. Especially in the region of the fully developed jet, the agreement is excellent. Using the available numerical data base, the influence of real-gas effects on the jet mixing process is studied in detail. The most important finding is that the reservoir and the post-shock temperature are not identical as it is the case under ideal gas conditions. For the present case, an average difference of approximately 70 K is found. This, in turn, results in highly different temperatures and speed of sound values downstream of the Mach disk when comparing the ideal and real gas closure to each other. Therefore, real-gas effects have to be taken into account fully consistently to accurately predict the mixing process. In this context, it is important to define the thermodynamic states rigorously when recalculating thermodynamic properties from, for instance, single-point speed of sound measurements. Based on these findings, an adiabatic mixing model is outlined. The mass fractions evaluated a posteriori from the measured sound velocities based on this mixing model collapse nicely to the present simulation results.

In the next part, the phase separation process in an extremely underexpanded jet is studied. Recent experimental investigations from the literature are employed where argon is injected through a single-hole injector into its own gas phase. From these experimental investigations, flow field and Mie scattering measurements are available. A Large-Eddy Simulation of this test case is conducted within this work. With regard to the flow field, the CFD results and the experiments agree well. Especially the near-nozzle flow field is captured accurately. In terms of the phase separation processes, an excellent agreement with the experimental measurements is found. Within the fully developed jet, the single-phase instabilities occur downstream of the nozzle exit and upstream of

the Mach disk. Hence, the region of two-phase states is confined by the characteristic shock barrel. Downstream of the Mach disk, no phase separation is present anymore, as the normal shock results in a large pressure and temperature recovery bringing the jet back into a single-phase (pure gas) state. The further evaluation of the numerical results shows that the underexpansion is even such strong that it crosses the triple point of argon. Therefore, the occurrence of a solid phase is possible but cannot be represented by the applied cubic equation of state.

Based on the thorough validation of the CFD tool within the first two parts, phase separation processes under GE-relevant operating conditions are investigated in the third part of the results. Two GE-typical fuels are considered: a hydrogen-based and a methane-based fuel. Three different test cases are defined to study the influence of the pressure ratio and of the fuel on the possibility of phase separation processes. For both methane-based test cases strong phase separation effects across large parts of the jet structure are found. A thorough analysis indicates that the single-phase instability is triggered by two mechanisms: In the jet center, the large underexpansion results in the crossing of the binodal similar to the pure argon jet. In the traveling spherical vortex at the jet tip, ambient gas mixes into the fuel and a combined expansion and dilution process yields an entry into the vapor-liquid equilibrium region. Reducing the nozzle pressure ratio in the methane-based fuel yields weaker two phase effects. Changing the injected fuel from methane- to hydrogen-based, the phase separation processes vanish. The reason for this disappearance is the drastically decreased critical temperature of the low volatile component of the mixture. In the hydrogen-based fuel, temperatures far below 100 K are necessary to trigger single-phase instabilities. Finally, the temporal development of the jet penetration depth is studied. The hydrogen-based fuel jet follows common theoretical approaches in the literature. In contrast, the methane-based jets strongly deviate from the common theory due to the permanent presence of two-phase effects within the jet. Here, an almost linear increase of the jet penetration depth in time is found. This is in contrast to ordinary single-phase jets which show a dependency on the square root of time.

Mixing under subsonic flow conditions

In a combined experimental and numerical study in close cooperation with the ITLR at the University of Stuttgart, mixture-induced phase separation processes under initially supercritical injection conditions are investigated. Using the identical experimental test facility as for the underexpanded n-hexane jets, the same fuel is injected at subsonic and almost isobaric flow conditions into the test chamber filled with nitrogen at rest. In the experiments, simultaneous shadowgraphy and elastic light scattering measurements are conducted to assess both the flow structure as well as the phase separation. Numerical investigations are performed by means of Large-Eddy Simulations. Three different test cases are defined based on the adiabatic mixing concept considering phase separation processes. The injection temperatures of n-hexane are selected such that they lead to regimes in which the occurrence of phase separation is possible and triggered gradually by lowering the injection temperature. The characteristics of the phase formation process agree well between experiments and numerical simulations. Both show phase separation phenomena for the identical injection conditions. Consequently, the transition from a dense-gas to a spray-like jet is captured by both the experiment and the numerical simulations.

Based on the good agreement of the previous investigation, the prediction capability of the QC density-based solver is assessed. The focal point is put on the predicted thermodynamic mixing trajectories of the density- and the pressure-based solvers. In the first step, a single-phase subsonic test case is used where a large number of experimental speed of sound measurements are available in the literature. Again, the experiments have been conducted at the ITLR and n-hexane is injected into nitrogen at rest. The numerical results of an LES using the FC pressure-based solver show a very good agreement with the experimental sound velocities. In contrast, the results generated with the density-based solver by means of a 2D planar simulation clearly deviate from the FC results. Large parts of the scatter data are located in the vapor-liquid equilibrium region of the binary mixture so that the speed of sound evaluation is not feasible. Using both high temperature test cases from the combined experimental and numerical study, the possibly nonphysical prediction of the QC scheme can be further confirmed. In conclusion, it is found that a fully-conservative solver and the adiabatic mixture model are most suitable for an estimation of the thermodynamic mixing trajectory of the jet mixing process in the present cases.

Single-phase instability in high-pressure combustion

In the final result part of this work, the possibility of phase separation processes during the high-pressure combustion under LRE-like operating conditions is assessed. The reference conditions are taken from two well-known experiments for LOx/hydrogen and LOx/methane combustion. First, nominal flamelet results are considered. Single-phase instabilities are found on both the oxidizer-rich and the fuel-rich side of the flamelet whereby the more pronounced effects occur on the oxygen side. The phase separation process can be attributed to the moderate temperatures and the presence of water. The a posteriori analysis of the phase separation processes shows that the thermodynamic states lie in the metastable region of the binary water/oxygen mixture. Therefore, the occurrence of a second phase is not triggered intrinsically. The results of the methane flame are tabulated and applied in a single element test case. An LES is conducted and the results show that the spatial extent of the phase separation phenomena are mostly restricted to the region around the LOx-core. Finally, line-of-sight integrated OH* emission images indicate that both flame length and shape are in good agreement with the experimental results.

10 Outlook

Based on the results of this work starting points for future investigations can be derived. Some ideas and potentially new fields of research are outlined below:

- More thorough investigations on the mixing process under LRE-like conditions using both the FC and QC solvers are necessary. Although very good agreement for the FC pressure-based solver is found in the present work with many experimental investigations, it is not clear if these findings hold when different fluids and operating conditions are considered. In this context, the influence and effect of more sophisticated transport models might be a key to new findings and a better understanding of the mixing process.
- The LES sub-grid models applied in this work and by many other researchers in the LRE and GE community have been derived originally for atmospheric flows. First a priori DNS studies of, for instance, Unnikrishnan et al. [329, 328] showed that the interaction between turbulence and real-gas thermodynamics yields not negligible contributions which should be reflected by the applied SGS model.
- The implementation of the applied thermodynamic framework is quite cumbersome and prone to errors. In addition, the evaluation of the TPD method and the subsequent flash is very costly. Therefore, the VLE model is currently limited to academic research. The application of tabulation methods or artificial neural networks are promising candidates to speed up the evaluation of the thermodynamic state and to give access to these approaches to a broader community and group of interest. In this context, preliminary investigations of Ge et al. [89] showed first promising results in the field of real-gas thermodynamics.
- The presence of phase separation processes motivates the consideration of surface tension effects within the numerical framework. In this context, some researchers [86, 275] recently focused on diffuse interface models based on the second gradient theory. On the one hand, these models enable the resolution of the gas/liquid interface. On the other hand, the additional terms introduced by the second gradient theory might help to further stabilize the flow solver under real-gas conditions, see, e.g., Gaillard et al. [86]. By introducing the Korteweg tensor into the momentum and energy equation, a universal tool for the simulation of sub- and supercritical injection and combustion processes might be formulated.
- The application of the VLE model in cavitating flows is another interesting field of research. Up to now, many investigations rely on simplified thermodynamic models like, for instance, the Tait equation [278, 277] or stiffened gas EoSs [275]. Using the thermodynamic VLE model presented in this work, a fully consistent framework could be applied to this flow problems which at its best is able to account for non-condensable gases. First own investigations showed that the newly implemented density-based solver is able to handle such flow problems. Here, the double-flux method can be dropped as the AUSM⁺-up scheme for all speeds is already suited well for cavitating flows, see, e.g., Edwards et al. [70].
- With regard to the underexpanded jet test cases, it would be interesting to test the capability of density-based solvers. On the one hand, density-based solvers employing the KNP and KT flux schemes are already available in the standard OpenFOAM libraries. To enable the simulation of the present test cases, these solvers have to be extended to multicomponent flows and real-gases. On the other hand, the newly implemented density-based solver can be tested and further developed in this context. Here, the application of the double-flux formulation should not be necessary and a fully conservative formulation can be used.
- The pressure-based solver could be further stabilized by applying a Newton linearization of the mass flux. For supersonic flows, this was recently demonstrated by, for instance, Xiao et al. [359] or Hanemann et al. [112]. Also the application of a fully coupled algorithm instead of the current segregated approach could further increase the stability. First implementations of a coupled pressure-based algorithm have been demonstrated recently by Uroic [330].

- The implementation of more general and sophisticated EoSs might be necessary to extend the present investigations to other fluids, e.g., fluoroketone. Here, the three parameter EoS due to Cismondi and Mollerup [53] is a first good step which is basically a blend between the SRK-EoS [296] and PR-EoS [226].
- In the field of combustion, two different topics could be tackled in the future: First, doubly transcritical combustion cases can be investigated with the current framework. Own a priori studies showed strong two-phase effects on both sides of the flame. A thorough numerical investigation might help to better understand the resulting flame shape and combustion process. Second, the implemented VLE model can be coupled with a tabulated non-adiabatic combustion model. Non-adiabatic flamelet models have been recently implemented and validated in OpenFOAM by Zips et al. [367, 369, 370] for ideal-gas flows. Combining this approach with the current thermodynamic framework, real-gas effects and condensation processes in, for instance, the wall-near region can be investigated.

Bibliography

- [1] OpenFOAM 4.1. <https://www.openfoam.org/version/4-1/>, 2016.
- [2] OpenFOAM v1806. <https://www.openfoam.com/releases/openfoam-v1806/>, 2018.
- [3] Abgrall, R. How to prevent pressure oscillations in multicomponent flow calculations: A quasi conservative approach. *Journal of Computational Physics*, 125(1):150–160, 1996.
- [4] Abgrall, R. and Karni, S. Computations of compressible multifluids. *Journal of Computational Physics*, 169(2):594–623, 2001.
- [5] Abraham, J. Entrapment characteristics of transient gas jets. *Numerical Heat Transfer, Part A Applications*, 30(4):347–364, 1996.
- [6] Anderko, A. Equation-of-state methods for the modelling of phase equilibria. *Fluid Phase Equilibria*, 61(1-2):145–225, 1990.
- [7] Anderson, J. D. *Computational Fluid Dynamics*. McGraw-Hill, New York, 1995.
- [8] Aparicio-Martínez, S. and Hall, K. R. Phase equilibria in water containing binary systems from molecular based equations of state. *Fluid Phase Equilibria*, 254(1-2):112–125, 2007.
- [9] Arp, V., Persichetti, J. M., and Guo-bang, C. The Grüneisen parameter in fluids. *Journal of Fluids Engineering*, 106(2):193–200, 1984.
- [10] Arrhenius, S. Über die Reaktionsgeschwindigkeit bei der Inversion von Rohrzucker durch Säuren. *Zeitschrift für physikalische Chemie*, 4(1):226–248, 1889.
- [11] Ashkenas, H. and Sherman, F. S. Structure and utilization of supersonic free jets in low density wind tunnels. Technical report, National Aeronautics and Space Administration, 1965.
- [12] Awad, M. and Muzychka, Y. Effective property models for homogeneous two-phase flows. *Experimental Thermal and Fluid Science*, 33(1):106–113, 2008.
- [13] Baab, S., Förster, F. J., Lamanna, G., and Weigand, B. Combined elastic light scattering and two-scale shadowgraphy of near critical fuel jets. In *26th Annual Conference on Liquid Atomization and Spray Systems*, 2014.
- [14] Baab, S., Förster, F. J., Lamanna, G., and Weigand, B. Speed of sound measurements and mixing characterization of underexpanded fuel jets with supercritical reservoir condition using laser-induced thermal acoustics. *Experiments in Fluids*, 57(11):172, 2016.
- [15] Baab, S., Lamanna, G., and Weigand, B. Two-phase disintegration of high-pressure retrograde fluid jets at near-critical injection temperature discharged into a subcritical pressure atmosphere. *International Journal of Multiphase Flow*, 107:116–130, 2018.
- [16] Baab, S., Steinhausen, C., Lamanna, G., Weigand, B., and Förster, F. J. A quantitative speed of sound database for multi-component jet mixing at high pressure. *Fuel*, 233:918–925, 2018.
- [17] Bader, G. and Deuflhard, P. A semi-implicit mid-point rule for stiff systems of ordinary differential equations. *Numerische Mathematik*, 41(3):373–398, 1983.
- [18] Baehr, H. D. and Kabelac, S. *Thermodynamik*. Springer, Berlin, 2012.
- [19] Baker, L. E., Pierce, A. C., and Luks, K. D. Gibbs energy analysis of phase equilibria. *Society of Petroleum Engineers Journal*, 22(05):731–742, 1982.
- [20] Banholzer, M. *Numerische Modellierung und Untersuchung der Hochdruckeindüsung nicht-idealener Fluide bei überkritischen Druckverhältnissen*. PhD thesis, Universität der Bundeswehr München, 2019.

- [21] Banholzer, M., Müller, H., and Pfitzner, M. Numerical investigation of the flow structure of underexpanded jets in quiescent air using real-gas thermodynamics. *23rd AIAA Computational Fluid Dynamics Conference*, 2017.
- [22] Banuti, D. T., Ma, P. C., Hickey, J. P., and Ihme, M. Sub- or supercritical? A flamelet analysis of high pressure rocket propellant injection. In *52nd AIAA/SAE/ASEE Joint Propulsion Conference*, 2016.
- [23] Banuti, D. T., Ma, P. C., Hickey, J.-P., and Ihme, M. Thermodynamic structure of supercritical LOX–GH₂ diffusion flames. *Combustion and Flame*, 196:364–376, 2018.
- [24] Banuti, D. T., Ma, P. C., and Ihme, M. Phase separation analysis in supercritical injection using large-eddy-simulation and vapor-liquid-equilibrium. In *53rd AIAA/SAE/ASEE Joint Propulsion Conference*, 2017.
- [25] Beegle, B. L., Modell, M., and Reid, R. C. Legendre transforms and their application in thermodynamics. *AIChE Journal*, 20(6):1194–1200, 1974.
- [26] Beegle, B. L., Modell, M., and Reid, R. C. Thermodynamic stability criterion for pure substances and mixtures. *AIChE Journal*, 20(6):1200–1206, 1974.
- [27] Bell, I., Wronski, J., Quoilin, S., and Lemort, V. Pure and pseudo-pure fluid thermophysical property evaluation and the open-source thermophysical property library CoolProp. *Industrial & Engineering Chemistry Research*, 53(6):2498–2508, 2014.
- [28] Bellan, J. Supercritical (and subcritical) fluid behavior and modeling: Drops, streams, shear and mixing layers, jets and sprays. *Progress in Energy and Combustion Science*, 26(4-6):329–366, 2000.
- [29] Bellan, J. Future challenges in the modelling and simulations of high-pressure flows. *Combustion Science and Technology*, 192(7):1199–1218, 2020.
- [30] Benedict, M., Webb, G. B., and Rubin, L. C. An empirical equation for thermodynamic properties of light hydrocarbons and their mixtures I. Methane, ethane, propane and n-butane. *The Journal of Chemical Physics*, 8(4):334–345, 1940.
- [31] Bhaskar, V., Prakash, R. H., and Prasad, B. D. Hydrogen fuelled ic engine—an overview. *IJITR*, 1(1):046–053, 2013.
- [32] Billet, G. and Abgrall, R. An adaptive shock-capturing algorithm for solving unsteady reactive flows. *Computers & Fluids*, 32(10):1473–1495, 2003.
- [33] Billet, G. and Ryan, J. A Runge–Kutta discontinuous Galerkin approach to solve reactive flows: The hyperbolic operator. *Journal of Computational Physics*, 230(4):1064–1083, 2011.
- [34] Billingsley, D. S. and Lam, S. Critical point calculation with nonzero interaction parameters. *AIChE Journal*, 32(8):1393–1396, 1986.
- [35] Birch, A., Brown, D., Dodson, M., and Swaffield, F. The structure and concentration decay of high pressure jets of natural gas. *Combustion Science and Technology*, 36(5-6):249–261, 1984.
- [36] Birch, A., Hughes, D., and Swaffield, F. Velocity decay of high pressure jets. *Combustion Science and Technology*, 52(1-3):161–171, 1987.
- [37] Blazek, J. *Computational Fluid Dynamics: Principles and Applications*. Elsevier, Amsterdam, 2005.
- [38] Bloomer, O. T. and Parent, J. D. Liquid-vapor phase behavior of the methane-nitrogen system. In *Chemical Engineering Progress Symposium Series*, volume 49, pages 11–24, 1953.
- [39] Bonelli, F., Viggiano, A., and Magi, V. A numerical analysis of hydrogen underexpanded jets under real gas assumption. *Journal of Fluids Engineering*, 135(12), 2013.
- [40] Cabrit, O. and Nicoud, F. Direct simulations for wall modeling of multicomponent reacting compressible turbulent flows. *Physics of Fluids*, 21(5):055108, 2009.
- [41] Callen, H. B. *Thermodynamics*. Wiley, New York, 1960.

- [42] Castier, M. Thermodynamic speed of sound in multiphase systems. *Fluid Phase Equilibria*, 306(2):204–211, 2011.
- [43] Castiglioni, G. and Bellan, J. On models for predicting thermodynamic regimes in high-pressure turbulent mixing and combustion of multispecies mixtures. *Journal of Fluid Mechanics*, 843:536–574, 2018.
- [44] Chang, S. and Lu, B. C. Y. Vapor-liquid equilibria in the nitrogen-methane-ethane system. In *Chemical Engineering Progress Symposium Series*, volume 63. University of Ottawa, Ontario, 1967.
- [45] Chehroudi, B. Recent experimental efforts on high-pressure supercritical injection for liquid rockets and their implications. *International Journal of Aerospace Engineering*, 2012, 2012.
- [46] Cheng, Z., Agranat, V., Tchouvelev, A., Houf, W., and Zhubrin, S. PRD hydrogen release and dispersion, a comparison of CFD results obtained from using ideal and real gas law properties. In *International Conference on Hydrogen Safety*, 2005.
- [47] Choi, D. and Merkle, C. L. Application of time-iterative schemes to incompressible flow. *AIAA Journal*, 23(10):1518–1524, 1985.
- [48] Chorin, A. J. A numerical method for solving incompressible viscous flow problems. *Journal of Computational Physics*, 2(1):12–26, 1967.
- [49] Chou, G. F. and Prausnitz, J. M. A phenomenological correction to an equation of state for the critical region. *AIChE Journal*, 35(9):1487–1496, 1989.
- [50] Chung, T. H., Ajlan, M., Lee, L. L., and Starling, K. E. Generalized multiparameter correlation for nonpolar and polar fluid transport properties. *Industrial & Engineering Chemistry Research*, 27(4):671–679, 1988.
- [51] Chung, T. H., Lee, L. L., and Starling, K. E. Applications of kinetic gas theories and multiparameter correlation for prediction of dilute gas viscosity and thermal conductivity. *Industrial & Engineering Chemistry Fundamentals*, 23(1):8–13, 1984.
- [52] Cines, M. R., Roach, J. T., Hogan, R. J., and Roland, C. H. Nitrogen-methane vapor-liquid equilibria. In *Chemical Engineering Progress Symposium Series*, volume 49, pages 1–10, 1953.
- [53] Cismonti, M. and Mollerup, J. Development and application of a three-parameter RK-PR equation of state. *Fluid Phase Equilibria*, 232(1-2):74–89, 2005.
- [54] Cook, A. and Cabot, W. Hyperviscosity for shock-turbulence interactions. *Journal of Computational Physics*, 203(3):2133–2144, 2005.
- [55] Crist, S., Glass, D. R., and Sherman, P. M. Study of the highly underexpanded sonic jet. *AIAA Journal*, 4(1):68–71, 1966.
- [56] Cutrone, L. *Predicting reactive flows for propulsion applications using a flamelet/progress-variable approach*. PhD thesis, Politecnico di Bari, 2009.
- [57] Dahms, R. N., Manin, J., Pickett, L. M., and Oefelein, J. C. Understanding high-pressure gas-liquid interface phenomena in Diesel engines. *Proceedings of the Combustion Institute*, 34(1):1667–1675, 2013.
- [58] Dahms, R. N. and Oefelein, J. C. On the transition between two-phase and single-phase interface dynamics in multicomponent fluids at supercritical pressures. *Physics of Fluids*, 25(9):092103, 2013.
- [59] Darwish, M. and Moukalled, F. A unified formulation of the segregated class of algorithms for fluid flow at all speeds. *Numerical Heat Transfer: Part B: Fundamentals*, 37(1):103–139, 2000.
- [60] Darwish, M. and Moukalled, F. TVD schemes for unstructured grids. *International Journal of Heat and Mass Transfer*, 46(4):599–611, 2003.
- [61] De Boer, C., Bonar, G., Sasaki, S., and Shetty, S. Application of supercritical gasoline injection to a direct injection spark ignition engine for particulate reduction. Technical report, SAE Technical Paper, 2013.

- [62] Debenedetti, P. G. *Metastable Liquids: Concepts and Principles*. Princeton University Press, Princeton, 1996.
- [63] Delplanque, J.-P. and Sirignano, W. A. Numerical study of the transient vaporization of an oxygen droplet at sub- and super-critical conditions. *International Journal of Heat and Mass Transfer*, 36(2):303–314, 1993.
- [64] Demirbas, A. *Methane Gas Hydrate*. Springer, London, 2010.
- [65] DeSouza, S. and Segal, C. Sub- and supercritical jet disintegration. *Physics of Fluids*, 29(4):047107, 2017.
- [66] Domingo, P., Vervisch, L., and Veynante, D. Large-eddy simulation of a lifted methane jet flame in a vitiated coflow. *Combustion and Flame*, 152:415–432, 2008.
- [67] Drikakis, D. and Tsangaritis, S. On the solution of the compressible Navier-Stokes equations using improved flux vector splitting methods. *Applied Mathematical Modelling*, 17(6):282–297, 1993.
- [68] Eaton, B. Calculation of critical points by the method of Heidemann and Khalil. Technical report, NBS Technical Note 1313, 1988.
- [69] Echekki, T. and Mastorakos, E. *Turbulent Combustion Modeling: Advances, New Trends and Perspectives*. Springer, Berlin, 2010.
- [70] Edwards, J. R., Franklin, R. K., and Liou, M.-S. Low-diffusion flux-splitting methods for real fluid flows with phase transitions. *AIAA Journal*, 38(9):1624–1633, 2000.
- [71] Edwards, J. R., Lin, K., Ryan, M., and Carter, C. Simulation of supercritical ethylene condensation using homogeneous nucleation theory. In *48th AIAA Aerospace Sciences Meeting Including the New Horizons Forum and Aerospace Exposition*, 2010.
- [72] Eliosa-Jiménez, G., Silva-Oliver, G., García-Sánchez, F., and de Ita de la Torre, A. High-pressure vapor-liquid equilibria in the nitrogen + n-hexane system. *Journal of Chemical & Engineering Data*, 52(2):395–404, 2007.
- [73] Elliott, J. R. and Lira, C. T. *Introductory Chemical Engineering Thermodynamics*. Prentice Hall, New Jersey, 2012.
- [74] Ewan, B. and Moodie, K. Structure and velocity measurements in underexpanded jets. *Combustion Science and Technology*, 45(5-6):275–288, 1986.
- [75] Ferziger, J. H. and Perić, M. *Computational Methods for Fluid Dynamics*. Springer, Berlin, 2002.
- [76] Fiala, T. and Sattelmayer, T. Assessment of existing and new modeling strategies for the simulation of OH* radiation in high-temperature flames. *CEAS Space Journal*, 8(1):47–58, 2016.
- [77] Firoozabadi, A. *Thermodynamics and Applications of Hydrocarbon Energy Production*. McGraw-Hill Education, New York, 2016.
- [78] Firoozabadi, A. and Pan, H. Two-phase isentropic compressibility and two-phase sonic velocity for multicomponent-hydrocarbon mixtures. *SPE Reservoir Evaluation & Engineering*, 3(4):335–341, 2000.
- [79] Fond, B., Xiao, C., T’Joen, C., Henkes, R., Veenstra, P., van Wachem, B. G. M., and Beyrau, F. Investigation of a highly underexpanded jet with real gas effects confined in a channel: Flow field measurements. *Experiments in Fluids*, 59(10):160, 2018.
- [80] Förster, F. J., Baab, S., Steinhäusen, C., Lamanna, G., Ewart, P., and Weigand, B. Mixing characterization of highly underexpanded fluid jets with real gas expansion. *Experiments in Fluids*, 59(3):44, 2018.
- [81] Franquet, E., Perrier, V., Gibout, S., and Brûlé, P. Free underexpanded jets in a quiescent medium: A review. *Progress in Aerospace Sciences*, 77:25–53, 2015.
- [82] Friedrichs, K. O. Symmetric hyperbolic linear differential equations. *Communications on Pure and Applied Mathematics*, 7(2):345–392, 1954.

- [83] Fröhlich, J. *Large Eddy Simulation turbulenter Strömungen*. Teubner, Wiesbaden, 2006.
- [84] Fuller, E. N., Ensley, K., and Giddings, J. C. Diffusion of halogenated hydrocarbons in helium. The effect of structure on collision cross sections. *The Journal of Physical Chemistry*, 73(11):3679–3685, 1969.
- [85] Fuller, E. N., Schettler, P. D., and Giddings, J. C. New method for prediction of binary gas-phase diffusion coefficients. *Industrial & Engineering Chemistry*, 58(5):18–27, 1966.
- [86] Gaillard, P., Giovangigli, V., and Matuszewski, L. A diffuse interface Lox/hydrogen trans-critical flame model. *Combustion Theory and Modelling*, 20(3):486–520, 2016.
- [87] Gaillard, P., Giovangigli, V., and Matuszewski, L. Nonmixing layers. *Physical Review Fluids*, 1(8):084001, 2016.
- [88] Garnier, E., Adams, N., and Sagaut, P. *Large Eddy Simulation for Compressible Flows*. Springer Science + Business Media, 2009.
- [89] Ge, Y., Hansinger, M., Traxinger, C., and Pfitzner, M. Deep residual learning applied to real-gas thermodynamics. In *AIP Conference Proceedings*, volume 2040. AIP Publishing LLC, 2018.
- [90] Gerold, J., Vogl, P., and Pfitzner, M. New correlation of subsonic, supersonic and cryo gas jets validated by highly accurate Schlieren measurements. *Experiments in Fluids*, 54(6):1542, 2013.
- [91] Gibbs, J. W. On the equilibrium of heterogeneous substances, part I. *Transactions of the Connecticut Academy of Arts and Sciences*, III, 1876.
- [92] Giovangigli, V., Matuszewski, L., and Gaillard, P. High pressure flames with multicomponent transport. In Bellan, J., editor, *High-Pressure Flows for Propulsion Applications*, pages 485–529. American Institute of Aeronautics and Astronautics, 2020.
- [93] Gnanaskandan, A. and Bellan, J. Numerical simulation of jet injection and species mixing under high-pressure conditions. In *Journal of Physics: Conference Series*, volume 821, page 012020. IOP Publishing, 2017.
- [94] Godlewski, E. and Raviart, P.-A. *Numerical Approximation of Hyperbolic Systems of Conservation Laws*. Springer, Berlin, 1996.
- [95] Godunov, S. K. A difference method for numerical calculation of discontinuous solutions of the equations of hydrodynamics. *Matematicheskii Sbornik*, 89(3):271–306, 1959.
- [96] Goodwin, D. G., Speth, R. L., Moffat, H. K., and Weber, B. W. Cantera: An object-oriented software toolkit for chemical kinetics, thermodynamics, and transport processes. <https://www.cantera.org>, 2018. Version 2.4.0.
- [97] Goos, E., Burcat, A., and Ruscic, B. Report ANL 05/20 TAE 960. Technical report, 2005. <http://burcat.technion.ac.il/dir>.
- [98] Gorlé, C. and Ham, F. Investigation of an underexpanded hydrogen jet in quiescent air using numerical simulations and experiments. *Annual Research Briefs, Center of Turbulence Research*, 2010.
- [99] Gorlé, C. and Iaccarino, G. Large eddy and Reynolds-averaged Navier-Stokes simulations of an underexpanded sonic jet. In *7th European Symposium on Aerothermodynamics*, volume 692, page 146, 2011.
- [100] Greenshields, C. J. *OpenFOAM Programmer's Guide*. 2015.
- [101] Greenshields, C. J., Weller, H. G., Gasparini, L., and Reese, J. M. Implementation of semi-discrete, non-staggered central schemes in a colocated, polyhedral, finite volume framework, for high-speed viscous flows. *International Journal for Numerical Methods in Fluids*, 63(1):1–21, 2010.
- [102] GRI-Mech 3.0. www.me.berkeley.edu/grimech/. University of California at Berkeley, 2000.

- [103] Gross, J. and Sadowski, G. Perturbed-chain SAFT: An equation of state based on a perturbation theory for chain molecules. *Industrial & Engineering Chemistry Research*, 40(4):1244–1260, 2001.
- [104] Hah, C. A Navier-Stokes analysis of three-dimensional turbulent flows inside turbine blade rows at design and off-design conditions. *Journal of Engineering for Gas Turbines and Power*, 106:421–429, 1984.
- [105] Hah, C. Navier-Stokes calculation of three-dimensional compressible flow across a cascade of airfoils with an implicit relaxation method. In *24th Aerospace Sciences Meeting*, 1986.
- [106] Haidn, O. J., Adams, N. A., Radespiel, R., Schröder, W., Stemmer, C., Sattelmayer, T., and Weigand, B. Fundamental technologies for the development of future space transportsystem components under high thermal and mechanical loads. In *2018 Joint Propulsion Conference*, 2018.
- [107] Haldenwang, P., Nicoli, C., and Daou, J. High pressure vaporization of LOX droplet crossing the critical conditions. *International Journal of Heat and Mass Transfer*, 39(16):3453–3464, 1996.
- [108] Hamzehloo, A. and Aleiferis, P. G. Large eddy simulation of highly turbulent under-expanded hydrogen and methane jets for gaseous-fuelled internal combustion engines. *International Journal of Hydrogen Energy*, 39(36):21275–21296, 2014.
- [109] Hamzehloo, A. and Aleiferis, P. G. Gas dynamics and flow characteristics of highly turbulent under-expanded hydrogen and methane jets under various nozzle pressure ratios and ambient pressures. *International Journal of Hydrogen Energy*, 41(15):6544–6566, 2016.
- [110] Hamzehloo, A. and Aleiferis, P. G. Numerical modelling of transient under-expanded jets under different ambient thermodynamic conditions with adaptive mesh refinement. *International Journal of Heat and Fluid Flow*, 61:711–729, 2016.
- [111] Hamzehloo, A. and Aleiferis, P. G. LES and RANS modelling of under-expanded jets with application to gaseous fuel direct injection for advanced propulsion systems. *International Journal of Heat and Fluid Flow*, 76:309–334, 2019.
- [112] Hanimann, L., Mangani, L., Casartelli, E., Vogt, D. M., and Darwish, M. Real gas models in coupled algorithms numerical recipes and thermophysical relations. *International Journal of Turbomachinery, Propulsion and Power*, 5(3), 2020.
- [113] Hardi, J. S., Beinke, S., Oschwald, M., and Dally, B. B. Coupling of cryogenic oxygen-hydrogen flames to longitudinal and transverse acoustic instabilities. *Journal of Propulsion and Power*, 30(4):991–1004, 2014.
- [114] Harstad, K. and Bellan, J. Global analysis and parametric dependencies for potential unintended hydrogen-fuel releases. *Combustion and Flame*, 144(1-2):89–102, 2006.
- [115] Harten, A. On the symmetric form of systems of conservation laws with entropy. *Journal of Computational Physics*, 49:151–164, 1983.
- [116] Harten, A., Lax, P. D., and van Leer, B. On upstream differencing and Godunov-type schemes for hyperbolic conservation laws. *SIAM Review*, 25(1):35–61, 1983.
- [117] Heidemann, R. A. and Khalil, A. M. The calculation of critical points. *AICHE Journal*, 26(5):769–779, 1980.
- [118] Hempert, F., Boblest, S., Ertl, T., Sadlo, F., Offenhäuser, P., Glass, C., Hoffmann, M., Beck, A., Munz, C.-D., and Iben, U. Simulation of real gas effects in supersonic methane jets using a tabulated equation of state with a discontinuous Galerkin spectral element method. *Computers & Fluids*, 145:167–179, 2017.
- [119] Hill, P. G. and Ouellette, P. Transient turbulent gaseous fuel jets for Diesel engines. *Journal of Fluids Engineering*, 121:93–101, 1999.
- [120] Hirsch, C. *Numerical Computation of Internal and External Flows*. Butterworth-Heinemann, Oxford, 1997.

- [121] Hirschfelder, J. O., Curtiss, C. F., Bird, R. B., and Mayer, M. G. *Molecular Theory of Gases and Liquids*. John Wiley & Sons, New York, 1964.
- [122] Holzmann, T. *Mathematics, Numerics, Derivations and OpenFOAM®*. Holzmann CFD, Loeben, 2016.
- [123] Hu, E., Huang, Z., Liu, B., Zheng, J., Gu, X., and Huang, B. Experimental investigation on performance and emissions of a spark-ignition engine fuelled with natural gas–hydrogen blends combined with EGR. *International Journal of Hydrogen Energy*, 34(1):528–539, 2009.
- [124] Idicheria, C. A. and Pickett, L. M. Quantitative mixing measurements in a vaporizing Diesel spray by Rayleigh imaging. *SAE Transactions*, 116:490–504.
- [125] Issa, R. and Lockwood, F. On the prediction of two-dimensional supersonic viscous interactions near walls. *AIAA Journal*, 15(2):182–188, 1977.
- [126] Issa, R. I., Gosman, A. D., and Watkins, A. P. The computation of compressible and incompressible recirculating flows by a non-iterative implicit scheme. *Journal of Computational Physics*, 62(1):66–82, 1986.
- [127] Japas, M. L. and Franck, E. High pressure phase equilibria and PVT-data of the water–oxygen system including water-air to 673 K and 250 MPa. *Berichte der Bunsengesellschaft für physikalische Chemie*, 89(12):1268–1275, 1985.
- [128] Jarczyk, M. M. *Numerische Modellierung von turbulenten Strömungen realger Gasgemische*. PhD thesis, Universität der Bundeswehr München, 2013.
- [129] Jarczyk, M. M. and Pfitzner, M. Large eddy simulation of supercritical nitrogen jets. In *50th AIAA Aerospace Sciences Meeting including the New Horizons Forum and Aerospace Exposition*, 2012.
- [130] Jasak, H. *Error analysis and estimation for the finite volume method with applications to fluid flows*. PhD thesis, Imperial College London (University of London), 1996.
- [131] Jasak, H., Weller, H., and Gosman, A. High resolution NVD differencing scheme for arbitrarily unstructured meshes. *International Journal for Numerical Methods in Fluids*, 31(2):431–449, 1999.
- [132] Jones, W. P. and Launder, B. The calculation of low-Reynolds-number phenomena with a two-equation model of turbulence. *International Journal of Heat and Mass Transfer*, 16(6):1119–1130, 1973.
- [133] Juanós, A. J. and Sirignano, W. A. Pressure effects on real-gas laminar counterflow. *Combustion and Flame*, 181:54–70, 2017.
- [134] Kalikmanov, V. *Nucleation Theory*. Springer, Berlin, 2013.
- [135] Karni, S. Multicomponent flow calculations by a consistent primitive algorithm. *Journal of Computational Physics*, 112(1):31–43, 1994.
- [136] Kay, W. B. Critical locus curve and the phase behavior of mixtures. *Accounts of Chemical Research*, 1(11):344–351, 1968.
- [137] Kemenov, K., Wang, H., and Pope, S. Modelling effects of subgrid-scale mixture fraction variance in LES of a piloted diffusion flame. *Combustion Theory and Modelling*, 16(4):611–638, 2012.
- [138] Khaksarfard, R., Kameshki, M. R., and Paraschivoiu, M. Numerical simulation of high pressure release and dispersion of hydrogen into air with real gas model. *Shock Waves*, 20(3):205–216, 2010.
- [139] Khalil, I. and Miller, D. R. The structure of supercritical fluid free-jet expansions. *AICHE Journal*, 50(11):2697–2704, 2004.
- [140] Kidnay, A. J., Miller, R. C., Parrish, W. R., and Hiza, M. J. Liquid-vapour phase equilibria in the N₂ CH₄ system from 130 to 180 K. *Cryogenics*, 15(9):531–540, 1975.
- [141] Kim, K., Kim, H., Kim, B., and Lee, K. Effect of natural gas composition on the performance of a CNG engine. *Oil & Gas Science and Technology-Revue de l'IFP*, 64(2):199–206, 2009.

- [142] Kim, T., Kim, Y., and Kim, S. Effects of pressure and inlet temperature on coaxial gaseous methane/liquid oxygen turbulent jet flame under transcritical conditions. *The Journal of Supercritical Fluids*, 81:164–174, 2013.
- [143] Kraposhin, M., Bovtrikova, A., and Strijhak, S. Adaptation of Kurganov-Tadmor numerical scheme for applying in combination with the PISO method in numerical simulation of flows in a wide range of Mach numbers. *Procedia Computer Science*, 66:43–52, 2015.
- [144] Kunz, O., Klimeck, R., Wagner, W., and Jaeschke, M. The GERG-2004 wide-range equation of state for natural gases and other mixtures. In *GERG TM15*, volume 6. Fortschritt-Berichte VDI, 2007.
- [145] Kunz, O. and Wagner, W. The GERG-2008 wide-range equation of state for natural gases and other mixtures: An expansion of GERG-2004. *Journal of Chemical & Engineering Data*, 57(11):3032–3091, 2012.
- [146] Kuo, K. K. *Principles of Combustion*. John Wiley & Sons, New Jersey, 2005.
- [147] Kuo, K. K. and Acharya, R. *Fundamentals of Turbulent and Multiphase Combustion*. John Wiley & Sons, New Jersey, 2012.
- [148] Kurganov, A. Central schemes: A powerful black-box solver for nonlinear hyperbolic PDEs. In *Handbook of Numerical Analysis*, volume 17, pages 525–548. Elsevier, 2016.
- [149] Kurganov, A., Noelle, S., and Petrova, G. Semidiscrete central-upwind schemes for hyperbolic conservation laws and Hamilton–Jacobi equations. *SIAM Journal on Scientific Computing*, 23(3):707–740, 2001.
- [150] Kurganov, A. and Petrova, G. A third-order semi-discrete genuinely multidimensional central scheme for hyperbolic conservation laws and related problems. *Numerische Mathematik*, 88(4):683–729, 2001.
- [151] Kurganov, A. and Petrova, G. Central-upwind schemes on triangular grids for hyperbolic systems of conservation laws. *Numerical Methods for Partial Differential Equations: An International Journal*, 21(3):536–552, 2005.
- [152] Kurganov, A. and Tadmor, E. New high-resolution central schemes for nonlinear conservation laws and convection–diffusion equations. *Journal of Computational Physics*, 160(1):241–282, 2000.
- [153] Lacaze, G., Misdariis, A., Ruiz, A., and Oefelein, J. C. Analysis of high-pressure Diesel fuel injection processes using LES with real-fluid thermodynamics and transport. *Proceedings of the Combustion Institute*, 35(2):1603–1611, 2015.
- [154] Lacaze, G. and Oefelein, J. C. A non-premixed combustion model based on flame structure analysis at supercritical pressures. *Combustion and Flame*, 159(6):2087–2103, 2012.
- [155] Lacaze, G. and Oefelein, J. C. Modeling high-density-gradient flows at supercritical pressures. In *49th AIAA/ASME/SAE/ASEE Joint Propulsion Conference*. 2013.
- [156] Lacaze, G., Schmitt, T., Ruiz, A., and Oefelein, J. C. Comparison of energy-, pressure- and enthalpy-based approaches for modeling supercritical flows. *Computers & Fluids*, 181:35–56, 2019.
- [157] Lallemand, M.-H. Dissipative properties of Runge-Kutta schemes with upwind spatial approximation for the Euler equations. *Rapport de Recherche INRIA*, No. 1173, 1990.
- [158] Lamanna, G., Oldenhof, E., Baab, S., Stotz, I., and Weigand, B. Disintegration regimes near the critical point. In *18th AIAA/3AF International Space Planes and Hypersonic Systems and Technologies Conference*, 2012.
- [159] Lapenna, P. E. *Mixing and non-premixed combustion at supercritical pressures*. PhD thesis, University of Rome, 2016.
- [160] Lapenna, P. E., Ciottoli, P. P., and Creta, F. Unsteady non-premixed methane/oxygen flame structures at supercritical pressures. *Combustion Science and Technology*, 189(12):2056–2082, 2017.

- [161] Launchbury, D. R. *Unsteady Turbulent Flow Modelling and Applications*. Springer, Berlin, 2016.
- [162] Lautrup, B. *Physics of Continuous Matter: Exotic and Everyday Phenomena in the Macroscopic World*. Taylor & Francis Group, Boca Raton, 2011.
- [163] Lax, P. D. Weak solutions of nonlinear hyperbolic equations and their numerical computation. *Communications on Pure and Applied Mathematics*, 7(1):159–193, 1954.
- [164] Lemmon, E. W., , Bell, I. H., Huber, M. L., and McLinden, M. O. NIST standard reference database 23: Reference fluid thermodynamic and transport properties-REFPROP, version 10.0, National Institute of Standards and Technology, 2018.
- [165] Lemmon, E. W., Huber, M. L., and McLinden, M. NIST standard reference database 23: Reference fluid thermodynamic and transport properties-REFPROP, version 9.1, National Institute of Standards and Technology, 2013.
- [166] Leschziner, M. A. Reynolds-averaged Navier–Stokes methods. *Encyclopedia of Aerospace Engineering*, 2010.
- [167] LeVeque, R. J. *Finite Volume Methods for Hyperbolic Problems*. Cambridge University Press, Cambridge, 2004.
- [168] Lilly, K. *The representation of small-scale turbulence in numerical simulation experiments*. 1966.
- [169] Lin, K.-C., Cox-Stouffer, S., and Jackson, T. Structures and phase transition processes of supercritical methane/ethylene mixtures injected into a subcritical environment. *Combustion Science and Technology*, 178(1-3):129–160, 2006.
- [170] Lin, K.-C., Cox-Stouffer, S., Kennedy, P., and Jackson, T. Expansion of supercritical methane/ethylene jets in a quiescent subcritical environment. In *41st Aerospace Sciences Meeting and Exhibit*, 2003.
- [171] Liou, M.-S. A sequel to AUSM, part II: AUSM+-up for all speeds. *Journal of Computational Physics*, 214(1):137–170, 2006.
- [172] Liou, M.-S. The evolution of AUSM schemes. *Defence Science Journal*, 60(6), 2010.
- [173] Liou, M.-S. and Steffen Jr., C. J. A new flux splitting scheme. *Journal of Computational Physics*, 107(1):23–39, 1993.
- [174] Litchford, R. and Jeng, S.-M. LOX vaporization in high-pressure, hydrogen-rich gas. In *26th Joint Propulsion Conference*, 1990.
- [175] Looijmans, K., Luijten, C., Hofmans, G., and Van Dongen, M. Classical binary nucleation theory applied to the real mixture n-nonane/methane at high pressures. *The Journal of Chemical Physics*, 102(11):4531–4537, 1995.
- [176] Lüdecke, D. and Lüdecke, C. *Thermodynamik: Physikalisch-chemische Grundlagen der thermischen Verfahrenstechnik*. Springer, Berlin, 2000.
- [177] Ma, P. C., Lv, Y., and Ihme, M. An entropy-stable hybrid scheme for simulations of trans-critical real-fluid flows. *Journal of Computational Physics*, 340:330–357, 2017.
- [178] Ma, P. C., Wu, H., Banuti, D. T., and Ihme, M. On the numerical behavior of diffuse-interface methods for transcritical real-fluids simulations. *International Journal of Multiphase Flow*, 113:231–249, 2019.
- [179] Manin, J., Bardi, M., Pickett, L. M., Dahms, R., and Oefelein, J. Microscopic investigation of the atomization and mixing processes of Diesel sprays injected into high pressure and temperature environments. *Fuel*, 134:531–543, 2014.
- [180] Manrique, J. A. and Borman, G. L. Calculations of steady state droplet vaporization at high ambient pressures. *International Journal of Heat and Mass Transfer*, 12(9):1081–1095, 1969.
- [181] Márquez Damián, S., Nigro, N. M., and Buscaglia, G. C. A central scheme for advecting scalars by velocity fields obtained from finite volume multiphase incompressible solvers. *Applied Mathematical Modelling*, 40(15-16):6934–6955, 2016.

- [182] Martin, J. J. Equations of state. *Industrial & Engineering Chemistry*, 59(12):34–52, 1967.
- [183] Martin, J. J. Cubic equations of state - which? *Industrial & Engineering Chemistry Fundamentals*, 18(2):81–97, 1979.
- [184] Masi, E., Bellan, J., Harstad, K. G., and Okong'o, N. A. Multi-species turbulent mixing under supercritical-pressure conditions: Modelling, direct numerical simulation and analysis revealing species spinodal decomposition. *Journal of Fluid Mechanics*, 721:578–626, 2013.
- [185] Mattheis, J. and Hickel, S. Multi-component vapor-liquid equilibrium model for LES of high-pressure fuel injection and application to ECN Spray A. *International Journal of Multiphase Flow*, 99:294–311, 2018.
- [186] Mattheis, J., Müller, H., Lenz, C., Pfitzner, M., and Hickel, S. Volume translation methods for real-gas computational fluid dynamics simulations. *The Journal of Supercritical Fluids*, 107:422–432, 2016.
- [187] Mausbach, P., Köster, A., Rutkai, G., Thol, M., and Vrabec, J. Comparative study of the Grüneisen parameter for 28 pure fluids. *The Journal of Chemical Physics*, 144(24):244505, 2016.
- [188] Mayer, W., Ivancic, B., Schik, A., and Hornung, U. Propellant atomization in LOX/GH2 rocket engines. In *34th AIAA/ASME/SAE/ASEE Joint Propulsion Conference and Exhibit*, 1998.
- [189] Mayer, W., Schik, A. H., Vielle, B., Chauveau, C., Gokalp, I., Talley, D. G., and Woodward, R. D. Atomization and breakup of cryogenic propellants under high-pressure subcritical and supercritical conditions. *Journal of Propulsion and Power*, 14(5):835–842, 1998.
- [190] Mayer, W., Telaar, J., Branam, R., Schneider, G., and Hussong, J. Raman measurements of cryogenic injection at supercritical pressure. *Heat and Mass Transfer*, 39(8-9):709–719, 2003.
- [191] Menter, F. Improved two-equation $k-\omega$ turbulence models for aerodynamic flows. *NASA Technical Memorandum*, 103975, 1992.
- [192] Menter, F. and Esch, T. Elements of industrial heat transfer predictions. In *16th Brazilian Congress of Mechanical Engineering (COBEM)*, volume 109, 2001.
- [193] Menter, F. R., Kuntz, M., and Langtry, R. Ten years of industrial experience with the SST turbulence model. *Turbulence, Heat and Mass Transfer*, 4(1):625–632, 2003.
- [194] Michelsen, M. L. The isothermal flash problem. Part I. Stability. *Fluid Phase Equilibria*, 9(1):1–19, 1982.
- [195] Michelsen, M. L. and Heidemann, R. A. Calculation of critical points from cubic two-constant equations of state. *AICHE Journal*, 27(3):521–523, 1981.
- [196] Michelsen, M. L. and Mollerup, J. M. *Thermodynamic Models: Fundamentals & Computational Aspects*. Tie-Line Publications, Holte, 2007.
- [197] Miles, R. B., Lempert, W. R., and Forkey, J. N. Laser Rayleigh scattering. *Measurement Science and Technology*, 12(5):R33, 2001.
- [198] Min, B. H., Chung, J. T., Kim, H. Y., and Park, S. Effects of gas composition on the performance and emissions of compressed natural gas engines. *Journal of Mechanical Science and Technology*, 16(2):219–226, 2002.
- [199] Mohamed, K. and Paraschivoiu, M. Real gas simulation of hydrogen release from a high-pressure chamber. *International Journal of Hydrogen Energy*, 30(8):903–912, 2005.
- [200] Moukalled, F. and Darwish, M. A high-resolution pressure-based algorithm for fluid flow at all speeds. *Journal of Computational Physics*, 168(1):101–130, 2001.
- [201] Moukalled, F., Mangani, L., and Darwish, M. *The Finite Volume Method in Computational Fluid Dynamics*. Springer, Berlin, 2016.
- [202] Müller, H. *Simulation turbulenter nicht-vorgemischter Verbrennung bei überkritischen Drücken*. PhD thesis, Universität der Bundeswehr München, 2016.

- [203] Müller, H., Ferraro, F., and Pfitzner, M. Implementation of a steady laminar flamelet model for non-premixed combustion in LES and RANS simulations. In *8th International Open-FOAM Workshop*, 2013.
- [204] Müller, H., Pfitzner, M., Matheis, J., and Hickel, S. Large-eddy simulation of coaxial LN₂/GH₂ injection at trans- and supercritical conditions. *Journal of Propulsion and Power*, 32(1):46–56, 2016.
- [205] Munday, D., Gutmark, E., Liu, J., and Kailasanath, K. Flow structure and acoustics of supersonic jets from conical convergent-divergent nozzles. *Physics of Fluids*, 23(11):116102, 2011.
- [206] Muthukumaran, C. and Vaidyanathan, A. Experimental study of elliptical jet from supercritical to subcritical conditions using planar laser induced fluorescence. *Physics of Fluids*, 27(3):034109, 2015.
- [207] Muthukumaran, C. and Vaidyanathan, A. Mixing nature of supercritical jet in subcritical and supercritical conditions. *Journal of Propulsion and Power*, 33(4):842–857, 2016.
- [208] Nessyahu, H. and Tadmor, E. Non-oscillatory central differencing for hyperbolic conservation laws. *Journal of Computational Physics*, 87(2):408–463, 1990.
- [209] Newman, J. A. and Brzustowski, T. Behavior of a liquid jet near the thermodynamic critical region. *AIAA Journal*, 9(8):1595–1602, 1971.
- [210] Nichita, D. V., Khalid, P., and Broseta, D. Calculation of isentropic compressibility and sound velocity in two-phase fluids. *Fluid Phase Equilibria*, 291(1):95–102, 2010.
- [211] Nicoud, F. and Ducros, F. Subgrid-scale stress modelling based on the square of the velocity gradient tensor. *Flow, Turbulence and Combustion*, 62(3):183–200, 1999.
- [212] O’Connaire, M., Curran, H., Simmie, J., Pitz, W., and Westbrook, C. A comprehensive modeling study of hydrogen oxidation. *International Journal of Chemical Kinetics*, 36:603–622, 2004.
- [213] O’Connell, J. P. and Haile, J. M. *Thermodynamics: Fundamentals for Applications*. Cambridge University Press, Cambridge, 2005.
- [214] Oefelein, J. C. Thermophysical characteristics of shear-coaxial LOX-H₂ flames at supercritical pressure. *Proceedings of the Combustion Institute*, 30(2):2929–2937, 2005.
- [215] Oefelein, J. C. Mixing and combustion of cryogenic oxygen-hydrogen shear-coaxial jet flames at supercritical pressure. *Combustion Science and Technology*, 178(1-3):229–252, 2006.
- [216] Oefelein, J. C. Advances in modeling supercritical fluid behavior and combustion in high-pressure propulsion systems. In *AIAA Scitech 2019 Forum*, 2019.
- [217] Okong’o, N. A. and Bellan, J. Direct numerical simulation of a transitional supercritical binary mixing layer: Heptane and nitrogen. *Journal of Fluid Mechanics*, 464:1–34, 2002.
- [218] Okong’o, N. A. and Bellan, J. Real-gas effects on mean flow and temporal stability of binary-species mixing layers. *AIAA Journal*, 41(12):2429–2443, 2003.
- [219] Okong’o, N. A. and Bellan, J. Small-scale dissipation in binary-species, thermodynamically supercritical, transitional mixing layers. *Computers & Fluids*, 39(7):1112–1124, 2010.
- [220] Oschwald, M., Schik, A., Klar, M., and Mayer, W. Investigation of coaxial LN₂/GH₂-injection at supercritical pressure by spontaneous Raman scattering. In *35th Joint Propulsion Conference and Exhibit*, 1999.
- [221] Oschwald, M., Smith, J., Branam, R., Hussong, J., Schik, A., Chehroudi, B., and Talley, D. Injection of fluids into supercritical environments. *Combustion Science and Technology*, 178(1-3):49–100, 2006.
- [222] Patankar, S. Calculation of unsteady compressible flows involving shocks. *Report UF/TN/A/4, Imperial College*, 1971.
- [223] Patankar, S. V. *Numerical Heat Transfer and Fluid Flow*. CRC Press, New York, 1980.

- [224] Patankar, S. V. and Spalding, D. B. A calculation procedure for heat, mass and momentum transfer in three-dimensional parabolic flows. In *Numerical Prediction of Flow, Heat Transfer, Turbulence and Combustion*, pages 54–73. Elsevier, 1983.
- [225] Pelletier, M., Schmitt, T., and Ducruix, S. A multifluid Taylor-Galerkin methodology for the simulation of compressible multicomponent separate two-phase flows from subcritical to supercritical states. *Computers & Fluids*, 206:104588, 2020.
- [226] Peng, D. and Robinson, D. B. A new two-constant equation of state. *Industrial & Engineering Chemistry Fundamentals*, 15(1):59–64, 1976.
- [227] Peng, D. and Robinson, D. B. A rigorous method for predicting the critical properties of multicomponent systems from an equation of state. *AICHE Journal*, 23(2):137–144, 1977.
- [228] Peters, N. Laminar diffusion flamelet models in non-premixed turbulent combustion. *Progress in Energy and Combustion Science*, 10(3):319–339, 1984.
- [229] Peters, N. Laminar flamelet concepts in turbulent combustion. In *Symposium (International) on Combustion*, volume 21, pages 1231–1250. Elsevier, 1986.
- [230] Peters, N. *Turbulent Combustion*. Cambridge University Press, Cambridge, 2000.
- [231] Picard, D. J. and Bishnoi, P. R. Calculation of the thermodynamic sound velocity in two-phase multicomponent fluids. *International Journal of Multiphase Flow*, 13(3):295–308, 1987.
- [232] Pickett, L. M., Manin, J., Genzale, C. L., Siebers, D. L., Musculus, M. P., and Idicheria, C. A. Relationship between Diesel fuel spray vapor penetration/dispersion and local fuel mixture fraction. *SAE International Journal of Engines*, 4(1):764–799, 2011.
- [233] Pitsch, H. Flamemaster. <https://www.itv.rwth-aachen.de/index.php?id=flamemaster>.
- [234] Pitzer, K. S., Lippmann, D. Z., Curl Jr., R., Huggins, C. M., and Petersen, D. E. The volumetric and thermodynamic properties of fluids. II. Compressibility factor, vapor pressure and entropy of vaporization. *Journal of the American Chemical Society*, 77(13):3433–3440, 1955.
- [235] Pohl, S., Jarczyk, M., Pfitzner, M., and Rogg, B. Real gas CFD simulations of hydrogen/oxygen supercritical combustion. *Progress in Propulsion Physics*, 4:583–614, 2013.
- [236] Poinsot, T. and Veynante, D. *Theoretical and Numerical Combustion*. R.T. Edwards, Inc., Philadelphia, 2005.
- [237] Poling, B. E., Prausnitz, J. M., and O'Connell, J. P. *The Properties of Gases and Liquids*. McGraw-Hill, New York, 2001.
- [238] Pope, S. B. *Turbulent Flows*. Cambridge University Press, Cambridge, 2000.
- [239] Poston, R. S. and McKetta, J. J. Vapor-liquid equilibrium in the n-hexane-nitrogen system. *Journal of Chemical and Engineering Data*, 11(3):364–365, 1966.
- [240] Prausnitz, J. M. Equations of state from van der Waals theory: The legacy of Otto Redlich. *Fluid Phase Equilibria*, 24(1-2):63–76, 1985.
- [241] Prausnitz, J. M., Lichtenthaler, R. N., and De Azevedo, E. G. *Molecular Thermodynamics of Fluid-Phase Equilibria*. Prentice Hall, New Jersey, 1999.
- [242] Preclik, D., Hagemann, G., Knab, O., Mäding, C., Haeseler, D., Haidn, O., Woschnak, A., and DeRosa, M. LOX/hydrocarbon preparatory thrust chamber technology activities in Germany. In *Proceedings of the 41st AIAA/ASME/SAE/ASEE Joint Propulsion Conference & Exhibit, Tucson, Arizona*, 2005.
- [243] Press, W. H., Teukolsky, S. A., Vetterling, W. T., and Flannery, B. P. *Numerical Recipes in C*. Cambridge University Press, Cambridge, 1992.
- [244] Qiu, L. and Reitz, R. D. Simulation of supercritical fuel injection with condensation. *International Journal of Heat and Mass Transfer*, 79:1070–1086, 2014.

- [245] Qiu, L. and Reitz, R. D. An investigation of thermodynamic states during high-pressure fuel injection using equilibrium thermodynamics. *International Journal of Multiphase Flow*, 72:24–38, 2015.
- [246] Qiu, L., Wang, Y., Jiao, Q., Wang, H., and Reitz, R. D. Development of a thermodynamically consistent, robust and efficient phase equilibrium solver and its validations. *Fuel*, 115:1–16, 2014.
- [247] Qiu, L., Wang, Y., and Reitz, R. D. Multiphase dynamic flash simulations using entropy maximization and application to compressible flow with phase change. *AICHE Journal*, 60(8):3013–3024, 2014.
- [248] Qiu, L., Wang, Y., and Reitz, R. D. On regular and retrograde condensation in multiphase compressible flows. *International Journal of Multiphase Flow*, 64:85–96, 2014.
- [249] Quarteroni, A., Sacco, R., and Saleri, F. *Numerical Mathematics*. Springer, Berlin, 2000.
- [250] Rachford Jr., H. H. and Rice, J. D. Procedure for use of electronic digital computers in calculating flash vaporization hydrocarbon equilibrium. *Journal of Petroleum Technology*, 4(10):19–3, 1952.
- [251] Redlich, O. and Kwong, J. N. On the thermodynamics of solutions. V. An equation of state. Fugacities of gaseous solutions. *Chemical Reviews*, 44(1):233–244, 1949.
- [252] Reid, R. C. and Beegle, B. L. Critical point criteria in Legendre transform notation. *AICHE Journal*, 23(5):726–732, 1977.
- [253] Reid, R. C., Prausnitz, J. M., and Poling, B. E. *The Properties of Gases and Liquids*. McGraw-Hill, New York, 1987.
- [254] Reiss, H. The kinetics of phase transitions in binary systems. *The Journal of Chemical Physics*, 18(6):840–848, 1950.
- [255] Reno, G. J. and Katz, D. L. Surface tension of n-heptane and n-butane containing dissolved nitrogen. *Industrial & Engineering Chemistry*, 35(10):1091–1093, 1943.
- [256] Rhie, C. M. and Chow, W. L. Numerical study of the turbulent flow past an airfoil with trailing edge separation. *AIAA Journal*, 21(11):1525–1532, 1983.
- [257] Rhie, C. M. and Stowers, S. T. Navier-Stokes analysis for high-speed flows using pressure correction algorithm. *Journal of Propulsion and Power*, 4(6):564–570, 1988.
- [258] Riazi, M. R. and Whitson, C. H. Estimating diffusion coefficients of dense fluids. *Industrial & Engineering Chemistry Research*, 32(12):3081–3088, 1993.
- [259] Ribert, G., Zong, N., Yang, V., Pons, L., Darabiha, N., and Candel, S. Counterflow diffusion flames of general fluids: Oxygen/hydrogen mixtures. *Combustion and Flame*, 154(3):319–330, 2008.
- [260] Ries, F. *Numerical modeling and prediction of irreversibilities in sub- and supercritical turbulent near-wall flows*. PhD thesis, Technische Universität Darmstadt, 2019.
- [261] Ries, F., Obando, P., Shevchuck, I., Janicka, J., and Sadiki, A. Numerical analysis of turbulent flow dynamics and heat transport in a round jet at supercritical conditions. *International Journal of Heat and Fluid Flow*, 66:172–184, 2017.
- [262] Rincon, J. and Elder, R. A high-resolution pressure-based method for compressible flows. *Computers & Fluids*, 26(3):217–231, 1997.
- [263] Roe, P. L. Approximate Riemann solvers, parameter vectors, and difference schemes. *Journal of Computational Physics*, 43(2):357–372, 1981.
- [264] Roe, P. L. Characteristic-based schemes for the Euler equations. *Annual Review of Fluid Mechanics*, 18(1):337–365, 1986.
- [265] Roy, A., Joly, C., and Segal, C. Disintegrating supercritical jets in a subcritical environment. *Journal of Fluid Mechanics*, 717:193–202, 2013.

- [266] Roy, A. and Segal, C. Experimental study of fluid jet mixing at supercritical conditions. *Journal of Propulsion and Power*, 26(6):1205–1211, 2010.
- [267] Ruiz, A. M., Lacaze, G., Oefelein, J. C., Mari, R., Cuenot, B., Selle, L., and Poinsot, T. Numerical benchmark for high-Reynolds-number supercritical flows with large density gradients. *AIAA Journal*, 54(5):1445–1460, 2016.
- [268] Rusanov, V. V. The calculation of the interaction of non-stationary shock waves with barriers. *Zhurnal Vychislitel'noi Matematiki i Matematicheskoi Fiziki*, 1(2):267–279, 1961.
- [269] Rusche, H. *Computational fluid dynamics of dispersed two-phase flows at high phase fractions*. PhD thesis, University of London, 2002.
- [270] Sagaut, P. *Large Eddy Simulation for Incompressible Flows: An Introduction*. Springer, Berlin, 2006.
- [271] Sanders, R. and Prendergast, K. H. The possible relation of the 3-kiloparsec arm to explosions in the galactic nucleus. *The Astrophysical Journal*, 188:489–500, 1974.
- [272] Sandler, S. I. *Models for Thermodynamic and Phase Equilibria Calculations*. Marcel Dekker, New York, 1994.
- [273] Saurel, R., Boivin, P., and Le Métayer, O. A general formulation for cavitating, boiling and evaporating flows. *Computers & Fluids*, 128:53–64, 2016.
- [274] Saurel, R., Cocchi, P., and Butler, P. B. Numerical study of cavitation in the wake of a hypervelocity underwater projectile. *Journal of Propulsion and Power*, 15(4):513–522, 1999.
- [275] Saurel, R. and Pantano, C. Diffuse-interface capturing methods for compressible two-phase flows. *Annual Review of Fluid Mechanics*, 50:105–130, 2018.
- [276] Schäfer, M. *Computational Engineering: Introduction to Numerical Methods*. Springer, Berlin, 2006.
- [277] Schmidt, S., Sezal, I., Schnerr, G., and Talhamer, M. Riemann techniques for the simulation of compressible liquid flows with phase-transistion at all Mach numbers-shock and wave dynamics in cavitating 3-D micro and macro systems. In *46th AIAA Aerospace Sciences Meeting and Exhibit*, 2008.
- [278] Schmidt, S., Sezal, I., and Schnerr, G. H. Compressible simulation of high-speed hydrodynamics with phase change. In *ECCOMAS CFD 2006: Proceedings of the European Conference on Computational Fluid Dynamics*, 2006.
- [279] Schmitt, T. Large-eddy simulations of the Mascotte test cases operating at supercritical pressure. *Flow, Turbulence and Combustion*, 105:159–189, 2020.
- [280] Schmitt, T., Méry, Y., Boileau, M., and Candel, S. Large-eddy simulation of oxygen/methane flames under transcritical conditions. *Proceedings of the Combustion Institute*, 33(1):1383–1390, 2011.
- [281] Schmitt, T., Selle, L., Ruiz, A., and Cuenot, B. Large-eddy simulation of supercritical-pressure round jets. *AIAA Journal*, 48(9):2133–2144, 2010.
- [282] Segal, C. and Polikhov, S. Subcritical to supercritical mixing. *Physics of Fluids*, 20(5):052101, 2008.
- [283] Seidl, M. *Numerische Simulation von Raketenbrennkammern mit transkritischer Einspritzung*. PhD thesis, Universität Stuttgart, 2017.
- [284] Seidl, M. J., Aigner, M., Keller, R., and Gerlinger, P. CFD simulations of turbulent nonreacting and reacting flows for rocket engine applications. *The Journal of Supercritical Fluids*, 121:63–77, 2017.
- [285] Selle, L. C., Okong'o, N. A., Bellan, J., and Harstad, K. G. Modelling of subgrid-scale phenomena in supercritical transitional mixing layers: An a priori study. *Journal of Fluid Mechanics*, 593:57–91, 2007.
- [286] Sengers, J. V., Kayser, R., Peters, C., and White, H. *Equations of State for Fluids and Fluid Mixtures*. Elsevier, Amsterdam, 2000.

- [287] Settles, G. S. *Schlieren and Shadowgraph Techniques: Visualizing Phenomena in Transparent Media*. Springer, Berlin, 2012.
- [288] Shtekkel, F. and Tsinn, N. *Zh.Khim.Prom.*, 16(8):24–28, 1939.
- [289] Siebers, D. L. Scaling liquid-phase fuel penetration in Diesel sprays based on mixing-limited vaporization. *SAE Transactions*, pages 703–728, 1999.
- [290] Sierra-Aznar, M., Pineda, D. I., Cage, B. S., Shi, X., Corvello, J. P., Chen, J., and Dibble, R. W. Working fluid replacement in gaseous direct-injection internal combustion engines: A fundamental and applied experimental investigation. In *10th US National Combustion Meeting*, 2017.
- [291] Simeoni, G. G., Bryk, T., Gorelli, F. A., Krisch, M., Ruocco, G., Santoro, M., and Scopigno, T. The Widom line as the crossover between liquid-like and gas-like behaviour in supercritical fluids. *Nature Physics*, 6(7):503, 2010.
- [292] Singla, G., Scouflaire, P., Rolon, C., and Candel, S. Transcritical oxygen/transcritical or supercritical methane combustion. *Proceedings of the Combustion Institute*, 30(2):2921–2928, 2005.
- [293] Sirignano, W. A. Compressible flow at high pressure with linear equation of state. *Journal of Fluid Mechanics*, 843:244–292, 2018.
- [294] Sirignano, W. A. and Delplanque, J.-P. Transcritical vaporization of liquid fuels and propellants. *Journal of Propulsion and Power*, 15(6):896–902, 1999.
- [295] Smagorinsky, J. General circulation experiments with the primitive equations: I. The basic experiment. *Monthly Weather Review*, 91(3):99–164, 1963.
- [296] Soave, G. Equilibrium constants from a modified Redlich-Kwong equation of state. *Chemical Engineering Science*, 27(6):1197–1203, 1972.
- [297] Spurk, J. H. and Aksel, N. *Fluid Mechanics*. Springer, Cham, 2020.
- [298] Star, A. M., Edwards, J. R., Lin, K.-C., Cox-Stouffer, S., and Jackson, T. A. Numerical simulation of injection of supercritical ethylene into nitrogen. *Journal of Propulsion and Power*, 22(4):809–819, 2006.
- [299] Steger, J. L. and Warming, R. Flux vector splitting of the inviscid gasdynamic equations with application to finite-difference methods. *Journal of Computational Physics*, 40(2):263–293, 1981.
- [300] Stephan, P., Schaber, K., Stephan, K., and Mayinger, F. *Thermodynamik: Grundlagen und technische Anwendungen-Band 1: Einstoffsysteme*. Springer, Berlin, 2010.
- [301] Stephan, P., Schaber, K., Stephan, K., and Mayinger, F. *Thermodynamik: Grundlagen und technische Anwendungen-Band 2: Mehrstoffsysteme und chemische Reaktionen*. Springer, Berlin, 2010.
- [302] Stotz, I., Lamanna, G., Hettrich, H., Weigand, B., and Steelant, J. Design of a double diaphragm shock tube for fluid disintegration studies. *Review of Scientific Instruments*, 79(12):125106, 2008.
- [303] Streett, W. B. and Calado, J. C. G. Liquid-vapour equilibrium for hydrogen + nitrogen at temperatures from 63 to 110 K and pressures to 57 MPa. *The Journal of Chemical Thermodynamics*, 10(11):1089–1100, 1978.
- [304] Stryjek, R., Chapplelear, P. S., and Kobayashi, R. Low-temperature vapor-liquid equilibria of nitrogen-methane system. *Journal of Chemical and Engineering Data*, 19(4):334–339, 1974.
- [305] Sutherland, W. The viscosity of gases and molecular force. *The London, Edinburgh, and Dublin Philosophical Magazine and Journal of Science*, 36(223):507–531, 1893.
- [306] Sutton, G. P. and Biblarz, O. *Rocket Propulsion Elements*. John Wiley & Sons, New York, 2016.
- [307] Svehla, R. A. Estimated viscosities and thermal conductivities of gases at high temperatures. Technical report, National Aeronautics and Space Administration, 1963.

- [308] Swanson, R. C. and Turkel, E. On central-difference and upwind schemes. In *Upwind and High-Resolution Schemes*, pages 167–181. Springer, 1992.
- [309] Takahashi, S. Preparation of a generalized chart for the diffusion coefficients of gases at high pressures. *Journal of Chemical Engineering of Japan*, 7(6):417–420, 1975.
- [310] Telaar, J., Schneider, G., and Mayer, W. Experimental investigation of breakup of turbulent liquid jets. In *16th Annual Conference on Liquid Atomization and Spray Systems*, 2000.
- [311] Terashima, H. and Koshi, M. Approach for simulating gas–liquid-like flows under supercritical pressures using a high-order central differencing scheme. *Journal of Computational Physics*, 231(20):6907–6923, 2012.
- [312] Tester, J. W. and Modell, M. *Thermodynamics and its Applications*. Prentice Hall, New Jersey, 1996.
- [313] Tezduyar, T. E. *Frontiers in Computational Fluid-Structure Interaction and Flow Simulation: Research from Lead Investigators under Forty–2018*. Springer, Berlin, 2018.
- [314] Theron, M., Martin Benito, M., Vieille, B., Vingert, L., Fdida, N., Mauriot, Y., Blouquin, R., Seitan, C., Onori, M., and Lequette, L. Experimental and numerical investigation of LOX/methane cryogenic combustion at low mixture ratio. In *8th European Conference for Aeronautics and Aerospace Sciences*, 2019.
- [315] Tisza, L. *Generalized Thermodynamics*. MIT press, Cambridge, 1966.
- [316] Toro, E. F. *Riemann Solvers and Numerical Methods for Fluid Dynamics: A Practical Introduction*. Springer, Berlin, 2013.
- [317] Trappehl, G. and Knapp, H. Vapour-liquid equilibria in the ternary mixtures N₂-CH₄-C₂H₆ and N₂-C₂H₆-C₃H₈. *Cryogenics*, 27(12):696–716, 1987.
- [318] Traxinger, C., Banholzer, M., and Pfitzner, M. Real-gas effects and phase separation in underexpanded jets at engine-relevant conditions. In *2018 AIAA Aerospace Sciences Meeting*, 2018.
- [319] Traxinger, C. and Pfitzner, M. Effect of nonideal fluid behavior on the jet mixing process under high-pressure and supersonic flow conditions. *Journal of Supercritical Fluids*, 172:105195, 2020.
- [320] Traxinger, C., Pfitzner, M., Baab, S., Lamanna, G., and Weigand, B. Experimental and numerical investigation of phase separation due to multi-component mixing at high-pressure conditions. *Physical Review Fluids*, 4(7):074303, 2019.
- [321] Traxinger, C., Zips, J., Banholzer, M., and Pfitzner, M. A pressure-based solution framework for sub- and supersonic flows considering real-gas effects and phase separation under engine-relevant conditions. *Computers & Fluids*, 202:104452, 2020.
- [322] Traxinger, C., Zips, J., and Pfitzner, M. Single-phase instability in non-premixed flames under liquid rocket engine relevant conditions. *Journal of Propulsion and Power*, 35(4):675–689, 2019.
- [323] Tully, P., DeVaney, W., and Rhodes, H. Phase equilibria of the helium-nitrogen system from 122 to 126 K. In *Advances in Cryogenic Engineering*, pages 88–95. Springer, 1971.
- [324] Tuner, M. Combustion of alternative vehicle fuels in internal combustion engines. *Report within project “A pre-study to prepare for interdisciplinary research on future alternative transportation fuels”, financed by The Swedish Energy Agency*, 3(2), 2016.
- [325] Tuner, M. Review and benchmarking of alternative fuels in conventional and advanced engine concepts with emphasis on efficiency, CO₂, and regulated emissions. Technical report, SAE Technical Paper, 2016.
- [326] Turkel, E., Fiterman, A., and van Leer, B. Preconditioning and the limit to the incompressible flow equations. Technical report, NASA-CR-191500, 1993.
- [327] Umemura, A. Supercritical liquid fuel combustion. In *Symposium (International) on Combustion*, volume 21, pages 463–471. Elsevier, 1988.

- [328] Unnikrishnan, U., Oefelein, J. C., and Yang, V. Direct numerical simulation of a turbulent reacting liquid-oxygen/methane mixing layer at supercritical pressure. In *2018 Joint Propulsion Conference*, 2018.
- [329] Unnikrishnan, U., Wang, X., Yang, S., and Yang, V. Subgrid scale modeling of the equation of state for turbulent flows under supercritical conditions. In *53rd AIAA/SAE/ASEE Joint Propulsion Conference*, 2017.
- [330] Uroic, T. *Implicitly coupled finite volume algorithms*. PhD thesis, University of Zagreb, 2019.
- [331] Valderrama, J. O. The state of the cubic equations of state. *Industrial & Engineering Chemistry Research*, 42(8):1603–1618, 2003.
- [332] van Albada, G. D., Van Leer, B., and Roberts, W. W. A comparative study of computational methods in cosmic gas dynamics. *Astronomy and Astrophysics*, 108:76–84, 1982.
- [333] van der Waals, J. D. *Over de Continuiteit van den Gas- en Vloeistoftoestand*. PhD thesis, University of Leiden, 1873.
- [334] van Doormaal, J., Turan, A., and Raithby, G. Evaluation of new techniques for the calculation of internal recirculating flows. In *25th AIAA Aerospace Sciences Meeting*, 1987.
- [335] van Konynenburg, P. H. and Scott, R. L. Critical lines and phase equilibria in binary van der Waals mixtures. *Philosophical Transactions of the Royal Society of London A: Mathematical, Physical and Engineering Sciences*, 298(1442):495–540, 1980.
- [336] van Leer, B. Towards the ultimate conservative difference scheme. II. Monotonicity and conservation combined in a second-order scheme. *Journal of Computational Physics*, 14(4):361–370, 1974.
- [337] van Leer, B. Towards the ultimate conservative difference scheme. V. A second-order sequel to Godunov’s method. *Journal of Computational Physics*, 32(1):101–136, 1979.
- [338] van Leer, B. Flux-vector splitting for the Euler equation. In *8th International Conference on Numerical Methods in Fluid Dynamics*, page 507–512. Springer, 1982.
- [339] van Leer, B. On the relation between the upwind-differencing schemes of Godunov, Engquist–Osher and Roe. *SIAM Journal on Scientific and Statistical Computing*, 5(1):1–20, 1984.
- [340] Vehkämäki, H. *Classical Nucleation Theory in Multicomponent Systems*. Springer Science & Business Media, Berlin, 2010.
- [341] Vreman, A. W. An eddy-viscosity subgrid-scale model for turbulent shear flow: Algebraic theory and applications. *Physics of Fluids*, 16(10):3670–3681, 2004.
- [342] Vuorinen, V., Keskinen, J.-P., Duwig, C., and Boersma, B. On the implementation of low-dissipative Runge–Kutta projection methods for time dependent flows using OpenFOAM®. *Computers & Fluids*, 93:153–163, 2014.
- [343] Vuorinen, V., Yu, J., Tirunagari, S., Kaario, O., Larmi, M., Duwig, C., and Boersma, B. Large-eddy simulation of highly underexpanded transient gas jets. *Physics of Fluids*, 25(1):016101, 2013.
- [344] Weatherill, N., Mathur, J., and Marchant, M. An upwind kinetic flux vector splitting method on general mesh topologies. *International Journal for Numerical Methods in Engineering*, 37(4):623–643, 1994.
- [345] Wei, Y. S. and Sadus, R. J. Equations of state for the calculation of fluid-phase equilibria. *AICHE Journal*, 46(1):169–196, 2000.
- [346] Weise, S. and Hasse, C. Reducing the memory footprint in large eddy simulations of reactive flows. *Parallel Computing*, 49:50–65, 2015.
- [347] Weiss, J. M. and Smith, W. A. Preconditioning applied to variable and constant density flows. *AIAA Journal*, 33(11):2050–2057, 1995.
- [348] Wesseling, P. *Principles of Computational Fluid Dynamics*. Springer, Berlin, 2001.
- [349] White, F. M. and Corfield, I. *Viscous Fluid Flow*. McGraw-Hill, New York, 2006.

- [350] Wichterle, I. and Kobayashi, R. Vapor-liquid equilibrium of methane-ethane system at low temperatures and high pressures. *Journal of Chemical and Engineering Data*, 17(1):9–12, 1972.
- [351] Wilcox, D. C. *Turbulence Modeling for CFD*. DCW Industries, Palm Drive, 2006.
- [352] Wilemski, G. Composition of the critical nucleus in multicomponent vapor nucleation. *The Journal of Chemical Physics*, 80(3):1370–1372, 1984.
- [353] Wilson, G. M. A modified Redlich-Kwong equation of state, application to general physical data calculations. In *65th National AIChE Meeting, Cleveland, OH*, 1965.
- [354] Wood, A. B. *A Textbook of Sound*. The Macmillan Company, New York, 1930.
- [355] Woodward, R. and Talley, D. Raman imaging of transcritical cryogenic propellants. In *34th Aerospace Sciences Meeting and Exhibit*, 1996.
- [356] Woodward, R., Talley, D., Anderson, T., and Winter, M. Shadowgraphy of transcritical cryogenic fluids. 1994.
- [357] Wu, P., Chen, T. H., Nejad, A. S., and Carter, C. D. Injection of supercritical ethylene in nitrogen. *Journal of Propulsion and Power*, 12(4):770–777, 1996.
- [358] Wu, P.-K., Shahnam, M., Kirkendall, K. A., Carter, C. D., and Nejad, A. S. Expansion and mixing processes of underexpanded supercritical fuel jets injected into superheated conditions. *Journal of Propulsion and Power*, 15(5):642–649, 1999.
- [359] Xiao, C.-N., Denner, F., and van Wachem, B. G. M. Fully-coupled pressure-based finite-volume framework for the simulation of fluid flows at all speeds in complex geometries. *Journal of Computational Physics*, 346:91–130, 2017.
- [360] Xiao, C.-N., Fond, B., Beyrau, F., T’Joen, C., Henkes, R., Veenstra, P., and van Wachem, B. G. M. Numerical investigation and experimental comparison of the gas dynamics in a highly underexpanded confined real gas jet. *Flow, Turbulence and Combustion*, 103(1):141–173, 2019.
- [361] XXiao, J., Liu, K., Du, Y., Jin, Z., and Lu, H. M. Measurement on and correlation of VLE of H₂-N₂-Ar system. *Huaxue Gongcheng*, 18:8–12, 1990.
- [362] Yang, V. Modeling of supercritical vaporization, mixing, and combustion processes in liquid-fueled propulsion systems. *Proceedings of the Combustion Institute*, 28(1):925–942, 2000.
- [363] Yang, V. and Shuen, J.-S. Vaporization of liquid oxygen (LOX) droplets in supercritical hydrogen environments. *Combustion Science and Technology*, 97(4-6):247–270, 1994.
- [364] Yao, M. X., Hickey, J.-P., Ma, P. C., and Ihme, M. Molecular diffusion and phase stability in high-pressure combustion. *Combustion and Flame*, 210:302–314, 2019.
- [365] Yu, J., Vuorinen, V., Kaario, O., Sarjovaara, T., and Larmi, M. Visualization and analysis of the characteristics of transitional underexpanded jets. *International Journal of Heat and Fluid Flow*, 44:140–154, 2013.
- [366] Yüceil, K. B. and Ötügen, M. V. Scaling parameters for underexpanded supersonic jets. *Physics of Fluids*, 14(12):4206–4215, 2002.
- [367] Zips, J. *Simulation turbulenter Verbrennung von Methan und Sauerstoff in Raketenbrennkammern*. PhD thesis, Universität der Bundeswehr München, 2019.
- [368] Zips, J., Müller, H., and Pfitzner, M. Efficient thermo-chemistry tabulation for non-premixed combustion at high-pressure conditions. *Flow, Turbulence and Combustion*, 101(3):821–850, 2018.
- [369] Zips, J., Traxinger, C., Breda, P., and Pfitzner, M. Assessment of presumed/transported probability density function methods for rocket combustion simulations. *Journal of Propulsion and Power*, 35(4):747–764, 2019.
- [370] Zips, J., Traxinger, C., and Pfitzner, M. Time-resolved flow field and thermal loads in a single-element GOx/GCH₄ rocket combustor. *International Journal of Heat and Mass Transfer*, 143:118474, 2019.

- [371] Zurbach, S., Thomas, J. L., Vuillermoz, P., Vingert, L., and Habiballah, M. Recent advances on LOx/methane combustion for liquid rocket engine injector. In *38th AIAA/ASME/SAE/ASEE Joint Propulsion Conference and Exhibit*, 2002.

A Numerical flux schemes

A.1 Short overview

The application of the FVM yields a grid with piecewise constant initial data in every cell. Therefore, the variation of the properties are continuous within every control volume but at the cell faces discontinuities may arise. To advance the flow field to the new time level, fluxes have to be calculated at every cell face to evaluate the Gauss integral of the convection term. In the subsonic pressure-based approach, a linear face flux calculation is combined with the blended differencing scheme to assure boundedness of the solution. In the supersonic case, i.e., hyperbolic problems, flow induced discontinuities like, e.g., shocks, can occur yielding additional demands for the numerical solver and the flux formulation. The resulting problem is commonly referred to as Riemann problem which has to be solved at every cell face to calculate the representative fluxes. Therefore, numerical schemes for hyperbolic problems are often called Riemann solvers. In the literature, a large number of different schemes can be found which are tailored for specific problems. In general, these approaches can be divided roughly into two categories [37]:

1. Upwind schemes,
2. Central schemes.

The major feature of upwind schemes is that the discretization of the equations is performed according to propagation direction of the information on the grid [316]. In 1959, Godunov [95] proposed a first order upwind scheme and hereby provided an exact solution to the Riemann problem of the Euler equations. The epoch-making character of Godunov's work [95] is recognized by the fact that FVM schemes are often referred to as Godunov-type schemes [148]. The exact solution of the Riemann problem can be both computationally very expensive and analytically very difficult or even not existing [172]. As a result, many different approximate Riemann solvers have been proposed since the 1960s. Some of the most outstanding and best known schemes are:

- 1961: Rusanov scheme [268],
- 1981: Roe scheme [263],
- 1982: van Leer scheme [338],
- 1983: Harten-Lax-van Leer (HLL) scheme [116].

The main difference between these schemes is the approximate representation of the wave structure induced by the discontinuities. In addition, the class of upwind schemes can be subdivided into flux difference splitting (FDS) and flux vector splitting (FVS) approaches [316, 172]. For a more detailed introduction of these and other approximate Riemann solvers it is referred to the textbooks of LeVeque [167] and Toro [316].

The category of central schemes can be considered a simple, efficient and universal Riemann-problem-solver-free alternative to upwind schemes [148]. The first numerically stable central scheme was proposed in 1954 by Lax [163] and Friedrichs [82] – the widely-known Lax-Friedrichs (LxF) scheme. The LxF scheme introduces a large numerical viscosity of order $\mathcal{O}(\Delta x^2/\Delta t)$ which results in a strong smearing of the solution. This is a general drawback of first-order schemes as demonstrated by Godunov [95]. However, the extension to high-order approximations is not straightforward as spurious oscillations can occur at discontinuities.

In 1979, van Leer [337] proposed the first second-order Godunov-type scheme called Monotonic Upstream-centered Scheme for Conservation Laws (MUSCL). In the MUSCL approach, piecewise linear functions are reconstructed from the constant initial data. To prevent oscillations at the cell interfaces, the gradients used in the reconstruction procedure have to be limited. In the literature, a huge number of limiters can be found, see the textbooks of, for instance, LeVeque [167] or Godlewski and Raviart [94]. In general, this idea can be combined with any approach to determine non-oscillatory (high-order) fluxes at cell interfaces in the FVM. This approach is also often referred

to as TVD method which was originally introduced by Harten [115]. The idea of TVD is similar to MUSCL and aims to prevent the generation of new extrema in the solution [37].

In 1990, Nessyahu and Tadmor [208] (NT) employed the concept of the piecewise linear reconstruction with slope limiter to central schemes and derived a second order generalization of the LxF scheme. With this step, Nessyahu and Tadmor [208] drastically decreased the numerical viscosity compared to the original LxF scheme, i.e., $\mathcal{O}(\Delta x^2/\Delta t)$ to $\mathcal{O}(\Delta x^4/\Delta t)$. However, the NT approach has two disadvantages:

1. The application of a staggered grid is necessary.
2. The numerical dissipation depends on the time step and therefore increases with a decrease in Δt .

In 2000, Kurganov and Tadmor [152] (KT) presented an improved second-order central scheme where both drawbacks have been removed, i.e., the numerical viscosity is only proportional to the spatial resolution, i.e., $\mathcal{O}(\Delta x^4)$, and a semi-discrete formulation for non-staggered grids can be derived. This was achieved by considering the local speeds of propagation and an integration over variable sized Riemann fans [149] for the derivation of the KT scheme. This approach was further improved by Kurganov, Noelle and Petrova [149] (KNP) by employing the one-sided local speeds of propagation. In this way, more precise estimates of the Riemann fan structure are incorporated making the KNP scheme [149] less dissipative compared to the KT scheme [152]. The KNP scheme [149] is deemed a central-upwind scheme as one-sided speeds of propagation are used and therefore advanced information about the direction of propagation are employed compared to standard central schemes. In the present work, a semi-discrete version of the KNP flux approach [149] is used and its derivation is shown in the following.

A.2 Derivation of the central-upwind scheme

For the derivation of the semi-discrete version of the KNP central-upwind scheme [149] the 1D hyperbolic conservation law

$$\frac{\partial u}{\partial t} + \frac{\partial}{\partial x} \mathcal{F}(u(x, t)) = 0 \quad (\text{A.1})$$

is considered, where \mathcal{F} denotes the flux of the property u . An equidistant mesh is applied where the cell width is denoted by Δx . In addition, the introduction of the following definitions is helpful [152, 181]:

- u : continuous function being integrated in space and time,
- \bar{u} : piecewise constant approximation,
- \tilde{u} : piecewise polynomial reconstruction.

Mathematically, \bar{u} and \tilde{u} can be expressed as [152]:

$$\bar{u}(x, t^n) := \frac{1}{|I_x|} \int_{I_x} u(\zeta, t) d\zeta \quad \text{with} \quad I_x := \left\{ \zeta : |\zeta - x| \leq \frac{\Delta x}{2} \right\} \quad (\text{A.2})$$

and

$$\tilde{u}(x, t^n) := \sum_j \left[\bar{u}_j^n + (u_x)_j^n (x - x_j) \right] \mathbf{1}_{[x_{j-1/2}, x_{j+1/2}]} \quad \text{with} \quad x_{j\pm 1/2} = x_j \pm \frac{\Delta x}{2}. \quad (\text{A.3})$$

Here, $\mathbf{1}_{[x_{j-1/2}, x_{j+1/2}]}$ is an indicator function having the value one inside the interval and zero otherwise. In addition, $(u_x)_j^n$ denotes the operator used for the piecewise reconstruction, i.e., an approximation to the exact derivative of u into the x -direction at position j . To avoid oscillations in the solutions process, the determination of $(u_x)_j^n$ relies on TVD approaches. Applying Eq. (A.3) at the interval limits yields the piecewise reconstruction of cell values onto the faces. In Fig. A.1, the resulting left- (- - direction) and right-sided (+ - direction) reconstructions onto the cell interfaces from the cell centroids are sketched. The reconstruction locations $x_{j+1/2}^-$ and $x_{j+1/2}^+$ are identical to the position of the cell interface, i.e., $x_{j+1/2} = x_{j+1/2}^- = x_{j+1/2}^+$. These interpolation directions

are identical to the definitions in the underlying literature [152, 149, 148]. In OpenFOAM, the directions are defined differently and both the reconstruction and the flux formulation have to be translated into the "OpenFOAM language" which is addressed in Sec. 3.3.5. Here, the notation according to Fig. A.1 is applied.

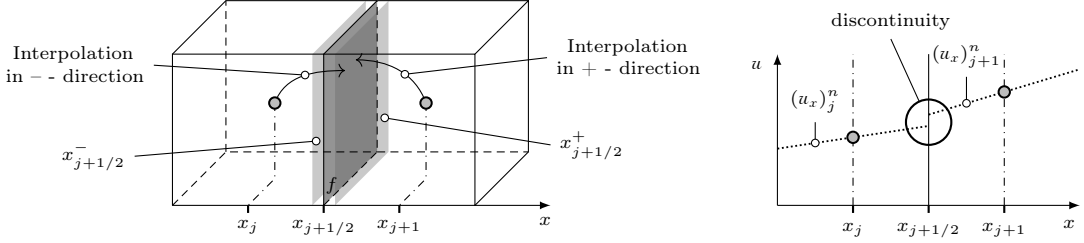


Figure A.1: Sketch of the piecewise reconstruction from cell to face values in central schemes.

The discontinuities at the cell interfaces resulting from the reconstruction process travel with left- and right-sided speeds of propagation which can be estimated as [149]:

$$a_{j+\frac{1}{2}}^- := \min_{\Pi \in \mathcal{C}(u_{j+\frac{1}{2}}^-, u_{j+\frac{1}{2}}^+)} \left[\lambda_1 \left(\frac{\partial \mathcal{F}}{\partial u} (\Pi) \right), 0 \right] \quad (\text{A.4})$$

and

$$a_{j+\frac{1}{2}}^+ := \max_{\Pi \in \mathcal{C}(u_{j+\frac{1}{2}}^-, u_{j+\frac{1}{2}}^+)} \left[\lambda_N \left(\frac{\partial \mathcal{F}}{\partial u} (\Pi) \right), 0 \right]. \quad (\text{A.5})$$

Here, λ_1 and λ_N denote the smallest and the largest eigenvalues of the flux Jacobian $\partial \mathcal{F} / \partial u$, respectively. In addition, $\mathcal{C}(u_{j+1/2}^-, u_{j+1/2}^+)$ is the curve in the state space that connects $u_{j+1/2}^-$ and $u_{j+1/2}^+$. In most practical applications, the propagation speeds can be deduced as [149]:

$$a_{j+\frac{1}{2}}^- := \min \left[\lambda_1 \left(\frac{\partial \mathcal{F}}{\partial u} (u_{j+\frac{1}{2}}^-) \right), \lambda_1 \left(\frac{\partial \mathcal{F}}{\partial u} (u_{j+\frac{1}{2}}^+) \right), 0 \right], \quad (\text{A.6})$$

$$a_{j+\frac{1}{2}}^+ := \max \left[\lambda_N \left(\frac{\partial \mathcal{F}}{\partial u} (u_{j+\frac{1}{2}}^-) \right), \lambda_N \left(\frac{\partial \mathcal{F}}{\partial u} (u_{j+\frac{1}{2}}^+) \right), 0 \right]. \quad (\text{A.7})$$

In the KNP scheme, these one-sided local speeds are used to estimate the width of the Riemann fan and sub-divide the solution domain into nonsmooth and smooth parts, see Fig. A.2 left. The

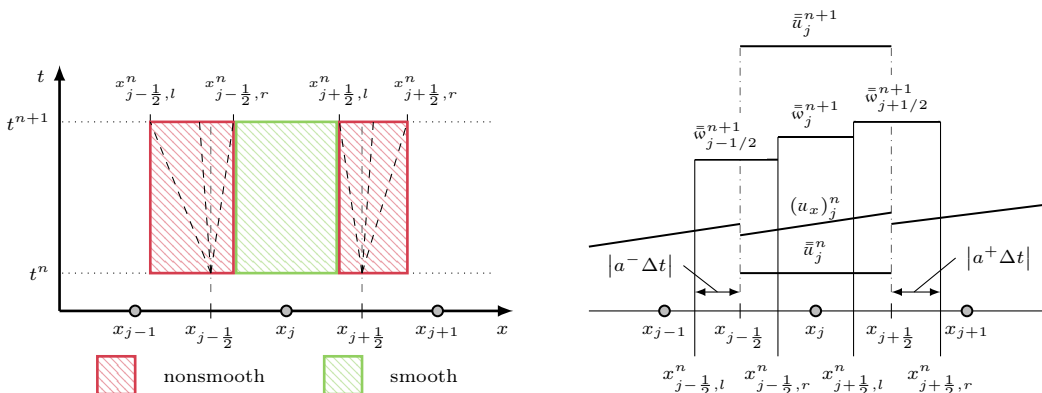


Figure A.2: Schematic of the KNP central-upwind scheme [149]. Left: Idea of the selection of the space-time control volumes. Right: Steps to evolve the numerical solution.

left and right-hand sided extent of the Riemann fan, $x_{j+\frac{1}{2},l}^n$ and $x_{j+\frac{1}{2},r}^n$, depend on the time step $\Delta t = t^{n+1} - t^n$ and the minimum and maximum propagation speeds:

$$x_{j+\frac{1}{2},l}^n := x_{j+\frac{1}{2}} + a_{j+\frac{1}{2}}^- \Delta t , \quad (\text{A.8})$$

$$x_{j+\frac{1}{2},r}^n := x_{j+\frac{1}{2}} + a_{j+\frac{1}{2}}^+ \Delta t . \quad (\text{A.9})$$

Therefore, the smooth and nonsmooth rectangular integration domains are $[x_{j-\frac{1}{2},r}^n, x_{j+\frac{1}{2},l}^n] \times [t^n, t^{n+1}]$ and $[x_{j+\frac{1}{2},l}^n, x_{j+\frac{1}{2},r}^n] \times [t^n, t^{n+1}]$, respectively. Integrating over these two intervals yields the new cell averages $\bar{\omega}_j^{n+1}$ and $\bar{\omega}_{j+1/2}^{n+1}$ [149]:

$$\begin{aligned} \bar{\omega}_j^{n+1} &= \frac{1}{x_{j+\frac{1}{2},l}^n - x_{j-\frac{1}{2},r}^n} \int_{x_{j-\frac{1}{2},r}^n}^{x_{j+\frac{1}{2},l}^n} \tilde{u}(\zeta, t^n) d\zeta \\ &\quad - \frac{1}{x_{j+\frac{1}{2},l}^n - x_{j-\frac{1}{2},r}^n} \int_{t^n}^{t^{n+1}} [\mathcal{F}(u(x_{j+\frac{1}{2},l}^n, \mathcal{T})) - \mathcal{F}(u(x_{j-\frac{1}{2},r}^n, \mathcal{T}))] d\mathcal{T} , \end{aligned} \quad (\text{A.10})$$

$$\begin{aligned} \bar{\omega}_{j+1/2}^{n+1} &= \frac{1}{x_{j+\frac{1}{2},r}^n - x_{j+\frac{1}{2},l}^n} \left[\int_{x_{j+\frac{1}{2},l}^n}^{x_{j+\frac{1}{2}}^n} \tilde{u}(\zeta, t^n) d\zeta + \int_{x_{j+\frac{1}{2}}^n}^{x_{j+\frac{1}{2},r}^n} \tilde{u}(\zeta, t^n) d\zeta \right] \\ &\quad - \frac{1}{x_{j+\frac{1}{2},r}^n - x_{j+\frac{1}{2},l}^n} \int_{t^n}^{t^{n+1}} [\mathcal{F}(u(x_{j+\frac{1}{2},r}^n, \mathcal{T})) - \mathcal{F}(u(x_{j+\frac{1}{2},l}^n, \mathcal{T}))] d\mathcal{T} . \end{aligned} \quad (\text{A.11})$$

These averages are defined in a staggered grid arrangement and therefore have to be projected back onto the original – collocated – mesh. In the work of Kurganov et al. [149] this is done by defining a piecewise polynomial interpolant \tilde{w}^{n+1} from the cell averages $\bar{\omega}_j^{n+1}$ and $\bar{\omega}_{j+1/2}^{n+1}$. The projection of this interpolant onto the collocated mesh yields the average solution \bar{u}_j^{n+1} at the new time level, see Fig. A.2 right. This procedure results in an explicit, fully discrete Godunov-type central-upwind scheme. On collocated meshes, the application of this kind of scheme is very inconvenient. Therefore, semi-discrete versions of the scheme are preferred.

To arrive at a semi-discrete formulation of the KNP scheme, the limit of $\Delta t \rightarrow 0$ has to be considered. Using the piecewise polynomial interpolant \tilde{w}^{n+1} the temporal derivative of \bar{u}_j can be expressed as [149]

$$\begin{aligned} \frac{d}{dt} \bar{u}_j(t) &= \lim_{\Delta t \rightarrow 0} \frac{\bar{u}_j^{n+1} - \bar{u}_j^n}{\Delta t} \\ &= \lim_{\Delta t \rightarrow 0} \frac{1}{\Delta t} \left[\frac{1}{\Delta x} \int_{x_{j-\frac{1}{2}}}^{x_{j+\frac{1}{2}}} \tilde{w}^{n+1}(\zeta) d\zeta - \bar{u}_j^n \right] . \end{aligned} \quad (\text{A.12})$$

Based on the conservation assumption, the integral of the interpolant can be further simplified applying the appropriate cell averages according to Fig. A.2 right:

$$\int_{x_{j-\frac{1}{2}}}^{x_{j+\frac{1}{2}}} \tilde{w}^{n+1}(\zeta) d\zeta = \int_{x_{j-\frac{1}{2}}}^{x_{j-\frac{1}{2},r}} \bar{\omega}_{j-\frac{1}{2}}^{n+1} d\zeta + \int_{x_{j-\frac{1}{2},r}}^{x_{j+\frac{1}{2},l}} \bar{\omega}_j^{n+1} d\zeta + \int_{x_{j+\frac{1}{2},l}}^{x_{j+\frac{1}{2}}} \bar{\omega}_{j+\frac{1}{2}}^{n+1} d\zeta . \quad (\text{A.13})$$

Using the estimations of the widths of the Riemann fan according to Eqs. (A.8) and (A.9), i.e., $x_{j-1/2,r}^n - x_{j-1/2}^n = a_{j-1/2}^+ \Delta t$ and $x_{j+1/2}^n - x_{j+1/2,l}^n = -a_{j+1/2}^- \Delta t$, yields:

$$\int_{x_{j-\frac{1}{2}}}^{x_{j+\frac{1}{2}}} \tilde{w}^{n+1}(\zeta) d\zeta = a_{j-\frac{1}{2}}^+ \Delta t \bar{\omega}_{j-\frac{1}{2}}^{n+1} + (x_{j+\frac{1}{2},l}^n - x_{j-\frac{1}{2},r}^n) \bar{\omega}_j^{n+1} - a_{j+\frac{1}{2}}^- \Delta t \bar{\omega}_{j+\frac{1}{2}}^{n+1} . \quad (\text{A.14})$$

Substituting this expression into Eq. (A.12) gives

$$\frac{d}{dt} \bar{u}_j(t) = \frac{a_{j-\frac{1}{2}}^+}{\Delta x} \lim_{\Delta t \rightarrow 0} \bar{\omega}_{j-\frac{1}{2}}^{n+1} + \lim_{\Delta t \rightarrow 0} \frac{1}{\Delta t} \left(\frac{x_{j+\frac{1}{2},l}^n - x_{j-\frac{1}{2},r}^n}{\Delta x} \bar{\omega}_j^{n+1} - \bar{u}_j^n \right) - \frac{a_{j+\frac{1}{2}}^-}{\Delta x} \lim_{\Delta t \rightarrow 0} \bar{\omega}_{j+\frac{1}{2}}^{n+1}. \quad (\text{A.15})$$

The three different terms on the right-hand side can be calculated separately. Using Eq. (A.10), the midpoint integration rule [249]

$$\int_a^b f(\zeta) d\zeta \approx (b-a) f\left(\frac{a+b}{2}\right) \quad (\text{A.16})$$

and the identities

$$u_{j+\frac{1}{2}}^- = \bar{u}_j^n + \frac{\Delta x}{2} (u_x)_j^n \quad \text{and} \quad u_{j-\frac{1}{2}}^+ = \bar{u}_j^n - \frac{\Delta x}{2} (u_x)_j^n, \quad (\text{A.17})$$

$\bar{\omega}_j^{n+1}$ can be determined as

$$\begin{aligned} \bar{\omega}_j^{n+1} = & \frac{1}{x_{j+\frac{1}{2},l}^n - x_{j-\frac{1}{2},r}^n} \left\{ \bar{u}_j^n \Delta x + \Delta t \left(a_{j+\frac{1}{2}}^- u_{j+\frac{1}{2}}^- - a_{j-\frac{1}{2}}^+ u_{j-\frac{1}{2}}^+ \right) \right. \\ & + \frac{(u_x)_j^n}{2} \left[\left(a_{j+\frac{1}{2}}^- \Delta t \right)^2 - \left(a_{j-\frac{1}{2}}^+ \Delta t \right)^2 \right] \\ & \left. - \Delta t \left[\mathcal{F}\left(u_{j+\frac{1}{2},l}^{n+\frac{1}{2}}\right) - \mathcal{F}\left(u_{j-\frac{1}{2},r}^{n+\frac{1}{2}}\right) \right] \right\}. \end{aligned} \quad (\text{A.18})$$

For $\Delta t \rightarrow 0$, the third term on the right-hand side vanishes and the fluxes \mathcal{F} can be approximated using the left and right-sided reconstructions. Therefore, the second term on the right-hand side of Eq. (A.15) can be obtained as

$$\lim_{\Delta t \rightarrow 0} \frac{1}{\Delta t} \left(\frac{x_{j+\frac{1}{2},l}^n - x_{j-\frac{1}{2},r}^n}{\Delta x} \bar{\omega}_j^{n+1} - \bar{u}_j^n \right) = \frac{a_{j+\frac{1}{2}}^- u_{j+\frac{1}{2}}^- - a_{j-\frac{1}{2}}^+ u_{j-\frac{1}{2}}^+}{\Delta x} - \frac{\mathcal{F}(u_{j+\frac{1}{2}}^-) - \mathcal{F}(u_{j-\frac{1}{2}}^+)}{\Delta x}. \quad (\text{A.19})$$

Applying similar mathematical relationships and using Eq. (A.11) as a basis yields the following expression for $\bar{\omega}_{j+\frac{1}{2}}^{n+1}$:

$$\begin{aligned} \bar{\omega}_{j+\frac{1}{2}}^{n+1} = & \frac{1}{\Delta t (a_{j+\frac{1}{2}}^+ - a_{j+\frac{1}{2}}^-)} \left\{ -u_{j+\frac{1}{2}}^- a_{j+\frac{1}{2}}^- \Delta t - (u_x)_j^n \frac{(a_{j+\frac{1}{2}}^- \Delta t)^2}{2} \right. \\ & + u_{j+\frac{1}{2}}^+ a_{j+\frac{1}{2}}^+ \Delta t + (u_x)_{j+1}^n \frac{(a_{j+\frac{1}{2}}^+ \Delta t)^2}{2} \\ & \left. - \Delta t \left[\mathcal{F}\left(u_{j+\frac{1}{2},r}^{n+\frac{1}{2}}\right) - \mathcal{F}\left(u_{j+\frac{1}{2},l}^{n+\frac{1}{2}}\right) \right] \right\}. \end{aligned} \quad (\text{A.20})$$

In the limit of $\Delta t \rightarrow 0$, this equation can be further simplified to

$$\lim_{\Delta t \rightarrow 0} \bar{\omega}_{j+\frac{1}{2}}^{n+1} = \frac{a_{j+\frac{1}{2}}^+ u_{j+\frac{1}{2}}^+ - a_{j+\frac{1}{2}}^- u_{j+\frac{1}{2}}^-}{a_{j+\frac{1}{2}}^+ - a_{j+\frac{1}{2}}^-} - \frac{\mathcal{F}(u_{j+\frac{1}{2}}^+) - \mathcal{F}(u_{j+\frac{1}{2}}^-)}{a_{j+\frac{1}{2}}^+ - a_{j+\frac{1}{2}}^-}. \quad (\text{A.21})$$

Analogous, the semi-discrete version of $\bar{\omega}_{j-\frac{1}{2}}^{n+1}$ reads:

$$\lim_{\Delta t \rightarrow 0} \bar{\omega}_{j-\frac{1}{2}}^{n+1} = \frac{a_{j-\frac{1}{2}}^+ u_{j-\frac{1}{2}}^+ - a_{j-\frac{1}{2}}^- u_{j-\frac{1}{2}}^-}{a_{j-\frac{1}{2}}^+ - a_{j-\frac{1}{2}}^-} - \frac{\mathcal{F}(u_{j-\frac{1}{2}}^+) - \mathcal{F}(u_{j-\frac{1}{2}}^-)}{a_{j-\frac{1}{2}}^+ - a_{j-\frac{1}{2}}^-}. \quad (\text{A.22})$$

Substituting Eqs. (A.19), (A.21) and (A.22) into Eq. (A.15) yields the semi-discrete KNP scheme in the following conservative form

$$\frac{d}{dt} \bar{u}_j(t) = -\frac{\mathcal{H}_{j+\frac{1}{2}}(t) - \mathcal{H}_{j-\frac{1}{2}}(t)}{\Delta x}, \quad (\text{A.23})$$

where \mathcal{H} denotes the numerical flux at the cell face. For the interface at $x_{j+1/2}$ the numerical flux reads:

$$\mathcal{H}_{j+\frac{1}{2}}(t) := \frac{a_{j+\frac{1}{2}}^+ \mathcal{F}(u_{j+\frac{1}{2}}^-) - a_{j+\frac{1}{2}}^- \mathcal{F}(u_{j+\frac{1}{2}}^+)}{a_{j+\frac{1}{2}}^+ - a_{j+\frac{1}{2}}^-} - \frac{a_{j+\frac{1}{2}}^+ a_{j+\frac{1}{2}}^-}{a_{j+\frac{1}{2}}^+ - a_{j+\frac{1}{2}}^-} (u_{j+\frac{1}{2}}^- - u_{j+\frac{1}{2}}^+). \quad (\text{A.24})$$

This flux formulation and the related reconstruction procedures form the basis for the hybrid pressure-based approach introduced in Sec. 3.3.5.

A.3 Flux-vector splitting approach

Following the suggestions of Billet and Abgrall [32] and Billet and Ryan [33], the flux-vector splitting scheme AUSM⁺-up for all speeds [171] is employed in the density-based double-flux solver. The FVS method belongs to the class of upwind schemes and incorporates the direction of propagation of information into the flux formulation [316]. First FVS approaches were proposed in the 1970s/80s by Sanders and Pendergast [271], Steger and Warming [299] and van Leer [338, 339] which were followed by many other groups, see, e.g., Drikakis and Tsangaris [67] and Weatherill et al. [344]. In FVS methods, the inviscid flux vector is decomposed into two parts. The following two approaches are found in the literature [37]:

1. Decomposition according to the sign of certain characteristic variables.
2. Decomposition into a convective and a pressure part.

The latter decomposition method was proposed by Liou and Steffen [173] in 1993 together with the introduction of the AUSM-family of schemes and is employed in the present work to determine the Euler fluxes in the double-flux method.

The common basis and key feature of the AUSM-family of schemes is the definition of the face Mach number based on left- and right-sided face states. An overview of the evolution of the AUSM family throughout the years and a discussion of the specific features can be found in the recent work of Liou [172]. In the present work, the AUSM⁺-up for all speeds scheme [171] together with the real-gas extension proposed by Edwards et al. [70] is employed. In the following, the AUSM⁺-up scheme is introduced for a pure fluid flow without viscous effects. The one-dimensional Euler equations with mass, momentum and energy conservation are considered:

$$\frac{\partial \mathbf{U}}{\partial t} + \frac{\partial \mathcal{F}(\mathbf{U})}{\partial x} = 0. \quad (\text{A.25})$$

Here, \mathbf{U} and $\mathcal{F}(\mathbf{U})$ denote the vector of the conserved variables and the flux vector, respectively. Both are given as

$$\mathbf{U} = \begin{bmatrix} \rho \\ \rho u \\ \rho e_t \end{bmatrix}, \quad \mathcal{F}(\mathbf{U}) = \begin{bmatrix} \rho u \\ \rho u^2 + p \\ u(\rho e_t + p) \end{bmatrix} = \begin{bmatrix} \rho u \\ \rho u^2 + p \\ \rho u h_t \end{bmatrix}. \quad (\text{A.26})$$

Employing an explicit time integration and the FVM to Eq. (A.25) yields the following linearized system of equations:

$$\mathbf{U}_j^{n+1} = \mathbf{U}_j^n - \frac{\Delta t}{\Delta x} [\mathcal{H}(x_{j+\frac{1}{2}}, t^n) - \mathcal{H}(x_{j-\frac{1}{2}}, t^n)]. \quad (\text{A.27})$$

According to the concept of upwinding schemes, the numerical flux \mathcal{H} at the cell face incorporates contributions from the left- and right-hand cells. Hence, the face flux at, for instance, $x_{j+1/2}$ can

be defined as [172]

$$\mathcal{H}\left(x_{j+\frac{1}{2}}, t^n\right) := \mathcal{H}(\mathbf{U}_j^n, \mathbf{U}_{j+1}^n) = \mathcal{H}(\mathbf{U}_L, \mathbf{U}_R) , \quad (\text{A.28})$$

where the subscripts refer to the respective reconstructions of the left (L) and the right (R) cell values onto the interface. In the following, the spatial indexing ($j + 1/2$ and $j - 1/2$) is omitted for the sake of simplicity and the subscript $1/2$ will be used to denote face values.

The core idea of the AUSM scheme is to split the flux into two distinct physical processes [173]: convection and acoustic waves. As a result, the Euler flux \mathcal{H} is expressed as the sum of a convective and a pressure term [172]:

$$\mathcal{H}(\mathbf{U}_L, \mathbf{U}_R) = \mathcal{H}^{(c)}(\mathbf{U}_L, \mathbf{U}_R) + \mathcal{H}^{(p)}(\mathbf{U}_L, \mathbf{U}_R) . \quad (\text{A.29})$$

These flux vectors ($\mathcal{H}^{(c)}$ and $\mathcal{H}^{(p)}$) read in the one-dimensional case

$$\mathcal{H}^{(c)}(\mathbf{U}_L, \mathbf{U}_R) = \begin{bmatrix} \rho u \\ \rho u^2 \\ \rho u h_t \end{bmatrix} = \rho u \begin{bmatrix} 1 \\ u \\ h_t \end{bmatrix} \quad (\text{A.30})$$

and

$$\mathcal{H}^{(p)}(\mathbf{U}_L, \mathbf{U}_R) = \begin{bmatrix} 0 \\ p \\ 0 \end{bmatrix} . \quad (\text{A.31})$$

Applying the concept of the common interface Mach number $\text{Ma}_{1/2}$ and the common interface pressure $p_{1/2}$ to the convective and pressure parts yields

$$\mathcal{H}^{(c)}(\mathbf{U}_L, \mathbf{U}_R) = \text{Ma}_{1/2} \begin{bmatrix} \rho_{L/R} a_{s,1/2} \\ \rho_{L/R} a_{s,1/2} u_{L/R} \\ \rho_{L/R} a_{s,1/2} h_{t,L/R} \end{bmatrix} = \text{Ma}_{1/2} a_{s,1/2} \rho_{L/R} \begin{bmatrix} 1 \\ u_{L/R} \\ h_{t,L/R} \end{bmatrix} \quad (\text{A.32})$$

and

$$\mathcal{H}^{(p)}(\mathbf{U}_L, \mathbf{U}_R) = \begin{bmatrix} 0 \\ p_{1/2} \\ 0 \end{bmatrix} . \quad (\text{A.33})$$

Here, $a_{s,1/2}$ is the interface speed of sound. In the present work, the real-gas approach due to Edwards et al. [70] is applied to determine $a_{s,1/2}$ as

$$a_{s,1/2} = \sqrt{\frac{\rho_L a_{s,L}^2 + \rho_R a_{s,R}^2}{\rho_L + \rho_R}} . \quad (\text{A.34})$$

The upwinding sources – denoted by the subscript L/R in Eq. (A.32) – depend on the interface Mach number:

$$(\bullet)_{L/R} = \begin{cases} (\bullet)_L & \text{if } \text{Ma}_{1/2} \geq 0 \\ (\bullet)_R & \text{if } \text{Ma}_{1/2} < 0 \end{cases} . \quad (\text{A.35})$$

Here, $(\bullet)_L$ and $(\bullet)_R$ denote the left- and right-hand reconstruction of cell values onto the faces. According to Fig. 3.4, these values correspond to $(\bullet)^+$ and $(\bullet)^-$ in OpenFOAM, respectively.

The crucial step of the AUSM schemes is the evaluation of the split Mach number and interface pressure. The interface Mach number $\text{Ma}_{1/2}$ is determined in the AUSM⁺-up scheme for all speeds [171] by means of a splitting based on two fourth-order polynomials $m_{(4)}$ and a contribution for low Mach number flows Ma_p [171]:

$$\text{Ma}_{1/2} = m_{(4)}^+(\text{Ma}_L) + m_{(4)}^-(\text{Ma}_R) + \text{Ma}_p . \quad (\text{A.36})$$

In general, the polynomials are functions of the reconstructed Mach number Ma (left- or right-sided) and their structure depends on whether the flow is subsonic ($|Ma| < 1$) or supersonic ($|Ma| \geq 1$) [171]:

$$m_{(4)}^{\pm}(\text{Ma}) = \begin{cases} m_{(1)}^{\pm}(\text{Ma}) & \text{if } |\text{Ma}| \geq 1 \\ m_{(2)}^{\pm}(\text{Ma}) [1 \mp 16\beta^{\text{AUSM}} m_{(2)}^{\mp}(\text{Ma})] & \text{if } |\text{Ma}| < 1 \end{cases}. \quad (\text{A.37})$$

Here, β^{AUSM} is a constant and $m_{(1)}^{\pm}$ and $m_{(2)}^{\pm}$ are expressed as [171]:

$$m_{(1)}^{\pm}(\text{Ma}) = \frac{1}{2} (\text{Ma} \pm |\text{Ma}|), \quad (\text{A.38})$$

$$m_{(2)}^{\pm}(\text{Ma}) = \pm \frac{1}{4} (\text{Ma} \pm 1)^2. \quad (\text{A.39})$$

The third term on the right-hand side of Eq. (A.36) – Ma_p – accounts for low Mach number effects [172], i.e., $u \ll a_s$. When the velocity tends towards zero an excessive amount of dissipation is introduced into compressible schemes employed in density-based solvers. The result is a slow/bad convergence behavior and the problem becomes numerically ill-conditioned. This problem can be avoided by re-scaling the speed of sound and the velocity to the same order. The most popular approach is pre-conditioning in combination with a dual time-stepping technique, see, e.g., Weiss and Smith [347]. In the applied AUSM scheme, additional coupling terms between the pressure and velocity fields are introduced to circumvent the scaling problem. According to Liou [171] the low Mach number term for the split Mach number is expressed as:

$$\text{Ma}_p = -\frac{K_p}{f_a} \max(1 - \sigma^{\text{AUSM}} \text{Ma}_m^2, 0) \frac{p_R - p_L}{\rho_{1/2} a_{s,1/2}^2}. \quad (\text{A.40})$$

Here, K_p and σ^{AUSM} are constants. Furthermore, the function f_a , the reference Mach number Ma_0 and Ma_m are defined as:

$$f_a = \text{Ma}_0 (2 - \text{Ma}_0), \quad (\text{A.41})$$

$$\text{Ma}_0 = \min(1.0, \max(\text{Ma}_m, \text{Ma}_{\infty})), \quad (\text{A.42})$$

$$\text{Ma}_m = \sqrt{\frac{u_L^2 + u_R^2}{2a_{s,1/2}^2}}. \quad (\text{A.43})$$

Here, Ma_{∞} is the cut-off Mach number, which was set to 0.3. The interface density is expressed as arithmetic average of the LHS and RHS face values:

$$\rho_{1/2} = \frac{\rho_L + \rho_R}{2}. \quad (\text{A.44})$$

Similarly to the interface Mach number, the split pressure $p_{1/2}$ is evaluated by means of two fifth-order polynomials and an additional low Mach number term p_u [171]:

$$p_{1/2} = \mathcal{P}_{(5)}^{+}(\text{Ma}_L) p_L + \mathcal{P}_{(5)}^{-}(\text{Ma}_R) p_R + p_u. \quad (\text{A.45})$$

The fifth-order pressure polynomials are again functions of the Mach number and can be determined as [171]

$$\mathcal{P}_{(5)}^{\pm}(\text{Ma}) = \begin{cases} \frac{1}{\text{Ma}} m_{(1)}^{\pm}(\text{Ma}) & \text{if } |\text{Ma}| \geq 1 \\ m_{(2)}^{\pm}(\text{Ma}) [(\pm 2 - \text{Ma}) \mp 16\alpha^{\text{AUSM}} \text{Ma} m_{(2)}^{\mp}(\text{Ma})] & \text{if } |\text{Ma}| < 1 \end{cases} \quad (\text{A.46})$$

where

$$\alpha^{\text{AUSM}} = \frac{3}{16} (-4 + 5f_a^2). \quad (\text{A.47})$$

Finally, the low Mach number contribution to the split pressure reads

$$p_u = -K_u \mathcal{P}_{(5)}^+ (\text{Ma}_L) \mathcal{P}_{(5)}^- (\text{Ma}_R) (\rho_L + \rho_R) f_a a_{s,1/2} (u_R - u_L) , \quad (\text{A.48})$$

where K_u is a constant. The constants required in the AUSM⁺-up scheme for all speeds [171] – β^{AUSM} , K_P , σ^{AUSM} and K_u – are listed in Tab. A.1. These constants are not fixed and can be adjusted to the respective flow problem. However, physical constraints have to be considered when the constants are parameterized. For more information, see the work of Liou [171]. In the present work, the original constants as proposed by Liou [171] are applied.

Table A.1: Constants used in the AUSM⁺-up scheme for all speeds [171].

β^{AUSM}	K_P	σ^{AUSM}	K_u
0.125	0.25	1.0	0.75

B Thermophysical properties

B.1 Critical properties, acentric factor and molar weight

In Tab. B.1, the critical properties, the acentric factor and the molar weight for the different fluids considered within this work are listed. The reference values are taken from CoolProp [27] and Zips [367].

Table B.1: Critical properties, acentric factor and molar weight of the applied fluids.

Fluid	p_c [bar]	T_c [K]	v_c [$\text{cm}^3 \text{ mol}^{-1}$]	Z_c [-]	ω [-]	M [g mol^{-1}]
C ₆ H ₁₄	30.34	507.82	369.57	0.2656	0.2990	86.18
N ₂	33.96	126.19	89.41	0.2894	0.0372	28.00
Ar	48.63	150.69	74.59	0.2895	-0.0022	39.95
H ₂	12.93	32.98	64.20	0.3030	-0.2170	2.00
CH ₄	45.99	190.56	98.63	0.2860	0.0114	16.04
C ₂ H ₆	48.72	305.32	145.84	0.2799	0.0990	30.07
C ₁₂ H ₂₆	18.17	658.10	751.88	0.2497	0.5742	170.33
O ₂	50.43	154.58	73.37	0.2879	0.0222	32.00
H ₂ O	221.20	647.30	55.95	0.2299	0.3443	18.02
CO	34.94	132.85	93.10	0.2920	0.0450	28.01
CO ₂	73.74	304.12	94.07	0.2740	0.2250	44.01
H	88.20	404.30	118.59	0.3112	0.0	1.01
O	76.00	367.40	125.07	0.3112	0.0	16.00
OH	85.40	443.70	134.41	0.3112	0.3290	17.01
HO ₂	33.96	126.19	89.41	0.2894	0.0372	33.01
H ₂ O ₂	33.96	126.19	89.41	0.2894	0.0372	34.01
C	33.96	126.19	89.41	0.2894	0.0372	12.01
CH	33.96	126.19	89.41	0.2894	0.0372	13.02
CH ₂	33.96	126.19	89.41	0.2894	0.0372	14.03
CH ₃	33.96	126.19	89.41	0.2894	0.0372	15.04
HCO	33.96	126.19	89.41	0.2894	0.0372	29.02
CH ₂ O	33.96	126.19	89.41	0.2894	0.0372	30.03
CH ₂ OH	33.96	126.19	89.41	0.2894	0.0372	31.03
CH ₃ O	33.96	126.19	89.41	0.2894	0.0372	31.03
CH ₃ OH	33.96	126.19	89.41	0.2894	0.0372	32.04
C ₂ H ₂	33.96	126.19	89.41	0.2894	0.0372	26.04
C ₂ H ₃	33.96	126.19	89.41	0.2894	0.0372	27.05
C ₂ H ₄	33.96	126.19	89.41	0.2894	0.0372	28.05
C ₂ H ₅	33.96	126.19	89.41	0.2894	0.0372	29.06
HCCO	33.96	126.19	89.41	0.2894	0.0372	41.03
CH ₂ CO	33.96	126.19	89.41	0.2894	0.0372	42.04
CH ₂ CHO	33.96	126.19	89.41	0.2894	0.0372	43.05

B.2 High-pressure diffusion coefficients

For the calculation of high-pressure diffusion coefficients, two different approaches are often used in the LRE community: a generalized chart due to Takahashi [309] and an analytical approach proposed by Riazi and Whitson [258]. In the present work, the latter is employed in the investigation of the binary n-hexane/nitrogen thermodynamic mixing trajectories. The equation to determine

the diffusion coefficient between species A and B according to Riazi and Whitson [258] reads:

$$D_{AB} = \frac{a_{\text{Riazi}} (D_{AB} p)^0}{\rho R T} \left(\frac{\mu}{\mu^0} \right)^{b_{\text{Riazi}} + c_{\text{Riazi}} p_r, \text{Riazi}}. \quad (\text{B.1})$$

Here, $a_{\text{Riazi}} = 1.07$ and the variables b_{Riazi} and c_{Riazi} can be determined as:

$$b_{\text{Riazi}} = -0.27 - 0.38\omega_{\text{Riazi}}, \quad (\text{B.2})$$

$$c_{\text{Riazi}} = -0.05 + 0.1\omega_{\text{Riazi}}. \quad (\text{B.3})$$

The pseudo-critical critical pressure $p_{c,\text{Riazi}}$ and the acentric factor of the binary mixture are calculated as molar weighted properties:

$$p_{c,\text{Riazi}} = z_A p_{c,A} + z_B p_{c,B}, \quad (\text{B.4})$$

$$\omega_{\text{Riazi}} = z_A \omega_A + z_B \omega_B. \quad (\text{B.5})$$

The ideal gas references of the viscosity μ^0 and the diffusion coefficient $(D_{AB} p)^0$ are estimated based on Sutherland's law, see Eq. (4.84), and the model due to Fuller et al. [85]

$$(D_{AB} p)^0 = 3.1209254 \times 10^{-8} \frac{T^{1.75} \sqrt{\frac{1}{M_A} + \frac{1}{M_B}}}{\left(\sum_A v_i^{1/3} + \sum_B v_i^{1/3} \right)^2}. \quad (\text{B.6})$$

Here, $\sum_A v_i$ and $\sum_B v_i$ are the diffusion volumes of the species A and B, respectively. According to Fuller et al. [84], theses volumes are $1.2774 \times 10^{-4} \text{ m}^3$ for n-hexane and $1.85 \times 10^{-5} \text{ m}^3$ for nitrogen.

C Departure functions for the state equation due to Soave, Redlich and Kwong

In the following the departure functions for the SRK-EoS [296] are briefly summarized. The best starting point is the departure function of the molar internal energy:

$$\underline{e}^r = \frac{a - T \frac{da}{dT}}{b} \ln \left(\frac{\underline{v}}{\underline{v} + b} \right). \quad (\text{C.1})$$

Here, the derivative of the attractive term with respect to the temperature reads:

$$\frac{da}{dT} = \sum_{i=1}^{N_c} \sum_{j=1}^{N_c} z_i z_j \frac{da_{ij}}{dT}, \quad (\text{C.2})$$

$$\frac{da_{ij}}{dT} = 0.42748 \frac{\mathcal{R}^2 T_{c,ij}^2}{p_{c,ij}} \frac{\kappa_{ij}}{\sqrt{T_{c,ij}}} \left(\frac{\kappa_{ij}}{\sqrt{T_{c,ij}}} - \frac{1 + \kappa_{ij}}{\sqrt{T}} \right). \quad (\text{C.3})$$

Based on the definition of the enthalpy, the real-gas contribution of h can be expressed as:

$$\underline{h}^r = \underline{e}^r + p\underline{v} - \mathcal{R}T = p\underline{v} - \mathcal{R}T + \frac{a - T \frac{da}{dT}}{b} \ln \left(\frac{\underline{v}}{\underline{v} + b} \right). \quad (\text{C.4})$$

The departure function of the entropy for the SRK-EoS [296] is:

$$\underline{s}^r = \mathcal{R} \ln \left[\frac{p(\underline{v} - b)}{\mathcal{R}T} \right] - \frac{da}{dT} \frac{1}{b} \ln \left(\frac{\underline{v}}{\underline{v} + b} \right). \quad (\text{C.5})$$

Using the analytical expressions for the internal energy, enthalpy and entropy, the departure functions of the Gibbs energy and the Helmholtz free energy can be written as:

$$\underline{g}^r = \underline{h}^r - T\underline{s}^r = p\underline{v} - \mathcal{R}T - \mathcal{R}T \ln \left[\frac{p(\underline{v} - b)}{\mathcal{R}T} \right] + \frac{a}{b} \ln \left(\frac{\underline{v}}{\underline{v} + b} \right), \quad (\text{C.6})$$

$$\underline{f}^r = \underline{e}^r - T\underline{s}^r = -\mathcal{R}T \ln \left[\frac{p(\underline{v} - b)}{\mathcal{R}T} \right] + \frac{a}{b} \ln \left(\frac{\underline{v}}{\underline{v} + b} \right). \quad (\text{C.7})$$

The heat capacity at isobaric conditions can be calculated according to:

$$c_p = \underline{c}_p^0(T, \mathbf{z}) - \mathcal{R} - \frac{T \frac{d^2 a}{dT^2}}{b} \left(\frac{\underline{v}}{\underline{v} + b} \right) - T \frac{\left(\frac{\partial p}{\partial T} \Big|_{\underline{v}} \right)^2}{\frac{\partial p}{\partial \underline{v}} \Big|_T}. \quad (\text{C.8})$$

Here, the second derivative of the attractive term with respect to the temperature is

$$\frac{d^2 a}{dT^2} = \sum_{i=1}^{N_c} \sum_{j=1}^{N_c} z_i z_j \frac{d^2 a_{ij}}{dT^2}, \quad (\text{C.9})$$

$$\frac{d^2 a_{ij}}{dT^2} = 0.42748 \frac{\mathcal{R}^2}{2T} \kappa_{ij} (1 + \kappa_{ij}) \frac{T_{c,ij}}{p_{c,ij}} \sqrt{\frac{T_{c,ij}}{T}}. \quad (\text{C.10})$$

The derivatives of the pressure with respect to the temperature and volume are:

$$\frac{\partial p}{\partial T} \Big|_{\underline{v}} = \frac{\mathcal{R}}{\underline{v} - b} - \frac{\frac{da}{dT}}{\underline{v}^2 + b\underline{v}}, \quad (\text{C.11})$$

$$\left. \frac{\partial p}{\partial \underline{v}} \right|_T = -\frac{\mathcal{R}T}{(\underline{v} - b)^2} + \frac{a(2\underline{v} + b)}{(\underline{v}^2 + b\underline{v})^2}. \quad (\text{C.12})$$

To calculate the partial derivative of the density with respect to the pressure at isenthalpic conditions, the following two partial derivatives are necessary:

$$\left(\left. \frac{\partial h}{\partial p} \right|_{\underline{v}} \right)^r = \underline{v} - \frac{\mathcal{R}}{\left. \frac{\partial p}{\partial T} \right|_{\underline{v}}} - \frac{T \frac{d^2 a}{dT^2} / \left. \frac{\partial p}{\partial T} \right|_{\underline{v}}}{b} \ln \left[\frac{\underline{v}}{\underline{v} + b} \right], \quad (\text{C.13})$$

$$\left(\left. \frac{\partial h}{\partial \underline{v}} \right|_p \right)^r = p - \mathcal{R} \left. \frac{\partial T}{\partial \underline{v}} \right|_p - \frac{T \frac{d^2 a}{dT^2} \left. \frac{\partial T}{\partial \underline{v}} \right|_p}{b} \ln \left[\frac{\underline{v}}{\underline{v} + b} \right] + \frac{a - T \frac{da}{dT}}{\underline{v}^2 + b\underline{v}}. \quad (\text{C.14})$$

Finally, the fugacity coefficient of the i -th component can be determined as:

$$\ln \varphi_i = -\ln \left[\frac{p(\underline{v} - b)}{\mathcal{R}T} \right] + \frac{b_i}{b} (Z - 1) - \frac{a}{b\mathcal{R}T} \left(\frac{2 \sum_{j=1}^{N_c} z_j a_{ij}}{a} - \frac{b_i}{b} \right) \ln \left(\frac{\underline{v} + b}{\underline{v}} \right). \quad (\text{C.15})$$

D Partial derivatives of the fugacity coefficient

For the flashing approaches and the construction of the phase envelopes, the partial derivatives of the fugacity coefficient with respect to the pressure, temperature and mole numbers are required. The derivation with respect to the mole numbers has advantages compared to the derivation with respect to the mole fractions. First of all, the resulting Jacobian matrix is symmetric

$$\frac{\partial \ln \varphi_i}{\partial n_j} \Big|_{p,T,n_k \neq j} = \frac{\partial \ln \varphi_j}{\partial n_i} \Big|_{p,T,n_k \neq i} \quad (\text{D.1})$$

which is not necessarily the case when the partial derivative is formulated with respect to the mole fractions [196]. Second, the derivatives can be used for both mole numbers as well as mole fractions, since mole fractions can be treated as mole numbers summing up to unity. When implementing the partial derivatives into the numerical code, consistency checks as described in the textbook of Michelsen and Mollerup [196] are recommended.

D.1 Equation of state due to Peng and Robinson

Applying the Peng-Robinson [226] EoS for deriving the natural logarithm of the fugacity coefficient of component i yields the following analytical expression:

$$\begin{aligned} \ln \varphi_i &= \ln \left(\frac{1}{Z - B} \right) + \frac{b_i}{b} (Z - 1) - \frac{A}{\sqrt{8B}} \left(\frac{2 \sum_{j=1}^{N_c} z_j a_{ij}}{a} - \frac{b_i}{b} \right) \ln \left[\frac{Z + B (1 + \sqrt{2})}{Z + B (1 - \sqrt{2})} \right] \\ &= \ln(\alpha) + \beta + \gamma \ln(\delta) . \end{aligned} \quad (\text{D.2})$$

Here, $A = pa(\mathcal{R}T)^{-2}$ and $B = pb(\mathcal{R}T)^{-1}$ are the dimensionless attractive and repulsive forces, respectively. The cubic form of the PR-EoS [226] in terms of the compressibility factor Z is:

$$Z^3 - (1 - B) Z^2 + (A - 3B^2 - 2B) Z - (AB - B^2 - B^3) = 0 . \quad (\text{D.3})$$

Splitting up Eq. (D.2) into four different parts, namely α , β , γ and δ , makes it easier to derive the analytical equations for the partial derivatives of $\ln \varphi_i$.

Derivation with respect to the pressure

The derivative of $\ln \varphi_i$ with respect to the pressure can be split up in

$$\begin{aligned} \frac{\partial \ln \varphi_i}{\partial p} \Big|_{T,\mathbf{n}} &= \frac{\partial \ln(\alpha)}{\partial p} + \frac{\partial \beta}{\partial p} + \ln(\delta) \frac{\partial \gamma}{\partial p} + \gamma \frac{\partial \ln(\delta)}{\partial p} \\ &= \frac{1}{\alpha} \frac{\partial \alpha}{\partial p} + \frac{\partial \beta}{\partial p} + \ln(\delta) \frac{\partial \gamma}{\partial p} + \frac{\gamma}{\delta} \frac{\partial \delta}{\partial p} . \end{aligned} \quad (\text{D.4})$$

The required partial derivatives read as follows:

$$\frac{\partial \alpha}{\partial p} = \frac{-\left(\frac{\partial Z}{\partial p} - \frac{\partial B}{\partial p}\right)}{(Z - B)^2} , \quad (\text{D.5})$$

$$\frac{\partial Z}{\partial p} = \frac{1}{p} \frac{(B - Z) A + [-Z^2 + Z(6B + 2) + A - 2B - 3B^2] B}{3Z^2 - 2Z(1 - B) + A - 3B^2 - 2B} , \quad (\text{D.6})$$

$$\frac{\partial B}{\partial p} = \frac{b}{\mathcal{R}T}, \quad (\text{D.7})$$

$$\frac{\partial \beta}{\partial p} = \frac{b_i}{b} \frac{\partial Z}{\partial p}, \quad (\text{D.8})$$

$$\frac{\partial \gamma}{\partial p} = 0, \quad (\text{D.9})$$

$$\frac{\partial \delta}{\partial p} = \frac{2\sqrt{2} \left(Z \frac{\partial B}{\partial p} - B \frac{\partial Z}{\partial p} \right)}{\left[Z + B (1 - \sqrt{2}) \right]^2}. \quad (\text{D.10})$$

Derivation with respect to the temperature

A very similar path has to be taken for the derivation of the partial derivative of the fugacity coefficient with respect to the temperature:

$$\begin{aligned} \frac{\partial \ln \varphi_i}{\partial T} \Big|_{p, n} &= \frac{\partial \ln(\alpha)}{\partial T} + \frac{\partial \beta}{\partial T} + \ln(\delta) \frac{\partial \gamma}{\partial T} + \gamma \frac{\partial \ln(\delta)}{\partial T} \\ &= \frac{1}{\alpha} \frac{\partial \alpha}{\partial T} + \frac{\partial \beta}{\partial T} + \ln(\delta) \frac{\partial \gamma}{\partial T} + \frac{\gamma}{\delta} \frac{\partial \delta}{\partial T}. \end{aligned} \quad (\text{D.11})$$

The required partial derivatives can be calculated analytically as follows:

$$\frac{\partial \alpha}{\partial T} = \frac{-\left(\frac{\partial Z}{\partial T} - \frac{\partial B}{\partial T}\right)}{(Z - B)^2}, \quad (\text{D.12})$$

$$\frac{\partial Z}{\partial T} = \frac{(B - Z) \frac{\partial A}{\partial T} + [-Z^2 + Z(6B + 2) + A - 2B - 3B^2] \frac{\partial B}{\partial T}}{3Z^2 - 2Z(1 - B) + A - 3B^2 - 2B}, \quad (\text{D.13})$$

$$\frac{\partial A}{\partial T} = \frac{p \frac{da}{dT} - pa \frac{2}{T}}{\mathcal{R}^2 T^2}, \quad (\text{D.14})$$

$$\frac{\partial B}{\partial T} = -\frac{B}{T}, \quad (\text{D.15})$$

$$\frac{\partial \beta}{\partial T} = \frac{b_i}{b} \frac{\partial Z}{\partial T}, \quad (\text{D.16})$$

$$\frac{\partial \gamma}{\partial T} = \frac{\left(\frac{da}{dT} b_i - 2b \sum_{j=1}^{N_c} z_j \frac{da_{ij}}{\partial T}\right) T - ab_i + 2b \sum_{j=1}^{N_c} z_j a_{ij}}{2\sqrt{2}\mathcal{R}b^2T^2}, \quad (\text{D.17})$$

$$\frac{\partial \delta}{\partial T} = \frac{2\sqrt{2} \left(Z \frac{\partial B}{\partial T} - B \frac{\partial Z}{\partial T} \right)}{\left[Z + B (1 - \sqrt{2}) \right]^2}. \quad (\text{D.18})$$

Derivation with respect to the mole number

The derivative of Eq. (D.2) with respect to the mole number of the j -th species is:

$$\begin{aligned} \frac{\partial \ln \varphi_i}{\partial n_j} \Big|_{p, T, n_k \neq j} &= \frac{\partial \ln(\alpha)}{\partial n_j} + \frac{\partial \beta}{\partial n_j} + \ln(\delta) \frac{\partial \gamma}{\partial n_j} + \gamma \frac{\partial \ln(\delta)}{\partial n_j} \\ &= \frac{1}{\alpha} \frac{\partial \alpha}{\partial n_j} + \frac{\partial \beta}{\partial n_j} + \ln(\delta) \frac{\partial \gamma}{\partial n_j} + \frac{\gamma}{\delta} \frac{\partial \delta}{\partial n_j}. \end{aligned} \quad (\text{D.19})$$

The derivative of α with respect to the mole number n_j reads:

$$\frac{\partial \alpha}{\partial n_j} = \frac{-\left(\frac{\partial Z}{\partial n_j} - \frac{\partial B}{\partial n_j}\right)}{(Z - B)^2}. \quad (\text{D.20})$$

This includes the partial derivative of the compressibility factor

$$\frac{\partial Z}{\partial n_j} = \frac{(B - Z) \frac{\partial A}{\partial n_j} + [-Z^2 + Z(6B + 2) + A - 2B - 3B^2] \frac{\partial B}{\partial n_j}}{3Z^2 - 2Z(1 - B) + A - 3B^2 - 2B} \quad (\text{D.21})$$

and the partial derivative of the normalized attractive force $A = pa(\mathcal{R}^2 T^2)^{-1}$:

$$\frac{\partial A}{\partial n_j} = \frac{p}{\mathcal{R}^2 T^2} \frac{\partial a}{\partial n_j} \quad (\text{D.22})$$

with

$$\frac{\partial a}{\partial n_j} = -\frac{2a}{n_t} + \frac{2}{n_t^2} \sum_{k=1}^{N_c} n_k a_{jk} . \quad (\text{D.23})$$

In addition, the partial derivative of the normalized co-volume B is required

$$\frac{\partial B}{\partial n_j} = \frac{p}{\mathcal{R}T} \frac{\partial b}{\partial n_j} \quad (\text{D.24})$$

with

$$\frac{\partial b}{\partial n_j} = -\frac{b}{n_t} + \frac{b_j}{n_t} . \quad (\text{D.25})$$

The partial derivative of β can be obtained with no additional derivatives necessary:

$$\frac{\partial \beta}{\partial n_j} = \frac{b_i \frac{\partial Z}{\partial n_j} b - b_i (Z - 1) \frac{\partial b}{\partial n_j}}{b^2} . \quad (\text{D.26})$$

For deriving the partial derivative of γ we split up the derivative into two parts χ and ζ

$$\frac{\partial \gamma}{\partial n_j} = -\frac{1}{\sqrt{8}\mathcal{R}T} \left(\frac{\partial \chi}{\partial n_j} - \frac{\partial \zeta}{\partial n_j} \right) \quad (\text{D.27})$$

with

$$\frac{\partial \chi}{\partial n_j} = \frac{2a_{ij}n_tb - 2\sum_{k=1}^{N_c} n_k a_{ik} \left(b + n_t \frac{\partial b}{\partial n_j} \right)}{(n_tb)^2} \quad (\text{D.28})$$

and

$$\frac{\partial \zeta}{\partial n_j} = \frac{b^2 b_i \frac{\partial a}{\partial n_j} - ab_i 2b \frac{\partial b}{\partial n_j}}{(b^2)^2} . \quad (\text{D.29})$$

The derivative of δ can be obtained as:

$$\frac{\partial \delta}{\partial n_j} = \frac{2\sqrt{2} \left(Z \frac{\partial B}{\partial n_j} - B \frac{\partial Z}{\partial n_j} \right)}{[Z + B(1 - \sqrt{2})]^2} . \quad (\text{D.30})$$

D.2 Equation of state due to Soave, Redlich and Kwong

In the following, the partial derivatives of the fugacity coefficient with respect to the pressure, temperature and mole numbers are shown for the cubic EoS of Soave-Redlich-Kwong [296]. Analogous to the derivation of the PR-EoS [226], the fugacity coefficient of component i is split up into four different terms:

$$\begin{aligned} \ln \varphi_i &= \ln \left(\frac{1}{Z - B} \right) + \frac{b_i}{b} (Z - 1) - \frac{A}{B} \left(\frac{2 \sum_{j=1}^{N_c} z_j a_{ij}}{a} - \frac{b_i}{b} \right) \ln \left[\frac{Z + B}{Z} \right] \\ &= \ln(\alpha) + \beta + \gamma \ln(\delta) . \end{aligned} \quad (\text{D.31})$$

To shorten the demonstration of the derivation only the derivatives which differ from the ones of the PR-EoS [226] are explicitly shown in the following. The cubic form of the SRK-EoS [296] in terms of the compressibility factor Z is:

$$Z^3 - Z^2 + (A - B - B^2)Z - AB = 0. \quad (\text{D.32})$$

Derivation with respect to the pressure

The derivative of $\ln \varphi_i$ with respect to the pressure can be split up in

$$\frac{\partial \ln \varphi_i}{\partial p} \Big|_{T,\mathbf{n}} = \frac{\partial \ln(\alpha)}{\partial p} + \frac{\partial \beta}{\partial p} + \ln(\delta) \frac{\partial \gamma}{\partial p} + \gamma \frac{\partial \ln(\delta)}{\partial p} = \frac{1}{\alpha} \frac{\partial \alpha}{\partial p} + \frac{\partial \beta}{\partial p} + \ln(\delta) \frac{\partial \gamma}{\partial p} + \frac{\gamma}{\delta} \frac{\partial \delta}{\partial p}. \quad (\text{D.33})$$

The following partial derivatives differ from the PR-EoS [226]:

$$\frac{\partial Z}{\partial p} = \frac{1}{p} \frac{(B - Z)A + ZB(1 + 2B) + AB}{3Z^2 - 2Z + A - B - B^2}, \quad (\text{D.34})$$

$$\frac{\partial \delta}{\partial p} = \frac{Z \frac{\partial B}{\partial p} - B \frac{\partial Z}{\partial p}}{Z^2}. \quad (\text{D.35})$$

Derivation with respect to the temperature

The basic expression for the derivation of the partial derivative of the fugacity coefficient with respect to the temperature is

$$\frac{\partial \ln \varphi_i}{\partial T} \Big|_{p,\mathbf{n}} = \frac{\partial \ln(\alpha)}{\partial T} + \frac{\partial \beta}{\partial T} + \ln(\delta) \frac{\partial \gamma}{\partial T} + \gamma \frac{\partial \ln(\delta)}{\partial T} = \frac{1}{\alpha} \frac{\partial \alpha}{\partial T} + \frac{\partial \beta}{\partial T} + \ln(\delta) \frac{\partial \gamma}{\partial T} + \frac{\gamma}{\delta} \frac{\partial \delta}{\partial T}. \quad (\text{D.36})$$

The required partial derivatives being different from the approaches in the PR-EoS [226] case read:

$$\frac{\partial Z}{\partial T} = \frac{(B - Z) \frac{\partial A}{\partial T} + [Z(1 + 2B) + A] \frac{\partial B}{\partial T}}{3Z^2 - 2Z + A - B - B^2}, \quad (\text{D.37})$$

$$\frac{\partial \gamma}{\partial T} = \frac{\left(\frac{da}{dT} b_i - 2b \sum_{j=1}^{N_c} z_j \frac{da_{ij}}{dT} \right) T - ab_i + 2b \sum_{j=1}^{N_c} z_j a_{ij}}{\mathcal{R} b^2 T^2}, \quad (\text{D.38})$$

$$\frac{\partial \delta}{\partial T} = \frac{Z \frac{\partial B}{\partial T} - B \frac{\partial Z}{\partial T}}{Z^2}. \quad (\text{D.39})$$

Derivation with respect to the mole number

The basic derivation for calculating the partial derivative of the fugacity coefficient with respect to the mole numbers is

$$\begin{aligned} \frac{\partial \ln \varphi_i}{\partial n_j} \Big|_{p,T,n_{k \neq j}} &= \frac{\partial \ln(\alpha)}{\partial n_j} + \frac{\partial \beta}{\partial n_j} + \ln(\delta) \frac{\partial \gamma}{\partial n_j} + \gamma \frac{\partial \ln(\delta)}{\partial n_j} \\ &= \frac{1}{\alpha} \frac{\partial \alpha}{\partial n_j} + \frac{\partial \beta}{\partial n_j} + \ln(\delta) \frac{\partial \gamma}{\partial n_j} + \frac{\gamma}{\delta} \frac{\partial \delta}{\partial n_j}. \end{aligned} \quad (\text{D.40})$$

The only two derivatives that are different due to the change of the EoS are the derivative of the compressibility factor

$$\frac{\partial Z}{\partial n_j} = \frac{(B - Z) \frac{\partial A}{\partial n_j} + [Z(1 + 2B) + A] \frac{\partial B}{\partial n_j}}{3Z^2 - 2Z + A - B - B^2} \quad (\text{D.41})$$

and of δ

$$\frac{\partial \delta}{\partial n_j} = \frac{Z \frac{\partial B}{\partial n_j} - B \frac{\partial Z}{\partial n_j}}{Z^2}. \quad (\text{D.42})$$

E Solver instabilities due to real-gas thermodynamics

The thermodynamic stability of a multicomponent system relies on three different mechanisms [77]: thermal stability, mechanical stability and chemical stability. According to Sec. 4.3, the thermodynamic equilibrium of a system can be defined by the equality of the temperature T , the pressure p and the chemical potentials μ_i :

$$T^I = T^{II} , \quad (\text{E.1})$$

$$p^I = p^{II} , \quad (\text{E.2})$$

$$\mu_i^I = \mu_i^{II} \quad i = 1, \dots, N_c . \quad (\text{E.3})$$

Within these equations, the superscripts indicate the different phases (here: two phases are considered denoted by I and II).

The first stability criterion which can be violated is the thermal one. In a closed system – molar volume \underline{v} and composition are constant – the thermal stability is satisfied when an isochoric heat supply, i.e., a rise in entropy \underline{s} , leads to a temperature increase. Therefore, the thermal stability criterion reads

$$\left. \frac{\partial T}{\partial \underline{s}} \right|_{\underline{v}, \mathbf{z}} > 0 . \quad (\text{E.4})$$

Applying the Maxwell Eq. (4.36) and using the fact that T is strictly positive, the thermal stability criterion can be expressed in terms of the specific heat at constant volume \underline{c}_v as

$$\underline{c}_v = \left. \frac{\partial \underline{e}}{\partial T} \right|_{\underline{v}, \mathbf{z}} > 0 . \quad (\text{E.5})$$

Due to the application of cubic equations of state in this work, \underline{c}_v is always larger than zero. Therefore, the thermal stability is ensured and of no concern [86].

The second thermodynamic stability criterion is the mechanical one. This condition can be violated whenever the pressure is below the critical pressure of the pure components. In the present work, such low pressure values occur during the high-speed fuel injection under GE-like operating conditions. In LREs, pressure conditions below the critical point of the fuel and oxidizer can be found during the start-up of an LRE [225]. In general, the mechanical stability criterion states that a decrease in volume must result in a pressure increase under isothermal conditions. Hence,

$$\left. \frac{\partial p}{\partial \underline{v}} \right|_{T, \mathbf{z}} < 0 \quad (\text{E.6})$$

must be fulfilled for ensuring the mechanical stability of the system. Equation (E.6) is related to phase separation in pure fluids, where it defines the spinodal region corresponding to the locus of intrinsic single-phase instability, i.e., the existence limit of metastable states [62], see Fig. E.1. The spinodal region cannot be entered and therefore a single phase (metastable) state instantaneously separates into a vapor and a liquid phase. For a pressure-based solver¹ an inadvertent crossing of the binodal can result in stability problems and usually in a crashing of the solver when real-gas equations of state are applied for the thermodynamic closure. This results from the fact that under subcritical conditions the cubic equation of state yields three real roots, see Fig. E.1. Focusing on the approximated isentropic expansion path shown in Fig. E.1, two possible scenarios can occur

¹Similar considerations can be made for a density-based solver. However, the main part of this work was conducted with a pressure-based solver and therefore the following statements are made with respect to this solver type.

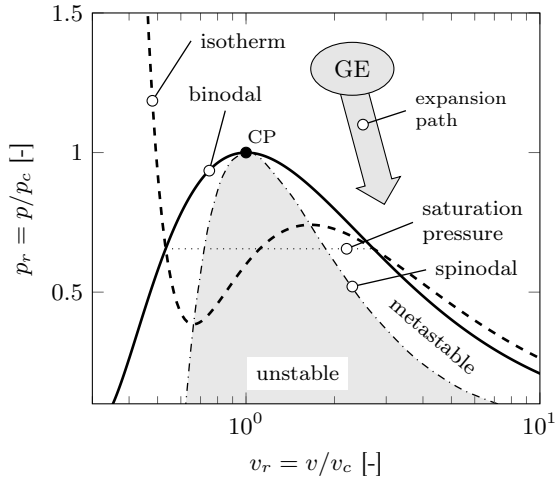


Figure E.1: Reduced p,v -diagram of a pure fluid together with an approximated expansion path as it can occur during the direct injection in gas engines.

during the simulation of high-pressure injection after crossing of the binodal: Either the root with the smallest Gibbs energy is chosen or the largest root, i.e., the gas root, is selected as solution. The latter results in an extrapolation of the gas state into the two phase region. This, in turn, yields large subcoolings in terms of temperature as the condensation process is suppressed, but stable results can be achieved until the spinodal is crossed. After the crossing of the spinodal, the solver crashes as, for instance, the speed of sound is proportional to $\sqrt{-\partial p/\partial v}|_T$ which has then no real solution anymore or in other words the square of the speed of sound gets negative [87]. If the Gibbs criterion is applied for the selection of the appropriate root [73], the equilibrium isotherm is obtained resulting in a discontinuous jump across the two-phase region highlighted by the saturation pressure in Fig. E.1. Depending on the iteration setup of the thermodynamic framework, i.e., the recalculation of the temperature from the transported energy and pressure, this can lead to the fact that no solution will be found or that the liquid root is selected which in turn results in a crash of the solver due to negative (here: nonphysical) pressures. The solution for these different problems is the consideration of the phase separation process after the crossing of the binodal within the thermodynamic framework which solves the convexity issue of the EoS [274, 273, 275].

The third and last stability criterion is the chemical instability which can occur during high-pressure injection when multicomponent mixtures are present. Similar to the mechanical stability limit, the chemical stability limit is associated with phase separation processes as it defines the limit of stability in mixtures. For a binary mixture at isothermal and isobaric conditions, the chemical stability limit can be defined by means of the partial derivative of the chemical potential with respect to the mole number as

$$\left. \frac{\partial \mu_1}{\partial n_1} \right|_{T,p,n_2} = 0. \quad (\text{E.7})$$

For a mixture of constant composition, Fig. E.2a shows a sketch of the binodal, often called isopleth, as well as the spinodal. A typical loop-like pattern can be seen for the mixture spinodal lying inside the two phase dome marking the limit of metastable states and hence the region of intrinsic phase separation. The chemical stability limit is reached before the mechanical one which lies inside the mixture spinodal. This fact gets highlighted in Fig. E.2b where the complete VLE of a binary mixture with a type-I critical locus is shown. Due to the location of the two different spinodals – the mechanical one lies inside the chemical one – the phase separation process will always be triggered by chemical instabilities in the case of multicomponent mixtures. Similar to the discussion of the pure fluid, the application of the single-phase treatment can also result in problems during numerical simulations. The main reason is that nonideal diffusion implies the

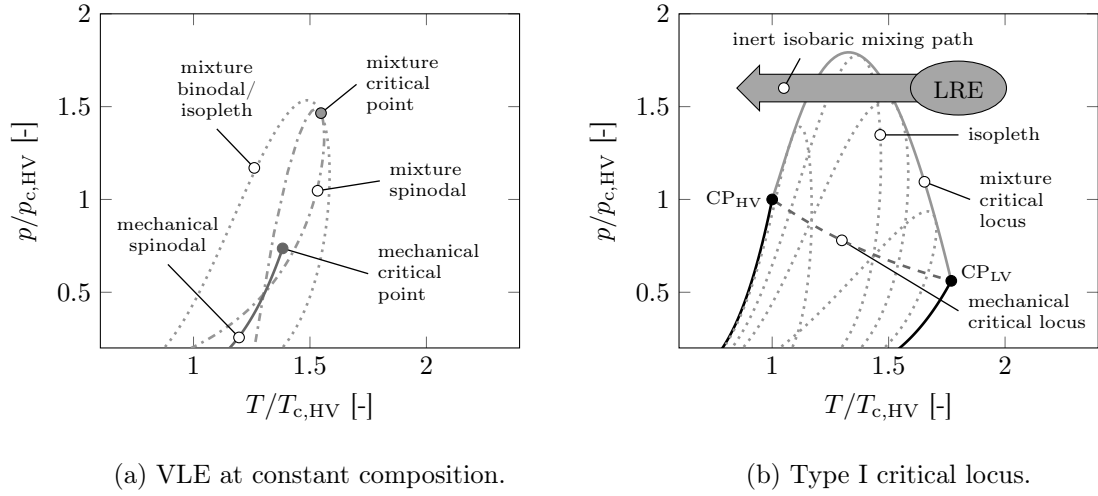


Figure E.2: Sketch of a vapor-liquid equilibrium of a binary mixture with a type-I critical locus according to van Konynenburg and Scott [335].

proportionality of the diffusion flux to the gradient of the chemical potential, cf. Sec. 2.1 and the work of Gaillard et al. [87]. This is usually of no concern in many solvers used in the LRE and GE community, as most of the numerical frameworks apply Fickian diffusion. However, depending on the fluids forming the mixture and the injection and combustion conditions, the chemical and the mechanical instability limit might not be far apart and hence might cause solver crashes, see, for instance, the area around the critical point of the LV component in Fig. E.2b.

F Additional material: Underexpanded jets

F.1 Validation of the hybrid pressure-based approach

For demonstrating the performance and shock capturing capability of the hybrid scheme described in Sec. 3.3.5, a 1D shock tube test case is used, see Fig. F.1. A fictional membrane initially separates a high pressure/high density (left) and a low pressure/low density (right) part. The

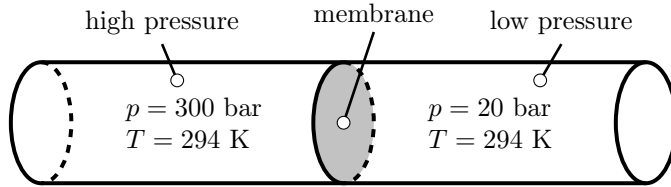


Figure F.1: Initial conditions of the 1D shock tube problem. Methane (CH_4) is considered as fuel and a pressure ratio of 15 is investigated.

membrane is placed in the middle of a one meter long 1D tube. Methane CH_4 is selected as a fluid due to its relevance for GEs. Both the ideal gas equation as well as the SRK-EoS [296] are used for the thermodynamic closure. The critical data and the acentric factor of methane are listed in Tab. B.1. By using two different EoSs, the influence of the neglect of intermolecular forces in the ideal gas EoS can be demonstrated and discussed. In the present test case, the initial temperature profile is assumed isothermal and the temperatures are therefore set to 294 K on both sides. At $t = 0$ s we let the membrane burst and study the temporal evolution of the fluid properties in the 1D tube. For the temporal and the spatial discretization second order schemes are used. The boundedness of the solution is achieved by means of the Minmod limiter [264]. The solver settings are listed in Tab. F.1

Table F.1: Numerical solver setup for the validation of the hybrid pressure-based approach.

Solver	TVD-limiter	EoS
pressure-based (supersonic)	Minmod [264]	SRK-EoS [296]

In Fig. F.2, the results of the 1D shock tube problem after 0.5 ms are shown. The numerical results obtained with the hybrid pressure-based scheme are compared to an exact solution calculated with a Riemann solver. For more information on the Riemann solver refer to the PhD thesis of Banholzer [20]. Three different mesh resolutions – coarse (100 cells), medium (400 cells) and fine (1600 cells) – are compared. On the left side the ideal gas and on the right side the real-gas results are shown. By comparing the two thermodynamic closures, not negligible differences arise: In the high-pressure part, the ideal-gas EoS predicts a 5.7% lower density compared to the SRK-EoS [296]. On the low-pressure side, the error of the ideal gas EoS is slightly reduced to -3.5%. As a consequence of the different thermodynamic closures, the rarefaction wave and shock discontinuity travel at different speeds and also the contact discontinuity can be found at a different axial position. Looking at the comparison of the exact Riemann solution and the results of the numerical simulations a very good agreement can be seen for the fine mesh (1600 cells). With coarser meshes, the solution gets gradually smeared out and is very diffusive for the coarsest version with 100 cells. In conclusion, the hybrid solver is able to capture the specific characteristics of the 1D shock tube problem for both thermodynamic closures.

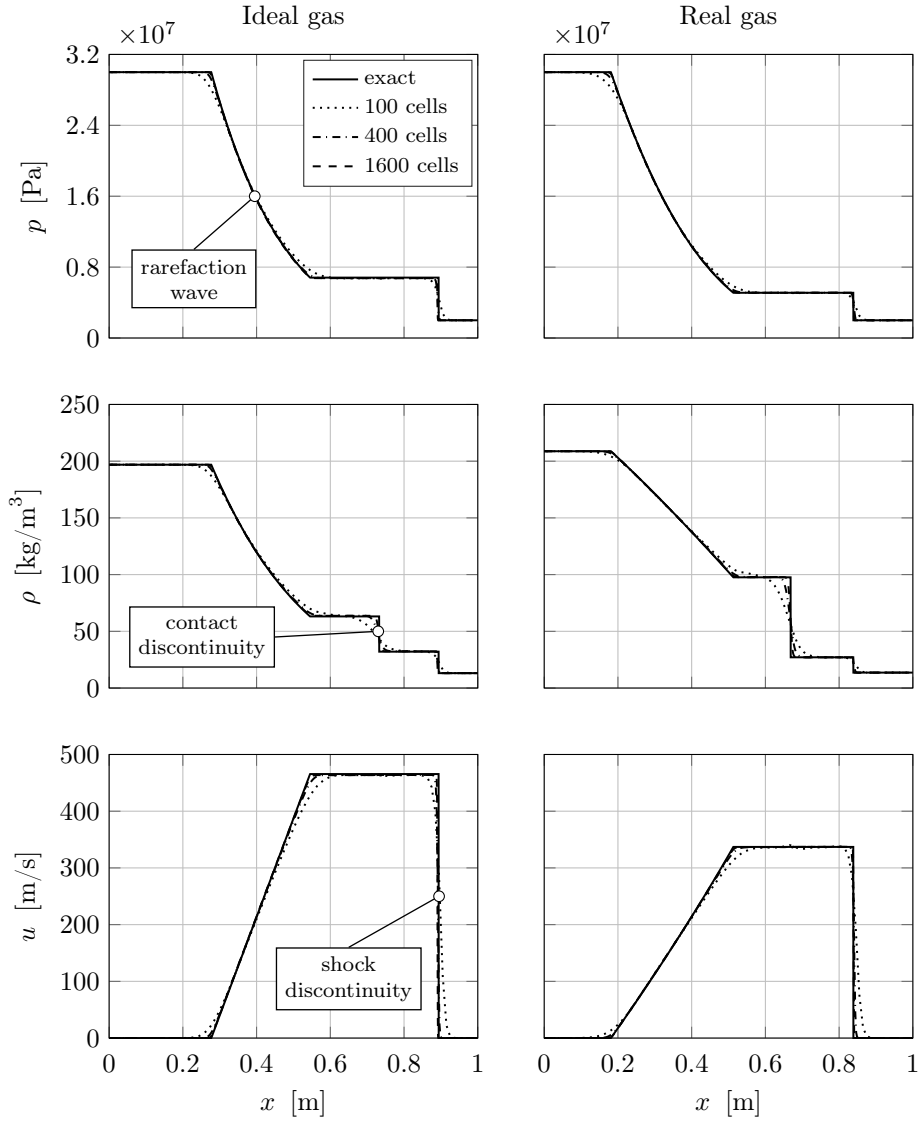


Figure F.2: Results of the 1D shock tube problem after 0.5 ms.

F.2 Determination of the choked flow conditions

For the calculation of the thermodynamic conditions of a choked pipe flow, a one-dimensional, steady and inviscid flow is considered. Under mass and energy conservation conditions, the governing equations read

$$\frac{d\rho}{\rho} + \frac{du}{u} + \frac{dA}{A} = 0 , \quad (\text{F.1a})$$

$$dh_t = dh + u du = 0 , \quad (\text{F.1b})$$

where A is the cross-section area of the nozzle. Applying the Gibbs equation (4.121) together with the assumption of an isentropic flow, i.e., constant entropy s , yields a relation between caloric and thermal properties:

$$dh = v dp . \quad (\text{F.2})$$

In addition, the change in density and velocity u can be related using the definition of the speed of sound, see Eq. (4.131), as:

$$a_s^2 d\rho = -\rho u du . \quad (\text{F.3})$$

Rearranging these equations yields

$$\frac{dA}{A} = - \left(1 - \frac{u^2}{a_s^2} \right) \frac{du}{u} = - (1 - Ma^2) \frac{du}{u} \quad (\text{F.4})$$

and demonstrates the equality of the Mach number Ma to one in the narrowest cross section of the nozzle under choked flow conditions. This fact is independent of the equation of state and hence applies for both ideal and nonideal fluids. Therefore, under choked flow conditions, the velocity u is equal to the speed of sound. Consequently, the solution of the choked nozzle flow (index: e) has to satisfy the following two relations, which are independent of the cross-section A :

$$h_t(p_t, T_t) = h_e(p_e, T_e) + \frac{a_s(p_e, T_e)^2}{2}, \quad (\text{F.5a})$$

$$s_t(p_t, T_t) = s_e(p_e, T_e). \quad (\text{F.5b})$$

For a more thorough discussion on choked flow conditions under both ideal and nonideal thermodynamic conditions it is referred to the work of Sirignano [293]. In the real-gas case, Eq. (F.5) can be solved by iteration. In this process, care has to be taken when the binodal is crossed. This region should be either avoided or a rigorous treatment of the thermodynamic states is necessary.

F.3 Assessment of the axial Mach disk position

Using the data from the simulations in Sec. 6.1, the axial position of the Mach disk can be assessed and compared to data being available in the literature. The axial position of the Mach disk is mainly governed by the nozzle pressure ratio, see, e.g., Franquet et al. [81]. According to Crist et al. [55] and Ashkenas and Sherman [11], the axial location of the Mach disk x_{md} can be calculated for $15 < \text{NPR} < 17000$ as:

$$\frac{x_{\text{md}}}{D} = 0.67 \sqrt{\frac{p_t}{p_{ch}}}. \quad (\text{F.6})$$

Here, the axial position is normalized by the nozzle diameter D which is 0.236 mm in the present study. The constant of 0.67 has been proposed by Ashkenas and Sherman [11] by fitting Eq. (F.6) to experimental data. In Fig. F.3, the Mach disk positions evaluated from the RANS simulations of Sec. 6.1 are compared to Eq. (F.6). The simulation results clearly reproduce the trend of a larger axial Mach disk position with increasing NPR. However, an almost constant shift in the log-log plot between the correlation and the RANS results becomes obvious. To further investigate this

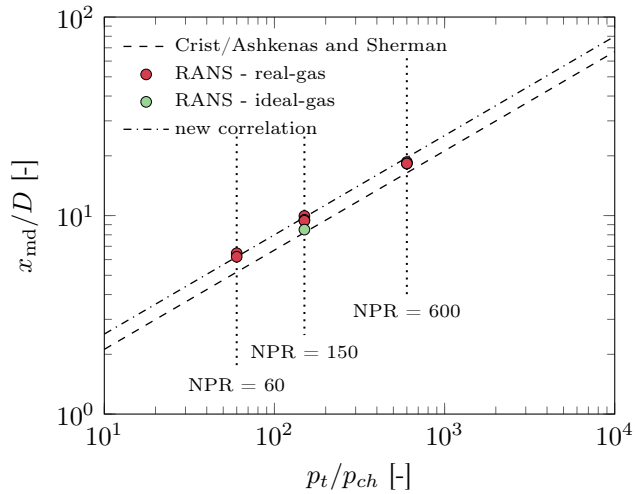


Figure F.3: Comparison of the axial position of the Mach disk in dependence of the NPR. The dashed line shows the correlation proposed by Crist et al. [55] and Ashkenas and Sherman [11]. The ideal-gas closure was used for case NPR150-T577.

issue, a RANS simulation has been conducted for the case NPR150-T577 employing the ideal gas closure. The result is shown as green dot in Fig. F.3. The shift of the ideal-gas result towards the correlation of Eq. (F.6) can be seen. Therefore, the deviation between the RANS results and the correlation of Eq. (F.6) is traced back to the strong real-gas effects being mainly present upstream of the Mach disk. Therefore, we slightly adjusted the correlation equation to better fit the present results:

$$\frac{x_{\text{md}}}{D} = 0.80 \sqrt{\frac{p_t}{p_{ch}}} . \quad (\text{F.7})$$

Changing the constant from 0.67 to 0.8 is a clear improvement for the present investigation and the result of the new fit is shown as a dash-dotted line in Fig. F.3.

G Validation of the density-based solver

In this section, the density-based solver is validated and its capability is demonstrated by means of both 1D and 2D test cases. The test cases are taken from the work of Ma et al. [177] and from appendix F.1. Nitrogen (N_2), methane (CH_4) and n-dodecane ($C_{12}H_{26}$) are considered as fluids and their critical properties together with their acentric factors are listed in Tab. B.1 in the appendix. The solver settings used for the validation are listed in Tab. G.1.

Table G.1: Numerical solver setup for the validation of the density-based solver.

Solver	TVD-limiter	EoS
density-based	limitedCubic	PR-EoS [226]

G.1 One-dimensional advection problem

The first test case is a 1D advection problem with periodic boundary conditions. A domain length of 1 m is selected and resolved with 150 grid points. Nitrogen is used as fluid and the pressure is set to 50 bar corresponding to a reduced critical pressure p/p_c of 1.47. A sharp density jump is introduced by means of a transcritical temperature jump ($T_{c,N_2} = 126.19$ K)

$$T = \begin{cases} 100 \text{ K}, & 0.25 \text{ m} < x < 0.75 \text{ m} \\ 300 \text{ K} & \text{otherwise} \end{cases} \quad (\text{G.1})$$

resulting in a maximum density of 792.66 kg/m³ and in a minimum density of 56.89 kg/m³ which corresponds to a density ratio of approximately 14. The resulting density profile is convected with a velocity of 100 m/s. The Euler equations are solved, i.e., viscous effects are neglected, enabling the comparison with an exact solution. A physical time of 0.01 s is simulated corresponding to one flow through period.

In Fig. G.1, the results of the 1D advection case are shown. The exact solution corresponds to

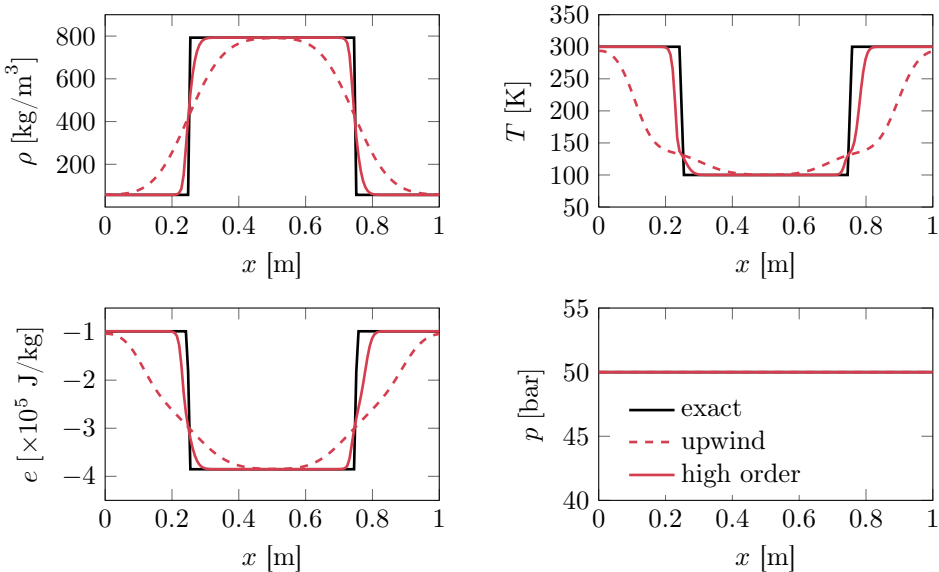


Figure G.1: Results of the 1D advection case after one flow through period.

the initial condition and is shown in black. First and high order reconstruction are compared to the exact solution. In the case of the density, temperature and energy fields, the upwind solution is heavily smeared out. With high order reconstruction, we achieve results which are very similar to the results of Ma et al. [177]. Due to the application of the double-flux method, the pressure and velocity equilibrium are conserved and no spurious pressure oscillations are induced across the sharp density interface. Ma et al. [177] reported that a fully conservative approach fails in this test case due to the large variation/discontinuity in γ^* and e_0^* across the interface.

G.2 Real-gas shock tube problem

As a second test case, the real-gas shock tube problem from Sec. F.1 is used. To accurately predict the fluid behavior of methane, the SRK-EoS [296] is employed. The Euler system is solved. Figure F.1 shows a schematic of the investigated shock tube problem. Initially, a high pressure section is separated from a low pressure section by an imaginary membrane which is removed at simulation start. Isothermal conditions ($T = 294$ K) are considered and a pressure ratio of 15 is imposed.

In Fig. G.2, the distributions of density, pressure, velocity and temperature after a time of 0.5 ms are shown. In addition, an exact solution to the Riemann problem is plotted. The comparison shows that the double-flux method in combination with the AUSM⁺-up flux-vector splitting scheme is able to capture the features of the shock tube problem. Three different mesh resolutions have been investigated. With increasing mesh resolution the contact discontinuity gets sharper. The same accounts for the traveling shock wave.

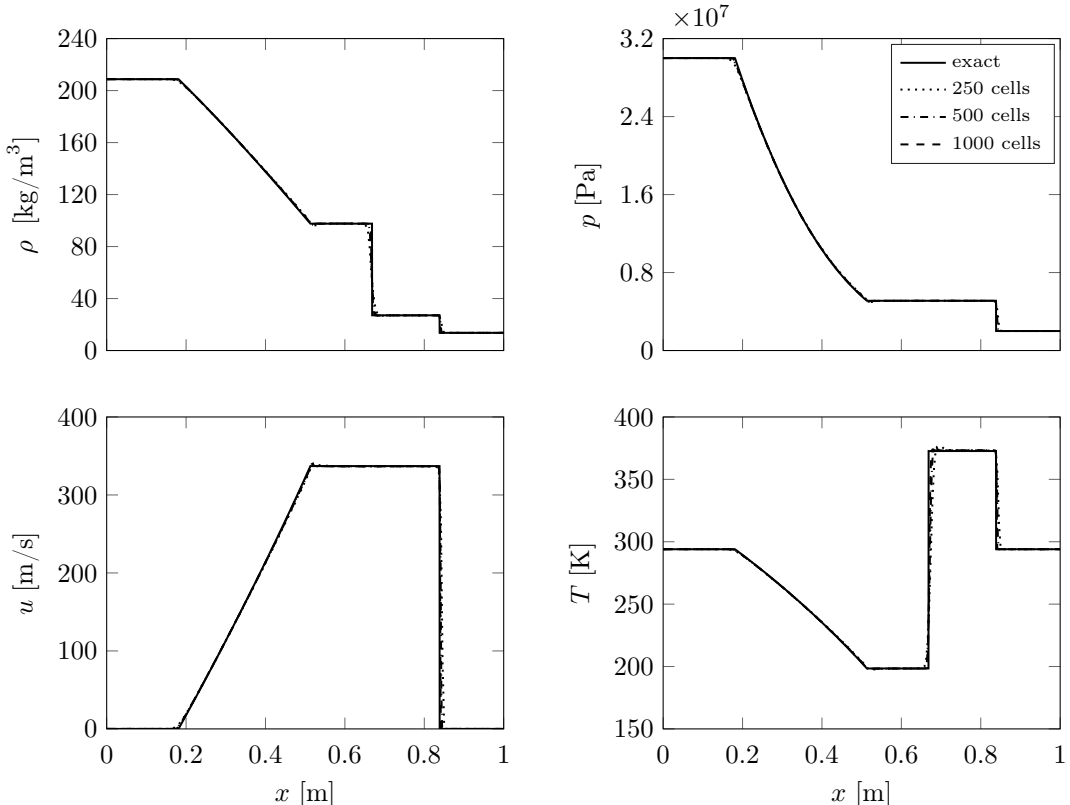


Figure G.2: Results of the real-gas shock tube problem at $t = 0.5$ ms in terms of density, pressure, velocity and temperature.

G.3 Transcritical planar jet - pure fluid

The third test case is a 2D transcritical planar jet where cryogenic nitrogen is injected into warm nitrogen gas. In Fig. G.3, the computational setup including the injection and chamber conditions is shown. According to Terashima and Koshi [311] and Ma et al. [177], the inlet height h is 1 mm and the inlet velocity was set to 100 m/s. A uniform grid spacing has been employed and the inlet is resolved with 50 cells. The full set of compressible conservation equations is used and no sub-grid turbulence model is applied.

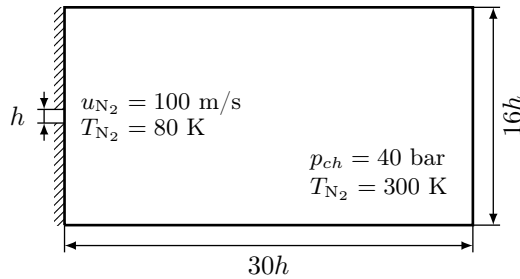


Figure G.3: Schematic of the computational domain for the 2D cryogenic planar jet configuration. The inlet height h is 1 mm.

In Fig. G.4, distributions of density, temperature, speed of sound and pressure after 0.35 ms are shown. The time was chosen such that the jet has not yet reached the end of the domain. A typical 2D cryogenic mixing process becomes obvious where the jet gradually dilutes into the environment and shows unphysical large-scale 2D vortical structures. The most important observation is that no spurious pressure oscillations occur. This is the main purpose for the implementation of the double-flux method and enables the investigation of the mixing behavior under high-pressure conditions.

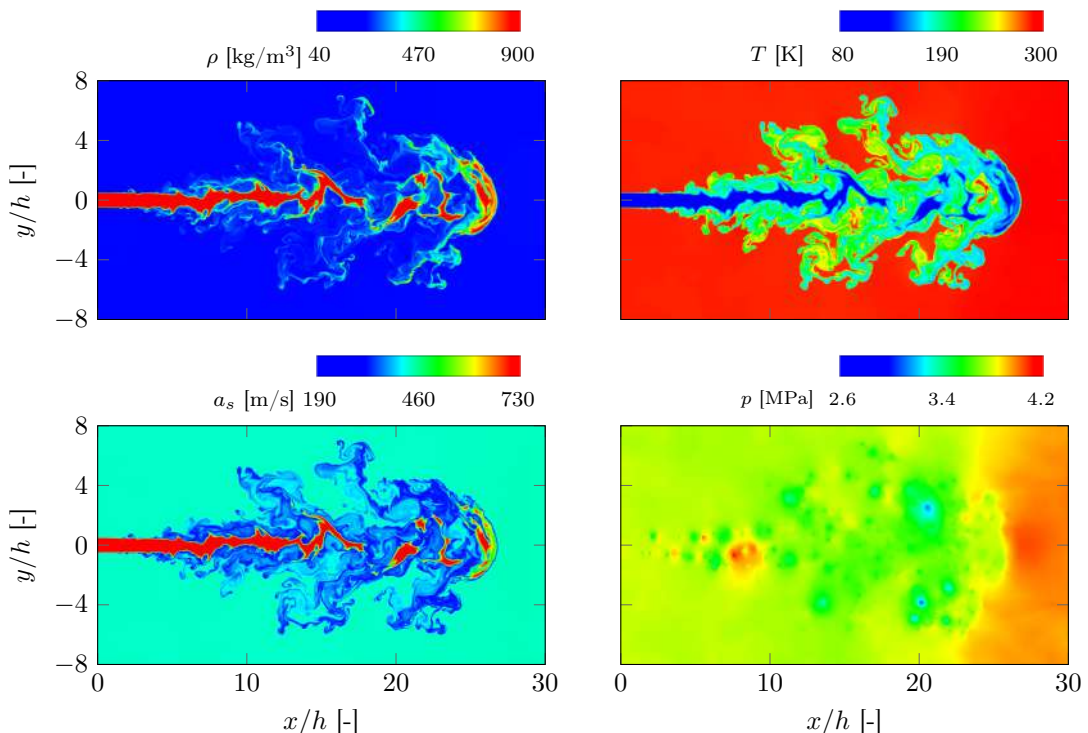


Figure G.4: Density, temperature, speed of sound and pressure distributions of the 2D planar nitrogen jet configuration after 0.35 ms.

G.4 Transcritical planar jet - binary mixture

Applying the configuration of the planar nitrogen jet, see Fig. G.3, the mixing process of a liquid-like fuel into a gaseous environment is studied as a final validation case. N-dodecane ($C_{12}H_{26}$) is injected into a quiescent nitrogen atmosphere. The conditions correspond to the ECN Spray A test case [232]: $T_{C_{12}H_{26}} = 363$ K, $T_{N_2} = 900$ K and $p = 60$ bar. As for the planar nitrogen jet, the injection velocity was selected as 100 m/s.

The instantaneous results ($t = 0.35$ ms) of the n-dodecane mass fraction, the density, the temperature and the pressure are shown in Fig. G.5. A typical 2D disintegration process with large-scale vortical structures is visible causing a steady mixing of n-dodecane with nitrogen. Therefore, only the jet core and regions of almost pure fuel have a large density or low temperature. The mixing process leads to a strong change in temperature and density which usually results in the occurrence of spurious pressure oscillations. As it can be seen from the instantaneous pressure field in Fig. G.5, this is not the case when the double-flux scheme is applied. A smooth pressure field results and both low and high pressure values are only present in regions where the jet break-up or large vortical structures occur.

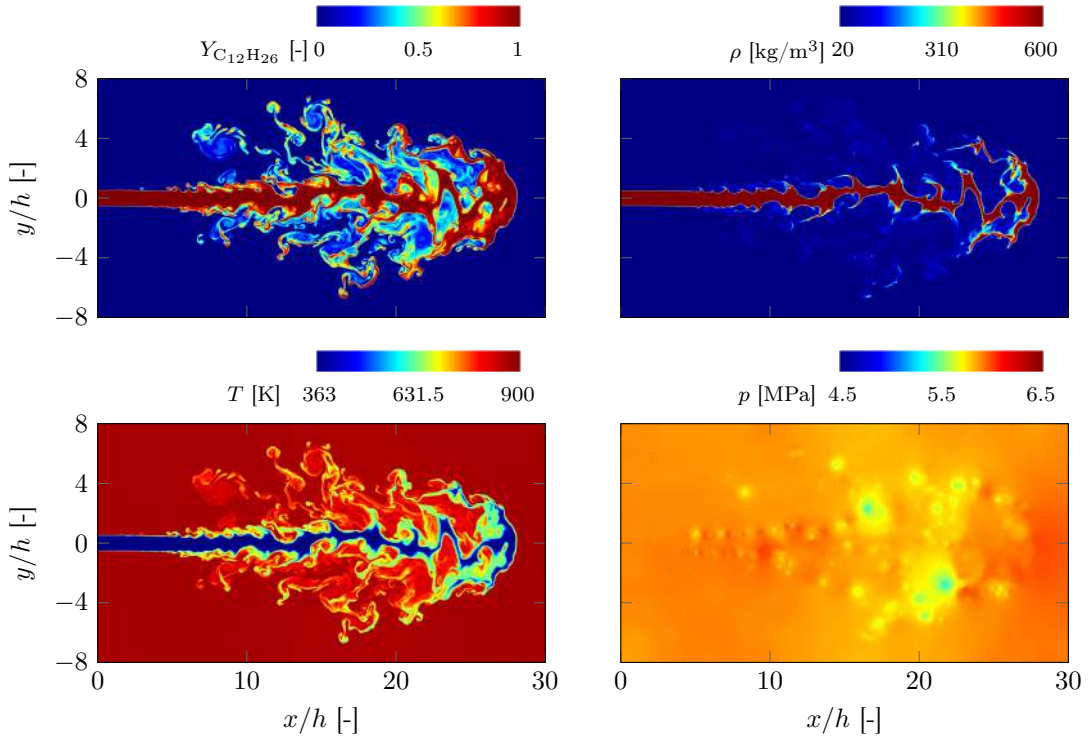


Figure G.5: Results of the 2D planar jet break-up of n-dodecane into a nitrogen environment. The instantaneous fields of n-dodecane mass fraction, density, temperature and pressure are shown at $t = 0.35$ ms.